frontiers | Research Topics

Fibrotic diseases in thorax and abdomainal viscera, volume II

Edited by
Jian Gao, Yang Zhou, Jing Qu, Enlong M. A and Xiaoxi Lv

Published in
Frontiers in Pharmacology

ISSN 1664-8714
ISBN 978-2-8325-2591-3
DOI 10.3389/978-2-8325-2591-3

About Frontiers

Frontiers is more than just an open access publisher of scholarly articles: it is a pioneering approach to the world of academia, radically improving the way scholarly research is managed. The grand vision of Frontiers is a world where all people have an equal opportunity to seek, share and generate knowledge. Frontiers provides immediate and permanent online open access to all its publications, but this alone is not enough to realize our grand goals.

Frontiers journal series

The Frontiers journal series is a multi-tier and interdisciplinary set of open-access, online journals, promising a paradigm shift from the current review, selection and dissemination processes in academic publishing. All Frontiers journals are driven by researchers for researchers; therefore, they constitute a service to the scholarly community. At the same time, the *Frontiers journal series* operates on a revolutionary invention, the tiered publishing system, initially addressing specific communities of scholars, and gradually climbing up to broader public understanding, thus serving the interests of the lay society, too.

Dedication to quality

Each Frontiers article is a landmark of the highest quality, thanks to genuinely collaborative interactions between authors and review editors, who include some of the world's best academicians. Research must be certified by peers before entering a stream of knowledge that may eventually reach the public - and shape society; therefore, Frontiers only applies the most rigorous and unbiased reviews. Frontiers revolutionizes research publishing by freely delivering the most outstanding research, evaluated with no bias from both the academic and social point of view. By applying the most advanced information technologies, Frontiers is catapulting scholarly publishing into a new generation.

What are Frontiers Research Topics?

Frontiers Research Topics are very popular trademarks of the *Frontiers journals series*: they are collections of at least ten articles, all centered on a particular subject. With their unique mix of varied contributions from Original Research to Review Articles, Frontiers Research Topics unify the most influential researchers, the latest key findings and historical advances in a hot research area.

Find out more on how to host your own Frontiers Research Topic or contribute to one as an author by contacting the Frontiers editorial office: frontiersin.org/about/contact

Fibrotic diseases in thorax and abdomainal viscera, volume II

Topic editors

Jian Gao — Shanghai Children's Medical Center, China
Yang Zhou — Brown University, United States
Jing Qu — Huazhong University of Science and Technology, China
Enlong M. A — Shenyang Pharmaceutical University, China
Xiaoxi Lv — Institute of Materia Medica, Chinese Academy of Medical Sciences and Peking Union Medical College, China

Citation

Gao, J., Zhou, Y., Qu, J., Enlong, M. A., E., Lv, X., eds. (2023). *Fibrotic diseases in thorax and abdomainal viscera, volume II*. Lausanne: Frontiers Media SA.
doi: 10.3389/978-2-8325-2591-3

Table of contents

frontiers | Frontiers in Pharmacology

ORIGINAL RESEARCH
published: 15 June 2022
doi: 10.3389/fphar.2022.919388

Investigation of the Pharmacological Effect and Mechanism of Jinbei Oral Liquid in the Treatment of Idiopathic Pulmonary Fibrosis Using Network Pharmacology and Experimental Validation

Aijun Zhang[1], Yixuan Zou[2], Qingcui Xu[1], Shuo Tian[2], Jie Wang[2], Yilin Li[2], Renchao Dong[2], Liangzong Zhang[1], Juanjuan Jiang[1], Lili Wang[1], Kai Tao[1], Zhaoqing Meng[1] and Yanqiu Liu[2]**

[1]Institute of Chinese Materia Medica, Shandong Hongji-tang Pharmaceutical Group Co., Ltd., Jinan, China, [2]Shandong University of Traditional Chinese Medicine, Jinan, China

OPEN ACCESS

Edited by:
Jian Gao,
Shanghai Children's Medical Center, China

Reviewed by:
Xin-guang Liu,
Henan University of Chinese Medicine, China
Chunlan Tang,
Ningbo University, China

***Correspondence:**
Zhaoqing Meng
mengzq@hjt.cn
Yanqiu Liu
60020218@sdutcm.edu.cn

Specialty section:
This article was submitted to Respiratory Pharmacology, a section of the journal Frontiers in Pharmacology

Received: 13 April 2022
Accepted: 06 May 2022
Published: 15 June 2022

Citation:
Zhang A, Zou Y, Xu Q, Tian S, Wang J, Li Y, Dong R, Zhang L, Jiang J, Wang L, Tao K, Meng Z and Liu Y (2022) Investigation of the Pharmacological Effect and Mechanism of Jinbei Oral Liquid in the Treatment of Idiopathic Pulmonary Fibrosis Using Network Pharmacology and Experimental Validation. Front. Pharmacol. 13:919388. doi: 10.3389/fphar.2022.919388

Overview: Idiopathic pulmonary fibrosis (IPF) is a disease caused by many factors, eventually resulting in lung function failure. Jinbei oral liquid (JBOL) is a traditional Chinese clinical medicine used to treat pulmonary diseases. However, the pharmacological effects and mechanism of the action of JBOL on IPF remain unclear. This study investigated the protective effects and mechanism of the action of JBOL on IPF using network pharmacology analysis, followed by *in vivo* and *in vitro* experimental validation.

Methods: The components of JBOL and their targets were screened using the TCMSP database. IPF-associated genes were obtained using DisGeNET and Drugbank. The common targets of JBOL and IPF were identified with the STRING database, and a protein–protein interaction (PPI) network was constructed. GO and KEGG analyses were performed. Sprague–Dawley rats were injected with bleomycin (BLM) to establish an IPF model and treated orally with JBOL at doses of 5.4, 10.8, and 21.6 ml/kg. A dose of 54 mg/kg of pirfenidone was used as a control. All rats were treated for 28 successive days. Dynamic pulmonary compliance (Cdyn), minute ventilation volume (MVV), vital capacity (VC), and lung resistance (LR) were used to evaluate the efficacy of JBOL. TGF-β–treated A549 cells were exposed to JBOL, and epithelial-to-mesenchymal transition (EMT) changes were assessed. Western blots were performed.

Results: Two hundred seventy-eight compounds and 374 targets were screened, and 103 targets related to IPF were identified. Core targets, including MAPK1 (ERK2), MAPK14 (p38), JUN, IL-6, AKT, and others, were identified by constructing a PPI network. Several pathways were involved, including the MAPK pathway. Experimentally, JBOL increased the levels of the pulmonary function indices (Cdyn, MVV, and VC) in a dose-dependent manner and reduced the RL level in the BLM-treated rats. JBOL increased the epithelial marker E-cadherin and suppressed the mesenchymal marker vimentin expression in the

TGF-β–treated A549 cells. The suppression of ERK1/2, JNK, and p38 phosphorylation by JBOL was validated.

Conclusion: JBOL had therapeutic effects against IPF by regulating pulmonary function and EMT through a systemic network mechanism, thus supporting the need for future clinical trials of JBOL.

Keywords: idiopathic pulmonary fibrosis, jinbei oral liquid, network pharmacology, MAPKS, pulmonary function, E-cadherin, vimentin

INTRODUCTION

Idiopathic pulmonary fibrosis (IPF) is a severe lung disease with the pathological characteristics of greatly diminished lung function, excessive fibroblast proliferation, and extracellular matrix deposition (Meyer 2017; Kim, Kugler et al., 2018). The 5-year survival rate for IPF is less than 30%. The pathogenetic mechanisms underlying IPF have not been fully established. Thus, the current drugs used to treat mild-to-moderate IPF, such as pirfenidone (PFD) and nintedanib, have limited benefit due to their failure to prolong the survival of IPF patients (Mazzei ME 2015). Moreover, PFD produces several adverse side effects, including gastrointestinal reactions, rashes, and photosensitivity (Antoniu, 2006). Therefore, novel drugs to effectively treat IPF need to be developed.

Jinbei oral liquid (JBOL) is a traditional Chinese herbal medicine (Tao K 1997, Tao, Zheng et al., 2013). It is composed of 12 herbs, *Astragalus membranaceus* (Fisch.) Bge, *Codonopsis pilosula* (Franch.) Nannf, *Glehnia littoralis* Fr. Schmidt ex Miq, *Salvia miltiorrhiza* Bge, *Angelica sinensis* (Oliv.) Diels, *Ligusticum striatum* DC, *Fritillaria cirrhosa* D. Don, *Pinellia ternata* (Thunb.) Breit, *Glycyrrhiza uralensis* Fisch, *Lonicera japonica* Thunb, *Scutellaria baicalensis* Georgi, and *Forsythia suspensa* (Thunb.) Vahl. (Zhang, Jie et al., 2012; Yu, Yang et al., 2020). JBOL is used to treat pulmonary interstitial fibrosis and acute lung injury (Zhang, Jie et al., 2012; Zhang, Wang et al., 2013). Most of the 12 herbs have been reported to have anti-inflammatory, antioxidative, antiviral, and immunomodulatory activities (Ng, Liu et al., 2004; Qi, Gao et al., 2017; Li Y 2021). Our previous study demonstrated that JBOL ameliorated bleomycin (BLM)-induced IPF in rats by inhibiting the production of inflammatory factors (Zhang, Cui et al., 2018; Xing, Qiang et al., 2020). However, the mechanism of action of JBOL on IPF is still largely unknown.

Network pharmacology is a valuable strategy to elucidate the mechanisms of action of traditional Chinese medicines (TCM), especially to specify their characteristics, including multiple components and numerous pathway targets (Hopkins and Andrew 2007; Shao and Bo 2013). The approach taken in this study utilized network analysis, combinations of targets, bioinformatics, and analysis of structure–activity relationships and connectivity. The results offered a new paradigm for verifying TCM efficacy and systematic determination of the function of different chemical components (Liu, Wang et al., 2013). Although network pharmacology was first described for drug discovery, its successful application in TCM studies has been explored by Professor Shao Li and others (Shao and Bo 2013). The network pharmacology of several Chinese medicines has been elucidated, including the mijianchangpu decoction (Xz, Jla et al., 2021), Moluodan (Zhou, Zhang et al., 2022), and Sinisan (Wei, Hou et al., 2021).

In the present study, an integrated investigation of JBOL was employed using active ingredient screening, target prediction, and network construction. The pharmacological mechanisms of JBOL on IPF and its potential targets were verified using ***in vitro*** and ***in vivo*** experimental methods.

MATERIALS AND METHODS

Network Pharmacology

Screening JBOL Chemical Components

The Traditional Chinese Medicine System Pharmacology (TCMSP) Database, http://lsp.nwu.edu.cn/tcmsp.php) was used. Additional reports were identified using the PubMed database searching the plant names in references that were published in the last 10 years. The JBOL active compounds were screened based on the properties of absorption, distribution, metabolism, and excretion (ADME). Two ADME-related models were developed. 1) Oral bioavailability (OB) is a critical pharmacokinetic parameter representing the percentage of a dose of an orally administered drug that reaches the systemic circulation. 2) DL is an index used to estimate the "drugability" (the ability of a compound to be used as a pharmaceutical drug) of potential drugs and is calculated using the Tanimoto coefficient. An OB > 20% and DL > 0.10 were used as criteria in the TCMSP screening. We also screened the available literature using the Latin names of the 12 herbs as keywords in the PubMed database to identify additional chemical components.

Screening Possible JBOL Targets

The drug–target network was mapped based on the source of the TCMSP database. For experimental validation of the compound targets, information was retrieved from the HIT database (Ye, Ye et al., 2011). Compounds without validated targets were screened using SysDT, a previously developed model that efficiently combines chemical and pharmacological information for drug targets using the random forest (RF) and support vector machine (SVM) algorithms. This method has demonstrated incredible success in predicting drug–target

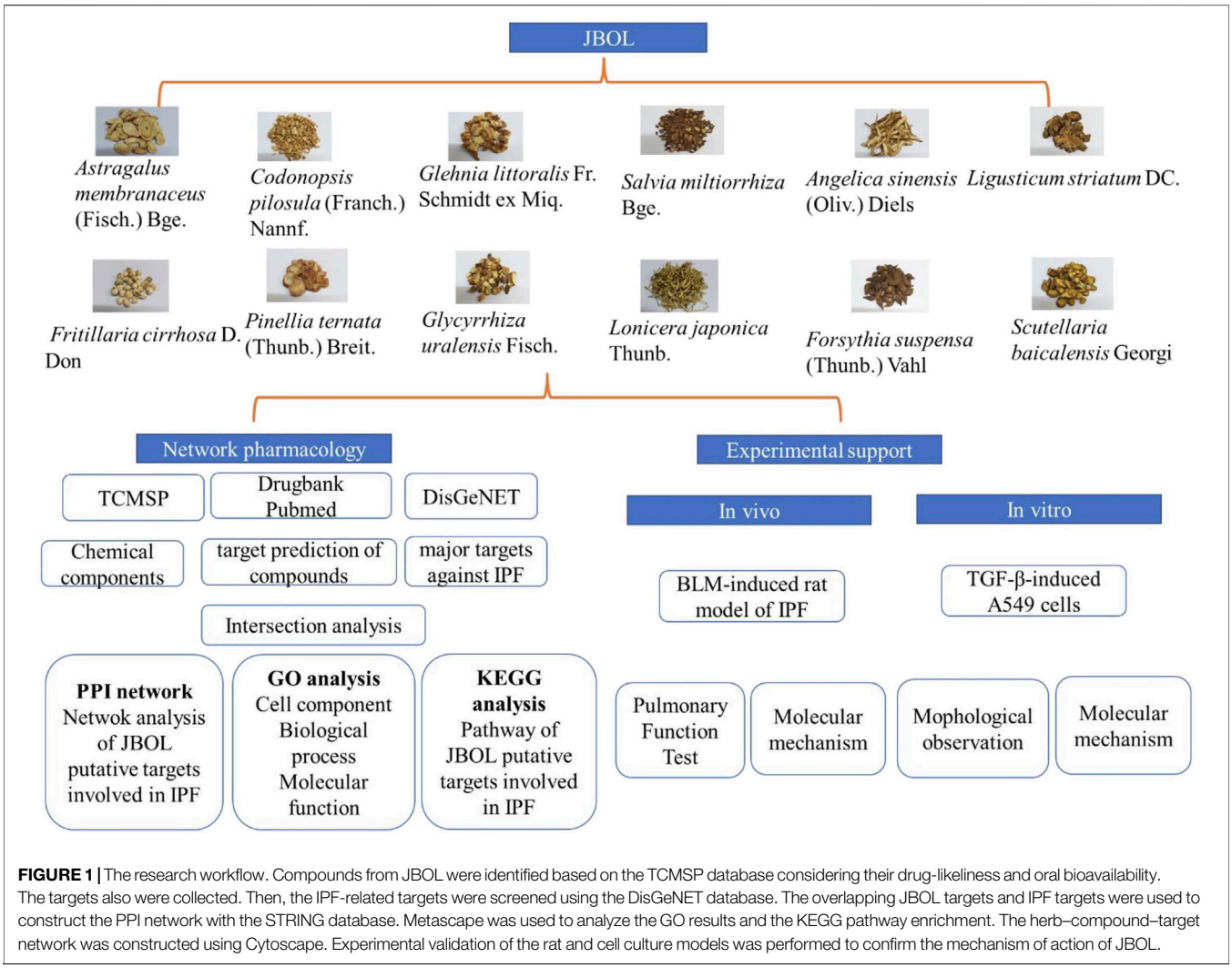

FIGURE 1 | The research workflow. Compounds from JBOL were identified based on the TCMSP database considering their drug-likeliness and oral bioavailability. The targets also were collected. Then, the IPF-related targets were screened using the DisGeNET database. The overlapping JBOL targets and IPF targets were used to construct the PPI network with the STRING database. Metascape was used to analyze the GO results and the KEGG pathway enrichment. The herb–compound–target network was constructed using Cytoscape. Experimental validation of the rat and cell culture models was performed to confirm the mechanism of action of JBOL.

interactions. A previous report indicated the specificity was 93%, concordance was 82%, and sensitivity was 81% (Yu, Chen et al., 2012). Based on the aforementioned methods, target information for JBOL compounds was obtained from the TCMSP database.

Screening for Possible IPF Targets

Target genes related to IPF were collected by searching the keyword "IPF" in the DisGeNET (https://www.disgenet.org/) (Paolacci, Precone et al., 2019) and DrugBank (Wishart, Feunang et al., 2017) (https://www.drugbank.ca/) databases. Genes identified in DisGeNET were scored, and the IPF-related genes were screened based on scores greater than the median score (Zhang, Li et al., 2019).

Overlapping JBOL and IPF Targets

Bioinformatics (http://www.bioinformatics.com.cn/) (Zhou, Zhou et al., 2019) was used to screen the overlapping targets between the JBOL compound targets and the IPF-related targets. The overlapping JBOL and IPF targets were utilized to construct the network and conduct additional analyses.

Protein–Protein Interaction Network Construction for the Overlapping Targets

The STRING database (https://string-db.org/) was the primary tool used to construct the PPI network. The interaction relationships between the functional proteins were included in this database (Franceschini, Szklarczyk et al., 2013; Lv, Xu et al., 2020). *Homo sapiens* was selected as the species of interest. The overlapping target proteins were imported, and the interaction information was analyzed. PPIs were selected based on a confidence score greater than 0.95 then the network was constructed and analyzed.

Gene Ontology and Kyoto Encyclopedia of Genes and Genomes Analyses

GO and KEGG analyses were performed based on the Metascape System (https://metascape.org/). The GO analysis of the biological processes, molecular functions, cell component annotation, and the KEGG pathway enrichment analysis were performed based on a p-value < 0.05 (Ashburner, Ball et al., 2000).

Network Construction

Cytoscape 3.2.1 software was employed to construct and visualize the networks, including the 12 herb–compound–target networks, the PPI network for overlapping targets for JBOL compounds and IPF targets, and the pathway–target network. All networks were plotted, and the network nodes indicated herbs, compounds, or target proteins. The edges represented interactions between compounds, targets, and pathways. The color and node size were proportional to the degree value, which was defined based on the number of connecting edges.

Experimental Verification

The study workflow is illustrated in **Figure 1**.

MATERIALS AND REAGENTS

Jinbei oral liquid (JBOL) (batch number: 2102001) was provided by Shandong Hongjitang Pharmaceutical Co., Ltd. (Jinan, China). The doses of each herb in 1,000 ml of JBOL were as follows: 66 g *Astragalus membranaceus*, 66 g *Codonopsis pilosula*, 70 g *Glehnia littoralis*, 66 g *Salvia miltiorrhiza*, 55 g *Angelica sinensis*, 55 g *Ligusticum striatum*, 46 g *Fritillaria cirrhosa*, 46 g *Pinellia ternata*, 35 g *Glycyrrhiza uralensis*, 115 g *Lonicera japonica*, 46 g *Scutellaria baicalensis*, and 46 g *Forsythia suspensa*. The plant names were checked on http://www.theplantlist.org. Bleomycin (BLM) was purchased from the Hanhui Pharmaceuticals Company (Shanghai, China). Pirfenidone was obtained from the Beijing Continent Pharmaceuticals Company (Beijing, China). TGF-β1 was purchased from MedChemExpress (Shanghai, China). Antibodies, including E-cadherin, vimentin, phospho-P38, phospho-ERK1/2, phospho-JNK, and GAPDH, were obtained from Cell Signaling Technology (MA. USA). The reference compounds, including adenosine (110879-201703), guanosine (111977-201501), chlorogenic acid (110753-202018), loganin (111640-201808), ferulic acid (110773-201614), imperialine (110767-201710), peimine (110750-201311), peiminine (110751-201712), imperatorin (110826-201918), and 18β-glycyrrhetinic acid (110723-201715) were provided by the National Institutes for Food and Drug Control. Rutin (120025-202004), liquiritigenin (070002-202011), and formononetin (130035-202003) were purchased from Shandong WoDeSen Bioscience Technology, Ltd. (Jinan, China). Isoliquiritigenin (B21525) was obtained from Yuanye Biotech Co., Ltd. (Shanghai, China). Tanshinone I (17122704) was obtained from Chengdu Pufei De Biotech Co., Ltd. (Chengdu, China). The purity of all reference compounds was greater than 98%.

UHPLC Analysis of JBOL

An Agilent 1290 UHPLC system (Agilent Technologies, Palo Alto, CA, United States) was used to analyze JBOL, and separation was achieved with a Waters ACQUITY UPLC® BEH C18 column (2.1 × 100 mm, 1.7 μm) (Shanghai, China). The column temperature was 30°C. The mobile phase was an elution composed of 0.1% formic acid water (A) and acetonitrile (B). One-μl samples were injected into the system, and the mobile phase flow rate was 0.3 ml/min.

Pulmonary Fibrosis Induced in Rats Using BLM

Sixty adult male Sprague–Dawley (SD) rats, weighing approximately 200 g, were obtained from the Vital River Laboratory Animal Technology Co., Ltd. (Beijing, China). The animal experiments were approved by the Animal Ethics Committee at Shandong University of Traditional Chinese Medicine. All rats were acclimated in an animal holding room at 25°C and provided food and water *ad libitum*. The rats were divided into six groups: 1) treatment with deionized water (control group); 2) treatment with 3 mg/kg BLM administered intratracheally (i.t, BLM group); 3) treatment with 3 mg/kg BLM (i.t.) and intragastric administration (i.g.,) of JBOL (5.4 ml/kg); 4) treatment with 3 mg/kg BLM (i.t.) and JBOL (10.8 ml/kg, i.g.); 5) treatment with 3 mg/kg BLM (i.t.) and JBOL (21.6 ml/kg, i.g.); 6) treatment with 3 mg/kg BLM (i.t.) and pirfenidone (54 mg/kg, i.g.) as a positive control. The doses of JBOL were chosen based on our previous reports (Zhang, Cui et al., 2018; Xing, Qiang et al., 2020). The compounds were administered once every day according to the aforementioned treatment groups. After 28 days of treatment, the rats were anesthetized, and the pulmonary function was assessed. Subsequently, the lung tissues were collected and frozen for protein expression assessment.

Pulmonary Function Assay

The rats were anesthetized and fixed in a supine position on a board. A trachea tube was inserted into the trachea and connected with the body plethysmograph. The change in gas pressure was measured to calculate the lung volume indirectly. The indices, including dynamic pulmonary compliance (Cdyn), minute ventilation volume (MVV), vital capacity (VC), and lung resistance (LR) data were determined.

Cell Culture and JBOL Treatment

Human type II alveolar epithelial A549 cells were purchased from the Type Culture Collection of the Chinese Academy of Sciences (Shanghai, China). Dulbecco's modified Eagle's medium (DMEM, Gibco, Paisley, United Kingdom) with 10% fetal calf serum (FCS), 100 μg/ml streptomycin, and 100 U/ml penicillin was used for cell culture. The A549 cells were maintained at 37°C with 5% CO_2 in a humidified chamber.

The A549 cells were treated with culture medium (control) or 5 ng/ml TGF-β1 with or without 0.05, 0.5, or 1% JBOL. JBOL was diluted using a culture medium. After incubation for 48 h, the cells were observed using an inverted phase-contrast microscope (Olympus, Japan). The cell morphology, including characteristics of mesenchymal–epithelial transition (EMT), was observed, and images were captured at ×200 magnification. For the protein expression assay, JBOL and 5 ng/ml TGF-β1 were added to the cells and incubated for 72 h. Then the cells were lysed for analysis.

Western Blot Assay

Lung tissue samples or A549 cells were treated for 40 min with RIPA lysis buffer containing phosphatase inhibitors, then centrifuged (12,000 rpm, 15 min) at 4°C. The protein concentration of the supernatant was assessed using bicinchoninic acid. Individual protein samples (10–30 μg) were loaded onto SDS-polyacrylamide gels for separation and then transferred to PVDF membranes

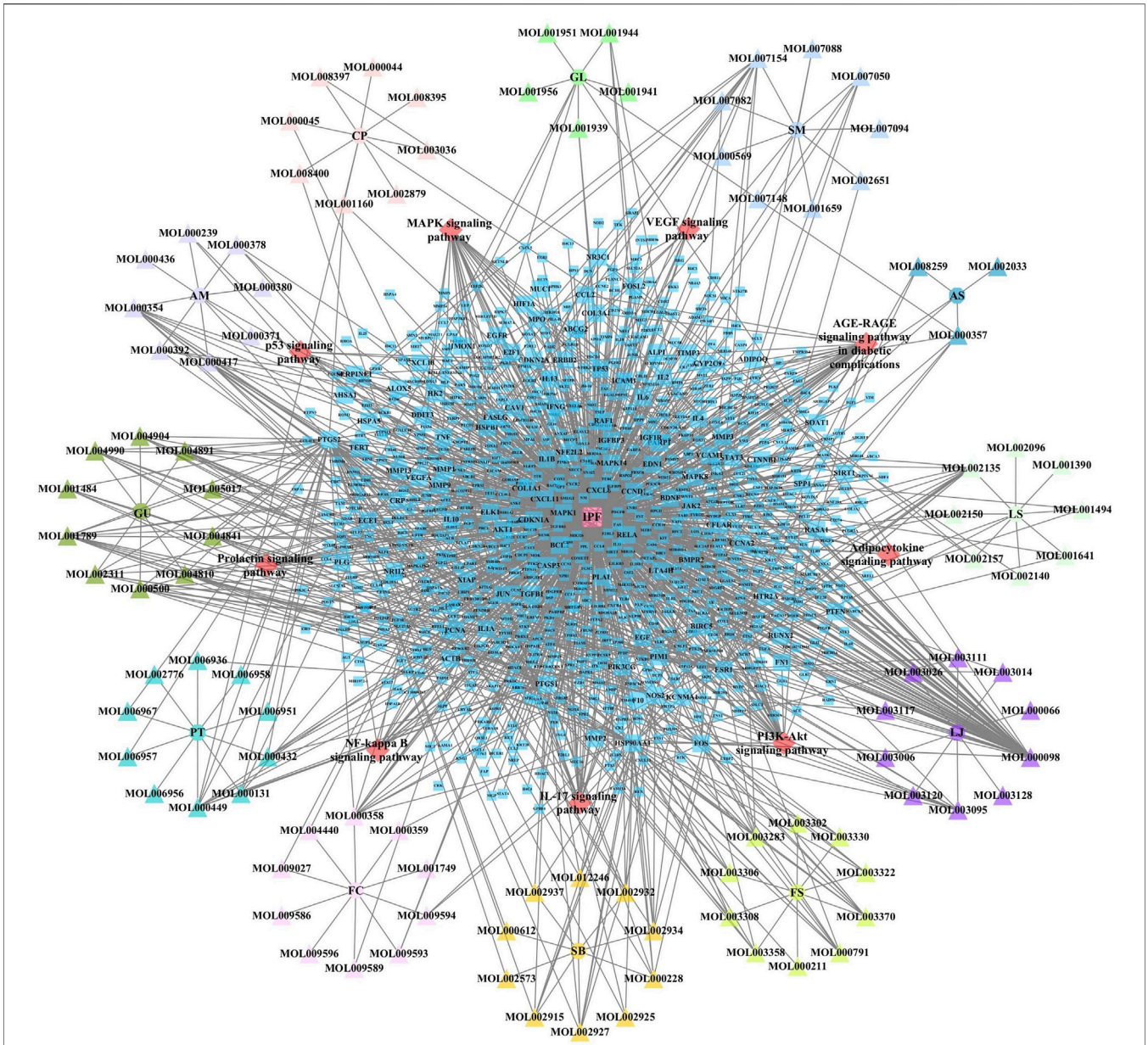

FIGURE 2 | The compound–target network of JBOL. Circles represent herbs, triangles represent compounds derived from herbs, and squares represent the predicted targets. The node size indicates the value of the degree.

(Millipore, Darmstadt, Germany). The membranes were incubated with different primary antibody solutions and shaken overnight. After the membranes were washed with Tris-buffered saline with Tween-20 (TBST), HRP-labeled secondary antibodies were added, and the membranes were incubated for 2 h. The protein bands were visualized using ECL-Plus detection (Biyuntian, Shanghai, China). The intensity of the protein bands was quantified using Image Pro-Plus 6.0 software.

Statistical Analysis

All data were expressed as means ± standard error of the mean (SEM). The one-way analysis of variance (ANOVA) was used for multiple comparisons. The Student's *t*-test was used to compare the differences between the two groups. A p-value < 0.05 was considered statistically significant.

RESULTS

JBOL Compound Screening and Target Prediction

JBOL contained 12 herbs, including Huangqi (*Astragalus membranaceus,* AM), Dangshen (*Codonopsis pilosula,* CP), Beishashen (*Glehnia littoralis*, GL), Danshen (*Salvia miltiorrhiza,*

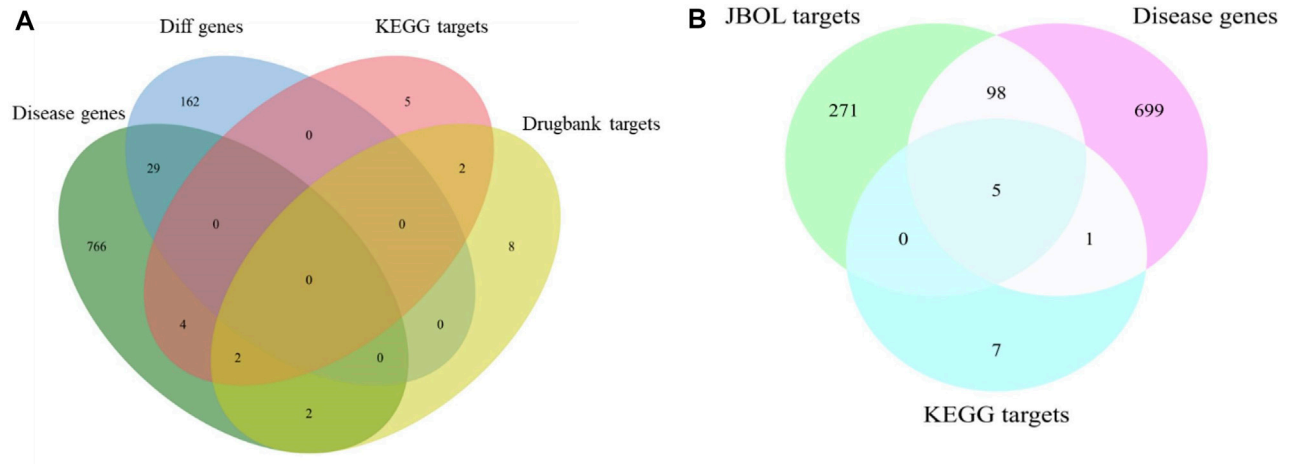

FIGURE 3 | Overlap of the target genes between IPF and JBOL. **(A)** Matching for the IPF genes, KEGG, and drug bank genes. **(B)** Matching for the IPF genes, KEGG drug target genes, and JBOL target genes.

SM), Danggui (*Angelica sinensis*, AS), Chuanxiong (*Ligusticum striatum,* LS), Chuanbeimu (*Fritillaria cirrhosa*, FC), Banxia (*Pinellia ternata*, PT), Gancao (*Glycyrrhiza uralensis*, GU), Jinyinhua (*Lonicera japonica*, LJ), Lianqiao (*Forsythia suspensa*, FS), and Huangqin (*Scutellaria baicalensis*, SB). The TCMSP database was used to determine the compounds present in JBOL and predict their targets. Two hundred seventy-eight candidate compounds were identified in JBOL, including 15 in AM, 20 in CP, 10 in GL, 27 in SM, 5 in AS, 9 in LS, 40 in FC, 29 in PT, 48 in RU, 15 in LJ, 22 in FS, and 97 in SB (**Supplementary Table S1**). The 278 compounds targeted 374 proteins (**Supplementary Table S2**). The screened compounds and their targets were mapped to generate the compound–target interaction network (**Figure 2**).

Potential Targets for IPF

The IPF-associated genes and targets were obtained from the DisGeNET (https://www.disgenet.org/) and DrugBank databases (**Supplementary Table S3**). The genes that overlapped with the JBOL compound targets were identified (**Figure 3**). One hundred and three overlapping targets were found based on the degree of correlation between the JBOL targets and the IPF targets. Information concerning the overlapping targets is shown in **Supplementary Table S4**.

Identifying Important JBOL Targets Using Intersection Analysis

The 103 overlapping JBOL targets, IPF genes, and anti-IPF drug targets were analyzed based on the STRING database. The protein–protein interactions (PPI) network was constructed using a confidence score of 0.4. The PPI network nodes represented the selected targets, and the edges represented target interactions. As seen in **Figure 4**, the PPI network consisted of 103 nodes and 501 edges. The degree value represented the connection intensity. The average node degree was 9.63. The central nodes with many more edges possibly played essential roles in the JBOL treatment of IPF, including MAPK1 (ERK2), MAPK14 (p38), MAPK8 (JNK1), JUN, IL-6, and AKT.

The GO and KEGG Enrichment Analyses

The 103 targets were imported into the Metascape system for the GO and KEGG pathway analyses. The GO analysis revealed targets associated with numerous cellular components, biological processes, and molecular functions critical for drug development and IPF treatment. One hundred and eleven enriched cell components were identified, and the top 10 cell components were closely associated with vesicle lumen, membrane rafts, endoplasmic reticulum lumen, cyclin-dependent protein kinase holoenzyme complex, and transcription regulator complex (**Figure 5A**). In addition, based on a p-value < 0.05, 1,956 enriched biological processes were identified, including response to lipopolysaccharide, response to steroid hormones, regulation of oxygen levels, response to growth factors, and others (**Figure 5B**). The molecular function targets included cytokine receptor binding, protein kinase binding, kinase regulator activity, and growth factor binding (**Figure 5C**). The identified cellular components, biological processes, and molecular functions indicated the critical actions of JBOL in IPF treatment.

To assess the molecular mechanism of JBOL in treating IPF in more detail, we enriched the KEGG pathways for the 103 targets. Forty-one pathways were identified based on a p-value < 0.05 (**Figure 6A**). These pathways included the MAPK signaling, cGMP-PKG, estrogen, thyroid hormone, HIF-1, cAMP, PI3K-Akt, IL-17, and AGE-RAGE pathways as well as others. A network involving these pathways was established to reveal their interaction relationships (**Figure 6B**).

JBOL Protected Against Pulmonary Fibrosis in the Rat and A549 Cell Models

The BLM-induced rat model and the TGF-β1–induced A549 cell model were used to validate the efficacy and mechanism of

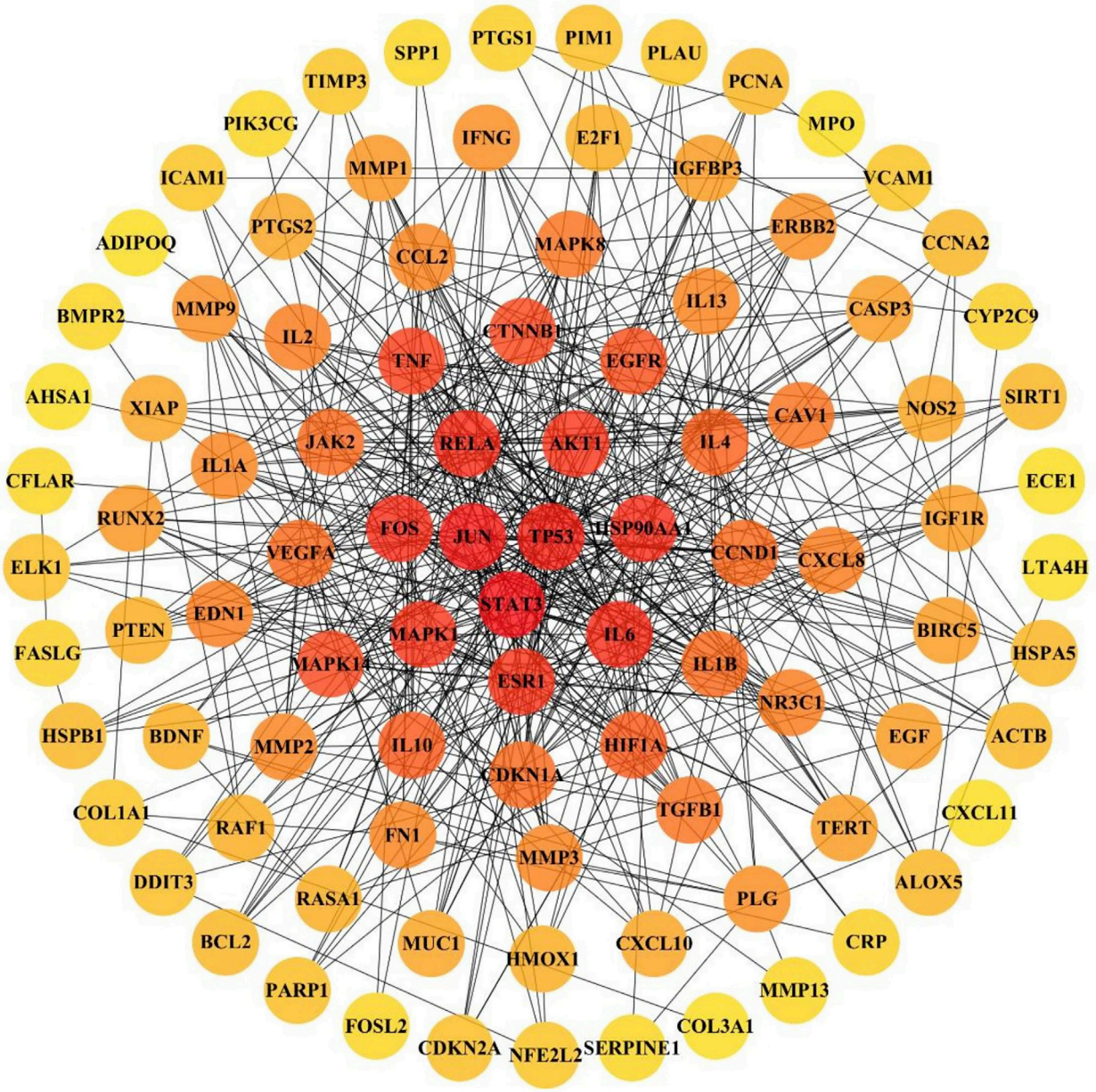

FIGURE 4 | The PPI network of overlapping targets between IPF and JBOL. 103 overlapping targets were plotted as nodes. The edges represent the interaction relationships between the nodes. The darker node color indicates a higher degree value.

JBOL actions on IPF. First, to monitor JBOL chemical stability, the major chemical components in JBOL were determined using the UHPLC analysis (**Figure 7**). Among the identified components, in addition to chlorogenic acid, which was present at high levels (**Table 1**), an additional seven components were identified in the TCMSP database, including guanosine, formononetin, liquiritigenin, isoliquiritigenin, imperatorin, tanshinone I, and 18β-glycyrrhetinic acid, based on the criteria of OB > 20% and DL > 0.10. Thus, these components were used as identifying components for JBOL (**Supplementary Table S5**).

To test for efficacy, rats were treated with BLM to establish the IPF model, and the effect of JBOL was evaluated. Compared with the BLM group, the Cdyn, MVV, and VC indices increased in the presence of JBOL or PFD, and the RL index decreased with treatment with JBOL or PFD (**Figure 8A**). These results indicated that JBOL reduced pulmonary functional damage in BLM-induced rats.

TGF-β1 is a critical cytokine capable of inducing epithelial-to-mesenchymal transitions (EMT) during pulmonary fibrosis (Zhang, Fan et al., 2021). We evaluated whether JBOL inhibited TGF-β1–induced EMT in A549 cells. The JBOL

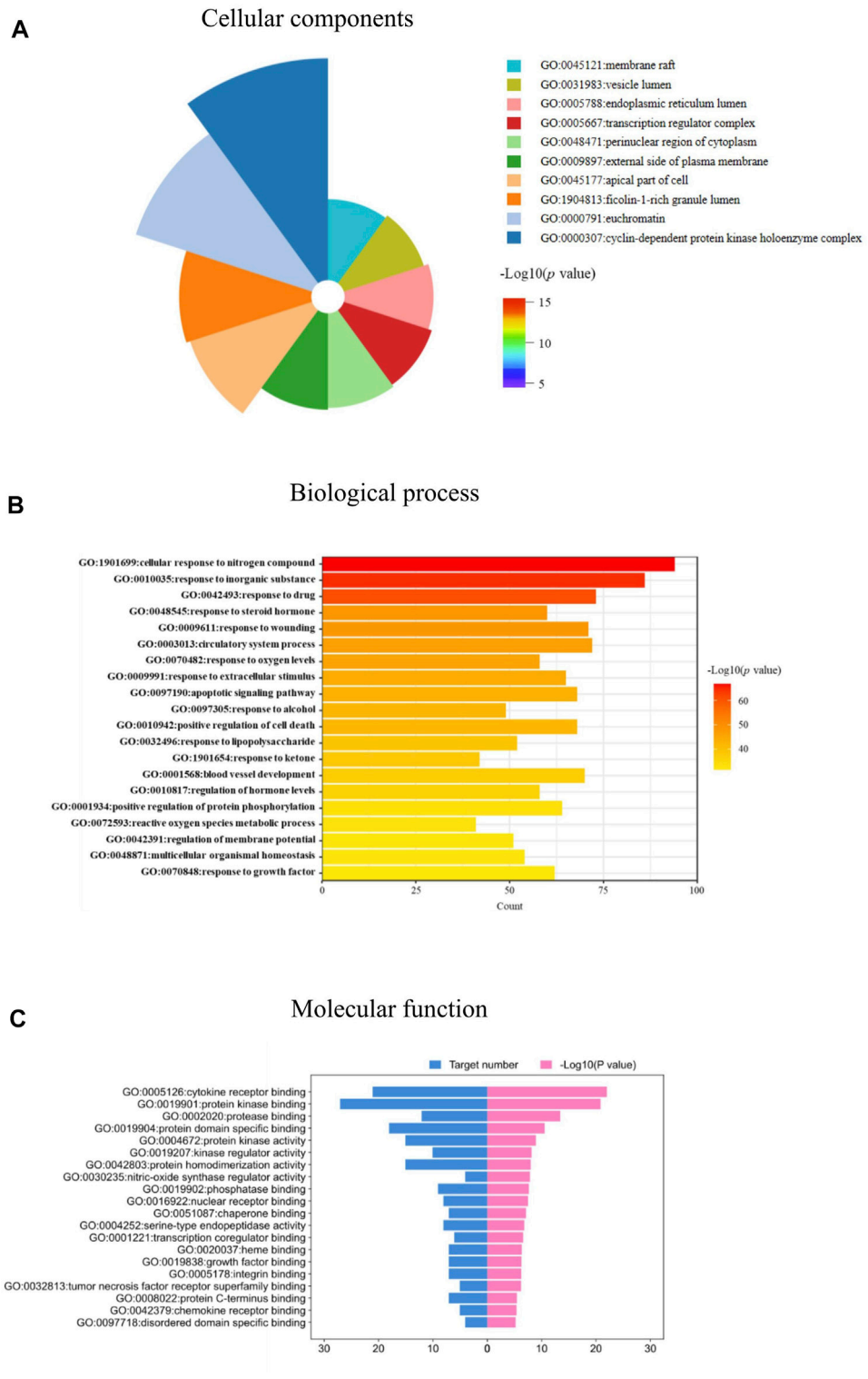

FIGURE 5 | biological function analysis of the overlapping targets. **(A)** Cellular components analyses. **(B)** Biological processes analyses. **(C)** Molecular function analyses related to JBOL treatment of IPF.

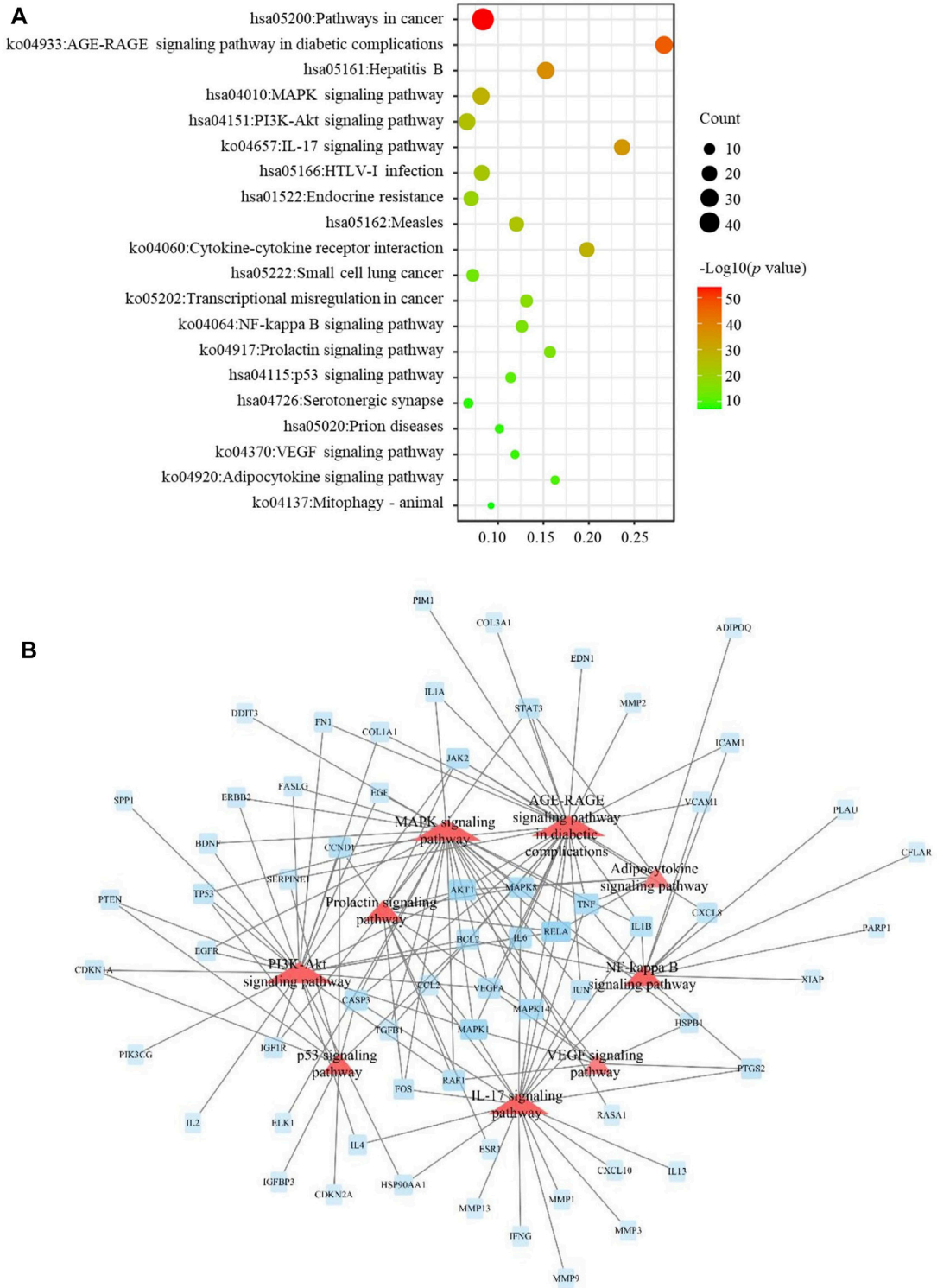

FIGURE 6 | KEGG pathway enrichment analysis. **(A)** Signaling pathways related to the JBOL treatment of IPF. **(B)** The key pathways related to IPF regulated by JBOL.

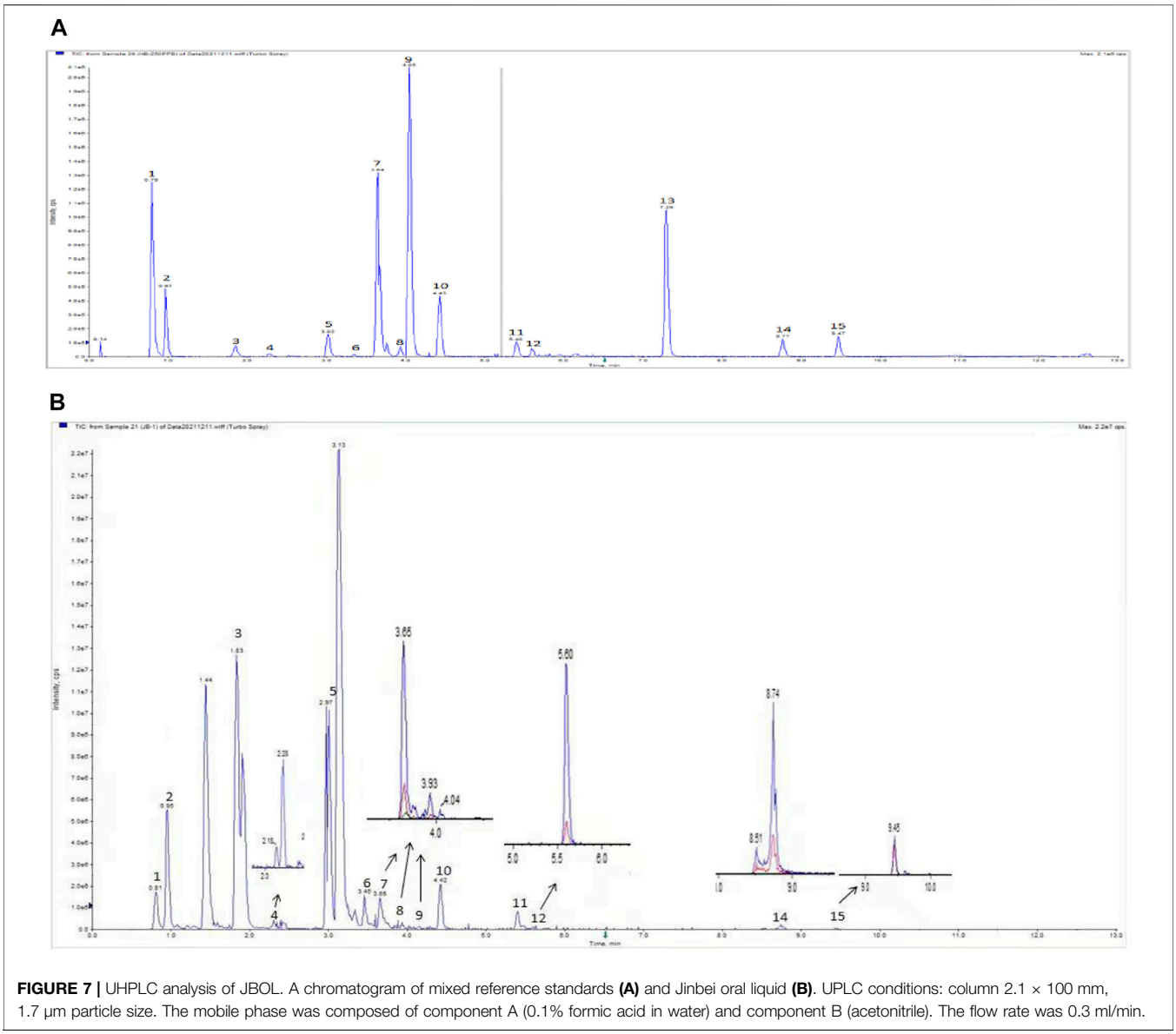

FIGURE 7 | UHPLC analysis of JBOL. A chromatogram of mixed reference standards **(A)** and Jinbei oral liquid **(B)**. UPLC conditions: column 2.1 × 100 mm, 1.7 μm particle size. The mobile phase was composed of component A (0.1% formic acid in water) and component B (acetonitrile). The flow rate was 0.3 ml/min.

dose, which was less than a 1% solution, did not exhibit cytotoxicity. As seen in **Figure 8B**, when the A549 cells were treated with TGF-β1, the cell shape-shifted from an epithelial form to a spindle-like fibroblast shape, representing the typical morphological characteristics of EMT. The addition of JBOL inhibited the TGF-β1–induced change in cellular morphology. Also, the expression of the mesenchymal marker vimentin was suppressed, and the expression of the epithelial marker E-cadherin increased with JBOL treatment (**Figure 8C**), indicating that JBOL inhibited the EMT process.

JBOL Inhibited MAPK ERK1/2, p38, and JNK Phosphorylation in BLM-Induced Rats

Since the hub nodes in the PPI network included MAPK proteins, and MAPK pathways are thought to act downstream of many of the aforementioned identified pathways (Antoniou, Margaritopoulos et al., 2010; Wang, Huang et al., 2018), the phosphorylation levels of extracellular signal-regulated kinase 1/2 (ERK1/2), p38, and c-Jun N-terminal protein kinase (JNK) were evaluated in JBOL-treated rats. The addition of JBOL reduced the increase in phosphorylation levels of ERK1/2, p38, and JNK induced by BLM in a dose-dependent manner (**Figure 9**). These results were consistent with the network pharmacological analysis suggesting that the MAPK proteins might be central to the JBOL mechanism of action that prevented IPF.

DISCUSSION

IPF is a chronic, progressive pulmonary disease with an unclear etiology and the pathological characteristics of progressive EMT transition, excessive extracellular matrix protein deposition, and,

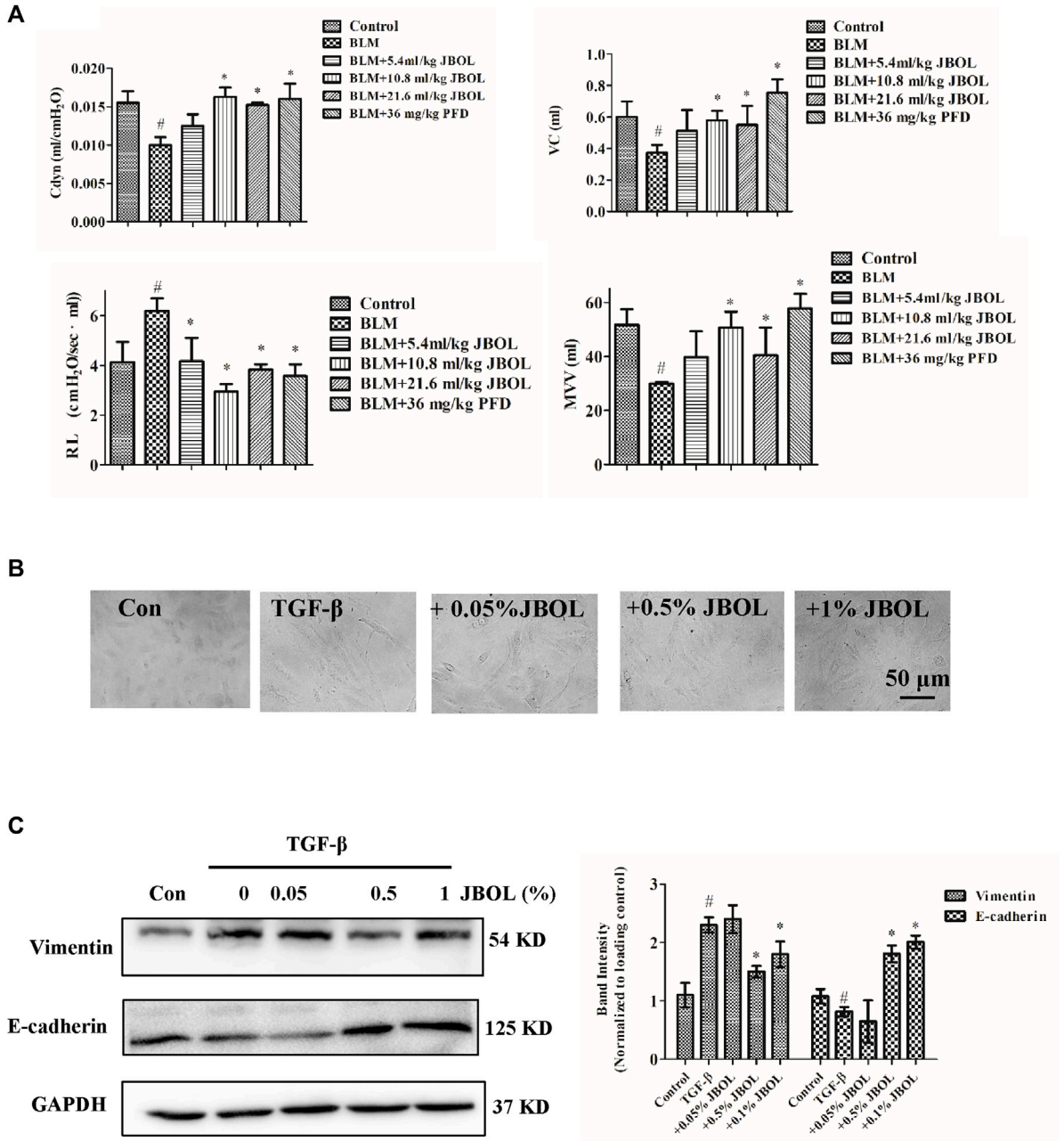

FIGURE 8 | Evaluation of JBOL effects on IPF *in vivo* and *in vitro*. **(A)** Pulmonary function test in the BLM-treated rats with JBOL or pirfenidone (PFD). n = 3–6, *$p <$ 0.05. **(B)** Morphological changes in A549 cells treated with TGF-β1 and/or JBOL. **(C)** The expression of vimentin and E-cadherin. n = 3, #$p < 0.05$ vs control; *$p < 0.05$ vs the TGF-β1-treated cells.

ultimately, respiratory system failure and death (Wilson and Wynn 2009; Degryse and Lawson 2011). Although several anti-inflammatory and immunomodulatory drugs are available to treat IPF, they fail to prevent its progression and exhibit adverse side effects (Walter and N. 2006; Michihito, Shinjiro et al., 2018). Therefore, novel drugs need to be developed.

JBOL currently is prescribed based on traditional Chinese medicine theory and has been used as a clinical treatment for interstitial lung disease (Tao K 1997). Recently, we reported that JBOL inhibited BLM-induced IPF by regulating the release of inflammatory factors, such as IFN-γ and IL-4 (Zhang, Cui et al., 2018). In this study, the protective effect of JBOL from pulmonary function impairment was observed. Furthermore, the underlying therapeutic mechanism of JBOL for IPF treatment was elucidated. However, the complicated characteristics of traditional Chinese medicine make it challenging to elucidate the underlying actions

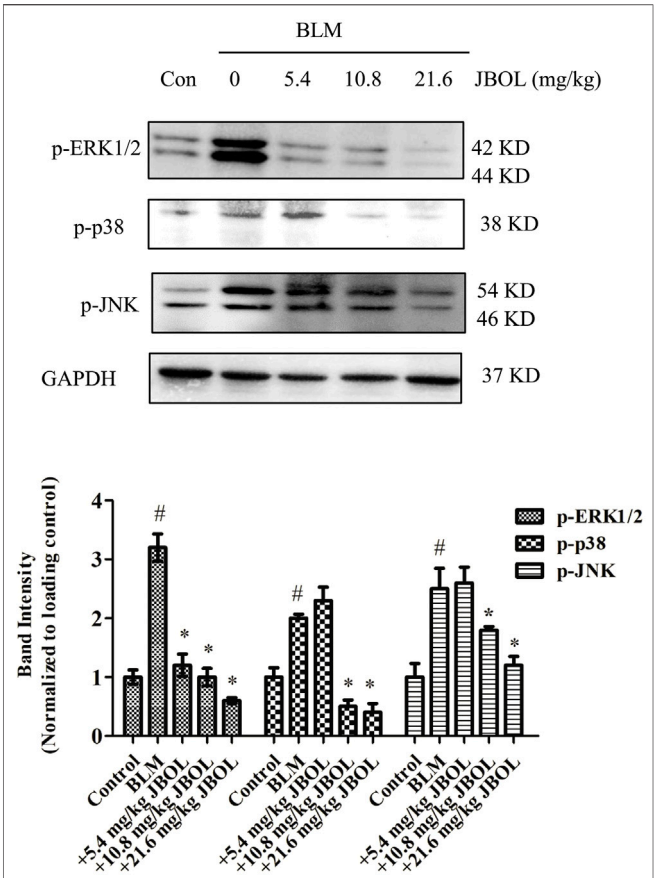

FIGURE 9 | Effect of MAPK phosphorylation *in vivo*. The expression of p-ERK1/2, p-P38, and p-JNK was determined using the Western blot analysis. n = 3–6, #$p < 0.05$ vs. control; *$p < 0.05$ vs. the BLM-treated group.

and mechanisms using the current reductionism research strategy of one gene, one target, and one compound.

In this study, systematic network pharmacology was used to discover the pharmacological mechanisms of JBOL underlying the IPF treatment. The process included JBOL chemical component screening, compound–target prediction, network construction, and experimental validation. Two hundred seventy-eight identified compounds in JBOL targeted 374 proteins. Among these targets, 103 targets were strongly associated with IPF (King, Pardo et al., 2011; Qiu, Wang et al., 2020). The key node targets that included many more edges, possibly have critical roles in the JBOL treatment of IPF, including MAPK1 (ERK2), MAPK14 (p38), MAPK8 (JNK1), JUN, IL-6, IL-4, and AKT. These targets corresponded to steroid hormones, oxygen levels, lipopolysaccharide, and responses to growth factors (Glass, Grossfeld et al., 2020). Il-4 has been validated as a target for JBOL, as we previously reported. Also, IFN-γ was inhibited by JBOL (Zhang, Cui et al., 2018). Additionally, JBOL has been reported to regulate the ratio of Th1/Th2 during chronic lung fibrosis (Xing, Qiang et al., 2020). In this study, additional targets for JBOL in response to the IPF-related inflammation and immune response were revealed.

TABLE 1 | Determination of 15 detected compounds in JBOL.

No.	Compound	Content (μg/ml)
1	Adenosine	12.5
2	Guanosine	8.03
3	Chlorogenic acid	70.25
4	Loganin	3.87
5	Rutin	4.25
6	Ferulic Acid	7.00
7	Imperialine	0.30
8	Peimine	0.01
9	Peiminine	0.03
10	Liquiritigenin	3.25
11	Isoliquiritigenin	0.87
12	Formononetin	1.05
13	Imperatorin	0
14	Tanshinone I	0.28
15	18β-Glycyrrhetinic Acid	0.23

There are numerous chemical components in JBOL. The active components are challenging to identify and were confirmed by the network pharmacology analysis. Therefore, we further identified major chemical components and determined their content in JBOL using UHPLC. By combining information from the TCMSP database and the UHPLC analysis, seven identified components, guanosine, formononetin, liquiritigenin, isoliquiritigenin, imperatorin, tanshinone I, and 18β-glycyrrhetinic acid, were confirmed as major active components. Although the content of most of the identified compounds was low, the efficacy of JBOL might be attributed to the combined and additive effects of these compounds.

Chlorogenic acid is thought to prevent IPF but has poor oral bioavailability (Wang, Dong et al., 2017). Isoliquiritigenin suppresses fibrogenesis through the PI3K/AKT/mTOR pathway in TGF-β1–treated human lung fibroblast-derived MRC-5 cells (He, Peng et al., 2020). Imperatorin exhibited anti-inflammatory properties on alveolar macrophages associated with pulmonary injury (Li, Chen et al., 2019). In addition, formononetin and tanshinone I target several signaling molecules related to IPF (Ma, Ji et al., 2013; Tao, Zheng et al., 2013); therefore, these components might have essential roles in treating IPF with JBOL. Although 278 compounds were identified using the TCMSP database, not all of these compounds were present in JBOL. We identified 15 compounds in JBOL using the UHPLC analysis. Additional compounds need to be identified in JBOL using the chemical analysis, such as UPLC/MS. Therefore, additional investigation of the active components in JBOL would be beneficial.

We performed an *in vivo* experiment to confirm that JBOL protected pulmonary function in BLM-induced rats. Previously, a histopathological assessment was performed to verify the protective effect of JBOL in the BLM-induced lung impairment (Zhang, Cui et al., 2018; Xing, Qiang et al., 2020). In this study, the protective role of JBOL in pulmonary function was confirmed. We also used TGF-β1 to treat A549 cells to create an *in vitro* IPF model (Oh, Kim et al., 2020). The EMT is critical in the pathology of IPF (Zhang, Fan et al., 2021), and JBOL exposure

resulted in a decrease in the spindle-like fibroblast cell shape induced by TGF-β1. EMT markers, including decreased expression of E-cadherin and increased expression of vimentin induced by TGF-β1, were reversed by the JBOL treatment, suggesting that JBOL could inhibit the EMT process in alveolar epithelial cells. The inhibitory effect on EMT in the cultured cells was consistent with a previous study demonstrating JBOL inhibition of EMT in the BLM-treated rats (Zhang, Cui et al., 2018). Also, the compounds in JBOL exhibited immune-modulatory, anti-inflammatory, and antifibrosis activities (Lin and Yang 2021; Yao, Ren et al., 2021). Combined with our previous study, the current results suggested that JBOL prevented IFP by reducing inflammation, fibrosis, and EMT.

To elucidate the molecular mechanism of action of JBOL in the treatment of IPF further, the GO and KEGG pathway analyses were performed to screen for critical candidate targets. The GO analysis revealed several biological processes, including responses to steroid hormones, growth factors, and lipopolysaccharide. The results of the KEGG pathway analysis indicated that a possible mechanism of JBOL for treating IPF involved the regulation of multiple signaling pathways related to inflammation, immunoregulation, and EMT, including MAPK, PI3K/Akt, and HIF-1 signaling pathways as well as others. Aberrant activation of the PI3K/Akt, HIF, and estrogen pathways contribute to fibroblast proliferation, alveolar epithelial cell apoptosis, and EMT (Lu, Azad et al., 2010; Elliot, Periera-Simon et al., 2019). The NF-κB pathway has been suggested as a therapeutic target in IPF (Jaffar J et al., 2021). NF-κB is capable of regulating IFN-γ action in lung fibroblasts through the Fas pathway (Wynes, MW et al., 2011). We proposed that JBOL inhibited IFN-γ possibly through targeting the NF-κB pathway. The cGMP–PKG pathway was involved in autophagy in BLM-induced IPF (Wang Y 2021). Thyroid hormone could inhibit lung fibrosis by improving epithelial mitochondrial function (Yu, Tzouvelekis et al., 2018), and BLM-mediated IPF was found to be dependent on the IL-17 pathway (Wilson and Wynn 2009). Increased AGE accelerated aging in fibrotic lung tissue (Machahua, Montes-Worboys et al., 2016).

The involved signaling pathways and molecular targets were varied and difficult to validate using single experiments. Among these pathways, we assumed that the MAPK proteins might play a central role because the signaling proteins of MAPK1 (ERK2), MAPK14 (p38), MAPK8 (JNK1), and JUN were key hub nodes in the PPI network. Simultaneously, they commonly act as downstream molecules of various signaling pathways to execute signaling functions, such as the PI3K/Akt and HIF-1 signaling pathways (Derynck and Zhang 2003; Roux and Blenis 2004). ERK1/2, p38, and JNK are three members of the MAPK protein family (van der Velden, Ye et al., 2016; Goda, Balli et al., 2020) and participate in the pathological mechanism of pulmonary fibrosis (Yu, Song et al., 2019). JNK was activated during the BLM-induced alveolar epithelial cell death (Lee, Schroedl et al., 2005). p38 and ERK were phosphorylated in the TGF-β–induced rat fibroblast NRK-49F cells (Chen, Zhou et al., 2013). MAPK also participated in regulating the production of inflammatory factors, TGF-β/Smads signaling or acted downstream of the PI3K and HIF pathways (Derynck and Zhang 2003), indicating a central role for the MAPK pathway in IPF pathology. In this study, JBOL inhibited the expression of phosphorylated ERK1/2, p38, and JNK in the BLM-treated rats, suggesting that JBOL inhibited the MAPK activation. Thus, we concluded that this might be a central event in the systematic network triggered by JBOL. In the future, the active components of JBOL targeting MAPK proteins and also other targets screened from network pharmacology regulated by JBOL require additional investigation.

CONCLUSION

This study is the first to show that JBOL could improve pulmonary function and inhibit EMT in the TGF-β1–induced A549 cells. The pharmacological mechanisms underlying the efficacy of JBOL might be related to systematic network regulation, including multiple components targeting several pathways centered on inhibiting phosphorylation of MAPK ERK1/2, p38, and JNK. Thus, these findings provide a theoretical and experimental basis for promoting the clinical application of JBOL.

DATA AVAILABILITY STATEMENT

The raw data supporting the conclusions of this article will be made available by the authors, without undue reservation.

ETHICS STATEMENT

The animal study was reviewed and approved by SDUTCM20190402012.

AUTHOR CONTRIBUTIONS

ZM and Y-QL designed the hypotheses. AZ, YZ, QX, ST, JW, YL, and TK conducted the experiments and data analyses. Y-QL, AZ, YZ, ST, YL, RD, and JW were responsible for writing and revising the manuscript. All authors approved the final version of the manuscript.

SUPPLEMENTARY MATERIAL

The Supplementary Material for this article can be found online at: https://www.frontiersin.org/articles/10.3389/fphar.2022.919388/full#supplementary-material

REFERENCES

Antoniou, K. M., Margaritopoulos, G. A., Soufla, G., Symvoulakis, E., Vassalou, E., Lymbouridou, R., et al. (2010). Expression Analysis of Akt and MAPK Signaling Pathways in Lung Tissue of Patients with Idiopathic Pulmonary Fibrosis (IPF). *J. Recept Signal Transduct. Res.* 30 (4), 262–269. doi:10.3109/10799893.2010.489227

Antoniu, S. A. (2006). Pirfenidone for the Treatment of Idiopathic Pulmonary Fibrosis. *Expert Opin. Investig. Drugs* 15 (15), 823–828. doi:10.1517/13543784.15.7.823

Ashburner, M., Ball, C. A., Blake, J. A., Botstein, D., Butler, H., Cherry, J. M., et al. (2000). Gene Ontology: Tool for the Unification of Biology. The Gene Ontology Consortium. *Nat. Genet.* 25 (1), 25–29. doi:10.1038/75556

Chen, H. H., Zhou, X. L., Shi, Y. L., and Yang, J. (2013). Roles of P38 MAPK and JNK in TGF-B1-Induced Human Alveolar Epithelial to Mesenchymal Transition. *Arch. Med. Res.* 44 (2), 93–98. doi:10.1016/j.arcmed.2013.01.004

Degryse, A. L., and Lawson, W. E. (2011). Progress toward Improving Animal Models for Idiopathic Pulmonary Fibrosis. *Am. J. Med. Sci.* 341 (6), 444–449. doi:10.1097/maj.0b013e31821aa000

Derynck, R., and Zhang, Y. E. (2003). Smad-dependent and Smad-independent Pathways in TGF-Beta Family Signalling. *Nature* 425 (6958), 577–584. doi:10.1038/nature02006

Elliot, S., Periera-Simon, S., Xia, X., Catanuto, P., Rubio, G., Shahzeidi, S., et al. (2019). MicroRNA Let-7 Downregulates Ligand-independent Estrogen Receptor-Mediated Male-Predominant Pulmonary Fibrosis. *Am. J. Respir. Crit. Care Med.* 200 (10), 1246–1257. doi:10.1164/rccm.201903-0508OC

Franceschini, A., Szklarczyk, D., Frankild, S., Kuhn, M., Simonovic, M., Roth, A., et al. (2013). STRING v9.1: Protein-Protein Interaction Networks, with Increased Coverage and Integration. *Nucleic Acids Res.* 41, D808–D815. doi:10.1093/nar/gks1094

Glass, D. S., Grossfeld, D., Renna, H. A., Agarwala, P., Spiegler, P., Kasselman, L. J., et al. (2020). Idiopathic Pulmonary Fibrosis: Molecular Mechanisms and Potential Treatment Approaches. *Respir. Investig.* 58 (5), 320–335. doi:10.1016/j.resinv.2020.04.002

Goda, C., Balli, D., Black, M., Milewski, D., Le, T., Ustiyan, V., et al. (2020). Loss of FOXM1 in Macrophages Promotes Pulmonary Fibrosis by Activating P38 MAPK Signaling Pathway. *PLoS Genet.* 16 (4), e1008692. doi:10.1371/journal.pgen.1008692

He, J., Peng, H., Wang, M., Liu, Y., Guo, X., Wang, B., et al. (2020). Isoliquiritigenin Inhibits TGF-B1-Induced Fibrogenesis through Activating Autophagy via PI3K/AKT/mTOR Pathway in MRC-5 Cells. *Acta Biochim. Biophys. Sin. (Shanghai)* 52 (8), 810–820. doi:10.1093/abbs/gmaa067

Hopkins, A. L., and Andrew, L. (2007). Network Pharmacology. *Nat. Biotechnol.* 25 (10), 1110–1111. doi:10.1038/nbt1007-1110

Jaffar, J., Glaspole, I., Symons, K., and Westall, G. (2021). Inhibition of NF-Kb by ACT001 Reduces Fibroblast Activity in Idiopathic Pulmonary Fibrosis. *Biomed. Pharmacother.* 138, 111471. doi:10.1016/j.biopha.2021.111471

Kim, K. K., Kugler, M. C., Wolters, P. J., Robillard, L., Brumwell, M. G. A. N., Sheppard, D., et al. (20182006). Alveolar Epithelial Cell Mesenchymal Transition Develops *In Vivo* during Pulmonary Fibrosis and Is Regulated by the Extracellular Matrix. *Proc. Natl. Acad. Sci. U. S. A.* 103 (35), 13180–13185. doi:10.1073/pnas.0605669103

King, T. E., Pardo, A., and Selman, M. (2011). Idiopathic Pulmonary Fibrosis. *Lancet* 378 (9807), 1949–1961. doi:10.1016/S0140-6736(11)60052-4

Lee, V. Y., Schroedl, C., Brunelle, J. K., Buccellato, L. J., Akinci, O. I., Kaneto, H., et al. (2005). Bleomycin Induces Alveolar Epithelial Cell Death through JNK-dependent Activation of the Mitochondrial Death Pathway. *Am. J. Physiol. Lung Cell Mol. Physiol.* 289 (4), L521–L528. doi:10.1152/ajplung.00340.2004

Li, S., and Zhang, B. (2013). Traditional Chinese Medicine Network Pharmacology: Theory, Methodology and Application. *Chin. J. Nat. Med.* 11 (2), 110–120. doi:10.1016/S1875-5364(13)60037-0

Li Y, Z. A., Wang, J., Zhang, Y., Suo, X., Wang, J., Zhang, L., et al. (2021). Clinical Efficacy of Jinbei Oral Liquid in the Treatment of COVID-19 by Retrospective Analysis. *Pharmacol. Clin. Chin. Mater. Med.* 37, 7–10.

Li, Y. Z., Chen, J. H., Tsai, C. F., and Yeh, W. L. (2019). Anti-inflammatory Property of Imperatorin on Alveolar Macrophages and Inflammatory Lung Injury. *J. Nat. Prod.* 82 (4), 1002–1008. doi:10.1021/acs.jnatprod.9b00145

Lin, Y., and Yang, P. (2021). Phillygenin Inhibits the Inflammation and Apoptosis of Pulmonary Epithelial Cells by Activating PPARγ Signaling via Downregulation of MMP8. *Mol. Med. Rep.* 24 (5), 775. doi:10.3892/mmr.2021.12415

Liu, H., Wang, J., Zhou, W., Wang, Y., and Yang, L. (2013). Systems Approaches and Polypharmacology for Drug Discovery from Herbal Medicines: An Example Using Licorice. *J. Ethnopharmacol.* 146 (3), 773–793. doi:10.1016/j.jep.2013.02.004

Lu, Y., Azad, N., Wang, L., Iyer, A. K., Castranova, V., Jiang, B. H., et al. (2010). Phosphatidylinositol-3-Kinase/Akt Regulates Bleomycin-Induced Fibroblast Proliferation and Collagen Production. *Am. J. Respir. Cell Mol. Biol.* 42 (4), 432–441. doi:10.1165/rcmb.2009-0002OC

Lv, X., Xu, Z., Xu, G., Li, H., Wang, C., Chen, J., et al. (2020). Investigation of the Active Components and Mechanisms of Schisandra Chinensis in the Treatment of Asthma Based on a Network Pharmacology Approach and Experimental Validation. *Food Funct.* 11 (4), 3032–3042. doi:10.1039/d0fo00087f

Ma, Z., Ji, W., Fu, Q., and Ma, S. (2013). Formononetin Inhibited the Inflammation of LPS-Induced Acute Lung Injury in Mice Associated with Induction of PPAR Gamma Expression. *Inflammation* 36 (6), 1560–1566. doi:10.1007/s10753-013-9700-5

Machahua, C., Montes-Worboys, A., Llatjos, R., Escobar, I., Dorca, J., Molina-Molina, M., et al. (2016). Increased AGE-RAGE Ratio in Idiopathic Pulmonary Fibrosis. *Respir. Res.* 17 (1), 144. doi:10.1186/s12931-016-0460-2

Mazzei, M. E., Richeldi, L., and Collard, H. R. (2015). Nintedanib in the Treatment of Idiopathic Pulmonary Fibrosis. *Ther. Adv. Respir. Dis.* 9, 121–129. doi:10.1177/1753465815579365

Meyer, K. C. (2017). Pulmonary Fibrosis, Part I: Epidemiology, Pathogenesis, and Diagnosis. *Expert Rev. Respir. Med.* 11 (5), 343–359. doi:10.1080/17476348.2017.1312346

Michihito, T., Shinjiro, M., Yukiko, M., Hiroko, Y. O., Takanori, A., Shoji, K., et al. (2018). Pirfenidone Suppresses Polarization to M2 Phenotype Macrophages and the Fibrogenic Activity of Rat Lung Fibroblasts. *J. Clin. Biochem. Nutr.* 63 (1), 58–65.

Ng, T. B., Liu, F., and Wang, H. X. (2004). The Antioxidant Effects of Aqueous and Organic Extracts of Panax Quinquefolium, Panax Notoginseng, Codonopsis Pilosula, Pseudostellaria Heterophylla and Glehnia Littoralis. *J. Ethnopharmacol.* 93 (2-3), 285–288. doi:10.1016/j.jep.2004.03.040

Oh, S. Y., Kim, Y. H., Kang, M. K., Lee, E. J., Kim, D. Y., Oh, H., et al. (2020). Aesculetin Attenuates Alveolar Injury and Fibrosis Induced by Close Contact of Alveolar Epithelial Cells with Blood-Derived Macrophages via IL-8 Signaling. *Int. J. Mol. Sci.* 21 (15). doi:10.3390/ijms21155518

Paolacci, S., Precone, V., Acquaviva, F., Chiurazzi, P., Fulcheri, E., Pinelli, M., et al. (2019). Genetics of Lipedema: New Perspectives on Genetic Research and Molecular Diagnoses. *Eur. Rev. Med. Pharmacol. Sci.* 23 (13), 5581–5594. doi:10.26355/eurrev_201907_18292

Qi, Y., Gao, F., Hou, L., and Wan, C. (2017). Anti-Inflammatory and Immunostimulatory Activities of Astragalosides. *Am. J. Chin. Med.* 45, 1157–1167. doi:10.1142/S0192415X1750063X

Qiu, Y., Wang, Z., Zhang, X., Huang, P., Zhang, W., Zhang, K., et al. (2020). A Long-Acting Isomer of Ac-SDKP Attenuates Pulmonary Fibrosis through SRPK1-Mediated PI3K/AKT and Smad2 Pathway Inhibition. *IUBMB life* 72 (12), 2611–2626. doi:10.1002/iub.2389

Roux, P. P., and Blenis, J. (2004). ERK and P38 MAPK-Activated Protein Kinases: a Family of Protein Kinases with Diverse Biological Functions. *Microbiol. Mol. Biol. Rev.* 68 (2), 320–344. doi:10.1128/MMBR.68.2.320-344.2004

Tao, K. Z. X. (1997). Feitong Oral Liquid in the Treatment of 20 Cases of Interstitial Lung Disease. *Beijing J. Trad. Chin. Med.* 16, 13–15. doi:10.1007/bf02843397

Tao, S., Zheng, Y., Lau, A., Jaramillo, M. C., Chau, B. T., Lantz, R. C., et al. (2013). Tanshinone I Activates the Nrf2-dependent Antioxidant Response and Protects against As(III)-induced Lung Inflammation *In Vitro* and *In Vivo*. *Antioxid. Redox Signal* 19 (14), 1647–1661. doi:10.1089/ars.2012.5117

van der Velden, J. L., Ye, Y., Nolin, J. D., Hoffman, S. M., Chapman, D. G., Lahue, K. G., et al. (2016). JNK Inhibition Reduces Lung Remodeling and Pulmonary Fibrotic Systemic Markers. *Clin. Transl. Med.* 5 (1), 36. doi:10.1186/s40169-016-0117-2

Walter, N., Collard, H. R., and King, T. E. 2006). "Current Perspectives on the Treatment of Idiopathic Pulmonary Fibrosis." *Proc. Am. Thorac. Soc.* 3(4): 330–338.doi:10.1513/pats.200602-016TK

Wang, Y., Huang, G., Wang, Z., Qin, H., Mo, B., and Wang, C. (2018). Elongation Factor-2 Kinase Acts Downstream of P38 MAPK to Regulate Proliferation, Apoptosis and Autophagy in Human Lung Fibroblasts. *Exp. Cell Res.* 363 (2), 291–298. doi:10.1016/j.yexcr.2018.01.019

Wang, Y. C., Dong, J., Nie, J., Zhu, J. X., Wang, H., Chen, Q., et al. (2017). Amelioration of Bleomycin-Induced Pulmonary Fibrosis by Chlorogenic Acid through Endoplasmic Reticulum Stress Inhibition. *Apoptosis* 22 (9), 1147–1156. doi:10.1007/s10495-017-1393-z

Wang, Y., Hu, S., Shen, L., Liu, S., Wan, L., Yang, S., et al. (2021). Dynamic Observation of Autophagy and Transcriptome Profiles in a Mouse Model of Bleomycin-Induced Pulmonary Fibrosis. *Front. Mol. Biosci.* 8, 664913. doi:10.3389/fmolb.2021.664913

Wei, X., Hou, W., Liang, J., Fang, P., Dou, B., Wang, Z., et al. (2021). Network Pharmacology-Based Analysis on the Potential Biological Mechanisms of Sinisan against Non-alcoholic Fatty Liver Disease. *Front. Pharmacol.* 12, 693701. doi:10.3389/fphar.2021.693701

Wilson, M. S., and Wynn, T. A. (2009). Pulmonary Fibrosis: Pathogenesis, Etiology and Regulation. *Mucosal Immunol.* 2 (2), 103–121. doi:10.1038/mi.2008.85

Wishart, D. S., Feunang, Y. D., Guo, A. C., Lo, E. J., Grant, A. J. R., Sajed, T., et al. (2017). DrugBank 5.0: A Major Update to the DrugBank Database for 2018. *Nucleic Acids Res.* 46 (Database issue), D1074–D1082. doi:10.1093/nar/gkx1037

Wynes, M. W., Edelman, B. L., Kostyk, A. G., Edwards, M. G., Coldren, C., Groshong, S. D., et al. (2011). Increased Cell Surface Fas Expression Is Necessary and Sufficient to Sensitize Lung Fibroblasts to Fas Ligation-Induced Apoptosis: Implications for Fibroblast Accumulation in Idiopathic Pulmonary Fibrosis. *J. Immunol.* 187 (1), 527–537. doi:10.4049/jimmunol.1100447

Xing, X.-y., Qiang, W.-j., Bao, J.-l., Yang, R.-c., Hou, J., Tao, K., et al. (2020). Jinbei Oral Liquid Ameliorates Bleomycin-Induced Idiopathic Pulmonary Fibrosis in Rats via Reversion of Th1/Th2 Shift. *Chin. Herb. Med.* 12, 273–280. doi:10.1016/j.chmed.2020.05.002

Xz, A., Jla, B., Ly, A., Yang, N. A., Rr, A., Chao, S. A., et al. (2021). Beneficial Effects of Mijianchangpu Decoction on Ischemic Stroke through Components Accessing to the Brain Based on Network Pharmacology. *J. Ethnopharmacol.* 285, 114882.

Yao, R., Ren, L., Wang, S., Zhang, M., and Yang, K. (2021). Euxanthone Inhibits Traumatic Spinal Cord Injury via Anti-oxidative Stress and Suppression of P38 and PI3K/Akt Signaling Pathway in a Rat Model. *Transl. Neurosci.* 12 (1), 114–126. doi:10.1515/tnsci-2021-0012

Ye, H., Ye, L., Kang, H., Zhang, D., Tao, L., Tang, K., et al. (2011). HIT: Linking Herbal Active Ingredients to Targets. *Nucleic Acids Res.* 39, D1055–D1059. doi:10.1093/nar/gkq1165

Yu, G., Tzouvelekis, A., Wang, R., Herazo-Maya, J. D., Ibarra, G. H., Srivastava, A., et al. (2018). Thyroid Hormone Inhibits Lung Fibrosis in Mice by Improving Epithelial Mitochondrial Function. *Nat. Med.* 24 (1), 39–49. doi:10.1038/nm.4447

Yu, H., Chen, J., Xu, X., Li, Y., Zhao, H., Fang, Y., et al. (2012). A Systematic Prediction of Multiple Drug-Target Interactions from Chemical, Genomic, and Pharmacological Data. *PloS one* 7 (5), e37608. doi:10.1371/journal.pone.0037608

Yu, W., Song, X., and Liu, Y. (2019). TRB3 Regulates Pulmonary Interstitial Fibrosis through the MAPK Signaling Pathway. *Int. J. Clin. Exp. Pathol.* 12 (9), 3247–3257.

Yu, X. Q., Yang, S. G., Xie, Y., and Li, J. S. (2020). Traditional Chinese Medicine in the Treatment of Idiopathic Pulmonary Fibrosis Based on Syndrome Differentiation: Study Protocol of an Exploratory Trial. *J. Integr. Med.* 18, 163–168. doi:10.1016/j.joim.2019.12.005

Zhang, C., Cui, Q., Tian, J., Wang, P., Hou, L., Gong, T., et al. (2018). Effect of Jinbei Oral Liquid on Bleomycin-Induced Pulmonary Fibrosis in Rats. *Pharmacol. Clin. Chin. Materia Medica* 34, 146–150.

Zhang, S., Fan, Y., Qin, L., Fang, X., Zhang, C., Yue, J., et al. (2021). IL-1β Augments TGF-β Inducing Epithelial-Mesenchymal Transition of Epithelial Cells and Associates with Poor Pulmonary Function Improvement in Neutrophilic Asthmatics. *Respir. Res.* 22 (1), 216. doi:10.1186/s12931-021-01808-7

Zhang, X., Jie, M. U., Wen-Cheng, Y. U., Liu, C. C., and Liu, Y. Y. (2012). Effect of Feitongkoufuye Treating Pulmonary Interstitial Fibrosis on Neutrophil Elastase. *J. Shandong Univ. Sci.* 50, 24–28.

Zhang, X., Wang, D., and Jie, M. U. (2013). Therapeutical Effect and Mechanism of Fei Tong Oral Liquid on the Acute Lung Injury in Rats. *Shandong Med. J.* 53, 8–10.

Zhang, Y., Li, X., Xu, X., and Yang, N. (2019). Mechanisms of Paeonia Lactiflora in Treatment of Ulcerative Colitis: A Network Pharmacological Study. *Med. Sci. Monit.* 25, 7574–7580. doi:10.12659/MSM.917695

Zhou, W., Zhang, H., Wang, X., Kang, J., Guo, W., Zhou, L., et al. (2022). Network Pharmacology to Unveil the Mechanism of Moluodan in the Treatment of Chronic Atrophic Gastritis. *Phytomedicine* 95, 153837. doi:10.1016/j.phymed.2021.153837

Zhou, Y., Zhou, B., Pache, L., Chang, M., Khodabakhshi, A. H., Tanaseichuk, O., et al. (2019). Metascape Provides a Biologist-Oriented Resource for the Analysis of Systems-Level Datasets. *Nat. Commun.* 10 (1), 1523. doi:10.1038/s41467-019-09234-6

Conflict of Interest: AZ, QX, LZ, JJ, LW, KT, and ZM were employed by Shandong Hongji-tang Pharmaceutical Group Co., Ltd.

The remaining authors declare that the research was conducted in the absence of any commercial or financial relationships that could be construed as a potential conflict of interest.

Publisher's Note: All claims expressed in this article are solely those of the authors and do not necessarily represent those of their affiliated organizations, or those of the publisher, the editors, and the reviewers. Any product that may be evaluated in this article, or claim that may be made by its manufacturer, is not guaranteed or endorsed by the publisher.

frontiers | Frontiers in Pharmacology

TYPE Review
PUBLISHED 11 August 2022
DOI 10.3389/fphar.2022.928933

OPEN ACCESS

EDITED BY
Yang Zhou,
Brown University, United States

REVIEWED BY
Krzysztof Bryniarski,
Jagiellonian University Medical College, Poland
Sandhya Bansal,
St. Joseph's Hospital and Medical Center, United States
Gagandeep Kaur,
University of Rochester, United States

*CORRESPONDENCE
Yi Li,
peach_adore@hotmail.com

SPECIALTY SECTION
This article was submitted to Respiratory Pharmacology, a section of the journal Frontiers in Pharmacology

RECEIVED 26 April 2022
ACCEPTED 15 July 2022
PUBLISHED 11 August 2022

CITATION
Yang Y, Huang H and Li Y (2022), Roles of exosomes and exosome-derived miRNAs in pulmonary fibrosis. *Front. Pharmacol.* 13:928933. doi: 10.3389/fphar.2022.928933

Roles of exosomes and exosome-derived miRNAs in pulmonary fibrosis

Yongfeng Yang[1], Hong Huang[1,2] and Yi Li[1]*

[1]Precision Medicine Key Laboratory, Institute of Respiratory Health, West China Hospital, Sichuan University, Chengdu, Sichuan, China, [2]Key Laboratory of Transplantation Engineering and Immunology, Institute of Clinical Pathology, Ministry of Health, West China Hospital, Sichuan University, Chengdu, Sichuan, China

Pulmonary fibrosis is a chronic, progressive fibrosing interstitial lung disease of unknown etiology that leads rapidly to death. It is characterized by the replacement of healthy tissue through an altered extracellular matrix and damage to the alveolar structure. New pharmacological treatments and biomarkers are needed for pulmonary fibrosis to ensure better outcomes and earlier diagnosis of patients. Exosomes are nanoscale vesicles released by nearly all cell types that play a central role as mediators of cell-to-cell communication. Moreover, exosomes are emerging as a crucial factor in antigen presentation, immune response, immunomodulation, inflammation, and cellular phenotypic transformation and have also shown promising therapeutic potential in pulmonary fibrosis. This review summarizes current knowledge of exosomes that may promote pulmonary fibrosis and be utilized for diagnostics and prognostics. In addition, the utilization of exosomes and their cargo miRNAs as novel therapeutics and their potential mechanisms are also discussed. This review aims to elucidate the role of exosomes in the pathogenesis of pulmonary fibrosis and paves the way for developing novel therapeutics for pulmonary fibrosis. Further in-depth research and clinical trials on this topic are encouraged in the future.

KEYWORDS

exosome, pulmonary fibrosis, biomark, therapy tool, microRNA

Abbreviations: AATD, alpha-1 antitrypsin deficiency; AD, adipose tissue; ADSCs, adipose mesenchymal stem cells; BALF, bronchoalveolar lavage fluid; BM, bone marrow; BMP, bone morphogenic protein; COPD, chronic obstructive pulmonary disease; ECM, extracellular matrix; EMT, epithelial–mesenchymal transition; EVs, extracellular vesicles; HBE, Chuman bronchial epithelial cell-derived; HILI, hyperoxia-induced lung injury; IPF, idiopathic pulmonary fibrosis; MHC, major histocompatibility complex; MSCs, mesenchymal stem cells/mesenchymal stromal cells; mTOR, mammalian target of rapamycin; NSCLC, non-small-cell lung cancer; PF, pulmonary fibrosis; TGF-β, transforming growth factor-β; TNF, tumor necrosis factor; 3′UTR, 3′untranslated region.

Introduction

Exosomes are small extracellular vesicles generated by inward budding of the membrane into the lumen of the compartment (Koh et al., 2020). The diameter of exosomes ranges from 40 to 160 nm (Li et al., 2022), and these structures play an important role in intercellular communication by transferring nucleotides or proteins, which then act accordingly (Merckx et al., 2020). Various exosomes can be detected in various body fluids, including blood, urine (Makler and Asghar, 2020), synovial fluid, breast milk, ascites, thorax-related sputum, bronchoalveolar lavage fluid (BALF), and pleural effusions, which represent a unique tool to study the pathophysiology and biomarker discovery of respiratory diseases (Kadota et al., 2016; Lucchetti et al., 2021). Recently, exosomes have been recognized as a novel disease biomarker because they reflect the physiological state and microenvironment of the cell of origin, are readily found in body fluids, and are stable in the extracellular environment (Kok and Yu, 2020).

In respiratory medicine, there is increasing evidence regarding the involvement of exosomes in the pathogenesis of lung diseases, such as chronic obstructive pulmonary disease (COPD), asthma, alpha-1 antitrypsin deficiency (AATD), pulmonary fibrosis (PF), and lung cancer (Trappe et al., 2021). For example, exosomes are reported to be involved in inflammation and immune activation in asthmatic patients (Admyre et al., 2003). Furthermore, exosomes can also transfer microRNAs (miRNAs) that are capable of inducing disease phenotypes in COPD target cells (Fujita et al., 2015). Current research has predominantly focused on the role of exosomes in lung cancer. There are numerous published reports on the pathophysiological role of exosomes in cancer initiation, progression, invasion, metastasis, and new therapeutic approaches using exosomes as drug delivery systems (Xunian and Kalluri, 2020). In addition, the number and profiles of exosomes are altered according to the pathophysiological status of the disease; therefore, exosomes can be used as biomarkers to monitor disease (Zheng et al., 2018). On clinicaltrials.gov, studies using exosomes as diagnostic tests or a molecular cargo that delivers miRNAs and proteins are underway in several lung diseases, such as clinical studies of circulating tumor DNA and combined detection of exosomes to identify benign and malignant pulmonary nodules (NCT04182893) and vaccination assays with dendritic cell-derived exosomes loaded with tumor antigens in non-small-cell lung cancer (NSCLC) (NCT01159288). Murine *in vitro* and *in vivo* models have suggested the potential involvement of exosomes in PF (Kadota et al., 2021; Zhou et al., 2021), but a direct correlation has not been clarified.

This review discusses the role of exosomes in PF to elucidate their potential application as diagnostic and prognostic biomarkers and therapeutic targets.

Exosomes

Exosomes are nanosized membrane-bound vesicles released from cells and transport lipids, proteins, and nucleic acids (including mRNA, miRNA, lncRNA, circular RNA, ribosomal RNA, tRNA, and DNA fragments) (Li et al., 2022). Exosomes were first discovered in circulation during sheep reticulocyte maturation (Pan et al., 1985), and subsequently in other biological fluids (Makler and Asghar, 2020) and cell culture supernatants. Exosomes and microvesicles are collectively referred to as extracellular vesicles. Exosomes derived from different cell sources share similar surface proteins, including tetraspanins CD9, CD63, CD81, and CD82, as well as Alix and TSG101 (Zhu et al., 2021), which are recognized and currently used as markers for exosomes. The formation and secretion of exosomes is regulated by Rab proteins (Ostrowski et al., 2010), the endosomal sorting complex required for transport proteins (Tamai et al., 2010), and intracellular Ca^{2+} levels (Kim et al., 2021). Exosomes also express cell surface proteins that are similar to their origin. For example, mesenchymal stem cell (MSC)-derived exosomes express CD29, CD44, CD73, CD90, and integrins so that they can adhere and fuse with circulating or distant resident cells (Szul et al., 2016).

Exosomes can bind to the surface of target cells (receptor cells) and enter directly or activate receptors on the target cell surface to perform biological functions such as mediating antigen presentation and immune regulation. Macrophage-derived exosomes contain major histocompatibility complex (MHC) class II and costimulatory molecules that play a role in antigen presentation and naive T cell priming (Ramachandra et al., 2010). Exosomes released from activated macrophages can enhance immune cell activity by delivering inflammatory cytokines such as tumor necrosis factor (TNF) (O'Neill and Quah, 2008), while exosomes released by T cells can target various different cells and induce immunomodulatory effects (Lindenbergh and Stoorvogel, 2018). In summary, exosomes are crucial for intercellular communication, immune responses, immunomodulation, inflammation, and the transformation of cellular phenotypes.

Exosomes contribute to the pathogenesis of pulmonary fibrosis

PF is a chronic, progressive, and destructive lung disease characterized by the accumulation of fibroblasts/myofibroblasts, increased deposition of extracellular matrix, and decreased lung function (Richeldi et al., 2017). The etiology of PF is currently unknown. There is increasing evidence that exosomes contribute to the pathogenesis of pulmonary fibrosis. Makiguchi et al. (2016) found that miR-21-5p was elevated in serum exosomes during acute inflammation and chronic fibrosis in a bleomycin-induced PF mouse model. In addition, patients with PF and high levels of

miR-21-5p had a significantly poorer prognosis over 30 months, indicating the potential of miR-21-5p as a prognostic biomarker for PF. Chen et al. (2022) demonstrated that exosomes derived from hypoxia-induced alveolar epithelial cells stimulated interstitial PF through a mechanism dependent on the lncRNA HOTAIRM1. Increased numbers of BALF exosomes were reported in mice with experimental PF as well as in patients with idiopathic PF (IPF). This was because exosomes carry fibrotic mediators, such as WNT5A, which lead to increased fibroblast proliferation (Martin-Medina et al., 2018). Lacedonia et al. (2021) reported that exosomal miRNAs let-7d and miR-16 were significantly downregulated in the serum of patients with IPF. Expression of let-7d was also repressed in exosomes derived from BALF of PF mice (Xie et al., 2020). Furthermore, numerous differentially expressed miRNAs were detected in the lung-tissue-derived exosomes of patients with IPF compared with non-smoking controls, and these data further revealed lung-specific miRNAs associated with chronic lung diseases that could serve as potential biomarkers or therapeutic targets (Kaur et al., 2021). Liu et al. (2018) found that miR-125b-5p, miR-128-3p, miR-21-5p, miR-100-5p, miR-140-3p, and miR-374b-5p were upregulated, while let-7d-5p, miR-103-3p, miR-27b-3p, and miR-30a-5p were downregulated in exosomes in BALF from patients with PF. In addition, in a miRNA branch of exosomes, miR-142-3p was significantly upregulated in both sputum and plasma from patients with PF (Guiot et al., 2019; Njock et al., 2019). In addition,miR-142-3p was also positively correlated with the percentage of sputum macrophages and negatively correlated with the percentage of sputum neutrophils in patients with PF (Guiot et al., 2020). Furthermore, miR-142-3p was inversely correlated with lung diffusing capacity for carbon monoxide/alveolar volume (Njock et al., 2019).

Yao et al. (2019) demonstrated that M2 macrophage-derived exosomes overexpressed miR-328 and played a vital role in pulmonary fibroblast proliferation and the progression of PF by regulating FAM13A. Parimon et al. (2019) indicated that overexpressed Syndecan-1 in patients with PF, mainly in type II alveolar epithelial cells, was instrumental in controlling miRNA packaging in extracellular vesicles, including miR-144-3p, miR-142(a)-3p, miR-142b, miR-503-5p, and miR-34b-5p. Fibronectin expression on the surface of extracellular vesicles derived from fibroblasts of patients with PF could mediate their invasion, which may be related to the pathogenesis of fibrotic diseases (Chanda et al., 2019). Kang et al. (2019) revealed that extracellular vesicles derived from transforming growth factor-β (TGF-β)-stimulated fibroblasts contained PD-L1, which could inhibit T-cell proliferation and mediate fibroblast migration. Furthermore, fibroblast-derived extracellular vesicles contained increased levels of miR-23b-3p and miR-494-3p in PF, which induced epithelial cell phenotypic changes and were positively correlated with disease severity (Kadota et al., 2020). Kuse et al. (2020) revealed that miR-22 expression in exosomes from serum was increased and then decreased in a bleomycin-induced PF model. In addition, administration of the miR-22 mimic could ameliorate fibrosis by regulating fibroblast-to-myofibroblast differentiation. The identification of altered exosomes and elucidation of their role in the pathogenesis of PF can serve as references for the development of diagnostic biomarkers and subsequent therapeutic targets (Yamada, 2020; Hua et al., 2021; Yamada, 2021) (Table 1; Figure 1A).

Exosomes as a therapeutic tool for pulmonary fibrosis

Recently, treatment aims for PF have been limited to prolonging life expectancy by slowing progression of the disease (Glass et al., 2022). Exosomes could improve management of PF and serve as an innovative therapeutic (Purghè et al., 2021). As early as 2014, Novelli and Neri's team demonstrated that the BALF of patients with PF, which contained procoagulant microparticles and tissue factor, could activate coagulation factor X to Xa and potentially contribute to the pathogenesis of PF by regulating fibroblast growth and differentiation (Novelli et al., 2014). This team later reported that pirfenidone, one of only two U.S. Food and Drug Administration (FDA)-approved drugs for IPF at the time of writing, could inhibit p38-mediated generation of tissue factor in microparticles from H_2O_2 to stimulate alveolar epithelial cells (Neri et al., 2016). These findings showed that exosomes could be used to develop therapeutic applications.

Stem cells exhibit strong self-renewal and proliferation potential. Mesenchymal stem cells/mesenchymal stromal cells (MSCs) are multipotent stromal cells derived from the mesoderm and exhibit immunomodulatory, anti-inflammatory, and most importantly, antifibrotic properties. These properties are due, in part, to the activity of growth factors and cytokines secreted by the MSCs. Recently, researchers revealed that exosomes were responsible for the antifibrotic efficacy of MSCs (Fujita et al., 2018; Ma et al., 2022). MSCs derived from bone marrow (BM), adipose tissue (AD), and placenta confirmed that exosomes from MSCs could reduce inflammation by regulating related signaling pathways and polarization, and could also reduce collagen deposition in bleomycin- (Mansouri et al., 2019; Dinh et al., 2020; Wan et al., 2020), silica- (Choi et al., 2014; Phinney et al., 2015; Bandeira et al., 2018; Dinh et al., 2020), PM2.5- (Gao et al., 2020), and radiation- (Lei et al., 2020) induced PF models and TGF-β stimulated myofibroblasts (Shentu et al., 2017). The effect was also reported in stem cells from menstrual blood (Sun L. et al., 2019). However, Dinh et al. (2020) indicated that lung spheroid cell-derived exosomes exhibited superior therapeutic benefits in damage control and tissue repair compared with those from MSCs; moreover, the regenerative effects were more robust in the bleomycin model compared with the silica model. Guiot et al. (2020) showed that macrophage-derived exosomes alleviated fibrosis in airway epithelial cells and lung fibroblasts

TABLE 1 Exosomes associated with pulmonary fibrosis.

Author	Species	Exosome source	Outcome	Expression	Reference
Makiguchi	Human	Serum	miR-21-5p	↑	Makiguchi et al. (2016)
Chen	Mouse	Hypoxia-induced alveolar epithelial cells	HOTAIRM1	↑	Chen et al. (2022)
Martin-Medina	Human, Mouse	BALF	WNT5A	↑	Martin-Medina et al. (2018)
Lacedonia	Human	Serum	let-7d	↓	Lacedonia et al. (2021)
			miR-16	↓	
Xie	Mouse	BALF	let-7d	↓	Xie et al. (2020)
Liu	Human	BALF	miR-30a-5p	↓	Liu et al. (2018)
			let-7d-5p	↓	
			miR-103-3p	↓	
			miR-27b-3p	↓	
			miR-125b-5p	↑	
			miR-128-3p	↑	
			miR-21-5p	↑	
			miR-100-5p	↑	
			miR-140-3p	↑	
			miR-374b-5p	↑	
Guiot and Njock	Human	Sputum, plasma	miR-142-3p	↑	Guiot et al. (2019); Njock et al. (2019); Guiot et al. (2020)
		Plasma	miR-200c-5p	↑	Guiot et al. (2020)
		Sputum	miR-33a-5p	↑	Guiot et al. (2019); Njock et al. (2019); Guiot et al. (2020)
		Sputum	let-7d-5p	↓	Guiot et al. (2019); Njock et al. (2019); Guiot et al. (2020)
		Sputum	miR-192-5p	↑	Njock et al. (2019)
		Sputum	miR-26a-5p	↓	Njock et al. (2019)
		Sputum	miR-29b-3p	↓	Njock et al. (2019)
		Sputum	miR-423-3p	↓	Njock et al. (2019)
Yao	Rat	M2 macrophage	miR-328	↑	Yao et al. (2019)
			FAM13A	↓	
Parimon	Human Mouse	BALF	Syndecan-1	↑	Parimon et al. (2019)
			miR-144-3p	↓	
			miR-142(a)-3p	↓	
			miR-142b	↓	
			miR-503-3p	↓	
			miR-34b-5p	↓	
Chanda	Human	Fibroblast	Fibronectin	↑	Chanda et al. (2019)
Kang	Human	Fibroblast	PD-L1	↑	Kang et al. (2019)
Kadota	Human	Fibroblast	miR-23b-3p	↑	Kadota et al. (2020)
			miR-494-3p	↑	
			miR-19a-3p	↑	
			miR-127-3p	↑	
			miR-145-5p	↑	
			miR-424-5p	↑	
Kuse	Mouse	Serum	miR-22-3p	↑	Kuse et al. (2020)
			miR-16-5p	↑	
			miR-15a-5p	↑	
			miR-15b-5p	↑	
			miR-21a-5p	↑	
			miR-25-3p	↑	

(Continued on following page)

TABLE 1 (*Continued*) Exosomes associated with pulmonary fibrosis.

Author	Species	Exosome source	Outcome	Expression	Reference
			miR-93-5p	↑	
			miR-23a-3p	↑	
			miR-17-5p	↑	
			miR-29a-3p	↑	
			miR-32-3p	↓	
			miR-15a-3p	↓	
			miR-29c-5p	↓	
			miR-29b-1-5p	↓	
			miR-28a-3p	↓	
			miR-23b-5p	↓	
			miR-26a-1-3p	↓	
			miR-34a-3p	↓	
			miR-34c-5	↓	
			miR-21a-3p	↓	

by delivering miR-142-3p, while Kadota et al. (2021) reported that human bronchial epithelial cell-derived extracellular vesicles (HBEC EVs) inhibited TGF-β-mediated induction of both myofibroblast differentiation and lung epithelial cellular senescence by attenuating WNT signaling. In the latter study, it was further suggested that administration of HBEC EVs was a promising antifibrotic modality of treatment for PF via miRNA-mediated inhibition of TGF-β-WNT crosstalk (Kadota et al., 2021). In addition, exosomes and their cargos, such as miRNAs, lncRNAs, and proteins, could promote or inhibit epithelial-mesenchymal transition (EMT), modulate the transformation of fibroblasts into myofibroblasts, contribute to the proliferation of fibroblasts, and promote immunoregulatory and mitochondrial damage during PF (Xie and Zeng, 2020). Thus, exosomes are emerging as a promising tool for the clinical benefit of cell therapy to treat PF and can potentially reduce the risks associated with cell transplantation (Table 2; Figure 1B).

Potential miRNA targets for pulmonary fibrosis

miR-21-5p: anti-apoptosis

Exosomal miRNAs were found to have potential applications in PF (Inomata et al., 2021; Peng et al., 2022; Yang et al., 2022). Since miR-21-5p is regarded as an oncogene in lung cancer, since the expression of miR-21-5p was significantly upregulated in patients with lung cancer, and it can be used as a biomarker for lung cancer (Zhou et al., 2022). Yan et al. (2018) reported that miR-21-5p inhibited TGF-βI to induce cell proliferation in NSCLC, while Tang et al. (2021) revealed that this miRNA boosted NSCLC progression by regulating SMAD7. Inhibition of miR-21-5p increased radiosensitivity in NSCLC (Song et al., 2017). The anti-apoptosis mechanism of miR-21-5p was subsequently investigated and was also found to play a role in many other lung diseases. Wu et al. (2022) indicated that ADMSC-EVs carrying miR-21-5p alleviated hyperoxia-induced lung injury (HILI) *via* the SKP2/Nr2f2/C/EBPα axis, and miR-21-5p could inhibit MAP2K3 expression and reduce cellular apoptosis in HILI (Qi et al., 2021). Liu et al. (2020) proved that miR-21-5p regulated hyperoxia-induced mitophagy and mitochondrial dysfunction by directly binding to the target gene PGAM5 (Liu et al., 2020). Moreover, miR-21-5p inhibited apoptosis of AEC II cells *via* PTEN/AKT in a hyperoxic acute lung injury rat model (Qin et al., 2019). Wang et al. (2018) demonstrated that resveratrol alleviated PF by regulating miR-21 through both the TGF-β1/SMAD and MAPK/AP-1 signaling pathways. Moreover, extracellular vesicles from MSCs pre-exposed to hypoxia exhibited increased miR-21-5p, which can promote lung cancer development by reducing apoptosis and promoting macrophage M2 polarization (Ren et al., 2019). In addition, exosomes from MSCs alleviated lung ischemia/reperfusion injury by delivering miR-21-5p targeting PTEN and PDCD4 (Ren et al., 2019). Administration of MSCs-derived exosomes or miR-21-5p agomir reduced pulmonary edema and dysfunction, M1 polarization of alveolar macrophages, and secretion of high mobility group box 1(HMGB1), IL-8, IL-1β, IL-6, IL-17, and TNF-α (Li et al., 2019). In conclusion, the above changes indicate a potential mechanism by which miR-21-5p regulates apoptotic/anti-apoptotic alterations in lung disease (Table 3).

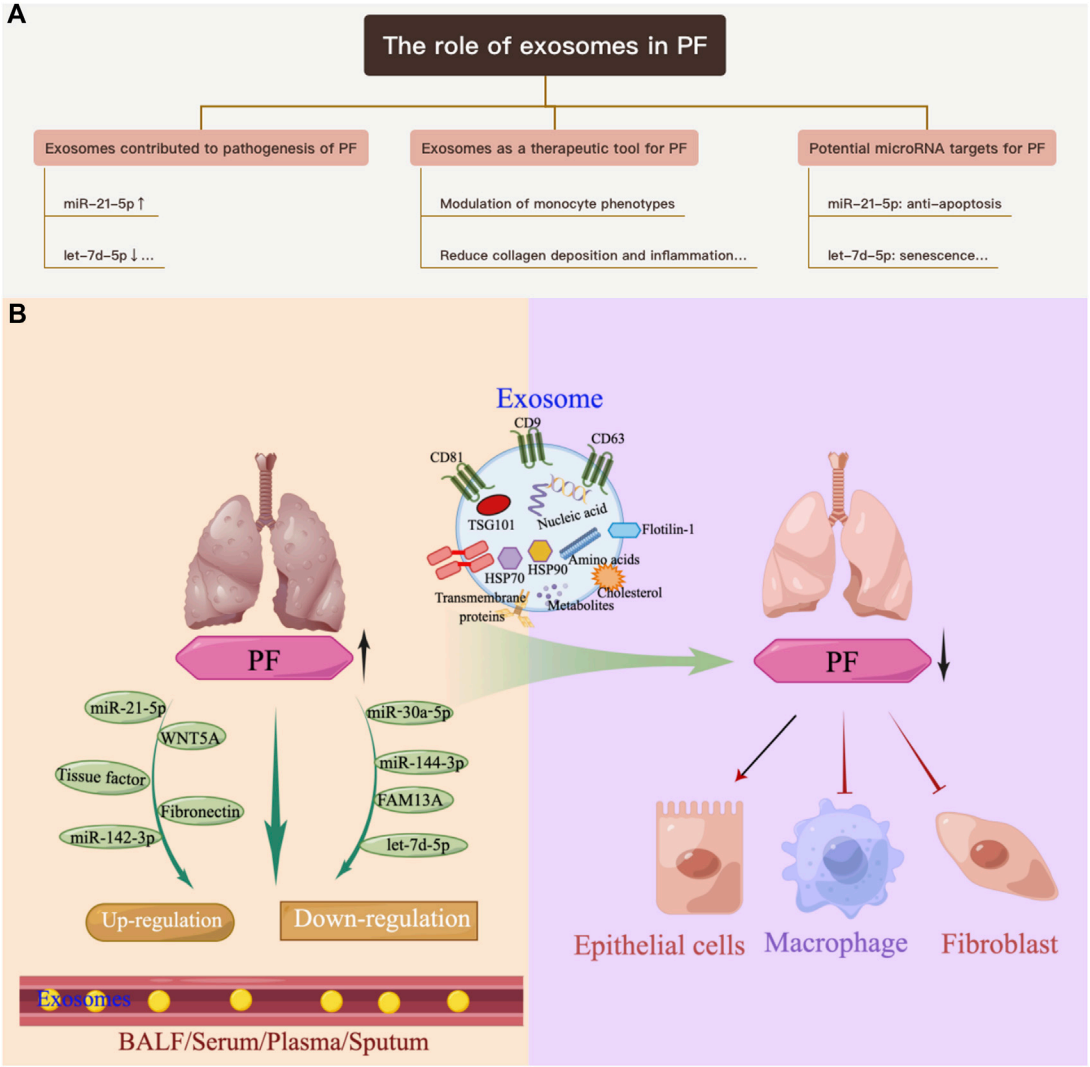

FIGURE 1
Overview of the role of exosomes in PF. **(A)** Exosomes contribute to the pathogenesis of PF. **(B)** Exosomes as a therapeutic tool for pulmonary PF.

Let-7d-5p: senescence

Previous studies revealed that let-7d-5p plays a key role in regulating the cell cycle and senescence, differentiation, and carcinogenesis (Markopoulos et al., 2017; Chen Y. N. et al., 2019). In addition, let-7d-5p affected the stemness and differentiation of MSCs, while transfection of fibroblasts with let-7d-5p reduced the expression of mesenchymal markers (Huleihel et al., 2014). In recent years, the role of let-7d-5p in degenerative diseases such as Alzheimer's disease and amyotrophic lateral sclerosis has been investigated, and it was significantly downregulated in both diseases (Kumar et al., 2013; Mendes-Silva et al., 2016; Chen et al., 2018; Liguori et al., 2018). Moreover, let-7d-5p showed anti-inflammatory properties and inhibited intestinal epithelial cell apoptosis in necrotizing enterocolitis of neonatal rats by negatively regulating the LGALS3-dependent TLR4/NF-κB signaling pathway (Sun et al., 2020). The expression of let-7d-5p was downregulated both in the skin of systemic sclerosis and in the lungs of PF (Bagnato et al., 2017). Furthermore, when patients had both acute exacerbation and stable PF, let-7d-5p expression was downregulated compared with controls (Min et al., 2016). Significant downregulation of let-7d-5p was also observed in the serum of patients with NSCLC, and its expression could predict overall survival (Gasparini et al.,

TABLE 2 Application of exosomes in experimental models of pulmonary fibrosis.

Author	Cell source	Model	Target	Reference
Dinh	Lung spheroid cell, hBM-MSC	Bleomycin, silica	Regulate miR-99a-5p, miR-100-5p, miR-30a-3p, let-7 family	Dinh et al. (2020)
Mansouri	hBM-MSC	Bleomycin	Modulation of monocyte phenotypes	Mansouri et al. (2019)
Wan	hBM-MSC	Bleomycin	Regulate miR-29b-3p and frizzled 6; inhibit fibroblast proliferation, migration, invasion, and differentiation	Wan et al. (2020)
Choi	hBM-MSC	Silica	Reduce collagen deposition and inflammation	Choi et al. (2014)
Phinney	hBM-MSC, mBM-MSC	Silica	Regulate miR-451a, miR-1202, miR-630, miR-638; inhibit toll-like receptor signaling in macrophages	Phinney et al. (2015)
Shentu	hBM-MSC	TGF-β-stimulated myofibroblast	Regulate miR-199a/b-3p, miR-21-5p, miR-630, miR-22-3p, miR-196a-5p, miR-199b-5p, miR-34a-5p, and miR-148a-3p	Shentu et al. (2017)
Bandeira	hAD-MSC	Silica	Reduce collagen fiber content, size of granuloma, number of macrophages, and IL-1β, TGF-β	Bandeira et al. (2018)
Gao	hAD-MSC	PM2.5	Regulate let-7-5p, TGF-βR1; reduce apoptosis and necrosis, ROS, inflammation	Gao et al. (2020)
Lei	Placenta MSCs	Radiation	Regulate miR-214-3p, ATM/P53/P21; inhibit vascular damage, inflammation, and fibrosis	Lei et al. (2020)
Sun	Menstrual blood stem cells	Bleomycin	Regulate let-7-5p; regulates ROS, mtDNA damage, NLRP3 inflammasome activation	Sun L. et al. (2019)
Guiot	Macrophage	TGF-β stimulated cells	Regulate miR-142-3p, TGF-βR1	Guiot et al. (2020)
Kadoda	Human bronchial epithelial cell	Bleomycin	Inhibit TGF-β-mediated induction of both myofibroblast differentiation and lung epithelial cellular senescence by attenuating WNT signaling	Kadota et al. (2021)
Xie	Bone marrow mesenchymal stem cells (BMSCs)	Under pathological and physiological conditions	May promote or inhibit EMT of type II alveolar epithelial cells and the transformation of fibroblasts into myofibroblasts	Xie and Zeng, (2020)

TABLE 3 The roles of miR-21-5p in lung disease.

Author	Disease	Target/pathway	Role	Expression	Reference
Zhou	NSCLC	—	Biomarker	↑	Zhou et al. (2022)
Yan	NSCLC	TGF-βI	Induce cell proliferation	↑	Yan et al. (2018)
Tang	NSCLC	SMAD7	Boost NSCLC progression	↑	Tang et al. (2021)
Song	NSCLC	—	Decrease radiosensitivity	↑	Song et al. (2017)
Wu	HILI	SKP2/Nr2f2/C/EBPα axis	Alleviate HILI	—	Wu et al. (2022)
Qi	HILI	MAP2K3	Reduce cellular apoptosis	—	Qi et al. (2021)
Liu	HILI	PGAM5	Regulate hyperoxia-induced mitophagy and mitochondrial dysfunction	—	Liu et al. (2020)
Qin	Hyperoxic acute lung injury	PTEN/AKT	Inhibit apoptosis of AEC II cells	—	Qin et al. (2019)
Wang	PF	TGF-β1/SMAD and MAPK/AP-1 signaling pathways	Alleviate PF	—	Wang et al. (2018)
Ren	Lung cancer	PTEN, PDCD4, and RECK	Promote lung cancer development	—	Ren et al. (2019)
Li	Lung ischemia/reperfusion injury	PTEN and PDCD4	Alleviate lung ischemia/reperfusion injury	—	Li et al. (2019)

TABLE 4 The roles of let-7d-5p in lung disease.

Author	Disease	Target/pathway	Role	Expression	Reference
Chen; Kumar; Mendes-Silva	Alzheimer's diseaseAlzheimer's disease	—	—	↓	Kumar et al. (2013); Mendes-Silva et al. (2016); Chen et al. (2018)
Liguori	Amyotrophic lateral sclerosis	—	—	↓	Liguori et al. (2018)
Sun	Necrotizing enterocolitis of neonatal rats	LGALS3-dependent TLR4/NF-κB signaling pathway	Anti-inflammatory properties and inhibited intestinal epithelial cell apoptosis	—	Sun et al. (2020)
Bagnato; Min	PF	—	—	↓	Min et al. (2016); Bagnato et al. (2017)
Gasparini; Kumar	NSCLC	—	Biomarker	↓	Gasparini et al. (2015); Kumar et al. (2020)
Gan	Lung cancer	NAP1L1	Repress angiogenesis	↓	Gan et al. (2022)
Ideozu	cystic fibrosis	—	—	↑	Ideozu et al. (2019)
Min	lung cysts/pneumothorax presentation of Birt-Hogg-Dubé Syndrome	—	—	↑	Min et al. (2020)
Tasena	COPD	—	—	↑	Tasena et al. (2018)
Gao	PF	TGF-ßRI	Mitigate PF	—	Gao et al. (2020)

2015; Kumar et al., 2020). The fungus *Trametes robiniophila*, which is used as a traditional Chinese medicine, represses angiogenesis and tumor growth of lung cancer via strengthening let-7d-5p and targeting NAP1L1 (Gan et al., 2022). In contrast, overexpression of let-7d-5p was detected in cystic fibrosis (Ideozu et al., 2019), lung cysts/pneumothorax presentation of Birt-Hogg-Dubé Syndrome (Min et al., 2020), and chronic mucus hypersecretion in COPD (Tasena et al., 2018). Furthermore, ADSCs-EVs inhibited TGF-βRI by transferring let-7d-5p and further mitigated PF (Gao et al., 2020). Given that let-7d-5p is highly enriched in stem cells such as MSCs, therapies with cells or cell-free exosomes provide novel strategies for various diseases (Table 4).

miR-100-5p: regulator of mammalian target of rapamycin

Accumulating studies have reported that miR-100 is a master regulator of PI3K/AKT/mTOR signaling in different diseases. The PI3K/AKT/mTOR signaling pathway is a critical regulator of cell growth and proliferation as well as stress responses. Wang et al. (2015) found that miR-100 regulated the proliferation of pulmonary artery smooth muscle cells in hypoxic pulmonary hypertension rats by inhibiting the expression of mTOR. Subsequently, miR-100-5p was confirmed to directly target the 3′-untranslated region (3′-UTR) of mTOR (Wu et al., 2019). Ye et al. (2015) reported that miR-100-5p promoted cell apoptosis and affected cell survival in amyloid *ß*-induced neuronal pathologies via the mTOR pathway, and Frith et al. (2018) demonstrated that miR-100-5p could modulate the fate of MSCs by altering mTOR signaling. A significant upregulation of mTOR was found in fibroproliferative diseases, suggesting mTOR inhibitors could be promising modulators of such diseases, including PF and liver fibrosis (Lawrence and Nho, 2018; Wang et al., 2019). Moreover, upregulation of miR-100-5p was also observed in PF and liver fibrosis (Peng et al., 2016; Liu et al., 2018), and it was assumed that miR-100-5p was a responsive factor rather than a pathogenic factor. Therefore, it is feasible that miR-100-5p could be utilized to repress mTOR expression and may be a potential therapy target for diseases. For example, miR-100-5p-abundant exosomes derived from MSCs provided a protective effect on articular cartilage and inhibited cell apoptosis in osteoarthritis (Wu et al., 2019). In a study by Dinh et al. (2020), miR-99a-5p and miR-100 were highly expressed in exosomes from lung spheroid cells and MSCs, and upregulated expression of miR-100 was identified in the exosomes of chronic PM2.5 exposure (Wang Y. C. et al., 2021). ReNcell-derived EVs inhibited hypoxia-induced proliferation, migration, and phenotype switching of pulmonary artery smooth muscle cells, at least in part, *via* the delivery of endogenous highly expressed miRNAs, let-7b-5p, miR-92b-3p, and miR-100-5p (Wang et al., 2020). These studies highlight that miR-100-5p can act as a potential target for fibroproliferative disease treatment (Table 5).

TABLE 5 The roles of miR-100-5p in lung disease.

Author	Disease	Target/ pathway	Role	Expression	Reference
Wang	Hypoxic pulmonary hypertension	mTOR	Regulate the proliferation of pulmonary artery smooth muscle cells	—	Wang et al. (2015)
Ye	Amyloid *β*-induced neuronal pathologies	mTOR pathway	Promote cell apoptosis and affect cell survival	—	Ye et al. (2015)
Frith	—	mTOR pathway	Modulate MSC fate		Frith et al. (2018)
Liu; Peng	PF and liver fibrosis	—	—	↑	Peng et al. (2016); Liu et al. (2018)
Wu	Osteoarthritis	mTOR	Provide a protective effect on articular cartilage and inhibit cell apoptosis	—	Wu et al. (2019)
Dinh	Exosomes from lung spheroid cells	—	—	↑	Dinh et al. (2020)
Wang	MSCs and chronic PM2.5 exposure	—	—	↑	Wang Y. et al. (2021)
Wang	—	—	Inhibit hypoxia-induced proliferation, migration, and phenotype switching of pulmonary artery smooth muscle cells	—	Wang et al. (2020)

miR-142-3p: antifibrosis

It was reported that miR-142-3p is highly expressed in the lung interstitium during early lung development (Carraro et al., 2014). This miRNA positively regulates WNT/CTNNB1 (β-catenin) signaling by targeting adenomatous polyposis (APC), which is a negative regulator of WNT signaling (Isobe et al., 2014; Bartel et al., 2018). Impaired proliferation of parabronchial smooth muscle cell progenitors and premature differentiation occurred when miR-142-3p lost its function (Carraro et al., 2014). Aberrant expression of miR-142-3p in PF has been reported. However, the changes in miR-142-3p in patients with PF versus healthy controls are under debate (Guo et al., 2017; Njock et al., 2019; Parimon et al., 2019). WNT/β-catenin signaling has also been reported to be activated in PF. In experimental models, inhibition of WNT/β-catenin signaling reduces lung inflammation and fibrosis (Shi et al., 2017). All the research teams that conducted the above-mentioned studies believed that miR-142-3p was an antifibrotic miRNA. Moreover, Wang et al. (2016) found that overexpression of miR-142-3p suppressed the expression of profibrotic genes in cardiomyocytes by targeting HMGB1. In addition, Yang X. et al. (2017) revealed that plasma miR-142-3p levels were significantly decreased in patients with liver cirrhosis, and that miR-142-3p inhibited the TGF-β/SMAD signaling pathway to prevent hepatic stellate cell activation and reduce profibrotic markers. Zhu et al. (2018) demonstrated that overexpression of miR-142-3p attenuated high glucose-induced EMT in aortic endothelial cells by blocking the TGF-β1/SMAD signaling pathway in myocardial fibrosis, which confirmed the antifibrotic role of miR-142-3p. Consequently, Guiot et al. (2020) utilized miR-142-3p-enriched exosomes derived from macrophages to repress TGF-βR1, leading to antifibrotic properties in PF. However, contrary to these findings, some profibrotic conclusions of miR-142-3p have recently emerged, as reported by Cai et al. (2020). Thus, miR-142-3p warrants further investigation for future therapeutic use (Table 6).

miR-29b-3p regulates collagen synthesis

The miR-29 family is considered a key regulator of tissue fibrosis, including heart, liver, lung, and kidney, as many reports have shown that members of this family inhibit collagen synthesis by directly binding to its 3′UTR in fibroblasts (He et al., 2013; Deng et al., 2017). Recently, accumulative reports demonstrated that miR-29b-3p regulated the TGF-β1/SMAD pathway in cardiac fibrosis (Liang et al., 2019; Xue et al., 2020). Moreover, the expression of miR-29b-3p was decreased in liver fibrosis, and miR-29b-3p overexpression repressed collagenous fibrosis and STAT3 (Tao et al., 2018; Gong et al., 2020). Lu et al. (2017) also reported that the lncRNA H19 promoted tendon differentiation by directly targeting miR-29b-3p, thus activating TGF-β1 and COL1A1 expression. In PF, downregulation of miR-29b-3p was detected (Mullenbrock et al., 2018), and downregulation of miR-29b promoted PF *via* the TGF-β1/SMAD pathway (Cushing et al., 2011; Pandit et al., 2011; Cushing et al., 2015). Conversely, overexpression of miR-29 prevented bleomycin-induced fibrosis as assessed by hydroxyproline content and collagen I mRNA expression (Cushing et al., 2015), suggesting that miR-29b might have a significant antifibrotic effect. In particular, miR-29b-3p-enriched BM-MSC exosomes suppressed fibroblast proliferation and decreased the level of hydroxyproline in the lung of a bleomycin-induced PF model (Wan et al., 2020). In

TABLE 6 The roles of miR-142-3p in lung disease.

Author	Disease	Target/pathway	Role	Expression	Reference
Carraro	—	—	Early lung development	↑	Carraro et al. (2014)
Isobe; Bartel	Breast cancer; asthma	WNT/CTNNB1 (β-catenin)	Regulate the tumorigenicity	—	Isobe et al. (2014); Bartel et al. (2018)
Guo	PF	Cox-2	Inhibit apoptosis and inflammation	—	Guo et al. (2017)
Njock	IPF	—	—	↑	Njock et al. (2019)
Parimon	PF	—	—	↓	Parimon et al. (2019)
Wang	PF	High mobility group box 1	Suppress the expression of profibrotic genes	—	Wang et al. (2016)
Yang	Liver cirrhosis	TGF-β/SMAD signaling pathway	Prevent hepatic stellate cell activation and reduce profibrotic markers	—	Yang X. et al. (2017)
Zhu	Myocardial fibrosis	TGF-β1/SMAD signaling pathway	Attenuate high glucose-induced EMT in aortic endothelial cells	—	Zhu et al. (2018)
Guiot	PF	TGF-βR1	Antifibrotic properties	—	Guiot et al. (2020)
Cai	Myocardial fibrosis	—	Profibrotic properties	—	Cai et al. (2020)

TABLE 7 The roles of miR-29b-3p in lung disease.

Author	Disease	Target/pathway	Role	Expression	Reference
Deng; He	Tissue fibrosis (including heart, liver, lung and kidney)	Binding to the 3′UTR	Inhibit collagen synthesist	—	He et al. (2013); Deng et al. (2017)
Liang; Xue	Cardiac fibrosis	TGF-β1/SMAD pathway	—	—	Liang et al. (2019); Xue et al. (2020)
Gong; Tao	Liver fibrosis	STAT3	Repress collagenous fibrosis	↓	Tao et al. (2018); Gong et al. (2020)
Lu	Liver fibrosis	TGF-β1	Activate COL1A1 expression	—	Lu et al. (2017)
Mullenbrock; Cushing; Pandit	PF	TGF-β1/SMAD pathway	Downregulate miR-29b and promote PF	↓	Cushing et al. (2011); Pandit et al. (2011); Cushing et al. (2015); Mullenbrock et al. (2018)
Wan	PF	—	Suppress fibroblast proliferation and decrease the level of hydroxyproline	—	Wan et al. (2020)

summary, drugs targeting miR-29b-3p could be considered as potential therapeutics for fibroproliferative diseases (Table 7).

miR-22-3p: tissue-specific regulator of fibrogenesis

MiR-22 has been proven to directly regulate bone morphogenic protein (BMP) by binding to its 3′UTR (Long et al., 2013). However, the effect of miR-22 on BMP seems to be tissue specific. For instance, an association between miR-22 and renal tubulointerstitial fibrosis was reported (Zhang et al., 2018), and similarly, miR-22 could promote the development of liver cirrhosis through BMP7 suppression in some studies (Ji et al., 2015; Zhou et al., 2018). The lncRNA Neat1 expedited the progression of liver fibrosis in mice through targeting miR-148a-3p and miR-22-3p to upregulate Cyth3 (Huang et al., 2021), and miR-30b-5p and miR-22-3p restrained fibrogenesis post-MI in mice *via* targeting PTAFR (Zhao et al., 2020). However, in contrast to these findings, downregulation of miR-22 increased the expression of collagen and fibrogenesis *in vitro*, whereas overexpression of miR-22 alleviated angiotensin II-induced cardiac fibrosis, indicating an antifibrotic effect of miR-22 (Hong et al., 2016). miR-22 expression was increased after bleomycin-induced PF in mice, while administration of an miR-22 mimic ameliorated lung lesions and decreased α-SMA expression (Kuse et al., 2020). Furthermore, miR-22 in MSC-derived extracellular vesicles was beneficial for PF (Shentu et al., 2017), demonstrating its antifibrotic effect in the lung. Due to the contrasting effects of miR-22 on fibrogenesis in different organs, local application of treatments is suggested to lessen the side effects of systemic administration (Table 8).

TABLE 8 The roles of miR-22-3p in lung disease.

Author	Disease	Target/pathway	Role	Expression	Reference
Long	Kidney fibrosis	Bone morphogenic protein (BMP)	Alleviate kidney fibrosis	—	Long et al. (2013)
Zhang	Renal tubulointerstitial fibrosis	—	—	—	Zhang et al. (2018)
Ji; Zhou	Liver fibrosis	BMP7	Promote the development of tissue cirrhosis	—	Ji et al. (2015); Zhou et al. (2018)
Huang	Liver fibrosis	Cyth3	Promote the development of tissue cirrhosis	—	Huang et al. (2021)
Zhao	Liver fibrosis	PTAFR	Promote the development of tissue cirrhosis	—	Zhao et al. (2020)
Hong	Cardiac fibrosis	—	Alleviate dangiotensin II-induced cardiac fibrosis	—	Hong et al. (2016)
Kuse; Shentu	PF	α-SMA	Antifibrotic effect in the lung	—	Shentu et al. (2017); Kuse et al. (2020)

TABLE 9 The roles of miR-15a in lung disease.

Author	Disease	Target/pathway	Role	Expression	Reference
Tijsen	Cardiac hypertrophy and fibrosis	TGF-β	Exacerbate cardiac hypertrophy and fibrosis	—	Tijsen et al. (2014)
Rawal; Jin	Diabetic cardiac fibroblasts	—	Suppress the activation of diabetic cardiac fibroblasts	↓	Rawal et al. (2017); Jin (2021)
Fu	Hepatic fibrosis	SOX9	Inhibit LX-2 cell viability and hepatic fibrosis	—	Fu et al. (2022)
Chen; Sun	PF	YAP1	Inhibit the activation of fibroblasts	↓	Chen Y. et al. (2019); Sun J. et al. (2019)
Kuse	PF	—	—	↑	Kuse et al. (2020)

miR-15a: Hippo-YAP mediator

Growing evidence implicates miR-15a in the cell cycle and fibrotic diseases. Tijsen et al. (2014) found that inhibiting miR-15a exacerbated cardiac hypertrophy and fibrosis in mice by manipulating TGF-β. Inhibition of miR-15a/b also promoted fibrotic remodeling in type 2 diabetic hearts, whereas overexpression of miR-15a/b suppressed the activation of diabetic cardiac fibroblasts (Rawal et al., 2017). Furthermore, miR-15a/-15b, miR-18a-5p, miR-20a-5p, miR-26b-5p, miR-29, miR-133a, miR-141, miR-146, miR-200b, miR-203, miR-222, and miR-551b-5p were all downregulated in the diabetic heart and exhibited antifibrosis activity when they were overexpressed (Jin 2021). Fu et al. (2022) reported that miR-15a could inhibit LX-2 cell viability and hepatic fibrosis pathogenesis by targeting SOX9. However, the role and mechanism of miR-15a in PF remain controversial. MiR-15a was one of 161 miRNAs that were previously reported to be differentially expressed in the lungs of bleomycin-treated and control mice (Xie et al., 2011). Recently, miR-15a was discovered to be one of the most important miRNAs regulating the Hippo pathway, and knockdown of miR-15a promoted Twist expression by targeting YAP1, resulting in fibroblast activation and lung fibrosis (Chen Y. et al., 2019). In contrast, the lncRNA PFAR was proven to participate in PF by binding to and sponging miR-15a and by regulating the expression of YAP1 (Sun J. et al., 2019). Restoration of miR-15a can inhibit fibrogenesis (Chen Y. et al., 2019; Sun J. et al., 2019). However, according to Kuse et al. (2020), the expression of miR-15a in exosomes was strongly upregulated in bleomycin-induced PF. The reason for this discrepancy has yet to be elucidated; therefore, the use of miR-15a, especially that from exosomes, as a diagnostic and therapeutic target remains to be determined (Table 9).

miR-23 regulates epithelial–mesenchymal transition

MiR-23 belongs to the miR-23/24/27 cluster and is highly correlated with cell proliferation, differentiation, invasion,

TABLE 10 The roles of let-7d-5p in lung disease.

Author	Disease	Target/ pathway	Role	Expression	Reference
Cao; Zheng	Cancer	EMT	Correlate with cell proliferation, differentiation, invasion, migration	—	Cao et al. (2012); Zheng et al. (2014)
Yang; Rogler	Liver fibrosis	COLA1 and ACTA2	Reverse TGF-β-induced liver fibrosis	↓	Yang L. et al. (2017); Rogler et al. (2017)
Kuse; Fang; Tan; Shi	PF	TGF-β/SMAD pathway	Alleviate PF	—	Fang et al. (2016); Tan et al. (2018); Kuse et al. (2020); Shi et al. (2021)

migration, and EMT in cancer (Cao et al., 2012; Zheng et al., 2014). Previous research demonstrated that miR-23 was significantly increased in high glucose-treated EMT in mesothelial peritoneal cells, and inhibition of miR-23 attenuated the process of EMT (Yang L. et al., 2017). Similarly, knockdown of miR-23b could reverse TGF-β-induced liver fibrosis by regulating COLA1 and ACTA2 expression and stellate cell activation (Rogler et al., 2017). Aberrant expression of miR-23a-3p, miR-23b-3p, and miR-23b-5p was recently detected in PF (Kuse et al., 2020). However, exosomal miR-23a inhibited myofibroblast differentiation through inhibition of the TGF-β/SMAD pathway during wound healing (Fang et al., 2016), and was thus used in the experimental treatment of PF (Tan et al., 2018). Moreover, extracellular vesicles derived from umbilical cord MSCs enriched with miR-23 alleviated PF by inhibition of TGF-β signaling (Shi et al., 2021). The precise effect and mechanism of the miR-23 family requires further investigation (Table 10).

Discussion and future perspectives

Interest in the contribution of exosomes to the maintenance of lung homeostasis and the progression of PF, as well as the potential therapeutic utilization of exosomes, has increased substantially in recent years. Exosomes are critical for intercellular communication, immune response, immune regulation, inflammation, and cell phenotype transformation, and play a vital role in PF. This review summarized recent advances regarding the status of exosomes as potential biomarkers and therapeutic tools in PF. The potential involvement of exosomes in the pathological process of PF was first reviewed by describing the relevant characteristics of exosomes in PF, which highlights the potential value of exosomes as PF markers and therapeutic targets. Second, mouse *in vivo* and *in vitro* models were reviewed to demonstrate that multiple sources of exosomes have therapeutic effects on PF. These studies have collectively indicated that exosomes can be used as a therapeutic tool for PF and can reduce the risk associated with cell engraftment. Furthermore, exosomes have the potential to develop cell-free therapies. The main contents of exosomes are discussed, and the potential miRNA targets of PF are enumerated to highlight future research directions for elucidating the mechanism of exosomes in the treatment of PF. Exploration of the functional properties of exosomes in the context of PF could also reveal new avenues for therapeutic approaches.

Exosomes have potential clinical application value as a therapeutic tool for PF. However, several issues need to be addressed before they can be used in clinics. First, the characteristics and functions of exosomes derived from multiple types of cells should be extensively studied for safety aspects in future clinical applications. Exosomes can target several signaling pathways and molecules and therefore may induce previously unknown effects. Furthermore, treatments aimed at specific targets can cause persistent or lethal outcomes. Thus, thorough investigations of exosomes should be conducted to provide comprehensive information. Second, the exosomes need to be delivered with precision. Identification of target cells and limiting the destination to specific cells, for instance, fibroblasts/myofibroblasts, abnormal alveolar epithelial cells or immune cells in PF, should be performed to accurately interpret and correct the biological function. Finally, a manufacturing practice-grade standard protocol for the isolation and utilization of cell-free exosomes should be proposed. For the use of exosomes as diagnostic, prognostic, and therapeutic targets, the related protocols should be optimized and standardized to minimize variations due to technical issues.

There are some limitations to this review. First, when discussing exosomes as a potential therapeutic tool for PF, the mechanism of action was not explored in depth; only the potential miRNA targets were listed, and the description focused on the role of exosomes through miRNAs. Second, the review does not systematically discuss the major cells in PF that are altered by exosomes—fibroblasts, epithelial cells, and macrophages—so the specific cellular targets of exosomes in PF remain unclear, and further discussion on the mechanism of action is needed. In addition, each miRNA is known to have multiple targets. For example, miR-21-5p could alleviate HILI via the SKP2/Nr2f2/C/EBPα axis (Wu et al., 2022), PTEN/

AKT signaling (Qin et al., 2019), inhibition of MAP2K3 (Qi et al., 2021) or by directly binding to the target gene PGAM5 (Liu et al., 2020). Although a single miRNA can often regulate multiple targets within a pathway or network, there are also risks of unpredictable and opposite effects on additional miRNA targets. Sun et al. (2015) demonstrated that miR-214 mediates cardiac fibroblast proliferation and collagen synthesis via inhibition of Mfn2 and activation of ERK1/2 MAPK signaling, but Dong et al. (2016) reported that miR-214 exerts cardio-protective effects by inhibition of fibrosis, and the inhibitory effect involves TGF-β1 suppression and MMP-1/TIMP-1 regulation. It is therefore feasible that the use of miRNA for disease therapy might have adverse implications for other essential biological pathways. Before clinical application in PF, further experiments are needed to explore the targets of miRNAs and their mimics *in vivo* and to determine their effects on other signaling pathways to avoid potential adverse effects.

Author contributions

YY and HH performed data collection and analysis. YL contributed to the study's conception and design.

Funding

The research leading to these results has received funding from the China Postdoctoral Science Foundation (2018M643504), the PostDoctor Research Project, West China Hospital, Sichuan University (2020HXBH089) and Sichuan University Full-time Postdoctoral Research and Development Fund (2020SCU12023).

Conflict of interest

The authors declare that the research was conducted in the absence of any commercial or financial relationships that could be construed as a potential conflict of interest.

Publisher's note

References

Admyre, C., Grunewald, J., Thyberg, J., Gripenbäck, S., Tornling, G., Eklund, A., et al. (2003). Exosomes with major histocompatibility complex class II and co-stimulatory molecules are present in human BAL fluid. *Eur. Respir. J.* 22 (4), 578–583. doi:10.1183/09031936.03.00041703

Bagnato, G., Roberts, W. N., Roman, J., and Gangemi, S. (2017). A systematic review of overlapping microRNA patterns in systemic sclerosis and idiopathic pulmonary fibrosis. *Eur. Respir. Rev.* 26 (144), 160125. doi:10.1183/16000617.0125-2016

Bandeira, E., Oliveira, H., Silva, J. D., Menna-Barreto, R. F. S., Takyia, C. M., Suk, J. S., et al. (2018). Therapeutic effects of adipose-tissue-derived mesenchymal stromal cells and their extracellular vesicles in experimental silicosis. *Respir. Res.* 19 (1), 104. doi:10.1186/s12931-018-0802-3

Bartel, S., Carraro, G., Alessandrini, F., Krauss-Etschmann, S., Ricciardolo, F. L. M., and Bellusci, S. (2018). miR-142-3p is associated with aberrant WNT signaling during airway remodeling in asthma. *Am. J. Physiol. Lung Cell. Mol. Physiol.* 315 (2), L328–L333. doi:10.1152/ajplung.00113.2018

Cai, L., Chao, G., Li, W., Zhu, J., Li, F., Qi, B., et al. (2020). Activated CD4(+) T cells-derived exosomal miR-142-3p boosts post-ischemic ventricular remodeling by activating myofibroblast. *Aging (Albany NY)* 12 (8), 7380–7396. doi:10.18632/aging.103084

Cao, M., Seike, M., Soeno, C., Mizutani, H., Kitamura, K., Minegishi, Y., et al. (2012). MiR-23a regulates TGF-β-induced epithelial-mesenchymal transition by targeting E-cadherin in lung cancer cells. *Int. J. Oncol.* 41 (3), 869–875. doi:10.3892/ijo.2012.1535

Carraro, G., Shrestha, A., Rostkovius, J., Contreras, A., Chao, C. M., El Agha, E., et al. (2014). miR-142-3p balances proliferation and differentiation of mesenchymal cells during lung development. *Development* 141 (6), 1272–1281. doi:10.1242/dev.105908

Chanda, D., Otoupalova, E., Hough, K. P., Locy, M. L., Bernard, K., Deshane, J. S., et al. (2019). Fibronectin on the surface of extracellular vesicles mediates fibroblast invasion. *Am. J. Respir. Cell Mol. Biol.* 60 (3), 279–288. doi:10.1165/rcmb.2018-0062OC

Chen, J., Qi, Y., Liu, C. F., Lu, J. M., Shi, J., and Shi, Y. (2018). MicroRNA expression data analysis to identify key miRNAs associated with Alzheimer's disease. *J. Gene Med.* 20 (6), e3014. doi:10.1002/jgm.3014

Chen, L., Yang, Y., Yue, R., Peng, X., Yu, H., and Huang, X. (2022). Exosomes derived from hypoxia-induced alveolar epithelial cells stimulate interstitial pulmonary fibrosis through a HOTAIRM1-dependent mechanism. *Lab. Invest* online ahead of print. doi:10.1038/s41374-022-00782-y

Chen, Y. N., Ren, C. C., Yang, L., Nai, M. M., Xu, Y. M., Zhang, F., et al. (2019). MicroRNA let-7d-5p rescues ovarian cancer cell apoptosis and restores chemosensitivity by regulating the p53 signaling pathway via HMGA1. *Int. J. Oncol.* 54 (5), 1771–1784. doi:10.3892/ijo.2019.4731

Chen, Y., Zhao, X., Sun, J., Su, W., Zhang, L., Li, Y., et al. (2019). YAP1/Twist promotes fibroblast activation and lung fibrosis that conferred by miR-15a loss in IPF. *Cell Death Differ.* 26 (9), 1832–1844. doi:10.1038/s41418-018-0250-0

Choi, M., Ban, T., and Rhim, T. (2014). Therapeutic use of stem cell transplantation for cell replacement or cytoprotective effect of microvesicle released from mesenchymal stem cell. *Mol. Cells* 37 (2), 133–139. doi:10.14348/molcells.2014.2317

Cushing, L., Kuang, P., and Lü, J. (2015). The role of miR-29 in pulmonary fibrosis. *Biochem. Cell Biol.* 93 (2), 109–118. doi:10.1139/bcb-2014-0095

Cushing, L., Kuang, P. P., Qian, J., Shao, F., Wu, J., Little, F., et al. (2011). miR-29 is a major regulator of genes associated with pulmonary fibrosis. *Am. J. Respir. Cell Mol. Biol.* 45 (2), 287–294. doi:10.1165/rcmb.2010-0323OC

Deng, Z., He, Y., Yang, X., Shi, H., Shi, A., Lu, L., et al. (2017). MicroRNA-29: A crucial player in fibrotic disease. *Mol. Diagn. Ther.* 21 (3), 285–294. doi:10.1007/s40291-016-0253-9

Dinh, P.-U. C., Paudel, D., Brochu, H., Popowski, K. D., Gracieux, M. C., Cores, J., et al. (2020). Inhalation of lung spheroid cell secretome and exosomes promotes lung repair in pulmonary fibrosis. *Nat. Commun.* 11 (1), 1064. doi:10.1038/s41467-020-14344-7

Dong, H., Dong, S., and Zhang, L. (2016). MicroRNA-214 exerts a cardio-protective effect by inhibition of fibrosis. *Anat. Rec. (Hoboken)* 299 (10), 1348–1357. doi:10.1002/ar.23396

Fang, S., Xu, C., Zhang, Y., Xue, C., Yang, C., Bi, H., et al. (2016). Umbilical cord-derived mesenchymal stem cell-derived exosomal microRNAs suppress myofibroblast differentiation by inhibiting the transforming growth factor-β/

SMAD2 pathway during wound healing. *Stem Cells Transl. Med.* 5 (10), 1425–1439. doi:10.5966/sctm.2015-0367

Frith, J. E., Kusuma, G. D., Carthew, J., Li, F., Cloonan, N., Gomez, G. A., et al. (2018). Mechanically-sensitive miRNAs bias human mesenchymal stem cell fate via mTOR signalling. *Nat. Commun.* 9 (1), 257. doi:10.1038/s41467-017-02486-0

Fu, M., Yin, W., Zhang, W., Zhu, Y., Ni, H., and Gong, L. (2022). MicroRNA-15a inhibits hepatic stellate cell activation and proliferation via targeting SRY-box transcription factor 9. *Bioengineered* 13 (5), 13011–13020. doi:10.1080/21655979.2022.2068895

Fujita, Y., Araya, J., Ito, S., Kobayashi, K., Kosaka, N., Yoshioka, Y., et al. (2015). Suppression of autophagy by extracellular vesicles promotes myofibroblast differentiation in COPD pathogenesis. *J. Extracell. Vesicles* 4, 28388. doi:10.3402/jev.v4.28388

Fujita, Y., Kadota, T., Araya, J., Ochiya, T., and Kuwano, K. (2018). Clinical application of mesenchymal stem cell-derived extracellular vesicle-based therapeutics for inflammatory lung diseases. *J. Clin. Med.* 7 (10), 355. doi:10.3390/jcm7100355

Gan, H., Xu, X., and Bai, Y. (2022). Trametes robiniophila represses angiogenesis and tumor growth of lung cancer via strengthening let-7d-5p and targeting NAP1L1. *Bioengineered* 13 (3), 6698–6710. doi:10.1080/21655979.2021.2012619

Gao, Y., Sun, J., Dong, C., Zhao, M., Hu, Y., and Jin, F. (2020). Extracellular vesicles derived from adipose mesenchymal stem cells alleviate PM2.5-induced lung injury and pulmonary fibrosis. *Med. Sci. Monit.* 26, e922782. doi:10.12659/msm.922782

Gasparini, P., Cascione, L., Landi, L., Carasi, S., Lovat, F., Tibaldi, C., et al. (2015). microRNA classifiers are powerful diagnostic/prognostic tools in ALK-EGFR-and KRAS-driven lung cancers. *Proc. Natl. Acad. Sci. U. S. A.* 112 (48), 14924–14929. doi:10.1073/pnas.1520329112

Glass, D. S., Grossfeld, D., Renna, H. A., Agarwala, P., Spiegler, P., DeLeon, J., et al. (2022). Idiopathic pulmonary fibrosis: Current and future treatment. *Clin. Respir. J.* 16 (2), 84–96. doi:10.1111/crj.13466

Gong, X., Wang, X., and Zhou, F. (2020). Liver microRNA-29b-3p positively correlates with relative enhancement values of magnetic resonance imaging and represses liver fibrosis. *J. Biochem.* 168 (6), 603–609. doi:10.1093/jb/mvaa074

Guiot, J., Cambier, M., Boeckx, A., Henket, M., Nivelles, O., Gester, F., et al. (2020). Macrophage-derived exosomes attenuate fibrosis in airway epithelial cells through delivery of antifibrotic miR-142-3p. *Thorax* 75 (10), 870–881. doi:10.1136/thoraxjnl-2019-214077

Guiot, J., Struman, I., Louis, E., Louis, R., Malaise, M., and Njock, M.-S. (2019). Exosomal miRNAs in lung diseases: From biologic function to therapeutic targets. *J. Clin. Med.* 8 (9), 1345. doi:10.3390/jcm8091345

Guo, F., Lin, S. C., Zhao, M. S., Yu, B., Li, X. Y., Gao, Q., et al. (2017). microRNA-142-3p inhibits apoptosis and inflammation induced by bleomycin through down-regulation of Cox-2 in MLE-12 cells. *Braz. J. Med. Biol. Res.* 50 (7), e5974. doi:10.1590/1414-431x20175974

He, Y., Huang, C., Lin, X., and Li, J. (2013). MicroRNA-29 family, a crucial therapeutic target for fibrosis diseases. *Biochimie* 95 (7), 1355–1359. doi:10.1016/j.biochi.2013.03.010

Hong, Y., Cao, H., Wang, Q., Ye, J., Sui, L., Feng, J., et al. (2016). MiR-22 may suppress fibrogenesis by targeting TGFβR I in cardiac fibroblasts. *Cell. Physiol. biochem.* 40 (6), 1345–1353. doi:10.1159/000453187

Hua, Y., Ding, Y., Hou, Y., Liu, Y., Mao, K., Cui, Y., et al. (2021). Exosomal MicroRNA: Diagnostic marker and therapeutic tool for lung diseases. *Curr. Pharm. Des.* 27 (26), 2934–2942. doi:10.2174/1381612827666210608150640

Huang, W., Huang, F., Zhang, R., and Luo, H. (2021). LncRNA Neat1 expedites the progression of liver fibrosis in mice through targeting miR-148a-3p and miR-22-3p to upregulate Cyth3. *Cell Cycle* 20 (5-6), 490–507. doi:10.1080/15384101.2021.1875665

Huleihel, L., Ben-Yehudah, A., Milosevic, J., Yu, G., Pandit, K., Sakamoto, K., et al. (2014). Let-7d microRNA affects mesenchymal phenotypic properties of lung fibroblasts. *Am. J. Physiol. Lung Cell. Mol. Physiol.* 306 (6), L534–L542. doi:10.1152/ajplung.00149.2013

Ideozu, J. E., Zhang, X., Rangaraj, V., McColley, S., and Levy, H. (2019). Microarray profiling identifies extracellular circulating miRNAs dysregulated in cystic fibrosis. *Sci. Rep.* 9 (1), 15483. doi:10.1038/s41598-019-51890-7

Inomata, M., Kamio, K., Azuma, A., Matsuda, K., Usuki, J., Morinaga, A., et al. (2021). Rictor-targeting exosomal microRNA-16 ameliorates lung fibrosis by inhibiting the mTORC2-SPARC axis. *Exp. Cell Res.* 398 (2), 112416. doi:10.1016/j.yexcr.2020.112416

Isobe, T., Hisamori, S., Hogan, D. J., Zabala, M., Hendrickson, D. G., Dalerba, P., et al. (2014). miR-142 regulates the tumorigenicity of human breast cancer stem cells through the canonical WNT signaling pathway. *Elife* 3, e01977. doi:10.7554/eLife.01977

Ji, D., Li, B., Shao, Q., Li, F., Li, Z., and Chen, G. (2015). MiR-22 suppresses BMP7 in the development of cirrhosis. *Cell. Physiol. biochem.* 36 (3), 1026–1036. doi:10.1159/000430276

Jin, Z. Q. (2021). MicroRNA targets and biomarker validation for diabetes-associated cardiac fibrosis. *Pharmacol. Res.* 174, 105941. doi:10.1016/j.phrs.2021.105941

Kadota, T., Fujita, Y., Araya, J., Watanabe, N., Fujimoto, S., Kawamoto, H., et al. (2021). Human bronchial epithelial cell-derived extracellular vesicle therapy for pulmonary fibrosis via inhibition of TGF-β-WNT crosstalk. *J. Extracell. Vesicles* 10 (10), e12124. doi:10.1002/jev2.12124

Kadota, T., Fujita, Y., Yoshioka, Y., Araya, J., Kuwano, K., and Ochiya, T. (2016). Extracellular vesicles in chronic obstructive pulmonary disease. *Int. J. Mol. Sci.* 17 (11), 1801. doi:10.3390/ijms17111801

Kadota, T., Yoshioka, Y., Fujita, Y., Araya, J., Minagawa, S., Hara, H., et al. (2020). Extracellular vesicles from fibroblasts induce epithelial cell senescence in pulmonary fibrosis. *Am. J. Respir. Cell Mol. Biol.* 63 (5), 623–636. doi:10.1165/rcmb.2020-0002OC

Kang, J. H., Jung, M. Y., Choudhury, M., and Leof, E. B. (2019). Transforming growth factor beta induces fibroblasts to express and release the immunomodulatory protein PD-L1 into extracellular vesicles. *FASEB J.* 34 (2), 2213–2226. doi:10.1096/fj.201902354R

Kaur, G., Maremanda, K. P., Campos, M., Chand, H. S., Li, F., Hirani, N., et al. (2021). Distinct Exosomal miRNA profiles from BALF and lung tissue of COPD and IPF patients. *Int. J. Mol. Sci.* 22 (21), 11830. doi:10.3390/ijms222111830

Kim, J., You, G. E., Woo, M., Chang, N. H., and Lee, J. (2021). Discovery of lactoferrin as a stimulant for hADSC-derived EV secretion and proof of enhancement of resulting EVs through skin model. *Int. J. Mol. Sci.* 22 (20), 10993. doi:10.3390/ijms222010993

Koh, Y. Q., Tan, C. J., Toh, Y. L., Sze, S. K., Ho, H. K., Limoli, C. L., et al. (2020). Role of exosomes in cancer-related cognitive impairment. *Int. J. Mol. Sci.* 21 (8), E2755. doi:10.3390/ijms21082755

Kok, V. C., and Yu, C. C. (2020). Cancer-derived exosomes: Their role in cancer biology and biomarker development. *Int. J. Nanomedicine* 15, 8019–8036. doi:10.2147/IJN.S272378

Kumar, P., Dezso, Z., MacKenzie, C., Oestreicher, J., Agoulnik, S., Byrne, M., et al. (2013). Circulating miRNA biomarkers for Alzheimer's disease. *PLoS One* 8 (7), e69807. doi:10.1371/journal.pone.0069807

Kumar, S., Sharawat, S. K., Ali, A., Gaur, V., Malik, P. S., Kumar, S., et al. (2020). Identification of differentially expressed circulating serum microRNA for the diagnosis and prognosis of Indian non-small cell lung cancer patients. *Curr. Probl. Cancer* 44 (4), 100540. doi:10.1016/j.currproblcancer.2020.100540

Kuse, N., Kamio, K., Azuma, A., Matsuda, K., Inomata, M., Usuki, J., et al. (2020). Exosome-derived microRNA-22 ameliorates pulmonary fibrosis by regulating fibroblast-to-myofibroblast differentiation *in vitro* and *in vivo*. *J. Nippon Med. Sch.* 87 (3), 118–128. doi:10.1272/jnms.JNMS.2020_87-302

Lacedonia, D., Scioscia, G., Soccio, P., Conese, M., Catucci, L., Palladino, G. P., et al. (2021). Downregulation of exosomal let-7d and miR-16 in idiopathic pulmonary fibrosis. *BMC Pulm. Med.* 21 (1), 188. doi:10.1186/s12890-021-01550-2

Lawrence, J., and Nho, R. (2018). The role of the mammalian target of rapamycin (mTOR) in pulmonary fibrosis. *Int. J. Mol. Sci.* 19 (3), 778. doi:10.3390/ijms19030778

Lei, X., He, N., Zhu, L., Zhou, M., Zhang, K., Wang, C., et al. (2020). Mesenchymal stem cell-derived extracellular vesicles attenuate radiation-induced lung injury via miRNA-214-3p. *Antioxid. Redox Signal.* 35, 849–862. doi:10.1089/ars.2019.7965

Li, J. W., Wei, L., Han, Z., and Chen, Z. (2019). Mesenchymal stromal cells-derived exosomes alleviate ischemia/reperfusion injury in mouse lung by transporting anti-apoptotic miR-21-5p. *Eur. J. Pharmacol.* 852, 68–76. doi:10.1016/j.ejphar.2019.01.022

Li, Y., Shen, Z., Jiang, X., Wang, Y., Yang, Z., Mao, Y., et al. (2022). Mouse mesenchymal stem cell-derived exosomal miR-466f-3p reverses EMT process through inhibiting AKT/GSK3β pathway via c-MET in radiation-induced lung injury. *J. Exp. Clin. Cancer Res.* 41 (1), 128. doi:10.1186/s13046-022-02351-z

Liang, J. N., Zou, X., Fang, X. H., Xu, J. D., Xiao, Z., Zhu, J. N., et al. (2019). The Smad3-miR-29b/miR-29c axis mediates the protective effect of macrophage migration inhibitory factor against cardiac fibrosis. *Biochim. Biophys. Acta. Mol. Basis Dis.* 1865 (9), 2441–2450. doi:10.1016/j.bbadis.2019.06.004

Liguori, M., Nuzziello, N., Introna, A., Consiglio, A., Licciulli, F., D'Errico, E., et al. (2018). Dysregulation of microRNAs and target genes networks in peripheral

blood of patients with sporadic amyotrophic lateral sclerosis. *Front. Mol. Neurosci.* 11, 288. doi:10.3389/fnmol.2018.00288

Lindenbergh, M. F. S., and Stoorvogel, W. (2018). Antigen presentation by extracellular vesicles from professional antigen-presenting cells. *Annu. Rev. Immunol.* 36 (1), 435–459. doi:10.1146/annurev-immunol-041015-055700

Liu, B., Jiang, T., Hu, X., Liu, Z., Zhao, L., Liu, H., et al. (2018). Downregulation of microRNA-30a in bronchoalveolar lavage fluid from idiopathic pulmonary fibrosis patients. *Mol. Med. Rep.* 18 (6), 5799–5806. doi:10.3892/mmr.2018.9565

Liu, G., Qian, M., Chen, M., Chen, T., and Qin, S. (2020). miR-21-5p suppresses mitophagy to alleviate hyperoxia-induced acute lung injury by directly targeting PGAM5. *Biomed. Res. Int.* 2020, 4807254. doi:10.1155/2020/4807254

Long, J., Badal, S. S., Wang, Y., Chang, B. H., Rodriguez, A., and Danesh, F. R. (2013). MicroRNA-22 is a master regulator of bone morphogenetic protein-7/6 homeostasis in the kidney. *J. Biol. Chem.* 288 (51), 36202–36214. doi:10.1074/jbc.M113.498634

Lu, Y. F., Liu, Y., Fu, W. M., Xu, J., Wang, B., Sun, Y. X., et al. (2017). Long noncoding RNA H19 accelerates tenogenic differentiation and promotes tendon healing through targeting miR-29b-3p and activating TGF-β1 signaling. *FASEB J.* 31 (3), 954–964. doi:10.1096/fj.201600722R

Lucchetti, D., Santini, G., Perelli, L., Ricciardi-Tenore, C., Colella, F., Mores, N., et al. (2021). Detection and characterisation of extracellular vesicles in exhaled breath condensate and sputum of COPD and severe asthma patients. *Eur. Respir. J.* 58 (2), 2003024. doi:10.1183/13993003.03024-2020

Ma, Y., Liu, X., Long, Y., and Chen, Y. (2022). Emerging therapeutic potential of mesenchymal stem cell-derived extracellular vesicles in chronic respiratory diseases: An overview of recent progress. *Front. Bioeng. Biotechnol.* 10, 845042. doi:10.3389/fbioe.2022.845042

Makiguchi, T., Yamada, M., and Yoshioka, Y. (2016). Serum extracellular vesicular miR-21-5p is a predictor of the prognosis in idiopathic pulmonary fibrosis. *Respir. Res.* 17 (1), 110. doi:10.1186/s12931-016-0427-3

Makler, A., and Asghar, W. (2020). Exosomal biomarkers for cancer diagnosis and patient monitoring. *Expert Rev. Mol. diagn.* 20 (4), 387–400. doi:10.1080/14737159.2020.1731308

Mansouri, N., Willis, G. R., Fernandez-Gonzalez, A., Reis, M., Nassiri, S., Mitsialis, S. A., et al. (2019). Mesenchymal stromal cell exosomes prevent and revert experimental pulmonary fibrosis through modulation of monocyte phenotypes. *JCI Insight* 4 (21), 128060. doi:10.1172/jci.insight.128060

Markopoulos, G. S., Roupakia, E., Tokamani, M., Vartholomatos, G., Tzavaras, T., Hatziapostolou, M., et al. (2017). Senescence-associated microRNAs target cell cycle regulatory genes in normal human lung fibroblasts. *Exp. Gerontol.* 96, 110–122. doi:10.1016/j.exger.2017.06.017

Martin-Medina, A., Lehmann, M., Burgy, O., Hermann, S., Baarsma, H. A., Wagner, D. E., et al. (2018). Increased extracellular vesicles mediate WNT5A signaling in idiopathic pulmonary fibrosis. *Am. J. Respir. Crit. Care Med.* 198 (12), 1527–1538. doi:10.1164/rccm.201708-1580OC

Mendes-Silva, A. P., Pereira, K. S., Tolentino-Araujo, G. T., Nicolau Ede, S., Silva-Ferreira, C. M., Teixeira, A. L., et al. (2016). Shared biologic pathways between alzheimer disease and major depression: A systematic review of microRNA expression studies. *Am. J. Geriatr. Psychiatry* 24 (10), 903–912. doi:10.1016/j.jagp.2016.07.017

Merckx, G., Hosseinkhani, B., Kuypers, S., Deville, S., Irobi, J., Nelissen, I., et al. (2020). Angiogenic effects of human dental pulp and bone marrow-derived mesenchymal stromal cells and their extracellular vesicles. *Cells* 9 (2), 312. doi:10.3390/cells9020312

Min, H., Fan, S., Song, S., Zhuang, Y., Li, H., Wu, Y., et al. (2016). Plasma microRNAs are associated with acute exacerbation in idiopathic pulmonary fibrosis. *Diagn. Pathol.* 11 (1), 135. doi:10.1186/s13000-016-0583-2

Min, H., Ma, D., Zou, W., Wu, Y., Ding, Y., Zhu, C., et al. (2020). FLCN-regulated miRNAs suppressed reparative response in cells and pulmonary lesions of Birt-Hogg-Dubé syndrome. *Thorax* 75 (6), 476–485. doi:10.1136/thoraxjnl-2019-213225

Mullenbrock, S., Liu, F., and Szak, S. (2018). Systems analysis of transcriptomic and proteomic profiles identifies novel regulation of fibrotic programs by miRNAs in pulmonary fibrosis fibroblasts. *Genes (Basel)* 9 (12), 588. doi:10.3390/genes9120588

Neri, T., Lombardi, S., Faìta, F., Petrini, S., Balìa, C., Scalise, V., et al. (2016). Pirfenidone inhibits p38-mediated generation of procoagulant microparticles by human alveolar epithelial cells. *Pulm. Pharmacol. Ther.* 39, 1–6. doi:10.1016/j.pupt.2016.05.003

Njock, M.-S., Guiot, J., Henket, M. A., Nivelles, O., Thiry, M., Dequiedt, F., et al. (2019). Sputum exosomes: Promising biomarkers for idiopathic pulmonary fibrosis. *Thorax* 74 (3), 309–312. doi:10.1136/thoraxjnl-2018-211897

Novelli, F., Neri, T., and Tavanti, L. (2014). Procoagulant, tissue factor-bearing microparticles in bronchoalveolar lavage of interstitial lung disease patients: An observational study. *PLoS One* 9 (4), e95013. doi:10.1371/journal.pone.0095013

O'Neill, H. C., and Quah, B. J. (2008). Exosomes secreted by bacterially infected macrophages are proinflammatory. *Sci. Signal.* 1 (6), pe8. doi:10.1126/stke.16pe8

Ostrowski, M., Carmo, N. B., Krumeich, S., Fanget, I., Raposo, G., Savina, A., et al. (2010). Rab27a and Rab27b control different steps of the exosome secretion pathway. *Nat. Cell Biol.* 12 (1), 19–30. sup pp 1-13. doi:10.1038/ncb2000

Pan, B. T., Teng, K., Wu, C., Adam, M., and Johnstone, R. M. (1985). Electron microscopic evidence for externalization of the transferrin receptor in vesicular form in sheep reticulocytes. *J. Cell Biol.* 101 (3), 942–948. doi:10.1083/jcb.101.3.942

Pandit, K. V., Milosevic, J., and Kaminski, N. (2011). MicroRNAs in idiopathic pulmonary fibrosis. *Transl. Res.* 157 (4), 191–199. doi:10.1016/j.trsl.2011.01.012

Parimon, T., Yao, C., Habiel, D. M., Ge, L., Bora, S. A., Brauer, R., et al. (2019). Syndecan-1 promotes lung fibrosis by regulating epithelial reprogramming through extracellular vesicles. *JCI Insight* 4 (17), 129359. doi:10.1172/jci.insight.129359

Peng, L., Chen, Y., Shi, S., and Wen, H. (2022). Stem cell-derived and circulating exosomal microRNAs as new potential tools for diabetic nephropathy management. *Stem Cell Res. Ther.* 13 (1), 25. doi:10.1186/s13287-021-02696-w

Peng, X., Yang, L., Liu, H., Pang, S., Chen, Y., Fu, J., et al. (2016). Identification of circulating microRNAs in biliary atresia by next-generation sequencing. *J. Pediatr. Gastroenterol. Nutr.* 63 (5), 518–523. doi:10.1097/mpg.0000000000001194

Phinney, D. G., Di Giuseppe, M., Njah, J., Sala, E., Shiva, S., St Croix, C. M., et al. (2015). Mesenchymal stem cells use extracellular vesicles to outsource mitophagy and shuttle microRNAs. *Nat. Commun.* 6, 8472. doi:10.1038/ncomms9472

Purghè, B., Manfredi, M., Ragnoli, B., Baldanzi, G., and Malerba, M. (2021). Exosomes in chronic respiratory diseases. *Biomed. Pharmacother.* 144, 112270. doi:10.1016/j.biopha.2021.112270

Qi, A., Wang, T., Li, W., Wang, Y., and Chai, Y. (2021). The effect of miR-21-5p on the MAP2K3 expressions and cellular apoptosis in the lung tissues of neonatal rats with hyperoxia-induced lung injuries. *Am. J. Transl. Res.* 13 (4), 2784–2793.

Qin, S., Wang, H., Liu, G., Mei, H., and Chen, M. (2019). miR-21-5p ameliorates hyperoxic acute lung injury and decreases apoptosis of AEC II cells via PTEN/AKT signaling in rats. *Mol. Med. Rep.* 20 (6), 4953–4962. doi:10.3892/mmr.2019.10779

Ramachandra, L., Qu, Y., Wang, Y., Lewis, C. J., Cobb, B. A., Takatsu, K., et al. (2010). *Mycobacterium tuberculosis* synergizes with ATP to induce release of microvesicles and exosomes containing major histocompatibility complex class II molecules capable of antigen presentation. *Infect. Immun.* 78 (12), 5116–5125. doi:10.1128/iai.01089-09

Rawal, S., Munasinghe, P. E., and Nagesh, P. T. (2017). Down-regulation of miR-15a/b accelerates fibrotic remodelling in the Type 2 diabetic human and mouse heart. *Clin. Sci. (Lond)* 131 (9), 847–863. doi:10.1042/CS2016091

Ren, W., Hou, J., Yang, C., Wang, H., Wu, S., Wu, Y., et al. (2019). Extracellular vesicles secreted by hypoxia pre-challenged mesenchymal stem cells promote non-small cell lung cancer cell growth and mobility as well as macrophage M2 polarization via miR-21-5p delivery. *J. Exp. Clin. Cancer Res.* 38 (1), 62. doi:10.1186/s13046-019-1027-0

Richeldi, L., Collard, H. R., and Jones, M. (2017). Idiopathic pulmonary fibrosis. *Lancet* 389 (10082), 1941–1952. doi:10.1016/S0140-6736(17)30866-8

Rogler, C. E., Matarlo, J. S., Kosmyna, B., Fulop, D., and Rogler, L. E. (2017). Knockdown of miR-23, miR-27, and miR-24 alters fetal liver development and blocks fibrosis in mice. *Gene Expr.* 17 (2), 99–114. doi:10.3727/105221616x693891

Shentu, T.-P., Huang, T.-S., Cernelc-Kohan, M., Chan, J., Wong, S. S., Espinoza, C. R., et al. (2017). Thy-1 dependent uptake of mesenchymal stem cell-derived extracellular vesicles blocks myofibroblastic differentiation. *Sci. Rep.* 7 (1), 18052. doi:10.1038/s41598-017-18288-9

Shi, J., Li, F., Luo, M., Wei, J., and Liu, X. (2017). Distinct roles of Wnt/β-catenin signaling in the pathogenesis of chronic obstructive pulmonary disease and idiopathic pulmonary fibrosis. *Mediat. Inflamm.* 2017, 3520581. doi:10.1155/2017/3520581

Shi, L., Ren, J., Li, J., Wang, D., Wang, Y., Qin, T., et al. (2021). Extracellular vesicles derived from umbilical cord mesenchymal stromal cells alleviate pulmonary fibrosis by means of transforming growth factor-β signaling inhibition. *Stem Cell Res. Ther.* 12 (1), 230. doi:10.1186/s13287-021-02296-8

Song, Y., Zuo, Y., Qian, X. L., Chen, Z. P., Wang, S. K., Song, L., et al. (2017). Inhibition of microRNA-21-5p promotes the radiation sensitivity of non-small cell lung cancer through HMSH2. *Cell. Physiol. biochem.* 43 (3), 1258–1272. doi:10.1159/000481839

Sun, J., Su, W., Zhao, X., Shan, T., Jin, T., Guo, Y., et al. (2019). LncRNA PFAR contributes to fibrogenesis in lung fibroblasts through competitively binding to miR-15a. *Biosci. Rep.* 39 (7), BSR20190280. doi:10.1042/bsr20190280

Sun, L., Sun, M., Ma, K., and Liu, J. (2020). Let-7d-5p suppresses inflammatory response in neonatal rats with necrotizing enterocolitis via LGALS3-mediated TLR4/NF-κB signaling pathway. *Am. J. Physiol. Cell Physiol.* 319 (6), C967–C979. doi:10.1152/ajpcell.00571.2019

Sun, M., Yu, H., Zhang, Y., Li, Z., and Gao, W. (2015). MicroRNA-214 mediates isoproterenol-induced proliferation and collagen synthesis in cardiac fibroblasts. *Sci Rep.* 5, 18351. doi:10.1038/srep1835

Sun, L., Zhu, M., Feng, W., Lin, Y., Yin, J., Jin, J., et al. (2019). Exosomal miRNA Let-7 from menstrual blood-derived endometrial stem cells alleviates pulmonary fibrosis through regulating mitochondrial dna damage. *Oxid. Med. Cell. Longev.* 2019, 4506303. doi:10.1155/2019/4506303

Szul, T., Bratcher, P. E., and Fraser, K. B. (2016). Toll-like receptor 4 engagement mediates prolyl endopeptidase release from airway epithelia via exosomes. *Am. J. Respir. Cell Mol. Biol.* 54 (3), 359–369. doi:10.1165/rcmb.2015-0108OC

Tamai, K., Tanaka, N., Nakano, T., Kakazu, E., Kondo, Y., Inoue, J., et al. (2010). Exosome secretion of dendritic cells is regulated by Hrs, an ESCRT-0 protein. *Biochem. Biophys. Res. Commun.* 399 (3), 384–390. doi:10.1016/j.bbrc.2010.07.083

Tan, J. L., Lau, S. N., and Leaw, B. (2018). Amnion epithelial cell-derived exosomes restrict lung injury and enhance endogenous lung repair. *Stem Cells Transl. Med.* 7 (2), 180–196. doi:10.1002/sctm.17-0185

Tang, J., Li, X., Cheng, T., and Wu, J. (2021). miR-21-5p/SMAD7 axis promotes the progress of lung cancer. *Thorac. Cancer* 12 (17), 2307–2313. doi:10.1111/1759-7714.14060

Tao, R., Fan, X. X., Yu, H. J., Ai, G., Zhang, H. Y., Kong, H. Y., et al. (2018). MicroRNA-29b-3p prevents Schistosoma japonicum-induced liver fibrosis by targeting COL1A1 and COL3A1. *J. Cell. Biochem.* 119 (4), 3199–3209. doi:10.1002/jcb.26475

Tasena, H., Faiz, A., Timens, W., Noordhoek, J., Hylkema, M. N., Gosens, R., et al. (2018). microRNA-mRNA regulatory networks underlying chronic mucus hypersecretion in COPD. *Eur. Respir. J.* 52 (3), 1701556. doi:10.1183/13993003.01556-2017

Tijsen, A. J., van der Made, I., van den Hoogenhof, M. M., Wijnen, W. J., van Deel, E. D., de Groot, N. E., et al. (2014). The microRNA-15 family inhibits the TGFβ-pathway in the heart. *Cardiovasc. Res.* 104 (1), 61–71. doi:10.1093/cvr/cvu184

Trappe, A., Donnelly, S. C., McNally, P., and Coppinger, J. A. (2021). Role of extracellular vesicles in chronic lung disease. *Thorax* 76 (10), 1047–1056. doi:10.1136/thoraxjnl-2020-216370

Wan, X., Chen, S., Fang, Y., Zuo, W., Cui, J., and Xie, S. (2020). Mesenchymal stem cell-derived extracellular vesicles suppress the fibroblast proliferation by downregulating FZD6 expression in fibroblasts via micrRNA-29b-3p in idiopathic pulmonary fibrosis. *J. Cell. Physiol.* 235 (11), 8613–8625. doi:10.1002/jcp.29706

Wang, A. P., Li, X. H., Gong, S. X., Li, W. Q., Hu, C. P., Zhang, Z., et al. (2015). miR-100 suppresses mTOR signaling in hypoxia-induced pulmonary hypertension in rats. *Eur. J. Pharmacol.* 765, 565–573. doi:10.1016/j.ejphar.2015.09.031

Wang, H., Liu, Y., Wang, D., Xu, Y., Dong, R., Yang, Y., et al. (2019). The upstream pathway of mTOR-mediated autophagy in liver diseases. *Cells* 8 (12), E1597. doi:10.3390/cells8121597

Wang, J., Hu, L., Huang, H., Yu, Y., Wang, J., Yu, Y., et al. (2020). CAR (CARSKNKDC) peptide modified ReNcell-derived extracellular vesicles as a novel therapeutic agent for targeted pulmonary hypertension therapy. *Hypertension* 76 (4), 1147–1160. doi:10.1161/HYPERTENSIONAHA.120.15554

Wang, J., He, F., Chen, L., Li, Q., Jin, S., Zheng, H., et al. (2018). Resveratrol inhibits pulmonary fibrosis by regulating miR-21 through MAPK/AP-1 pathways. *Biomed. Pharmacother.* 105, 37–44. doi:10.1016/j.biopha.2018.05.104

Wang, Y. C., Xie, H., Zhang, Y. C., Meng, Q. H., Xiong, M. M., Jia, M. W., et al. (2021). Exosomal miR-107 antagonizes profibrotic phenotypes of pericytes by targeting a pathway involving HIF-1α/Notch1/PDGFRβ/YAP1/Twist1 axis *in vitro*. *Am. J. Physiol. Heart Circ. Physiol.* 320 (2), H520–H534. doi:10.1152/ajpheart.00373.2020

Wang, Y., Ouyang, M., Wang, Q., and Jian, Z. (2016). MicroRNA-142-3p inhibits hypoxia/reoxygenation-induced apoptosis and fibrosis of cardiomyocytes by targeting high mobility group box 1. *Int. J. Mol. Med.* 38 (5), 1377–1386. doi:10.3892/ijmm.2016.2756

Wang, Y., Zhong, Y., Sun, K., Fan, Y., Liao, J., and Wang, G. (2021). Identification of exosome miRNAs in bronchial epithelial cells after PM2.5 chronic exposure. *Ecotoxicol. Environ. Saf.* 215, 112127. doi:10.1016/j.ecoenv.2021.112127

Wu, J., Kuang, L., Chen, C., Yang, J., Zeng, W. N., Li, T., et al. (2019). miR-100-5p-abundant exosomes derived from infrapatellar fat pad MSCs protect articular cartilage and ameliorate gait abnormalities via inhibition of mTOR in osteoarthritis. *Biomaterials* 206, 87–100. doi:10.1016/j.biomaterials.2019.03.022

Wu, Y., Zhang, Z., Li, J., Zhong, H., Yuan, R., Deng, Z., et al. (2022). Mechanism of adipose-derived mesenchymal stem cell-derived extracellular vesicles carrying miR-21-5p in hyperoxia-induced lung injury. *Stem Cell Rev. Rep.* 18 (3), 1007–1024. doi:10.1007/s12015-021-10311-x

Xie, H., Gao, Y. M., Zhang, Y. C., Jia, M. W., Peng, F., Meng, Q. H., et al. (2020). Low let-7d exosomes from pulmonary vascular endothelial cells drive lung pericyte fibrosis through the TGFβRI/FoxM1/Smad/β-catenin pathway. *J. Cell. Mol. Med.* 24 (23), 13913–13926. doi:10.1111/jcmm.15989

Xie, L., and Zeng, Y. (2020). Therapeutic potential of exosomes in pulmonary fibrosis. *Front. Pharmacol.* 11, 590972. doi:10.3389/fphar.2020.590972

Xie, T., Liang, J., Guo, R., Liu, N., Noble, P. W., and Jiang, D. (2011). Comprehensive microRNA analysis in bleomycin-induced pulmonary fibrosis identifies multiple sites of molecular regulation. *Physiol. Genomics* 43 (9), 479–487. doi:10.1152/physiolgenomics.00222.2010

Xue, Y., Fan, X., Yang, R., Jiao, Y., and Li, Y. (2020). miR-29b-3p inhibits post-infarct cardiac fibrosis by targeting FOS. *Biosci. Rep.* 40 (9), BSR20201227. doi:10.1042/bsr20201227

Xunian, Z., and Kalluri, R. (2020). Biology and therapeutic potential of mesenchymal stem cell-derived exosomes. *Cancer Sci.* 111 (9), 3100–3110. doi:10.1111/cas.14563

Yamada, M. (2021). Extracellular vesicles: Their emerging roles in the pathogenesis of respiratory diseases. *Respir. Investig.* 59 (3), 302–311. doi:10.1016/j.resinv.2021.02.006

Yamada, M. (2020). The roles of microRNAs and extracellular vesicles in the pathogeneses of idiopathic pulmonary fibrosis and acute respiratory distress syndrome. *Tohoku J. Exp. Med.* 251 (4), 313–326. doi:10.1620/tjem.251.313

Yan, L., Ma, J., Wang, Y., Zan, J., Wang, Z., Zhu, Y., et al. (2018). miR-21-5p induces cell proliferation by targeting TGFBI in non-small cell lung cancer cells. *Exp. Ther. Med.* 16 (6), 4655–4663. doi:10.3892/etm.2018.6752

Yang, L., Fan, Y., Zhang, X., and Ma, J. (2017). miRNA-23 regulates high glucose induced epithelial to mesenchymal transition in human mesotheial peritoneal cells by targeting VDR. *Exp. Cell Res.* 360 (2), 375–383. doi:10.1016/j.yexcr.2017.09.029

Yang, X., Dan, X., Men, R., Ma, L., Wen, M., Peng, Y., et al. (2017). MiR-142-3p blocks TGF-β-induced activation of hepatic stellate cells through targeting TGFβRI. *Life Sci.* 187, 22–30. doi:10.1016/j.lfs.2017.08.017

Yang, Z., Xu, X., and Song, C. (2022). Circular RNA La-Related Protein 4 inhibits non-small cell lung cancer cell proliferation while promotes apoptosis through sponging microRNA-21-5p. *Cancer biother. Radiopharm.* 37 (2), 111–118. doi:10.1089/cbr.2020.3707

Yao, M.-Y., Zhang, W.-H., Ma, W.-T., Liu, Q.-H., Xing, L.-H., and Zhao, G.-F. (2019). MicroRNA-328 in exosomes derived from M2 macrophages exerts a promotive effect on the progression of pulmonary fibrosis via FAM13A in a rat model. *Exp. Mol. Med.* 51 (6), 1–16. doi:10.1038/s12276-019-0255-x

Ye, X., Luo, H., Chen, Y., Wu, Q., Xiong, Y., Zhu, J., et al. (2015). MicroRNAs 99b-5p/100-5p regulated by endoplasmic reticulum stress are involved in Abeta-induced pathologies. *Front. Aging Neurosci.* 7, 210. doi:10.3389/fnagi.2015.00210

Zhang, Y., Zhao, S., Wu, D., Liu, X., Shi, M., Wang, Y., et al. (2018). MicroRNA-22 promotes renal tubulointerstitial fibrosis by targeting PTEN and suppressing autophagy in diabetic nephropathy. *J. Diabetes Res.* 2018, 4728645. doi:10.1155/2018/4728645

Zhao, X. S., Ren, Y., Wu, Y., Ren, H. K., and Chen, H. (2020). MiR-30b-5p and miR-22-3p restrain the fibrogenesis of post-myocardial infarction in mice via targeting PTAFR. *Eur. Rev. Med. Pharmacol. Sci.* 24 (7), 3993–4004. doi:10.26355/eurrev_202004_20869

Zheng, H., Li, W., Wang, Y., Xie, T., Cai, Y., Wang, Z., et al. (2014). miR-23a inhibits E-cadherin expression and is regulated by AP-1 and NFAT4 complex during Fas-induced EMT in gastrointestinal cancer. *Carcinogenesis* 35 (1), 173–183. doi:10.1093/carcin/bgt274

Zheng, J., Yu, L., Chen, W., Lu, X., and Fan, X. (2018). Circulating exosomal microRNAs reveal the mechanism of Fructus Meliae Toosendan-induced liver injury in mice. *Sci. Rep.* 8 (1), 2832. doi:10.1038/s41598-018-21113-6

Zhou, X., Liu, H., Pang, Y., Wang, M., and Liu, S. (2022). UTMD-mediated delivery of miR-21-5p inhibitor suppresses the development of lung cancer. *Tissue Cell* 74, 101719. doi:10.1016/j.tice.2021.101719

Zhou, Y., Gao, Y., Zhang, W., Chen, Y., Jin, M., and Yang, Z. (2021). Exosomes derived from induced pluripotent stem cells suppresses M2-type macrophages during pulmonary fibrosis via miR-302a-3p/TET1 axis. *Int. Immunopharmacol.* 99, 108075. doi:10.1016/j.intimp.2021.108075

Zhou, Y., Lv, X., Qu, H., Zhao, K., Fu, L., Zhu, L., et al. (2018). Preliminary screening and functional analysis of circular RNAs associated with hepatic stellate cell activation. *Gene* 677, 317–323. doi:10.1016/j.gene.2018.08.052

Zhu, G. H., Li, R., Zeng, Y., Zhou, T., Xiong, F., and Zhu, M. (2018). MicroRNA-142-3p inhibits high-glucose-induced endothelial-to-mesenchymal transition through targeting TGF-β1/Smad pathway in primary human aortic endothelial cells. *Int. J. Clin. Exp. Pathol.* 11 (3), 1208–1217.

Zhu, J., Zhang, J., Ji, X., Tan, Z., and Lubman, D. M. (2021). Column-based technology for CD9-HPLC immunoaffinity isolation of serum extracellular vesicles. *J. Proteome Res.* 20 (10), 4901–4911. doi:10.1021/acs.jproteome.1c00549

frontiers | Frontiers in Pharmacology

TYPE Review
PUBLISHED 20 September 2022
DOI 10.3389/fphar.2022.999604

OPEN ACCESS

EDITED BY
Jian Gao,
Shanghai Children's Medical Center, China

REVIEWED BY
Ming Ding,
China Pharmaceutical University, China
Yuping Zhou,
Ningbo University, China

*CORRESPONDENCE
Chenghai Liu,
chenghailiu@hotmail.com
Yuan Peng,
pengyuan1026@shutcm.edu.cn

SPECIALTY SECTION
This article was submitted to Gastrointestinal and Hepatic Pharmacology, a section of the journal Frontiers in Pharmacology

RECEIVED 21 July 2022
ACCEPTED 09 September 2022
PUBLISHED 20 September 2022

CITATION
Yang Z, Qi J, Ping D, Sun X, Tao Y, Liu C and Peng Y (2022), Salvia miltiorrhiza in thorax and abdomainal organ fibrosis: A review of its pharmacology. *Front. Pharmacol.* 13:999604. doi: 10.3389/fphar.2022.999604

Salvia miltiorrhiza in thorax and abdomainal organ fibrosis: A review of its pharmacology

Zhao Yang[1], Jingshu Qi[1], Dabing Ping[1], Xin Sun[2], Yanyan Tao[1], Chenghai Liu[1,2,3]* and Yuan Peng[1]*

[1]Institute of Liver Diseases, Shuguang Hospital Affiliated to Shanghai University of Traditional Chinese Medicine, Shanghai, China, [2]Shanghai Key Laboratory of Traditional Chinese Clinical Medicine, Shanghai, China, [3]Key Laboratory of Liver and Kidney Diseases, Ministry of Education, Shanghai, China

Organ fibrosis is a common pathological change that finally results in organ failure, which involves the destruction of parenchyma cells, the activation of mesenchymal cells and the imbalance of immunological cells. In recent years, although some breakthroughs have been made in understanding the pathogenesis and therapeutics of organ fibrosis, no registered drugs could directly target the fibrotic process, which constitutes a major biomedical challenge. *Salvia miltiorrhiza* (SM) is a well-known medicinal plant in China, which has been widely applied because of its pharmacological effects on anti-oxidative, anti-myocardial infarction, anti-fibrotic, anti-inflammatory, and anti-neoplastic properties. Accumulated evidence suggested that SM played critical roles against organ fibrosis *in vivo* and *in vitro* experiments by its multiple biological compounds. In this review, we discussed the recent advances on the phytochemistry and pharmacological mechanisms of SM and its active ingredients in liver, lung, kidney, and heart fibrosis, which might help to promote the treatment of fibrotic diseases in thorax and abdomainal viscera in clinic.

KEYWORDS

organ fibrosis, *Salvia miltiorrhiza*, ingredients, pharmacological mechanism, review

Introduction

Fibrosis, defined as fibroblast proliferation and excessive accumulation of extracellular matrix (ECM) in the broadest sense, was associated with a high cost in morbidity and mortality at a global level (Wynn and Ramalingam, 2012). In solid organ fibrosis, such as thorax and abdomainal organ fibrosis, activated fibroblasts presented overwhelming proliferating and invasion capacities, which could accelerate the development of fibrosis pathogenesis (Deng et al., 2021). Myofibroblasts, differentiated from fibroblasts, were then accumulated dramatically while ECMs were simultaneously synthesizd and deposited. Thus, these abnormal cell populations could contribute to the induction of fibrosis in major organs.

To date, many human diseases, including those of lung, heart, liver, kidney, bone marrow, brain blood vessels, and skin, correlated strongly with fibrosis. The main

characteristics of organ fibrosis were typically presented with the chronic inflammation, the microvascular disturbances, the missing organ parenchyma and the loss-off function (Eddy, 2005). Therefore, fibrosis is a common pathway that might finally lead to organ failure. It was clear that organ fibrosis was a major clinical challenge. Currently, no registered drugs could directly target the fibrotic process. In contrast, traditional Chinese medicine (TCM) and its active ingredients had potential to target fibrosis in one organ or synchronously reversing fibrosis in multiple other fibrotic organs, which were increasingly recognized as effective therapies for fibrosis.

Herbal medicine and its active ingredients were believed to treat disease as a trusted source of medicine from ancient times. *Salvia miltiorrhiza* (SM) Bunge (Lamiaceae), known as danshen (Chinese), is a widely used medicinal plant in TCM (Figure 1). It has been used in China with a long history of two thousand years, which was recorded in the oldest materia medica book "Shen Nongs Classic of Materia Medica" (Shen Nong Ben Cao Jing, 100 BCE to 200 CE). Historically, SM was used to promote blood circulation for removing blood stasis, improving microcirculation and assuaging pain. In addition, SM was demonstrated to exert numerous pharmacological effects, including anti-oxidative, myocardial infarction, anti-fibrotic (Su et al., 2015), anti-inflammatory (Ma et al., 2016), anti-hypertension (Lee et al., 2009), and anti-neoplastic (Chen et al., 2014) and anti-bacterial (Lee and Kim, 2016) properties.

Salvia miltiorrhiza Bunge contains ethanol-soluble compounds (such as various tanshinone analogues) and water-soluble active components (such as salvianolic acids) (Li et al., 2009; Pang et al., 2016). Accumulated evidence suggested that SM played critical roles against organ fibrosis in both animal experiments and clinical studies by its multiple biological ingredients, including anti-inflammation, anti-fibrosis, anti-oxidation and anti-apoptosis. In order to adequately define and elucidate the pharmacological functions of SM in organ fibrosis, pharmacology, phytochemistry, and safety of SM in organ fibrosis were hereby reviewed. For better understanding the pharmacological actions of SM against organ fibrosis, phytochemistry of SM were firstly summarized (Figures 2, 3).

Phytochemistry of *Salvia miltiorrhiza*

There are more than 100 ingredients that were identified from SM so far, including lipid-soluble tanshinones and water-soluble phenolic compounds (Ma et al., 2015). Over 30 phenolic acids had been isolated from SM(Pang et al., 2016), including salvianolic acid A/B/C/D/E/F/G/H/I/J/K/N, rosmarinic acid, danshensu, protocatechuic acid, caffeic acid, lithospermic acid, caffeic acid, etc and other derivatives. Most of the phenolic acids had been conventionally isolated by continuous refluxing extraction and sonication in different solvents such as methanol, aqueous methanol (75%–95%, *v*/*v*) and aqueous ethanol (60%–95%, v/v) (XD et al., 2019). However, these methods also have some shortcomings. Most of them were time-consuming, which might promote phenolic acids converted into another kinds of compounds. In the last few years, novel emerging methods have been applied to extract phenolic acids, including microwave-assisted extraction (Gallo et al., 2010), supercritical fluid extraction (SFE) (Li et al., 2002), ultrasonic extraction (UAE) (Li et al., 2009), tissue-smashing based ultra-rapid extraction (Fan et al., 2014) and microsphere resin chromatography combined with microbial biotransformation (Kan et al., 2009).

Besides the hydrophilic salvianolic acids, the lipophilic terpenoids were also the major bioactive constituents of SM. Until now, at least 40 liposoluble compounds had been isolated from SM. Tanshinones and their analogues, including tanshinone I, tanshinone IIA, tanshinol A, tanshinol B, cryptotanshinone, dihydrotanshinone, danshenxinkun A, przewaquinone A, etc, were the main

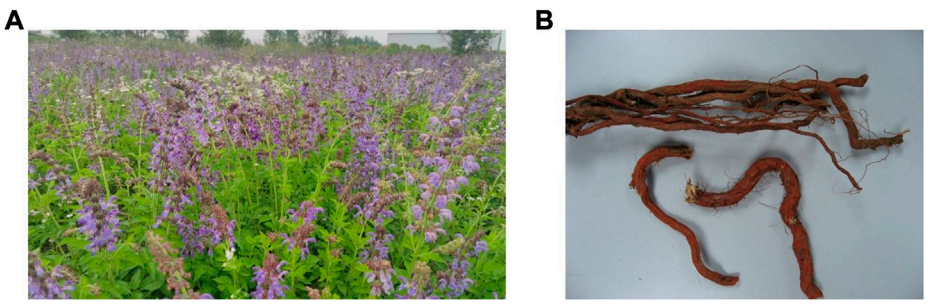

FIGURE 1
Overall appearance of *Salvia miltiorrhiza* Bunge (SM). **(A)**The aerial parts of SM. **(B)** The raw herb of SM.

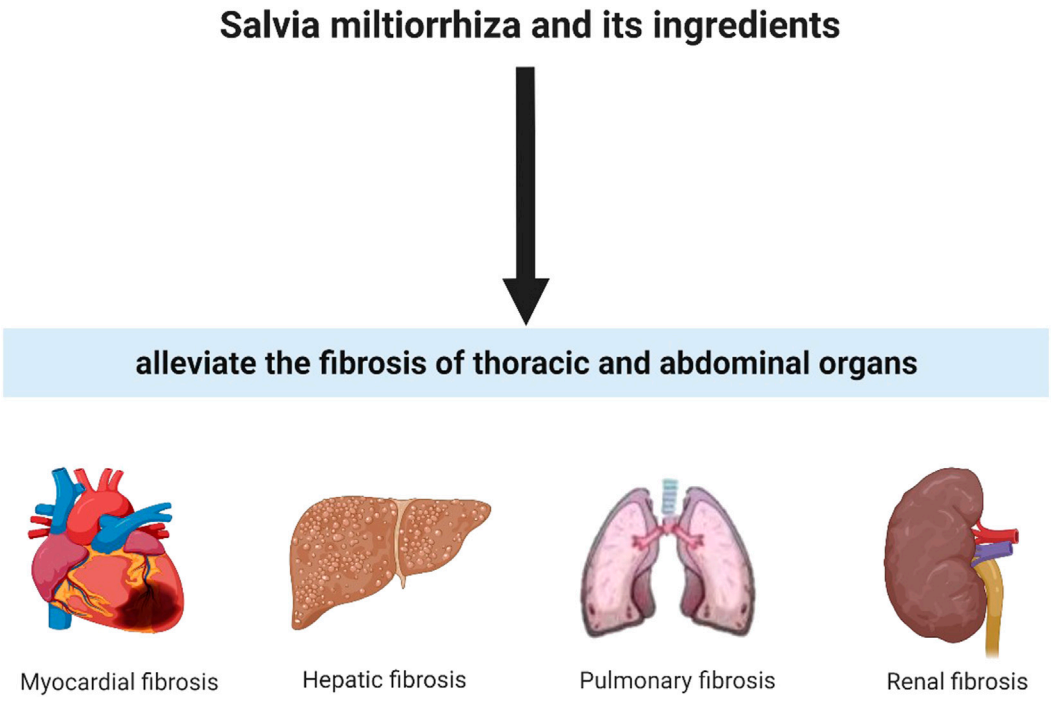

FIGURE 2
Salvia miltiorrhiza and its ingredients could alleviate fibrotic condition in thoracic and abdominal organs.

active diterpenoids in SM (Su et al., 2015). Some conventional extraction reagents, such as CHCl3, ethyl acetate, or petroleum ether, were used as the initial extraction solvent to isolate the tanshinones (XD et al., 2019). Besides these, extraction techniques such as soaking, percolation, reflux as well as ultrasound were generally applied for the extraction of tanshinones. However, tanshinones were present at lower concentrations than in the original SM, and many liposoluble constituents were instability, eg. cryptotanshinone and tanshinone IIA, etc (Li et al., 2008). Nowadays, these problems could be solved by a wide range of technique or approach, including infrared-assisted extraction (Chen et al., 2010), UAE (Li et al., 2009), surfactant-assisted extraction (Bi et al., 2011), SFE (Li et al., 2002) and pressurized-liquid extraction (Jiang et al., 2010).

Apart from the above, as SM was cultivation is scattered all over the country, the contents of main active constituents of SM might be influenced by environmental, altitude and cultivars factors (Wang et al., 2013; Zhao et al., 2016a). In addition, the active constituents might differ in intrinsically because of the various germplasms (Zhang et al., 2013; Zhao et al., 2016b). And the different genotypes of SM possessed their own specific ethylene responsive element binding protein gene (Cui et al., 2010).

Pharmacological actions of *Salvia miltiorrhiza* in treatment for organ fibrosis

Liver fibrosis

Liver fibrosis is a key pathological hallmark of various chronic liver diseases, including auto-immune liver disease, viral hepatitis, alcohol, and non-alcoholic fatty liver disease (Friedman, 2010; Tsochatzis et al., 2014). Although significant achievements have been made in our understanding of the pathogenenic actions of hepatic fibrosis and cirrhosis, effective anti-fibrotic agents and therapies remain the unconquered areas in the fields of drug research and development (Schuppan and Kim, 2013). "Deficiency of vital essential and blood stasis" was response in development of liver fibrosis and cirrhosis, which was the basic TCM pathogenesis of this condition. Among these, blood stasis was a central component. In TCM theory, SM was considered to promote blood circulation for removing blood stasis and resolving microcirculation (Sun et al., 2005). SM was applied in treating splenomegaly due to schistosomiasis in the fifties of the last century in China. Since then, many Chinese patent medicines, typified by Fuzheng Huayu tablet/capsule, contained SM as an integral part against liver fibrosis and cirrhosis. Both *in vitro* and *in vivo* experiments confirmed

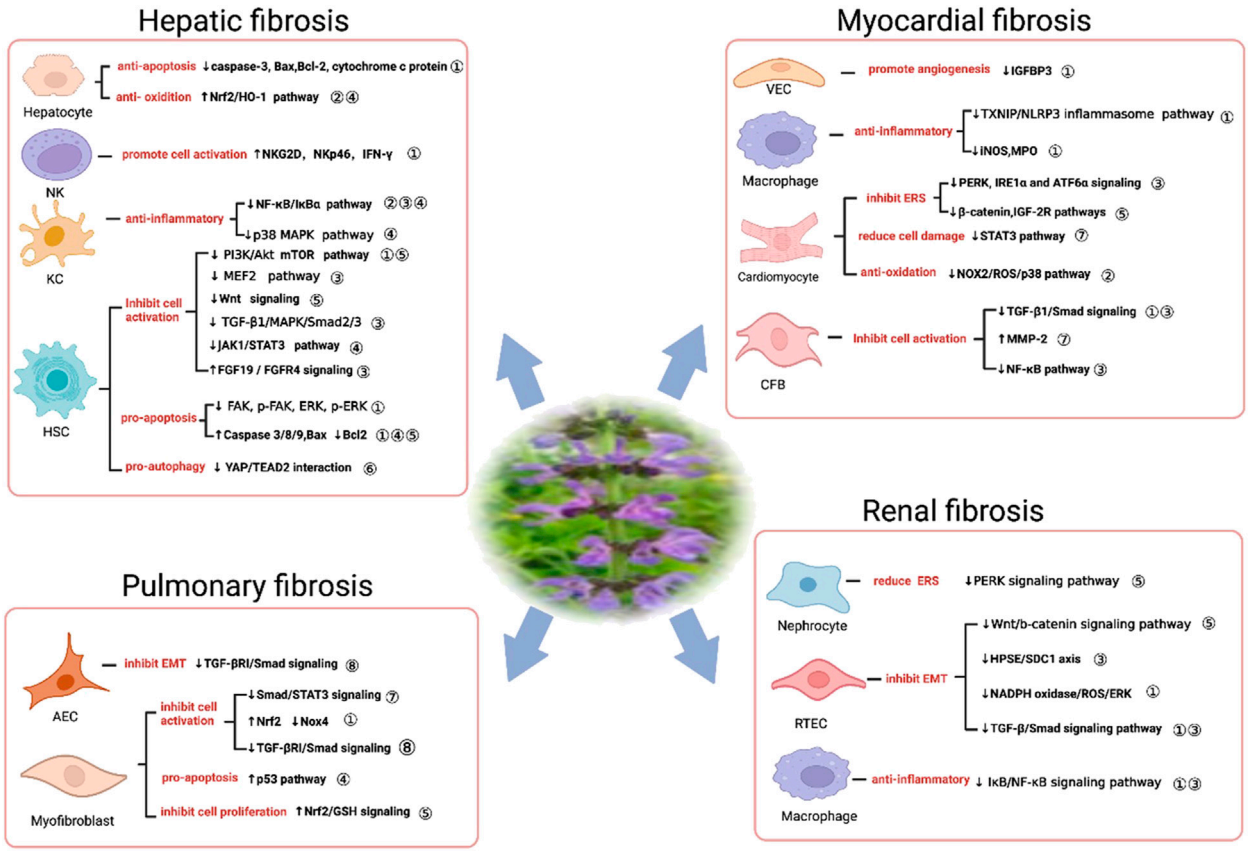

FIGURE 3
Pharmacological mechanisms of SM and its active ingredients in liver, lung, kidney and heart fibrosis. Ingredients in SM, ① *Salvia miltiorrhiza*; ② Tanshinol; ③ Salvianolic acid B; ④ Salvianolic acid A; ⑤ Tanshinone IIA; ⑥ Dihydrotanshinone I; ⑦ Cryptotanshinone; ⑧ Magnesium Lithospermate B. Abbreviations, NK, natural killer cells; KC, Kupffer cell; HSC, Hepatic stellate cell; VEC, vascular endothelial cell; CFB, myocardial fibroblast; AEC, alveolar epithelial cell; RTEC, renal tubular epithelial cell; Bax, B-cell lymphoma-2-associated X protein; BCL2, B-cell lymphoma-2; Nrf2, nuclear factor-erythroid 2-related factor 2; HO-1, heme oxygenase-1; NKG2D, natural killer cell group 2D; NF-κB, nuclear factor kappa-B; IκB, inhibitor of nuclear factor kappa-B; MAPK, mitogen-activated protein kinase; PI3K, phosphatidylinositol-3-kinase; Akt, protein kinase B; mTOR, molecular target of rapamycin; MEF2, myocyte enhancer factor 2; TGFβ1, transforming growth factor β1; Smad, *drosophila* mothers against decapentaplegic protein 2/3; JAK1, Janus kinase one; STAT3, signal transducer and activator of transcription three; FGF19, fibroblast growth factor 19; FGFR4, fibroblast growth factor receptor 4; FAK, focal adhesion kinase; p-FAK, phosphorylated focal adhesion kinase; ERK, extracellular regulated protein kinases; p-ERK, phosphorylated extracellular regulated protein kinases; YAP, yes-associated protein; TEAD2, TEA domain family member two; IGFBP3,insulin-like growth factor-binding protein 3; TXNIP, thioredoxin interacting protein; NLRP3, Nucleotide-binding oligomerization domain; leucine-rich repeat and pyrin domain-containing three; iNOS, inductible nitric oxide synthase; MPO, myeloperoxidase; PERK, protein kinase R-like endoplasmic reticulum kinase; IRE1α, Inositol requiring enzyme1α; ATF6α, activating transcription factor 6α; IGF-2R, insulin-like growth factor 2 receptor; NOX2, nicotinamide adenine dinucleotide phosphate oxidase two; ROS, reactive oxygen species; MMP-2, matrix metalloproteinase-2; EMT, epithelial-mesenchymal transition; TGF-βRI, transforming growth factor β receptor I; GSH, glutathione; ERS, endoplasmic reticulum stress; HPSE, heparinase; SDC1,syndecan-1; NADPH oxidase, reduced nicotinamide adenine dinucleotide phosphate oxidase; ↑ activate; ↓ inhibit).

that SM played anti-fibrotic roles in liver fibrosis and cirrhosis (Peng et al., 2018). These hepatoprotective mechanisms of SM were shown to be attributed to inhibiting inflammation, reducing oxidant stress, enhancing apoptosis of HSCs, decreasing hepatocellular injury and suppressing the functions of activation of HSCs without damaging the hepatocytes. In addition to the direct effects of inhibiting the activated HCSs, SM could indirectly enhance the activities of NK cell to reduce liver fibrosis (Peng et al., 2018). Several experimental studies had reported that SM could couple with some herbal medicines, such as radix astragali (Yang et al., 2008; Cao et al., 2020), stephania tetrandra (Chor et al., 2009), ligusticum chuanxiong and glycyrrhiza glabra (Lin et al., 2008), to exert the antifibrotic effects *via* alleviating collagen deposition and reducing inflammation in the liver. Moreover, the active anti-fibrotic ingredients from SM have gained an increasing amount of attention. Salvianolic acid A/B/C, danshensu, tanshinone IIA and dihydrotanshinone I were reported to have noticeable pharmacological activities and were also representative active ingredients in SM. The anti-fibrotic activities of these

TABLE 1 Effects of SM and its active ingredients against liver fibrosis *in vivo* and *in vitro*.

Animals/ Cells	Inducer	Drug and dose	Mechanism	References
In vivo				
C57BL/6 mice	10% CCl_4 2 ml/kg i.p	SM extract 3.0 g/kg i.g	NKG2D, Nkp46, IFN-γ↑	Peng et al. (2018)
SD rats	TAA 350 mg/kg i.p	PF2401-SF 1 or 2.5 mg/kg i.g	collagen 1(α), TIMP1, α-SMA↓	Parajuli et al. (2015)
SD rats	BDL	IH764-3 40 mg/kg i.p	α-SMA, FAK, p-FAK, ERK, p-ERK↓	Liu et al. (2012)
SD rats	50% CCl_4 1 ml/kg i.g	tanshinol 20 or 40 mg/kg i.g	SOD, GSH-Px, HO-1, NQO-1, GCLC, NF-κB, IκBα ↑ HA, LN, IV-C, PIIIP, MDA, Cox-2, TGF-β, TNF-α, IL-1β, IL-6, NF-κB in the nucleolus↓	Wang et al. (2018b)
SD rats	BDL	hot-water extract of SM 100 mg/kg i.g	TCHO, MDA, Hyp, α-SMA↓	Nan et al. (2001)
Kunming mice	0.1% DEN 10 ml/kg i.p	salvianolic acid B 10 or 30 mg/kg i.g	p-Smad3C↑ α-SMA,CollagenI, p-Smad2C, p-Smad2L,p-Smad3L↓	Wu et al. (2019)
SD rats	CCl_4 0.75 ml/kg i.g	PF2401-SF 50 mg/kg i.g	α-SMA↓	Parajuli et al. (2013)
Wistar rats	CCl_4 1 ml/kg i.p	Tanshinone IIA 10 mg/kg i.g	α-SMA, COL1A2, c-Jun, p-c-Jun, c-Myc, CCND1, MMP9, P65, p-P65, PI3K, P38↓	Shi et al. (2020)
Wistar rats	CCl_4 0.5 ml/kg i.p	SM extract 25 or 50 mg/kg i.g	GSH↑ GST, TGFβ1, TIMP-1, procollagen I↓	Lee et al. (2003)
SD rats	BDL	dihydrotanshinone I 25 mg/kg i.p	γ-GT, COL1A1¸ ACTA2, TGFβ1, MMP-2, TIMP-1, TIMP-2↓	Ge et al. (2017)
SD rats	CCl_4	tanshinol 20 or 40 mg/kg i.g	MMP-13, MMP-1,Bax, Caspase- 3↑ PIIINP, HA, CollagenIV, LN, HOP, TIMP-1, Collagen I, Collagen II, α-SMA, TGFβ, Cox-2, TNF-α, IL-1, IL-6, Bcl-2, β-FGF, PD-ECGF↓, PI3K/AKT/mTOR/p70S6K1↓	Peng et al. (2017)
Wistar rats	CCl_4 0.5 ml kg i.p	water-soluble extract of SM 50 mg/kg i.g	GSH↑ caspase-3, Bax, Bcl-2, cytochrome c protein, calpain-μ↓	Lee et al. (2006)
SD rats	CCl_4 1 ml/kg i.g	salvianolic acid B 10 or 20 mg/kg i.g	NF-κB, IκBα in the cytoplasm↑ HA, LN, IV-C, PIIIP, NF-κB in the nucleolus↓	Wang et al. (2012)
In vitro				
JS-1 cell line	TGF-β1 5 ng/ml	SM extract 12.5–50 μg/ml	RAE-1ε↑ α-SMA↓	Peng et al. (2018)
T6 and LX-2 cell lines	TGF-β1 9p.m.	salvianolic acid B 25, 50 and 100 μM	p-ERK1/2, p-JNK1/2, p-P38, p-Smad2C, p-Smad2L, p-Smad3C, p-Smad3L, PAI-1↓	Wu et al. (2019)
LX-2 cell line	LPS 100 ng/ml	salvianolic acid B 1, 2.5 and 5 μM	FGF19, FGFR4 ↑ α-SMA, COL1A1↓	Tian et al. (2021)
t-HSC/Cl-6 cell line	Null	PF2401-SF 20 μg/ml	Caspase -3, Caspase -8, Caspase- 9, Bax↑ Bcl2↓	Parajuli et al. (2013)
LX-2 cell line	TGF-β1 2 ng/ml	dihydrotanshinone I 1, 5 and 10 μM	MAP1LC3B, LC3B↑ TGFβ1, α-SMA, COL1A1, pHSCs, ACTA2, CTGF, SOX4, p62↓	Ge et al. (2017)
LX-2 cell line	7-days culture	salvianolic acid B (6 μM, 48 μM), caffeic acid (6 μM, 48 μM) and rosmarinic acid (48 μM)	α-SMA↓	Yang et al. (2013)
human primary HSCs	TGF-β1 10 ng/ml	salvianolic acid B 1 μM	MEF2, α-SMA, Collagen I↓	Zhang et al. (2019a)
T6 cell line	acetaldehyde 200 μM	danshensu 100, 125 and 150 μM	uPA↑ TGF-β1, PAI-1↓	Zhang et al. (2012)
t-HSC/Cl-6 cell line	null	tanshinone IIA 20 μM	Caspase -3, cytochrome c, cyclin E, cyclin A, cdk2, Bax/Bcl-2↑	Che et al. (2010)
primary rat HSCs	TGF-β1 1 ng/ml	salvianolic acid B 280 μM	DPPH, MDA, ROS, α-SMA↓	Lin et al. (2006b)
T6 cell line	PDGF-BB	salvianolic acid A 10 mM	Caspase -3↑ Bcl-2, p21, p27, Akt, cyclinsD1/E, PDGF↓	Lin et al. (2006a)
primary rat HSCs	24-h culturing	salvianolic acid A 1 and 10 μM	Collagen I↓	Liu et al. (2000)

Note: i.p: intraperitoneal injection; i.g.: intragastric administration.

TABLE 2 Effects of SM and its active ingredients against renal fibrosis *in vivo* and *in vitro*.

Animals/ Cells	Inducer	Drug and dose	Mechanism	References
In vivo				
SD rats	adenine 150 mg/kg i.g	Ethanol extract of SM 0.46 g/kg i.g. and water extract of SM 1.03 g/kg i.g	UP, Scr, BUN, ISF, E-cadherin, α-SMA, FN, p-ERK, NOX1, NOX2, NOX4, TGF-β↓	Cai et al. (2018b)
C57BL/6 mice	UUO model	protocatechualdehyde (PCA) 10 or 40 mg/kg i.g	Smad7↑	Yang et al. (2021)
			KIM-1, BUN, SCR, α-SMA, collagenI, fibronectin, TNF-α, IL-1β, MCP-1, COX2, iNOS, NF-κB, Smad3↓	
C57BL/6 mice	UUO model	salvianolic acid B 6.25–25 mg/kg i.g	SDC1, E-cadherin↑	Hu et al. (2020)
			BUN, CR, HPSE, α-SMA, TGF-β1, FGF-2↓	
SD rats	streptozotocin 60 mg/kg i.p	tanshinone IIA 2, 4, 8 mg/kg i.p	SOD↑	Xu et al. (2020)
			TGF-β1, TSP-1, Grp78, CHOP, p-PERK, p-elf2α, ATF4 ↓	
SD rats	5/6 nephrectomy	tanshinone IIA 10 mg/kg i.g	Ang II, TGF-β1, collagen IV↓	Ahn et al. (2010)
SD rats	streptozotocin 60 mg/kg i.p	danshen injection 0.5–1 ml/kg i.p	SOD↑	Xu et al. (2016)
			ROS, MDA, TGF-β1,Smad2/3, TNF-α, IL-1β, IL-6, p-IκBα, p-NF-κB p65 ↓	
	streptozotocin 55 mg/kg i.p	danshen injection 0.78 ml/kg i.p	GSH-Px, SOD↑	Yin et al. (2014)
			AGEs, LPO, TGF-β1↓	
In vitro				
HK-2 cell line	ISF 250 μM	Ethanol or water extract of SM, 5–100 μM	α-SMA, FN, E-cadherin↑	Cai et al. (2018b)
			NOX1, NOX2, NOX4, p-ERK ↓	
			TGF-β, TGF-βRI, TGF-βRII, Smad2, Smad3, Smad7 ↓	
primary renal TECs	TGF-β1 2 ng/ml	protocatechualdehyde 20–80 μM	LRNA9884, iNOS, COX2, IL-6, MCP-1, NF-κB, IL-6, α-SMA, collagen I, fibronectin↓	Yang et al. (2021)
HK-2 cell line	AngII 1 μM	salvianolic acid B 0.1–10 μM	SDC1, E-cadherin↑	Hu et al. (2020)
			TGF-β1, FGF-2, HPSE, α-SMA↓	
HK-2 cell line	glucose 30 mM	Tanshinone IIA 5 or 10 μM	VDR, E-cadherin↑ a-SMA, b-catenin, GSK-3b↓	Zeng and Bao, (2021b)
HK-2 cell line	glucose 30 mM	Tanshinone IIA 1–50 μM	E-cadherin↑	Cao et al. (2017)
			α-SMA, vimentin, fibronectin, Snail↓	

compounds were exhibited significantly, especially inhibiting the activation of HSCs which was a stromal cell in the liver well known for its role in triggering the fibrogenic process both *in vitro* and *in vivo*. These results indicated that SM alone or in combination with other herbs were highly effective in anti-fibrotic therapeutic strategy. And the inhibitory effect of the ingredients from SM might be a continuation of its anti-fibrotic effect. More details were shown in Table 1.

Renal fibrosis

Renal fibrosis is a common feature of a range of chronic kidney diseases (CKDs) with the progressive and irreversible declines in renal functions. Renal tubulointerstitial fibrosis, glomerulosclerosis, and arteriosclerosis with perivascular fibrosis are the established characteristic of renal fibrosis (Liu, 2011). Excessive deposition of ECM, inflammatory cell infiltration, fibroblast accumulation, and myofibroblast expansion disrupt the local vasculature and impede the tissue repair, which accelerates the development of renal fibrosis in CKDs and eventually leads to kidney failure. Therefore, renal fibrosis is a hallmark of end-stage kidney disease.

Currently, despite remarkable progress in preclinical animal experiments, very limited therapeutics could inhibit or even reverse renal fibrosis effectively and safely. Haemodialysis, peritoneal dialysis and kidney transplantation are largely to the symptomatic approaches and palliation of symptoms, but cannot fundamentally improve the condition. In contrast, TCM can provide an alternative approach for treating renal fibrosis. SM and its main ingredients were demonstrated to have nephroprotective activities and anti-fibrotic functions via multiple pathways in adenine diet, streptozotocin (STZ) injection, 5/6 nephrectomy and unilateral urethral obstruction (UUO) induced renal fibrosis models (Table 2). Both water and ethanol extracts of SM presented protections in nephropathy and renal fibrosis *via* inhibiting the elevation of renal functions, improving the clinical symptoms of glomerular and tubular atrophy, alleviating focal calcium deposits, altering metabolites and reversing renal interstitial fibrosis and inflammation.

Furthermore, it was revealed that SM suppressed renal fibrosis and epithelial trans-differentiation by inhibiting TGF-β/Smad and NADPH oxidase/ROS/ERK signaling pathways (Cai et al., 2018a). Beyond that, therapeutic application of SM was effective in combination with other agents. Astragalus membranaceus and SM could alleviate collagen deposition and metabolism, especially Tryptophan metabolism and Butanoate metabolism, in cyclosporin A-induced chronic nephrotoxicity and renal fibrosis. The further underlying mechanism might be lied in regulating the "gut-kidney axis" and modulating the disorder of miRNA-mRNA interaction profiles (Han et al., 2021).

In addition, active compounds in SM, such as protocatechualdehyde, salvianolic acid B, and tanshinone IIA, were also exert effects against renal fibrosis (Hu et al., 2020; Xu et al., 2020; Yang et al., 2021) in several renal fibrosis models. Protocatechualdehyde, a natural compound in the root of SM, was reported to decrease renal inflammation and fibrosis via mediating NF-κB/TGF-β1/Smad3/lncRNA9884/MCP-1 signaling pathway (Yang et al., 2021). Salvianolic acid B could notably reduce the renal injury and fibrosis in murine UUO model *in vivo*. The mechanism was confirmed to be related with the downregulation of HPSE/FGF-2/TGF-β1/α-SMA expression and upregulation of SDC1/E-cadherin levels *in vitro* (Hu et al., 2020). Tanshinone IIA was demonstrated to have excellent anti-fibrotic properties in streptozotocin-induced and 5/6 nephrectomy models, respectively (Ahn et al., 2010; Xu et al., 2020). More importantly, the mechanism for SM against renal fibrosis might be related to reducing endoplasmic reticulum stress to attenuate PERK signaling activities, decreasing expressions of Ang II, TGF-β1 and collagen IV, attenuating high glucose-induced EMT by up-regulating VDR levels on Wnt/β-catenin pathway and inhibiting HG-induced the epithelial-myofibroblast trans differentiation pathway (Ahn et al., 2010; Cao et al., 2017; Xu et al., 2020; Zeng and Bao, 2021a).

Pulmonary fibrosis

Pulmonary fibrosis is a chronic interstitial pulmonary disease caused by a diversity of insults, including smoke, chemical materials, microbial infection, and environment contamination (Noble et al., 2012). Pulmonary fibrosis (rather difficult to reverse), consisting of progressive and irreversible destruction of lung architecture caused by scar formation, could ultimately lead to organ malfunction, disruption of gas exchange, and death from respiratory failure (Wynn, 2011). Till now, no effective therapy could prevent or reverse the development of pulmonary fibrosis. Nintedanib and pirfenidone are proved by FDA to alleviate lung function and lung fibrosis, however, neither of these drugs are able to reverse pulmonary fibrosis. Currently, the only life-saving treatment available for patients with progressive lung fibrosis is lung transplantation. Thus, identifying drugs to ameliorate the pulmonary fibrogenesis is urgently needed.

Recently, TCM has played an indispensable role in the treatment of pulmonary fibrosis *via* its multi-components, multi-targets and multi-pathways. SM and its ingredients were demonstrated to have effects in extenuating pulmonary fibrosis (Peng et al., 2019). The effect of SM for treatment in pingyangmycin-induced experimental model, was reported for the first time in 1987 in China (Chen, 1987). In Table 3, we summarized the available literatures related to the mechanisms of SM and its ingredients against pulmonary fibrosis during the past 35 years. Among these, bleomycin (BLM) and silica were commonly used to induce pulmonary fibrosis in rats and mice. And TGF-β1-stimulated cultured lung fibroblast, such as HLFs and MRC-5, exerted as an excellent model for evaluating anti-fibrotic compounds *in vitro*.

Peng et al. (2019) found that ethyl acetate extract of SM could alleviate bleomycin-induced lung fibrosis. The mechanism was associated with the reduction of ROS generation in fibroblasts, activation of Nrf2 pathway and inhibition TGF-β1/Smad3 pathway *in vivo* and *in vitro*. Single use of SM significantly ameliorated experimental lung fibrosis, and such effect was also exerted when combined with other herbal medicine. Combination of SM and ligustrazine were viewed to attenuate bleomycin-induced pulmonary fibrosis in rats *via* modulating TNF-α and TGF (Huang et al., 2018). Both the lipophilic ingredients (tanshinone IIA and cryptotanshinone) and hydrophilic ingredients (salvianolic acid A, salvianolic acid B, and magnesium lithospermate B) from SM have protective effects against pulmonary fibrosis, including reducing the proliferation of lung fibroblasts and protecting the alveolar epithelial integrity (Pan et al., 2014; Liu et al., 2018; Zhang Y. et al., 2019; Luo et al., 2021a).

Salvianolic acid B (SAB) was the most well studied active hydrophilic compound of SM against lung fibrosis. SAB had potent anti-fibrotic effects via blocking proliferation of lung fibroblasts, trans-differentiation and oxidative stress levels (Liu et al., 2018; Jiang et al., 2020). The pharmacological mechanisms of SAB were mainly related to the inhibition of TGF-βRI/Smad signaling in activated pulmonary fibroblasts. Tanshinone IIA were also weakened the myofibroblast proliferation by activating Nrf2/GSH signaling pathway to limit glutaminolysis (An et al., 2019).

Myocardial fibrosis

Myocardial fibrosis (MF) is characterized by excessive deposition of ECM in the cardiac interstitium, which is a pathophysiologic component of many chronic myocardial diseases. Although the pathological processes of MF involved the complex interaction of multiple cell types, activated fibroblasts and myofibroblasts are the major contributors, serving as the main source of collagen fibres in cardiac fibrosis (Gonzalez et al., 2018). Clinically available drugs for

TABLE 3 Effects of SM and its active ingredients against pulmonary fibrosis *in vivo* and *in vitro*.

Animals/Cells	Inducer	Drug and dose	Mechanism	References
In vivo				
SD rats	intratracheal instillation of bleomycin 5 mg/kg	Cryptotanshinone 7.5–60 mg/kg	E-cadherin↑ Fibronectin, COL-I, COL-III, α-SMA, PAI-1, IL-6, TNF-α, p-STAT3Tyr705, p-STAT3Ser727↓	Zhang et al. (2019b)
C57BL/6 mice	intratracheal injection of bleomycin 1.25 U/kg	ethyl acetate extract of SM(EASM) 20, 40, 80 mg/kg	Nrf2↑ TGF-β, p-Smad3, α-SMA, Col-I, Nox4, acid-soluble collagen↓	Peng et al. (2019)
SD rats	intratracheal instillation of bleomycin 2 mg/kg	Magnesium Lithospermate B 50 mg/kg i.p	Col1A1, α-SMA, Col3A1, IL-4, IL-6, IL-13, TGF-β↓	Luo et al. (2021b)
Wistar rats	intratracheal injection of bleomycin 5 mg/kg	salvianolic acid A 2.5, 5, and 10 mg/kg i.v	TGF-β mRNA↓	Pan et al. (2014)
C57BL/6 mice	intratracheal injection of bleomycin 0.025U/mice	tanshinone IIA 5, 10, 20 mg/kg, i.g	Nrf2↑ Nox4, Smad3, TGF-β1, fibronectin, Col-I, Col-III, α-SMA↓	An et al. (2019)
SD rats	intratracheal instillation of bleomycin 3.5 U/kg	Salvianolic Acid B 10 mg/kg i.p	Col1a1, Col1a2, Ctgf, PAI-1, α-SMA↓	Liu et al. (2016)
Wistar rats	intratracheal injection of bleomycin 5 mg/kg	Salvianolic acid B 20 mg/kg i.v	GSH, Nrf2↑ α-SMA, MDA↓	Liu et al. (2018)
Human fetal lung fibroblasts (HLFs)	TGF-β1 5 ng/ml	Cryptotanshinone 1.5–6 mg/L	E-cadherin↑ Fibronectin, COL-I, COL-III, α-SMA, PAI-1↓ TGF-βR I, TGF-βR II, Smad2, Smad3 ↓	Zhang et al. (2019b)
Mice embryo fibroblasts (NIH-3T3)	TGF-β1 10 ng/ml	EASM 0.1, 1, 3 μg/ml	Nrf2↑ TGF-β1, Nox4, PKC-δ, p-Smad3, α-SMA↓	Peng et al. (2019)
Human lung fibroblasts (MRC-5)	TGF-β1 10 ng/ml	salvianolic acid B 20 μg/ml or sodium tanshinone IIA sulfonate 50 μg/ml	IL-1β, TNF-α, COL1A1, α-SMA, ACTA2↓	Jiang et al. (2020)
Human type II alveolar epithelial cell line (A549) or MRC-5 cell	TGF-β1 10 ng/ml	Magnesium Lithospermate B 30 or 50 μM	Col 1A1, Col 3A1, α-SMA↓ TGF-βRI, Smad3 ↓	Luo et al. (2021b)
Murine 3T6 fibroblasts	null	salvianolic acid A 6.25–25 μg/ml	p21, p53, caspase-3↑ cyclin D1, cyclin E1, cyclin B1, Bcl-2↓	Pan et al. (2014)
NIH-3T3	TGF-β1 10 ng/ml	tanshinone IIA 1–10 μM	Nrf2, GSH↑ Nox4, α-SMA, Col-I, Smad3, Col-III, PKCδ↓	An et al. (2019)
A549 cell line	TGF-β1 10 ng/ml and TNF-α 10 ng/ml	salvianolic acid B 50 μg/ml	CDH1↑ FN1, p-Smad3, p-ERK1/2, p-JNK↓	Liu et al. (2016)
MRC-5 cell line	TGF-β1 10 ng/ml	salvianolic acid B 40 μM	GSH, Nrf2↑ α-SMA, vimentin, fibronectin, ROS, MDA↓	Liu et al. (2018)

treating MF were applied including angiotensin-converting enzyme inhibitors (lisinopril) (Brilla et al., 2000), type1 angiotensin II-receptor antagonists (losartan) (Diez et al., 2002) and mineralocorticoid-receptor antagonists (spironolactone) (Izawa et al., 2005), which target renin-angiotensin-aldosterone system. Besides, loop diuretics (torasemide) were also applied in clinical practice that targeting extracellular collagen processing (Lopez et al., 2004). However, no specific drugs exist for reversing myocardial fibrosis to the present date.

SM has been used in Chinese folk medicine to treat heart diseases for a long history in China. In recent years, multiple SM preparations such as compound Danshen tablets, compound Danshen Dripping Pill, Danshen injections, Danshen tablets and Danshen capsules have been used in treatment of cardiovascular problems. According to Chinese medicine theory, SM is considered to promote blood circulation and alleviate blood stasis so as to relieve pain, eliminate blood stasis and promote blood flow in treatment of MF. Similar to PF, SM, and its ingredients (e.g., Salvanic acid B) restrained fibroblasts activation and inhibited collagen deposition through suppressing oxidative stress and TGF-β1/smad signaling pathway in MF, especially blocking cardiac fibroblast proliferation and ECM synthesis (Zhang

TABLE 4 Effects of SM and its active ingredients against myocardial fibrosis *in vivo* and *in vitro*.

Animals/Cells	Inducer	Drug and dose	Mechanism	References
In vivo				
Kunming mice	Iron Dextran Injection 50 mg/kg i.p	SM injection 3 g/kg and 6 g/kg i.p	SOD↑ Hyp,MDA,COL-I,COL-III,TGF-β1, MMP-9↓	Zhang et al. (2015)
C57BL/6J mice	Streptozotocin (STZ) 60 mg/kg i.p	Salvianolic acid B (Sal B) 15 or 30 mg/kg i.p	VEGFA, VEGFR2, p-AKT, p-ERK↑ Collagen I, Collagen Ⅲ, IGFBP3↓	Li et al. (2020)
Kunming mice	Isoproterenol hydro-chloride injection (ISO) 2.5 mg/kg i.p	Salvanic acid B	Smad7↑ TGF-β1, Smad2/3↓	Gao et al. (2019b)
SD rats	left anterior descending (LAD) ligation	Danshen Injection (DSI) 1.5 ml/kg/d i.m	Bcl-2, Bax↑ MMP-2, iNOS, MPO↓	Wang et al. (2017)
SD rats	left aortic descending coronary artery ligation	Cryptotanshinone (CTS) 30 and 60 mg/kg i.g	FN, COX-2, NOX-2,NOX-4↓	Ma et al. (2014)
SD rats	left anterior descending coronary artery ligation	Salvianolate 10, 20 and 40 mg/kg i.p	TGFβ1, p-Smad2/Smad2, p-Smad3/ Smad3, Collagen I, Collagen III, MMP9, TIMP1, TXNIP, IL-1β, IL-18, NLRP3, Caspase-1, CRP, IL-6, BNP↓	Qiu et al. (2018b)
SD rats	left and right renal artery ligation	Tanshinone II-A 35 and 70 mg/kg i.g	MMP-9, TIMP-1, TIMP-2↓	Fang et al. (2010)
Wistar rats	Streptozotocin 65 mg/kg i.v	Cryptotanshinone 10 mg/kg i.g	STAT3, CTGF, MMP-9↓	Lo et al. (2017)
SD rats	isoprenaline 0.25 mg/kg i.p	isopropyl 3-(3,4-dihydroxyphenyl)-2-hydroxylpropanoate (IDHP) 50 mg/kg	Collagen I, Collagen III↓	Yin et al. (2015)
C57BL/6 mice	Isoprenaline 3 mg/kg s.c	Cryptotanshinone 20 mg/kg i.g	MMP-2↑	Ma et al. (2012)
In vitro				
Rat embryonic ventricular H9c2 cardiomyocytes	oxygen-glucose deprivation/ reoxygenation (OGD/R) condition	PCA 1.25, 2.5 and 5.0 μM	Caspase-3, Bax↓ CHOP, BiP, PERK, Ero1-Lα, IRE1α, ATF6, HIF-1α↓	Wan et al. (2021)
Mouse cardiac fibroblasts (CFs) cells	TGF-β1 20 ng/ml	Sal B 5, 10, and 20 ng/ml	Smad7↑ Smad2/3, MMP-2, MMP-9↓	Gao et al. (2019b)
primary rat cardiac fibroblasts (CFs)	Ang II 100 nM	Cryptotanshinone (CTS) 2.5–20 mM	FN, CTGF, p-ERK1/2, ROS, NOX-2, NOX-4, COX-2↓	Ma et al. (2014)
primary neonatal rat cardiac fibroblasts	Ang II 1 μM	Salvianolic acid B (SalB) 12.5–50 μM	Collagen I, FN, CTGF, p-IκB, p-p65, α-SMA↓	Wang et al. (2018a)
Primary neonatal rat cardiomyocytes	D-glucose 30 mM	cryptotanshinone 3 μM	STAT3, CTGF, MMP-9↓	Lo et al. (2017)
neonatal rat cardiac fibroblasts (NRCFs)	isoprenaline	isopropyl 3-(3,4-dihydroxyphenyl)-2-hydroxylpropanoate (IDHP) 1–100 μM	ROS, p-p38, NOX2↓	Yin et al. (2015)
H9c2 cardiomyoblast cell	AngII 10^{-8}M	Tanshinone IIA 40 μM	ERα, ERβ↑ β-catenin, p-ERK1/2, IGF-2R, LEF-1, MMP-9, MMP-2, TGF-β1, p-Smad2/3, SP-1,CTGF↓	Chen et al. (2017b)
Primary cardiac myocytes and cardiac fibroblasts from neonatal rats	endothelin-1 (ET-1) 10–8 M, phenylephrine (PE) 10–6 M, or insulin-like growth factor-1 (IGF-1) 10^{-8} M	tanshinone VI (tsh) 10^{-5} M	ET-1, PE, IGF-1↓	Maki et al. (2002)

et al., 2015; Qiu et al., 2018a; Gao et al., 2019a). The mechanisms were mainly associated with inhibiting TGF-β1 expression and Smad2/3 phosphorylation, as well as restraining the release of myeloperoxidase (MPO) (Wang et al., 2017). In addition, tanshinone IIA, the main lipophilic bioactive components of SM, reduced the Ang II-induced activation of β-catenin and IGF-2R pathways, apoptosis and cardiac remodeling via ERs (Chen et al., 2017a). More details were shown in Table 4.

Conclusions and outlooks

Organ fibrosis was a common endpoint of diverse chronic diseases with progressive tissue scarring and organ dysfunction that eventually led to organ failure and significant mortality world-wide (Wynn, 2004). Pulmonary fibrosis, cardiac fibrosis, hepatic fibrosis, and renal fibrosis were the most common four types of organ fibrosis in thorax and abdomainal viscera, which shared the same histopathological features, including the destruction of parenchyma cells, the activation of mesenchymal cells, and the imbalance of immunological cells. Fibrosis is a highly dynamic process in various organ systems. Indeed, despite certain achievements were made in clinic treatment, no specific drug for reversing fibrosis of either organ was approved by Food and Drug Administration. Numerous anti-fibrotic drugs against single-target and single-pathway single target have failed in clinical experiments, which revealed that the candidate drug against organ fibrosis should shift to multi-target and multi-pathway.

SM has been regarded as the most frequent used hepatoprotective and cardioprotective drug in TCM practice. Accumulated evidence suggests that SM and its active ingredients exerted protective effects on fibrotic diseases in thorax and abdomainal viscera. The mechanism of how SM and its ingredients benefit fibrosis treatment including but not limited to decreasing inflammation, alleviating oxidative stress, regulating collagen production and degradation, and preventing tissue injury through different signaling pathways (Figures 2, 3). In fibrotic diseases, SM and its ingredients exerted anti-fibrotic functions in different organs via different mechanisms. But they share the same core aim: to lower the fibrous septa in the viscera. It has been known that the activated fibroblasts and myofibroblasts, mainly activated by TGF-β1, are the principal cells of producing ECM (Henderson et al., 2020). On the one hand, SM and its ingredients could inhibit the activation of fibroblasts and myofibroblasts through TGF-β/Smad signaling pathway in fibrotic organs, which contributed the acceleration of ECM degradation, decrease of collagen cross-linking and inhibition of collagen/ECM deposition. And on the other hand, ECM degradation, blocked by SM and its ingredients, could alleviate the cell-ECM interactions to limit the excessive activation of fibroblasts and myofibroblasts.

However, despite of the encouraging progress in our understanding of the efficacy of SM in organ fibrosis, a nonnegligible translational gap remained between bioactive novel constituents extracted form SM and conversion into effective patient therapies and pharmacological agents. Besides, most of the known mechanisms were explored from *in vitro* experiments with a single cell line. Some advanced experimental designs, such as 3D culture system of co-culturing with a diverse array of cells *in vitro* and transgenic mice experiments *in vivo*, were urgent needed to verity the above discoveries. And although the efficacy of Chinese patent medicine from SM and its ingredients have been repeatedly tested in clinical treatment of organ fibrosis, more further studies are needed to better understand the mechanism and to serve the patients. In addition, because of the insufficient bioavailability of SM and its ingredients in poor solubleness, which leads to low oral bioavailability and delivery problems, advanced drug carriers are meaningful to develop, so as to enhance the tissue targeting, expand the clinical applications for the patients suffering from organ fibrosis.

In summary, though many shortcomings exist in the current studies, pharmacological studies and clinical practices have demonstrated that SM and its ingredients are considered to have good clinical efficacy and widespread application prospects. With the implementations of further research, it is believed that more systematic molecular mechanisms and anti-fibrotic targets of SM and its ingredients could be identified and elucidated to improve the treatment for patients with organ fibrosis.

Author contributions

ZY and YP wrote the manuscript; JQ, DP, and XS assisted with the data collection; CL, YT, and YP made critical revision for the manuscript; CL and YP co-correspond for the whole project.

Funding

This work was supported by grants from the National Natural Science Foundation of China (Nos. 81503322, 81730109, 81874363 and 82174057), the National Key Research and Development Program of China (2020YFC0845000), Shanghai Science and technology innovation action plan (21S21900300), the Science and Technology Innovation Action Plan of the Shanghai Municipal Science and Technology Commission (No. 19401901500) and Shuguang Siming Scholar Plan (SGXZ-201910).

Acknowledgments

We thank Yifeng Pan, Shanghai Huanghai Pharmaceutical Co., Ltd., for providing the pictures of SM.

Conflict of interest

The authors declare that the research was conducted in the absence of any commercial or financial relationships that could be construed as a potential conflict of interest.

Publisher's note

References

Ahn, Y. M., Kim, S. K., Lee, S. H., Ahn, S. Y., Kang, S. W., Chung, J. H., et al. (2010). Renoprotective effect of Tanshinone IIA, an active component of Salvia miltiorrhiza, on rats with chronic kidney disease. *Phytother. Res.* 24, 1886–1892. doi:10.1002/ptr.3347

An, L., Peng, L. Y., Sun, N. Y., Yang, Y. L., Zhang, X. W., Li, B., et al. (2019). Tanshinone IIA activates nuclear factor-erythroid 2-related factor 2 to restrain pulmonary fibrosis via regulation of redox homeostasis and glutaminolysis. *Antioxid. Redox Signal.* 30, 1831–1848. doi:10.1089/ars.2018.7569

Bi, W., Tian, M., and Row, K. H. (2011). Extraction and concentration of tanshinones in*Salvia miltiorrhiza*Bunge by task-specific non-ionic surfactant assistance. *Food Chem.* 126, 1985–1990. doi:10.1016/j.foodchem.2010.12.059

Brilla, C. G., Funck, R. C., and Rupp, H. (2000). Lisinopril-mediated regression of myocardial fibrosis in patients with hypertensive heart disease. *Circulation* 102, 1388–1393. doi:10.1161/01.cir.102.12.1388

Cai, H., Su, S., Li, Y., Zeng, H., Zhu, Z., Guo, J., et al. (2018b). Protective effects of Salvia miltiorrhiza on adenine-induced chronic renal failure by regulating the metabolic profiling and modulating the NADPH oxidase/ROS/ERK and TGF-β/Smad signaling pathways. *J. Ethnopharmacol.* 212, 153–165. doi:10.1016/j.jep.2017.09.021

Cai, H., Su, S., Li, Y., Zeng, H., Zhu, Z., Guo, J., et al. (2018a). Protective effects of Salvia miltiorrhiza on adenine-induced chronic renal failure by regulating the metabolic profiling and modulating the NADPH oxidase/ROS/ERK and TGF-β/Smad signaling pathways. *J. Ethnopharmacol.* 212, 153–165. doi:10.1016/j.jep.2017.09.021

Cao, L., Huang, B., Fu, X., Yang, J., Lin, Y., and Lin, F. (2017). Effects of tanshinone IIA on the regulation of renal proximal tubular fibrosis. *Mol. Med. Rep.* 15, 4247–4252. doi:10.3892/mmr.2017.6498

Cao, T., Lu, Y., Zhu, M., Cheng, J., Ye, B., Fang, N., et al. (2020). Effects of Salvia miltiorrhiza and Radix astragali on the TGF-Î²/Smad/Wnt pathway and the pathological process of liver fibrosis in rats. *Cell. Mol. Biol.* 66, 46–51. doi:10.14715/cmb/2020.66.6.9

Che, X. H., Park, E. J., Zhao, Y. Z., Kim, W. H., and Sohn, D. H. (2010). Tanshinone II A induces apoptosis and S phase cell cycle arrest in activated rat hepatic stellate cells. *Basic Clin. Pharmacol. Toxicol.* 106, 30–37. doi:10.1111/j.1742-7843.2009.00465.x

Chen, X., Guo, J., Bao, J., Lu, J., and Wang, Y. (2014). The anticancer properties of salvia miltiorrhiza Bunge (danshen): A systematic review. *Med. Res. Rev.* 34, 768–794. doi:10.1002/med.21304

Chen, X. Y., Yin, W. P., and Yin, Q. Z. (1987). The dorsal raphe nucleus is involved in the inhibitory effect of hypothalamic arcuate stimulation on pain-evoked unit discharges of the thalamic parafascicular nucleus. *Sheng Li Xue Bao* 12, 46–53.

Chen, Y., Duan, G., Xie, M., Chen, B., and Li, Y. (2010). Infrared-assisted extraction coupled with high-performance liquid chromatography for simultaneous determination of eight active compounds in Radix Salviae miltiorrhizae. *J. Sep. Sci.* 33, 2888–2897. doi:10.1002/jssc.201000234

Chen, Y. F., Day, C. H., Lee, N. H., Chen, Y. F., Yang, J. J., Lin, C. H., et al. (2017a). Tanshinone IIA inhibits beta-catenin nuclear translocation and IGF-2R activation via estrogen receptors to suppress angiotensin II-induced H9c2 cardiomyoblast cell apoptosis. *Int. J. Med. Sci.* 14, 1284–1291. doi:10.7150/ijms.20396

Chen, Y. F., Day, C. H., Lee, N. H., Chen, Y. F., Yang, J. J., Lin, C. H., et al. (2017b). Tanshinone IIA inhibits β-catenin nuclear translocation and IGF-2R activation via estrogen receptors to suppress angiotensin II-induced H9c2 cardiomyoblast cell apoptosis. *Int. J. Med. Sci.* 14, 1284–1291. doi:10.7150/ijms.20396

Chor, J. S., Yu, J., Chan, K. K., Go, Y. Y., and Sung, J. J. (2009). Stephania tetrandra prevents and regresses liver fibrosis induced by carbon tetrachloride in rats. *J. Gastroenterol. Hepatol.* 24, 853–859. doi:10.1111/j.1440-1746.2008.05720.x

Cui, G. H., Feng, H., Li, W. Y., Wang, W. Y., and Huang, L. Q. (2010). Cloning and polymorphism analysis of SmERF in Salvia miltiorrhiza. *Yao Xue Xue Bao* 45, 1188–1193.

Deng, C. C., Hu, Y. F., Zhu, D. H., Cheng, Q., Gu, J. J., Feng, Q. L., et al. (2021). Single-cell RNA-seq reveals fibroblast heterogeneity and increased mesenchymal fibroblasts in human fibrotic skin diseases. *Nat. Commun.* 12, 3709. doi:10.1038/s41467-021-24110-y

Diez, J., Querejeta, R., Lopez, B., Gonzalez, A., Larman, M., and Martinez Ubago, J. L. (2002). Losartan-dependent regression of myocardial fibrosis is associated with reduction of left ventricular chamber stiffness in hypertensive patients. *Circulation* 105, 2512–2517. doi:10.1161/01.cir.0000017264.66561.3d

Eddy, A. A. (2005). Progression in chronic kidney disease. *Adv. Chronic Kidney Dis.* 12, 353–365. doi:10.1053/j.ackd.2005.07.011

Fan, Y., Yan, C. P., Chen, C., So, K. F., Li, P., and Qi, L. W. (2014). Tissue-smashing based ultra-rapid extraction of chemical constituents in herbal medicines. *J. Pharm. Biomed. Anal.* 95, 213–219. doi:10.1016/j.jpba.2014.03.004

Fang, J., Xu, S. W., Wang, P., Tang, F. T., Zhou, S. G., Gao, J., et al. (2010). Tanshinone II-A attenuates cardiac fibrosis and modulates collagen metabolism in rats with renovascular hypertension. *Phytomedicine* 18, 58–64. doi:10.1016/j.phymed.2010.06.002

Friedman, S. L. (2010). Evolving challenges in hepatic fibrosis. *Nat. Rev. Gastroenterol. Hepatol.* 7, 425–436. doi:10.1038/nrgastro.2010.97

Gallo, M., Ferracane, R., Graziani, G., Ritieni, A., and Fogliano, V. (2010). Microwave assisted extraction of phenolic compounds from four different spices. *Molecules* 15, 6365–6374. doi:10.3390/molecules15096365

Gao, H., Bo, Z., Wang, Q., Luo, L., Zhu, H., and Ren, Y. (2019b). Salvanic acid B inhibits myocardial fibrosis through regulating TGF-β1/Smad signaling pathway. *Biomed. Pharmacother.* 110, 685–691. doi:10.1016/j.biopha.2018.11.098

Gao, H., Bo, Z., Wang, Q., Luo, L., Zhu, H., and Ren, Y. (2019a). Salvanic acid B inhibits myocardial fibrosis through regulating TGF-β1/Smad signaling pathway. *Biomed. Pharmacother.* 110, 685–691. doi:10.1016/j.biopha.2018.11.098

Ge, M., Liu, H., Zhang, Y., Li, N., Zhao, S., Zhao, W., et al. (2017). The anti-hepatic fibrosis effects of dihydrotanshinone I are mediated by disrupting the yes-associated protein and transcriptional enhancer factor D2 complex and stimulating autophagy. *Br. J. Pharmacol.* 174, 1147–1160. doi:10.1111/bph.13766

Gonzalez, A., Schelbert, E. B., Diez, J., and Butler, J. (2018). Myocardial interstitial fibrosis in heart failure: Biological and translational perspectives. *J. Am. Coll. Cardiol.* 71, 1696–1706. doi:10.1016/j.jacc.2018.02.021

Han, C., Jiang, Y. H., Li, W., and Liu, Y. (2021). Astragalus membranaceus and Salvia miltiorrhiza ameliorates cyclosporin A-induced chronic nephrotoxicity through the "gut-kidney axis. *J. Ethnopharmacol.* 269, 113768. doi:10.1016/j.jep.2020.113768

Henderson, N. C., Rieder, F., and Wynn, T. A. (2020). Fibrosis: From mechanisms to medicines. *Nature* 587, 555–566. doi:10.1038/s41586-020-2938-9

Hu, Y., Wang, M., Pan, Y., Li, Q., and Xu, L. (2020). Salvianolic acid B attenuates renal interstitial fibrosis by regulating the HPSE/SDC1 axis. *Mol. Med. Rep.* 22, 1325–1334. doi:10.3892/mmr.2020.11229

Huang, C., Wu, X., Wang, S., Wang, W., Guo, F., Chen, Y., et al. (2018). Combination of Salvia miltiorrhiza and ligustrazine attenuates bleomycin-induced pulmonary fibrosis in rats via modulating TNF-α and TGF-β. *Chin. Med.* 13, 36. doi:10.1186/s13020-018-0194-9

Izawa, H., Murohara, T., Nagata, K., Isobe, S., Asano, H., Amano, T., et al. (2005). Mineralocorticoid receptor antagonism ameliorates left ventricular diastolic dysfunction and myocardial fibrosis in mildly symptomatic patients with idiopathic dilated cardiomyopathy: A pilot study. *Circulation* 112, 2940–2945. doi:10.1161/CIRCULATIONAHA.105.571653

Jiang, L., Wang, J., Ju, J., and Dai, J. (2020). Salvianolic acid B and sodium tanshinone II A sulfonate prevent pulmonary fibrosis through anti-inflammatory and anti-fibrotic process. *Eur. J. Pharmacol.* 883, 173352. doi:10.1016/j.ejphar.2020.173352

Jiang, Y., David, B., Tu, P., and Barbin, Y. (2010). Recent analytical approaches in quality control of traditional Chinese medicines--a review. *Anal. Chim. Acta* 657, 9–18. doi:10.1016/j.aca.2009.10.024

Kan, S., Li, J., Huang, W., Shao, L., and Chen, D. (2009). Microsphere resin chromatography combined with microbial biotransformation for the separation and purification of salvianolic acid B in aqueous extract of roots of Salvia

multiorrihza Bunge. *J. Chromatogr. A* 1216, 3881–3886. doi:10.1016/j.chroma.2009.02.084

Lee, H. S., and Kim, Y. (2016). Antifungal activity of salvia miltiorrhiza against Candida albicans is associated with the alteration of membrane permeability and (1, 3)-beta-D-Glucan synthase activity. *J. Microbiol. Biotechnol.* 26, 610–617. doi:10.4014/jmb.1511.11009

Lee, S. J., Park, W. H., and Moon, H. I. (2009). Bioassay-guided isolation of antiplasmodial anacardic acids derivatives from the whole plants of Viola websteri Hemsl. *Parasitol. Res.* 104, 463–466. doi:10.1007/s00436-008-1205-z

Lee, T. Y., Chang, H. H., Wang, G. J., Chiu, J. H., Yang, Y. Y., and Lin, H. C. (2006). Water-soluble extract of Salvia miltiorrhiza ameliorates carbon tetrachloride-mediated hepatic apoptosis in rats. *J. Pharm. Pharmacol.* 58, 659–665. doi:10.1211/jpp.58.5.0011

Lee, T. Y., Wang, G. J., Chiu, J. H., and Lin, H. C. (2003). Long-term administration of Salvia miltiorrhiza ameliorates carbon tetrachloride-induced hepatic fibrosis in rats. *J. Pharm. Pharmacol.* 55, 1561–1568. doi:10.1211/0022357022098

Li, C. L., Liu, B., Wang, Z. Y., Xie, F., Qiao, W., Cheng, J., et al. (2020). Salvianolic acid B improves myocardial function in diabetic cardiomyopathy by suppressing IGFBP3. *J. Mol. Cell. Cardiol.* 139, 98–112. doi:10.1016/j.yjmcc.2020.01.009

Li, M. H., Chen, J. M., Peng, Y., Wu, Q., and Xiao, P. G. (2008). Investigation of Danshen and related medicinal plants in China. *J. Ethnopharmacol.* 120, 419–426. doi:10.1016/j.jep.2008.09.013

Li, Y. C., Zeng, J. Q., Liu, L. M., and Jin, X. S. (2002). Extraction of three tanshinones from the root of Salvia miltiorrhiza Bunge by supercritical carbon dioxide fluid and their analysis with high performance liquid chromatography. *Se Pu* 20, 40–42.

Li, Y. G., Song, L., Liu, M., Hu, Z. B., and Wang, Z. T. (2009). Advancement in analysis of Salviae miltiorrhizae Radix et Rhizoma (Danshen). *J. Chromatogr. A* 1216, 1941–1953. doi:10.1016/j.chroma.2008.12.032

Lin, Y. L., Hsu, Y. C., Chiu, Y. T., and Huang, Y. T. (2008). Antifibrotic effects of a herbal combination regimen on hepatic fibrotic rats. *Phytother. Res.* 22, 69–76. doi:10.1002/ptr.2265

Lin, Y. L., Lee, T. F., Huang, Y. J., and Huang, Y. T. (2006a). Antiproliferative effect of salvianolic acid A on rat hepatic stellate cells. *J. Pharm. Pharmacol.* 58, 933–939. doi:10.1211/jpp.58.7.0008

Lin, Y. L., Wu, C. H., Luo, M. H., Huang, Y. J., Wang, C. N., Shiao, M. S., et al. (2006b). *In vitro* protective effects of salvianolic acid B on primary hepatocytes and hepatic stellate cells. *J. Ethnopharmacol.* 105, 215–222. doi:10.1016/j.jep.2005.10.021

Liu, C. H., Liu, P., Hu, Y. Y., Xu, L. M., Tan, Y. Z., Wang, Z. N., et al. (2000). Effects of salvianolic acid-A on rat hepatic stellate cell proliferation and collagen production in culture. *Acta Pharmacol. Sin.* 21, 721–726.

Liu, L., Wei, J., Huo, X., Fang, S., Yao, D., Gao, J., et al. (2012). The Salvia miltiorrhiza monomer IH764-3 induces apoptosis of hepatic stellate cells *in vivo* in a bile duct ligation-induced model of liver fibrosis. *Mol. Med. Rep.* 6, 1231–1238. doi:10.3892/mmr.2012.1076

Liu, M., Xu, H., Zhang, L., Zhang, C., Yang, L., Ma, E., et al. (2018). Salvianolic acid B inhibits myofibroblast transdifferentiation in experimental pulmonary fibrosis via the up-regulation of Nrf2. *Biochem. Biophys. Res. Commun.* 495, 325–331. doi:10.1016/j.bbrc.2017.11.014

Liu, Q., Chu, H., Ma, Y., Wu, T., Qian, F., Ren, X., et al. (2016). Salvianolic acid B attenuates experimental pulmonary fibrosis through inhibition of the TGF-β signaling pathway. *Sci. Rep.* 6, 27610. doi:10.1038/srep27610

Liu, Y. (2011). Cellular and molecular mechanisms of renal fibrosis. *Nat. Rev. Nephrol.* 7, 684–696. doi:10.1038/nrneph.2011.149

Lo, S. H., Hsu, C. T., Niu, H. S., Niu, C. S., Cheng, J. T., and Chen, Z. C. (2017). Cryptotanshinone inhibits STAT3 signaling to alleviate cardiac fibrosis in type 1-like diabetic rats. *Phytother. Res.* 31, 638–646. doi:10.1002/ptr.5777

Lopez, B., Querejeta, R., Gonzalez, A., Sanchez, E., Larman, M., and Diez, J. (2004). Effects of loop diuretics on myocardial fibrosis and collagen type I turnover in chronic heart failure. *J. Am. Coll. Cardiol.* 43, 2028–2035. doi:10.1016/j.jacc.2003.12.052

Luo, X., Deng, Q., Xue, Y., Zhang, T., Wu, Z., Peng, H., et al. (2021b). Anti-fibrosis effects of magnesium lithospermate B in experimental pulmonary fibrosis: By inhibiting TGF-βri/smad signaling. *Molecules* 26, 1715. doi:10.3390/molecules26061715

Luo, X., Deng, Q., Xue, Y., Zhang, T., Wu, Z., Peng, H., et al. (2021a). Anti-fibrosis effects of magnesium lithospermate B in experimental pulmonary fibrosis: By inhibiting TGF-βri/smad signaling. *Molecules* 26, 1715. doi:10.3390/molecules26061715

Ma, S., Yang, D., Wang, K., Tang, B., Li, D., and Yang, Y. (2012). Cryptotanshinone attenuates isoprenaline-induced cardiac fibrosis in mice associated with upregulation and activation of matrix metalloproteinase-2. *Mol. Med. Rep.* 6, 145–150. doi:10.3892/mmr.2012.866

Ma, S., Zhang, D., Lou, H., Sun, L., and Ji, J. (2016). Evaluation of the anti-inflammatory activities of tanshinones isolated from Salvia miltiorrhiza var. alba roots in THP-1 macrophages. *J. Ethnopharmacol.* 188, 193–199. doi:10.1016/j.jep.2016.05.018

Ma, X. H., Ma, Y., Tang, J. F., He, Y. L., Liu, Y. C., Ma, X. J., et al. (2015). The biosynthetic pathways of tanshinones and phenolic acids in salvia miltiorrhiza. *Molecules* 20, 16235–16254. doi:10.3390/molecules200916235

Ma, Y., Li, H., Yue, Z., Guo, J., Xu, S., Xu, J., et al. (2014). Cryptotanshinone attenuates cardiac fibrosis via downregulation of COX-2, NOX-2, and NOX-4. *J. Cardiovasc. Pharmacol.* 64, 28–37. doi:10.1097/FJC.0000000000000086

Maki, T., Kawahara, Y., Tanonaka, K., Yagi, A., and Takeo, S. (2002). Effects of tanshinone VI on the hypertrophy of cardiac myocytes and fibrosis of cardiac fibroblasts of neonatal rats. *Planta Med.* 68, 1103–1107. doi:10.1055/s-2002-36337

Nan, J. X., Park, E. J., Kang, H. C., Park, P. H., Kim, J. Y., and Sohn, D. H. (2001). Anti-fibrotic effects of a hot-water extract from Salvia miltiorrhiza roots on liver fibrosis induced by biliary obstruction in rats. *J. Pharm. Pharmacol.* 53, 197–204. doi:10.1211/0022357011775406

Noble, P. W., Barkauskas, C. E., and Jiang, D. (2012). Pulmonary fibrosis: Patterns and perpetrators. *J. Clin. Invest.* 122, 2756–2762. doi:10.1172/JCI60323

Pan, Y., Fu, H., Kong, Q., Xiao, Y., Shou, Q., Chen, H., et al. (2014). Prevention of pulmonary fibrosis with salvianolic acid a by inducing fibroblast cell cycle arrest and promoting apoptosis. *J. Ethnopharmacol.* 155, 1589–1596. doi:10.1016/j.jep.2014.07.049

Pang, H., Wu, L., Tang, Y., Zhou, G., Qu, C., and Duan, J. A. (2016). Chemical Analysis of the Herbal Medicine Salviae miltiorrhizae Radix et Rhizoma (Danshen). *Molecules* 21, 51. doi:10.3390/molecules21010051

Parajuli, D. R., Park, E. J., Che, X. H., Jiang, W. Y., Kim, Y. C., Sohn, D. H., et al. (2013). PF2401-SF, standardized fraction of Salvia miltiorrhiza, induces apoptosis of activated hepatic stellate cells *in vitro* and *in vivo*. *Molecules* 18, 2122–2134. doi:10.3390/molecules18022122

Parajuli, D. R., Zhao, Y. Z., Jin, H., Chi, J. H., Li, S. Y., Kim, Y. C., et al. (2015). Anti-fibrotic effect of PF2401-SF, a standardized fraction of Salvia miltiorrhiza, in thioacetamide-induced experimental rats liver fibrosis. *Arch. Pharm. Res.* 38, 549–555. doi:10.1007/s12272-014-0425-2

Peng, L. Y., An, L., Sun, N. Y., Ma, Y., Zhang, X. W., Liu, W. H., et al. (2019). Salvia miltiorrhiza restrains reactive oxygen species-associated pulmonary fibrosis via targeting nrf2-nox4 redox balance. *Am. J. Chin. Med.* 47, 1113–1131. doi:10.1142/S0192415X19500575

Peng, R., Wang, S., Wang, R., Wang, Y., Wu, Y., and Yuan, Y. (2017). Antifibrotic effects of tanshinol in experimental hepatic fibrosis by targeting PI3K/AKT/mTOR/p70S6K1 signaling pathways. *Discov. Med.* 23, 81–94.

Peng, Y., Yang, T., Huang, K., Shen, L., Tao, Y., and Liu, C. (2018). Salvia miltiorrhiza ameliorates liver fibrosis by activating hepatic natural killer cells *in vivo* and *in vitro*. *Front. Pharmacol.* 9, 762. doi:10.3389/fphar.2018.00762

Qiu, H., Liu, W., Lan, T., Pan, W., Chen, X., Wu, H., et al. (2018b). Salvianolate reduces atrial fibrillation through suppressing atrial interstitial fibrosis by inhibiting TGF-β1/Smad2/3 and TXNIP/NLRP3 inflammasome signaling pathways in post-MI rats. *Phytomedicine* 51, 255–265. doi:10.1016/j.phymed.2018.09.238

Qiu, H., Liu, W., Lan, T., Pan, W., Chen, X., Wu, H., et al. (2018a). Salvianolate reduces atrial fibrillation through suppressing atrial interstitial fibrosis by inhibiting TGF-β1/Smad2/3 and TXNIP/NLRP3 inflammasome signaling pathways in post-MI rats. *Phytomedicine* 51, 255–265. doi:10.1016/j.phymed.2018.09.238

Schuppan, D., and Kim, Y. O. (2013). Evolving therapies for liver fibrosis. *J. Clin. Invest.* 123, 1887–1901. doi:10.1172/JCI66028

Shi, M. J., Yan, X. L., Dong, B. S., Yang, W. N., Su, S. B., and Zhang, H. (2020). A network pharmacology approach to investigating the mechanism of Tanshinone IIA for the treatment of liver fibrosis. *J. Ethnopharmacol.* 253, 112689. doi:10.1016/j.jep.2020.112689

Su, C. Y., Ming, Q. L., Rahman, K., Han, T., and Qin, L. P. (2015). Salvia miltiorrhiza: Traditional medicinal uses, chemistry, and pharmacology. *Chin. J. Nat. Med.* 13, 163–182. doi:10.1016/S1875-5364(15)30002-9

Sun, J., Huang, S. H., Tan, B. K., Whiteman, M., Zhu, Y. C., Wu, Y. J., et al. (2005). Effects of purified herbal extract of Salvia miltiorrhiza on ischemic rat myocardium after acute myocardial infarction. *Life Sci.* 76, 2849–2860. doi:10.1016/j.lfs.2004.11.016

Tian, S., Chen, M., Wang, B., Han, Y., Shang, H., and Chen, J. (2021). Salvianolic acid B blocks hepatic stellate cell activation via FGF19/FGFR4 signaling. *Ann. Hepatol.* 20, 100259. doi:10.1016/j.aohep.2020.07.013

Tsochatzis, E. A., Bosch, J., and Burroughs, A. K. (2014). Liver cirrhosis. *Lancet* 383, 1749–1761. doi:10.1016/S0140-6736(14)60121-5

Wan, Y. J., Wang, Y. H., Guo, Q., Jiang, Y., Tu, P. F., and Zeng, K. W. (2021). Protocatechualdehyde protects oxygen-glucose deprivation/reoxygenation-induced myocardial injury via inhibiting PERK/ATF6α/IRE1α pathway. *Eur. J. Pharmacol.* 891, 173723. doi:10.1016/j.ejphar.2020.173723

Wang, C., Luo, H., Xu, Y., Tao, L., Chang, C., and Shen, X. (2018a). Salvianolic acid B-alleviated angiotensin II induces cardiac fibrosis by suppressing NF-κB pathway *in vitro*. *Med. Sci. Monit.* 24, 7654–7664. doi:10.12659/MSM.908936

Wang, L., Yu, J., Fordjour, P. A., Xing, X., Gao, H., Li, Y., et al. (2017). Danshen injection prevents heart failure by attenuating post-infarct remodeling. *J. Ethnopharmacol.* 205, 22–32. doi:10.1016/j.jep.2017.04.027

Wang, R., Wang, J., Song, F., Li, S., and Yuan, Y. (2018b). Tanshinol ameliorates CCl(4)-induced liver fibrosis in rats through the regulation of Nrf2/HO-1 and NF-κB/IκBα signaling pathway. *Drug Des. devel. Ther.* 12, 1281–1292. doi:10.2147/DDDT.S159546

Wang, R., Yu, X. Y., Guo, Z. Y., Wang, Y. J., Wu, Y., and Yuan, Y. F. (2012). Inhibitory effects of salvianolic acid B on CCl(4)-induced hepatic fibrosis through regulating NF-κB/IκBα signaling. *J. Ethnopharmacol.* 144, 592–598. doi:10.1016/j.jep.2012.09.048

Wang, Y., Peng, H., Shen, Y., Zhao, R., and Huang, L. (2013). The profiling of bioactive ingredients of differently aged Salvia miltiorrhiza roots. *Microsc. Res. Tech.* 76, 947–954. doi:10.1002/jemt.22253

Wu, C., Chen, W., Ding, H., Li, D., Wen, G., Zhang, C., et al. (2019). Salvianolic acid B exerts anti-liver fibrosis effects via inhibition of MAPK-mediated phospho-Smad2/3 at linker regions *in vivo* and *in vitro*. *Life Sci.* 239, 116881. doi:10.1016/j.lfs.2019.116881

Wynn, T. A. (2004). Fibrotic disease and the T(H)1/T(H)2 paradigm. *Nat. Rev. Immunol.* 4, 583–594. doi:10.1038/nri1412

Wynn, T. A. (2011). Integrating mechanisms of pulmonary fibrosis. *J. Exp. Med.* 208, 1339–1350. doi:10.1084/jem.20110551

Wynn, T. A., and Ramalingam, T. R. (2012). Mechanisms of fibrosis: Therapeutic translation for fibrotic disease. *Nat. Med.* 18, 1028–1040. doi:10.1038/nm.2807

Xd, M. E., Cao, Y. F., Che, Y. Y., Li, J., Shang, Z. P., Zhao, W. J., et al. (2019). Danshen: A phytochemical and pharmacological overview. *Chin. J. Nat. Med.* 17, 59–80. doi:10.1016/S1875-5364(19)30010-X

Xu, L., Shen, P., Bi, Y., Chen, J., Xiao, Z., Zhang, X., et al. (2016). Danshen injection ameliorates STZ-induced diabetic nephropathy in association with suppression of oxidative stress, pro-inflammatory factors and fibrosis. *Int. Immunopharmacol.* 38, 385–394. doi:10.1016/j.intimp.2016.06.024

Xu, S., He, L., Ding, K., Zhang, L., Xu, X., Wang, S., et al. (2020). Tanshinone IIA ameliorates streptozotocin-induced diabetic nephropathy, partly by attenuating PERK pathway-induced fibrosis. *Drug Des. devel. Ther.* 14, 5773–5782. doi:10.2147/DDDT.S257734

Yang, J., Li, J., Tan, R., He, X., Lin, X., Zhong, X., et al. (2021). Protocatechualdehyde attenuates obstructive nephropathy through inhibiting lncRNA9884 induced inflammation. *Phytother. Res.* 35, 1521–1533. doi:10.1002/ptr.6919

Yang, T., Shen, D. P., Wang, Q. L., Tao, Y. Y., and Liu, C. H. (2013). Investigation of the absorbed and metabolized components of Danshen from Fuzheng Huayu recipe and study on the anti-hepatic fibrosis effects of these components. *J. Ethnopharmacol.* 148, 691–700. doi:10.1016/j.jep.2013.05.031

Yang, Y., Yang, S., Chen, M., Zhang, X., Zou, Y., and Zhang, X. (2008). Compound Astragalus and Salvia miltiorrhiza Extract exerts anti-fibrosis by mediating TGF-beta/Smad signaling in myofibroblasts. *J. Ethnopharmacol.* 118, 264–270. doi:10.1016/j.jep.2008.04.012

Yin, D., Yin, J., Yang, Y., Chen, S., and Gao, X. (2014). Renoprotection of Danshen Injection on streptozotocin-induced diabetic rats, associated with tubular function and structure. *J. Ethnopharmacol.* 151, 667–674. doi:10.1016/j.jep.2013.11.025

Yin, Q., Lu, H., Bai, Y., Tian, A., Yang, Q., Wu, J., et al. (2015). A metabolite of Danshen formulae attenuates cardiac fibrosis induced by isoprenaline, via a NOX2/ROS/p38 pathway. *Br. J. Pharmacol.* 172, 5573–5585. doi:10.1111/bph.13133

Zeng, J., and Bao, X. (2021b). Tanshinone IIA attenuates high glucose-induced epithelial-to-mesenchymal transition in HK-2 cells through VDR/Wnt/β-catenin signaling pathway. *Folia histochem. Cytobiol.* 59, 259–270. doi:10.5603/FHC.a2021.0025

Zeng, J., and Bao, X. (2021a). Tanshinone IIA attenuates high glucose-induced epithelial-to-mesenchymal transition in HK-2 cells through VDR/Wnt/β-catenin signaling pathway. *Folia histochem. Cytobiol.* 59, 259–270. doi:10.5603/FHC.a2021.0025

Zhang, L., Wu, T., Chen, J. M., Yang, L. L., Song, H. Y., and Ji, G. (2012). Danshensu inhibits acetaldehyde-induced proliferation and activation of hepatic stellate cell-T6. *Zhong Xi Yi Jie He Xue Bao* 10, 1155–1161. doi:10.3736/jcim20121013

Zhang, W., Ping, J., Zhou, Y., Chen, G., and Xu, L. (2019a). Salvianolic acid B inhibits activation of human primary hepatic stellate cells through downregulation of the myocyte enhancer factor 2 signaling pathway. *Front. Pharmacol.* 10, 322. doi:10.3389/fphar.2019.00322

Zhang, Y., Li, X., and Wang, Z. (2013). Diversity evaluation of Salvia miltiorrhiza using ISSR markers. *Biochem. Genet.* 51, 707–721. doi:10.1007/s10528-013-9600-2

Zhang, Y., Lu, W., Zhang, X., Lu, J., Xu, S., Chen, S., et al. (2019b). Cryptotanshinone protects against pulmonary fibrosis through inhibiting Smad and STAT3 signaling pathways. *Pharmacol. Res.* 147, 104307. doi:10.1016/j.phrs.2019.104307

Zhang, Y., Wang, H., Cui, L., Zhang, Y., Liu, Y., Chu, X., et al. (2015). Continuing treatment with Salvia miltiorrhiza injection attenuates myocardial fibrosis in chronic iron-overloaded mice. *PLoS One* 10, e0124061. doi:10.1371/journal.pone.0124061

Zhao, Q., Pan, Y. L., Dou, H. T., Hua, J. H., Fu, X. X., and Wang, J. H. (2016a). Effect of different locations and genotypes on yield and accumulation of bioactive constituents in salvia miltiorrhiza. *Zhong Yao Cai* 39, 1935–1939.

Zhao, Q., Song, Z., Fang, X., Pan, Y., Guo, L., Liu, T., et al. (2016b). Effect of genotype and environment on salvia miltiorrhiza roots using LC/MS-Based metabolomics. *Molecules* 21, 414. doi:10.3390/molecules21040414

frontiers | Frontiers in Pharmacology

TYPE Clinical Trial
PUBLISHED 20 September 2022
DOI 10.3389/fphar.2022.1014486

OPEN ACCESS

EDITED BY
Jian Gao,
Shanghai Children's Medical Center, China

REVIEWED BY
Chun Yang,
Nanjing Medical University, China
Jian-Jun Yang,
Zhengzhou University, China

*CORRESPONDENCE
Xuesheng Liu,
liuxuesheng@ahmu.edu.cn

SPECIALTY SECTION
This article was submitted to Gastrointestinal and Hepatic Pharmacology, a section of the journal Frontiers in Pharmacology

RECEIVED 08 August 2022
ACCEPTED 06 September 2022
PUBLISHED 20 September 2022

CITATION
Tang L, Ye C, Wang N, Chen C, Chen S, Gao S and Liu X (2022), The median effective doses of propofol combined with two different doses of nalbuphine for adult patients during painless gastroscopy.
Front. Pharmacol. 13:1014486.
doi: 10.3389/fphar.2022.1014486

The median effective doses of propofol combined with two different doses of nalbuphine for adult patients during painless gastroscopy

Lili Tang[1], Chenxuan Ye[1], Nan Wang[1], Chen Chen[1], Sirui Chen[2], Shan Gao[3] and Xuesheng Liu[1]*

[1]Department of Anesthesiology, The First Affiliated Hospital of Anhui Medical University, Hefei, China, [2]Department of Biomedical Engineering, City University of Hong Kong, Kowloon Tong, Hong Kong SAR, China, [3]Department of Pharmacology, Basic Medical College, Anhui Medical University, Hefei, China

Objective: Propofol is the most widely administered intravenous anesthetic to induce deep sedation for gastroscopy procedures. Coadministration of nalbuphine can provide analgesia and sedation to patients experiencing visceral pain, thereby decreasing the amount of propofol needed and reducing the risk of propofol-induced adverse events. We carried out this study to determine the median effective dose (ED50) of propofol in combination with different dosages of nalbuphine and the optimal dosage of nalbuphine during painless gastroscopy.

Methods: We recruited sixty-five patients aged 18–60 years who underwent elective painless gastroscopy. A total of sixty-one patients were allocated randomly to the N1 group (nalbuphine 0.1 mg/kg) or N2 group (nalbuphine 0.15 mg/kg). Three minutes after administration of nalbuphine, patients received a preset dose of propofol at 2.0 mg/kg with a dose gradient of 0.2 mg/kg according to Dixon's "up-and-down" method. The primary outcome was the ED50 of propofol in combination with nalbuphine. Hemodynamic parameters, recovery time, pain score, and adverse events were recorded as secondary outcomes.

Results: The ED50 of propofol in the N2 group was significantly lower than that observed in the N1 group ($p < 0.01$). Using probit analysis, the ED50 and ED95 of propofol were 1.632 mg/kg and 2.759 mg/kg in the N1 group and 1.111 mg/kg and 2.243 mg/kg in the N2 group, respectively. The incidence of hypotension in the N2 group was lower than that in the N1 group ($p < 0.05$), and the recovery time was shorter than that of the N1 group ($p < 0.05$).

Conclusion: In adult patients, 0.15 mg/kg nalbuphine led to a significant reduction in the ED50 and ED95 of propofol during gastroscopy. This dose of nalbuphine also reduced the incidence of hypotension and shortened the recovery time. Therefore, nalbuphine (0.15 mg/kg) combined with propofol is a safe option for enhancing recovery after painless gastroscopy in adult patients.

Clinical Trial Registration: [https://www.chictr.org.cn/edit.aspx?pid=126699&htm=4], identifier [ChiCTR2100053204].

KEYWORDS

nalbuphine, propofol, gastroscopy, dose-effect relationship, ED50

Introduction

Gastroscopy is widely used to diagnose or treat esophageal and gastric diseases and may reduce the incidence and mortality rates of upper gastrointestinal tract cancer in areas with high cancer risk in China (Xia et al., 2021). In 2018, 22.2 million gastrointestinal endoscopies were performed in the United States, and 284,844 new cases of gastrointestinal cancer were diagnosed (Peery et al., 2022). However, gastroscopy is a painful and unbearable procedure without sedation and analgesia. Therefore, the vast majority of endoscopic examinations (>98%) were performed under sedation (Cohen et al., 2006).

Propofol sedation in gastroscopy has become a mainstay of clinical practice due to its shorter onset, faster recovery, antiemetic effect, better acceptance and higher diagnostic accuracy of the procedure (Meining et al., 2007; Wang et al., 2013; Committee et al., 2018). However, propofol alone appears to have several dose-dependent adverse effects, such as respiratory depression, hypotension, hypoxemia and injection pain (Vaessen and Knape, 2016; Yin et al., 2019; Stogiannou et al., 2018). Thus, μ-receptor opioids, such as remifentanil, fentanyl or sufentanil, can be combined with propofol to reduce propofol-related adverse events in clinical practice (Xu et al., 2008; Zhang et al., 2014; Li et al., 2016; Yin et al., 2019; Yu et al., 2019; Wang et al., 2020; Dossa et al., 2021). However, there is still a high incidence of severe hypoxemia (SPO_2 < 90%) and hypotension when these μ-receptor opioids are combined with propofol during gastrointestinal endoscopy (Xu et al., 2008; Lin et al., 2019), which may result in longer recovery time and higher financial burden.

Nalbuphine, a κ-opioid receptor agonist and μ-opioid receptor antagonist, provides analgesia, a sedative effect, less respiratory depression, and increased patient comfort (Chestnutt, 1987; Jaffe et al., 1988; Sury and Cole, 1988). Compared to sufentanil, Sun suggested that nalbuphine provides a better analgesic effect for visceral pain and higher patient satisfaction after cesarean section (Sun et al., 2020). Nalbuphine at 0.162 mg/kg combined with propofol was reported to be effective and safe for painless gastroscopy in adults (Li et al., 2021). Our center also found that 0.1 mg/kg nalbuphine could effectively inhibit the injection pain associated with propofol and reduce the total dosage of propofol needed for gastroscopy (Wang et al., 2020). However, the minimum effective dose of propofol in combination with nalbuphine has not yet been determined. Therefore, the current study was to investigate the median effective dose (ED50) of propofol combined with different doses of nalbuphine during gastroscopy in adult patients.

Materials and methods

The current randomized controlled trial was approved by the Ethical Committee of The First Affiliated Hospital of Anhui Medical University (China, Approval No. PJ 2021-14-15) and registered in the Chinese Clinical Trial Registry (https://www.chictr.org.cn/edit.aspx?pid=126699&htm=4, ChiCTR2100053204; 14 November 2021). All patients in our study provided written informed consent.

Patients

We recruited patients who were scheduled for painless gastroscopy or biopsy with American Society of Anesthesiologists (ASA) physical status I or II. All patients were adults aged 18–60 y with a body mass index (BMI) between 18 and 24 kg/m^2.

The exclusion criteria were as follows: age <18 y or >60 y; ASA III or higher; overweight (body mass index >24 kg/m^2); allergy to nalbuphine or propofol; liver or kidney dysfunction; history of neurologic, respiratory or heart diseases; mental illness, sedative or analgesic drug abuse; duration of gastroscopy >30 min; inability to provide informed consent.

Clinical protocol

Based on the dose of nalbuphine (Rui Jing, Yichang Humanwell Pharmaceutical, Hubei, China; lot no. 21J04021), patients were assigned randomly to an N1 group (0.1 mg/kg nalbuphine) or an N2 group (0.15 mg/kg nalbuphine) at a 1:1 ratio using computer-generated randomized numbers.

All patients fasted for 8 h, had no water for 2 h and did not receive any preoperative medication before the gastroscopy. Standard physiological monitoring, including oxygen saturation (SpO_2), blood pressure, respiratory rate (RR) and electrocardiogram, was applied every 2 min, and venous access to the upper limb was secured in the operating room. Nalbuphine in both groups was diluted into 10-ml syringe by an anesthesiologist who did not participate in the case collection. When nalbuphine was given intravenously, oxygen was supplied by a mask (5 L/min). Approximately 3 min after nalbuphine administration, propofol (AstraZeneca, Cambridge, United Kingdom; lot no. RX455) was injected within 60 s. Sedation levels were assessed with the Modified Observer's Assessment of Alertness/Sedation Scale (MOAA/S) every minute during gastroscopy (score of 5: responds quickly to name spoken in normal tone; score of 4: lethargic response to name spoken in normal tone; score of 3: responds only after

name is called loudly and/or repeatedly; score of 2: responds only after mild prodding or shaking; score of 1: responds only after painful trapezius squeeze; 0 score: no response after painful trapezius squeeze). Gastroscopy was performed after the patient's MOAA/S score was ≤2 (Patel et al., 2005; Kang et al., 2021). All anesthetic injections and management were performed by the same senior anesthesiologist, and the examination was conducted by the same group of experienced endoscopists.

We assessed the threshold for all-or-none responses to gastroscopy using the up-and-down method (Dixon, 1991). Propofol was administered at a preselected dose of 2.0 mg/kg, and a booster injection of 0.5 mg/kg propofol was administered if the patient could not tolerate the operation of the gastroscope, which was indicated by frowning, cough, or any physical movement when gastroscopy was placed within 5 min after propofol injection. Accordingly, the dosage of propofol for the next patient was increased by a step size of 0.2 mg/kg, and if the gastroscopic examination was successfully completed, the dose for the next patient to be examined was decreased by 0.2 mg/kg. The corresponding propofol dose at the midpoint of negative and positive responses was defined as the effective dose of propofol for 1 crossover, and the effective dose in each group was the average of the 7 crossovers in this group.

The primary outcome was the ED50 of propofol in the two groups. Secondary outcomes included initial dose of propofol; duration of procedure (the time from endoscopic implantation to endoscopic withdrawal); time of opening eyes (the time from losing consciousness to opening eyes); orientation recovery time (the time from losing consciousness to answer the name and location); systolic blood pressure (SBP), diastolic blood pressure (DBP), heart rate (HR) and respiratory rate (RR) before induction (T1), after induction (T2), end of gastroscopy (T3), and opening eyes (T4); adverse events; pain score at the time of anesthesia recovery by visual analog scale (VAS, 0 = painless and 10 = severe pain); and duration of stay in the postanesthesia care unit (PACU; the time from endoscopic withdrawal to Steward score of 6). An anesthesiology resident who was blinded to group assignment recorded the data.

Systolic blood pressure decreased by more than 20% compared with the preoperative baseline value, or the mean arterial pressure was less than 60, which was regarded as perioperative hypotension. Patients with intraoperative hypotension were immediately treated with phenylephrine (20 μg). Atropine (0.5 mg) was administered if patients had bradycardia (HR < 50 bpm). If hypoxemia (SpO_2 < 95%) appeared, the lower jaw was lifted; if the SpO_2 did not improve or continued to drop to less than 90% (severe hypoxia), pressure-assisted ventilation with a mask was performed.

Statistical analysis

According to another article in our center, the incidence of hypotension during gastroscopy was 44% with 0.1 mg/kg nalbuphine combined with propofol (Wang et al., 2020). We assumed a 50% reduction in hypotension with 0.15 mg/kg nalbuphine, requiring 50 samples per group to achieve a power of 0.8, an α significance level of 0.05, and a loss to follow-up rate of 0.1. We also applied the 7 crossovers recommended by the up-down method of Dixon's approach for sample size calculation (Dixon, 1991; Chen et al., 2021). All data analyses were performed by SPSS version 23.0 (IBM Inc., Armonk, NY, United States), provided by the Medical Data Processing Center of the School of Public Health of Anhui Medical University. Normally distributed continuous variables were expressed as the means ± standard deviations (SD) and compared by independent-samples *t* test. Nonnormally distributed data are presented as medians (interquartile ranges, IQR) and analyzed by the Mann–Whitney U test. Categorical variables were expressed as frequencies (%) and compared with Fischer's exact test. The ED50 of each group was calculated as the average of 7 crossovers of the dose of propofol, and then, the ED50 values in the two groups were compared by independent-samples *t* test. We also applied the probit method (probability unit regression) to analyze the up-and-down sequences in each group and to calculate the ED50 and 95% effective dose (ED95) of propofol in the two groups. Repeated measures ANOVA was used to analyze hemodynamic and respiratory changes. A p value less than 0.05 was considered statistically significant.

Results

Included patient information

From November 2021 to March 2022, sixty-five patients were assessed for eligibility, and four patients were excluded: two patients declined to participate, and two patients did not meet the inclusion criteria. When 31 patients were included in the N1 group and 30 patients in the N2 group, the 7 crossovers of each group occurred. Therefore, sixty-one patients were enrolled and allocated randomly to the N1 and N2 groups, and the data of 61 patients were finally analyzed (shown in Figure 1). The baseline data between the two groups showed no significant difference (Table 1).

The ED50/ED95 of propofol combined with different doses of nalbuphine

The ED50 of propofol in the N2 group was significantly lower than that observed in the N1 group (1.20 ± 0.38 vs. 1.66 ± 0.38 mg/kg, $p < 0.01$) (Table 2). The results of the ED50 of propofol in the two groups were similar using probit analysis, which were 1.632 mg/kg in the N1 group and 1.111 mg/kg in the N2 group. The ED95 values of propofol in the N1 and N2 groups were 2.759 mg/kg and 2.243 mg/kg,

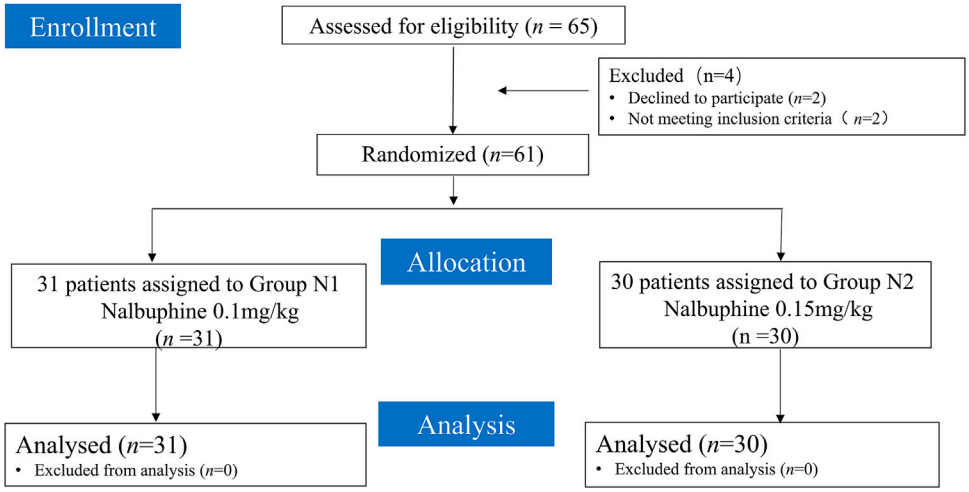

FIGURE 1
Flowchart of patient enrollment, allocation, and analysis.

TABLE 1 The general characteristics of patients in the two groups.

Values	Group N1 (n = 31)	Group N2 (n = 30)	p value
Age (years)	42.29 ± 11.30	43.30 ± 10.50	0.449
Sex (M/F)	10/21	10/20	0.572
Height (cm)	163 (160, 170)	162 (157.75, 168)	0.127
Weight (kg)	59.31 ± 7.19	58.45 ± 7.33	0.653
BMI (kg/m^2)	21.22 (20.55, 22.83)	22.26 (21.05, 23.44)	0.132
ASA status			0.527
I	7 (22.58%)	6 (20%)	
II	24 (77.42%)	24 (80%)	

Values are expressed as the mean ± SD, median (IQR), or the number of patients and percent. M, male; F, female; BMI, body mass index; ASA, American Society of Anesthesiologists (ASA). No significant differences were found in these characteristics between the two groups. Group N1: 0.1 mg/kg nalbuphine; Group N2: 0.15 mg/kg nalbuphine; 3 min after nalbuphine administration, propofol was given to the two groups.

respectively. (shown in Figures 2, 3). The sequential doses of propofol combined with different doses of nalbuphine in gastroscopy are shown in Figures 2, 3.

Comparison of intravenous anesthesia outcomes, procedure time and adverse effects

The initial time of propofol and the time of procedure did not differ between the two groups. Compared to the N1 group, the initial dose of propofol in the N2 group was significantly reduced (72.67 ± 23.54 vs. 102.35 ± 23.49 mg, $p < 0.001$). The total dose of propofol had similar results (88.1 [62.85, 118.20] vs. 108 [93.60, 134.80] mg, $p < 0.01$). The corresponding time of eye opening (5.31 [3.99, 6.22] vs. 6.43 [5.52, 7.93] min, $p < 0.05$), orientation recovery time (6.00 [4.99, 7.36] vs. 7.38 [6.25, 8.65] min, $p < 0.01$) and stay in the PACU (13 [12.10, 14.16] vs. 15 [13.20, 17.00] min, $p < 0.05$) were shorter in the N2 group than in the N1 group. There was a statistically significant difference in VAS score between the N1 and N2 groups (0 [0, 1] vs. 0 [0, 0]); $p < 0.05$). The incidence of injection pain of propofol and respiratory

TABLE 2 Comparison of perioperative outcomes and adverse events between the two groups.

Values	Group N1 (n = 31)	Group N2 (n = 30)	p value
Initial dose of propofol (mg)	102.35 ± 23.49	72.67 ± 23.54	0.000
Initial time of propofol (s)	64 (52, 77)	62 (53.75, 74)	0.874
Total dose of propofol (mg)	108 (93.60–134.80)	88.1 (62.85, 118.20)	0.002
ED50 of propofol	1.66 ± 0.38	1.20 ± 0.38	0.005
Duration of procedure (min)	4.66 ± 1.22	4.30 ± 1.90	0.390
Time of opening eyes (min)	6.43 (5.52, 7.93)	5.31 (3.99, 6.22)	0.014
Orientation recovery time	7.38 (6.25, 8.65)	6.00 (4.99, 7.36)	0.007
Stay of PACU (min)	15 (13.2, 17)	13 (12.10, 14.16)	0.018
VAS scores	0 (0, 1)	0 (0, 0)	0.030
Hypotension	11 (35.48%)	2 (6.67%)	0.011
Injection pain	9 (29.03%)	4 (13.33%)	0.118
Respiratory depression	8 (25.81%)	2 (6.67%)	0.081
PONV	1 (3.23%)	2 (6.67%)	0.612

Values are expressed as the mean ± SD, median (IQR), or the number of patients and percent. ED50, median effective dose; PACU, postanesthesia care unit; VAS, visual analog scale; PONV, postoperative nausea and/or vomiting.

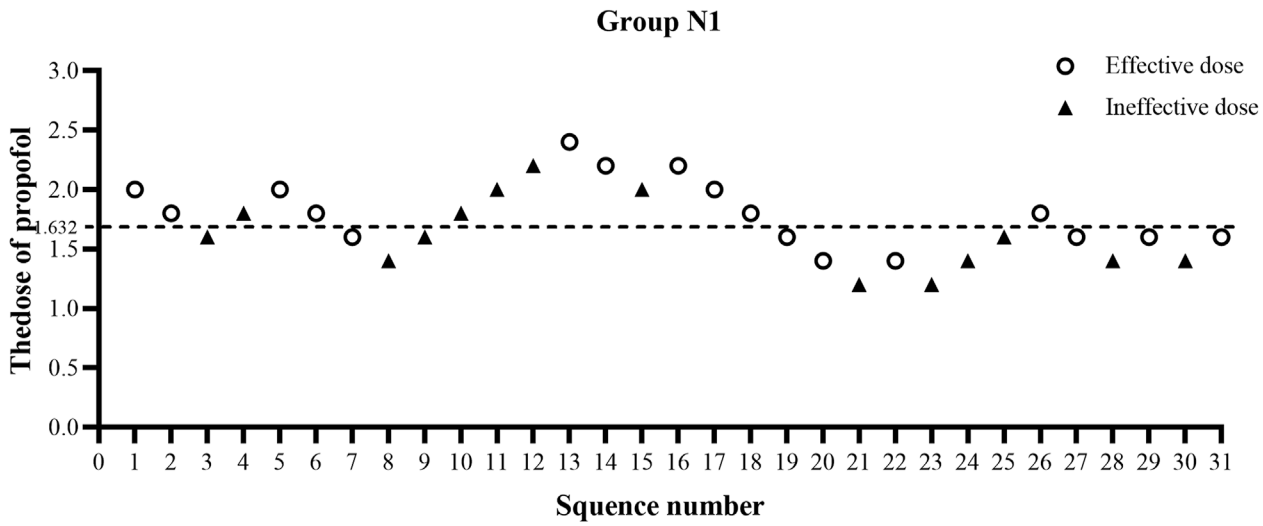

FIGURE 2
Sequential dose adjustment of propofol when combined with 0.1 mg/kg nalbuphine by the Dixon method in the N1 group. The open circle represents an effective dose; the filled triangle indicates an ineffective dose. The ED50 and ED95 were 1.632 mg/kg and 2.759 mg/kg, respectively, in the N1 group.

depression in the N2 group was slightly lower than that in the N1 group; however, there was no statistically significant difference between the two groups ($p > 0.05$). The incidence of nausea and vomiting between the two groups also showed no significant difference ($p > 0.05$). The results are all presented in Table 2.

Comparison of hemodynamic and respiratory parameters at different time points

Table 3 shows that systolic blood pressure (SBP), diastolic blood pressure (DBP) and heart rate (HR) in the two groups were both

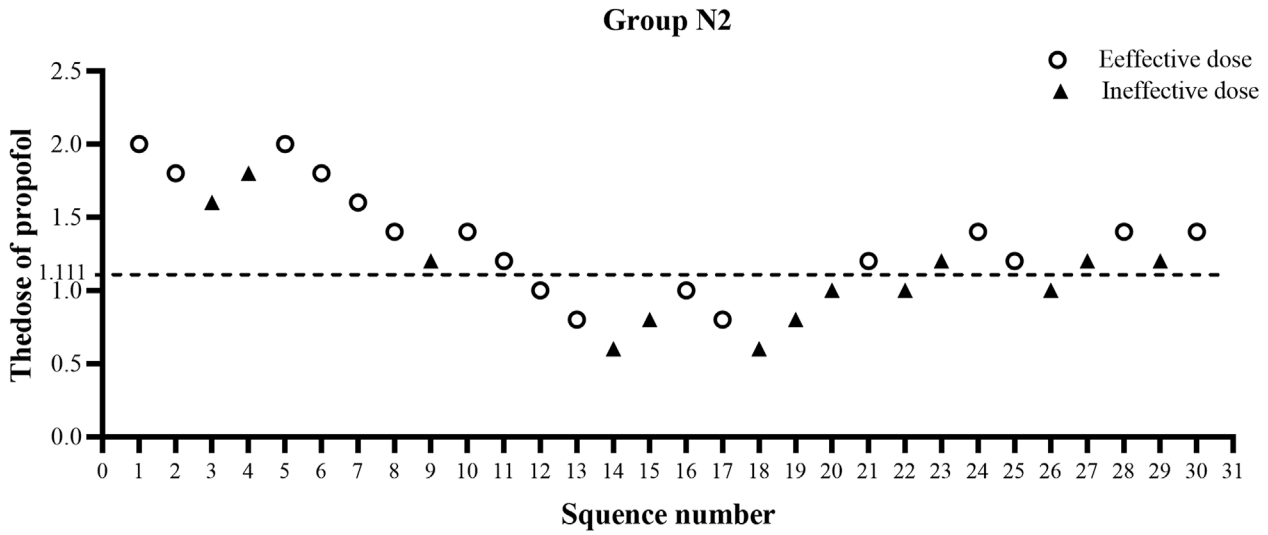

FIGURE 3
Sequential dose adjustment of propofol when combined with 0.15 mg/kg nalbuphine by the Dixon method in the N2 group. The open circle represents an effective dose; the filled triangle indicates an ineffective dose. The ED50 and ED95 were 1.111 mg/kg and 2.243 mg/kg, respectively, in the N2 group.

TABLE 3 Comparison of hemodynamic parameters and respiratory rate between the two groups at different time points.

Values	Time points	Group N1 (n = 31)	Group N2 (n = 30)
SBP (mmHg)	T1	131 ± 15.66	131.60 ± 15.49
	T2	113.71 ± 14.95*	121 ± 23.72*
	T3	108 ± 11.95*	112.60 ± 13.70*
	T4	112.35 ± 11.93	117.13 ± 11.71
DBP (mmHg)	T1	84.03 ± 13.80	86.20 ± 10.32
	T2	71.97 ± 13.20*	71.77 ± 11.28*
	T3	69.13 ± 10.30*	72.03 ± 11.47*
	T4	71.38 ± 12.65*	75.26 ± 11.93*
HR (bpm)	T1	84.35 ± 17.39	82.83 ± 11.31
	T2	79.38 ± 12.21*	75.23 ± 8.56*
	T3	74.74 ± 12.41*	75.63 ± 11.11*
	T4	80.13 ± 13.63	78.40 ± 11.06
RR (bpm)	T1	16.45 ± 3.37	15.77 ± 3.54
	T2	14.06 ± 3.07	14.03 ± 3.43
	T3	14.81 ± 3.36	14.2 ± 3.66
	T4	15.65 ± 3.13	16.00 ± 2.63

Values are expressed as the mean ± SD. SBP, systolic blood pressure; DBP, diastolic blood pressure; HR, heart rate; RR, respiratory rate. T1: before induction; T2: after induction; T3: end of gastroscopy; T4: opening eyes. Compared with T1, *$p < 0.05$.

significantly lower at T2 and T3 than at T1 ($p < 0.05$) (Table 3). The above indicators fluctuated more in the N1 group, and the incidence of hypotension in the N1 group was significantly higher than that in the N2 group (35.48% vs. 6.67%, $p < 0.05$). No difference was found in the respiratory rate values at different timepoints in each group or between the two groups (Table 3).

Discussion

Previous studies demonstrated that propofol is a safe and effective anesthetic for all endoscopy procedures, even for high-risk patients, including those with hepatic encephalopathy (Wang et al., 2013; Yin et al., 2019; Edelson et al., 2020;

Dossa et al., 2021; Kang et al., 2021). However, propofol alone would likely lead to inadequate conditions for esophageal instrumentation (Cris D LaPierre et al., 2012). Therefore, opioids are added to improve tolerability and minimize adverse events associated with high-dose propofol in clinical practice. Several studies have shown that sufentanil, fentanyl, and ketamine reduce the ED50 of propofol and the incidence of propofol-related changes in hemodynamics for patients during different endoscopy procedures (Li et al., 2016; Hayes et al., 2018; Yu et al., 2019; Chen et al., 2021). Compared with μ receptor agonists, nalbuphine did not cause significant respiratory or cardiovascular depression, nausea and vomiting, or pruritus (Charuluxananan et al., 2001; Riviere, 2004). Another study in our group showed that 0.1 mg/kg nalbuphine can effectively inhibit pain caused by uterine contraction. Consequently, nalbuphine combined with propofol is superior to sufentanil combined with propofol for first-trimester abortion surgeries (Fang et al., 2022). Li and colleagues determined the safety and feasibility of nalbuphine combined with propofol for painless gastroscopy in adults (Li et al., 2021). Our study is the first randomized dose–response study to evaluate the effect of different doses of nalbuphine on the ED50 of propofol during gastroscopy in adult patients.

Our study showed that 0.15 mg/kg nalbuphine leads to a significant reduction in the ED50 of propofol required to prevent cough or body movement during gastroscopy implantation in adult patients (BMI 18-24). The probit method demonstrated that the ED50 of propofol in combination with 0.15 mg/kg nalbuphine was 1.111 mg/kg and 1.632 mg/kg when combined with 0.1 mg/kg nalbuphine. The ED50 of propofol in the N2 group decreased by a dose of 0.521 mg/kg compared with that in the N1 group (an approximately 32% decrease). The ED95 of propofol in the N2 group also decreased by 18.7%. Thus, the effect of κ-mediated sedation depends on increasing the nalbuphine dose, which was consistent with previous studies (Chestnutt et al., 1987; Li et al., 2021). Additionally, the results of the initial dose and total dose of propofol were consistent with those between the two groups, which led to a shorter recovery time (6.00 [4.99, 7.36] vs. 7.38 [6.25, 8.65]) and a lower incidence of hypotension (35.48% vs. 6.67%). The incidence of hypotension in the N2 group decreased by more than 50% when our sample size was calculated at the time of 7 crossovers, which was less than the sample size we initially calculated. Consequently, this drug combination may be more suitable and safer for elderly patients and patients with cardiovascular disease. The higher turnover efficiency of painless gastroscopy (stay of PACU, 13 [12.10, 14.16] vs. 15 [13.20, 17.00]) reduced waiting time to improve patient satisfaction due to the large number of gastrointestinal endoscopies. However, 0.2 mg/kg nalbuphine combined with propofol was reported to not achieve more benefits than the 0.1 mg/kg nalbuphine group for hysteroscopy in Chen's study (Chen et al., 2021), which was different from our results. This may be related to different types of procedural variables and gender.

A review reported that nalbuphine was equivalent to 0.8 to 0.9 times the analgesic effect of morphine and had a longer duration than morphine at equianalgesic doses, while there was a ceiling effect of respiratory depression and minimal effects on cardiovascular function (Heel, 1983). Therefore, nalbuphine is suitable for outpatient analgesia. As expected, two different doses of nalbuphine both provided effective analgesia for visceral pain and relieved patient discomfort caused by gastroscopy. Evidence showed a statistically significant difference in VAS scores between the two groups (0 [0, 1] vs. 0 [0, 0]), although it had no clinical significance. Our data of nalbuphine doses are in line with a recent prospective study, in which the ED50 and ED95 of nalbuphine combined with propofol for adult patients during gastroscopy were 0.078 and 0.162 mg/kg, respectively (Li et al., 2021). The incidence of propofol-induced Injection pain in the N1 group (29.03%) was similar to that in previous reports (27%) of our center (Wang et al., 2020), while that in the N2 group (13.33%) was lower. In our study, the incidence of respiratory depression (<SpO_2 95%) was 25.81% in the N1 group and 6.67% in the N2 group. No severe hypoxia occurred in either group, which was lower than the rate reported in a previous study (8.4%), while the prevalence of subclinical hypoxia in the N2 group was lower than that reported in a previous study (16.3%) (Lin et al., 2019). The two groups had similar fluctuations in SBP, DBP, and HR at T1, T2, T3 and T4. SBP, DBP and HR at T2 and T3 significantly decreased compared with those at T1. The hemodynamic decline was slightly greater in the N1 group. This should be attributed to the larger propofol dose. The respiration rate (RR) in the two groups did not differ much at T1, T2, T3 and T4. In conclusion, nalbuphine can effectively suppress visceral pain during gastroscopy with stable hemodynamics and mild respiratory depression.

Our study has some limitations. First, we only evaluated the ED50 of patients with BMI 18-24, excluding overweight and obese patients. Second, all of the participants were healthy adults with ASA I or II, excluding elderly patients or ASA III or higher patients. Accordingly, the recommended dose of nalbuphine combined with propofol in our study cannot be extended to these populations. Future studies should examine the dosages of nalbuphine combined with propofol among other populations.

Conclusion

In summary, the current study indicates that the ED50 values of propofol combined with nalbuphine are 1.632 (0.1 mg/kg of nalbuphine) and 1.111 mg/kg (0.15 mg/kg of nalbuphine), respectively. Treatment with 0.15 mg/kg nalbuphine led to a significant reduction in the

ED50 of propofol, reduced the incidence of hypotension and shortened the recovery time. Therefore, nalbuphine (0.15 mg/kg) is a safe option for enhancing recovery after painless gastroscopy.

Data availability statement

The raw data supporting the conclusions of this article will be made available by the authors, without undue reservation.

Ethics statement

The studies involving human participants were reviewed and approved by the Ethical Committee of The First Affiliated Hospital of Anhui Medical University, Hefei, China (Approval No. PJ 2021-14-15). The patients/participants provided their written informed consent to participate in this study.

Author contributions

LT: Study design, data collection and analysis, article drafting; CY: data collection; NW: data collection; CC: randomization implementation and drug preparation; XL: study design, data interpretation, and critical revision of the article. SG: critical revision of the article. SC: critical revision of the article.

Funding

This study was supported by the Joint Project of Anesthesiology and Pharmacology of Anhui Medical University (No. 2021lcxk002).

Acknowledgments

We sincerely thank Professor Cheng-yang Hu, School of Public Health, Anhui Medical University, for his contribution to the statistical analysis of our paper.

Conflict of interest

The authors declare that the research was conducted in the absence of any commercial or financial relationships that could be construed as a potential conflict of interest.

Publisher's note

All claims expressed in this article are solely those of the authors and do not necessarily represent those of their affiliated organizations, or those of the publisher, the editors and the reviewers. Any product that may be evaluated in this article, or claim that may be made by its manufacturer, is not guaranteed or endorsed by the publisher.

References

Charuluxananan, S., Somboonviboon, W., Lertmaharit, S., Ngamprasertwong, P., and Nimcharoendee, K. (2001). Nalbuphine versus propofol for treatment of intrathecal morphine-induced pruritus after cesarean delivery. *Anesth. Analg.* 93 (1), 162–165. doi:10.1097/00000539-200107000-00032

Chen, C., Tang, W., Ye, W., Zhong, W., and Li, Y. (2021). ED50 of propofol combined with nalbuphine on the sedative effect in painless hysteroscopy. *Pain Ther.* 10 (2), 1235–1243. doi:10.1007/s40122-021-00280-x

Chestnutt, W. N., Clarke, R. S., and Dundee, J. W. (1987). Comparison of nalbuphine, pethidine and placebo as premedication for minor gynaecological surgery. *Br. J. Anaesth.* 59 (5), 576–580. doi:10.1093/bja/59.5.576

Cohen, L. B., Wecsler, J. S., Gaetano, J. N., Benson, A. A., Miller, K. M., Durkalski, V., et al. (2006). Endoscopic sedation in the United States: Results from a nationwide survey. *Am. J. Gastroenterol.* 101 (5), 967–974. doi:10.1111/j.1572-0241.2006.00500.x

Committee, A. S. o. P., Early, D. S., Lightdale, J. R., Vargo, J. J., 2nd, Acosta, R. D., Chandrasekhara, V., et al. (2018). Guidelines for sedation and anesthesia in GI endoscopy. *Gastrointest. Endosc.* 87 (2), 327–337. doi:10.1016/j.gie.2017.07.018

Cris D LaPierre, K. B. J., Randall, B. R., TalmageEgan, D., and Egan, T. D. (2012). A simulation study of common propofol and propofol-opioid dosing regimens for upper endoscopy: Implications on the time course of recovery. *Anesthesiology* 117 (2), 252–262. doi:10.1097/ALN.0b013e31825fb1b2

Dixon, W. J. (1991). Staircase bioassay: The up-and-down method. *Neurosci. Biobehav. Rev.* 15 (1), 47–50. doi:10.1016/s0149-7634(05)80090-9

Dossa, F., Megetto, O., Yakubu, M., Zhang, D. D. Q., and Baxter, N. N. (2021). Sedation practices for routine gastrointestinal endoscopy: A systematic review of recommendations. *BMC Gastroenterol.* 21 (1), 22. doi:10.1186/s12876-020-01561-z

Edelson, J., Suarez, A. L., Zhang, J., and Rockey, D. C. (2020). Sedation during endoscopy in patients with cirrhosis: Safety and predictors of adverse events. *Dig. Dis. Sci.* 65 (4), 1258–1265. doi:10.1007/s10620-019-05845-7

Fang, P., Qian, J., Ding, J., Pan, X., Su, H., and Liu, X. (2022). Comparison of analgesic effects between nalbuphine and sufentanil in first-trimester surgical abortion: A randomized, double-blind, controlled trial. *Pain Ther.* 11 (1), 121–132. doi:10.1007/s40122-021-00334-0

Hayes, J., Matava, C., Pehora, C., El-Beheiry, H., Jarvis, S., and Finkelstein, Y. (2018). Determination of the median effective dose of propofol in combination with different doses of ketamine during gastro-duodenoscopy in children: A randomised controlled trial. *Br. J. Anaesth.* 121 (2), 453–461. doi:10.1016/j.bja.2018.03.037

Heel, K. E. R. C., and Heel, R. C. (1983). Nalbuphine. A preliminary review of its pharmacological properties and therapeutic efficacy. *Drugs* 3 (26), 191–211. doi:10.2165/00003495-198326030-00002

Jaffe, R. S., Moldenhauer, C. C., Hug, C. C., Finlayson, D. C., Tobia, V., and Kopel, M. E. (1988). Nalbuphine antagonism of fentanyl-induced ventilatory depression: A randomized trial. *Anesthesiology* 68 (2), 254–260. doi:10.1097/00000542-198802000-00012

Kang, S., Lu, J., and Zhou, H. M. (2021). Anesthetic strategy for obese patients during gastroscopy: Deep sedation or conscious sedation? A prospective randomized controlled trial. *J. Anesth.* 35 (4), 555–562. doi:10.1007/s00540-021-02951-7

Li, S., Wang, Y., Chen, X., Huang, T., and Li, N. (2021). Effective doses of nalbuphine combined with propofol for painless gastroscopy in adults: A randomized controlled trial. *Front. Pharmacol.* 12, 673550. doi:10.3389/fphar.2021.673550

Li, S., Yu, F., Zhu, H., Yang, Y., Yang, L., and Lian, J. (2016). The median effective concentration (EC50) of propofol with different doses of fentanyl during colonoscopy in elderly patients. *BMC Anesthesiol.* 16, 24. doi:10.1186/s12871-016-0189-y

Lin, Y., Zhang, X., Li, L., Wei, M., Zhao, B., Wang, X., et al. (2019). High-flow nasal cannula oxygen therapy and hypoxia during gastroscopy with propofol sedation: A randomized multicenter clinical trial. *Gastrointest. Endosc.* 90 (4), 591–601. doi:10.1016/j.gie.2019.06.033

Meining, A., Semmler, V., Kassem, A. M., Sander, R., Frankenberger, U., Burzin, M., et al. (2007). The effect of sedation on the quality of upper gastrointestinal endoscopy: An investigator-blinded, randomized study comparing propofol with midazolam. *Endoscopy* 39 (4), 345–349. doi:10.1055/s-2006-945195

Patel, S., Vargo, J. J., Khandwala, F., Lopez, R., Trolli, P., Dumot, J. A., et al. (2005). Deep sedation occurs frequently during elective endoscopy with meperidine and midazolam. *Am. J. Gastroenterol.* 100 (12), 2689–2695. doi:10.1111/j.1572-0241.2005.00320.x

Peery, A. F., Crockett, S. D., Murphy, C. C., Jensen, E. T., Kim, H. P., Egberg, M. D., et al. (2022). Burden and cost of gastrointestinal, liver, and pancreatic diseases in the United States: Update 2021. *Gastroenterology* 162 (2), 621–644. doi:10.1053/j.gastro.2021.10.017

Riviere, P. J. (2004). Peripheral kappa-opioid agonists for visceral pain. *Br. J. Pharmacol.* 141 (8), 1331–1334. doi:10.1038/sj.bjp.0705763

Stogiannou, D., Protopapas, A., and Tziomalos, K. (2018). Is propofol the optimal sedative in gastrointestinal endoscopy? *Acta Gastroenterol. belg.* 81 (4), 520–524.

Sun, S., Guo, Y., Wang, T., and Huang, S. (2020). Analgesic effect Comparison between nalbuphine and sufentanil for patient-controlled intravenous analgesia after cesarean section. *Front. Pharmacol.* 11, 574493. doi:10.3389/fphar.2020.574493

Sury, M. R., and Cole, P. V. (1988). Nalbuphine combined with midazolam for outpatient sedation. An assessment in fibreoptic bronchoscopy patients. *Anaesthesia* 43 (4), 285–288. doi:10.1111/j.1365-2044.1988.tb08974.x

Vaessen, H. H., and Knape, J. T. (2016). Considerable variability of procedural sedation and analgesia practices for gastrointestinal endoscopic procedures in europe. *Clin. Endosc.* 49 (1), 47–55. doi:10.5946/ce.2016.49.1.47

Wang, D., Chen, C., Chen, J., Xu, Y., Wang, L., Zhu, Z., et al. (2013). The use of propofol as a sedative agent in gastrointestinal endoscopy: A meta-analysis. *PLoS One* 8 (1), e53311. doi:10.1371/journal.pone.0053311

Wang, J., Duan, J., Xie, C., Yu, Y., and Lu, Y. (2020). Comparison between intravenous nalbuphine and lidocaine in reducing propofol-induced injection pain during gastroscopy: A randomized controlled trial. *Pain Ther.* 9 (2), 563–571. doi:10.1007/s40122-020-00188-y

Xia, R., Zeng, H., Liu, W., Xie, L., Shen, M., Li, P., et al. (2021). Estimated cost-effectiveness of endoscopic screening for upper gastrointestinal tract cancer in high-risk areas in China. *JAMA Netw. Open* 4 (8), e2121403. doi:10.1001/jamanetworkopen.2021.21403

Xu, Z. Y., Wang, X., Si, Y. Y., Wu, J. C., Zuo, Y. X., Xue, F. S., et al. (2008). Intravenous remifentanil and propofol for gastroscopy. *J. Clin. Anesth.* 20 (5), 352–355. doi:10.1016/j.jclinane.2008.03.006

Yin, S., Hong, J., Sha, T., Chen, Z., Guo, Y., Li, C., et al. (2019). Efficacy and tolerability of sufentanil, dexmedetomidine, or ketamine added to propofol-based sedation for gastrointestinal endoscopy in elderly patients: A prospective, randomized, controlled trial. *Clin. Ther.* 41 (9), 1864–1877. doi:10.1016/j.clinthera.2019.06.011

Yu, J., Xiang, B., Song, Y., Chen, H., Li, Y., and Liu, C. (2019). ED50 of propofol in combination with low-dose sufentanil for intravenous anaesthesia in hysteroscopy. *Basic Clin. Pharmacol. Toxicol.* 125 (5), 460–465. doi:10.1111/bcpt.13280

Zhang, L., Bao, Y., and Shi, D. (2014). Comparing the pain of propofol via different combinations of fentanyl, sufentanil or remifentanil in gastrointestinal endoscopy. *Acta Cir. Bras.* 29 (10), 675–680. doi:10.1590/s0102-8650201400160008

frontiers | Frontiers in Pharmacology

TYPE Original Research
PUBLISHED 11 October 2022
DOI 10.3389/fphar.2022.1025814

OPEN ACCESS

EDITED BY
Jian Gao,
Shanghai Children's Medical Center, China

REVIEWED BY
Antonio Molino,
University of Naples Federico II, Italy
Xiaoping Zhu,
Tongji University, China

*CORRESPONDENCE
Huiping Li,
liw2013@126.com

†These authors have contributed equally to this work

SPECIALTY SECTION
This article was submitted to Respiratory Pharmacology, a section of the journal Frontiers in Pharmacology

RECEIVED 23 August 2022
ACCEPTED 29 September 2022
PUBLISHED 11 October 2022

CITATION
Yin C, Xie H, He X, Zhang Y, Zhang A and Li H (2022), Small airway dysfunction in idiopathic pulmonary fibrosis. *Front. Pharmacol.* 13:1025814. doi: 10.3389/fphar.2022.1025814

Small airway dysfunction in idiopathic pulmonary fibrosis

Chengsheng Yin[1,2†], Huikang Xie[3†], Xian He[2†], Yuan Zhang[2†], Aihong Zhang[4] and Huiping Li[2*]

[1]Department of Pulmonary and Critical Care Medicine, Yijishan Hospital, The first Affiliated Hospital of Wannan Medical College, Wuhu, Anhui, China, [2]Department of Respiratory Medicine, Shanghai Pulmonary Hospital, Tongji University, School of Medicine, Shanghai, China, [3]Department of Pathology, Shanghai Pulmonary Hospital, Tongji University, School of Medicine, Shanghai, China, [4]Department of Medical Statistics, Tongji University, School of Medicine, Shanghai, China

It is generally accepted that the pathophysiology of idiopathic pulmonary fibrosis (IPF) can be attributed to impaired lung interstitium and alveoli, while airway involvement has rarely been reported. In the present study, we aimed to investigate the actual occurrence of IPF comorbid small airway dysfunction (SAD) and its impact on survival. Data from inpatients diagnosed with IPF at Shanghai Pulmonary Hospital (Shanghai, China) from 2011 to 2021 were retrospectively collected and analyzed. Lung function parameters were used to assess SAD. A total of 243 IPF patients were included in this retrospective study, and 84 cases (84/243, 34.57%) were diagnosed with SAD. The lung histopathology showed that all 48 cases undergoing lung transplantation presented various degrees of airway lesions, of which 18 patients (18/48, 37.5%) diagnosed with SAD before lung transplantation had a higher proportion of airway distortion and obliteration. The possible risk factors associated with IPF comorbid SAD were smoking, male, younger age, and high CT fibrosis and emphysema scores. By univariate Fine-Grey regression, the hazard ratio (HR) of IPF comorbid SAD was 1.725 (95% CI 1.071, 2.777, $p < 0.05$). After adjusting the CTPF model and GAP model, the value of HR was 1.714 (95% CI 1.043, 2.816, $p < 0.05$) and 1.731 (95% CI 1.074, 2.788, $p < 0.05$), respectively. These findings suggested that IPF comorbid SAD was an independent risk factor for the mortality of IPF patients.

KEYWORDS

idiopathic pulmonary fibrosis, small airway dysfunction, mortality risk, combined with pulmonary fibrosis and emphysema, IPF combined obstructive ventilator dysfunction

Abbreviations: IPF, idiopathic pulmonary fibrosis; ILD, interstitial lung disease; PFT, pulmonary function test; TLC, total lung capacity; FVC, forced vital capacity; DLCO, diffusing capacity of the lung for carbon monoxide; CPFE, combined with pulmonary fibrosis and emphysema; O-IPF, IPF patients have obstructive ventilator dysfunction; FEV1, forced expiratory volume in one second; COPD, chronic obstructive pulmonary disease; SAD, small airway dysfunction; CT, computed tomography; CPI, composite physiologic index; GAP, gender, age, and physiologic variables; SaO_2, oxyhemoglobin saturation; SpO_2, oxygen saturation of peripheral blood; HRCT, high-resolution computed tomography; UIP, usual interstitial pneumonia; PF, pulmonary function and physiological features; CTPF, HRCT combined pulmonary function andphysiological features.

Introduction

Idiopathic pulmonary fibrosis (IPF) is the most common interstitial lung disease (ILD) (Raghu et al., 2018). Its pathophysiological process is generally recognized as that pulmonary interstitial hyperplasia leads to alveolar occlusion and damage. At the same time, the airways are spared, and the pulmonary function test (PFT) shows restrictive ventilation disorders, decreased total lung capacity (TLC), increased forced expiratory volume in one second (FEV1), normal or increased FEV1/FVC%, and decreased diffusing capacity for carbon monoxide (DLCO) (Gibson and Pride, 1977; Nicholson et al., 2002; Katzenstein et al., 2008). In recent years, IPF combined with pulmonary fibrosis and emphysema (CPFE) has been found in some studies, which usually exhibits fibrosis in the lower lobes combined with emphysema in the upper lobes (Cottin et al., 2005; Silva et al., 2008; Mitchell et al., 2015). Therefore, it is interesting to understand whether ILD/IPF patients combined with emphysema and bullae can cause airway dysfunction, which is a problem that has attracted the attention of scholars (Cottin et al., 2005). In 1977, Fulmer et al. (1977) have reported 12 patients (12/18, 66%) with airway stenosis in the lumen diameter of less than 2-mm air tube, and this stenosis lesion may be related to the patient's clinical symptoms and disease severity by observing the pathological sections of 18 IPF patients by open-chest lung biopsy. Verleden et al. (2020) have compared pathological lung tissues of end-stage IPF patients undergoing lung transplantation with healthy donors without lung disease and found that the loss of terminal bronchioles is significant in IPF patients' lung tissues. Guiot et al. (2022) have recently reported that about 15% of ILD patients have combined obstructive ventilator dysfunction diagnosed based on the PFT criteria FEV1/FVC < 70%, 7% (5/68) of IPF patients have obstructive ventilator dysfunction (O-IPF), and their small airway function is impaired significantly. Based on the above studies, we hypothesized that small airway dysfunction (SAD) might be a risk factor affecting the prognosis of IPF patients.

A review of the IPF genetics by Evans et al. (2016) has concluded that IPF is a complex genetic disorder with abnormal mucus cilia function, and the MUC5B promoter mutation rs35705950 is the most common risk factor for the development of IPF. Moreover, this mutation leads to overproduction of the mucus protein MUC5B, which obstructs the peripheral airways, leading to distortion, suppuration, and occlusion of small airways and resulting in pathological changes, such as infection and inflammatory cell infiltration. Some studies (Kirkham et al., 2008; Seibold et al., 2011) have reported that MUC5B is one of the primary mucins in the sputum of patients with chronic obstructive pulmonary disease (COPD). It can be seen that mutations in the MUC5B gene affect both IPF and COPD, which may be one of the mechanisms that complicate emphysema in IPF patients. The small airway is defined as bronchi with a lumen diameter of less than 2 mm (Macklem, 1998). SAD is commonly seen in COPD, bronchial asthma, and other chronic airway diseases (Halpin et al., 2021; Reddel et al., 2022). However, the incidence rate, major risk factors, and prognosis of IPF comorbid SAD remain unclear. At present, only very few clinical studies have focused on IPF comorbid SAD. Especially, there is a lack of large cohort studies to detect the incidence rate of IPF comorbid SAD and the impact on disease mortality.

In the present study, we explored the actual incidence rate of IPF comorbid SAD and its effect on mortality by retrospectively analyzing the lung function parameters, lung tissue pathology, and other clinical data of the IPF cohort. Collectively, our findings might help explore suitable preventive and therapeutic methods for them.

Materials and methods

Patient's clinical data

In the present study, the medical records and survival statuses of 308 patients who were diagnosed with IPF in the Department of Respiratory Medicine at Shanghai Pulmonary Hospital from 2011 to 2021 were retrospectively analyzed. The cases were reviewed according to diagnostic criteria of the 2018 IPF International Guidelines (Raghu et al., 2018) by a multidisciplinary team composed of two respiratory physicians, two radiologists, two thoracic surgeons, and two pathologists. Information, such as the patient's gender, age, PFT paraments, SpO_2% (or SaO_2%), chest HRCT, occupation, and smoking history, was collected. The artificial intelligence HRCT pulmonary fibrosis assessment system developed by our team was adopted to calculate the extent of fibrosis and emphysema patterns (Wu et al., 2022). All patients were followed up by clinical visits and telephone follow-ups. The follow-up data included patient survival, time of death (the year and month of death), cause of death, other complications, whether undergoing lung transplantation, and the time of lung transplantation. In addition, two pathologists interpreted the lung histopathology of patients undergoing lung transplantation at Shanghai Pulmonary Hospital. All donor's lungs were deemed appropriate for transplantation on review of the clinical files, and each patient undergoing transplantation signed informed consent. All data used in this study were approved by the Ethics Committee of Shanghai Pulmonary Hospital (No. K17-016). The flowchart of patient screening and enrollment and the follow-up results are presented in Figure 1.

Small airway dysfunction diagnostic criteria by pulmonary function test

According to previous studies on lung function in the Chinese population (McFadden and Linden, 1972; Ciprandi et al., 2006; Perez et al., 2013; Lin et al., 2014; Xiao et al., 2020), three indicators of lung function were used to assess

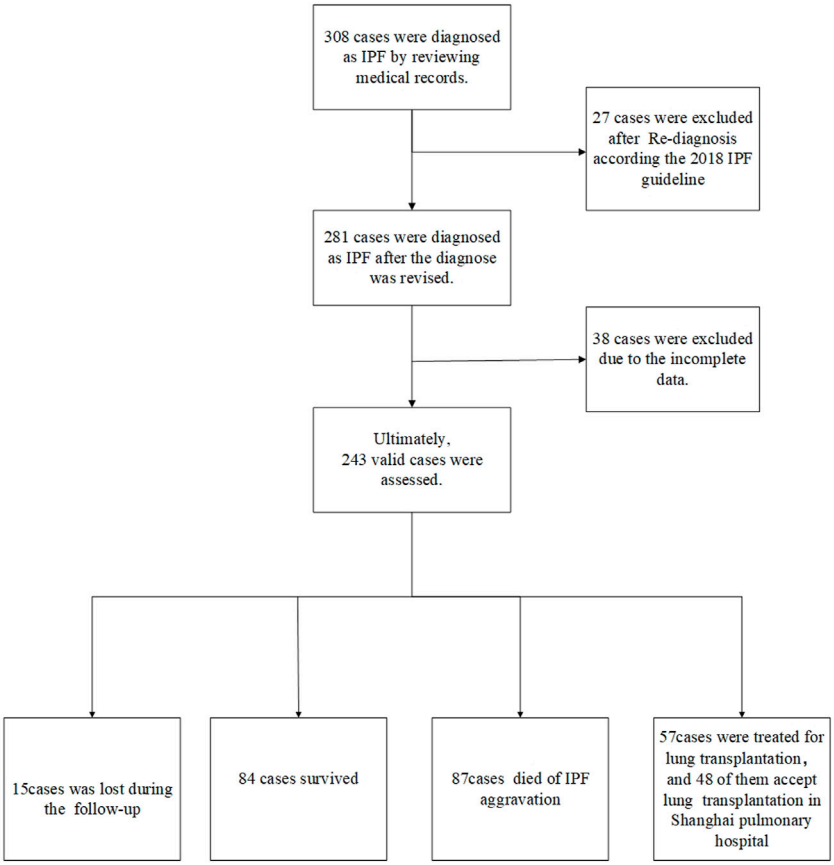

FIGURE 1
Case screening process A total of 308 cases were diagnosed with IPF by reviewing the medical records. Moreover, 27 cases were excluded after re-diagnosis according to the 2018 IPF guideline. Besides, 38 cases had incomplete CT and lung function data. Finally, 243 cases were included in the final retrospective analysis, including 57 cases undergoing lung transplantation. There were 84 surviving cases, and 15 cases were lost during follow-up. Besides, 87 deaths happened due to acute exacerbation of IPF, 57 patients underwent lung transplantation, and 48 of them accepted transplantation in Shanghai Pulmonary Hospital.

SAD, namely mid-maximum expiratory flow (MMEF), forced expiratory flow (FEF) at 50% of vital capacity (FEF50%), and FEF at 75% of vital capacity (FEF75%), and SAD was diagnosed when at least two of these three indicators were less than 65% of those predicted in the absence of bronchodilators.

Histopathological diagnostic criteria for small airway dysfunction

According to the literature on small airway disease (Kawabata et al., 2008; Katzenstein et al., 2010; Chen et al., 2013; Koo et al., 2018; Higham et al., 2019), small airway lesions are often caused by inflammation or inflammatory injury response around the airway. In our present study, the pathologists evaluated the pathologic morphology of the small airway as follows. 1. Airway distortion: the wall thickness of the small airway was significantly increased (but the lumen was unobstructed), and the structure was distorted. 2. Airway obliteration: submucosal fibrous hyperplasia accompanied by significant stenosis or even complete occlusion of the small airway lumen. 3. Airway metaplasia: the alveolar septum around the bronchioles had slight fibrosis, and the alveolar epithelium around the bronchioles was replaced by cuboidal or columnar cells. 4. Airway inflammation and mucous: the number of inflammatory cells in small airway submucosa was significantly increased and caused embolization of the lumen.

Statistical analysis

All analyses were performed using the statistical software IBM SPSS24.0, Stata/MP14.0, and GraphPad Prism 9. Measurement data were expressed as mean ± standard deviation (SD). Count data were presented as percentage (%) or proportion (%). The Kolmogorov-Smirnov test was used to analyze the distribution of variables. The *t*-test was used to analyze normally distributed

TABLE 1 Comparison of case characteristics.

	Small airway dysfunction	Non-small airway dysfunction	*P*-value
Case	84	159	
States (survive/death/lung transplantation)	25/38/21	74/49/36	0.028
Survive	25	74	0.013
Death	38	49	0.035
Lung transplantation	21	36	0.751
Male/female	74/10	149/10	0.130
Age	62.75 ± 8.50	64.7 ± 7.46	0.164
Smoking/Non-smoking	56/28	118/41	0.215
Fibrosis rate%	15.76 ± 11.16	14.24 ± 10.84	0.291
Emphysema rate%	1.59 ± 3.15	0.98 ± 1.80	0.117
Median survival time (months)	34 ± 7.59	52 ± 5.34	0.028
SpO_2%	94.27 ± 4.14	94.94 ± 4.78	0.052
FVC	2.17 ± 0.73	2.50 ± 0.72	0.002
FVC pred%	62.86 ± 19.32	74.60 ± 21.01	<0.001
FEV1	1.68 ± 0.50	2.15 ± 0.55	<0.001
FEV1 pred%	60.89 ± 16.94	80.64 ± 21.01	<0.001
FEV1/FVC	79.55 ± 9.82	86.90 ± 5.57	<0.001
FEF25 pred%	67.00 ± 24.24	92.91 ± 23.72	<0.001
FEF50 pred%	62.49 ± 22.79	114.83 ± 30.98	<0.001
FEF75 pred%	39.9 ± 16.07	97.70 ± 44.22	<0.001
MMEF pred%	44.84 ± 14.38	94.24 ± 25.61	<0.001
DLcopred%	42.85 ± 25.00	55.44 ± 29.33	0.003
CPI index	50.54 ± 20.05	43.19 ± 20.47	0.014
CT stage((I/II/III)	13/54/17	36/99/24	0.317
PF grade(a/b/c)	26/40/18	74/62/23	0.055
GAP stage	31/36/17	88/48/23	0.010

Notes: Measurement data are presented as mean ± standard deviation (SD). Count data are presented as percentage or proportion. SpO_2%, oxygen saturation of peripheral blood. SpO_2 is the resting arterial oxygen saturation measured at fingertips. FVC, forced vital capacity; FVC% pred, the percentage of the actual FVC over the predicted FVC; FEV1, forced expiratory volume in one second. FEV1% pred, the percentage of the actual FEV1 over the predicted FEV1; DLco, diffusing capacity of the lung for carbon monoxide; DLco% pred, the percentage of the actual DLco over the predicted DLco; FEV1/FVC%, the percentage of FEV1 over FVC. Fibrosis Rate and Emphysema Rate calculated by AI according to the system established by Wu et al. (2022) FEF25 pred%, Forced expiratory flow at 25 of vital capacity; FEF50 pred%, Forced expiratory flow at 25 of vital capacity; FEF75 pred%, Forced expiratory flow at 75 of vital capacity; MMEF pred%, Maximal mid-expiratory flow; CT stage, The stage was determined by using AI according to the system established by Li HP et al. PF-based grade: The grade was determined by using the pulmonary function and physiological parameters (age, gender, FVC% pred, DLco% pred, and SpO_2%) and following the CTPF model recommendation by Li HP et al. The grade was defined as: mild (a), moderate (b), and severe (c). GAP (gender, age, and physiologic variables) stage followed the recommendation by Brett Ley, and a higher stage represented a greater death risk. CPI: composite physiologic index. In 2002, Athol U. Wells and others proposed to use CPI, which combined chest CT and pulmonary functional parameters, to assess the severity of interstitial lung diseases (ILDs). A higher CPI represents a more severe ILD.

variables in the bivariate analysis, while the Mann-Whitney *U*-test was used to analyze non-normally distributed variables. The chi-square test was used to compare qualitative variables. According to the collected data, logistic regression was used to determine the possible risk factors of IPF comorbid SAD. The variables that presented statistically significant differences ($p < 0.05$) in the bivariate analysis and were of clinical interest were included as the independent variables in the model. The forward stepwise technique (i.e., the Wald test) was then used to remove any variables with $p > 0.1$ from the final model. Patients' survival time was defined from the date when patients' data were acquired to the date of death endpoint or the last follow-up. The endpoint of this study was defined as the death caused by lung diseases. Lung transplantation was considered a competing risk event in this study. Other outcomes were treated as censored data. The Fine-Grey mortality risk regression model was adopted to analyze univariate risk and multivariate risk of SAD on the survival of IPF patients, and the hazard ratio (HR) and 95% confidence interval of each independent variable were calculated. A $p < 0.05$ was considered statistically significant.

Results

Patients' clinical characteristics

Figure 1 illustrates the patient screening flow chart. A total of 308 IPF cases were included by reviewing the medical records.

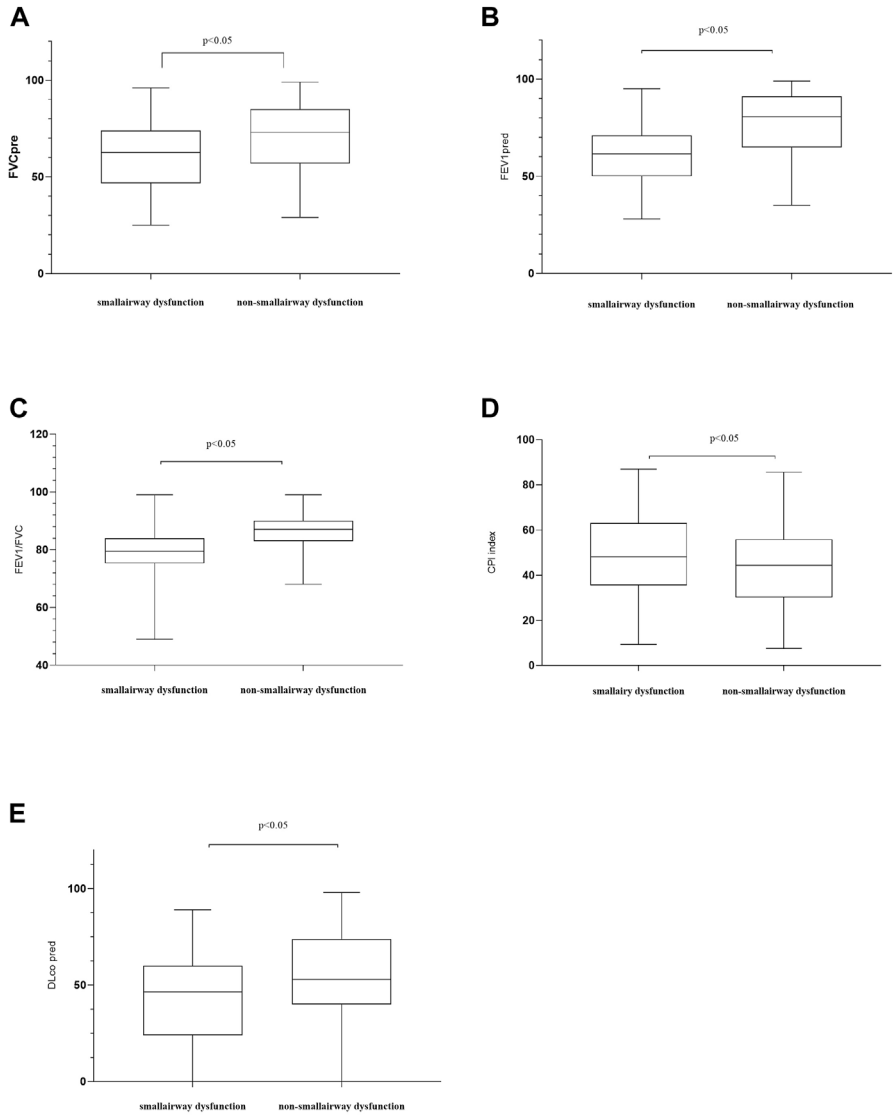

FIGURE 2
Comparisons of patients' characteristics between the SAD and non-SAD groups. **(A)** FVC, forced vital capacity. FVC pred: the percentage of the actual FVC over the predicted FVC; **(B)** forced expiratory volume in 1 s (FEV1) % predicted; **(C)** FEV1/FVC ratio; **(D)** CPI, composite physiologic index. In 2002, Athol U. Wells and others proposed to use CPI, which combined chest CT and pulmonary functional parameters, to assess the severity of ILDs. A higher CPI represents a more severe ILD; **(E)** DLco, diffusing lung capacity for carbon monoxide. DLco% pred, the percentage of the actual DLco over the predicted DLco; Moreover, $p < 0.05$ indicates statistical significance.

Moreover, 27 (27/308) cases were excluded according to the updated IPF guideline in 2018 (Raghu et al., 2018). Besides, 38 cases were excluded because of their incomplete data in CT and/or lung function. Finally, 243 cases were included in the final retrospective analysis. Of 243 IPF patients, 57 patients received lung transplants (48 of 57 performed in Shanghai Pulmonary Hospital). Other patients were treated by routine therapies, including oxygen therapy, antifibrotic drugs, and antioxidants. According to the diagnostic criteria of PFT, 84 patients (84/243, 34.57%) were diagnosed with IPF comorbid SAD, and 159 patients were non-SAD. Table 1 shows the case characteristics of the two groups. There was a statistical difference in lung function parameters between the two groups, while other clinical features had no significant difference (Figure 2). In addition, as shown in Table 2, 11 patients (11/84, 13%) in the SAD group were diagnosed with O-IPF by the PFT criteria FEV1/FVC < 70%. Compared with non-O-IPF patients, O-IPF patients had worse small airway lesions (FEF50 pred%, FEF75 pred%, and MMEF pred%) ($p < 0.05$). Moreover, O-IPF patients had lower

TABLE 2 Comparison between with and without obstructive ventilatory dysfunction in patients with IPF combined small airway dysfunction.

	O-IPF (FEV1/FVC <70%)	Non OIPF (FEV1/FVC >70%)	*P*
Cases	11	73	
FEF25 pred%	46.10 ± 24.12	70.14 ± 22.79	0.002
FEF50 pred%	29.56 ± 15.38	67.42 ± 19.37	<0.001
FEF75 pred%	22.65 ± 11.99	42.49 ± 15.02	<0.001
MMEF pred%	25.64 ± 14.55	47.73 ± 12.02	<0.001
Emphysema rate%	2.38 ± 2.37	1.48 ± 3.26	0.380
Fibrosis rate%	13.30 ± 9.40	16.13 ± 11.40	0.437
Median survival time (months)	20	27	0.237
SpO_2%	93.18 ± 3.57	94.43 ± 4.22	0.352
FVC	2.51 ± 0.77	2.12 ± 0.71	0.096
FVC pred%	73.10 ± 18.25	61.31 ± 19.12	0.052
FEV1	1.57 ± 0.45	1.70 ± 0.51	0.462
FEV1 pred%	56.75 ± 16.72	61.52 ± 17.00	0.387
DLcopred%	52.94 ± 28.56	41.33 ± 24.23	0.152
CPI index	37.14 ± 20.52	52.56 ± 19.32	0.016

[a]Airway obstruction was defined by a Tifeneau index FEV1/FVC <70%. Notes: Measurement data are presented as mean ± standard deviation (SD). O-IPF, combined obstructive and idiopathic pulmonary fibrosis. SpO_2%, oxygen saturation of peripheral blood. SpO_2 is the resting arterial oxygen saturation measured at fingertips. FVC, forced vital capacity; FVC% pred, the percentage of the actual FVC over the predicted FVC; FEV1, forced expiratory volume in one second; FEV1% pred, the percentage of the actual FEV1 over the predicted FEV1; DLco, diffusing capacity of the lung for carbon monoxide; DLco% pred, the percentage of the actual DLco over the predicted DLco. Fibrosis Rate and Emphysema Rate calculated by AI according to the system established by Li HP et al. FEF25 pred%, Forced expiratory flow at 25 of vital capacity; FEF50 pred%, Forced expiratory flow at 25 of vital capacity; FEF75 pred%, Forced expiratory flow at 75 of vital capacity; MMEF pred%, Maximal mid-expiratory flow; CPI, composite physiologic index. In 2002, Athol U. Wells and others proposed to use CPI, which combined chest CT and pulmonary functional parameters, to assess the severity of interstitial lung diseases (ILDs). A higher CPI represents a more severe ILD.

FEV1 pred%, higher emphysema score, and lower median survival. However, the difference was not significant, which might be attributed to the small number of cases.

Characteristics of patients receiving lung transplantation

A total of 57 patients underwent lung transplantation. Among them, 48 patients accepted the operation at Shanghai Pulmonary Hospital, and their pathological lung tissue sections were preserved after transplantation. According to the latest PFT before transplantation, 18 patients (18/48, 37.5%) were diagnosed with IPF comorbid SAD. Table 3 lists the patient characteristics. The FEV1 pred% of the SAD group was lower (p = 0.004), and other lung function parameters showed no statistical differences. Patients receiving lung transplantation were younger in the SAD group (58, 66, p = 0.023). According to the assessment report of the pathological lung tissue section evaluated by the pathologist, all 48 cases exhibited pathological manifestations of usual interstitial pneumonitis (UIP) and had different degrees of airway lesions. Figure 3 shows the microscopic manifestations of pathological sections. Notably, Figure 4 and Table 3 reveal that the proportion of airway distortion and obliteration was higher in the SAD group.

Risk factors of idiopathic pulmonary fibrosis comorbid small airway dysfunction

Table 4 shows the results of univariate and multivariate logistic regression analyses. Male patients with young age and high scores of pulmonary fibrosis and emphysema were more likely to be diagnosed with IPF comorbid SAD. However, p > 0.05 was found in both analyses. Therefore, independent risk factors associated with IPF comorbid SAD were not identified.

Survival analysis

As shown in Table 5, on univariate Fine-Grey competitive risk regression analysis of IPF comorbid SAD, the HR value was 1.725 (95% CI: 1.071, 2.777, p < 0.05). After adjusting the CT fibrosis stage and pulmonary function, as well as physiological condition grade (CTPF model) and GAP model, the HR value became 1.714 (95% CI: 1.043, 2.816, p < 0.05, p < 0.05) and 1.731 (95% CI 1.074, 2.78). According to mortality risk curves after adjusting the different assessment predict models shown in Figures 5, 6, SAD patients had a higher risk of death than non-SAD patients in all models. These results suggested that patients with IPF comorbid SAD could be an independent risk factor for mortality.

TABLE 3 Characteristics of lung transplantation cases.

	Small airway dysfunction	Non-small airway dysfunction	*P*-value
Case	18	30	
Male/Female	13/5	27/3	0.110
Operation type			
BLTx/LSLTx/RSLTx	2/1/15	5/6/19	
Operation age	58 ± 11	66 ± 6.4	0.023
Smoking/Non-smoking	14/16	11/7	0.083
SpO_2%	91.6 ± 9.4	91.2 ± 10.9	0.30
FVC pred%	55.0 ± 22.5	67.1 ± 24.5	0.083
FEV1 pred%	53.2 ± 19.8	74.0 ± 24.9	0.004
FVE1/FVC%	84.2 ± 12.9	89.0 ± 5.6	0.092
DLco pred%	37.8 ± 31.1	47.6 ± 23.9	0.327
Pathological interpretation (n/%)			
Airway distortion	17/94.4%	20/66.7%	0.027*
Airway metaplasia	6/33.3%	11/36.7%	0.815*
Airway obliteration	8/44.4%	5/16.7%	0.036*
Airway inflammationand mucous	8/44.4%	9/30.0%	0.311*

Notes: Measurement data are presented as mean ± standard deviation (SD). Count data are presented as percentage or proportion. BLTx, Bilateral lung transplant; LSLx, left-side lung transplant; RSLTx, right-sided lung transplant; SpO_2%, oxygen saturation of peripheral blood. SpO_2 is the resting arterial oxygen saturation measured at fingertips. FVC, forced vital capacity; FVC% pred, the percentage of the actual FVC over the predicted FVC; FEV1, forced expiratory volume in one second; FEV1% pred, the percentage of the actual FEV1 over the predicted FEV1; DLco, diffusing capacity of the lung for carbon monoxide; DLco% pred, the percentage of the actual DLco over the predicted DLco; FEV1/FVC%, the percentage of FEV1 over FVC. * The comparison is using the percentage.

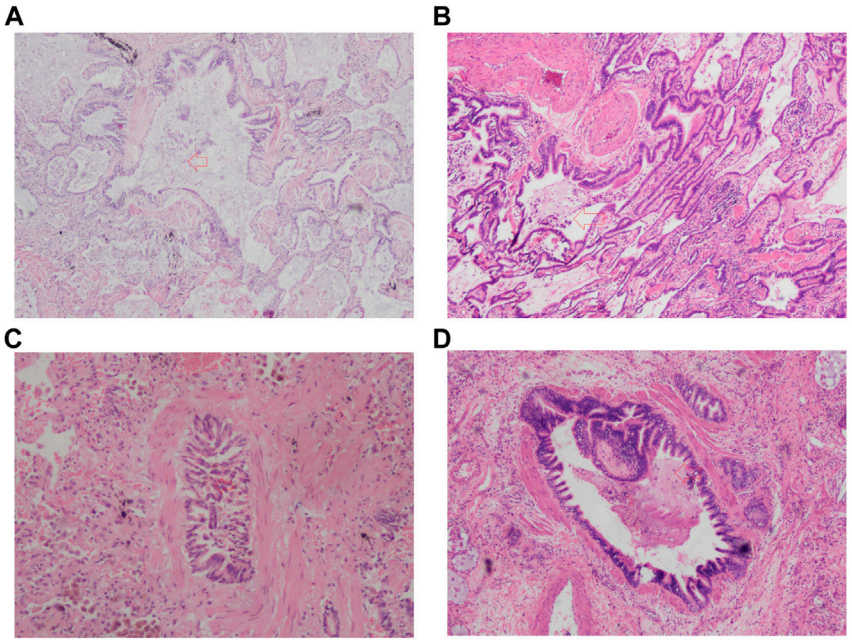

FIGURE 3
The pathologic image of SAD. **(A)** Airway distortion; **(B)** Airway metaplasia; **(C)** Airway obliteration; **(D)** Airway inflammation and mucous. The red arrow points to the lesion.

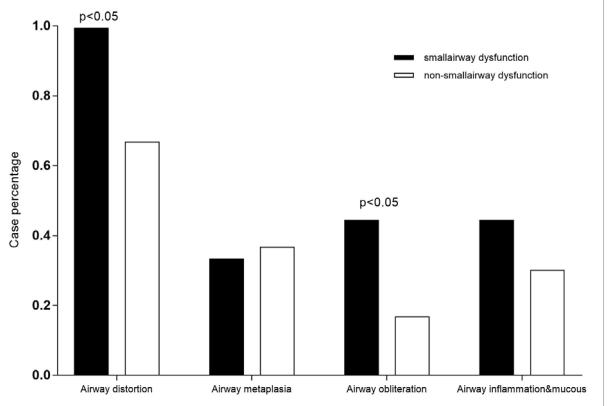

FIGURE 4
Comparisons of pathological characteristics between the SAD and non-SAD groups The pathological lesion types of airway distortion proportion and airway obliteration proportion were significantly high in SAD patients.

TABLE 4 Factors associated with small airway Dysfunction logistic regression analysis.

	Odd ratios (OR)	*P*-value	95% CI	
			Lower	Upper
Univariate analysis				
Smoking	1.439	0.216	0.809	2.560
Gender	2.014	0.136	0.803	5.051
Age	0.969	0.068	0.937	1.002
Fibrosis rate	1.013	0.304	0.989	1.037
Emphysema rate	1.111	0.067	0.993	1.243
Multivariate analysis				
Smoking	1.260	0.494	0.650	2.441
Gender	1.988	0.202	0.691	5.721
Age	0.967	0.067	0.934	1.002
Fibrosis rate	1.004	0.786	0.978	1.030
Emphysema rate	1.113	0.071	0.991	1.250

Notes: CI, confidence interval. Fibrosis rate, the percentage of fibrosis in chest CT calculated by AI according to the system established by Li HP et al.; Emphysema rate, the percentage of Emphysema in chest CT calculated by AI according to the system established by Li HP et al.

Discussion

The pathophysiology of IPF is generally considered to be impaired lung interstitium and alveoli but rare airway involvement (Mead, 1970; Gibson and Pride, 1977; Nicholson et al., 2002). Our retrospective analysis consisting of 243 IPF patients showed that one-third (84/243, 34.57%) of IPF patients had SAD, and these patients had a significantly higher mortality risk compared with non-SAD patients (HR 1.725, $p < 0.05$), and the median survival was significantly shortened (34 ± 7.59 vs. 52 ± 5.34 months). Further stratified analysis showed that IPF comorbid SAD at different CTPF stages and GAP stages had a substantially higher risk of death compared with those non-SAD patients. Previous studies on IPF mortality prediction have mostly focused on FVC, DLCO, chest CT pulmonary fibrosis range, age, gender, and other parameters (King et al., 2001; Zappala et al., 2010; Ley et al., 2014), while no large-scale case-cohort studies have focused on SAD in IPF patients. In the present study, the sample size of IPF patients in our cohort reached 243, and our study showed that IPF comorbid SAD was an independent risk factor associated with the mortality of IPF patients.

Among the 84 patients diagnosed with SAD, only 11 cases (11/84, 13%) had significant obstructive ventilatory dysfunction (FEV1/FVC < 0.7), which was slightly higher than the value of 7% (5/68) reported by Guiot et al. (2022). In contrast, the majority of patients (87%) showed no significant obstructive ventilatory dysfunction by routine PFT. The results showed that the changes in small airway function indexes (MMEF, FEF50%, FEF75%) were more sensitive than normal airway function indexes (FEV1/FVC < 70%), by which abnormalities in IPF patients could be detected earlier. Table 2 shows that once IPF was combined with O-IPF, their SAD became worse ($p < 0.001$), and their median survival time was shortened.

The histopathology of patients undergoing lung transplantation in our cohort showed that all 48 IPF patients had diverse degrees of small airway lesions in their pathological section, while the proportion of airway distortion and obliteration was higher in patients with SAD diagnosed by the preoperative PFT (Table 3). The lesions of airway distortion and obliteration might be more critical pathological changes affecting SAD. SAD patients undergoing lung transplantation were younger compared with the non-SAD group, suggesting that patients with SAD progressed to the end stage of the disease more quickly. Some studies have found that in end-stage ILD, there is a significant reduction in the number of small terminal airways, showing loss of terminal bronchioles, fibroblastic foci, lymphocyte-dominated immune cell infiltration inflammation, increased lymphatic follicular volume fraction, and even emphysema with increased alveolar volume and more severe clinical symptoms through micro-CT, new *in-vivo* imaging methods, and other means (Fulmer et al., 1977; Kawabata et al., 2008; Katzenstein et al., 2010; Galban et al., 2012; Chen et al., 2013; Koo et al., 2018; Higham et al., 2019; Vasilescu et al., 2019; Verleden et al., 2020), which can partially explain why IPF patients are combined with small airway lesions and develop to CPFE eventually. Our study confirmed that the small airway lesion was a common feature of all end-stage IPF diseases. Based on our research, we speculated that the progression of IPF damaged pulmonary alveoli and interstitium first by fibroblast proliferation. Then it spread to the small airway to gradually impair the small airway function, finally invading the large airway. PFT would show apparent ventilation dysfunction when the airway obliteration and distortion developed

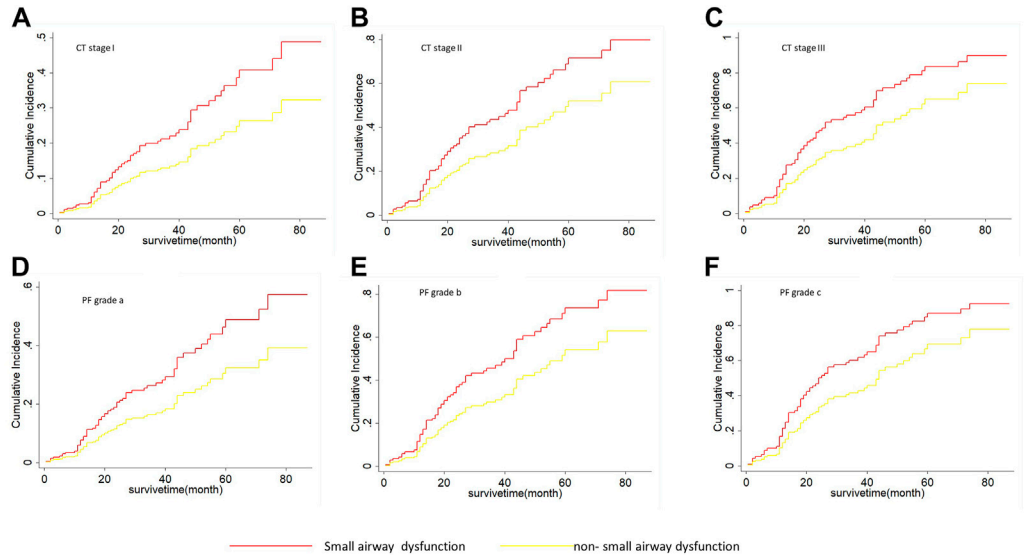

FIGURE 5
The cumulative risk of death with SAD and non-SAD in different CTPF stages based on the Fine-Gray regression model. **(A)** Cumulative death risk curve of patients with SAD and non-SAD in CT stage I; **(B)** Cumulative death risk curve of patients with SAD and non-SAD in CT stage II; **(C)** Cumulative death risk curve of patients with SAD and non-SAD in CT stage III; **(D)** Cumulative death risk curve of patients with SAD and non-SAD in grade a; **(E)** Cumulative death risk curve of patients with SAD and non-SAD in grade b; **(F)** Cumulative death risk curve of patients with SAD and non-SAD in grade c. As the cumulative dearth risk curve show, IPF comorbid SAD had a high dearth risk in all different CTPF stages. The red curve indicates that PFT diagnoses SAD. The yellow curve indicates that PFT diagnoses non-SAD. Note: CTPF model: A Mortality Risk Prediction model used to evaluate the severity of IPF based on Artificial Intelligence which was established by Li HP et al. CT stage: The stage was determined by using AI according to the system installed by Li HP et al. CT I: Honeycomb area rate was <5% of the entire lung. CT II: Honeycomb area rate was 5%–25% of the entire lung. CT III: Honeycomb area rate was >25%. PF grade: The grade was determined by using the pulmonary function and physiological parameters (age, gender, FVC% pred, DLco% pred, and SpO_2%). The grade was defined as: mild **(A)**, moderate **(B)**, and severe **(C)**.

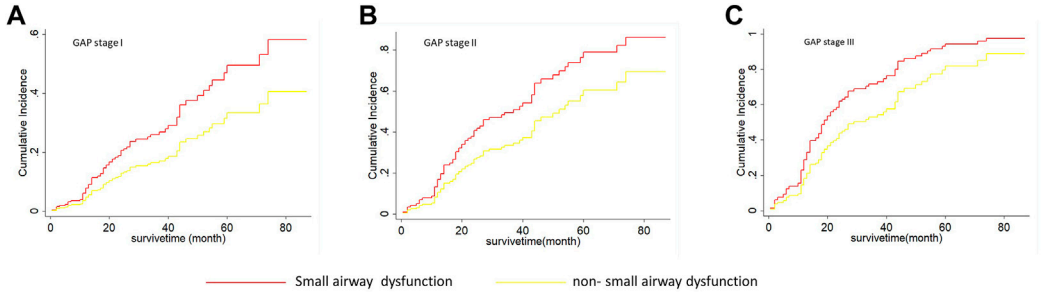

FIGURE 6
The cumulative risk of death with SAD and non-SAD in different GAP stages based on the Fine-Gray regression model. **(A)** Cumulative death risk curve of patients with SAD and non-SAD in GAP stage I; **(B)** Cumulative death risk curve of patients with SAD and non-SAD in GAP stage II; **(C)** Cumulative death risk curve of patients with SAD and non-SAD in GAP stage III; IPF comorbid SAD had the high dearth risk in all GAP stages. Note: The red curve indicates that PFT diagnoses SAD; the yellow curve indicates that PFT diagnoses non-SAD. GAP (gender, age, and physiologic variables) stage followed the recommendation by Brett Ley, and a higher stage represented a greater death risk.

severely. Therefore, clinicians should pay more attention to the changes in small airway function in IPF patients, adjust the therapeutic measures timely, and improve the effectiveness of treatment outcomes.

Previous studies of SAD have mainly focused on chronic airway diseases, such as COPD and asthma, and the risk factors associated with SAD are air pollutant exposure and smoking (Konstantinos Katsoulis et al., 2016; Usmani et al., 2016). Few clinical studies have focused on ILD with small airway lesions. Guiot et al. (2022) have reported that about 15% of ILD patients are complicated with obstructive ventilator dysfunction. Among them, 7% (5/68) of patients have IPF comorbid obstructive

TABLE 5 Fine-gray death risk regression analysis results from different model factors.

	Hazard ratio (HR)	*P*-value	95% CI	
			Lower	Upper
Univariate factors				
Small airway dysfunction	1.725	0.025	1.071	2.778
Multivariate factors (Adjust CTPF model)				
Small airway dysfunction	1.714	0.033	1.043	2.816
CT I	referent			
CT II	2.393	0.017	1.171	4.894
CT III	3.425	0.009	1.368	8.571
PF(a)	referent			
PF(b)	2.000	0.014	1.151	3.465
PF(c)	3.021	0.004	1.420	6.424
Multivariate factors (Adjust GAP stage)				
Small airway dysfunction	1.675	0.035	1.038	2.705
GAP I	referent			
GAP II	2.276	0.002	1.356	3.820
GAP III	4.189	<0.001	2.134	8.222

Notes: CI, confidence interval; CTPF model, A Mortality Risk Prediction model used to evaluate the severity of IPF based on Artificial Intelligence which established by Li HP et al. CT stage: The stage was determined by using AI according to the system established by Li HP et al. CT I: Honeycomb lesion area was <5% of the entire lung. CT II: Honeycomb lesion area was 5%–25% of the entire lung. CT III: Honeycomb lesion area was >25%. PF grade: The grade was determined by using the pulmonary function and physiological parameters (age, gender, FVC% pred, DLco% pred, and SpO_2%) and following the CTPF model recommendation by Li HP et al. The grade was defined as: mild (a), moderate (b), and severe (c). GAP (gender, age, and physiologic variables) stage followed the recommendation by Brett Ley, and a higher stage represented a greater death risk.

ventilator dysfunction and impaired small airway function. However, due to the small sample size, the risk factors are not analyzed. Our case-cohort logistic regression analysis found that patients with IPF comorbid SAD had higher proportions of smoking, male, younger age, and a larger range of pulmonary fibrosis and emphysema patterns in chest CT. However, the *p* values were not statistically significant in both multivariate and univariate regression analyses. Therefore, the independent risk factors associated with IPF comorbid SAD needed to be analyzed in a larger sample, multicenter, and long-term follow-up cohort.

There were several limitations in our study. First, even though our research found that O-IPF (11 cases) patients had a higher proportion of emphysema and shorter survival time, there was no significant difference due to the small sample size. Second, the detailed therapeutic process was not analyzed because of the retrospective analysis. Whether the patients with IPF comorbid SAD need to be treated by inhaled glucocorticoid and bronchodilators like COPD or other chronic airway diseases? Whether the patients can benefit from this treatment or not? All these questions need to be answered in future studies. Third, this study was a single-center retrospective analysis, and multicenter prospective studies with large samples are required.

In conclusion, we found that 30% of IPF patients had comorbid SAD, and the mortality risk of these patients was significantly higher compared with the non-SAD group. Moreover, no significant obstructive ventilatory dysfunction was found in 87% of patients with IPF comorbid SAD. When IPF patients had combined significant ventilatory dysfunction, the degree of SAD was worse, and the median survival time was shorter. These findings suggested that clinicians should pay more attention to the small airway function in IPF patients, and appropriate treatment should be explored.

Data availability statement

The raw data supporting the conclusion of this article will be made available by the authors, without undue reservation.

Ethics statement

The studies involving human participants were reviewed and approved by the Institutional Ethics Committee of Shanghai Pulmonary Hospital (No. K17-016). Written informed consent for participation was not required for this study in accordance with the national legislation and the institutional requirements.

Author contributions

HL, CY, YZ, and XH participated in the conception, hypothesis, and design of the study. CY and AZ carried out the statistical analyses. All authors contributed to the interpretation of the data. HX participated in pathological slice interpretation. CY and HL drafted the manuscript, and all authors made critical revisions. All authors read and approved the final manuscript.

Funding

This study was financially supported by grants from the National Science Foundation of China (Grant No.: 81730002) and the Shanghai Family Planning Commission Health Industry Clinical Research Project (20184Y0084, 20194Y0054, 20204Y0383).

Conflict of interest

The authors declare that the research was conducted in the absence of any commercial or financial relationships that could be construed as a potential conflict of interest.

The reviewer XZ declared a shared parent affiliation with the authors to the handling editor at the time of the review.

Publisher's note

All claims expressed in this article are solely those of the authors and do not necessarily represent those of their affiliated organizations, or those of the publisher, the editors and the reviewers. Any product that may be evaluated in this article, or claim that may be made by its manufacturer, is not guaranteed or endorsed by the publisher.

References

Chen, Y. S., Li, X. Q., Li, H. R., Miao, Y., Lian, S. q., Lu, F. f., et al. (2013). Risk factors for small airway obstruction among Chinese island residents: A case-control study. *PLoS One* 8 (7), e68556. doi:10.1371/journal.pone.0068556

Ciprandi, G., Cirillo, I., Klersy, C., Marseglia, G. L., Vizzaccaro, A., Pallestrini, E., et al. (2006). Role of FEF25-75 as an early marker of bronchial impairment in patients with seasonal allergic rhinitis. *Am. J. Rhinol.* 20 (6), 641–647. doi:10.2500/ajr.2006.20.2914

Cottin, V., Nunes, H., Brillet, P. Y., Delaval, P., Devouassoux, G., TillIe-Leblond, I., et al. (2005). Combined pulmonary fibrosis and emphysema: A distinct underrecognised entity. *Eur. Respir. J.* 26 (4), 586–593. doi:10.1183/09031936.05.00021005

Evans, C. M., Fingerlin, T. E., Schwarz, M. I., Lynch, D., Kurche, J., Warg, L., et al. (2016). Idiopathic pulmonary fibrosis: A genetic disease that involves mucociliary dysfunction of the peripheral airways. *Physiol. Rev.* 96 (4), 1567–1591. doi:10.1152/physrev.00004.2016

Fulmer, J. D., Roberts, W. C., von Gal, E. R., and Crystal, R. G. (1977). Small airways in idiopathic pulmonary fibrosis. Comparison of morphologic and physiologic observations. *J. Clin. Invest.* 60 (3), 595–610. doi:10.1172/JCI108811

Galban, C. J., Han, M. K., Boes, J. L., Chughtai, K. A., Meyer, C. R., Johnson, T. D., et al. (2012). Computed tomography-based biomarker provides unique signature for diagnosis of COPD phenotypes and disease progression. *Nat. Med.* 18 (11), 1711–1715. doi:10.1038/nm.2971

Gibson, G. J., and Pride, N. B. (1977). Pulmonary mechanics in fibrosing alveolitis: The effects of lung shrinkage. *Am. Rev. Respir. Dis.* 116 (4), 637–647. doi:10.1164/arrd.1977.116.4.637

Guiot, J., Henket, M., Frix, A. N., Gester, F., Thys, M., Giltay, L., et al. (2022). Combined obstructive airflow limitation associated with interstitial lung diseases (O-ILD): The bad phenotype. *Respir. Res.* 23 (1), 89. doi:10.1186/s12931-022-02006-9

Halpin, D. M. G., Criner, G. J., Papi, A., Singh, D., Anzueto, A., Martinez, F. J., et al. (2021). Global initiative for the diagnosis, management, and prevention of chronic obstructive lung disease. The 2020 GOLD science committee report on COVID-19 and chronic obstructive pulmonary disease. *Am. J. Respir. Crit. Care Med.* 203 (1), 24–36. doi:10.1164/rccm.202009-3533SO

Higham, A., Quinn, A. M., Cancado, J. E. D., and Singh, D. (2019). The pathology of small airways disease in COPD: Historical aspects and future directions. *Respir. Res.* 20 (1), 49. doi:10.1186/s12931-019-1017-y

Katzenstein, A. L., Mukhopadhyay, S., and Myers, J. L. (2008). Diagnosis of usual interstitial pneumonia and distinction from other fibrosing interstitial lung diseases. *Hum. Pathol.* 39 (9), 1275–1294. doi:10.1016/j.humpath.2008.05.009

Katzenstein, A. L., Mukhopadhyay, S., Zanardi, C., and Dexter, E. (2010). Clinically occult interstitial fibrosis in smokers: Classification and significance of a surprisingly common finding in lobectomy specimens. *Hum. Pathol.* 41 (3), 316–325. doi:10.1016/j.humpath.2009.09.003

Kawabata, Y., Hoshi, E., Murai, K., Ikeya, T., TakahashiN.Saitou, Y., et al. (2008). Smoking-related changes in the background lung of specimens resected for lung cancer: A semiquantitative study with correlation to postoperative course. *Histopathology* 53 (6), 707–714. doi:10.1111/j.1365-2559.2008.03183.x

King, T. E., Jr., Tooze, J. A., Schwarz, M. I., Brown, K. R., and Cherniack, R. M. (2001). Predicting survival in idiopathic pulmonary fibrosis: Scoring system and survival model. *Am. J. Respir. Crit. Care Med.* 164 (7), 1171–1181. doi:10.1164/ajrccm.164.7.2003140

Kirkham, S., Kolsum, U., Rousseau, K., Singh, D., Vestbo, J., and Thornton, D. J. (2008). MUC5B is the major mucin in the gel phase of sputum in chronic obstructive pulmonary disease. *Am. J. Respir. Crit. Care Med.* 178 (10), 1033–1039. doi:10.1164/rccm.200803-391OC

Konstantinos Katsoulis, K., Kostikas, K., and Kontakiotis, T. (2016). Techniques for assessing small airways function: Possible applications in asthma and COPD. *Respir. Med.* 119, e2–e9. doi:10.1016/j.rmed.2013.05.003

Koo, H. K., Vasilescu, D. M., Booth, S., Hsieh, A., Katsamenis, O. L., Fishbane, N., et al. (2018). Small airways disease in mild and moderate chronic obstructive pulmonary disease: A cross-sectional study. *Lancet. Respir. Med.* 6 (8), 591–602. doi:10.1016/S2213-2600(18)30196-6

Ley, B., Elicker, B. M., Hartman, T. E., Ryerson, C. J., Vittinghoff, E., Ryu, J. H., et al. (2014). Idiopathic pulmonary fibrosis: CT and risk of death. *Radiology* 273 (2), 570–579. doi:10.1148/radiol.14130216

Lin, S. P., Shih, S. C., Chuang, C. K., Lee, K. S., Chen, M. R., Niu, D. M., et al. (2014). Characterization of pulmonary function impairments in patients with mucopolysaccharidoses--changes with age and treatment. *Pediatr. Pulmonol.* 49 (3), 277–284. doi:10.1002/ppul.22774

Macklem, P. T. (1998). The physiology of small airways. *Am. J. Respir. Crit. Care Med.* 157 (2), S181–S183. doi:10.1164/ajrccm.157.5.rsaa-2

McFadden, E. R., Jr., and Linden, D. A. (1972). A reduction in maximum mid-expiratory flow rate. A spirographic manifestation of small airway disease. *Am. J. Med.* 52 (6), 725–737. doi:10.1016/0002-9343(72)90078-2

Mead, J. (1970). The lung's "quiet zone. *N. Engl. J. Med.* 282 (23), 1318–1319. doi:10.1056/NEJM197006042822311

Mitchell, P. D., Das, J. P., Murphy, D. J., Keane, M. P., Donnelly, S. C., Dodd, J. D., et al. (2015). Idiopathic pulmonary fibrosis with emphysema: Evidence of synergy among emphysema and idiopathic pulmonary fibrosis in smokers. *Respir. Care* 60 (2), 259–268. doi:10.4187/respcare.03389

Nicholson, A. G., Fulford, L. G., Colby, T. V., du Bois, R. M., Hansell, D. M., and Wells, A. U. (2002). The relationship between individual histologic features and disease progression in idiopathic pulmonary fibrosis. *Am. J. Respir. Crit. Care Med.* 166 (2), 173–177. doi:10.1164/rccm.2109039

Perez, T., Chanez, P., Dusser, D., and Devillier, P. (2013). Small airway impairment in moderate to severe asthmatics without significant proximal

airway obstruction. *Respir. Med.* 107 (11), 1667–1674. doi:10.1016/j.rmed.2013.08.009

Raghu, G., Remy-Jardin, M., Myers, J. L., Richeldi, L., Ryerson, C. J., Lederer, D. J., et al. (2018). Diagnosis of idiopathic pulmonary fibrosis. An official ATS/ERS/JRS/ALAT clinical practice guideline. *Am. J. Respir. Crit. Care Med.* 198 (5), e44–e68. doi:10.1164/rccm.201807-1255ST

Reddel, H. K., Bacharier, L. B., Bateman, E. D., Brightling, C. E., Brusselle, G. G., Buhl, R., et al. (2022). Global initiative for asthma strategy 2021. Executive summary and rationale for key changes. *Arch. Bronconeumol.* 58 (1), 35–51. doi:10.1016/j.arbres.2021.10.003

Seibold, M. A., Wise, A. L., Speer, M. C., Steele, M. P., Brown, K. K., Loyd, J. E., et al. (2011). A common MUC5B promoter polymorphism and pulmonary fibrosis. *N. Engl. J. Med.* 364 (16), 1503–1512. doi:10.1056/NEJMoa1013660

Silva, D. R., Gazzana, M. B., Barreto, S. S., and Knorst, M. M. (2008). Idiopathic pulmonary fibrosis and emphysema in smokers. *J. Bras. Pneumol.* 34 (10), 779–786. doi:10.1590/s1806-37132008001000005

Usmani, O. S., Singh, D., Spinola, M., Bizzi, A., and Barnes, P. J. (2016). The prevalence of small airways disease in adult asthma: A systematic literature review. *Respir. Med.* 116, 19–27. doi:10.1016/j.rmed.2016.05.006

Vasilescu, D. M., Martinez, F. J., Marchetti, N., Galban, C. J., Hatt, C., Meldrum, C. A., et al. (2019). Noninvasive imaging biomarker identifies small airway damage in severe chronic obstructive pulmonary disease. *Am. J. Respir. Crit. Care Med.* 200 (5), 575–581. doi:10.1164/rccm.201811-2083OC

Verleden, S. E., Tanabe, N., McDonough, J. E., Vasilescu, D. M., Xu, F., Wuyts, W. A., et al. (2020). Small airways pathology in idiopathic pulmonary fibrosis: A retrospective cohort study. *Lancet. Respir. Med.* 8 (6), 573–584. doi:10.1016/S2213-2600(19)30356-X

Wu, X., Yin, C., Chen, X., Zhang, Y., Su, Y., Shi, J., et al. (2022). Idiopathic pulmonary fibrosis mortality risk prediction based on artificial intelligence: The CTPF model. *Front. Pharmacol.* 13, 878764. doi:10.3389/fphar.2022.878764

Xiao, D., Chen, Z., Wu, S., Huang, K., Xu, J., Yang, L., et al. (2020). Prevalence and risk factors of small airway dysfunction, and association with smoking, in China: Findings from a national cross-sectional study. *Lancet. Respir. Med.* 8 (11), 1081–1093. doi:10.1016/S2213-2600(20)30155-7

Zappala, C. J., Latsi, P. I., Nicholson, A. G., Colby, T. V., Cramer, D., Renzoni, E. A., et al. (2010). Marginal decline in forced vital capacity is associated with a poor outcome in idiopathic pulmonary fibrosis. *Eur. Respir. J.* 35 (4), 830–836. doi:10.1183/09031936.00155108

frontiers | Frontiers in Pharmacology

TYPE Original Research
PUBLISHED 12 October 2022
DOI 10.3389/fphar.2022.1016552

OPEN ACCESS

EDITED BY
Jian Gao,
Shanghai Children's Medical Center, China

REVIEWED BY
Chuantao Tu,
Tongji University School of Medicine, China
Zhishen Xie,
Henan University of Chinese Medicine, China

*CORRESPONDENCE
Wei Liu,
lwhzayl@163.com
Ping Liu,
liuliver@vip.sina.com

†These authors have contributed equally to this work

SPECIALTY SECTION
This article was submitted to Gastrointestinal and Hepatic Pharmacology, a section of the journal Frontiers in Pharmacology

RECEIVED 11 August 2022
ACCEPTED 29 September 2022
PUBLISHED 12 October 2022

CITATION
He X-L, Hu Y-H, Chen J-M, Zhang D-Q, Yang H-L, Zhang L-Z, Mu Y-P, Zhang H, Chen G-F, Liu W and Liu P (2022), SNS-032 attenuates liver fibrosis by anti-active hepatic stellate cells via inhibition of cyclin dependent kinase 9. *Front. Pharmacol.* 13:1016552. doi: 10.3389/fphar.2022.1016552

SNS-032 attenuates liver fibrosis by anti-active hepatic stellate cells *via* inhibition of cyclin dependent kinase 9

Xiao-Li He[1,2†], Yong-Hong Hu[1†], Jia-Mei Chen[1], Ding-Qi Zhang[1], Hai-Lin Yang[1], Lin-Zhang Zhang[1,3], Yong-Ping Mu[1], Hua Zhang[1], Gao-Feng Chen[1], Wei Liu[1*] and Ping Liu[1,3*]

[1]Key Laboratory of Liver and Kidney Diseases (Ministry of Education), Institute of Liver Diseases, Shanghai Key Laboratory of Traditional Chinese Clinical Medicine, Shuguang Hospital Affiliated to Shanghai University of Traditional Chinese Medicine, Shanghai, China, [2]Department of Endocrinology, Yueyang Hospital of Integrated Traditional Chinese and Western Medicine, Shanghai University of Traditional Chinese Medicine, Shanghai, China, [3]Shanghai Frontiers Science Center of TCM Chemical Biology, Institute of Interdisciplinary Integrative Medicine Research, Shanghai University of Traditional Chinese Medicine, Shanghai, China

Liver fibrosis is a common pathological process of all chronic liver diseases. Hepatic stellate cells (HSCs) play a central role in the development of liver fibrosis. Cyclin-dependent kinase 9 (CDK9) is a cell cycle kinase that regulates mRNA transcription and elongation. A CDK9 inhibitor SNS-032 has been reported to have good effects in anti-tumor. However, the role of SNS-032 in the development of liver fibrosis is unclear. In this study, SNS-032 was found to alleviate hepatic fibrosis by inhibiting the activation and inducing the apoptosis of active HSCs in carbon tetrachloride-induced model mice. *In vitro*, SNS-032 inhibited the activation and proliferation of active HSCs and induced the apoptosis of active HSCs by downregulating the expression of CDK9 and its downstream signal transductors, such phosphorylated RNA polymerase II and Bcl-2. CDK9 short hairpin RNA was transfected into active HSCs to further elucidate the mechanism of the above effects. Similar results were observed in active HSCs after CDK9 knockdown. In active HSCs with CDK9 knockdown, the expression levels of CDK9, phosphorylated RNA polymerase II, XIAP, Bcl-2, Mcl-1, and α-SMA significantly decreased, whereas those of cleaved-PARP1 and Bax decreased prominently. These results indicated that SNS-032 is a potential drug and CDK9 might be a new prospective target for the treatment of liver fibrosis.

KEYWORDS

liver fibrosis, hepatic stellate cell, cyclin-dependent kinase 9, apoptosis, activation, proliferation

Introduction

Liver fibrosis is a general pathological change that is induced by several chronic liver diseases, such as viral hepatitis, nonalcoholic steatohepatitis, primary cholestatic cirrhosis, and drug-induced liver disease. It is characterized by the excess accumulation of the extracellular matrix (ECM) in liver tissue (Strowitzki et al., 2019). The core event of fibrosis is the activation of hepatic stellate cells (HSCs), which synthesize and secrete large amounts of ECM (Tanwar et al., 2020). Acta2 (α-smooth muscle actin, α-SMA), the marker of active HSCs, and collagen type Iα1 (Col1A1), one of the most crucial ECM proteins, are usually detected to evaluate the activation of HSCs and the stage of fibrosis (Chen et al., 2010a; Jin et al., 2011). When fibrosis develops, the production and apoptosis of active HSCs increase, with production exceeding apoptosis. This condition leads to the increase in the total number of active HSCs. In the recovery stage of fibrosis, the opposite phenomenon occurs, and the number of active HSCs decreases. Recent studies have demonstrated that the apoptosis of active HSCs could be induced by aquaporins and cytokines, such as nerve growth factors, and eliminated by natural killer cells (Oakley et al., 2003; Lakner et al., 2011; Kisseleva and Brenner, 2012). Although the apoptosis of active HSCs was observed many years ago, methods for selectively inducing this process remain lacking.

Cyclin-dependent kinase 9 (CDK9) is a member of the cyclin-dependent kinase (CDK) family (Matrone et al., 2015). Recent studies have suggested that CDKs play an important role in cell apoptosis, proliferation, activation, and survival (Santo et al., 2015). The CDK subfamily members CDK2, CDK4, and CDK6 regulate the cell cycle, whereas other CDK subfamily members, such as CDK7 and CDK9, affect the transcription of mRNA (Gérard and Goldbeter, 2016). CDK9 binds with cyclin families (cyclin T1, T2a, T2b, or K) to form a heterodimer kinase called positive transcription elongation factor b (P-TEFb), which is necessary and crucial for promoting the transcription and elongation of mRNA by activating RNA polymerase II (RNAP II) (Fujinaga, 2020). P-TEFb has two states: inactive and catalytically active. Commonly, P-TEFb is inactive when it is bound with hexamethylene bis-acetamide-inducible protein 1 (HEXIM1), methylphosphate capping enzyme (MePCE), Larp7, and 7SK small nuclear ribonucleoprotein (7SK snRNP) (Fujinaga et al., 2014). When DNA damage is induced by ultraviolet rays or other physical and chemical injuries, inactive P-TEFb releases HEXIM1, MePCE, Larp7, and 7SK snRNP and recruits bromodomain-containing protein 4 (BRD4) (or super elongation complex [SEC]; whichever factor is recruited varies in different cells), which activates the phosphorylation of CDK9 and provides the catalytic activity that can phosphorylate RNAP II (Zheng et al., 2021). RNAP II is one of the most important synthetic enzymes of mRNA elongation in eukaryotes (Liang et al., 2015). Phosphorylated CDK9 is the core of active P-TEFb, which finally determines the catalytic activity of P-TEFb. CDK9 inhibitors can inhibit the phosphorylation of RNAP II *via* inhibiting the phosphorylation of CDK9 and degrading CDK9 to block the activation of P-TEFb (Bose et al., 2013; Zhou et al., 2022).

SNS-032, a CDK9 inhibitor, has the IC_{50} ratio of inhibition with CDK9 of 4 nM, which indicates 10-fold selectivity over other CDKs (48 nM to CDK2, 62 nM to CDK7, 340 nM to CDK5, and little inhibitory effect on CDK6) *in vitro* (Chen et al., 2009; Conroy et al., 2009). The safety of SNS-032 has been evaluated in phase I clinical trial. And it has been used to treat hematopoietic diseases, such as B-lymphoid malignancies, chronic lymphocytic leukemia, mantle cell lymphoma, and multiple myeloma (NCT00446342), as well as some advanced solid tumors (NCT00292864) (Tong et al., 2010; Walsby et al., 2011). Recently, it has also been used to treat solid tumors, such as ovarian carcinoma, by preventing the proliferation and formation of capillaries through the inhibition of vascular endothelial growth factors (Misra et al., 2004; Ali et al., 2007). A recent study has shown that knockdown of CDK9 and a CDK9 inhibitor (LDC000067) could remarkably ameliorate renal fibrosis by blocking the phosphorylation of the Smad3 linker (Thr179) (Qu et al., 2015). However, the role of CDK9 inhibitors in the development of liver fibrosis is unclear. Therefore, the purpose of this study is to clarify the antiliver fibrosis effects of the CDK9 inhibitor SNS-032 and elucidate its possible mechanism *in vivo* and *in vitro*.

Materials and methods

Drugs and reagents

SNS-032 (lot CSN12378, a specific CDK9 inhibitor) was purchased from CSNpharm, Inc. (Shanghai, China). SB431542 [lot S1067, a transforming growth factor-β [TGF-β] receptor inhibitor and used as the positive drug for inhibiting activated HSCs (Gupta et al., 2016)], was obtained from Selleckchem, Inc. (Shanghai, China). Sorafenib tosylate, which was used as the positive drug *in vivo* as previously described (Lin et al., 2016), was bought from ChemBest Research Laboratories Ltd. (Shanghai, China). CCl_4 was acquired from China Pharmaceutical Group Co., Ltd. (Beijing, China). Fetal bovine serum (FBS), Dulbecco modified Eagle's medium (DMEM), penicillin–streptomycin solution, 0.25% trypsin with ethylenediamine tetra-acetic acid (EDTA), and 0.25% trypsin without EDTA were bought from Gibco (Thermo Fisher Scientific, Inc., MA, United States). Dimethyl sulfoxide was purchased from Sigma-Aldrich, LLC. (MUC, GER). Phosphate-buffered saline (PBS) was procured from Hyclone (Thermo Fisher Scientific, Inc., MA, United States). Recombinant human TGF-β1 was obtained from R&D (R&D Systems Inc., MN, United States). Serum alanine aminotransferase (ALT), aspartate transaminase (AST),

Sirius red staining kit, and hematoxylin–eosin (HE) staining kit were provided by Jiancheng Bioengineering Institute (Nanjing, China). Annexin V–fluorescein isothiocyanate (FITC)/propidium iodide (PI) apoptosis kit and annexin V–allophycocyanin (APC) dye were purchased from BD Biosciences, Inc. (NJ, United States). Diaminyl phenyl indole (DAPI) dye was acquired from Beyotime Biotechnology, Inc. (Shanghai, China).

Animals and treatment

Forty-eight male C57BL6 mice (6-week-old, 18–20 g) were caged individually in a temperature- and humidity-controlled environment under a 12:12 light–dark cycle. After acclimation, they were kept in the Shanghai Model Organisms Center, Inc. (Shanghai, China) with the license number SCXK 2019-0002. Then, they were assigned into two groups randomly. The first group (control group, $n = 8$) was fed with normal diet and water freely. The second group ($n = 40$) was intraperitoneally injected with 2 ml·kg^{-1} 15% carbon tetrachloride (CCl_4)–olive oil on Mondays, Wednesdays, and Fridays for 3 weeks. Then, the mice in the second group were randomly allocated into five groups (experimental, low-dose SNS-032, medium-dose SNS-032, high-dose SNS-032, and sorafenib groups; $n = 8$). Subsequently, the mice in the low-, medium-, and high-dose SNS-032 and sorafenib groups were treated with 2.5, 5, and 10 mg·kg^{-1}·day SNS-032 through intraperitoneal administration or 5 mg·kg^{-1}·day sorafenib through intragastric administration for 3 weeks with the continuous injection of CCl_4–olive oil. The CCl_4 mouse model was used as the liver fibrosis model as previously described (Strnad et al., 2008).

All experiments were approved (ID. PZSHUTCM190315006) by the experimental animal ethics committee of the Shanghai University of Traditional Chinese Medicine and conducted in accordance with the Guide for the Care and Use of Laboratory Animals (National Institutes of Health, NIH Publication 86–23, revised 1996).

Cell culture

The human hepatic stellate cell line LX-2 was obtained from the Institute of Liver Disease affiliated with the Shanghai University of Traditional Chinese Medicine. LX-2 was cultured with DMEM containing 10% FBS in 5% CO_2 at 37 C. The cells were passaged when their density reached 80%.

Cell treatment

The human hepatic stellate cell line LX-2 was cultured on six-well plates or 6 cm culture dishes at the density of 2×10^6 cells per well or 4×10^6 cells per dish for 24 h. LX-2 was incubated with 5 ng·mL^{-1} TGF-β1 for 24 h to construct the activated HSC model *in vitro* as previously described (He et al., 2020). Then, the activated LX-2 cell line was treated with 0.04, 0.2, and 1 μM SNS-032 for 24 h H_2O_2 with the concentration of 200 μM was used as the positive drug in apoptosis induction (Shang et al., 2020), and 10 μM SB431542 was used as the positive drug in the inhibition of activated LX-2 (Premkumar and Shankar, 2021). Then, the cell lysates of each group were collected and stored at −80 °C in a refrigerator.

Establishment of the CDK9 knockdown LX-2 cell line

A CDK9 knockdown strategy using lentiviral vectors encoding CDK9 short hairpin RNA (shRNA) was utilized. LX-2 cells were incubated with lentiviral vectors at MOI ratio = 40 for 8 h. Then, the transfected cells were cultured and incubated with 4 μg·mL^{-1} purinomycin for 48 h to screen LX-2 cells with CDK9 knockdown. The lentiviral vectors (GV248) that carried CDK9 shRNA, green fluorescent protein (GFP), and antipurinomycin genes were designed, synthesized, and packed into the GV248 lentivirus by Genechem, Inc. (Shanghai, China). The RNA sequences of the three CDK9 shRNAs are listed in Supplementary Table S1.

HE staining

Liver tissues were dehydrated in a gradient series of alcohol and embedded in paraffin wax blocks. Before staining, 4 μm-thick liver tissue sections were dewaxed in xylene, rehydrated in decreasing concentrations of ethanol, and washed in PBS. Then, the sections were stained with HE. After staining, the sections were dehydrated in increasing concentrations of ethanol and xylene and covered with neutral resin.

Sirius red staining

Liver paraffin sections were dewaxed and rehydrated. Next, the slices were incubated with Sirius red dye for 10 min at 37 C. After being washed with ethanol for 2 min twice, the slices were immersed in dimethylbenzene for 10 min and covered with neutral resin and cover slips. High-resolution scanning and photography were performed with a Leica SCN400 Slide Scanning System (Leica, Inc., Wetzlar, GER). The positive area of collagen was semiquantitatively analyzed by using Aperio Scope software (Leica, Inc., Wetzlar, GER).

Biochemical assays

The serum levels of AST, ALT, TBIL, and ALB were measured with test kits purchased from Jiancheng Bioengineering Institute (Nanjing, China) and a Beckman Coulter Synchron DXC800 Automatic Biochemical Analyzer (CA, United States) as described by the manufacturer.

Immunohistochemical staining

The liver paraffin sections were dewaxed and rehydrated first. After antigen repair and endogenous peroxidase elimination, the sections were treated with 10% goat serum for 30 min and subsequently covered with 1 μg·mL^{-1} Acta2 primary antibody (see Supplementary Table S2) at 4 C for 12 h. Horseradish peroxidase solution was added to conjugate the primary antibody, and 2% diaminobenzidine solution was used to visualize the positive area. The sections were stained with hematoxylin dye to visualize nuclei. Positive stained areas were semiquantitatively analyzed by using Aperio Scope software (Leica, Inc., Wetzlar, GER).

Annexin V–FITC/propidium iodide staining

After TGF-β1 and SNS-032 treatment for 24 h, the cells were digested with 0.25% trypsin, washed twice with cold PBS, and resuspended in 1× binding buffer at the concentration of 1 × 10^5 cells·mL^{-1}. The cells were then stained with annexin V–FITC or annexin V–APC and PI dyes for 15 min at room temperature as described by the product protocol, detected through flow cytometry (FITC, peak excitation wavelength [Ex]: 495 nm/ peak emission wavelength [Em]: 525 nm; PI, Ex: 535 nm/Em: 615 nm; APC, Ex: 650 nm/Em: 660 nm), and analyzed with WinMDI 2.9 software (Purdue University Cytometry Laboratories, IN, United States).

Immunofluorescence staining

LX-2 cells cultured on slides were washed with PBS and fixed with 4% polyformaldehyde for 20 min. Then, the cells were permeated with 0.5% Triton-X 100 for 15 min, blocked with 5% BSA in PBS for 30 min at room temperature, and incubated with the Col1A1 primary antibody (Supplementary Table S2) at 4 C for 12 h Cy3-conjugated or FITC-conjugated secondary antibodies (Supplementary Table S2) were used to visualize the primary antibodies, and DAPI or Hoechst 33342 was applied to visualize nuclei. The stained cells were mounted with antifluorescence quenching solution and viewed with a FV10C-W3 laser confocal microscope or a DP80 fluorescence inverted microscope (Olympus, Inc., TKY, Japan).

RNA isolation, reverse transcription, and qPCR

After treatment, the liver tissues were homogenized, and the LX-2 cells were lysed. Then, the total mRNA was extracted through the Trizol method in accordance with the manufacturer's instructions. Reverse transcription and PCR were conducted as previously described (Liu et al., 2020). Primers (Supplementary Table S3) were designed and synthesized by Takara Bio (Takara Biotechnology Inc., Dalian, China).

Western blot analysis

Tissue homogenates or cell lysates were prepared and Western blot analysis was performed in accordance with previously described methods (Zhang et al., 2021). The gray value was analyzed, and the relative expression level of proteins was obtained by using ImageJ 1.51 software (NIH Image, Bethesda, MD, United States). The primary and secondary antibodies were purchased from Abcam (Abcam Inc., Shanghai, China) and are listed in Supplementary Table S2.

Statistical analysis

All the experiments were performed three times, and data were expressed as mean ± standard deviation. Student's *t* test was used to compare the differences between two groups, whereas those among three and more groups were compared by using one-way analysis of variance with Tukey's posthoc test. All statistical tests were two-sided, and $p < 0.05$ was considered as statistically significant.

Results

SNS-032 improves liver function and fibrotic stage *in vivo*

Male C57BL/6 mice were intraperitoneally injected with 2 ml·kg^{-1} 15% CCl_4–olive oil on Mondays, Wednesdays, and Fridays for 6 weeks to establish a murine model of hepatic fibrosis. After 3 weeks of injection, the mice were treated with 2.5, 5, or 10 mg·kg^{-1} SNS-032 and 5 mg·kg^{-1} sorafenib for 3 weeks (Figure 1A). Then, the sera and liver tissues of each group were collected. We found that the liver weight and liver/ body weight ratio of the mice in the experimental group had

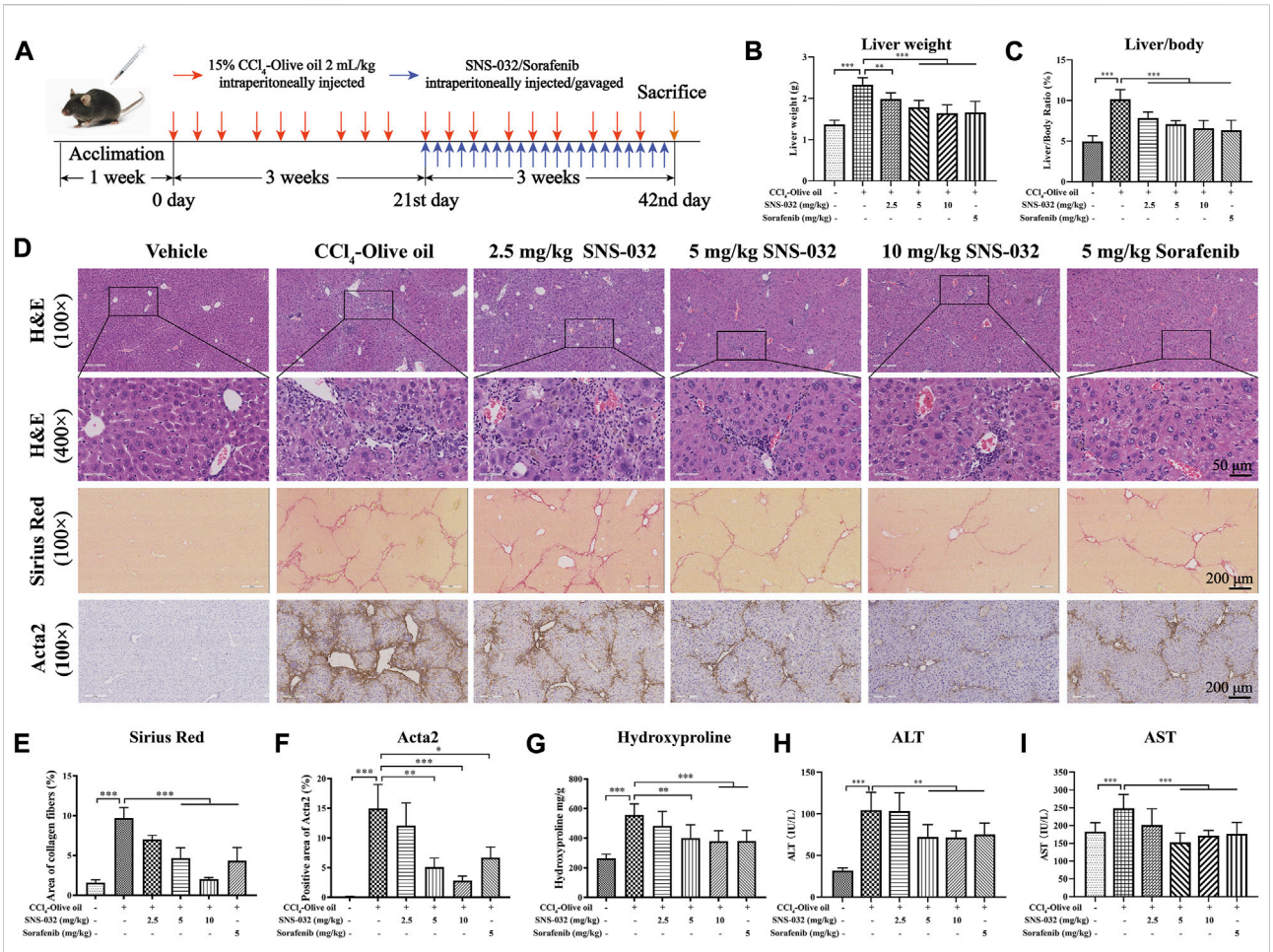

FIGURE 1
SNS-032 improves hepatic injury and liver fibrosis in CCl_4-induced mice. Male C57BL/6 mice were intraperitoneally injected with 2 ml/kg 15% CCl_4-olive oil on Monday, Wednesday and Friday for 6 weeks to establish a hepatic fibrosis model and treated with 2.5, 5, and 10 mg·kg^{-1} SNS-032 or 5 mg·kg^{-1} sorafenib for 3 weeks. Each group had 8 samples (n = 8). **(A)** The flowchart of murine model establishment and treatment. **(B)** Liver weight. **(C)** Liver/body ratio. **(D)** H&E staining (magnification: ×100 and ×400), Sirius Red staining (magnification: ×100), and immunohistochemical staining of Acta2 (magnification: ×100) were performed to observe the histopathological characteristics of liver tissue after the treatment of SNS-032 or sorafenib. Then, the semi-quantitative of Sirius Red staining **(E)**, and Acta2 staining **(F)**, were calculated. And the content of hydroxylysine in liver tissue **(G)**, serum ALT **(H)**, and AST **(I)**, were detect. Comparing with experimental group, *p < 0.05, **p < 0.01, ***p < 0.001.

significantly increased compared with those of the mice in the normal group (p < 0.001). Liver weight and liver/body weight ratio prominently decreased after treatment with 2.5, 5, or 10 mg·kg^{-1} SNS-032 and 5 mg·kg^{-1} sorafenib (p < 0.05; p < 0.001; p < 0.001) (Figures 1B,C).

HE and Sirius red staining revealed that the deposition of fibers and collagen, the infiltration of inflammatory cells, and the degree of liver fibrosis had increased in the experimental group. We found that after treatment with 5 and 10 mg·kg^{-1} SNS-032, collagen deposition, inflammatory cell infiltration, and liver fibrosis degree significantly decreased (Figure 1D). The semiquantitatively analyzed Sirius red positive area and hydroxyproline content in liver tissue significantly increased in the experimental group but decreased in the 5 and 10 mg·kg^{-1} SNS-032 and 5 mg·kg^{-1} sorafenib groups (p < 0.05; p < 0.001; p < 0.001) (Figures 1D,E,G). The percentage of the Acta2-positive area significantly increased in the experimental group but decreased in the 5 and 10 mg·kg^{-1} SNS-032 and 5 mg·kg^{-1} sorafenib groups (p < 0.01; p < 0.001; p < 0.05) (Figures 1D,F). In terms of biochemical profiles, the serum levels of ALT and AST were significantly elevated in the experimental group and significantly decreased in the 5 and 10 mg·kg^{-1} SNS-032 and 5 mg·kg^{-1} sorafenib groups (p < 0.05; p < 0.001; p < 0.001) (Figures 1H,I).

Then, the protein and mRNA expression levels of Acta2 and Col1A1 were assessed in liver tissues. The protein expression of Acta2 significantly increased in the experimental group but decreased in the 5 and 10 mg·kg^{-1} SNS-032 groups (p < 0.05; p < 0.01) (Figures 2A,B). Compared with that in the experimental group, the protein expression of CDK9 had significantly decreased in the 5 and 10 mg·kg^{-1} SNS-032 and 5 mg·kg^{-1} sorafenib groups

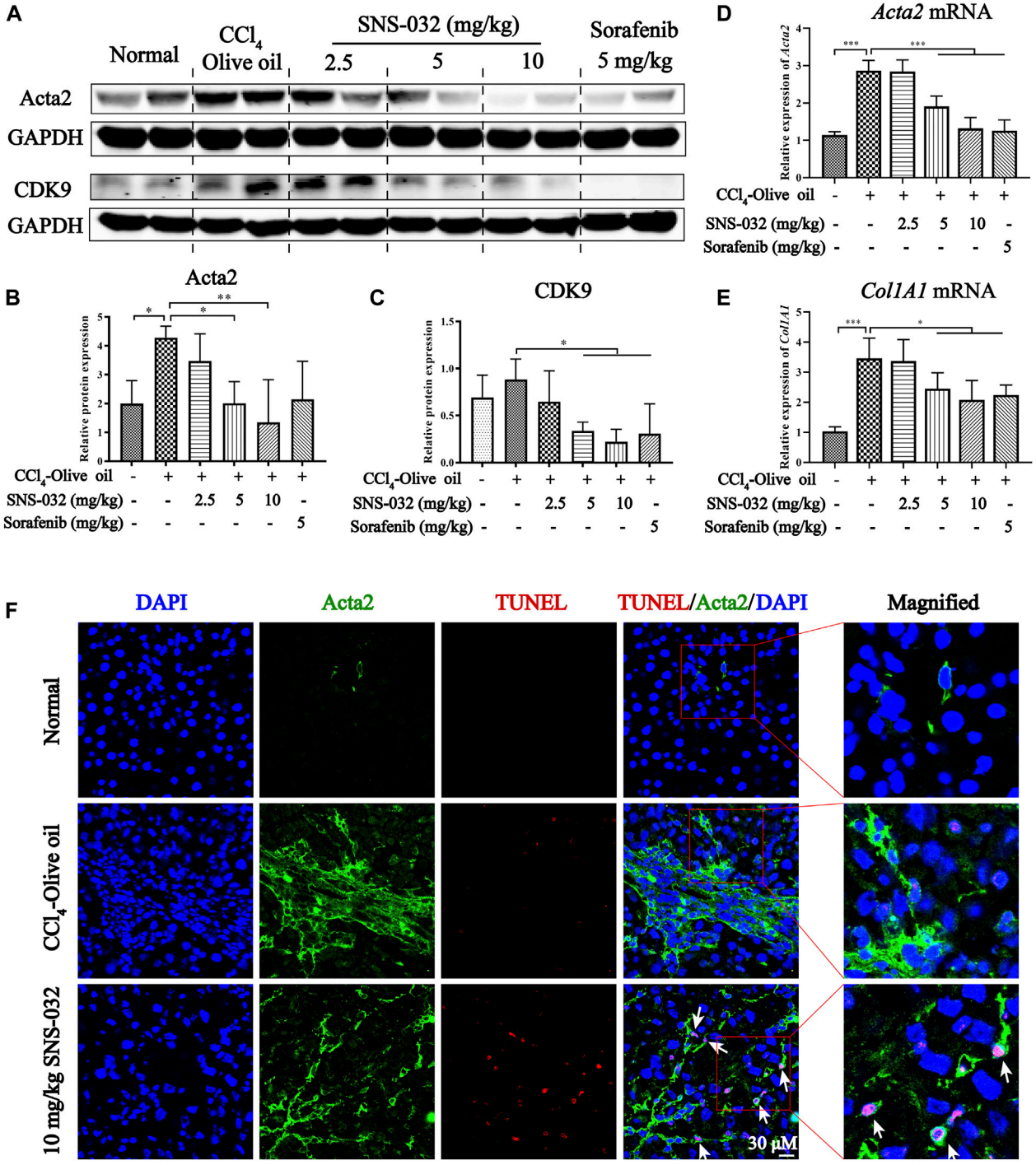

FIGURE 2
SNS-032 alleviates liver fibrosis and induces the apoptosis of active HSCs *in vivo*. Male C57BL/6 mice were intraperitoneally injected with 2 ml/kg 15% CCl_4-olive oil on Monday, Wednesday and Friday for 6 weeks to establish a hepatic fibrosis model and treated with 2.5, 5, and 10 mg·kg^{-1} SNS-032 or 5 mg·kg^{-1} sorafenib for 3 weeks **(A)** The protein expressions of Acta2 and CDK9. **(B,C)** The relative grey values of Acta2 and CDK9. **(D,E)** The mRNA expressions of *Acta2* and *Col1A1*. **(F)** The co-immunofluorescence staining of Acta2, TUNEL, and DAPI in liver tissue (magnification: ×600). Comparing with experimental group, $^*p < 0.05$, $^{**}p < 0.01$, $^{***}p < 0.001$.

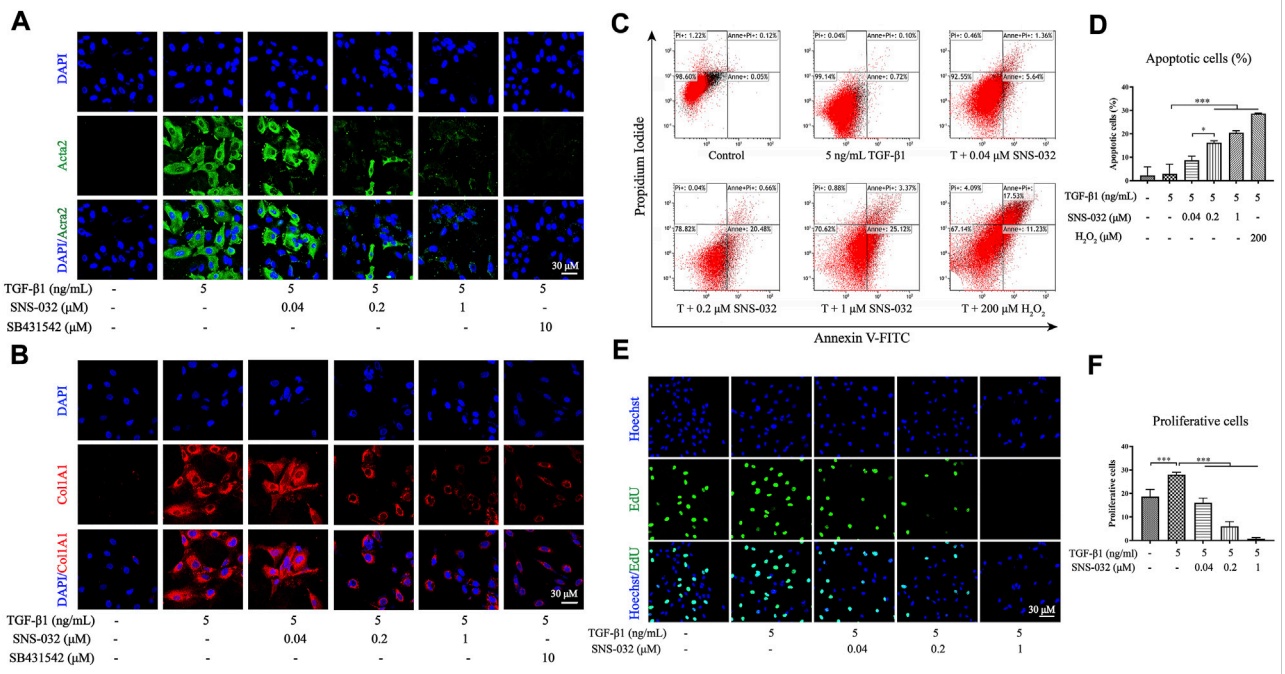

FIGURE 3
SNS-032 inhibits the activation and proliferation of LX-2 induced by TGF-β1, and promotes its apoptosis. LX-2 cells were incubated with 5 ng·mL^{-1} TGF-β1 and treated with 0.04, 0.2, 1 μM SNS-032, and 10 μM SB431542 (TGF-β1 inhibitor) for 24 h. The immunofluorescence staining of Acta2 (**A**, red) and Col1A1 (**B**, red) were observed by laser confocal microscope (magnification: ×600). Then, LX-2 cells were incubated with 5 ng mL^{-1} TGF-β1 and treated with 0.04, 0.2, 1 μM SNS-032 for 24 h, and 200 μM H_2O_2 for 6 h. The apoptotic cells of active LX-2 were stained with Annexin V-FITC/PI/PI and analyzed by flow cytometry **(C)**. **(D)** The percentage of apoptotic cells. **(E)** The proliferation of active LX-2 detected by EdU (green) staining in LX-2 induced by 5 ng·mL^{-1} TGF-β1 (magnification: ×300). **(F)** The numbers of proliferating cells in each high power field. Magnification: ×300. Comparing with experimental group, *p < 0.05, **p < 0.01, ***p < 0.001.

($p < 0.05$; $p < 0.05$; $p < 0.05$) (Figures 2A,C). The mRNA expression levels of *Acta2* ($p < 0.001$; $p < 0.001$; $p < 0.001$) and *Col1A1* ($p < 0.05$; $p < 0.05$; $p < 0.05$) significantly increased in the experimental group but decreased in the 5 and 10 mg·kg^{-1} SNS-032 and 5 mg·kg^{-1} sorafenib groups (Figures 2D,E). Compared with that in the experimental group, the protein expression of CDK9 in the liver tissues in the 10 mg·kg^{-1} SNS-032 group had significantly decreased (Figures 2A,C). Interestingly, we found that active HSCs expressing Acta2 (green) underwent significant apoptosis after treatment with 10 mg·kg^{-1} SNS-032 (Figure 2F). These results illustrated that SNS-032 improves liver function and ameliorates hepatic inflammation and fibrosis in fibrotic model mice. Moreover, it induces the apoptosis of active HSCs *in vivo*. This effect may be related to the inhibition of CDK9.

SNS-032 induces the apoptosis of active HSCs and inhibits the proliferation and activation of HSCs *in vitro*

In vitro, LX-2 cells were activated through incubation with 5 ng·mL^{-1} recombinant human TGF-β1 for 24 h as previously described (He et al., 2020). Acta2, a biomarker of active HSCs, and Col1A1 in TGF-β1-induced LX-2 were detected *via* immunofluorescence staining, and 10 μM SB431542 was used as the positive drug. The results showed that the expression levels of Acta2 and Col1A1 significantly increased in the experimental group but decreased in the 0.2 and 1 μM SNS-032 groups (Figures 3A,B). Then, the active LX-2 cells were treated with different concentrations of SNS-032 and 200 μM H_2O_2 for 24 h. Apoptotic cells were stained with Annexin V–FITC/PI dye and detected through flow cytometry. Compared with the treatment received by the experimental group, treatment with 0.2 or 1 μM SNS-032 and 200 μM H_2O_2 significantly increased the percentage of active LX-2 in the early and late stages of apoptosis ($p < 0.001$; $p < 0.001$; $p < 0.001$) (Figures 3C,D). Then, proliferative cells were marked through EdU (Azide 488, green) staining. Compared with the treatment received by the experimental group, treatment with 0.04, 0.2, or 1 μM SNS-032 significantly decreased the quantities of proliferative active LX-2 ($p < 0.001$; $p < 0.001$; $p < 0.001$) (Figures 3E,F). These results indicated that SNS-032 induced the apoptosis of active HSCs and inhibited the proliferation and activation of HSCs.

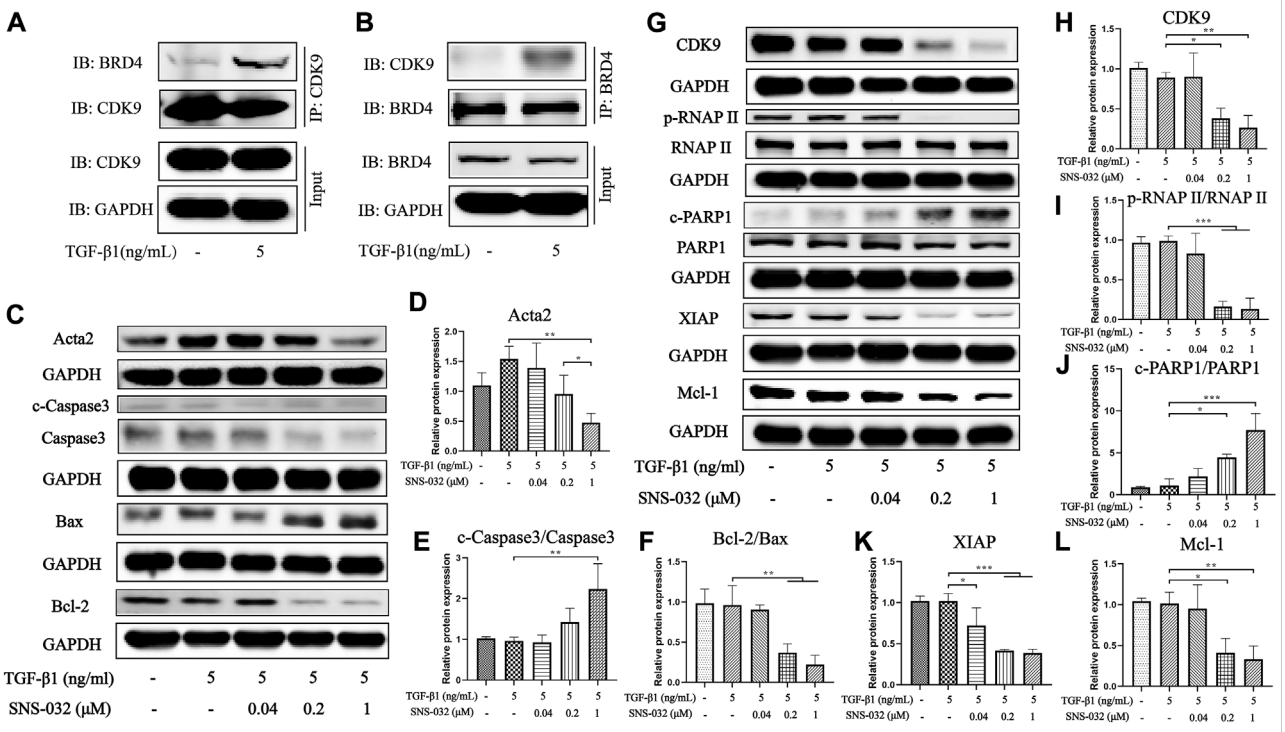

FIGURE 4
SNS-032 inhibits the expression of CDK9 and its downstream, down-regulates Acta2 and Bcl-2, and up-regulates cleaved-Caspase3 and Bax. LX-2 cells were incubated with 5 ng·mL^{-1} TGF-β1 and treated with 0.04, 0.2, 1 μM SNS-032 for 24 h **(A,B)** The immunocoprecipitation (IP) assay between BRD4 and CDK9 in LX-2 cells incubated with 5 ng·mL^{-1} TGF-β1 for 24 h. **(C)** The immunoblot of Acta2 (the activation marker of HSCs), cleaved-Caspase3, Caspase3, Bax, and Bcl-2 (the apoptosis related markers). **(D–F)** The relative protein expression of Acta2, cleaved-Caspase3/Caspase3, Bcl-2/Bax. **(G)** The immunoblot of CDK9 and its downstream (phosphorylated RNAP II, RNAP II, cleaved-PARP1, PARP1, XIAP, and Mcl-1). **(H–L)** The relative protein expression of CDK9, phosphorylated RNAP II/RNAP II, XIAP, Mcl-1, and cleaved-PARP1/PARP1.

SNS-032 decreases CDK9 and inhibits the phosphorylation of RNAP II and its downstream signal transductors

We further investigated the protein expression levels of CDK9 and its downstream factors to clarify the mechanism of SNS-032. First, we compared the expression levels of CDK9 in normal and active LX-2 cells. Interestingly, the protein expression of CDK9 in LX-2 cells was unchanged after treatment with 5 ng·mL^{-1} TGF-β1. According to the literature, CDK9 binds to cyclins (T1, T2a, T2b, and K) to form the heterodimer kinase P-TEFb (Fujinaga, 2020). Usually, P-TEFb is inactive when it is bound to HEXIM1, MePCE, Larp7, and 7SK snRNP (Fujinaga et al., 2014). When cells experience DNA damage as a result of chemical or physical injury, inactive P-TEFb releases HEXIM1, MePCE, Larp7, and 7SK snRNP and recruits BRD4 to form a catalytically active complex that promotes the phosphorylation of RNAP II (Zheng et al., 2021). Therefore, we investigated the combination of CDK9 and BRD4 in active LX-2 cells and found that the conjugation of CDK9 and BRD4 had increased significantly in active LX-2 cells relative to that in normal LX-2 cells (Figures 4A,B). As the CDK9–cyclin–BRD4 complexes increased, the activity of RNAP II significantly increased.

Then, the expression of CDK9 significantly decreased after treatment with 0.2 and 1 μM SNS-032 ($p < 0.05$; $p < 0.01$) (Figures 4G,H). Treatment with 0.2 and 1 μM SNS-032 significantly blocked the phosphorylation of the carboxyterminal domain of RNAP II at Ser2 in the initial stage ($p < 0.001$; $p < 0.001$) (Figures 4G,I). Recent studies have reported that phosphorylated RNAP II promotes the elongation of mRNA and regulates several apoptosis- and proliferation-related proteins, such as XIAP, Mcl-1, and PARP1 (Maccallum et al., 2005). In this study, treatment with 0.2 and 1 μM SNS-032 prominently increased the ratio of cleaved PARP1/PARP1 ($p < 0.05$; $p < 0.001$), and decreased the ratio of Bcl-2/Bax ($p < 0.01$; $p < 0.01$) and the expression levels of XIAP ($p < 0.001$; $p < 0.001$) and Mcl-1 ($p < 0.05$; $p < 0.01$) (Figures 4C,F,G,J–L). Treatment with 1 μM SNS-032 significantly elevated the ratio of cleaved-Caspase3/Caspase3 ($p < 0.01$), and reduced the expression of Acta2

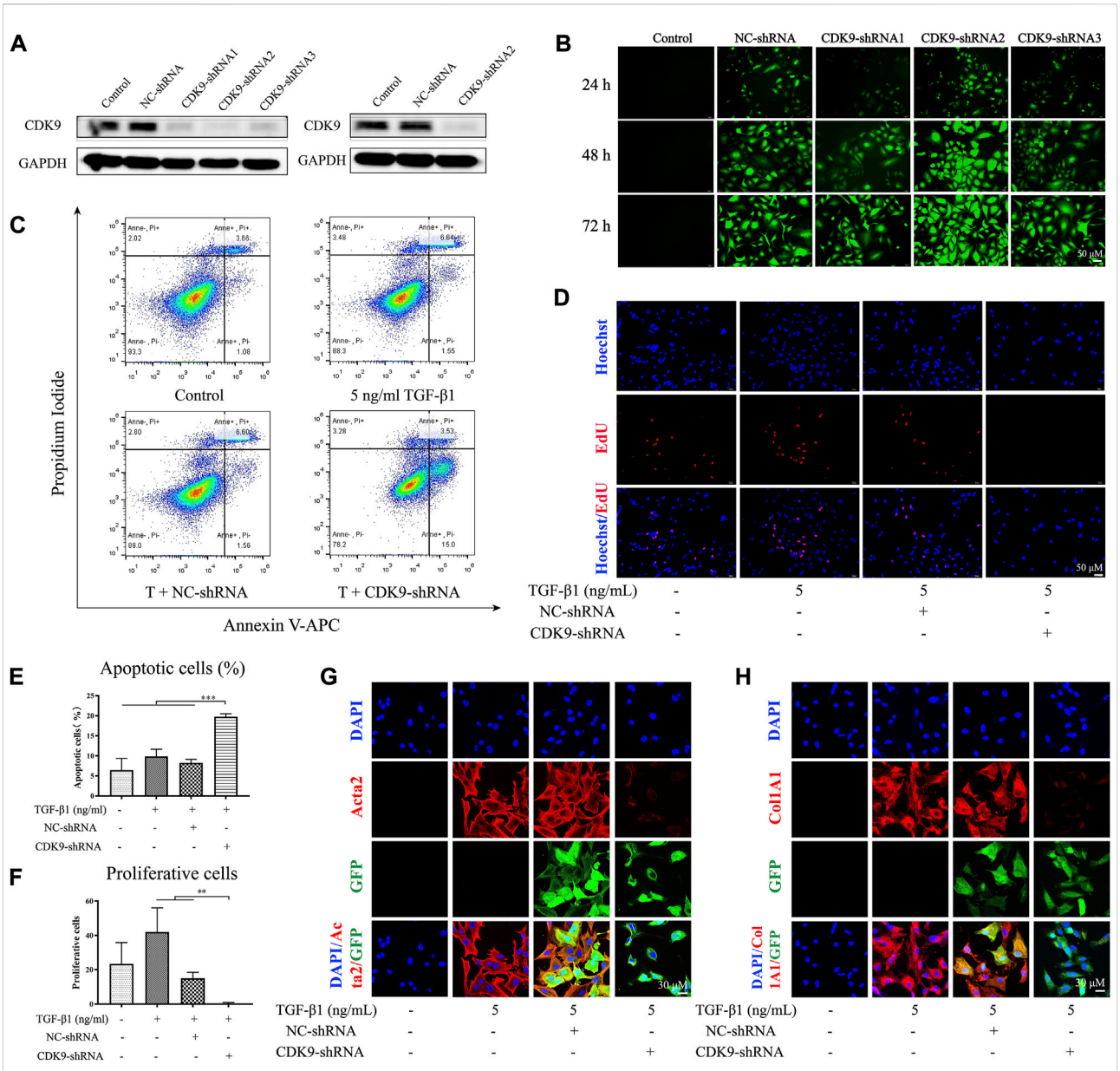

FIGURE 5
Knocking down CDK9 induces the apoptosis of active LX-2 and inhibits its activation and proliferation. LX-2 were transfected with CDK9-shRNA vectors which also encoded GFP and puromycin resistance genes. The most efficient CDK-shRNA vector was used to transfect LX-2 cells and the protein expression of CDK9 was detected by immunoblot **(A)**. **(B)** The immunofluorescence of GFP (green) after the transfection of CDK9-shRNA for 24, 48, and 72 h. Then, CDK9-shRNA transfected LX-2 cells were incubated with 5 ng·mL^{-1} TGF-β1 for 24 h and the apoptosis of cells were stained with Annexin V-FITC/PI and detected by flow cytometry **(C)**. **(D)** CDK9-shRNA transfected LX-2 cells were stained with EdU (red) and observed by fluorescence inverted microscope (magnification: ×300). **(E)** The percentage of apoptotic cells. **(F)** The numbers of proliferating cells in each high power field. After incubated with 5 ng·mL^{-1} TGF-β1, CDK9-shRNA transfected LX-2 cells were stained with Acta2 **(G)** and Col1A1 **(H)** (magnification: ×600). Acta2 (red), Col1A1 (red), GFP (green), and DAPI (blue). Comparing with experimental group, $^{*}p < 0.05$, $^{**}p < 0.01$, $^{***}p < 0.001$.

($p < 0.01$) (Figures 4C–E). These results illustrated that SNS-032 induced the apoptosis of active HSCs and inhibited the proliferation and activation of HSCs by downregulating CDK9, p-RNAP II, XIAP, Mcl-1, Bcl-2, and Acta2 and upregulating Bax, cleaved PARP1, and cleaved Caspase3.

CDK9 knockdown induces apoptosis and inhibits the proliferation and activation of active LX-2

Although SNS-032 is a CDK9 inhibitor and shows good effects in liver fibrosis treatment, the mechanisms of CDK9 in the

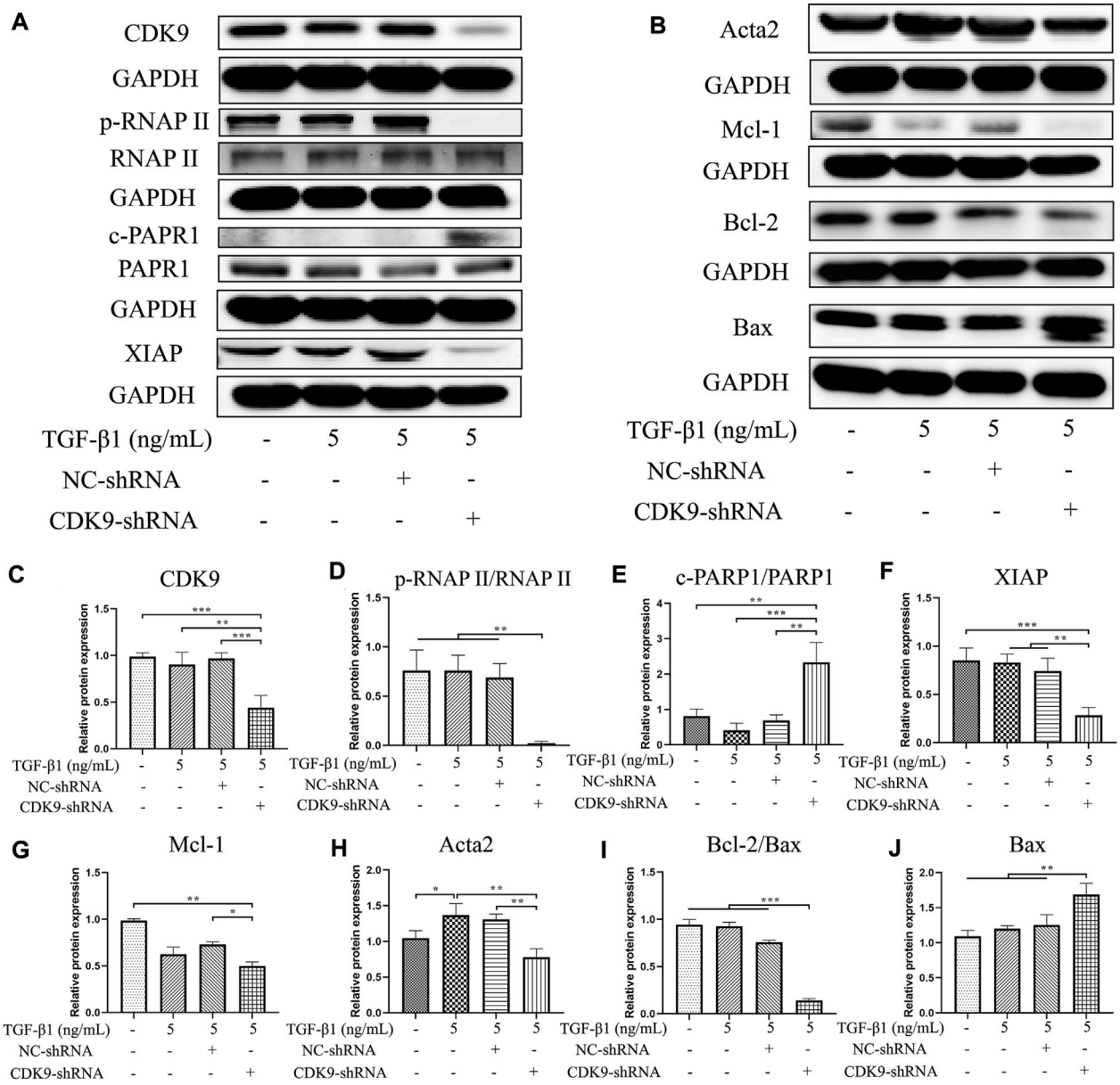

FIGURE 6
Knocking down CDK9 inhibits the expression of CDK9 and its downstream, down-regulates Acta2 and Bcl-2, and up-regulates Bax. CDK9-shRNA transfected LX-2 cells were incubated with 5 ng·mL^{-1} TGF-β1 for 24 h and the protein expressions of CDK9 and its downstream were detected by immunoblot. **(A,B)** The immunoblot of CDK9, its downstream (phosphorylated RNAP II, RNAP II, cleaved-PARP1, PARP1, XIAP, and Mcl-1), Acta2 (the activation marker of HSCs), Bcl-2, and Bax (the apoptosis related markers). **(C–J)** The relative protein expressions of CDK9, phosphorylated RNAP II/RNAP II, cleaved-PARP1/PARP1, XIAP, Mcl-1, Acta2, Bcl-2/Bax, and Bax. Comparing with experimental group, *$p < 0.05$, **$p < 0.01$, ***$p < 0.001$.

development of liver fibrosis remain unclear. Therefore, we utilized a CDK9-shRNA-loaded lentivirus (GV248) to knockdown CDK9 in LX-2. Three CDK9 shRNAs encoded with base sequences were transfected into LX-2 cells (the three sequences of the CDK9 shRNAs are listed in Supplementary Table S1). Then, the expression of CDK9 and the fluorescence intensity of GFP were detected. Given that CDK9 shRNA2 showed the best transfection and knockdown effects among the three shRNAs (Figures 5A,B), it was used for transfection in further experiments. After transfection with CDK9 shRNA, LX-2 was treated with 4 ng·mL^{-1} puromycin to select stably transfected LX-2 cells (Figures 5A,B). The stably transfected LX-2 cells were cultured with 5 ng·mL^{-1} TGF-β1 in six-well dishes for 24 h, stained with Annexin V–APC/PI, and

subjected to flow cytometry. Compared with the negative control (NC shRNA) group, the CDK9 shRNA group showed a higher percentage of apoptosis ($p < 0.001$) (Figures 5C,E). Then, the CDK9 shRNA LX-2 cells were cultured with 5 ng·mL^{-1} TGF-β1 in 48-well dishes for 24 h, stained with EdU (Azide 594, red), and observed by using a laser confocal microscope. Compared with those in the NC shRNA group, the proliferative cells in the CDK9 shRNA group had decreased significantly ($p < 0.01$) (Figures 5D,F). Subsequently, CDK9 shRNA LX-2 cells were cultured with 5 ng·mL^{-1} TGF-β1 in 6 cm dishes for 24 h, incubated with Acta2 and Col1A1 primary antibodies, stained with Cy3 and DAPI, and observed by using a laser confocal microscope. Compared with those in the NC shRNA group, the expression levels of Acta2 and Col1A1 had decreased significantly in the CDK9 shRNA group (Figures 5G,H). Therefore, the knockdown of CDK9 induces the apoptosis of active LX-2 and inhibits the proliferation and activation of active LX-2.

Knocking down CDK9 decreases CDK9 and inhibits the phosphorylation of RNAP II and its downstream factors

Compared with that in the NC shRNA group, the expression of CDK9 significantly decreased in the group with CDK9 gene knockdown ($p < 0.001$) (Figures 6A,C). Knockdown of CDK9 significantly blocked the phosphorylation of the carboxyterminal domain of RNAP II at Ser2 in the initial stage ($p < 0.01$) (Figures 6A,D). Knockdown of CDK9 significantly decreased the ratio of cleaved PARP1/PARP1 increased ($p < 0.01$) and the expression levels of XIAP ($p < 0.01$) and Mcl-1 ($p < 0.05$) (Figures 6A,B,E–G). Knockdown of CDK9 prominently increased the expression of Bax ($p < 0.01$), and reduced the expression of Acta2 ($p < 0.01$) and the ratio of Bcl-2/Bax ($p < 0.001$) (Figures 6B,E–G). Similar to the effects of SNS-032, knockdown of CDK9 induced the apoptosis of active HSCs and inhibited the proliferation and activation of HSCs by downregulating CDK9, p-RNAP II, XIAP, Mcl-1, Bcl-2, and Acta2 and upregulating Bax and cleaved PARP1.

Discussion

CDK9 is a potential target that has widely attracted attention in cancer studies. Similar to traditional CDKs, CDK9 plays an important role in the transcription of mRNA and is closely related to the survival and proliferation of cells (Santo et al., 2015). A growing body of evidence suggests that the expression of CDK9 is elevated in malignant cells, such as chronic lymphocytic leukemia, multiple myeloma, breast cancer, and lung cancer cells (Franco et al., 2018). Liver fibrosis is a pathological process that occurs along with the combination of damage and repair. Excessive ECM accumulation results in fiber and collagen deposition in hepatic sinuses; this effect blocks the regeneration of liver tissue (Parola and Pinzani, 2019). ECM is secreted by active HSCs, which are activated and proliferate vigorously when liver injury occurs (Reichert et al., 2021). Therefore, antiactive HSCs are the key points in the treatment of liver fibrosis. Given that mRNA synthesis can be promoted when cell division or DNA repair occurs, actively proliferating cells exhibit active mRNA synthesis with the phosphorylation of RNAP II (Jia et al., 2021).

Recent studies have reported that CDK inhibitors have antiliver fibrosis effects. Roscovitine (a Cdc2, CDK2, and CDK5 inhibitor) protects against liver diseases by inhibiting macrophage inflammatory actions and HSC activation at the onset of liver injury (Liu et al., 2021). CR8, a pan-CDK inhibitor and a derivative of roscovitine, reduces the proliferation and viability of LX-2 cells and attenuates the profibrotic properties of primary murine HSCs while preserving the proliferation and viability of primary murine hepatocytes *in vitro* (Hübbers et al., 2020). In this study, we found that SNS-032 prominently alleviated hepatic fibrosis in CCl_4-induced model mice. In the experimental group, the expression of CDK9 significantly increased after CCl_4 induction. Then, after SNS-032 treatment, the expression levels of CDK9 and Acta2 decreased significantly and the apoptosis of active HSCs increased. Notably, CDK9 expression in active and quiescent HSCs *in vitro* did not significantly vary. Similar results were also observed in TGF-β1-induced primary mouse fibroblasts (Qu et al., 2015). Therefore, we further detected the expression of active P-TEFb, which contains CDK9 and BRD4, and found that although the expression of CDK9 was unchanged, the conjugation of CDK9 and BRD4 had increased. Generally speaking, under physical or chemical irritation, inactive P-TEFb (CDK9–cyclin–HEXIM1–MePCE–Larp7–7SK snRNP complex) releases HEXIM1, MePCE, Larp7, and 7SK snRNP and recruits BRD4 for combination into active P-TEFb, which catalyzes the phosphorylation of RNAP II (Zheng et al., 2021). The main function of phosphorylated RNAP II in eukaryotic cells is the transcription elongation of nascent mRNA strands; this process is quite active during cell proliferation (Baluapuri et al., 2019). SNS-032 decreases active HSCs to alleviate hepatic fibrosis by inducing the apoptosis of active HSCs and inhibiting their activation and proliferation by inhibiting the expression of CDK9 and blocking the phosphorylation of RNAP II and its downstream factors (Figure 7).

In this study, we found that SNS-032 significantly downregulated the expression levels of Bcl-2, XIAP, and Mcl-1 (Figure 4). However, some previous studies on other cell types found that SNS-032 has no major effects on the protein levels of XIAP and Bcl-2 (Zhang et al., 2019; Zeng et al., 2021). In our opinion, given that different cell lines undergo different transformations, the regulatory effects of SNS-032 may vary across different cell lines. To illustrate, Chen et al. found that

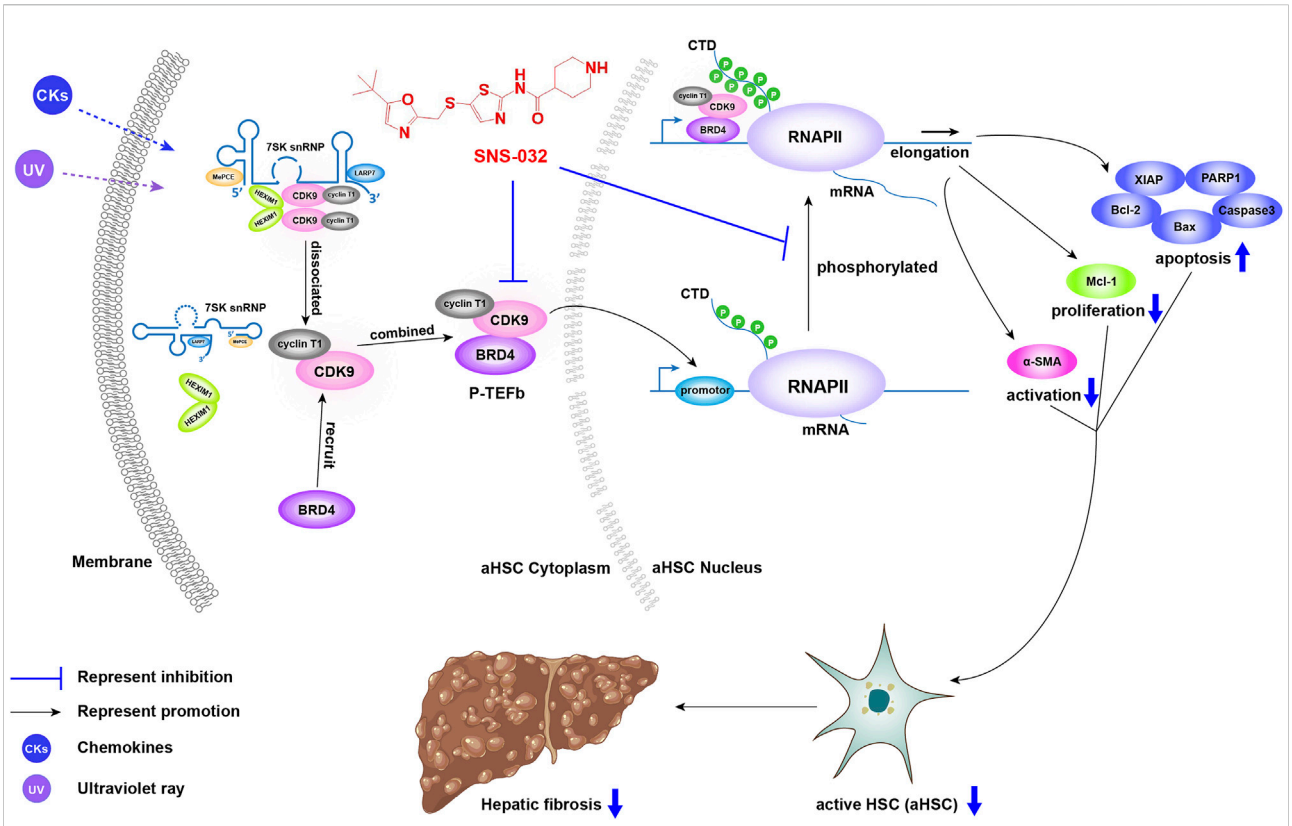

FIGURE 7
The illustration of the mechanism of CDK9 to promote liver fibrosis and the inhibitory effect of SNS-032. Under physical or chemical irritation, inactive P-TEFb (CDK9–cyclin–HEXIM1–MePCE–Larp7–7SK snRNP complex) releases HEXIM1, MePCE, Larp7, and 7SK snRNP and recruits BRD4 to form active P-TEFb, which catalyzes the phosphorylation of RNAP II. Then, phosphorylated RNAP II upregulates the transcription of anti-apoptosis, proliferation and activation related genes, and downregulates the transcription of apoptosis related genes. SNS-032 inhibits the expression of CDK9, block the phosphorylation of RNAP II and its downstream. It decreases the active HSCs to alleviate the hepatic fibrosis *via* inducing the apoptosis of active HSCs and inhibiting its activation and proliferation.

the expression levels of Mcl-1 and XIAP decreased in chronic lymphocytic leukemia cells after 24 h of treatment with SNS-032. Bcl-2 exhibited significantly decreased mRNA expression but not protein expression (Chen et al., 2009). Meanwhile, some studies suggested that even in the same cell type but in different cell lines, the regulatory effects of SNS-032 differ. For example, under SNS-032 treatment, the protein expression of cleaved PARP1 increased significantly in JeKo.1 but not in Granta 519; these cell lines are both human mantle cell lymphoma cell lines (Chen et al., 2010b). Another recent study also supported the supposition that SNS-032 significantly decreased the protein expression of Bcl-2 in SU-DHL-4, a human diffuse large B-cell lymphoma cell line, but had no effect on SU-DHL-2 (Jiang et al., 2022).

In liver tissue, CDK9 has two isoforms with the molecular weights of 55 and 42 kDa (Liu and Herrmann, 2005). Although these isoforms have the same 42 kDa amino acid sequence, $CDK9_{55}$ has an additional 13 kDa amino acid chain (117 residue terminal extension), and its three-dimensional structure differs from that of $CDK9_{42}$. Moreover, they are encoded by the same genes but are regulated by different promoter regions (Shore et al., 2005; Liu et al., 2010). The predominant isoform of CDK9 differs during different stages of the cell cycle. Specifically, $CDK9_{42}$ predominates after the cell cycle, whereas $CDK9_{55}$ predominates before the cell cycle. $CDK9_{42}$ and $CDK9_{55}$ have different locations: $CDK9_{42}$ is located in the nucleoplasm, whereas $CDK9_{55}$ is located in the nucleus (Shore et al., 2003). The specific physiological functions of $CDK9_{55}$ and $CDK9_{42}$ remain unclear. We noticed that the expression of CDK9 varied considerably in the same group, whereas the expression of $CDK9_{55}$ was consistent with that of $CDK9_{42}$ in the same sample (Supplementary Material, uncropped WB figures). In addition, $CDK9_{42}$ is predominant in HSCs, whereas $CDK9_{55}$ is predominant in hepatocytes (Shore et al., 2003). $CDK9_{42}$ inhibitors, if selectively targeting $CDK9_{42}$, may selectively affect HSCs in addition to hepatocytes. This characteristic may help the development of highly selective inhibitors for liver fibrosis treatment.

CDK9 is not only closely related to proliferation and survival, it also regulates activation, growth, and inflammation directly.

CDK9 could phosphorylate the Smad linker to drive Smad transcriptional activation and turnover through the BMP and TGF-β pathways (Alarcón et al., 2009). In a mouse model of unilateral ureteral obstruction, CDK9 could also conjugate with Smad3 and Smad4 to form a complex to promote renal fibrosis (Qu et al., 2015). Recent studies have reported that the transient induction of CDK9 in the early stage of differentiation is critical for myogenesis (Tarhriz et al., 2019). CDK9 could also phosphorylate glucocorticoid receptor-interacting protein-1 to regulate the anti-inflammatory effects of glucocorticoids (Rollins et al., 2017). Given that CDK9 could bind with numerous other proteins to form active complexes, future studies may need to focus on the active complexes formed by CDK9 and the upstream and downstream factors of CDK9 to elucidate the mechanism of CDK9 further.

Conclusion

The CDK9 inhibitor SNS-032 has definite effects in liver fibrosis treatment *in vivo* and *in vitro*. SNS-032 can induce the apoptosis of active HSCs and inhibit the proliferation and activation of active HSCs to alleviate fibrosis by downregulating the expression of CDK9 and its downstream factors. The knockdown of CDK9 exerts the same antifibrosis effects by regulating the CDK9/RNAP II signaling pathway. These pieces of evidence strongly suggest that CDK9 is a potential powerful target against liver fibrosis.

Data availability statement

The original contributions presented in the study are included in the article/Supplementary Material, further inquiries can be directed to the corresponding authors.

Ethics statement

The animal study was reviewed and approved by the experimental animal ethics committee of the Shanghai University of Traditional Chinese Medicine.

Author contributions

PL, WL, and XH contributed to the design of this study. XH, YH, JC, YM, HZ, DZ, HZ, LZ, GC, WL, and PL conducted the experiments and statistics analysis. XH, YH, WL, and PL drafted the main manuscript text. All the authors participated in the interpretation of results. All the authors have read and approved the final manuscript.

Funding

This work was supported by National Natural Foundation of China (Grant Nos. 82130120, 81530101, 82205009), Shanghai Science and Technology Innovation Action Plans supported by Shanghai Science and Technology Committee (No. 20S21902600), Young Elite Scientists Sponsorship Program by CAST (No. 2020QNRC001), "Chen Guang" project supported by Shanghai Municipal Education Commission and Shanghai Education Development Foundation (No. 20CG50), Special Project for Clinical Research of Shanghai Municipal Health Commission (No. 20214Y0178), Budget Project of Shanghai University of Traditional Chinese Medicine (No. 2021LK092), Science Foundation of Yueyang Hospital of Integrated Traditional Chinese and Western Medicine (No. 2021yygq01), China Postdoctoral Science Foundation (No. 2021M702218), Shanghai Post-doctoral Excellence Program (No. 2020372).

Acknowledgments

We would like to deeply thank Weiliang Zhu (Shanghai Institute of Materia Medica, Chinese Academy of Sciences) to contribute the anti-liver fibrosis targets *via* high throughout screening of molecular docking. We also deeply thank the BioRender App to facilitate the completion of graphic abstract.

Conflict of interest

The authors declare that the research was conducted in the absence of any commercial or financial relationships that could be construed as a potential conflict of interest.

Publisher's note

Supplementary material

The Supplementary Material for this article can be found online at: https://www.frontiersin.org/articles/10.3389/fphar.2022.1016552/full#supplementary-material

SUPPLEMENTARY FIGURE S1
Graphical abstract.

References

Alarcón, C., Zaromytidou, A. I., Xi, Q., Gao, S., Yu, J., Fujisawa, S., et al. (2009). Nuclear CDKs drive Smad transcriptional activation and turnover in BMP and TGF-beta pathways. *Cell* 139, 757–769. doi:10.1016/j.cell.2009.09.035

Ali, M. A., Choy, H., Habib, A. A., and Saha, D. (2007). SNS-032 prevents tumor cell-induced angiogenesis by inhibiting vascular endothelial growth factor. *Neoplasia* 9, 370–381. doi:10.1593/neo.07136

Baluapuri, A., Hofstetter, J., Dudvarski Stankovic, N., Endres, T., Bhandare, P., Vos, S. M., et al. (2019). MYC recruits SPT5 to RNA polymerase II to promote processive transcription elongation. *Mol. Cell* 16, 674–687. e11. doi:10.1016/j.molcel.2019.02.031

Bose, P., Simmons, G. L., and Grant, S. (2013). Cyclin-dependent kinase inhibitor therapy for hematologic malignancies. *Expert Opin. Investig. Drugs* 22, 723–738. doi:10.1517/13543784.2013.789859

Chen, P., Han, Z. Y., Yang, P., Zhu, L., Hua, Z. C., and Zhang, J. F. (2010). Loss of clock gene mPer2 promotes liver fibrosis induced by carbon tetrachloride. *Hepatol. Res.* 40, 1117–1127. doi:10.1111/j.1872-034X.2010.00695.x

Chen, R., Chubb, S., Cheng, T., Hawtin, R. E., Gandhi, V., and Plunkett, W. (2010). Responses in mantle cell lymphoma cells to SNS-032 depend on the biological context of each cell line. *Cancer Res.* 70, 6587–6597. doi:10.1158/0008-5472.CAN-09-3578

Chen, R., Wierda, W. G., Chubb, S., Hawtin, R. E., Fox, J. A., Keating, M. J., et al. (2009). Mechanism of action of SNS-032, a novel cyclin-dependent kinase inhibitor, in chronic lymphocytic leukemia. *Blood* 113, 4637–4645. doi:10.1182/blood-2008-12-190256

Conroy, A., Stockett, D. E., Walker, D., Arkin, M. R., Hoch, U., Fox, J. A., et al. (2009). SNS-032 is a potent and selective CDK 2, 7 and 9 inhibitor that drives target modulation in patient samples. *Cancer Chemother. Pharmacol.* 64, 723–732. doi:10.1007/s00280-008-0921-5

Franco, L. C., Morales, F., Boffo, S., and Giordano, A. (2018). CDK9: A key player in cancer and other diseases. *J. Cell. Biochem.* 119, 1273–1284. doi:10.1002/jcb.26293

Fujinaga, K., Luo, Z., and Peterlin, B. M. (2014). Genetic analysis of the structure and function of 7SK small nuclear ribonucleoprotein (snRNP) in cells. *J. Biol. Chem.* 289, 21181–21190. doi:10.1074/jbc.M114.557751

Fujinaga, K. (2020). P-TEFb as A Promising therapeutic target. *Molecules* 25, 838. doi:10.3390/molecules25040838

Gérard, C., and Goldbeter, A. (2016). Dynamics of the mammalian cell cycle in physiological and pathological conditions. *Wiley Interdiscip. Rev. Syst. Biol. Med.* 8, 140–156. doi:10.1002/wsbm.1325

Gupta, S., Hau, A. M., Al-Ahmadie, H. A., Harwalkar, J., Shoskes, A. C., Elson, P., et al. (2016). Transforming growth factor-β is an upstream regulator of mammalian target of rapamycin complex 2-dependent bladder cancer cell migration and invasion. *Am. J. Pathol.* 186, 1351–1360. doi:10.1016/j.ajpath.2016.01.008

He, X., Chen, J., Mu, Y., Zhang, H., Chen, G., Liu, P., et al. (2020). The effects of inhibiting the activation of hepatic stellate cells by lignan components from the fruits of Schisandra chinensis and the mechanism of schisanhenol. *J. Nat. Med.* 74, 513–524. doi:10.1007/s11418-020-01394-w

Hübbers, A., Hennings, J., Lambertz, D., Haas, U., Trautwein, C., Nevzorova, Y. A., et al. (2020). Pharmacological inhibition of cyclin- dependent kinases triggers anti-fibrotic effects in hepatic stellate cells *in vitro*. *Int. J. Mol. Sci.* 21, 3267. doi:10.3390/ijms21093267

Jia, N., Guo, C., Nakazawa, Y., van den Heuvel, D., Luijsterburg, M. S., and Ogi, T. (2021). Dealing with transcription-blocking DNA damage: Repair mechanisms, RNA polymerase II processing and human disorders. *DNA Repair (Amst)* 106, 103192. doi:10.1016/j.dnarep.2021.103192

Jiang, L., Wen, C., Zhou, H., Liu, A., Zhang, H., Chen, X., et al. (2022). Cyclin-dependent kinase 7/9 inhibitor SNS-032 induces apoptosis in diffuse large B-cell lymphoma cells. *Cancer Biol. Ther.* 23, 319–327. doi:10.1080/15384047.2022.2055421

Jin, Z., Sun, R., Wei, H., Gao, X., Chen, Y., and Tian, Z. (2011). Accelerated liver fibrosis in Hepatitis B virus transgenic mice: Involvement of natural killer T cells. *Hepatology* 53, 219–229. doi:10.1002/hep.23983

Kisseleva, T., and Brenner, D. A. (2012). The phenotypic fate and functional role for bone marrow-derived stem cells in liver fibrosis. *J. Hepatol.* 56, 965–972. doi:10.1016/j.jhep.2011.09.021

Lakner, A. M., Walling, T. L., Mckillop, I. H., and Schrum, L. W. (2011). Altered aquaporin expression and role in apoptosis during hepatic stellate cell activation. *Liver Int.* 31, 42–51. doi:10.1111/j.1478-3231.2010.02356.x

Liang, K., Woodfin, A. R., Slaughter, B. D., Unruh, J. R., Box, A. C., Rickels, R. A., et al. (2015). Mitotic transcriptional activation: Clearance of actively engaged pol II via transcriptional elongation control in mitosis. *Mol. Cell* 60, 435–445. doi:10.1016/j.molcel.2015.09.021

Lin, T., Gao, D. Y., Liu, Y. C., Sung, Y. C., Wan, D., Liu, J. Y., et al. (2016). Development and characterization of sorafenib-loaded PLGA nanoparticles for the systemic treatment of liver fibrosis. *J. Control. Release* 221, 62–70. doi:10.1016/j.jconrel.2015.11.003

Liu, D., Zhang, P., Zhou, J., Liao, R., Che, Y., Gao, M. M., et al. (2020). TNFAIP3 interacting protein 3 overexpression suppresses nonalcoholic steatohepatitis by blocking TAK1 activation. *Cell Metab.* 31, 726–740. e8. doi:10.1016/j.cmet.2020.03.007

Liu, H., Herrmann, C. H., Chiang, K., Sung, T. L., Moon, S. H., Donehower, L. A., et al. (2010). 55K isoform of CDK9 associates with Ku70 and is involved in DNA repair. *Biochem. Biophys. Res. Commun.* 397, 245–250. doi:10.1016/j.bbrc.2010.05.092

Liu, H., and Herrmann, C. H. (2005). Differential localization and expression of the Cdk9 42k and 55k isoforms. *J. Cell. Physiol.* 203, 251–260. doi:10.1002/jcp.20224

Liu, Y., Li, J., Liao, L., Huang, H., Fan, S., Fu, R., et al. (2021). Cyclin-dependent kinase inhibitor roscovitine attenuates liver inflammation and fibrosis by influencing initiating steps of liver injury. *Clin. Sci.* 135, 925–941. doi:10.1042/CS20201111

Maccallum, D. E., Melville, J., Frame, S., Watt, K., Anderson, S., Gianella-Borradori, A., et al. (2005). Seliciclib (CYC202, R-Roscovitine) induces cell death in multiple myeloma cells by inhibition of RNA polymerase II-dependent transcription and down-regulation of Mcl-1. *Cancer Res.* 65, 5399–5407. doi:10.1158/0008-5472.CAN-05-0233

Matrone, G., Wilson, K. S., Maqsood, S., Mullins, J. J., Tucker, C. S., and Denvir, M. A. (2015). CDK9 and its repressor LARP7 modulate cardiomyocyte proliferation and response to injury in the zebrafish heart. *J. Cell Sci.* 128, 4560–4571. doi:10.1242/jcs.175018

Misra, R. N., Xiao, H. Y., Kim, K. S., Lu, S., Han, W. C., Barbosa, S. A., et al. (2004). N-(cycloalkylamino)acyl-2-aminothiazole inhibitors of cyclin-dependent kinase 2. N-[5-[[[5-(1, 1-dimethylethyl)-2-oxazolyl]methyl]thio]- 2-thiazolyl]-4-piperidinecarboxamide (BMS-387032), a highly efficacious and selective antitumor agent. *J. Med. Chem.* 47, 1719–1728. doi:10.1021/jm0305568

Oakley, F., Trim, N., Constandinou, C. M., Ye, W., Gray, A. M., Frantz, G., et al. (2003). Hepatocytes express nerve growth factor during liver injury: Evidence for paracrine regulation of hepatic stellate cell apoptosis. *Am. J. Pathol.* 163, 1849–1858. doi:10.1016/S0002-9440(10)63544-4

Parola, M., and Pinzani, M. (2019). Liver fibrosis: Pathophysiology, pathogenetic targets and clinical issues. *Mol. Asp. Med.* 65, 37–55. doi:10.1016/j.mam.2018.09.002

Premkumar, K., and Shankar, B. S. (2021). TGF-βR inhibitor SB431542 restores immune suppression induced by regulatory B-T cell axis and decreases tumour burden in murine fibrosarcoma. *Cancer Immunol. Immunother.* 70, 153–168. doi:10.1007/s00262-020-02666-w

Qu, X., Jiang, M., Sun, Y. B., Jiang, X., Fu, P., Ren, Y., et al. (2015). The Smad3/Smad4/CDK9 complex promotes renal fibrosis in mice with unilateral ureteral obstruction. *Kidney Int.* 88, 1323–1335. doi:10.1038/ki.2015.235

Reichert, D., Adolph, L., Köhler, J. P., Buschmann, T., Luedde, T., Häussinger, D., et al. (2021). Improved recovery from liver fibrosis by crenolanib. *Cells* 10, 804. doi:10.3390/cells10040804

Rollins, D. A., Kharlyngdoh, J. B., Coppo, M., Tharmalingam, B., Mimouna, S., Guo, Z., et al. (2017). Glucocorticoid-induced phosphorylation by CDK9 modulates the coactivator functions of transcriptional cofactor GRIP1 in macrophages. *Nat. Commun.* 8, 1739. doi:10.1038/s41467-017-01569-2

Santo, L., Siu, K. T., and Raje, N. (2015). Targeting cyclin-dependent kinases and cell cycle progression in human cancers. *Semin. Oncol.* 42, 788–800. doi:10.1053/j.seminoncol.2015.09.024

Shang, M., Sun, H., Wu, Y., Gong, Y., Tang, Z., Meng, F., et al. (2020). *In vivo* and *in vitro* studies using Clonorchis sinensis adult-derived total protein (CsTP) on cellular function and inflammatory effect in mouse and cell model. *Parasitol. Res.* 119, 1641–1652. doi:10.1007/s00436-020-06651-1

Shore, S. M., Byers, S. A., Dent, P., and Price, D. H. (2005). Characterization of Cdk9(55) and differential regulation of two Cdk9 isoforms. *Gene* 350, 51–58. doi:10.1016/j.gene.2005.01.015

Shore, S. M., Byers, S. A., Maury, W., and Price, D. H. (2003). Identification of a novel isoform of Cdk9. *Gene* 307, 175–182. doi:10.1016/s0378-1119(03)00466-9

Strnad, P., Tao, G. Z., Zhou, Q., Harada, M., Toivola, D. M., Brunt, E. M., et al. (2008). Keratin mutation predisposes to mouse liver fibrosis and unmasks differential effects of the carbon tetrachloride and thioacetamide models. *Gastroenterology* 134, 1169–1179. doi:10.1053/j.gastro.2008.01.035

Strowitzki, M. J., Ritter, A. S., Kimmer, G., and Schneider, M. (2019). Hypoxia-adaptive pathways: A pharmacological target in fibrotic disease? *Pharmacol. Res.* 147, 104364. doi:10.1016/j.phrs.2019.104364

Tanwar, S., Rhodes, F., Srivastava, A., Trembling, P. M., and Rosenberg, W. M. (2020). Inflammation and fibrosis in chronic liver diseases including non-alcoholic fatty liver disease and hepatitis C. *World J. Gastroenterol.* 26, 109–133. doi:10.3748/wjg.v26.i2.109

Tarhriz, V., Eyvazi, S., Musavi, M., Abasi, M., Sharifi, K., Ghanbarian, H., et al. (2019). Transient induction of Cdk9 in the early stage of differentiation is critical for myogenesis. *J. Cell. Biochem.* 120, 18854–18861. doi:10.1002/jcb.29204

Tong, W. G., Chen, R., Plunkett, W., Siegel, D., Sinha, R., Harvey, R. D., et al. (2010). Phase I and pharmacologic study of SNS-032, a potent and selective Cdk2, 7, and 9 inhibitor, in patients with advanced chronic lymphocytic leukemia and multiple myeloma. *J. Clin. Oncol.* 28, 3015–3022. doi:10.1200/JCO.2009.26.1347

Walsby, E., Lazenby, M., Pepper, C., and Burnett, A. K. (2011). The cyclin-dependent kinase inhibitor SNS-032 has single agent activity in AML cells and is highly synergistic with cytarabine. *Leukemia* 25, 411–419. doi:10.1038/leu.2010.290

Zeng, H., Yang, H., Song, Y., Fang, D., Chen, L., Zhao, Z., et al. (2021). Transcriptional inhibition by CDK7/9 inhibitor SNS-032 suppresses tumor growth and metastasis in esophageal squamous cell carcinoma. *Cell Death Dis.* 5, 1048. doi:10.1038/s41419-021-04344-w

Zhang, J., Liu, S., Ye, Q., and Pan, J. (2019). Transcriptional inhibition by CDK7/9 inhibitor SNS-032 abrogates oncogene addiction and reduces liver metastasis in uveal melanoma. *Mol. Cancer* 18 (1), 140. doi:10.1186/s12943-019-1070-7

Zhang, L., Tian, R., Yao, X., Zhang, X. J., Zhang, P., Huang, Y., et al. (2021). Milk fat globule-epidermal growth factor-factor 8 improves hepatic steatosis and inflammation. *Hepatology* 73, 586–605. doi:10.1002/hep.31277

Zheng, B., Aoi, Y., Shah, A. P., Iwanaszko, M., Das, S., Rendleman, E. J., et al. (2021). Acute perturbation strategies in interrogating RNA polymerase II elongation factor function in gene expression. *Genes Dev.* 35, 273–285. doi:10.1101/gad.346106.120

Zhou, K., Zhuang, S., Liu, F., Chen, Y., Li, Y., Wang, S., et al. (2022). Disrupting the Cdk9/Cyclin T1 heterodimer of 7SK snRNP for the Brd4 and AFF1/4 guided reconstitution of active P-TEFb. *Nucleic Acids Res.* 50, 750–762. doi:10.1093/nar/gkab1228

Glossary

Acta2 actin alpha 2
ALT alanine aminotransferase
APC allophycocyanin
AST aspartate transaminase
Bax Bcl-2 associated X
Bcl-2 B-cell lymphoma-2
BRD4 bromodomain-containing protein 4
CCl4 Carbon tetrachloride
CDK9 cyclin-dependent kinase 9
Col1A1 collagen type Iα1
DAPI diaminyl phenyl indole
DMEM Dulbecco modified Eagle's medium
ECM extracellular matrix
FBS fetal bovine serum
FITC fluorescein isothiocyanate
GFP green fluorescent protein
HE hematoxylin–eosin
HEXIM1 hexamethylene bis-acetamide-inducible protein 1
HSCs hepatic stellate cells
Mcl-1 myeloid cell leukemia-1
MePCE methylphosphate capping enzyme
NC negative control
PARP1 poly ADP-ribose polymerase 1
PI propidium iodide
RNAP II RNA polymerase II
P-TEFb positive transcription elongation factor b
shRNA short hairpin RNA
SEC super elongation complex
TGF-β transforming growth factor-β
XIAP X-linked inhibitor of apoptosis protein
7SK snRNP 7SK small nuclear ribonucleoprotein.

frontiers | Frontiers in Pharmacology

TYPE Original Research
PUBLISHED 28 October 2022
DOI 10.3389/fphar.2022.1053356

OPEN ACCESS

EDITED BY
Jian Gao,
Shanghai Children's Medical Center, China

REVIEWED BY
Hui Hui Zhao,
School of Traditional Chinese Medicine, Beijing University of Chinese Medicine, China
Yong Xu,
Nanjing University of Chinese Medicine, China

*CORRESPONDENCE
Jiansheng Li,
li_js8@163.com

SPECIALTY SECTION
This article was submitted to Respiratory Pharmacology, a section of the journal Frontiers in Pharmacology

RECEIVED 25 September 2022
ACCEPTED 17 October 2022
PUBLISHED 28 October 2022

CITATION
Li J, Yu X-q, Xie Y, Yang S-g, Zhao L, Zhou M and Meng Y (2022), Efficacy and safety of traditional Chinese medicine treatment for idiopathic pulmonary fibrosis: An exploratory, randomized, double-blinded and placebo controlled trial.
Front. Pharmacol. 13:1053356.
doi: 10.3389/fphar.2022.1053356

Efficacy and safety of traditional Chinese medicine treatment for idiopathic pulmonary fibrosis: An exploratory, randomized, double-blinded and placebo controlled trial

Jiansheng Li[1,2,3]*, Xue-qing Yu[1,2,3], Yang Xie[1,2,3], Shu-guang Yang[1,2,3], Limin Zhao[4], Miao Zhou[5] and Yong Meng[6]

[1]Collaborative Innovation Center for Chinese Medicine and Respiratory Diseases Co-constructed by Henan Province and Education Ministry of China, Henan University of Chinese Medicine, Zhengzhou, Henan, China, [2]Henan Key Laboratory of Chinese Medicine for Respiratory Disease, Henan University of Chinese Medicine, Zhengzhou, Henan, China, [3]Department of Respiratory Diseases, The First Affiliated Hospital of Henan University of Chinese Medicine, Zhengzhou, Henan, China, [4]Department of Respiratory Diseases, Henan Provincial People's Hospital, Zhengzhou, Henan, China, [5]Department of Respiratory Diseases, The Third Affiliated Hospital of Henan University of Chinese Medicine, Zhengzhou, Henan, China, [6]Department of Respiratory Diseases, Henan Province Hospital of Traditional Chinese Medicine, Zhengzhou, Henan, China

Background and objective: Idiopathic pulmonary fibrosis (IPF) is a critical disease, with limited treatments available. Clinical practices show that traditional Chinese medicine (TCM) has certain efficacy. This study was preliminarily to evaluate the efficacy and safety of TCM treatment based on syndrome differentiation in IPF.

Methods: A study design of exploratory, multi-centers, randomized, double-blinded, placebo controlled trial has been adopted. A total of 80 IPF patients from four sub-centers were enrolled. All the patients were randomly assigned into TCM group (TCMG) or control group (CG) in 1:1. Patients in TCMG were given CM granules, as patients in CG given with the placebo of CM granule. All the patients received a 26-week treatment. The efficacy was assessed by acute exacerbations (AEs) of IPF, pulmonary function, clinical symptoms, dyspnea scores (mMRC), health-related quality of life (HRQoL), 6-min walk test (6MWT) and all-cause mortality. Safety has also been assessed.

Results: A total of 67 patients completed the trial with 35 in TCM group and 32 in control group. Meaningful differences have been observed in mean changes in AEs (−1.56 times; 95% CI, −2.69 to −0.43, $p = 0.01$), DLco% (5.29; 95% CI, 0.76 to 9.81, $p = 0.02$), cough scores (−0.38 points; 95% CI, −0.73 to −0.04, $p = 0.03$), and 6MWT (30.43 m; 95% CI, 2.85 to 58.00, $p = 0.03$), with no statistical differences in FEV1, FVC, expectoration, chest tightness, Shortness of breath, Fatigue, Cyanosis, mMRC, CAT, SF-36, and SGRQ total scores in 26 weeks after treatment than before treatment. At of the end of follow-up, a total of 10 patients died, including three and seven in

the TCM and control group respectively. And the HR (Hazard ratio) for CM granules in all-cause mortality was 0.39 (95% CI, 0.10–1.52). The drug-related adverse events were not observed.

Conclusion: CM granules, as compared with placebo, could reduce frequencies of AEs, improve pulmonary function, HRQoL, exercise capacity and symptoms and signs for IPF to some extent with acceptable side-effect.

KEYWORDS

idiopathic pulmonary fibrosis, Chinese medicine, syndrome differentiation, efficacy, randomized controlled trial

1 Introduction

Idiopathic pulmonary fibrosis (IPF) is a progressive and ultimately fatal interstitial lung disease (Raghu et al., 2011; Gao et al., 2021). With worsened dyspnea and an increasing loss of pulmonary function, IPF patients will have poor health-related quality of life (HRQoL) (Hopkins et al., 2016). It has also caused an increasing social-economic burden (Raimundo et al., 2016; Maher et al., 2021; Cox et al., 2022). Researches show that pirfenidone and nintedanib could be certain effective to IPF (Wu et al., 2021; Pitre et al., 2022), which were also recommended by the guideline (Raghu et al., 2015). However, its application has been limited by side effects and high prices. And the case fatality rate is still on the rise (Dove et al., 2019). It is urgent to develop other effective treatments and strategies to manage IPF.

TCM has a long history and definite efficacy on respiratory diseases. IPF can be treated referring to *fei-wei* or *fei-bi*. According to TCM theory that lung is the dominator of qi and kidney is the root of qi, they can both affect the development of IPF. So, the methods of regulating and reinforcing lung and kidney have been the most commonly used treatment in clinical practice for TCM. In previous studies, our research team also found that it can reduce the incidence of acute exacerbations (AEs) of IPF and delay the loss of lung function. However, most of the present studies are limited to summary of clinical experiences. It is urgent to manage further researches to obtain evidence-based supports. In our previous literature research, we concluded that the common TCM syndromes of stable IPF included lung-qi deficiency, lung-kidney qi deficiency, yin deficiency and internal heat, meanwhile had prescriptions for each syndromes of Bao-fei Hua-xian (Bu-fei Yi-qi) granule, Jin-shui Huan-xian (Bu-fei Yi-shen) granule, and Yang-qing Kang-xian (Yang-yin Qing-re) granule, respectively. We systematically searched the clinical trial registration platform and other related databases. This is the first registered RCT for TCM in treating IPF. So, we have performed this study to evaluate the efficacy and safety of CM granule based on above prescriptions for each syndrome of IPF. The results will also provide evidence-based supports for TCM treatment in IPF and critical references for further TCM studies. The study protocol has been registered in www.chictr.org.cn (ChiCTR-IIR-17013532) and published in *JIM* (Yu et al., 2020).

2 Subjects and methods

2.1 Study design

The study was an exploratory, randomized, double-blinded, placebo controlled, and parallel-group trial, performed in four sub-centers in Zhengzhou China, which include the First Affiliated Hospital of Henan University of CM, Henan Province Hospital of CM, Third Affiliated Hospital of Henan University of CM, and Henan Provincial People's Hospital. An expert committee, included clinicians, statisticians and ethics experts, had been set up to perform the study design. The trial has been approved and supervised by Ethic Committee of the First Affiliated Hospital of Henan University of CM.

2.2 Patients

Patients were eligible to participate in the trial if they were aged 40–80 years old and met the diagnosis criteria of stable IPF (Raghu et al., 2011) 1 and syndrome differentiation of TCM (Lung qi deficiency syndrome, yin deficiency and internal heat Syndrome and of lung and kidney qi deficiency syndrome) (Professional Committee of Pulmonary Diseases of China Association of Chinese Medicine, 2012). They should not participate in any other trial within 1 month before enrollment. It was also necessary to sign informed consent before entering the study for all the subjects.

However, the patients with AEs of IPF, pregnancy or breast-feeding should be excluded, as should the subjects with obnubilation, dementia or mental disorders. Patients with severe cardiac insufficiency, severe liver and kidney diseases (ALT, AST, BUN, and Cr are more than twice the value of normal upper limit.) or being allergic to any of the used drugs should not be involved in the study.

Traditional Chinese medicine syndromes differentiation have been performed referring to the following diagnostic criteria:

Lung qi deficiency syndrome: ① Cough, or dyspnea, or shortness of breath; ② Fatigue with worsen symptom when moving; ③ Spontaneous sweating, which is also aggravated when moving; ④ Afraid of wind and cold, or easy to catch cold; ⑤ The tongue is light, or the pulse is thin or weak. On the basis of items ①, any other plus two items among ②, ③, ④, and ⑤ should be met.

Yin deficiency and internal heat syndrome: ① Dyspnea or shortness of breath; ② Dry cough, or cough with little or unpleasant sputum; ③ Dry mouth or throat; ④ Hands, feet and hearts are hot or hot in the afternoon; ⑤ Night sweat; ⑥ The tongue is red, or has little or no coating with dry or thin veins. On the basis of items ① and ②, any other plus two items among③, ④, ⑤, and ⑥ should be met.

Lung and kidney qi deficiency syndrome: ① Dyspnea, or cough, or shortness of breath, and symptoms will be worsen when moving; ② Mental weakness and fatigue or spontaneous sweating, with worse condition when moving; ③ Easy to catch a cold, or afraid of wind and cold; ④ Soreness of waist and knees; ⑤ Tinnitus or dizziness; ⑥ The face is puffy; ⑦ Frequent urination, increased nocturia, or enuresis when coughing; ⑧ The tongue is light, or the pulse is thin. On the basis of any two items among ①, ② and ③, other plus three items among ④, ⑤, ⑥, ⑦, and ⑧ should also be met.

2.3 Study procedure

After a washout period of 2 weeks, participants were randomly assigned into traditional Chinese medicine group (TCMG) or control group (CG) with 1:1 to receive CM granules or the placebo of CM granules for 26 weeks. CM granules have been applied according to TCM syndromes including Bao-fei Hua-xian granule for lung qi deficiency syndrome, Jin-shui Huan-xian granule for lung-kidney qi deficiency syndrome, and Yang-qing Kang-xian granule for yin deficiency and inter heat syndrome. A follow-up visit would be managed in every 13 weeks during the treatment period.

Central randomization was adopted by third party organization through SAS9.2 software. Patients, investigators, data collectors and the study sponsor were all blind to the treatment assignments in the whole process of study. To minimize the missing data, patients, who discontinued the trial, would be contacted through phone or other ways as soon as possible and complete all the questionnaires that should be completed. Any adverse event, which would be reported and dealt with in 24 h, was centrally collected. Informed consent and record should be completed for no uniform appointment on the application of pifenidone and nintedanib. If necessary, the symptomatic medication, such as ambroxol hydrochloride tablets, compound methoxyphenamine capsules and budesonide formoterol inhalants, would be applied. All the enrollments and follow-up visits have been managed in a special place. The study procedure could be found in Figure 1.

2.4 Outcomes

The primary outcomes were pulmonary function and AEs of IPF. Forced expiratory volume in one second (FEV1) and forced vital capacity (FVC) were measured in milliliter. Carbon monoxide diffusion capacity (DLCO) was measured in a percentage of the predicted value (DLCO%), and annual numbers of AE were also calculated. The diagnosis of AEs should meet the criterion published by the American Thoracic Society (Collard et al., 2016).

The secondary outcomes included clinical symptoms, dyspnea scores, HRQoL, 6MWT and all-cause mortality. The clinical symptoms were measured by cough, expectoration, chest tightness, shortness of breath, fatigue, and cyanosis, with the scoring criteria in Table 1. Dyspnea score was assessed with modified Medical Research Council (mMRC). HRQoL was assessed by the total score of the St. George's Respiratory Questionnaire (SGRQ), COPD assessment test (CAT)and short form 36 (SF-36) health survey questionnaire. Pulmonary function test was conducted at baseline and 26 weeks. 6MWT, mMRC, SGRQ, CAT, and SF-36 were assessed at baseline and every follow-up visit. All-cause deaths were counted separately to calculate all-cause mortality at 26 weeks.

Safety was assessed by routine blood, urine and stool test, liver and kidney function, electrocardiogram and adverse events. Routine blood, urine and stool test, liver and kidney function, electrocardiogram will be evaluated pre- and post-treatment. Adverse events will be recorded and dealt with as soon as possible.

2.5 Statistical analysis

Estimation method of sample size for exploratory research was adopted. And a lost-rate of 20% was also taken into account. The target total sample size was 80. Both efficacy and safety analysis were managed for all the patients in the trial. SAS 9.2 statistical software was applied in data analysis. The measurement data with normal distribution were represented by mean ± standard deviation ($\bar{x} \pm s$), as with non-normal distribution represented by median ± quartile (M ± Q). Paired *t*-test was applied in the comparison within group with normal distribution and homogeneous data, as Wilcoxon rank sum test used with non-normal distribution or non-homogeneous data; Variance analysis or independent sample *t*-test was applied in the comparison between groups with normal-distribution and

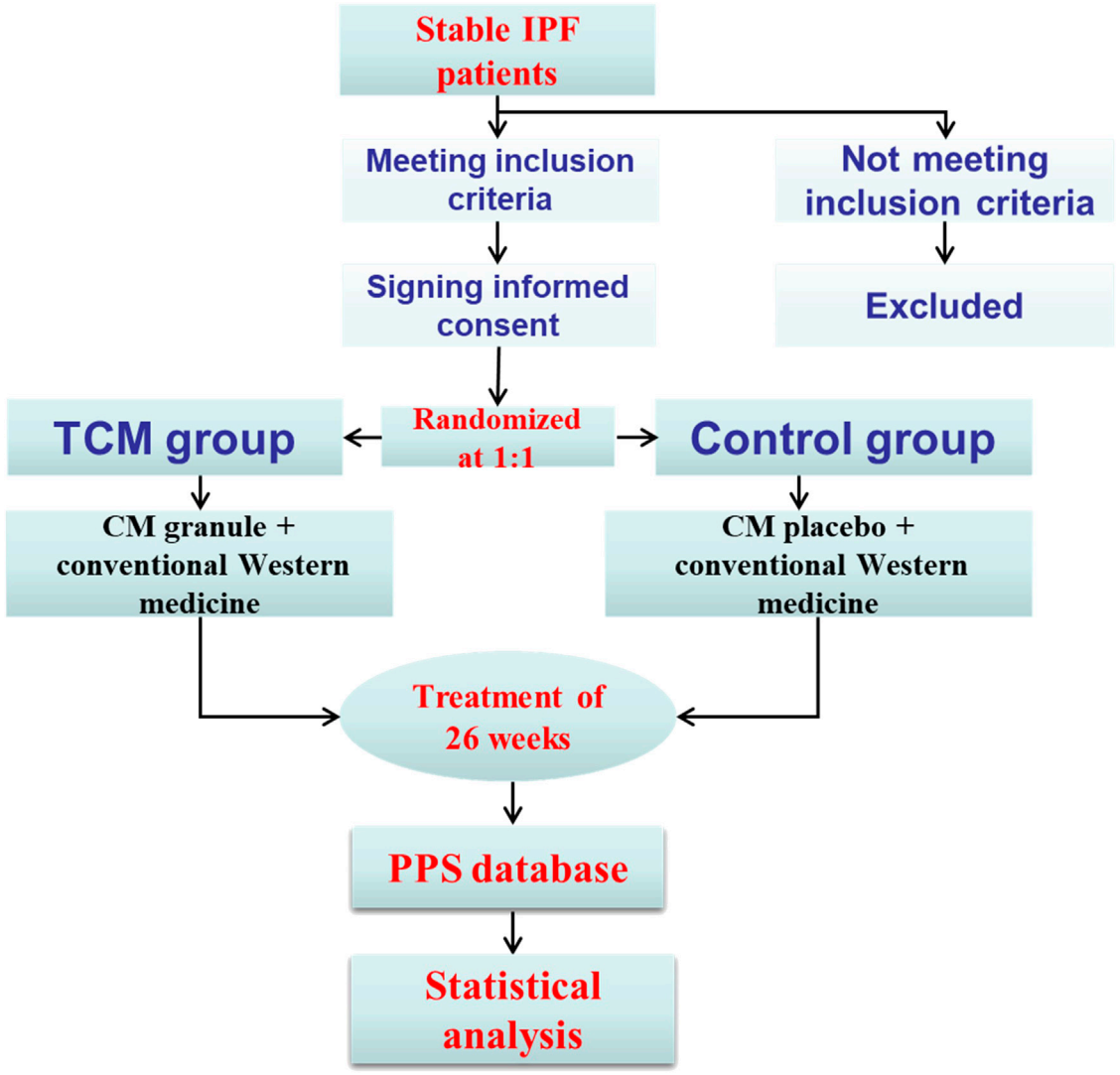

FIGURE 1
Study procedure of the trial.

TABLE 1 Scoring criteria of clinical symptoms and signs.

	0	1	2	3
Cough	No	Only in the morning	Through the day	Frequent cough through the day
Expectoration	No	10–20 ml through the day	20–30 ml through the day	30 ml and above through the day
Chest tightness	No	Once in a while	Often and post-activity aggravation	Obvious with incidence even rest
Shortness of breath	No	With heavy activity	With light activity	Even rest
Fatigue	No	Light	Moderate	Severe
Cyanosis	No	Light	Moderate	Severe

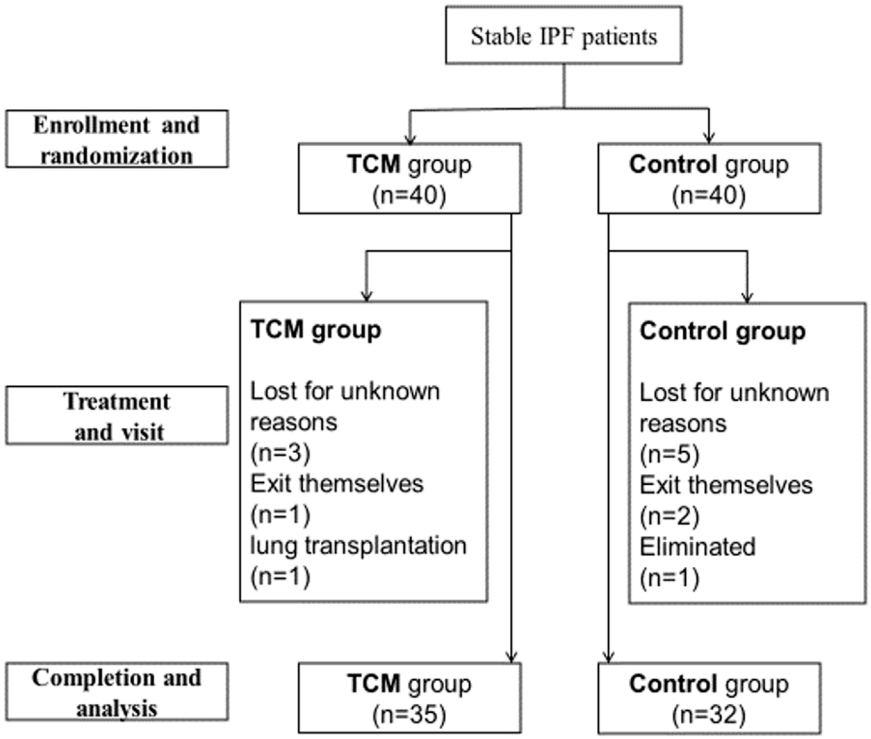

FIGURE 2
Presentation of patients' completion in the study.

homogeneous data, as Wilcoxon rank sum test used with non-normal distribution or non-homogeneous data. The counting data were described by frequency, number of incidence or constituent ratio, and the differences among groups was tested by contingency table chi-square test. Two-sided significance tests with an alpha value of 0.05 have been adopted. All the statistical analysis would be performed by third-party professional statisticians named Jiangsu Famous Medical Technology Co. Ltd. in Nanjing, China.

3 Results

3.1 Baseline characteristics of patients

From August 2016 to June 2017, a total of 80 stable IPF patients from outpatient of the above four sub-centers were enrolled (Figure 2). Among these patients, five in TCMG and seven in CG discontinued the trial, and one in CG was eliminated because of not taking medicine. Statistical analysis was completed on data from 35 patients in CMG and 32 in CG (Figure 2). Five patients in TCMG and one in CG took pifenidone with no statistical difference. There were also no statistical differences between the two groups in sex, nation, ages, occupations, education levels, smoking histories, disease durations, pulmonary function, annual incidences of acute exacerbation, mMRC, 6MWT, and HRQoL (Table 2).

3.2 Acute exacerbations of idiopathic pulmonary fibrosis

After treatment, there was statistical difference between the two groups in annual numbers of AEs ($p = 0.0008$). And the mean annual numbers were 0.69 and 2.19 times in TCMG and CG (mean difference, −1.50 times; 95%CI, −2.60 to 0.40), respectively. The mean changes from baseline in annual numbers of AEs were −0.37 and 1.19 times in TCMG and CG (mean difference, −1.56 times; 95% CI, −2.69 to −0.43). Annual number of AEs was significantly higher in CG than TCMG after treatment. Details could be got in Table 3 and Figure 3.

3.3 Pulmonary function

There were no significant differences in FVC and FEV1 between TCMG and CG. However, a meaningful

TABLE 2 General characteristics of patients at baseline[b].

Characteristics	TCM group	Control group	χ^2/F	p
Average age—years[a]	64.54 ± 6.50	63.00 ± 8.32	−0.849	0.399
Male sex—no. (%)	21 (60.0)	22 (68.75)	0.557	0.456
Han nationality—no. (%)	34 (97.14)	31 (96.88)	0.004	0.949
Education levels				
Illiteracy/Semiliterate—no. (%)	1 (2.86)	1 (3.13)	9.596	0.143
Primary school—no. (%)	8 (22.86)	9 (28.13)		
Junior middle school—no. (%)	7 (20.00)	11 (34.38)		
Senior middle school—no. (%)	7 (20.00)	8 (25.00)		
Junior college—no. (%)	10 (28.57)	1 (3.13)		
Undergraduate—no. (%)	2 (5.71)	1 (3.13)		
Postgraduate—no. (%)	0 (0)	1 (3.13)		
Occupations				
Worker—no. (%)	2 (5.71)	2 (6.25)	2.763	0.838
Farmer—no. (%)	10 (28.57)	13 (40.63)		
Intellectual—no. (%)	1 (2.86)	1 (3.13)		
Manager—no. (%)	2 (5.71)	0 (0)		
Service—no. (%)	1 (2.86)	1 (3.13)		
Retirement—no. (%)	18 (51.43)	14 (43.75)		
Unemployed—no. (%)	1 (2.86)	1 (3.13)		
Patients with smoking history—no. (%)	18 (51.43)	17 (53.13)	0.019	0.89
Patients with co-morbidity—no. (%)	6 (17.14)	9 (28.13)	1.16	0.281
Diseases duration—months[a]	27.97 ± 27.39	24.98 ± 25.69	−0.459	0.648
Annual numbers acute exacerbation[a]	1.06 ± 1.08	1.00 ± 1.07	−0.216	0.829
Scores of mMRC[a]	1.71 ± 0.66	1.56 ± 0.71	−0.898	0.372
6MWT—m[a]	342.57 ± 81.18	374.38 ± 87.67	1.542	0.128
Symptoms and signs total scors	8.54 ± 3.00	8.41 ± 2.38	0.651	0.838
mMRC scors	1.71 ± 0.66	1.56 ± 0.71	−0.898	0.372
CAT total scors	15.06 ± 6.66	13.22 ± 5.66	1.212	0.230
SGRQ total scors	47.86 ± 15.33	45.50 ± 17.92	0.314	0.563
SF-36 total scors	104.09 ± 15.73	104.91 ± 12.40	1.397	0.815
Lung function				
FEV 1—L	1.91 ± 0.62	1.99 ± 0.54	0.565	0.574
FVC—L	2.36 ± 0.76	2.42 ± 0.83	0.312	0.756
DLCO%—%	40.26 ± 13.60	44.18 ± 15.73	0.453	0.278

[a]Plus–minus values are means ± SD.
[b]There were no statistical differences between the two groups in any characteristic at baseline.

difference was shown in DLCO%. The mean changes from baseline in DLCO% were 4.40 and −0.88 (mean difference, 5.29; 95% CI, 0.76 to 9.81, p = 0.02) in TCMG and CG, respectively. Other results could be found in Table 3 and Figure 4.

3.4 Clinical symptoms and signs

There were no meaningful inter-group difference in clinical symptoms and signs expect cough. The mean changes from baseline in cough score were −0.14 and 0.03 points in TCMG and CG (mean difference, −0.18 points; 95% CI, −0.47 to 0.12) at week 13 and −0.26 points and 0.13 points at week 26 (mean difference, −0.38 points; 95% CI, −0.73 to −0.04, p = 0.03), respectively. Other details were shown in Table 3 and Figure 5.

3.5 mMRC

There was no significant inter-groups difference in mMRC scores. However, there were intra-group significant differences in TCMG between three or 6 months after treatment and baseline,

TABLE 3 Efficacy outcomes assessment after treatment.

Outcomes	TCM group		Control group		Difference (95% CI)	*p*
	No. of patients	Mean change from baseline[a]	No. of patients	Mean change from baseline[a]		
Annual numbers of AEs	35	−0.37 ± 1.96	32	1.19 ± 2.66	−1.56 (−2.69, −0.43)	0.01
Pulmonary function						
FEV1(L)-at week 26	35	−0.06 ± 0.22	32	−0.10 ± 0.20	0.05 (−0.06, 0.15)	0.38
FVC(L)-at week 26	35	−0.10 ± 0.27	32	−0.11 ± 0.24	0.01 (−0.11, 0.13)	0.86
DLCO%-at week 26	35	4.40 ± 9.89	32	−0.88 ± 8.66	5.29 (0.76, 9.81)	0.02
Clinical symptoms and signs						
Cough score						
At week 13	35	−0.14 ± 0.65	32	0.03 ± 0.54	−0.18 (−0.47, 0.12)	0.24
At week 26	35	−0.26 ± 0.78	32	0.13 ± 0.61	−0.38 (−0.73, −0.04)	0.03
Expectoration score						
At week 13	35	0.00 ± 0.91	32	0.19 ± 0.64	−0.19 (−0.58, 0.2)	0.34
At week 26	35	0.00 ± 0.94	32	0.25 ± 0.72	−0.25 (−0.66, 0.16)	0.23
Chest tightness score						
At week 13	35	−0.23 ± 0.77	32	−0.03 ± 0.54	−0.20 (−0.52, 0.13)	0.23
At week 26	35	−0.20 ± 1.11	32	−0.13 ± 0.66	−0.08 (−0.53, 0.38)	0.74
Shortness of breath score						
At week 13	35	−0.06 ± 0.64	32	−0.06 ± 0.62	0.01 (−0.30, 0.31)	0.97
At week 26	35	−0.26 ± 0.78	32	−0.03 ± 0.70	−0.23 (−0.59, 0.14)	0.22
Fatigue score						
At week 13	35	−0.26 ± 0.70	32	−0.13 ± 0.71	−0.13 (−0.48, 0.21)	0.45
At week 26	35	−0.37 ± 0.97	32	−0.16 ± 0.68	−0.22 (−0.63, 0.20)	0.30
Cyanosis score						
At week 13	35	−0.17 ± 0.51	32	−0.03 ± 0.54	−0.14 (−0.40, 0.12)	0.28
At week 26	35	−0.29 ± 0.57	32	−0.13 ± 0.55	−0.16 (−0.44, 0.12)	0.25
mMRC score						
At week 13	35	−0.31 ± 0.80	32	−0.16 ± 0.72	−0.16 (−0.53, 0.21)	0.40
At week 26	35	−0.43 ± 1.07	32	−0.22 ± 0.79	−0.21 (−0.67, 0.25)	0.37
HRQoL						
CAT total score						
At week 13	35	−1.17 ± 6.90	32	0.28 ± 5.62	−1.45 (−4.54, 1.63)	0.35
At week 26	35	−1.60 ± 7.50	32	0.19 ± 6.87	−1.79 (−5.31, 1.73)	0.31
SF-36 total score						
At week 13	35	5.91 ± 12.31	32	6.35 ± 13.36	−0.44 (−6.70, 5.82)	0.89
At week 26	35	6.62 ± 16.50	32	6.12 ± 13.91	0.50 (-6.98, 7.98)	0.89
SGRQ total score						
At week 13	35	−5.02 ± 15.44	32	−1.29 ± 11.76	−3.73 (−1078, 3.01)	0.27
At week 26	35	−5.66 ± 18.04	32	−0.86 ± 10.69	−4.80 (−12.13, 2.52)	0.20
6MWD (m)						
At week 13	35	14.11 ± 34.26	32	−8.91 ± 39.28	23.02 (5.07, 40.97)	0.01
At week 26	35	24.46 ± 63.07	32	−5.97 ± 48.18	30.43 (2.85, 58.00)	0.03
All-cause mortality	No. of patients	No. of patients with events (%)	No. of patients	No. of patients with event (%)	Hazard Ratio (95% CI)	
	35	3 (8.6)	32	7 (21.9)	0.39 (0.10, 1.52)	0.13

[a]mean ± SD.

Data presented as between-time mean (95% CI) differences by groups.

6MWT, 6-min walk test; AE, acute exacerbation; CAT, COPD assessment test; DLco%, diffusing capacity percentage of the predicted value; FEV1, forced expiratory volume in one second percentage; FVC, forced vital capacity; HRQoL, health-related quality of life; mMRC, modified medical research council; SF-36, 36-item short-form health survey; SGRQ, St. George's respiratory questionnaire.

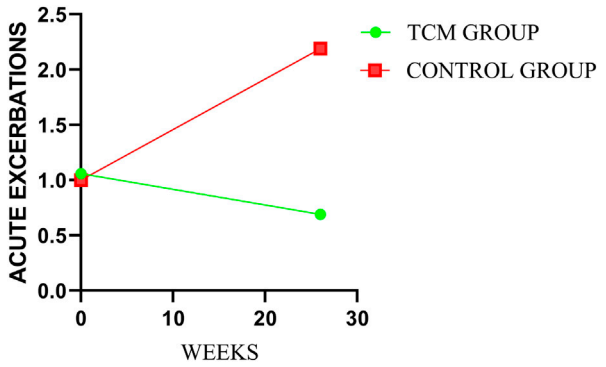

FIGURE 3
Comparison of differences between groups on AEs.

with no intra-group significant differences for CG. As shown in Table 3, the mean changes in mMRC score from baseline were −0.31 points in TG and −0.16 points in the CG at week 13 (mean difference = −0.16 points, 95% CI,−0.53 to 0.21; p = 0.40), and −0.43 points and −0.22 points at week 26 (mean difference = −0.21 points, 95% CI, −0.67 to 0.25; p = 0.37), respectively. Details could be found in Table 3 and Figure 6.

3.6 All-cause mortality

Three of the 35 patients in the TCMG died in the whole trial period, with seven of 32 patients in the CG. Harzard Ratio (HR) for CM granules in all-cause mortality is 0.39 (95% CI, 0.10–1.52) (Table 3). Please found details in Table 3 and Figure 7.

3.7 Health-related quality of life

In our study, no significant between-group difference has emerged in HRQoL assessed by SGRQ, CAT, and SF-36. However, as shown in Table 3, the results indicated a trend of improvement in HRQoL in both groups, and the TCMG may be better than CG. See details in Table 3 and Figure 8.

3.7 6-min walk test

In the treatment period, there were significant inter-group differences in mean change at every follow-up visit and post-treatment in 6MWT. The mean changes from baseline were 14.11 m in TCMG and −8.91 m in CG (mean difference = 23.02 m; 95% CI, 5.07–40.97, p = 0.01) at week 13 and 24.46 m and −5.97 m in respectively (mean difference, 30.43 m; 95% CI, 2.85–58.00, p = 0.03) at week 26. Details have been presented in Table 3 and Figure 9.

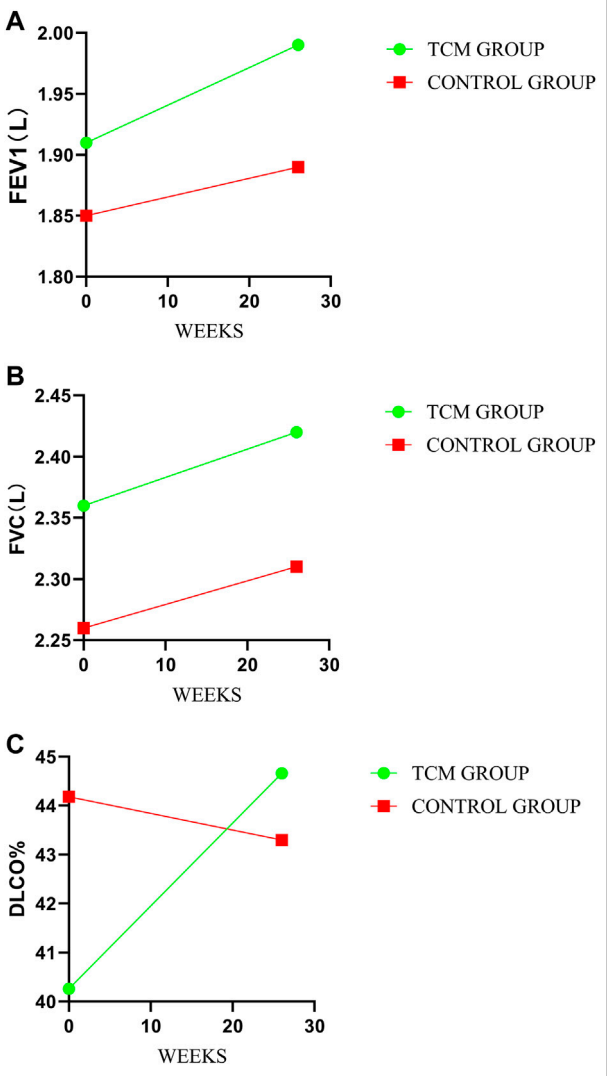

FIGURE 4
Comparison of differences between groups on pulmonary function. **(A–C)** represent the treatment change trends of FEV1, FVC, and DLco%, respectively.

3.8 Adverse events

In the whole trial, very few patients suffered from transient gastric discomfort, and no other significant adverse events were observed. None of adverse events were assessed to be related to the study drug.

4 Discussion

To our knowledge, this is the first randomized, controlled trial showing efficacy and safety of CM granules in IPF. Throughout the trail, only a few patients were prescribed with anti-fibrosis

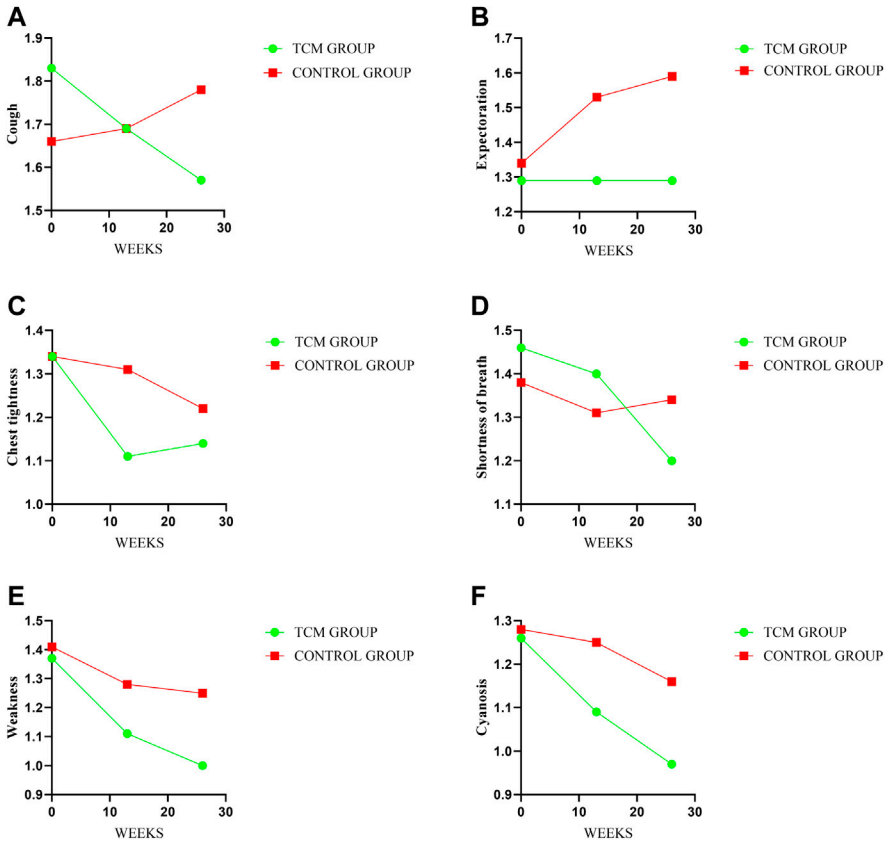

FIGURE 5
Comparison of differences between groups on symptoms and signs. Treatment change trends of cough, expectoration, chest tightness, shortness of breath, weakness and cyanosis have been shown in **(A–F)** respectively. The higher score will reflect the worse symptoms.

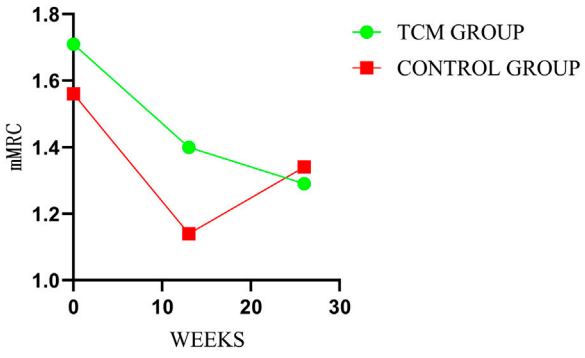

FIGURE 6
Comparison of differences between groups on mMRC.

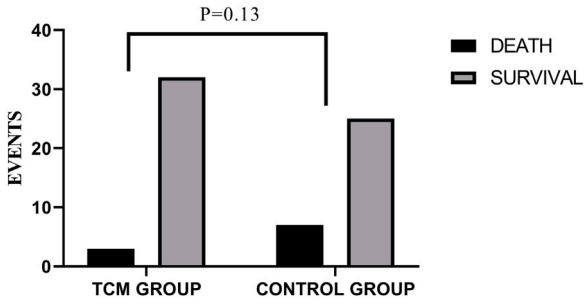

FIGURE 7
Comparison of differences between groups on mortality.

medicines. The efficacy and advantages of TCM in the treatment of IPF were initially highlighted. The results indicated that TCM granules could reduce incidences of AEs and risk of death, slow down the decline of pulmonary function, and improve HRQoL and exercise capacity for IPF to some extent. No obvious adverse reactions have been observed. However, the clinical symptoms and signs have also been improved to some extent with no statistical significance expect for cough.

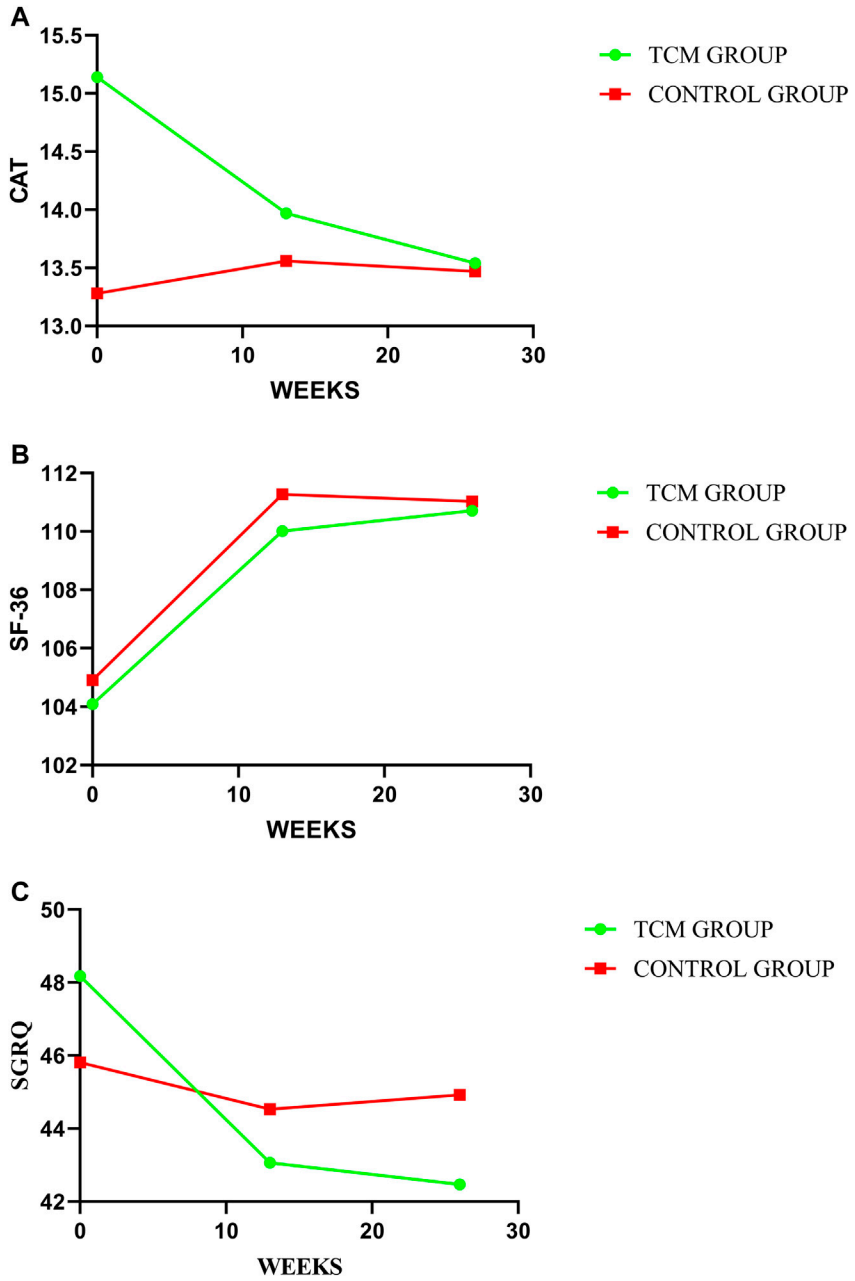

FIGURE 8
Comparison of differences between groups on HRQoL. In this study, HRQoL has been assessed by CAT, SF-36, and SGRQ, with treatment change trends shown in (A–C) respectively. A higher value indicate a better HRQoL for SF-36 with a worse HRQoL for CAT and SGRQ.

AEs, which could usually induce worsen HRQoL, disease-progression and even death (Collard et al., 2016; Kakugawa et al., 2016; Qiu et al., 2018), has been a primary outcome to assess efficacy of CM granules in the study. We could find that incidences of AEIPF in CG increased with the course of disease, as was no obvious trend in TG. CM granules can reduce incidences of AEs.

Pulmonary function, which is the most susceptible physiological function for IPF patients, is also the common efficacy indicator. So, it has also been another primary outcome. DLCO or DLCO% may be the most sensitive and be consistent with prognosis (Behr et al., 2009). FVC can also indicate the disease-progression and prognosis (Salisbury et al., 2016) and also be applied in other researches (King

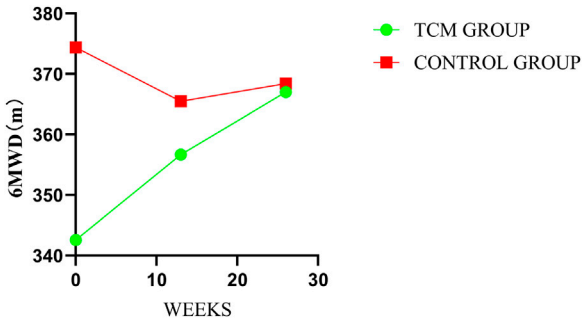

FIGURE 9
Comparison of differences between groups on 6MWD.

et al., 2014; Richeldi et al., 2014). Our study find that FVC and FEV1 decrease in both groups, with more pronounced in CG than that in TCMG. And DLCO% rose in TCMG as decreased in CG. CM granules may delay the deterioration of pulmonary function for IPF patients.

IPF is a critical disease with a poor prognosis and high-mortality. So some scholars insist that it could be applied as main outcome in the clinical study for IPF (Raghu et al., 2012; Collard et al., 2014). However, other scholars insist the converse opinion (Wells et al., 2012). They deem that a longer treatment period would be needed if death was applied as outcome. This may be the possible reason why there is no inter-group difference in all-cause mortality in this study.

IPF patients often undergo with poor HRQoL (Hopkins et al., 2016). So, improving HRQoL is also one of the goals for IPF. In our study, HRQoL, which was assessed by SF-36, CAT and SGRQ, has also been adopted as outcomes. There are no inter-group differences in SF-36, CAT and SGRQ, with some intra-group differences and better improvement trends in TCMG. The results indicated that CM granules may have improvement in HRQoL for IPF.

For IPF, some clinical symptoms and signs including cough, expectoration, chest tightness and so on, often occur in the process of disease. According to TCM theory, CM granules is based on clinical symptoms and signs. The improvement in clinical symptoms and signs should be the first step. However, the results showed that CM granules has a good tendency in improving symptoms and signs with no statistical difference. This may also indicate that clinical symptoms and signs are difficulty to improve for IPF.

Exercise capacity, which is assessed by 6MWT in this study, will decrease with disease progression in IPF. It is also an important indicator of disease severity and HRQoL in IPF (Bahmer et al., 2017). And because of its simple operation and good repeatability (du Bois et al., 2014; Holland et al., 2018), 6MWT has been applied to assess exercise capacity and clinical efficacy (Holland et al., 2014; Baddini-Martinez, 2018). Our results indicate that CM granules could improve 6MWT in IPF. The result may also indicate that CM granules could improve exercise capacity, HRQoL and disease severity.

In addition, characteristic changes in HRCT are the critical and objective efficacy and prognosis references for IPF evaluation. However, at the beginning of this study, the efficacy evaluation value of HRCT has not been highlighted, and not been adopted by the contemporary international studies. Therefore, the deficiency remains in this study, which will be improved in the future researches.

Although more and more relevant treatment researches have been conducted or being conducted in IPF, only pifenidone and nintedanib obtained evidence-based efficacy and were recommended in the guidelines up to now (King et al., 2014; Richeldi et al., 2014; Raghu et al., 2015; Behr, 2016; Cottin et al., 2017; Behr et al., 2018; Homma et al., 2018; Jo et al., 2018; Lee et al., 2019; Raghu et al., 2022). Drug-related side effects and their high prices have also caused limitations for clinical application. Other effective treatments are still needed to be developed. The pathogenesis of IPF has not been completely clear, so the drug development has also been restricted. The advantages of CM granules emerged. According to TCM theory, names of diseases, TCM pathogenesis and syndromes should be determined according to clinical symptoms and signs first. And then, the treatment would be completed. The process is called TCM syndrome differentiation. So, the pathogenesis in Western medicine is not necessary. The application of CM granules is more convenient and worth to promote. In addition, compared with the anti-fibrosis drugs being used, pifenidone and nintedanib, CM may also have the health economics advantage with cheap price. In our study, we could also find that, the adverse reactions of CM were few and well tolerated. More IPF patients will also have another treatment option and benefited in the absence or intolerance of anti-fibrosis treatment.

As we known, blood stasis and phlegm turbidity are also important pathological factors. According to the standards issued in 2012 by the Professional Committee of Pulmonary Diseases of China Association of Chinese Medicine, the syndromes for IPF include three types, which have seven syndromes, namely, deficiency syndrome (lung qi deficiency, yin deficiency and internal heat, lung and kidney qi deficiency, lung and kidney qi yin deficiency), excess syndrome (phlegm heat obstructing the lung, phlegm turbidity obstructing the lung), and concurrent syndrome (blood stasis). However, because of small sample, not all the syndromes could be taken into account. So, this study only selected the main TCM syndromes, including patterns of lung qi deficiency, lung-kidney qi deficiency, and yin deficiency inner heat, for observation on the basis of previous research, and there are also relevant single Chinese medicine for reducing phlegm and blood circulation given in the compound CM granules. Other syndromes will be considered in the future researches.

The sample size is also too small for this study as a multicenter research. However, IPF is a rare disease, and it is difficult to enroll patients to participate the study in clinical

practice. Then, this is an exploratory trial without sufficient preliminary data support. The sample size cannot be estimated exactly. So, we estimated sample size referring to sample size estimation method for exploratory clinical trial and to provide references for further confirmatory study.

Although some achievements have been obtained, there are still some limitations in the study. First, as an exploratory study with a deficiency of foundation, this trial does not have an ample sample size, which may also be the possible reason for that there was no statistical significance in some results. Second, although CM granules brings an advantage for TCM with no need for clear and complex pathogenesis of Western medicine, its shortcomings has also appeared. TCM syndromes often depend on the subjective judgement by researchers, with a deficiency of objective indicators. So, further confirmative researches with appropriate sample size and core TCM pathogenesis need to be carried out in the future. Developing objective indicators combining of IPF and TCM syndromes will also be another direction as well as mechanism of TCM in IPF.

Data availability statement

The datasets presented in this article are not readily available because the follow-up research is in progress. Data sharing will be available at the end of all studies. Requests to access the datasets should be directed to JL, li_js8@163.com.

Ethics statement

The studies involving human participants were reviewed and approved by the Ethic Committee of the First Affiliated Hospital of Henan University of CM. The patients/participants provided their written informed consent to participate in this study.

Author contributions

JL contributed to the conception and design, critical revision, and should be the corresponding author. XY contributed to the conception and design of trial. SY contributed to the data collection, data analysis and draft manuscript writing. YX contributed to the data collection, analysis and updated manuscript writing. XY, LZ, MZ, and YM contributed to the enrollment and visit of participants. All the authors have read and approved the final manuscript.

Funding

This study is supported by Special Scientific Research Project of National Clinical Research Base of Traditional Chinese Medicine (JDZX2015155, 2018JDZX006), National Natural Science Foundation of China (No. 81973779) and Natural Science Foundation of Henan Youth Fund (212300410056). All the participant experts are appreciated for their diligence in this study.

Conflict of interest

The authors declare that the research was conducted in the absence of any commercial or financial relationships that could be construed as a potential conflict of interest.

Publisher's note

All claims expressed in this article are solely those of the authors and do not necessarily represent those of their affiliated organizations, or those of the publisher, the editors and the reviewers. Any product that may be evaluated in this article, or claim that may be made by its manufacturer, is not guaranteed or endorsed by the publisher.

References

Baddini-Martinez, J. A. (2018). Six-minute walk test in patients with idiopathic pulmonary fibrosis. *J. Bras. Pneumol.* 44 (4), 257–258. doi:10.1590/S1806-37562018000040001

Bahmer, T., Kirsten, A. M., Waschki, B., Rabe, K. F., Magnussen, H., Kirsten, D., et al. (2017). Prognosis and longitudinal changes of physical activity in idiopathic pulmonary fibrosis. *BMC Pulm. Med.* 17 (1), 104. doi:10.1186/s12890-017-0444-0

Behr, J., Demedts, M., Buhl, R., Costabel, U., Dekhuijzen, R. P., Jansen, H. M., et al. (2009). Lung function in idiopathic pulmonary fibrosis--extended analyses of the IFIGENIA trial. *Respir. Res.* 10 101. doi:10.1186/1465-9921-10-101

Behr, J. (2016). Guidelines or guidance for better idiopathic pulmonary fibrosis management? *BMC Med.* 14 24. doi:10.1186/s12916-016-0567-9

Behr, J., Günther, A., Bonella, F., Geißler, K., Koschel, D., Kreuter, M., et al. (2018). German guideline for idiopathic pulmonary fibrosis - update on pharmacological therapies 2017. *Pneumologie* 72 (2), 155–168. doi:10.1055/s-0043-123035

Collard, H. R., Brown, K. K., Martinez, F. J., Raghu, G., Roberts, R. S., and Anstrom, K. J. (2014). Study design implications of death and hospitalization as end points in idiopathic pulmonary fibrosis. *Chest* 146 (5), 1256–1262. doi:10.1378/chest.14-0492

Collard, H. R., Ryerson, C. J., Corte, T. J., Jenkins, G., Kondoh, Y., Lederer, D. J., et al. (2016). Acute exacerbation of idiopathic pulmonary fibrosis. An international working group report. *Am. J. Respir. Crit. Care Med.* 194 (3), 265–275. doi:10.1164/rccm.201604-0801CI

Cottin, V., Crestani, B., Cadranel, J., Cordier, J. F., Marchand-Adam, S., Prévot, G., et al. (2017). French practical guidelines for the diagnosis and management of idiopathic pulmonary fibrosis - 2017 update. Full-length version. *Rev. Mal. Respir.* 34 (8), 900–968. doi:10.1016/j.rmr.2017.07.017

Cox, I. A., Otahal, P., de Graaff, B., Corte, T. J., Moodley, Y., Zappala, C., et al. (2022). Incidence, prevalence and mortality of idiopathic pulmonary fibrosis in Australia. *Respirology* 27 (3), 209–216. doi:10.1111/resp.14194

Dove, E. P., Olson, A. L., and Glassberg, M. K. (2019). Trends in idiopathic pulmonary fibrosis-related mortality in the United States: 2000-2017. *Am. J. Resp. Crit. care* 200 (7), 929–931. doi:10.1164/rccm.201905-0958LE

du Bois, R. M., Albera, C., Bradford, W. Z., Costabel, U., Leff, J. A., Noble, P. W., et al. (2014). 6-Minute walk distance is an independent predictor of mortality in patients with idiopathic pulmonary fibrosis. *Eur. Respir. J.* 43 (5), 1421–1429. doi:10.1183/09031936.00131813

Gao, J., Kalafatis, D., Carlson, L., Pesonen, I. H. A., Li, C. X., Wheelock, Å., et al. (2021). Baseline characteristics and survival of patients of idiopathic pulmonary fibrosis: A longitudinal analysis of the Swedish IPF registry. *Respir. Res.* 22 (1), 40. doi:10.1186/s12931-021-01634-x

Holland, A. E., Hill, C. J., Dowman, L., Glaspole, I., Goh, N., Lee, A. L., et al. (2018). Short- and long-term reliability of the 6-minute walk test in People with idiopathic pulmonary fibrosis. *Respir. Care* 63 (8), 994–1001. doi:10.4187/respcare.05875

Holland, A. E., Spruit, M. A., Troosters, T., Puhan, M. A., Pepin, V., Saey, D., et al. (2014). An official European respiratory society/American thoracic society technical standard: Field walking tests in chronic respiratory disease. *Eur. Respir. J.* 44 (6), 1428–1446. doi:10.1183/09031936.00150314

Homma, S., Bando, M., Azuma, A., Sakamoto, S., Sugino, K., Ishii, Y., et al. (2018). Japanese guideline for the treatment of idiopathic pulmonary fibrosis. *Respir. Investig.* 56 (4), 268–291. doi:10.1016/j.resinv.2018.03.003

Hopkins, R. B., Burke, N., Fell, C., Dion, G., and Kolb, M. (2016). Epidemiology and survival of idiopathic pulmonary fibrosis from national data in Canada. *Eur. Respir. J.* 48 (1), 187–195. doi:10.1183/13993003.01504-2015

Jo, H. E., Prasad, J. D., Troy, L. K., Mahar, A., Bleasel, J., Ellis, S. J., et al. (2018). Diagnosis and management of idiopathic pulmonary fibrosis: Thoracic Society of Australia and New Zealand and Lung Foundation Australia position statements summary. *Med. J. Aust.* 208 (2), 82–88. doi:10.5694/mja17.00799

Kakugawa, T., Sakamoto, N., Sato, S., Yura, H., Harada, T., Nakashima, S., et al. (2016). Risk factors for an acute exacerbation of idiopathic pulmonary fibrosis. *Respir. Res.* 17 (1), 79. doi:10.1186/s12931-016-0400-1

King, T. E., Bradford, W. Z., Castro-Bernardini, S., Fagan, E. A., Glaspole, I., Glassberg, M. K., et al. (2014). A phase 3 trial of pirfenidone in patients with idiopathic pulmonary fibrosis. *N. Engl. J. Med.* 370 (22), 2083–2092. doi:10.1056/NEJMoa1402582

Lee, S. H., Yeo, Y., Kim, T. H., Lee, H. L., Lee, J. H., Park, Y. B., et al. (2019). Korean guidelines for diagnosis and management of interstitial lung diseases: Part 2. Idiopathic pulmonary fibrosis. *Tuberc. Respir. Dis.* 82 (2), 102–117. doi:10.4046/trd.2018.0091

Maher, T. M., Bendstrup, E., Dron, L., Langley, J., Smith, G., Khalid, J. M., et al. (2021). Global incidence and prevalence of idiopathic pulmonary fibrosis. *Respir. Res.* 22 (1), 197. doi:10.1186/s12931-021-01791-z

Pitre, T., Mah, J., Helmeczi, W., Khalid, M. F., Cui, S., Zhang, M., et al. (2022). *Medical treatments for idiopathic pulmonary fibrosis: A systematic review and network meta-analysis*. London: Thorax. doi:10.1136/thoraxjnl-2021-217976

Professional Committee of Pulmonary Diseases of China Association of Chinese Medicine (2012). Diagnostic criteria of traditional Chinese medicine syndromes for diffuse interstitial lung disease (2012Edition). *J. Traditional Chin. Med.* 53, 1163–1165.

Qiu, M., Chen, Y., and Ye, Q. (2018). Risk factors for acute exacerbation of idiopathic pulmonary fibrosis: A systematic review and meta-analysis. *Clin. Respir. J.* 12 (3), 1084–1092. doi:10.1111/crj.12631

Raghu, G., Collard, H. R., Anstrom, K. J., Flaherty, K. R., Fleming, T. R., King, T. E., et al. (2012). Idiopathic pulmonary fibrosis: Clinically meaningful primary endpoints in phase 3 clinical trials. *Am. J. Respir. Crit. Care Med.* 185 (10), 1044–1048. doi:10.1164/rccm.201201-0006PP

Raghu, G., Collard, H. R., Egan, J. J., Martinez, F. J., Behr, J., Brown, K. K., et al. (2011). An official ATS/ERS/JRS/ALAT statement: Idiopathic pulmonary fibrosis: Evidence-based guidelines for diagnosis and management. *Am. J. Respir. Crit. Care Med.* 183 (6), 788–824. doi:10.1164/rccm.2009-040GL

Raghu, G., Remy-Jardin, M., Richeldi, L., Thomson, C. C., Inoue, Y., Johkoh, T., et al. (2022). Idiopathic pulmonary fibrosis (an update) and progressive pulmonary fibrosis in adults: An official ATS/ERS/JRS/ALAT clinical practice guideline. *Am. J. Respir. Crit. Care Med.* 205 (9), e18–e47. doi:10.1164/rccm.202202-0399ST

Raghu, G., Rochwerg, B., Zhang, Y., Garcia, C. A., Azuma, A., Behr, J., et al. (2015). An official ATS/ERS/JRS/ALAT clinical practice guideline: Treatment of idiopathic pulmonary fibrosis. An update of the 2011 clinical practice guideline. *Am. J. Respir. Crit. Care Med.* 192 (2), e3–e19. doi:10.1164/rccm.201506-1063ST

Raimundo, K., Chang, E., Broder, M. S., Alexander, K., Zazzali, J., and Swigris, J. J. (2016). Clinical and economic burden of idiopathic pulmonary fibrosis: A retrospective cohort study. *BMC Pulm. Med.* 16 2. doi:10.1186/s12890-015-0165-1

Richeldi, L., du Bois, R. M., Raghu, G., Azuma, A., Brown, K. K., Costabel, U., et al. (2014). Efficacy and safety of nintedanib in idiopathic pulmonary fibrosis. *N. Engl. J. Med.* 370 (22), 2071–2082. doi:10.1056/NEJMoa1402584

Salisbury, M. L., Xia, M., Zhou, Y., Murray, S., Tayob, N., Brown, K. K., et al. (2016). Idiopathic pulmonary fibrosis: Gender-Age-Physiology index stage for predicting future lung function decline. *Chest* 149 (2), 491–498. doi:10.1378/chest.15-0530

Wells, A. U., Behr, J., Costabel, U., Cottin, V., Poletti, V., Richeldi, L., et al. (2012). Hot of the breath: Mortality as a primary end-point in IPF treatment trials: The best is the enemy of the good. *Thorax* 67 (11), 938–940. doi:10.1136/thoraxjnl-2012-202580

Wu, W., Qiu, L., Wu, J., Liu, X., and Zhang, G. (2021). Efficacy and safety of pirfenidone in the treatment of idiopathic pulmonary fibrosis patients: A systematic review and meta-analysis of randomised controlled trials. *BMJ Open* 11 (12), e050004. doi:10.1136/bmjopen-2021-050004

Yu, X. Q., Yang, S. G., Xie, Y., and Li, J. S. (2020). Traditional Chinese medicine in the treatment of idiopathic pulmonary fibrosis based on syndrome differentiation: Study protocol of an exploratory trial. *J. Integr. Med.* 18 (2), 163–168. doi:10.1016/j.joim.2019.12.005

frontiers | Frontiers in Pharmacology

TYPE Original Research
PUBLISHED 31 October 2022
DOI 10.3389/fphar.2022.1013098

OPEN ACCESS

EDITED BY
Yang Zhou,
Brown University, United States

REVIEWED BY
Xingxin Wu,
Nanjing University, China
Raúl Vivar,
University of Chile, Chile

*CORRESPONDENCE
Guiwu Qu,
quguiwu@aliyun.com
Changjun Lv,
lucky_lcj@sina.com
Xiaodong Song,
songxd71@163.com

†These authors have contributed equally to this work

SPECIALTY SECTION
This article was submitted to Respiratory Pharmacology, a section of the journal Frontiers in Pharmacology

RECEIVED 06 August 2022
ACCEPTED 19 October 2022
PUBLISHED 31 October 2022

CITATION
Zhu Q, Wang J, Ji Y, Luan J, Yue D, Liu W, Li H, Zhang J, Qu G, Lv C and Song X (2022), Danshensu methyl ester enhances autophagy to attenuate pulmonary fibrosis by targeting lncIAPF–HuR complex. *Front. Pharmacol.* 13:1013098. doi: 10.3389/fphar.2022.1013098

Danshensu methyl ester enhances autophagy to attenuate pulmonary fibrosis by targeting lncIAPF–HuR complex

Qi Zhu[1†], Jing Wang[1†], Yunxia Ji[2†], Jianlin Luan[1], Dayong Yue[1], Weili Liu[2], Hongbo Li[2], Jinjin Zhang[3], Guiwu Qu[4*], Changjun Lv[2*] and Xiaodong Song[1*]

[1]Department of Cellular and Genetic Medicine, School of Pharmaceutical Sciences, Binzhou Medical University, Yantai, China, [2]Department of Respiratory and Critical Care Medicine, Binzhou Medical University Hospital, Binzhou Medical University, Binzhou, China, [3]Medical Research Center, Binzhou Medical University, Yantai, China, [4]School of Gerontology, Binzhou Medical University, Yantai, China

Pulmonary fibrosis is an irreversible fibrotic process that has a high mortality rate and limited treatment options; thus, developing a novel therapeutic drug is critical. In this study, we synthesized danshensu methyl ester (DME) and explored its anti-pulmonary fibrotic ability on TGF-β1-stimulated lung fibroblast *in vitro* and on bleomycin-induced pulmonary fibrosis *in vivo*. Results showed that DME decreased the expression of differentiation-related proteins, including fibroblast activation protein 1 (FAP1) and S100 calcium-binding protein A4 (S100A4), and fibrotic markers, such as *a*-SMA, vimentin, and collagen *in vivo* and *in vitro*. In addition, DME markedly repressed myofibroblast proliferation and migration. Mechanistically, chromatin immunoprecipitation–PCR, RNA immunoprecipitation, half-life, and other experiments revealed that DME inhibited activating transcription factor 3 expression *via* TGF-β1 signal transduction leading to a decrease in lncIAPF transcription and stability. Moreover, DME blocked human antigen R (HuR) nucleocytoplasmic translocation and promoted its degradation *via* downregulating lncIAPF, which markedly decreased the expression of HuR target genes such as negative autophagic regulators (EZH2, STAT1, and FOXK1). Collectively, our results demonstrated that DME enhanced autophagy to attenuate pulmonary fibrosis *via* downregulating the lncIAPF–HuR-mediated autophagic axis and the lncIAPF–HuR complex can be the target for drug action.

KEYWORDS

pulmonary fibrosis, danshensu, lncRNA, autophagy, HuR (ELAVL1)

Introduction

Pulmonary fibrosis is the common end stage for many diseases, such as Sjogren's syndrome, systemic lupus erythematosus, dermatomyositis, and rheumatoid arthritis. It is primarily characterized by morphological and functional abnormalities within the lung. Morphological abnormalities include progressive deposition of the extracellular matrix (ECM), thickening of the alveolar wall, and a large number of fibroblast proliferation and migration. Functional abnormalities include the decline in forced vital capacity (FVC), vital capacity, total lung capacity, and diffusion capacity of the lungs for carbon monoxide (Johannson et al., 2021). Environmental exposure, genetic factors, and aging have been described as potential risk factors (Moss et al., 2022). In addition, acute respiratory syndrome coronavirus can cause pulmonary fibrosis in many patients (Aveyard et al., 2021; Bando et al., 2022). Despite major advances in the mechanism of pulmonary fibrosis, no effective therapeutic methods have been developed. Therefore, research on effective treatment is of great practical importance.

At present, long non-coding RNAs (lncRNAs) are considered as RNA transcript with >200 nucleotides, which does not encode protein. They are multifaceted, versatile regulators of most cellular processes, including cell death, proliferation, migration, and differentiation. Accumulating studies have revealed that lncRNAs contribute to disease initiation, progression, and metastasis by modulating transcription, translation, posttranslational modification, and epigenetic modification and to protein/RNA stability by interacting with DNA, RNA, and/or proteins (de Goede et al., 2021; Quinodoz et al., 2021). For example, Hua et al. have revealed that a risk SNP-mediated promoter–enhancer switching can promote the initiation and progression of aggressive prostate cancer through lncRNA-PCAT19 (Hua et al., 2018). lncRNA-EPS serves as a transcriptional brake to restrain inflammation (Atianand et al., 2016). Similarly, lncRNA application in pharmaceutical research can be a powerful tool for drug research, such as the validation of drug targets and the study of resistance mechanisms and drug toxicity. For example, an integrated genome-wide CRISPRa approach is developed to functionalize lncRNAs in drug resistance (Bester et al., 2018). Chemotherapy-induced lncRNA-CILA1 promotes chemo-resistance in tongue squamous cell carcinoma (TSCC), and it is a therapeutic target for TSCC treatment (Lin et al., 2018). In addition, lncRNA-HIF1A-AS2 induces osimertinib resistance in patients with lung adenocarcinoma by regulating the miR-146b-5p/IL-6/STAT3 axis (Si et al., 2021). Therefore, understanding lncRNA-mediated mechanisms of drug responses will improve responses to chemotherapy and outcomes of disease treatment. In pulmonary fibrosis, RNA-binding motif protein 7 promotes the development of fibrosis by controlling the expression of selected target lncRNA-NEAT1 (Fukushima et al., 2020). lncRNA-DNM3OS promotes pulmonary fibrogenesis in trans by producing three miRNAs (i.e., miR-199a-5p/3p and miR-214-3p). Pharmacological approaches aiming at interfering with DNM3OS not only prevent lung fibrosis but also improve established pulmonary (Savary et al., 2019). To date, many lncRNA-based therapies are being investigated, including gene therapy, medical treatment, and stem cell therapy.

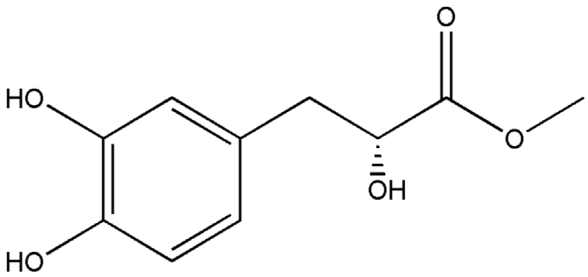

FIGURE 1
Molecular formula of DME (C10H12O5).

lncIAPF, as a pro-fibrotic factor, can be presented in both nucleus and cytoplasm in normal lung tissue. Human antigen R (HuR), as an RNA binding protein, enhances the stability of RNA and increases its expression. In a recent study (Zhang Q et al., 2022), lncIAPF and HuR function as lncIAPF-HuR complex to accelerate pulmonary fibrosis by blocking autophagy. But, whether lncIAPF-HuR complex can be a drug target is yet to be explored. Our team once has extracted danshensu from salvia miltiorrhiza, which has the effect of anti-pulmonary fibrosis. But it also exhibits physical and chemical defects, such as poor chemical stability, easy oxidation, and discoloration, which limit its clinical application (Zhao et al., 2018). Then we prepared a new compound based on danshensu (Figure 1). Because it is an esterified derivative of danshensu, we named it danshensu methyl ester (DME). In the present study, we further investigated the anti-pulmonary fibrosis and mechanism of DME targeting lncIAPF–HuR complex in TGFβ1-stimulated lung fibroblast and bleomycin (BLM)-treated mice.

Materials and methods

Animal model and ethical statement

Animal experiments were carried out in accordance with the regulation of the Animal Experiment Ethics Committee of Binzhou Medical College. 8-week-old C57/BL6 mice with an average weight of 20 ± 5 g were divided into 5 groups: sham group, bleomycin (BLM) group, BLM + danshensu methyl ester (DME) treatment group (5, 10, 20 mg/kg). The BLM model

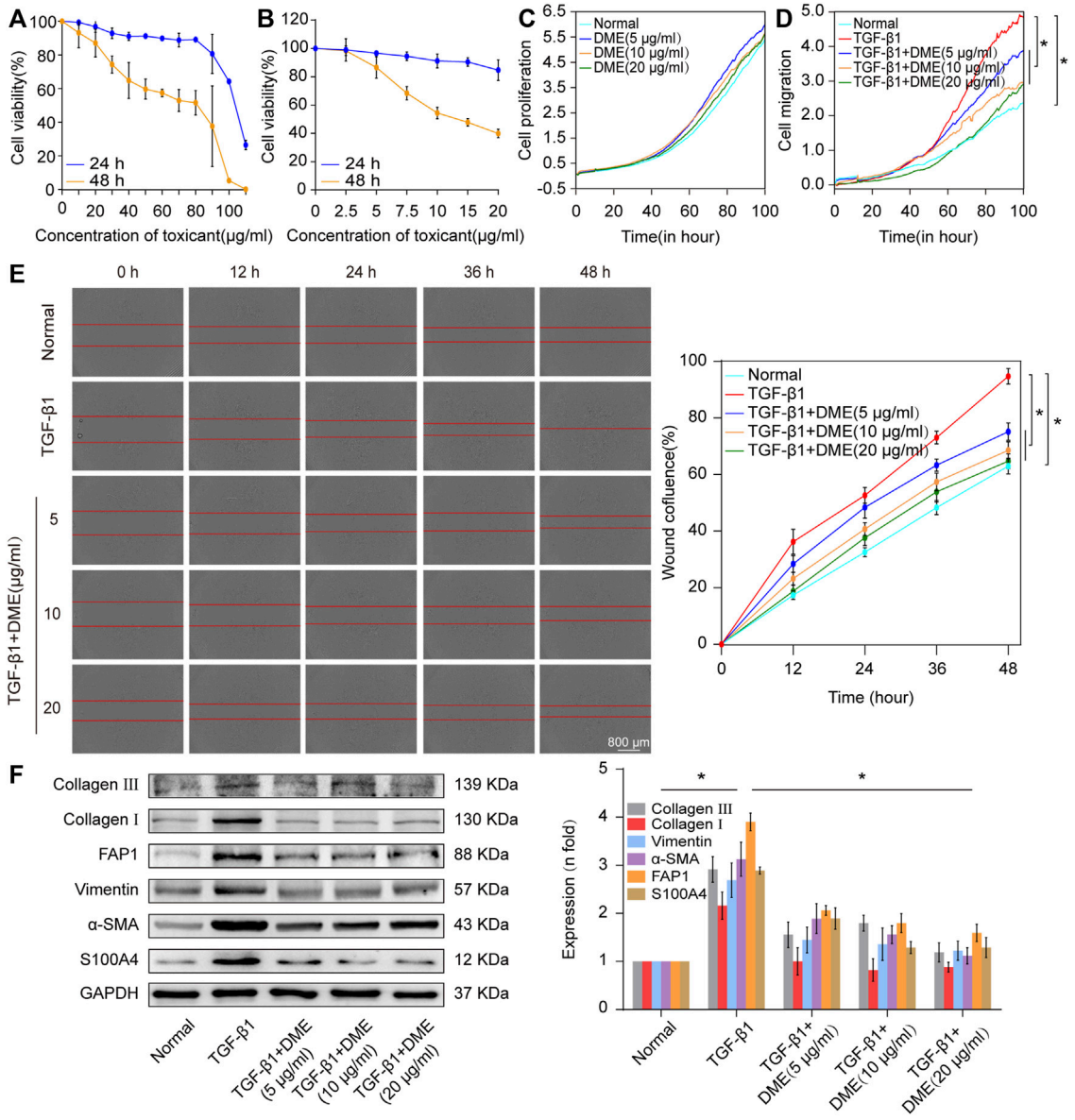

FIGURE 2
Concentration screening of DME and its anti-pulmonary fibrotic effect on MRC-5 cells. **(A)** CCK-8 was performed to test the drug toxicity of DME in normal MRC-5 cells. IC50 was approximately from 100 to 110 μg/ml under DME treated for 24 h and 80–90 μg/ml under DME treated for 48 h. **(B)** Inhibition of DME on TGF-β1-treated cells in a time- and dose-dependent manner. MRC-5 cells were initially cultured with 5 ng/ml of TGF-β1 for 72 h and then co-cultured with different concentrations of DME for 24 and 48 h respectively. **(C)** Real-time cell analysis identified that 5, 10, and 20 μg/ml of DME showed little toxicity against normal cell proliferation. **(D)** The curves of real-time cellular analysis revealed that 5, 10, and 20 μg/ml of DME significantly repressed the activated-fibroblast migration compared with those in the TGF-β1 treatment group **(E)** Analysis by using incuCyte S3 instrument confirmed that 5, 10, and 20 μg/ml of DME markedly inhibited the migration of cells treated with TGF-β1. **(F)** Western blot showed that DME decreased the expression level of S100A4, FAP1, vimentin, *a*-SMA, and collagen I and III. Each bar represents the mean ± SD; n = 6; *$p < 0.05$.

group was sprayed with 5 mg/kg BLM through the trachea by using Penn-Century MicroSprayer (Penn-Century Inc., Wyndmoor, PA, United States). The sham group was sprayed with the same amount of normal saline. The DME group was treated with different concentrations DME by intraperitoneal injection after BLM spraying. After 28 days of modeling, the lung tissue of the right lobe of mice was frozen in liquid nitrogen to extract tissue protein and RNA. The lung tissue of the left lobe was perfused and fixed with 4% paraformaldehyde for follow-up experiments.

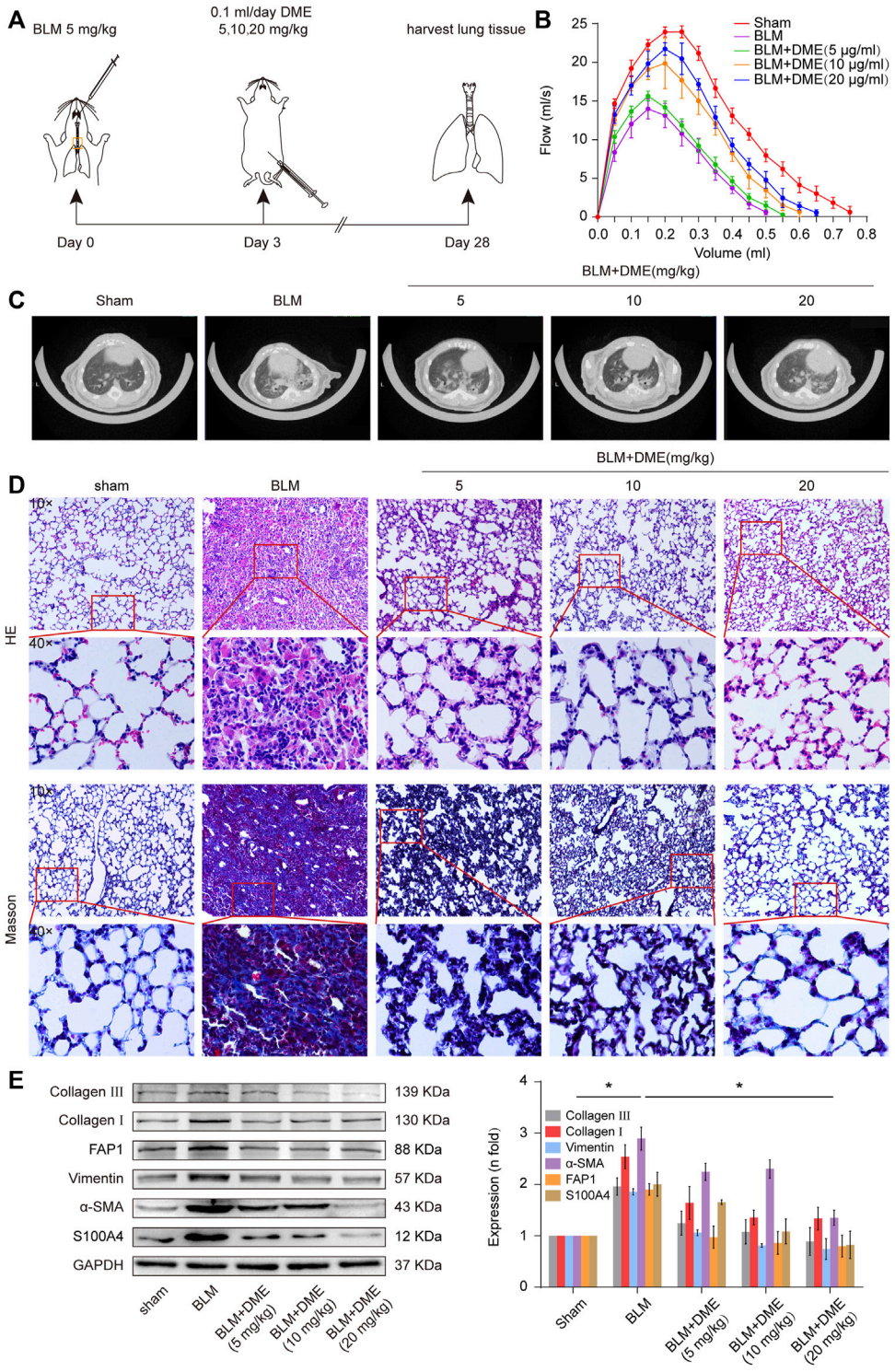

FIGURE 3
DME alleviated pulmonary fibrosis in BLM-treated mice. **(A)** Schematic illustration of DME injection to mice. **(B)** FVC results showed that DME enhanced the pulmonary function of mice compared with those in the BLM group. **(C)** MicroCT images exhibited that the BLM group had evident honeycomb-like changes and uneven patchy shadows compared with the sham group. The fibrotic symptoms were significantly improved in the DME group. **(D)** H&E and Masson staining unveiled that the alveolar structure was relatively complete; the alveolar septum became thinner, and collagen deposition was reduced in DME-treated mice compared with those of the BLM-treated group. **(E)** Western blot analysis showed that DME reduced the expression level of S100A4, FAP1, vimentin, *a*-SMA, and collagen I and III. Each bar represents the mean ± SD; $n = 6$; $^{*}p < 0.05$.

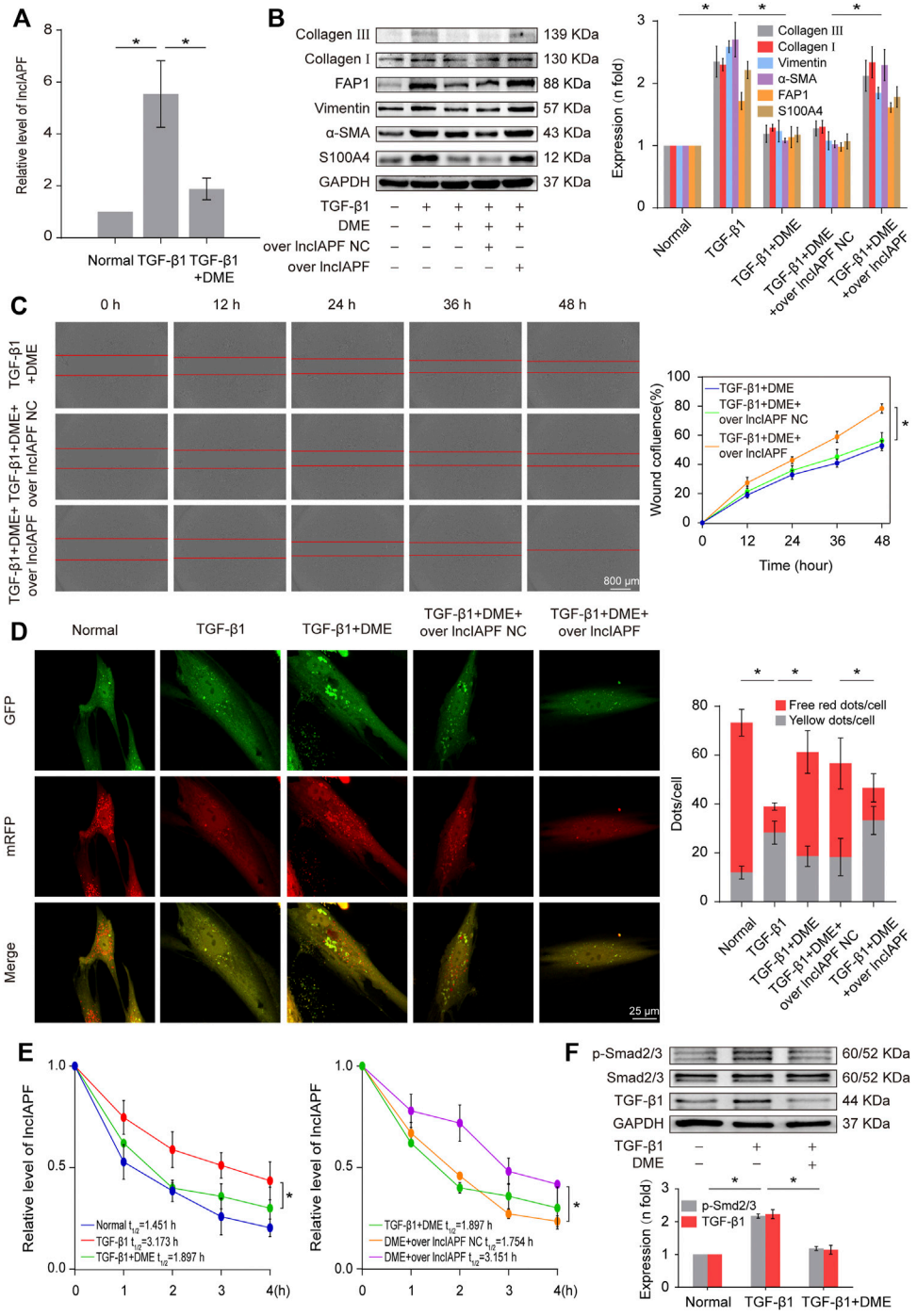

FIGURE 4
(Continued).

Cell model

Human fetal lung fibroblast MRC-5 cells were purchased from the American Type Culture Collection and cultured in advanced minimum essential medium containing 10% fetal bovine serum, 1% GlutaMAX, 1% sodium pyruvate, 1% NEAA, and 100 × penicillin/streptomycin solutions at 37°C and 5% CO_2 incubator. The cells were divided into different groups according to the experimental requirement: normal group, TGF-β1 treatment group, TGF-β1 + DME treatment

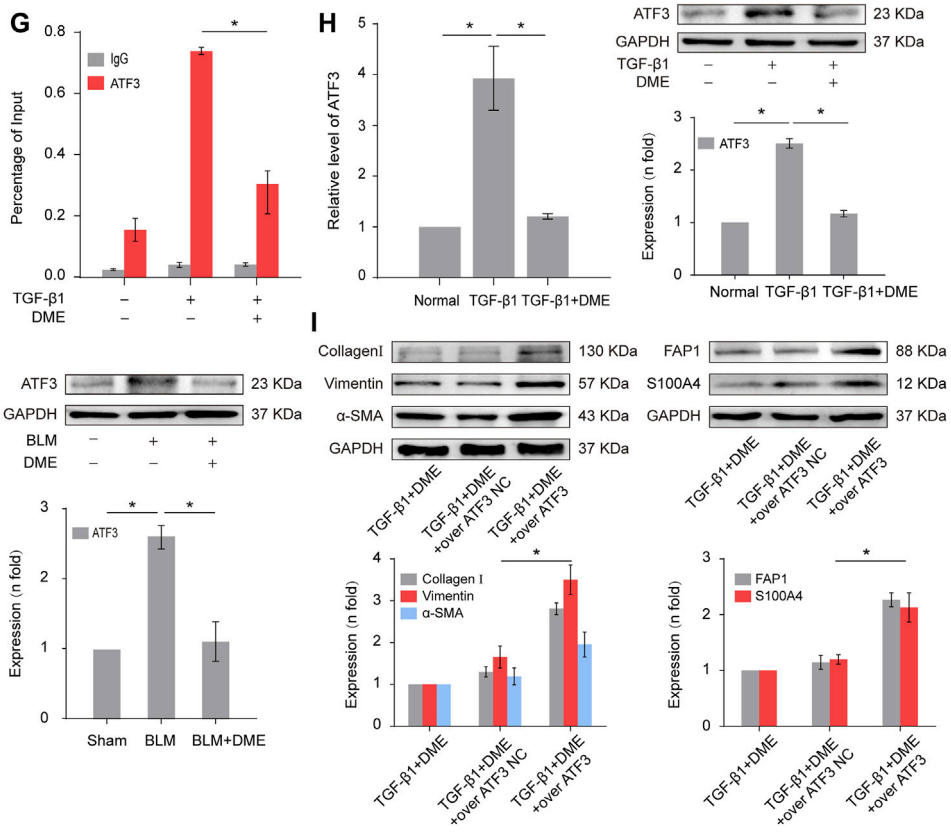

FIGURE 4
(Continued). DME alleviated pulmonary fibrosis by weakening lncIAPF stability and transcription to promote autophagy. **(A)** qRT-PCR result showed that DME reduced the expression level of lncIAPF. **(B)** The rescue experiment of Western blot showed that DME reduced the expression of S100A4, FAP1, α-SMA, vimentin, and collagen I and III. lncIAPF overexpression increased the expression of S100A4, FAP1, α-SMA, vimentin, and collagen I and III and reversed the downward trend caused by DME. **(C)** The rescue experiment of scratch assay showed that lncIAPF overexpression reversed the downward trend of migration caused by DME. **(D)** Red fluorescence indicates autolysosomes in normal autophagy. Yellow fluorescence indicates autolysosomes in abnormal autophagy. The yellow dots increased in the TGF-β1 group compared with the normal group. The red dots increased in the DME group compared with the TGF-β1 group. **(E)** Actinomycin D experiment showed that lncIAPF gradually decreased with the prolongation of actinomycin D action. However, lncIAPF overexpression reversed this trend. **(F)** Western blot result showed that DME decreased the expression levels of TGF-β1 and p-Smad2/3. **(G)** CHIP-PCR showed that TGF-β1 enhanced the binding between the lncIAPF promoter region and ATF3. DME partially blocked the binding of the lncIAPF promoter region to ATF3. **(H)** qRT-PCR and Western blot results showed that DME decreased ATF3 expression at mRNA and protein levels. **(I)** The rescue experiment of Western blot showed that overexpression of ATF3 increased S100A4, FAP1, α-SMA, vimentin and collagen I and reversed the downward trend caused by DME. The concentration of DME used was 10 μg/ml. Over lncIAPF NC indicates a negative control. Each bar represents the mean ± SD; n = 6; *$p < 0.05$.

group. Cells were treated with or without 5 ng/ml TGF-β1 for 72 h, and then treated with or without DME for 48 h. For rescue assay, cells were treated with TGF- β1 for 72 h and then transfected with an overexpression lncIAPF plasmid for 6 h, followed by treatment with DME for 48 h.

Cell counting kit-8 (CCK-8) toxicity experiment

5×10^3 MRC-5 cells were cultured for 24 h in the 96-well plates. 100 μl different concentrations of DME was added to each well and cultured for 24 h or 48 h. Then 10 μl CCK-8 solution was added to each well. After 4 h, the absorbance was measured at 450 nm with a microplate reader. Cell viability was calculated according to the kit formula.

Wound healing assay

MRC-5 cells were seeded in 96-well plates. When the cell density reached 60%, the complete medium was replaced by serum-free medium with or without TGF-β1 for 72 h. After an even line was drew on the surface of cultured cells, cells

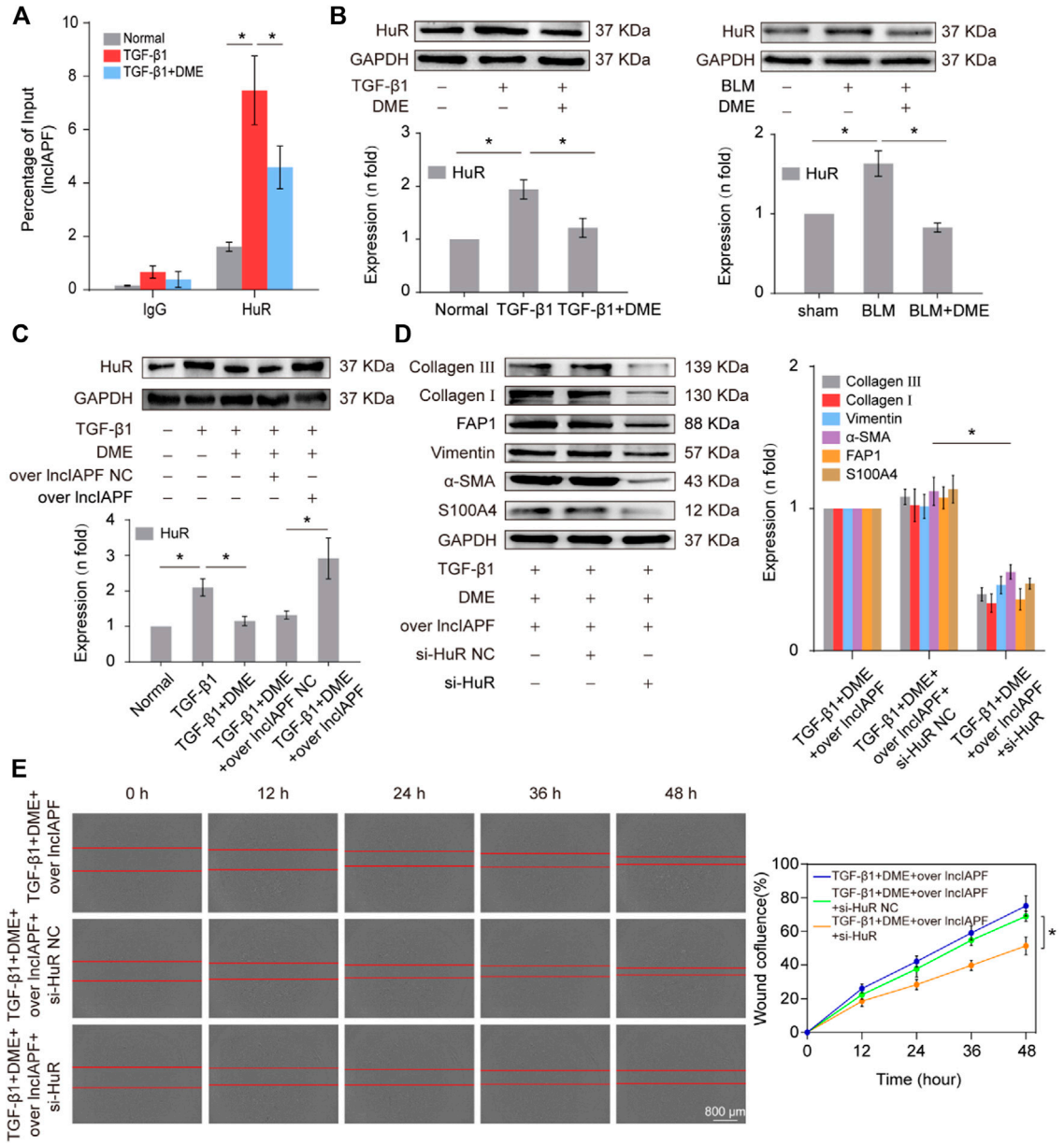

FIGURE 5
(Continued)

were washed three times with 1 × PBS to wash away the dead cells. Then, the different concentrations of DME were added to the plates and the plates were incubated in an IncuCyte S3 live-cell analysis system (Essen BioScience). The instrument automatically monitored and analyzed the live cells growth.

Hematoxylin-eosin staining and Masson's trichrome staining

The fixed lung tissue was dehydrated, soaked in paraffin overnight, embedded in paraffin, cut into 4 μM sections with a Leica microtome (RM2255), and stained with H&E or Masson

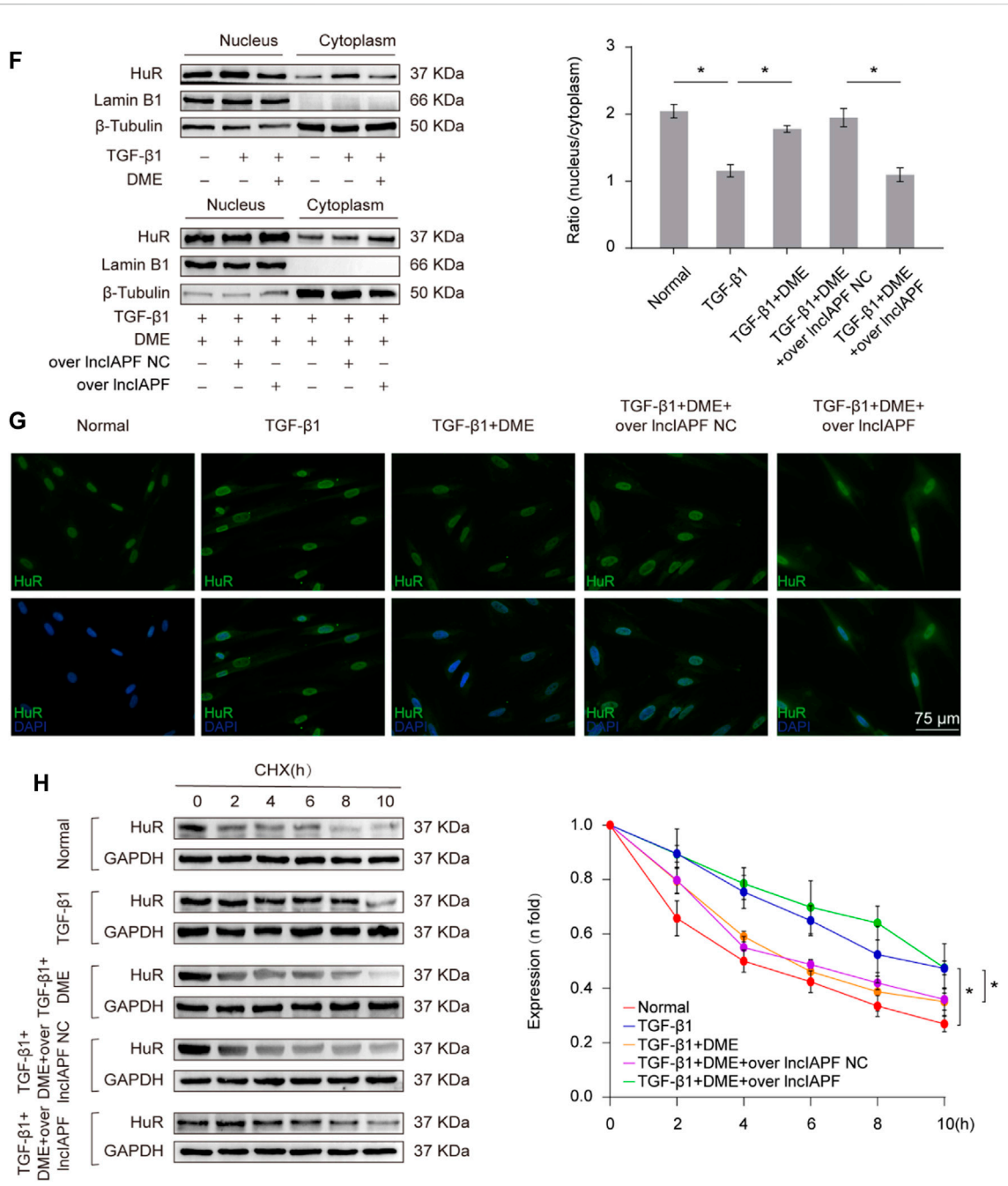

FIGURE 5
(Continued). Regulatory mechanism of DME on lncIAPF–HuR. **(A)** The RIP experiment verified the binding relationship between lncIAPF and HuR and the effect of DME on their binding. **(B)** Western blot result showed that the expression of HuR increased in the model group and decreased in the treatment group. **(C)** The rescue experiment of Western blot showed that DME reduced HuR expression, and lncIAPF overexpression increased HuR expression and reversed the downward trend caused by DME. **(D)** The rescue experiment of Western blot showed that interference with HuR decreased the expression of S100A4, FAP1, α-SMA, vimentin, collagen I and III, and reversed the upward trend caused by lncIAPF overexpression. **(E)** The rescue experiment of scratch assay showed that HuR interinterference reversed the trend of accelerated migration caused by lncIAPF overexpression. **(F)** Nucleocytoplasmic separation experiment showed that DME blocked the nucleocytoplasmic translocation of HuR, but lncIAPF overexpression reversed the effect of DME. β-Tubulin was used as the cytoplasmic reference, and Lamin B1 was used as the nucleus. The results of nucleoplasmic separation were quantitatively analyzed by Image J software as follows: Normal: nucleus/plasm = 2.0, TGF-β1: nucleus/plasm = 1.3, TGF-β1+DME: nucleus/plasm = 1.8, TGF-β1+DME + overlncIAPF NC: nucleus/plasm = 1.9, TGF-β1+DME + overlncIAPF: nucleus/plasm = 1.1. **(G)** Immunofluorescence experiment showed that HuR was primarily localized in the nucleus of normal cells, and it transferred from the nucleus to the cytoplasm under the action of TGF-β1 or lncIAPF overexpression. DME blocked the nucleocytoplasmic translocation of HuR, but lncIAPF overexpression reversed the effect of DME. **(H)** Cycloheximide experiment verified the stability of the HuR protein. DME weakened HuR stability, but lncIAPF overexpression reversed this trend. The half-life of HuR in each group was presented as follows: normal: T1/2 = 3.07 h, TGF-β1: T1/2 = 10.17 h, DME: T1/2 = 3.92 h, DME + over lncIAPF NC: T1/2 = 4.76 h, DME + lncIAPF: T1/2 = 12.33 h. The concentration of DME used was 10 μg/ml. Each bar represents the mean ± SD; n = 6; *$p < 0.05$.

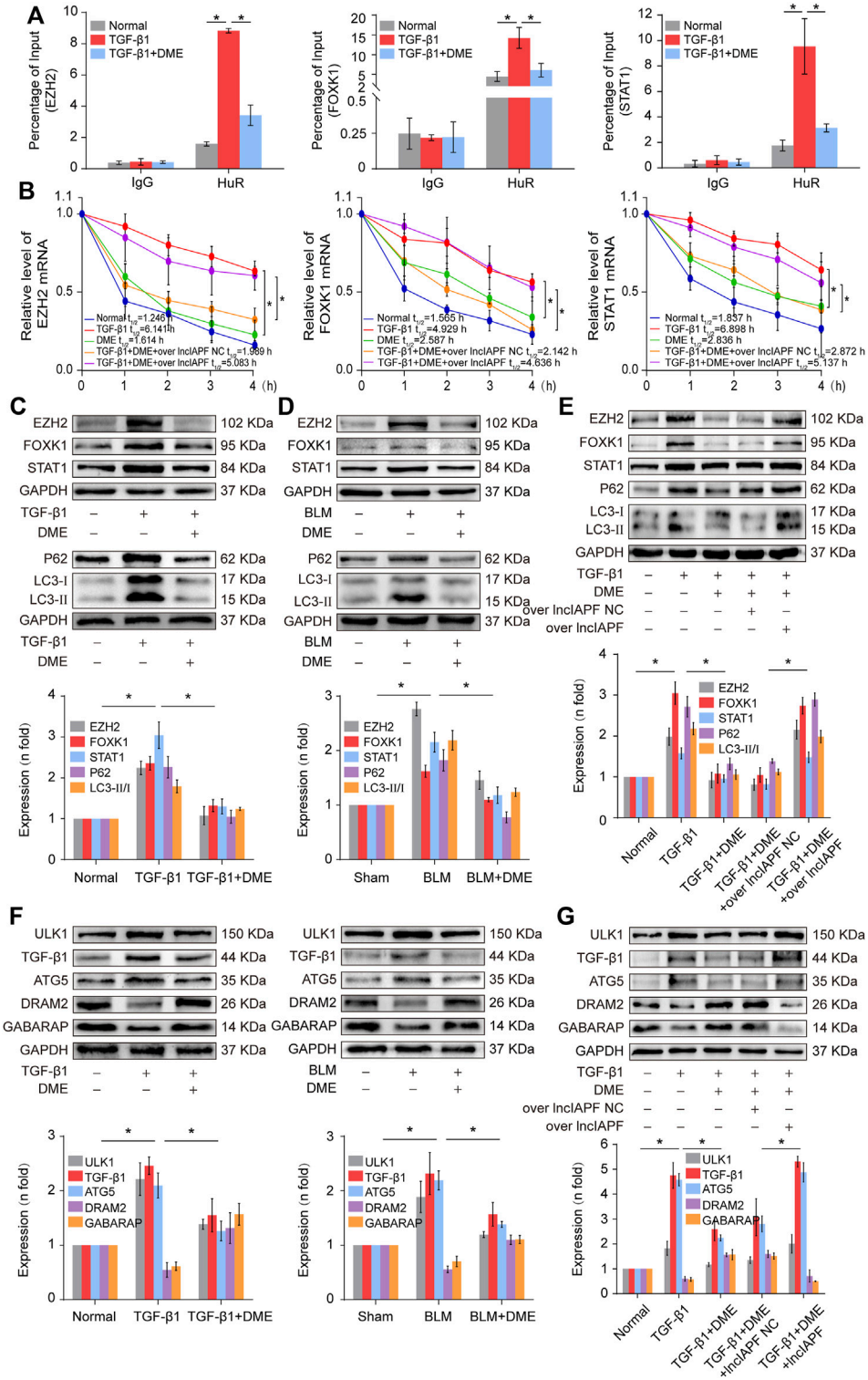

FIGURE 6
DME promoted autophagy through downregulating the target genes EZH2, STAT1, and FOXK1 depending on lncIAPF **(A)** RIP experiment showed that the mRNAs of EZH2, STAT1, and FOXK1 bound to HuR, and the binding amount decreased under DME treatment compared with TGF-β1 treatment **(B)** Half-life analysis revealed that DME treatment weakened the stability of EZH2, STAT1, and FOXK1 at the mRNA level, but lncIAPF overexpression reversed this trend. **(C)** Western blot result demonstrated that DME reduced the expression level of EZH2, STAT1, and FOXK1 in BLM-treated mice and TGF-β1-treated MRC-5 cells. **(D)** P62, LC3-II, and LC3-I expression levels in the DME group decreased compared with those in
(*Continued*)

FIGURE 6 (Continued)
the TGF-β1/BLM-treated group. **(E)** The rescue experiment validated that lncIAPF overexpression reversed the effect of DME on target and autophagic genes. **(F)** Western blot identified that ATG5 and ULK1 decreased *in vivo* and *in vitro* in the DME group compared with those in the TGF-β1 group. In addition, GABARAP and DRAM2 levels increased *in vivo* and *in vitro* in the DME group compared with those in the TGF-β1 group. **(G)** The rescue experiment clarified that lncIAPF overexpression reversed the enhancement effect of DME treatment on autophagy. The concentration of DME used was 10 μg/ml. Each bar represents the mean ± SD; $n = 6$; $^*p < 0.05$.

staining kits (Solarbio, China), respectively. The paraffin sections were dewaxed and stained, dehydrated with absolute ethanol, transparent in xylene, dripped with neutral gum, and sealed with a cover glass. The lung tissues of each group were observed under a light microscope.

Quantitative real-time reverse transcription PCR assay

Total RNA was extracted from MRC-5 cells or lung tissues with Trizol, then reverse transcribed into cDNA by reverse transcription kit (TaKaRa Biotechnology). A total volume of 20 μL system was as the following: 2 μl cDNA, 7.2 μl RNA free water, 0.4 μl lncIAPF/GAPDH forward primer, 0.4 μl lncIAPF/GAPDH reverse primer, 10 μL SYBR® Premix Ex TaqTM. The reaction program was as the following: holding temperature at 95°C for 30 s. 45 cycles of PCR amplification at 95°C for 5 s, 60°C for 20 s and 72°C for 30 s.

Immunofluorescence observation

MRC-5 cells were seeded on the cell slides in a 24-well plate, fixed with 4% tissue cell fixative for 30 min, and punched with 0.3% TritonX-100. The slides were washed with 1 × PBS, blocked with goat serum for 1 h, and incubated with anti-HuR (1:1,000, Proteintech, China) at 4°C overnight. Fluorescently labeled secondary antibody was added, incubated at room temperature for 60 min in the dark, and then discarded. 200 μl DAPI was added to each well to stain cell nuclei for 6 min and washed with 1 × PBS. Finally, the anti-fluorescence quencher was dropped on the cell slides. All images were collected under a laser scanning confocal microscope (Zeiss LSM880, Germany).

Western blot

Cells or lung tissues were harvested and lysed in radio immunoprecipitation assay buffer and phenylmethanesulfonyl fluoride (100:1). The protein concentration was measured using bicinchoninic acid protein assay kit (Coolaber, China). After separation in sodium dodecyl sulfate-polyacrylamide gel electrophoresis, the proteins were transferred to a polyvinylidene fluoride membrane, and the protein bands were blocked with 5% nonfat dry milk for 2 h, and mixed with anti-collagen III (1:1,000, Affinity, China), anti-collagen I (1:1,000, Affinity, China), anti-α-SMA (1:1,000, Affinity, China), anti-Vimentin (1:1,000, Affinity, China), Anti-GAPDH (1:10,000, Affinity, China), anti-ULK1 (1:1,000, Affinity, China), anti-FAP1 (1:1,000, Cell Signaling, United States), anti-TGF-β1, anti-ATG5, anti-DRAM2 (1:1,000, Cell Signaling, United States) 1,000, Bioss, China), anti-GABARAP (1:1,000, Affinity, China), anti-EZH2, anti-FOXK1, anti-STAT1 (1:1,000, Abcam, United Kingdom), anti-P62, anti-HuR (1:1,000, Proteintech, China)), anti-ATF3 (1:1,000, Proteintech, China), anti-LC3 polyclonal antibody and incubated overnight. Membranes were washed three times with 1× tris buffered saline tween and then incubated with goat anti-rabbit/mouse secondary antibody for 1 h. Finally, protein expression was detected by enhanced chemiluminescence kit (Spark Jade, China).

Nuclear and cytoplasmic extraction

The cell samples collected in 1.5 ml centrifuge tubes. Pre-cooled cytoplasmic extraction reagent (CER) I and CER II were added and mixed. After centrifugation, the supernatant was aspirated to obtain the cytoplasmic extraction. Then pre-cooled nuclear extraction reagent was added to the remaining precipitation, mixed and incubate on ice for 10 min. After centrifugation, the supernatant was aspirated to obtain the nucleus extraction.

Dual fluorescence HBAD-mcherry-EGFP-LC3 detection

MRC-5 cells were seeded in glass-bottom dishes. When the cell density reached 60%–70%, the complete medium was replaced with 500 μl serum-free medium. 5 μl HBAD-mcherry-EGFP-LC3 (HANBIO, China) was added into the medium. After 6 h, the medium containing HBAD-mcherry-EGFP-LC3 was removed. Then the cells were treated with/without TGF-β1 and medium containing DME for 48 h. Fluorescence images were examined under a laser scanning confocal microscope.

Half-life analysis

1×10^6/ml MRC-5 cells were seeded in cell dishes. Cells were treated with TGF-β1 for 72 h, and then treated with DME for 48 h. Finally, 2 ml serum-free medium containing 5 μg/ml actinomycin D was added into the cell samples for different times (0, 1, 2, 3, 4 h). Cells were collected and total RNA was extracted for subsequent qRT-PCR detection.

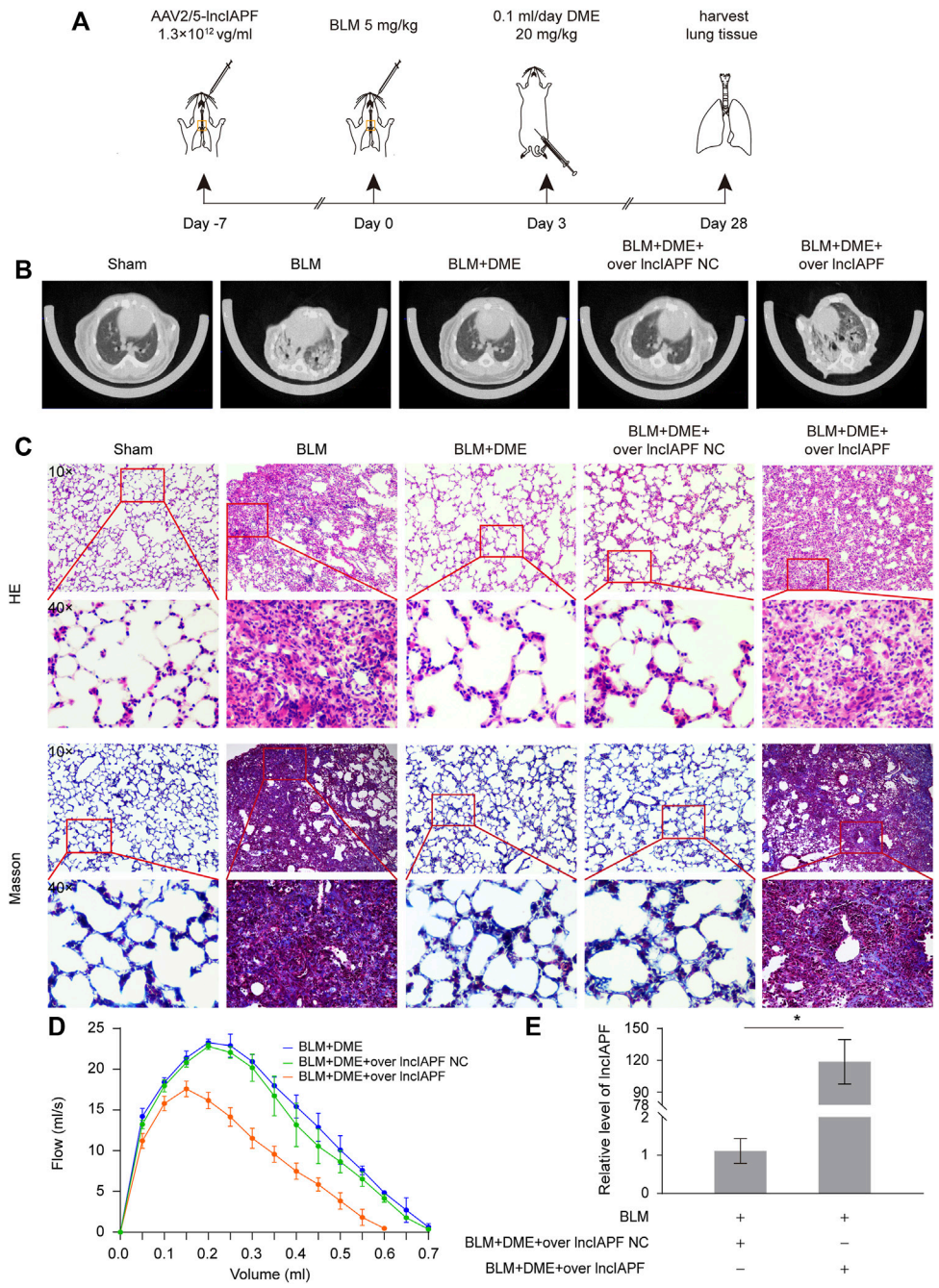

FIGURE 7
DME alleviated pulmonary fibrosis *via* downregulating the ATF3-lncIAPF–HuR–EZH2/STAT1/FOXK1 autophagic axis in mice **(A)** Schematic illustration of spraying overexpressed lncIAPF into mice **(B)** MicroCT images showed that the lungs of BLM-treated mice had evident honeycomb lung and uneven patchy shadows. DME treatment dramatically attenuated these fibrotic symptoms and lncIAPF overexpression reversed the effect of DME. **(C)** H&E and Masson staining showed that DME treatment lessened pulmonary fibrosis, but the alveolar walls in the lncIAPF overexpression group were thickened; collagen deposition increased, and the lung structure was changed. **(D)** FVC results showed that overexpression of lncIAPF worsened lung function and reversed the effect of DME on lung function. **(E)** qRT-PCR result showed that lncIAPF was highly expressed in the mouse model, indicating that adenovirus had been successfully constructed **(F)** In mice treated with overexpressed lncIAPF, the expression of fibrotic proteins (collagen, vimentin, and *a*-SMA) and autophagy-related proteins (EZH2, FOXK1, STAT1, P62, HuR, ATF3) increased, whereas that of E-cadherin, DRAM2, and GABARAP decreased compared with those in the BLM group. Each bar represents the mean ± SD; n = 6; *$p < 0.05$.

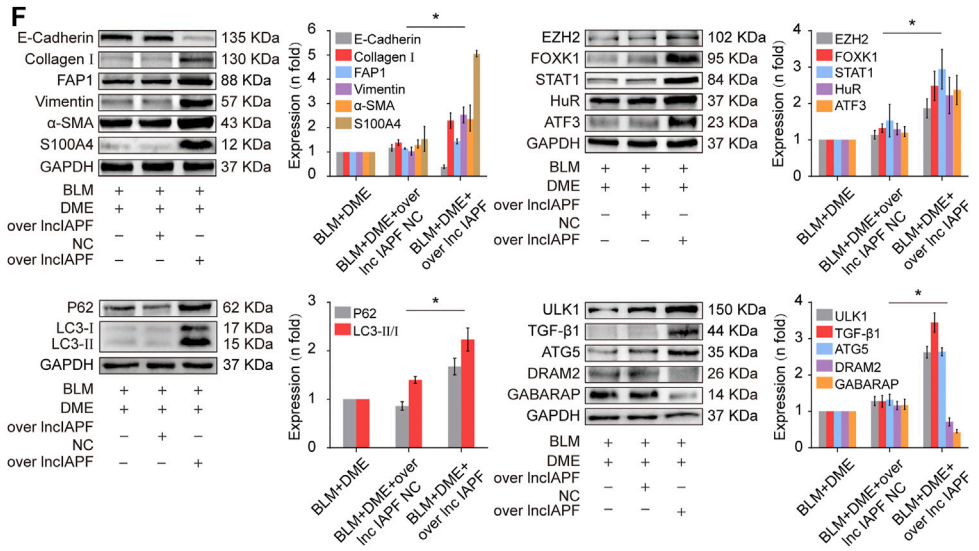

FIGURE 7
(Continued)

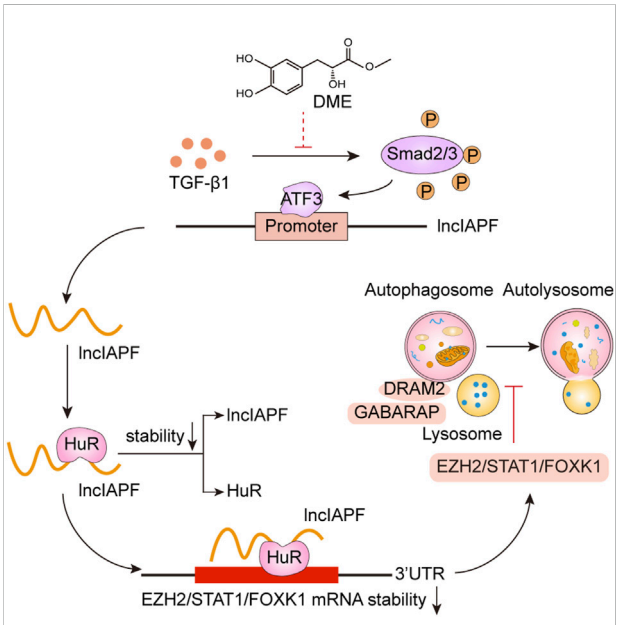

FIGURE 8
Therapeutic mechanism of DME treatment in pulmonary fibrosis.

HuR stability assay

1 × 10^6/ml MRC-5 cells were seeded in cell dishes. 2 ml serum-free medium containing 10 μg/ml cycloheximide was added into the cell samples. Cell proteins were extracted after cycloheximide treatment for different times. HuR and GAPDH protein levels were detected by Western blot.

RNA-binding protein immunoprecipitation analysis

RIP assay was performed by using the RNA immunoprecipitation kit (GENESEED, China) according to the manufacturer's instructions. The cell samples were collected and lysed by the lysis buffer containing protease inhibitors and RNase inhibitors. 100 μL supernatant was taken as input control, the negative control was normal rabbit anti-IgG antibody (Cell Signaling Technology, United States). The antibody was linked to the magnetic beads in advance to capture the antigen. Finally the RNA bound to the magnetic beads was eluted and purified for qRT-PCR analysis.

Chromatin immunoprecipitation PCR analysis

CHIP- PCR assay was performed by using the SimpleChIP® enzymatic chromatin IP kit (Cell Signaling Technology, United States) according to the manufacturer's instructions. The cell samples were collected and incubated with formaldehyde for 10 min. 2.5 M glycine was added and mixed. After centrifugation, the precipitation was prepared for nuclear preparation and chromatin digestion. The chromatin was immunoprecipitated with anti-ATF3 or rabbit IgG antibodies

and incubated overnight. 30 µl CHIP-grade protein G agarose beads was added and incubated for 2 h. NaCl and protease K were added and the enriched DNA-protein complex was de crosslinked to release DNA fragments. DNA was purified using a DNA centrifuge column and amplified by PCR. Primers for lncIAPF promoter were as follows: Forward-CTACCTTCAAGCCTTACTTCCTCCG, Reverse-GAATACAAGGCGCTATGCTAGGAAC.

Statistical analysis

Data were expressed as the means ± standard deviation (SD) and analyzed using the GraphPad Prism statistic software program. Differences between groups were assessed by two-sided Student's t-test. All experiments were repeated thrice. $p < 0.05$ was considered statistically significant.

Results

Danshensu methyl ester attenuated pulmonary fibrosis *In vivo* and *In vitro*

First, CCK-8 was used to evaluate the *in vitro* toxicity of DME. Human lung fibroblast MRC-5 cells were incubated in a medium containing different concentrations of DME for 24 and 48 h. Normal cell viability indicated that the IC50 of DME was approximately from 100 to 110 µg/ml at 24 h and 80–90 µg/ml at 48 h (Figure 2A). Then, 5 ng/ml of transforming growth factor β1 (TGF-β1) was used to establish a pulmonary fibrosis model in MRC-5 cells. MRC-5 cells were treated with TGF-β1 for 72 h, and then treated with different concentrations of DME (0, 2.5, 5, 7.5, 10, 15, 20 ug/mL) for 24 h and 48 h respectively. The results showed that DME inhibited TGF-β1-treated cells in a time- and concentration-dependent manner. Starting from the condition of 5 µg/ml DME-treated for 48 h, DME treatment showed a significant inhibitory effect (Figure 2B). The proliferation curve further confirmed that 5, 10, and 20 µg/ml of DME showed slight toxicity against normal cells (Figure 2C). Real-time cellular analysis (RTCA) experiment was performed to monitor the migration of TGF-β1-activated MRC-5 cells. The curves demonstrated that 5, 10, and 20 µg/ml of DME markedly inhibited the migration of cells treated with TGF-β1 (Figure 2D). The result of migration was further confirmed by scratch wound-healing assay by using an IncuCyte S3 instrument (Figure 2E). Western blot showed that DME decreased the expression level of differentiation-related proteins, including fibroblast activation protein 1 (FAP1) and S100 calcium-binding protein A4 (S100A4), and fibrotic markers, including vimentin, α-SMA, and collagen I and III (Figure 2F). Thus, 10 µg/ml of DME treated for 48 h was selected for further studies. These findings indicated that DME alleviated pulmonary fibrosis by inhibiting the differentiation of fibroblast into myofibroblast, myofibroblast proliferation and migration, and ECM deposition *in vitro*.

Then, the anti-pulmonary fibrotic ability of DME was assessed in BLM-treated mice (Figure 3A). Lung-function assessment revealed that DME treatment obviously promoted the forced vital capacity (FVC) of mice (Figure 3B). The images of the MicroCT system for small animals depicted that the honeycomb lung and uneven patchy shadows were evident in the BLM-treated group. The fibrotic symptoms were remarkably alleviated under DME treatment (Figure 3C). H&E staining displayed that BLM-treated mice had evident collagen deposition, damaged alveolar structure, and mild inflammatory cell infiltration. After DME treatment, collagen deposition was reduced, and the alveolar structure was clear and complete. Masson staining demonstrated that the alveolar structure of the treatment group was more complete, and collagen deposition was reduced in DME-treated mice (Figure 3D). Western blot indicated that DME reduced the expression level of pulmonary fibrotic proteins, including vimentin, collagen, and *a*-SMA, and differentiation-related proteins, including FAP1 and S100A4 (Figure 3E). The abovementioned results indicated the anti-pulmonary fibrotic ability of DME *in vivo*.

Danshensu methyl ester mitigated pulmonary fibrosis through downregulating lncIAPF–HuR complex to promote autophagy

Autophagy is repressed in pulmonary fibrosis. lncIAPF–HuR complex can promote pulmonary fibrogenesis through inhibiting autophagy. Thus, we explored if lncIAPF–HuR could be the target for DME action. The results of qRT-PCR illustrated that DME reduced the expression level of lncIAPF (Figure 4A). An overexpressed plasmid of lncIAPF (over lncIAPF) and an empty vector without lncIAPF (lncIAPF negative control) were designed to transfect into MRC-5 cells. The rescue experiment of Western blot indicated that lncIAPF overexpression reversed the downward expression of S100A4, FAP1, α-SMA, vimentin, and collagen I and III caused by DME (Figure 4B). Moreover, the rescue experiment of scratch assay confirmed that lncIAPF overexpression reversed the therapeutic effect of DME (Figure 4C). The effect of DME on autophagy was tested by using the tandem dual-fluorescence HBAD-mcherry-EGFP-LC3 method. Red fluorescence indicates autolysosomes in normal autophagy. Yellow fluorescence indicates autolysosomes in abnormal autophagy, which suggests that autolysosomes can form, but can not be degraded and autophagy is partially blocked. The yellow dots increased in the TGF-β1 group compared with the normal group. The red dots increased in the DME group compared with the TGF-β1 group, which indicated that DME promoted autophagy. The

rescue experiment further confirmed that lncIAPF overexpression reversed the enhanced effect of DME on autophagy (Figure 4D). Stable experiments demonstrated that DME weakened lncIAPF stability, and lncIAPF overexpression reversed the effect of DME on its stability (Figure 4E). The abovementioned findings indicated that DME attenuated pulmonary fibrosis *via* inhibiting lncIAPF to promote autophagy.

The regulatory mechanism of DME on the upstream signal pathway of lncIAPF was further explored. TGF-β1 signal transduction can be activated *via* the translocation of Smad2/3 in pulmonary fibrosis. Smad2/3 translocates from cytoplasm to nucleus *via* phosphorylation to realize TGF-β1 signal transduction. So we detected the expression of TGF-β1, Smad2/3 and p-Smad2/3. The result showed that DME inhibited TGF-β1 and p-Smad2/3, indicating DME inhibited TGF-β1 signal transduction directly (Figure 4F). Then, primers of the lncIAPF promoter were designed for CHIP-PCR to identify which transcription factor affected lncIAPF transcription under DME action. The data demonstrated that TGF-β1 enhanced the binding between the lncIAPF promoter region and activating transcription factor 3 (ATF3). The binding of the lncIAPF promoter region to ATF3 was partially blocked under DME action (Figure 4G). The results of qRT-PCR and Western blot further indicated that DME decreased ATF3 expression at mRNA and protein levels (Figure 4H). An overexpression plasmid ATF3 was designed and transfected into MRC-5 cells. The rescue experiment of Western blot indicated that ATF3 overexpression reversed the downward expression of S100A4, FAP1, α -SMA, vimentin, collagen I and collagen III caused by DME (Figure 4I). The abovementioned findings indicated that the inhibition of DME depended on ATF3 expression *via* TGF-β1 signal transduction.

Then, an RNA immunoprecipitation (RIP) experiment was performed to test whether lncIAPF bound to HuR and investigate the effect of DME on their binding. The results confirmed that lncIAPF bound to HuR, and the binding amount increased under TGF-β1 action and decreased under DME treatment (Figure 5A). HuR expression was verified by Western blot experiment. HuR expression increased in the model group and decreased in the DME treatment group (Figure 5B). The rescue experiment further demonstrated that lncIAPF overexpression increased HuR expression and reversed the downward trend caused by DME (Figure 5C). Meanwhile, a small interfering RNA plasmid of HuR (si-HuR) was designed and transfected into MRC-5 cells after transfection of overexpressing lncIAPF. The rescue experiment of Western blot indicated that HuR interference reversed the high expression of S100A4, FAP1, α-SMA, vimentin, collagen type I and collagen type III induced by lncIAPF overexpression (Figure 5D). The rescue experiment of scratch assay showed that interference with HuR reversed the trend of accelerated migration caused by lncIAPF overexpression (Figure 5E). The data indicated that the effect of DME was dependent on lncIAPF- HuR complex. HuR, as an RNA-binding protein, can enhance the stability of lncIAPF and increase its expression. The regulatory mechanism of DME on HuR *via* lncIAPF was further explored. First, the location of HuR in the cell was detected by nucleocytoplasmic separation and immunofluorescence experiments. The results showed that HuR primarily existed in the nucleus of normal cells. Under the action of TGF-β1 or overexpressed lncIAPF, HuR was transferred from the nucleus to the cytoplasm. DME blocked HuR nucleocytoplasmic translocation, but lncIAPF overexpression reversed this effect (Figures 5F,G), indicating that DME blocked HuR nucleocytoplasmic translocation *via* lncIAPF. Cycloheximide experiment verified that DME weakened HuR stability depending on lncIAPF (Figure 5H). Collectively, these studies demonstrated that DME attenuated pulmonary fibrosis by inhibiting the lncIAPF–HuR-mediated autophagic signaling pathway.

Danshensu methyl ester promoted autophagy by targeting the enhancer of zeste homolog 2, signal transducers and activators of transcription 1, and forkhead box K1

EZH2, STAT1, and FOXK1 are the target genes of HuR. Then, the effect of DME on autophagy through EZH2, STAT1, and FOXK1 was explored. The RIP experiment elucidated that the mRNAs of EZH2, STAT1, and FOXK1 bound to HuR, and the binding amount decreased under DME treatment compared with TGF-β1 treatment (Figure 6A). Half-life analysis revealed that DME treatment weakened the stability of EZH2, STAT1, and FOXK1 at the mRNA level, but lncIAPF overexpression reversed this trend, indicating that DME weakened the stability of EZH2, STAT1, and FOXK1 depending on lncIAPF (Figure 6B). Western blot detection showed that EZH2, STAT1, and FOXK1 decreased in the DME group compared with those in the TGF-β1/BLM group (Figure 6C). Autophagic marker proteins, such as P62, LC3I, and II, increased in the TGF-β1/BLM group and decreased in the DME group (Figure 6D). The rescue experiment showed that lncIAPF overexpression reversed this protein trend caused by DME, indicating that the enhancement effect of DME treatment on the target genes and autophagic flux was dependent on lncIAPF (Figure 6E).

Autophagosome accumulation was remarkably increased in pulmonary fibrosis (Figure 4D), indicating that autophagy was blocked in the later stage, and DME treatment promoted autophagy in pulmonary fibrosis. Thus, the effect of DME on autophagy was further explored. Autophagy-related gene 5 (ATG5) and unc-51-like kinase 1 (ULK1) play a role in the early stage of autophagy, and GABA type A receptor-associated protein (GABARAP) and DNA damage-regulated autophagy modulator 2 (DRAM2) contribute to the autophagosome–lysosome fusion in the later stage of

autophagy. The Western blot result displayed that ATG5 and ULK1 decreased *in vivo* and *in vitro* in the DME group compared with those in the TGF-β1 group. Moreover, GABARAP and DRAM2 levels increased *in vivo* and *in vitro* in the DME group compared with those in the TGF-β1 group (Figure 6F). The rescue experiment verified that lncIAPF overexpression reversed this protein trend caused by DME, indicating that the enhancement effect of DME treatment on autophagy was dependent on lncIAPF (Figure 6G).

Danshensu methyl ester alleviated pulmonary fibrosis *via* targeting lncIAPF–HuR-mediated autophagic signal pathway in mice

Rescue experiment was performed in mice to elucidate the action mechanism of DME targeting lncIAPF–HuR. The overexpressed lncIAPF was packaged into the adenovirus vector to spray into the mouse lung (Figure 7A). MicroCT images showed that the lungs of BLM-treated mice had evident honeycomb lung and uneven patchy shadows. DME treatment dramatically attenuated these fibrotic symptoms and lncIAPF overexpression reversed the effect of DME (Figure 7B). H&E and Masson staining presented the lung tissue structure and collagen deposition in mice. The results showed that DME treatment lessened pulmonary fibrosis, but the lncIAPF overexpression group had severe pulmonary fibrosis and more collagen deposition, which reversed the anti-pulmonary fibrosis of DME (Figure 7C). Lung function assessment revealed that lncIAPF overexpression worsened lung function, which reversed the effect of DME on lung function (Figure 7D). qRT-PCR data illustrated that lncIAPF overexpression increased lncIAPF expression and reversed the effect of DME on lncIAPF expression (Figure 7E). Western blot confirmed that lncIAPF overexpression increased the expression of fibrotic proteins (collagen, vimentin, and *a*-SMA), differentiation-related proteins (S100A4 and FAP1), and autophagy-related proteins (HuR, ATF3, EZH2, STAT1, FOXK1, P62, LC3I/II, and ULK1) and decreased DRAM2, GABARAP, and the epithelial marker protein E-cadherin, which reversed the effect of DME on these proteins (Figure 7F). The abovementioned finding indicated that DME alleviated pulmonary fibrosis in mice *via* downregulating the ATF3-lncIAPF–HuR–EZH2/STAT1/FOXK1 autophagic axis.

Discussion

Pulmonary fibrosis is characterized by fibroblast-to-myofibroblast differentiation, excessive proliferation and migration of myofibroblast, and accumulation of ECM components (Wu et al., 2020). Therefore, fibroblast-to-myofibroblast differentiation and excessive proliferation and migration of myofibroblast are the targets for anti-fibrotic drug development. For example, MBNL1 drives dynamic transition between fibroblasts and myofibroblasts, and tactical control of MBNL1 activity can alter fibrotic outcomes (Bugg et al., 2022). The methyl-CpG-binding domain 2 (MBD2) facilitates pulmonary fibrosis by orchestrating fibroblast-to-myofibroblast differentiation, and strategies aimed at silencing MBD2 can be potential therapeutic approaches for the prevention and treatment of pulmonary fibrosis (Wang et al., 2022). In addition, lncITPF accelerates fibroblast-to-myofibroblast differentiation to promote pulmonary fibrosis by targeting H3 and H4 histone acetylation in the ITGBL1 promoter depending on hnRNP-L (Song et al., 2019). Even, SARS-CoV-2 infection can drive fibroblast-to-myofibroblast transition leading to COVID-19 pulmonary fibrosis (Wang et al., 2021). Based on the results of atomic force microscopy, the mechanical stiffness of myofibroblast increases compared with normal fibroblast, which drives pulmonary fibrogenesis (Xu et al., 2022). In the present study, our results demonstrated that DME promoted autophagy to repress fibroblast-to-myofibroblast differentiation and proliferation and migration of myofibroblast *via* downregulating the lncIAPF–HuR-mediated autophagic axis (Figure 8). Mechanistically, DME inhibited ATF3 expression *via* TGF-β1 signal transduction leading to a decrease in lncIAPF transcription and stability. Moreover, DME blocked HuR nucleocytoplasmic translocation and promoted its degradation *via* downregulating lncIAPF, which markedly decreased the expression of HuR target genes such as negative autophagic regulators EZH2, STAT1, and FOXK1.

Autophagy is a normal cellular homeostatic process responsible for the lysosomal degradation of microorganisms, damaged organelles, and proteins that cannot be degraded by the ubiquitin–proteasome pathway (Klionsky et al., 2021; Ma et al., 2022). Abnormal autophagy contributes to the pathogenesis of human diseases targeting dysfunctional organelles, intracellular microbes, and pathogenic proteins (Levine and Kroemer., 2019). lncRNA-GBCDRlnc1 induces chemoresistance of gallbladder cancer cells by activating autophagy (Cai et al., 2019). The inhibition of lncRNA-Gm15834 attenuates autophagy-mediated myocardial hypertrophy *via* the miR-30b-3p/ULK1 axis in mice (Song et al., 2021). Under normal lung conditions, autophagy is critical for inhibiting spontaneous pulmonary inflammation and for the response of pulmonary stress. However, persistent and inefficient autophagy can promote lung injury (Racanelli et al., 2018). ATG4b-deficient mice displayed that autophagy disruption contributed to BLM-induced lung fibrosis (Cabrera et al., 2015). Annexin A2 is a specific BLM target to induce pulmonary fibrosis by impeding TFEB-mediated autophagic flux (Wang et al., 2018). Regarding lncRNA-related autophagy in pulmonary fibrosis, studies have reported that lncRNAs are involved in autophagy regulation. lncRNA-MEG3 restrained pulmonary fibrosis induced by NiO NPs *via* regulating autophagy mediated by the Hedgehog

signaling pathway (Gao et al., 2022). lncIAPF promotes fibroblast-to-myofibroblast differentiation to accelerate pulmonary fibrosis through lncIAPF-mediated autophagic flux *in vivo* and *in vitro* in patients with idiopathic pulmonary fibrosis (IPF). The receiver operating characteristic curve (ROC) between lncIAPF and FVC shows that the sensitivity and specificity values are 87.5% and 75.0% in patients with IPF, respectively. The area under the ROC curve is 0.879 (Zhang J et al., 2022). In this study, we further proved that the lncIAPF–HuR complex can be a target related to autophagy for drug action. Autophagy is a continuous dynamic process and mainly contains 4 steps: formation of phagocytes, formation of autophage, formation of autophagosome and degradation of autophagosome. Our results showed that autophagosome accumulation was remarkably increased in pulmonary fibrosis, indicating that autophagy was blocked in the later stage, and DME treatment promoted autophagy *via* downregulating lncIAPF–HuR siganal pathway to mitigate pulmonary fibrosis.

HuR and its target genes EZH2, STAT1, and FOXK1 are negative autophagic regulators. m^6A reader YTHDC1 interacts and cooperates with HuR in modulating autophagy by targeting SQSTM1 in diabetic skin (Liang et al., 2022). HuR usually serves as a RNA binding protein to regulate the stability and translation of messenger RNAs (Xiao et al., 2019). Our results indicated that DME weakened HuR stability to promote autophagy *via* inhibiting lncIAPF stability and transcription. The collected evidence indicates that overexpression or mutation of EZH2, STAT1, and FOXK1 is closely related to the occurrence and poor prognosis of multiple diseases; thus, they are attractive therapeutic targets for the treatment of diseases (Bowman et al., 2014; Kong et al., 2020; Patoli et al., 2020; Zhang J et al., 2022). Our mechanistic dissection revealed that DME inhibits EZH2, STAT1, and FOXK1 to block autophagy flux *via* weakening lncIAPF–HuR complex stability.

Conclusion

In conclusion, the novel compound DME prepared by our group has remarkable anti-fibrotic effects *in vivo* and *in vitro*, and the lncIAPF–HuR can be the target for drug action. Our study provides valuable insights into the design of new drugs and presents candidate therapeutic targets for drug treatment.

Data availability statement

The original contributions presented in the study are included in the article/Supplementary Material, further inquiries can be directed to the corresponding authors.

Ethics statement

The animal study was reviewed and approved by the Ethics Committee of Animal Experiments of Binzhou Medical University (Permit No. 2020-201).

Author contributions

XS and CL designed the project and drafted the manuscript. GQ prepared the compound DME. QZ, JW, and YJ performed the experiments. JL, DY, HL, and JZ analyzed the data and provided suggestions.

Funding

This work was supported by the National Natural Science Foundation of China (82170085, 81970064, 81870001, 81670064, and 31670365), the Natural Science Foundation of Shandong Province (ZR2020MH009, ZR2020MH010), and the regenerative medicine research program of Xu Rongxiang (50012305179).

Conflict of interest

The authors declare that the research was conducted in the absence of any commercial or financial relationships that could be construed as a potential conflict of interest.

Publisher's note

All claims expressed in this article are solely those of the authors and do not necessarily represent those of their affiliated organizations, or those of the publisher, the editors and the reviewers. Any product that may be evaluated in this article, or claim that may be made by its manufacturer, is not guaranteed or endorsed by the publisher.

References

Atianand, M. K., Hu, W., Satpathy, A. T., Shen, Y., Ricci, E. P., Alvarez-Dominguez, J. R., et al. (2016). A long noncoding RNA lincRNA-EPS acts as a transcriptional brake to restrain inflammation. *Cell.* 165 (7), 1672–1685. doi:10.1016/j.cell.2016.05.075

Aveyard, P., Gao, M., Lindson, N., Hartmann-Boyce, J., Watkinson, P., Young, D., et al. (2021). Association between pre-existing respiratory disease and its treatment, and severe COVID-19: A population cohort study. *Lancet. Respir. Med.* 9 (8), 909–923. doi:10.1016/S2213-2600(21)00095-3

Bando, T., Takei, R., Mutoh, Y., Sasano, H., Yamano, Y., Yokoyama, T., et al. (2022). Acute exacerbation of idiopathic pulmonary fibrosis after SARS-CoV-2 vaccination. *Eur. Respir. J.* 59 (3), 2102806. doi:10.1183/13993003.02806-2021

Bester, A. C., Lee, J. D., Chavez, A., Lee, Y. R., Nachmani, D., Vora, S., et al. (2018). An integrated genome-wide CRISPRa approach to functionalize lncRNAs in drug resistance. *Cell.* 173 (3), 649–664. e20. doi:10.1016/j.cell.2018.03.052

Bowman, C. J., Ayer, D. E., and Dynlacht, B. D. (2014). Foxk proteins repress the initiation of starvation-induced atrophy and autophagy programs. *Nat. Cell. Biol.* 16 (12), 1202–1214. doi:10.1038/ncb3062

Bugg, D., Bailey, L., Bretherton, R. C., Beach, K. E., Reichardt, I. M., Robeson, K. Z., et al. (2022). MBNL1 drives dynamic transitions between fibroblasts and myofibroblasts in cardiac wound healing. *Cell. Stem Cell.* 29 (3), 419–433.e10. e10. doi:10.1016/j.stem.2022.01.012

Cabrera, S., Maciel, M., Herrera, I., Nava, T., Vergara, F., Gaxiola, M., et al. (2015). Essential role for the ATG4B protease and autophagy in bleomycin-induced pulmonary fibrosis. *Autophagy* 11 (4), 670–684. doi:10.1080/15548627.2015.1034409

Cai, Q., Wang, S., Jin, L., Weng, M., Zhou, D., Wang, J., et al. (2019). Long non-coding RNA GBCDRlnc1 induces chemoresistance of gallbladder cancer cells by activating autophagy. *Mol. Cancer* 18 (1), 82. doi:10.1186/s12943-019-1016-0

de Goede, O. M., Nachun, D. C., Ferraro, N. M., Gloudemans, M. J., Rao, A. S., Smail, C., et al. (2021). Population-scale tissue transcriptomics maps long non-coding RNAs to complex disease. *Cell.* 184 (10), 2633–2648.e19. doi:10.1016/j.cell.2021.03.050

Fukushima, K., Satoh, T., Sugihara, F., Sato, Y., Okamoto, T., Mitsui, Y., et al. (2020). Dysregulated expression of the nuclear exosome targeting complex component Rbm7 in nonhematopoietic cells licenses the development of fibrosis. *Immunity* 52 (3), 542–556. e13. doi:10.1016/j.immuni.2020.02.007

Gao, Q., Chang, X., Yang, M., Zheng, J., Gong, X., Liu, H., et al. (2022). LncRNA MEG3 restrained pulmonary fibrosis induced by NiO NPs via regulating hedgehog signaling pathway-mediated autophagy. *Environ. Toxicol.* 37 (1), 79–91. doi:10.1002/tox.23379

Hua, J. T., Ahmed, M., Guo, H., Zhang, Y., Chen, S., Soares, F., et al. (2018). Risk SNP-mediated promoter-enhancer switching drives prostate cancer through lncRNA PCAT19. *Cell.* 174 (3), 564–575. doi:10.1016/j.cell.2018.06.014

Johannson, K. A., Chaudhuri, N., Adegunsoye, A., and Wolters, P. J. (2021). Treatment of fibrotic interstitial lung disease: Current approaches and future directions. *Lancet* 398 (10309), 1450–1460. doi:10.1016/S0140-6736(21)01826-2

Klionsky, D. J., Abdel-Aziz, A. K., Abdelfatah, S., Abdellatif, M., Abdoli, A., Abel, S., et al. (2021). Guidelines for the use and interpretation of assays for monitoring autophagy (4th edition)1. *Autophagy* 17 (1), 1–382. doi:10.1080/15548627.2020.1797280

Kong, E., Kim, H. D., and Kim, J. (2020). Deleting key autophagy elongation proteins induces acquirement of tumor-associated phenotypes via ISG15. *Cell. Death Differ.* 27 (8), 2517–2530. doi:10.1038/s41418-020-0519-y

Levine, B., and Kroemer, G. (2019). Biological functions of autophagy genes: A disease perspective. *Cell.* 176 (1-2), 11–42. doi:10.1016/j.cell.2018.09.048

Liang, D., Lin, W. J., Ren, M., Qiu, J., Yang, C., Wang, X., et al. (2022). m6A reader YTHDC1 modulates autophagy by targeting SQSTM1 in diabetic skin. *Autophagy* 18 (6), 1318–1337. doi:10.1080/15548627.2021.1974175

Lin, Z., Sun, L., Xie, S., Zhang, S., Fan, S., Li, Q., et al. (2018). Chemotherapy-induced long non-coding RNA 1 promotes metastasis and chemo-resistance of TSCC via the wnt/β-catenin signaling pathway. *Mol. Ther.* 26 (6), 1494–1508. doi:10.1016/j.ymthe.2018.04.002

Ma, X., Lu, C., Chen, Y., Li, S., Ma, N., Tao, X., et al. (2022). CCT2 is an aggrephagy receptor for clearance of solid protein aggregates. *Cell.* 185 (8), 1325–1345.e22. e22. doi:10.1016/j.cell.2022.03.005

Moss, B. J., Ryter, S. W., and Rosas, I. O. (2022). Pathogenic mechanisms underlying idiopathic pulmonary fibrosis. *Annu. Rev. Pathol.* 17, 515–546. doi:10.1146/annurev-pathol-042320-030240

Patoli, D., Mignotte, F., Deckert, V., Dusuel, A., Dumont, A., Rieu, A., et al. (2020). Inhibition of mitophagy drives macrophage activation and antibacterial defense during sepsis. *J. Clin. Invest.* 130 (11), 5858–5874. doi:10.1172/JCI130996

Quinodoz, S. A., Jachowicz, J. W., Bhat, P., Ollikainen, N., Banerjee, A. K., Goronzy, I. N., et al. (2021). RNA promotes the formation of spatial compartments in the nucleus. *Cell.* 184 (23), 5775–5790.e30. doi:10.1016/j.cell.2021.10.014

Racanelli, A. C., Kikkers, S. A., Choi, A., and Cloonan, S. M. (2018). Autophagy and inflammation in chronic respiratory disease. *Autophagy* 14 (2), 221–232. doi:10.1080/15548627.2017.1389823

Savary, G., Dewaeles, E., Diazzi, S., Buscot, M., Nottet, N., Fassy, J., et al. (2019). The long noncoding RNA DNM3OS is a reservoir of FibromiRs with major functions in lung fibroblast response to TGF-β and pulmonary fibrosis. *Am. J. Respir. Crit. Care Med.* 200 (2), 184–198. doi:10.1164/rccm.201807-1237OC

Si, J., Ma, Y., Lv, C., Hong, Y., Tan, H., and Yang, Y. (2021). HIF1A-AS2 induces osimertinib resistance in lung adenocarcinoma patients by regulating the miR-146b-5p/IL-6/STAT3 axis. *Mol. Ther. Nucleic Acids* 26, 613–624. doi:10.1016/j.omtn.2021.09.003

Song, C., Qi, H., Liu, Y., Chen, Y., Shi, P., Zhang, S., et al. (2021). Inhibition of lncRNA Gm15834 attenuates autophagy-mediated myocardial hypertrophy via the miR-30b-3p/ULK1 Axis in mice. *Mol. Ther.* 29 (3), 1120–1137. doi:10.1016/j.ymthe.2020.10.024

Song, X., Xu, P., Meng, C., Song, C., Blackwell, T. S., Li, R., et al. (2019). lncITPF promotes pulmonary fibrosis by targeting hnRNP-L depending on its host gene ITGBL1. *Mol. Ther.* 27 (2), 380–393. doi:10.1016/j.ymthe.2018.08.026

Wang, K., Zhang, T., Lei, Y., Li, X., Jiang, J., Lan, J., et al. (2018). Identification of ANXA2 (annexin A2) as a specific bleomycin target to induce pulmonary fibrosis by impeding TFEB-mediated autophagic flux. *Autophagy* 14 (2), 269–282. doi:10.1080/15548627.2017.1409405

Wang, S., Yao, X., Ma, S., Ping, Y., Fan, Y., Sun, S., et al. (2021). A single-cell transcriptomic landscape of the lungs of patients with COVID-19. *Nat. Cell. Biol.* 23 (12), 1314–1328. doi:10.1038/s41556-021-00796-6

Wang, Y., Zhang, L., Huang, T., Wu, G. R., Zhou, Q., Wang, F. X., et al. (2022). The methyl-CpG-binding domain 2 facilitates pulmonary fibrosis by orchestrating fibroblast to myofibroblast differentiation. *Eur. Respir. J.* 60, 2003697. doi:10.1183/13993003.03697-2020

Wu, H., Yu, Y., Huang, H., Hu, Y., Fu, S., Wang, Z., et al. (2020). Progressive pulmonary fibrosis is caused by elevated mechanical tension on alveolar stem cells. *Cell.* 180 (1), 107–121. doi:10.1016/j.cell.2019.11.027

Xiao, L., Li, X. X., Chung, H. K., Kalakonda, S., Cai, J. Z., Cao, S., et al. (2019). RNA-binding protein HuR regulates paneth cell function by altering membrane localization of TLR2 via post-transcriptional control of CNPY3. *Gastroenterology* 157 (3), 731–743. doi:10.1053/j.gastro.2019.05.010

Xu, P., Zhang, J., Wang, M., Liu, B., Li, R., Li, H., et al. (2022). hnRNPL-activated circANKRD42 back-splicing and circANKRD42-mediated crosstalk of mechanical stiffness and biochemical signal in lung fibrosis. *Mol. Ther.* 30 (6), 2370–2387. doi:10.1016/j.ymthe.2022.01.045

Zhang, J., Wang, H., Chen, H., Li, H., Xu, P., Liu, B., et al. (2022). ATF3 -activated accelerating effect of LINC00941/lncIAPF on fibroblast-to-myofibroblast differentiation by blocking autophagy depending on ELAVL1/HuR in pulmonary fibrosis. *Autophagy*, 1–20. doi:10.1080/15548627.2022.2046448

Zhang, Q., Yang, H., Feng, Q., Cao, J., Zhang, Y., Li, L., et al. (2022). Focus on the classical and non-classical functions of EZH2: Guide the development of inhibitors and degraders. *Pharmacol. Res.* 178, 106159. doi:10.1016/j.phrs.2022.106159

Zhao, X., Qu, G., Song, C., Li, R., Liu, W., Lv, C., et al. (2018). Novel formononetin-7-sal ester ameliorates pulmonary fibrosis via MEF2c signaling pathway. *Toxicol. Appl. Pharmacol.* 356, 15–24. doi:10.1016/j.taap.2018.07.005

frontiers | Frontiers in Pharmacology

TYPE Original Research
PUBLISHED 03 November 2022
DOI 10.3389/fphar.2022.986199

OPEN ACCESS

EDITED BY
Enlong M. A.,
Shenyang Pharmaceutical University, China

REVIEWED BY
Xiao-Mei Li,
The First Affiliated Hospital of University of Science and Technology of China (USTC), China
Wenfeng Tan,
Nanjing Medical University, China

*CORRESPONDENCE
Hong-Yan Wen,
wenhongyan@sxmu.edu.cn

†These authors have contributed equally to this work and share first authorship

SPECIALTY SECTION
This article was submitted to Respiratory Pharmacology, a section of the journal Frontiers in Pharmacology

RECEIVED 04 July 2022
ACCEPTED 21 October 2022
PUBLISHED 03 November 2022

CITATION
Guo R-H, Cheng H, Zhang X-Y, Yu Z, Wang G-H, Hao S-Y, Gao X-P and Wen H-Y (2022), Changes in peripheral T-lymphocyte subsets and serum cytokines in patients with systemic sclerosis.
Front. Pharmacol. 13:986199.
doi: 10.3389/fphar.2022.986199

Changes in peripheral T-lymphocyte subsets and serum cytokines in patients with systemic sclerosis

Rong-Hong Guo†, Hao Cheng†, Xiao-Ying Zhang, Zhen Yu, Guang-Hui Wang, Shu-Ya Hao, Xiao-Peng Gao and Hong-Yan Wen*

Department of Rheumatology, Shanxi Medical University, The Second Hospital of Shanxi Medical University, Taiyuan, Shanxi, China

Objective: T cells represent a predominant cell type in autoimmune disease. However, their exact roles are not fully clear in systemic sclerosis (SSc). This study aimed to mainly investigate the alteration in the absolute numbers of T-lymphocyte subsets and the serum levels of cytokines in SSc patients.

Methods: A total of 76 patients with SSc and 76 age- and sex-matched healthy controls (HCs) were enrolled. The levels of circulating T cell subsets and serum cytokines were measured by flow cytometry. T cell subsets or serum cytokines correlations with disease activity and organ involvement were analyzed.

Results: The absolute numbers of Th2 and Treg cells in SSc patients were lower than those in HCs ($p < 0.05$), resulting in the ratios of Th1/Th2 [25.01 (12.24, 38.61) vs. 11.64 (6.38, 20.34)] and Th17/Treg [0.42 (0.17, 0.66) vs. 0.17 (0.13, 0.29)] were increased significantly ($p < 0.001$). The absolute numbers of total T, Th, and Treg cells were negatively correlated with CRP ($r = -0.406$, $p = 0.002$; $r = -0.263$, $p < 0.05$; $r = -0.367$ $p < 0.01$). The serum levels of IL-2, SIL-2R, IL-6, IL-10, INF-γ, and TNF-α were significantly higher than those in HCs ($p < 0.001$). Increasing IL-2 in the wake of the augment of ESR ($r = 0.671$, $p = 0.004$), so did IL-6 ($r = 0.378$, $p < 0.05$). The ratio of Th17/Treg in SSc-ILD patients had lower levels than that in other patients [0.35 (0.14, 0.53) vs. 0.64 (0.26, 0.93) $p = 0.028$]; Treg cells were lessened in patients with Raynaud's phenomenon relative to controls [3.00 (2.41, 4.28) vs. 3.55 (2.86, 4.53) $p < 0.05$]. The levels of IL-2, IL-10 and INF-γ [3.32 (1.05,11.73) vs. 2.32 (0.44,6.45), $p = 0.045$], [8.08 (3.63, 355,77) vs. 4.89 (0.78, 21.44), $p = 0.02$], [6.31 (2.66, 44.03) vs. 4.03 (0.22, 16.96), $p = 0.009$] were elevated in patients with arthralgia, while the level of Th17 was decreased [0.62 (0.20,2.16) vs. 1.26 (0.22,10.93), $p = 0.026$]. ROC curve analysis yielded an optimal cut-off IL-2, IL-10, and INF-γ levels of 2.67, 5.93, and 5.32 pg/ml for the presence of arthralgia.

Conclusion: We exhibited abnormalities in T subsets and the production of their cytokines in SSc, as compared with those in HCs. This may allow the pathogenesis of SSc and the development of novel therapeutic interventions aimed at targeting these cells and the cytokines they produce.

KEYWORDS

T-lymphocyte subsets, cytokines, systemic sclerosis, interstitial lung disease (ILD), arthralgia

Introduction

Systemic sclerosis (SSc) is a complex and heterogeneous autoimmune connective disease characterized by vascular abnormalities, autoimmunity, and extensive fibrosis of the skin and internal organs. It is universally accepted that the pathophysiology of SSc was a progressive self-amplifying process, which first started the microvascular damage, then run an autoimmune response, and was followed by progressive fibrosis (Cutolo et al., 2019). There is growing evidence of epigenetic abnormalities in this intractable disease, including specific modifications affecting the three main cell types that influence SSc pathogenesis: immune cells, endothelial cells, and fibroblasts (Tsou et al., 2021). Many patients have higher mortality due to vital organ involvement such as interstitial fibrosis, pulmonary hypertension, and renal crisis, which can also symptoms that severely affect the quality of life, such as Raynaud's phenomenon, digital ulcerations, and arthralgia (Georges et al., 2006). It is a challenge for physicians who diagnose in the early oligosymptomatic stage of SSc and understand the pathogenesis for developing new targeted therapies (Herrick et al., 2017).

T cells have been reported to modulate the development of autoimmunity, inflammation, and fibrosis by the secretion of cytokines. It also has been found to be necessary to produce autoantibodies against a variety of nuclear proteins in SSc (Stochmal et al., 2020). Studies conducted in the progression of SSc have led to the recognition that T helper (TH) cells are involved in the early inflammatory response and late fibrotic phases by producing cytokines and interacting with fibroblasts (O'Reilly et al., 2012). Abnormal levels of T cell-derived cytokines, which act as humoral mediators during the immune response, have been found in the serum of SSc patients (Baraut et al., 2012). The concept of polarization of Th1/Th2 has been widely known as the classical pattern, Th1 cell-derived cytokines (such as IFN-γ, TNF-α, IL-1, IL-2, and IL-12) participate in pro-inflammatory responses, whereas Th2 cell-derived cytokines (IL-4, IL-13, IL-5, IL-6, and IL-10) promote the overproduction of collagen by fibroblasts (Baraut et al., 2010). Thus, Th2 is mostly involved in fibrosis, whereas Th1 rather induces inflammation at the early stages of SSc. Indeed, several cell types can produce cytokines, including $CD8^+$ T, dendritic, Th17, and regulator T (Treg) cells. Understanding the mechanisms that generate this pattern of immune response and analyzing the levels of cytokines as diagnostic and prognostic markers in SSc patients is significant.

This study aimed to investigate the alteration of peripheral T-lymphocyte subpopulations and serum cytokines in SSc patients. We exhibited abnormalities in these cells and the production of cytokines by them, as compared with NCs. We observed the correlation between cytokines with disease activity and organ involvement. Furthermore, abnormal expression of cytokines has joint diagnostic significance. This may allow the pathogenesis of SSc and the development of novel therapeutic interventions aimed at targeting these cells and the cytokine they produce.

Materials and methods

Patients and controls

A total of 76 SSc patients enrolled, who visited the Rheumatology and Immunology Department of the Second Hospital of Shanxi Medical University from January 2018 to December 2020, and enrolled in the study were initial treatment and aged between 18 and 80 years. The diagnosis of SSc was based on the American College of Rheumatology/European League Against Rheumatism (ACR/EULAR) classification criteria (van den Hoogen et al., 2013). The patients were excluded from this study if they were suffering from malignant disease, had a history of malignancy, had a recent clinically significant infection, or had any other connective tissue disease. We also included 76 healthy controls (HCs), who visited the physical examination center of our hospital during the same period, had no rheumatic immunological and family history, and were matched with SSc patients in age and gender. Each subject provided a signed consent form. Peripheral blood and serum samples were taken; the clinical and laboratory indexes and auto-antibodies were detected using freshly blood samples at the same time. Our study was approved by the Ethics Committee of the Shanxi Medical University Second Affiliated Hospital and all candidates have signed informed consent. (No.2019YX009).

Clinical measurements

The clinical data of SSc patients were collected through retrospective medical records. Disease duration, which is the clinical period of the disease, was defined as the period from the first appearance of symptoms and signs to this visit. Esophageal dysfunction was defined as symptoms of acid reflux heartburn or findings of reflux esophagitis on gastrointestinal endoscopy. Cardiovascular diseases were assessed by color Doppler echocardiography (EF, ECO, PHILIPS EPIQ7C). The diagnosis of interstitial lung disease (ILD) was determined by a review of a high-resolution computed tomography scan (HRCT, GE DiscoveryRT). Lung involvement and fibrosis

were evaluated using HRCT, which has four features: single ground glass lesions, ground glass lesions and reticular nodular lesions (mixed pattern), single reticular nodular lesions (reticular-nodular), and honeycomb changes. Diagnosed renal involvement with blood pressure exceeding 140/90 mmHg and decreased renal function (Renal dysfunction was defined as an increase in serum creatinine concentration of more than 30% above baseline levels at any study time point). In addition, the presence of joint contractures and Raynaud's phenomenon were noted.

Flow cytometry

Th1, Th2, and Th17 Cell cultures and Labeling: An 80 μl blood sample together with 10 μl phorbol myristate acetate working solution (final concentration, 30 ng/ml), 10 μl ionomycin working solution (final concentration, 750 ng/ml), and 1 μl GolgiStop was incubated at 37°C and 5% CO2 for 5 h. The samples were then divided into two tubes, followed by staining with anti-CD4-FITC antibodies at room temperature in the dark for 30 min. To the tubes was added 1 ml freshly prepared fixation/permeabilization solution; the tubes were then placed in an incubator at 4°C in the dark for 30 min. Anti-IL-4-PE and anti-interferon gamma (IFN-γ)-APC were added to tube A; Anti-FITC-CD4 and anti-IFN-γ-APC (intracellular staining) were used to detect Th1 cells, while anti-FITC-CD4, and anti-IL-4-PE (intracellular staining) were used to detect Th2 cells. Anti-human IL-17-PE (intracellular staining) was added to tube B for Th17-cell analysis. The two tubes of cells were stored at room temperature for 30 min in the dark and then washed with phosphate-buffered saline (PBS). The absolute numbers of $CD4^+$ T lymphocyte subsets were automatically detected using BD Multitest software (BD Biosciences, Franklin Lakes, NJ, United States). All immunofluorescence antibodies were purchased from BD Biosciences.

Detection of Treg Cells: Anti-CD4-FITC and anti-CD25-APC were added to an 80 μl blood sample and incubated at room temperature in the dark for 30 min. Then, 1 ml freshly prepared fixation/permeabilization solution was added to each tube, mixed, and incubated at 4°C for 30 min AntiFOXP3-PE (intracellular staining) was added and incubated at room temperature for 30 min in the dark, followed by washing with PBS and detection of Treg cells using flow cytometry. All immunofluorescence antibodies were purchased from BD Biosciences.

Flow cytometry: The stained cells were measured using flow cytometry (Calibur; BD Biosciences) within 24 h. Based on the scatter plot of the forward angular scattered light relative to the lateral angular dispersive light (side scatter (SSC)), the lymphocytes were gated to distinguish them. CD4 was used to distinguish $CD4^+$ T cells from the SSc gate; 10,000 cells from the gate were taken. The relative percentages were obtained and analyzed using CellQuest software. The absolute number of cells in each subgroup was calculated using the following equation: absolute cell number = percentage of positive cells in each subset × the absolute number of $CD4^+$ T cells (cells/μl) cells/μl whole blood.

Measurement of laboratory assessment

C3 and C4 complement levels, total serum immunoglobulin titers, and Erythrocyte Sedim entation Rate (ESR) were measured by nephelometry. The serum was separated from 4 ml venous blood after 1–2 h and stored at −20°C. The levels of serum cytokines [interleukin-2 (IL-2), IL-4, IL-6, IL-10, tumor necrosis factor-α (TNF-α), interferon-γ (IFN-γ), and IL-17] in SSc were measured using flow cytometry. A cytometric bead array (CBA) kit was purchased from Jiangsu Sage Biotechnology Co. Ltd. (Jiangsu, China) and used according to the manufacturer's instructions; the results were expressed as pg/ml.

Statistical analysis

Dichotomous variables were expressed as percentages and absolute frequencies, and continuous features were expressed as mean ± standard deviation (SD) or median four quantile method [M (P25, P75)]. The count data were measured using the chi-square goodness-of-fit test. The independent sample *t*-test was used for comparisons between the two groups. Nonnormal distribution data were performed using the Mann–Whitney's *U*-test for the comparisons of differences between groups, using the Kruskal-Wallis H test among multiple groups. Correlation analysis was performed using Spearman's rank correlation coefficient. All reported p values were 2-sided and were not adjusted for multiple testing. The level of significance was set at $p < 0.05$. All analyses were conducted using SPSS software version 26.0 (IBM, Armonk, NY, United States).

Results

Patients' disposition and baseline characteristics

Clinical data on the 76 patients with SSc were shown in Table 1. Of the 76 patients, 9.21% were male, and 90.79% were female. The average age of disease onset was 56.47 ± 12.42 years. The average hospitalization time was 15.60 ± 10.09 days. The course of the disease was 8.00 (3.00, 11.00) years. SSc was clinically classified into three groups: patients with diffuse cutaneous SSc (dcSSc) (65, 85.83%), an overlapping syndrome in which multiple diseases occur simultaneously (9, 11.84%), and limited cutaneous SSc (lcSSc) (2, 2.63%). Our cohort of patients

10.3389/fphar.2022.986199

TABLE 1 Overview of patients with SSc and healthy controls (HCs).

Clinical data	SSc patients	HCs	*p* Value
Age at disease onset (years)	56.47 ± 12.42	53.63 ± 8.10	0.097
The hospitalization time (days)	15.60 ± 10.09	—	—
The course of the disease (years)	8.00 (3.00,11.00)	—	—
Male	9.21% (7/76)	10.53% (8/76)	0.786
Female	90.79% (69/76)	89.47% (68/76)	0.786
ESR (mm/h)	22.50 (13.00,47.00)	9.00 (5.00,14.00)	**<0.001**
CRP (mg/L)	6.92 (2.01,13.05)	2.89 (1.33,3.56)	**<0.001**
Immunoglobulin G (g/L)	11.80 (9.28,14.15)	10.65 (8.61,12.45)	0.107
PLT (*10^9/L)	198.50 (153.00,265.25)	238.00 (212.00,291.50)	**0.008**
C3 (g/L)	0.78 (00.67,0.89)	—	—
C4 (g/L)	0.17 (0.13,0.21)	—	—
Anti-nuclear antibodies	76.32% (58/76)	—	—
Anti-centromere antibodies	7.89% (6/76)	—	—
Anti-Scl-70 antibodies	25% (19/76)	—	—
Anti-Ro52 antibodies	10.53% (8/76)	—	—
No. of organs affected	32.89% (26/76)	—	—
Organ involvement	67.1% (51/76)	—	—
Cardiovascular diseases	11.8% (7/76)	—	—
Pulmonary disease	65.78% (50/76)	—	—
Gastrointestinal disease	11.8% (7/76)	—	—
Renal involvement	9.21% (7/76)	—	—
Arthralgia	31.58% (24/76)	—	—
Raynaud's phenomenon	86.84% (66/76)	—	—
diffuse cutaneous SSc (dcSSc)	85.83% (65/76)	—	—
overlapping syndrome	11.84% (5/76)	—	—
limited cutaneous SSc (lcSSc)	2.63% (2/76)	—	—

*Among those with active disease. Results are given as mean ± SD, M (P25, P75) or percentage; ESR, erythrocyte sedimentation rate; CRP, C-reactive protein; PLT, platelet; Anti-Scl-70, Anti-topoisomerase I antibody; Bold values mean statistical significance.

with SSc represented untreated patients with diverse disease presentations, with some patients having none of the organs affected (32.89%), and others having a more systemic multiorgan disease (e.g., cardiovascular diseases, pulmonary disease, gastrointestinal disease, and renal involvement) (see Table 1). The proportion of patients who had ILD was 65.79%, while patients with cardiovascular diseases were 11.84%. Other involvement included arthralgia and Raynaud's phenomenon were 31.58% and 86.84% in the study subjects respectively. Anti-nuclear antibodies were positive in 76.32% of the patients. Among them, 7.89%, 25%, and 10.53% were also positive for anti-centromere antibodies (ACA), anti-Scl-70 antibodies, and anti- Ro52 antibodies, respectively (Table 1). The values of each inflammatory indicator in SSc patients and HCs were shown in Table 1. Among them, ESR (22.50 (13.00,47.00) vs. 9.00 (5.00,14.00) mm/h) and CRP (6.92 (2.01,13.05) vs. 2.89 (1.33,3.56) mg/L) in SSc were higher compared with HCs. However, the value of PLT (198.50 (153.00,265.25) *109/L vs. 238.00 (212.00,291.50) *109/L) was the opposite.

Differences in T-lymphocyte subsets and cytokines between patients and healthy controls

The values of T-lymphocyte subsets and cytokines in SSc patients and HCs were shown in Figure 1. For analyzing the changes of the adaptive immune cells in peripheral blood in SSc patients, we simultaneously quantified the T and B cells of 76 patients. Although the numbers of both T and B cells were prominent, the absolute numbers of T cells were greater than those of B cells. Among them, total T cells in SSc were lower than those in HCs. Given the varied literature regarding CD4+T cell subsets in the context of SSc, we directly quantified CD4+T cell subsets in patients. We observed that the absolute numbers of Th2 and Treg cells were all decreased in SSc ($p < 0.001$, $p < 0.001$, respectively); their percentages came up with similar results. Interestingly, the absolute numbers of Th1 and Th17 had no significant change. In addition, the ratios of Th1/Th2 and Th17/Treg were comparable between the two groups. Th1/Th2 [25.01 (12.24, 38.61) vs. 11.64 (6.38, 20.34), $p < 0.001$] and Th17/Treg

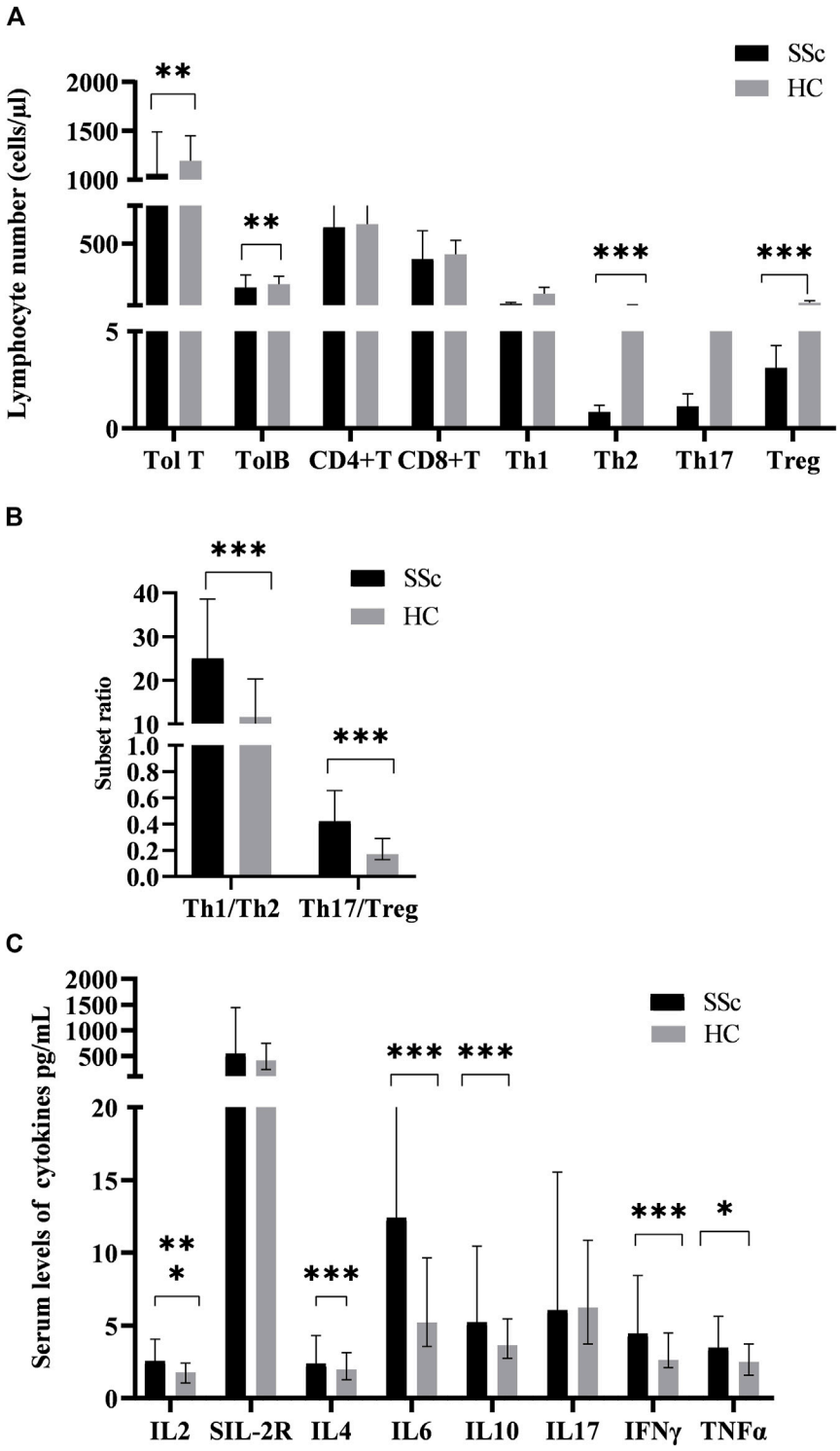

FIGURE 1
The levels of peripheral lymphocyte subsets and serum cytokines in SSc patients and HCs. **(A)**The absolute numbers of total T (Tol T), total B (Tol B), Th2, and Treg cells in SSc were significantly lower than those in HCs. **(B)**The ratios of Th1/Th2 and Th17/Treg in SSc were significantly higher than those in HCs. **(C)**The serum levels of cytokines in SSc were significantly increased. HC, Healthy controls; SSc, systemic sclerosis; *$p < 0.05$; **$p < 0.01$; ***$p < 0.001$ by Mann–Whitney's *U*-test.

10.3389/fphar.2022.986199

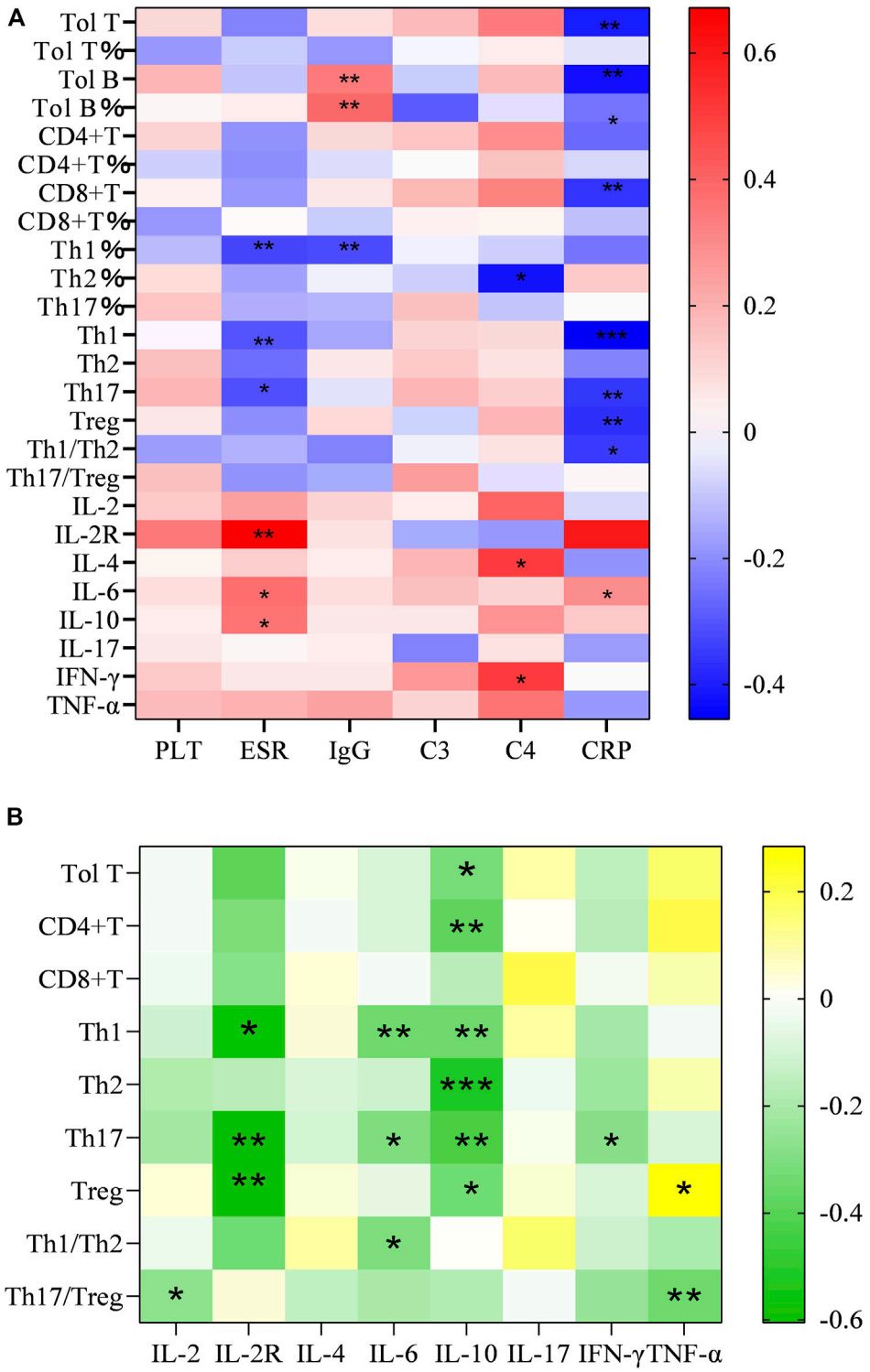

FIGURE 2
(A) Heatmap of correlation of the number and proportion of the circulating T-lymphocyte subsets and serum levels of cytokine with PLT, ESR, CRP, IgG, C3 and C4 in SSc patients; **(B)** Heatmap of correlation of the serum cytokine levels of IL-2, IL-4, IL-6, IL-10, INF-γ, TNF-α with Total T, Th, Th1, Th2, Th17, Treg, Th1/Th2, and Th17/Treg (*$p < 0.05$, **$p < 0.01$, and***$p < 0.001$ by Spearman's correlation test).

[0.42 (0.17, 0.66) vs. 0.17 (0.13, 0.29), $p < 0.001$] in SSc were higher compared with HCs. These results suggested that T-lymphocyte subsets seem to be involved in the pathogenesis of SSc.

Serum interleukin-2 (IL-2) levels in SSc patients [2.55 (1.05,2.41) pg/ml] were significantly higher than those in HCs [1.78 (1.05,2.41) pg/ml] ($p < 0.001$, Figure 1B). Similarly, serum levels of soluble interleukin-2 receptor (sIL-2R) [544.00 (374.00,1442.75) vs. 414.00 (235.50,682.25) pg/ml], interleukin-6 (IL-6) (12.42(5.43,23.05) vs. 5.16 (3.65,9.94)pg/ml), interleukin-10 (IL-10) [5.23(3.96,10.46) vs. 3.66 (2.74,5.50) pg/ml], INF-γ [4.44 (3.15,8.44) vs. 2.65 (2.12,4.56) pg/ml], and TNF-α [3.46 (2.02,5.64) vs. 2.49 (1.60,3.84) pg/ml] had a similar effect. Furthermore, there was no significant difference in serum interleukin-4 (IL-4) and interleukin-17 (IL-17) levels between SSc and HCs ($p = 0.146$; $p = 0.958$). Similarly, it has the significance that such high expression of cytokines in the pathogenesis of SSc cannot be underestimated.

The correlation of T-lymphocyte subsets and cytokines with inflammatory indexes

The serum levels of CRP, ESR, C3, C4, IgG, and PLT tended to be deemed as an indicator of disease activity frequently. As mentioned before, they were higher in the SSc than in the normal group. In addition, we examined the correlation between inflammatory index levels and these T-lymphocyte subsets and cytokines in SSc patients. As a result, total T cells, CD4+T cell, Treg cells and the ratio of Th1/Th2 were negatively correlated with CRP ($r = -0.406$, $p = 0.002$; $r = -0.263$, $p < 0.05$; $r = -0.367$ $p < 0.01$; $r = -0.346$, $p < 0.05$). We found a significantly negative correlation of Th1 cell levels with ESR and CRP ($r = -0.302$, $p = 0.026$; r = −0.455, $p < 0.001$), it equally applied to the relevance of Th17 with ESR and CRP (r = −0.311, $p = 0.022$; r = −0.56, $p < 0.01$). We also analyzed the correlation between other T-cell subsets and inflammatory indicators, but the difference was not statistically significant (Figure 2A).

Analogously, the results emerged a positive correlation between considerable cytokines and inflammatory markers. Increasing sIL-2R in the wake of the augment of ESR ($r = 0.671$, $p = 0.004$), so did IL-6 ($r = 0.378$, $p < 0.05$).

The correlations of T-lymphocyte subsets and cytokine levels with organ involvements

Next, we examined the association between them and organ involvements. For organ involvements, we evaluated the presence of skin sclerosis, interstitial lung disease (ILD), cardiac involvement, esophageal motility disorders, joint contractures, and Raynaud's phenomenon. In terms of the ILD, only the ratio of Th17/Treg was correlated, and simultaneously had lower levels relative to other patients [0.35 (0.14, 0.53) vs. 0.64 (0.26, 0.93) $p = 0.028$] (Figure 3A). On the other hand, Treg cells were lessened in patients with Raynaud's phenomenon relative to controls [3.00 (2.41, 4.28) vs. 3.55 (2.86, 4.53) $p < 0.05$] (Figure 3B). We also examined the circulating T-lymphocyte subsets and serum cytokine levels in the presence of arthralgia. IL-2, IL-10 and INF γ [3.32 (1.05, 11.73) vs. 2.32 (0.44, 6.45), $p = 0.045$], [8.08 (3.63, 355,77) vs. 4.89 (0.78, 21.44), $p = 0.02$], [6.31 (2.66, 44.03) vs. 4.03 (0.22, 16.96), $p = 0.009$] were elevated in patients with arthralgia while Th17 was decreased [0.62 (0.20, 2.16) vs. 1.26 (0.22, 10.93), $p = 0.026$]. The ratio of Th17/Treg also decreased [0.21 (0.05, 2.05) vs. 0.45 (0.07, 7.01); $p = 0.009$] (Figure 3C). There were changes in other ratios, but the differences were not statistically significant (not shown, in supplementary data). These findings suggested that the T-lymphocyte subsets and cytokine levels could be potentially useful biomarkers for organ involvement, particularly in arthralgia, which may be an important organ involvement for the early presentation of SSc.

Serum T-lymphocyte subsets and cytokines for arthralgia

Therefore, we calculated the cut-off value of each cytokine for the presence of arthralgia using ROC curve analysis (Figure 4A). Patients with arthralgia had higher levels of IL-2, IL-10, and INF-γ (Figure 3C). ROC curve analysis yielded an optimal cut-off value (2.67 pg/ml) of IL-2 for the presence of arthralgia. Similarly, levels of IL-10 and INFγ were elevated in patients with arthralgia. (Figure 3C). Subsequent ROC curve analysis yielded an optimal cut-off value of 5.93 and 5.32 pg/ml, respectively (Figure 4A). We then evaluated the usefulness of these optimal thresholds, and as shown in Figure 4B, they all showed a high prevalence of these optimal thresholds. We found that the proportion was significantly higher in patients with IL-2 >2.67 pg/ml; similarly, IL-10, INF-γ. When optimal thresholds for all three cytokines were used, arthralgia was found to have a higher incidence (Figure 4C).

Discussion

The roles of the immune effector network in the pathogenesis of SSc remain incompletely understood. Our results shed new insights into immune pathologies in SSc by demonstrating the T-lymphocyte subset and cytokine profiles in peripheral blood. First and foremost, we showed the association between dysregulated serum cytokines and altered T-lymphocyte subsets in SSc patients. Furthermore, assessing their correlation with disease activity and organ involvement, we found that abnormal expression of cytokines in joint

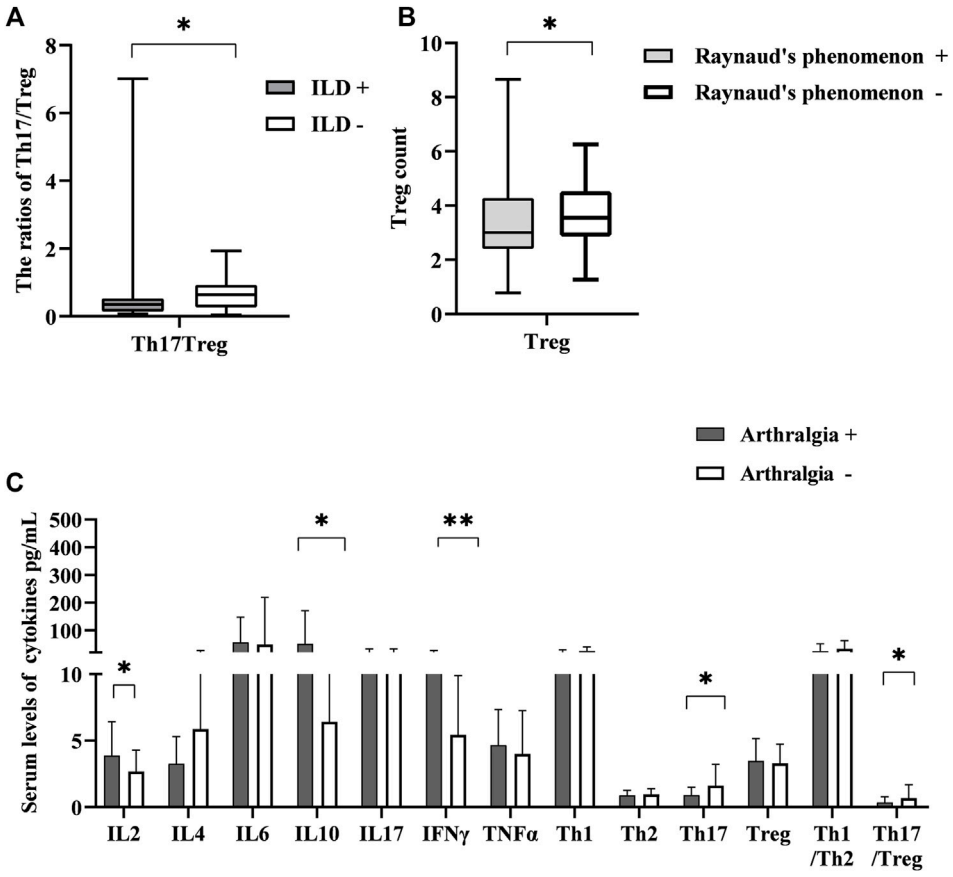

FIGURE 3
The correlation between the levels of T-lymphocyte subsets and cytokines with different symptoms. **(A)** The ratio of Th17/Treg in SSc patients with interstitial lung disease (ILD) had lower levels than that in those without ILD. **(B)** Treg cell number was lessened in patients with Raynaud's phenomenon relative to controls. **(C)** The correlation between T-lymphocyte subsets and cytokines levels with the presence of arthralgia. HC, Healthy controls; SSc, systemic sclerosis; *$p < 0.05$ **$p < 0.01$, ***$p < 0.001$ by Mann–Whitney's *U*-test.

involvement has joint diagnostic significance. This may allow the development of novel therapeutic strategies aimed at targeting these cells and the cytokine they produce.

It has long been studied that T lymphocytes isolated from the blood or fibrotic skin of SSc patients show oligoclonal libraries (Sakkas et al., 2002). From the perspective of what is known as immunity, the different phenotypes of T cell subsets (such as Th1, Th2, Th17, and Treg) stem from naïve T cells under the action of a variety of cytokine environments. The mediators, released by Th1 and Th2 lymphocytes, can inhibit each other. Th17 and Treg differentiations are interconnected analogously. Indeed, IL-6 plays an important role in determining whether the immune response will be dominated by pro-inflammatory Th17 or by anti-inflammatory Treg cells. The interaction between Th1/Th2 and Th17/Treg also generates a loop effect due to cytokines. IL-17 produced by Th17 can suppress Th1 differentiation (Zhang and Zhang, 2020).

The numbers of $CD4^+$ and $CD8^+$ T cells represent the predominant T cell subsets in the blood and hardened skin biopsies of SSc patients during the inflammatory phase, as well as the production of pro-fibrotic cytokines such as IL-4 and IL-13 (Fuschiotti, 2016), which play significant roles in activating angiogenesis and promoting collagen production and fibrosis. It has been proposed that an imbalance between the Th1 and Th2 cytokines leads to abnormal responses to tissue damage. Th2 cytokines stimulate the synthesis of collagen, while Th1 cytokines, such as IFN-γ, by contrast, do the opposite (Wynn, 2004). Therefore, the skin or lung fibrosis of SSc can be infiltrated by Th2 rather than Th1 generally (Boin et al., 2008).

However, the reports about Th17 and Treg infiltration in the tissues of SSc patients are controversial. The levels of Th17 cells and cytokines in peripheral blood, skin lesions, and lung tissues of SSc patients have also been found to increase to varying degrees (Rodríguez-Reyna et al., 2012; Zhou et al., 2015), while another study demonstrated their elevated levels of

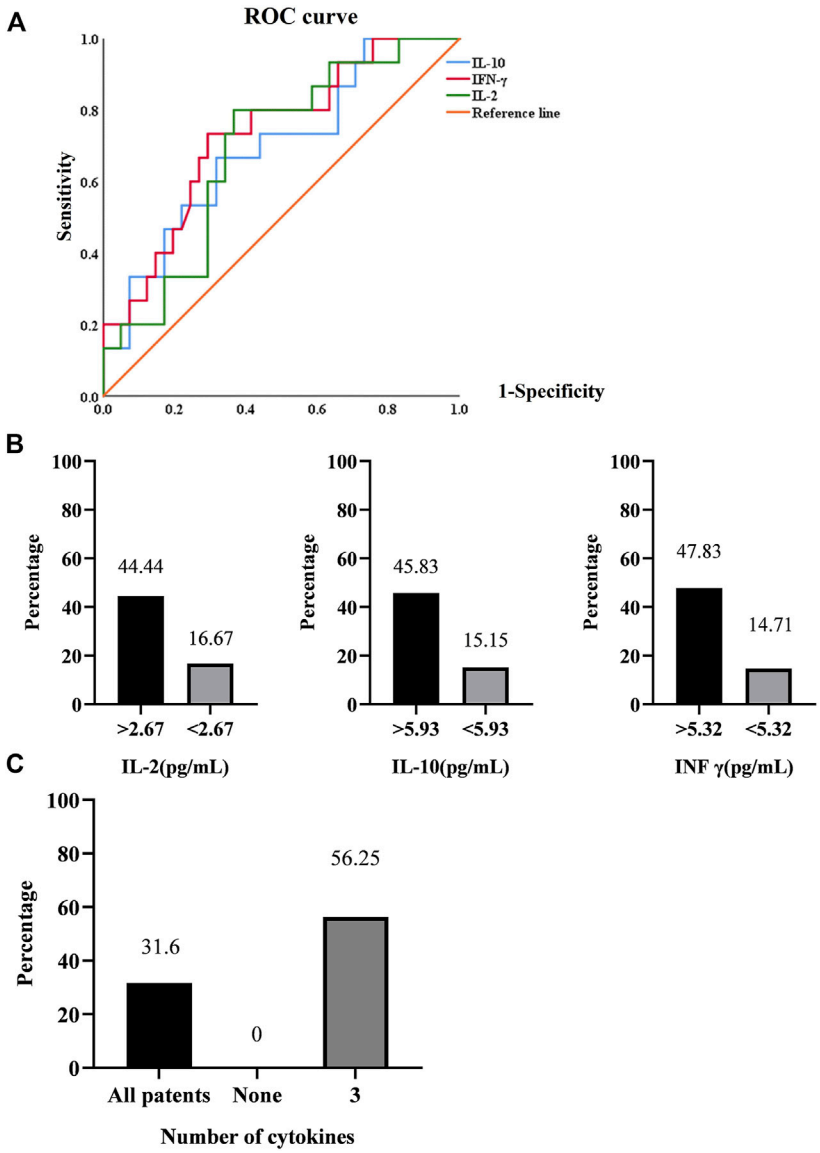

FIGURE 4
(A). ROC curve analysis in the presence of arthralgia. **(B)**. Prediction rates of arthralgia by IL-2, IL-10, INF-γ. **(C)**. Prediction rates of arthralgia by the synergistic effect of cytokines.

them and a positive correlation with disease activity and collagen overproduction (Yang et al., 2014). Studies have shown that there may be a positive feedback loop betweenTh17 cells that produce IL-17 in SSc, which directly or indirectly stimulates the activation of fibroblasts, vascular endothelial cells, and smooth muscle cells. After activation, cytokines such as IL-6 and IL-8 can enhance the activation of Th17 cells (Liu et al., 2016). The number of Treg cells in peripheral blood can be increased, decreased, or have no difference with weakened function (Boin et al., 2008; Zhou et al., 2015). They participated in autoimmune and tissue fibrosis by producing IL-4 and IL-13.

Different from these, we found that the absolute numbers of Th2 and Treg in blood were lower than those in healthy controls. The distinct results may be affected by factors such as disease course and activity. Considering the limited number of patients in this study, our results need, however, to be validated on a larger number of patients, probably in a multicenter study. Kataoka et al. (2015) found that the decrease of Treg cell subsets and immunosuppressive ability in skin tissues with SSc lesions may be caused by microRNA, DNA methylation, and histone modification affecting FoxP3 (Wang et al., 2014). Notably, patients had higher ratios

(imbalance) of Th1/Th2 and Th17/Treg. This result shed light on that T lymphocyte subsets do not wield a single influence independently, rather than play an immune role under the interaction of related circuits or patterns. In addition, our study indicated that there is a general trend of a reduction in T cells and an increase in markers of disease activity (Figure 2A).

Several lines of evidence suggested that effector T cells dominate the inflammatory infiltrates in the involved tissues during the early stages of the disease. Abnormal levels of T cell-derived cytokines, including TNFα, IL-6, IL-10 (Sato et al., 2001), IL-17, IL-4, and IL-13 (Fuschiotti et al., 2009; Hügle et al., 2013; Kang et al., 2019), have been found in the serum of SSc patients. Among these cytokines are thought to promote fibroblast overproduction of collagen, leading to excessive fibrosis. Consistent with previous reports, our conclusion illustrated that most cytokines increased significantly, IL-6 and IL-10 aggrandized particularly is especially obvious. IL-6 is a multifunctional acute-phase inflammatory cytokine that regulates cellular proliferation, activation, and immune responses. It is involved in a wide variety of pathophysiologic processes, such as increasing collagen production and driving differentiation of naive CD4-positive T cells into Th17 cells, which produce inflammatory cytokines (Abdel-Magied et al., 2016). Moreover, it is up-regulation was found to correlate with skin involvement and SSc-ILD (Abdel-Magied et al., 2016). However, no significant changes in IL-6 in patients with ILD were found in our study. In spite of this, the overwhelming majority of those cytokines showed a positive relationship with activity indexes as shown in Figure 2A.

In order to further investigate whether there are differences in T cells and cytokines among different organ-affected groups, we found that Th17/Treg was lower in patients with ILD, which is quite different from what we previously thought possible. Whereas, Treg has been lower in patients with Raynaud's phenomenon. Of note, recent studies demonstrated that the progression of the disease can attribute to Treg transformation to pathogenic effector T cells, such as Th17-like or Th2-like cells, which produce inflammatory and profibrotic cytokines respectively (MacDonald et al., 2015; Slobodin and Rimar, 2017). Hence, it is hard not to speculate that there is a transformation of Treg in patients with ILD and Raynaud's phenomenon. Despite these results, the transformation in the ILD and Raynaud's phenomenon needs to be understood and clarified.

As mentioned above, the serological IL-2, IL-6 and INF γ levels in the presence of arthralgia elevated, while Th17 and Th17/Treg decreased. We used ROC curves to determine their optimal bounds and, in turn, the optimal bounds were used to predict a higher prevalence. Little is known about IL-10 participation in the pathogenesis of SSc. Almost all leukocytes produce IL-10, which has a short half-life and short range of activity (Saxena et al., 2015). Treg suppresses inflammation and autoimmunity by utilizing IL-10. Furthermore, IL-10 has been shown to downregulate the mRNA expression of type I collagen and fibronectin (Antiga et al., 2010). Similarly, IL-10 was associated with many T lymphocytes in this study (Figure 2B). We also showed high levels of IL-10 and low levels of Treg in patients with arthralgia. The reason for this phenomenon is not only Treg transformation but also IL-10 playing a joint damage process, which of course needs further study.

A cross-sectional analysis of the EUSTAR registry disclosed that the prevalence of articular symptoms was 28% in SSc (Avouac et al., 2010), which frequency is obviously high. Articular symptoms of any form were also found to have a higher incidence of 31.6% in our study. In addition, arthralgia may often occur in the early stages of the disease and was associated with disease activity and inflammatory responses. Jérôme Avouac et al. (2016) conducted a prospective cohort study using the systematic longitudinal follow-up of SSc patients with the EUSTAR registry, which has determined the value of joint synovitis as a predictor of disease progression. Current management of articular involvement is largely supportive and symptomatic. In most cases, simple NSAIDs are effective. Recently, biologics have been widely used to treat inflammatory rheumatism, like using TNF-α inhibitors to get a significant decrease in signs of inflammation or joint symptoms (Lam et al., 2007). However, it is regrettable that randomized controlled trials of SSc were lacking. An expert consensus on the use of TNF-α inhibitors in SSc among EUSTAR centers, which subjected arthritis might respond and should be conducted in more detailed investigation (Distler et al., 2011). Thus, accurate identification of high-risk patients with arthralgia may control the disease progression and optimal efficacy through implementing sufficient treatment at the right time.

A known problem is that it is difficult to distinguish whether joint involvement is an SSc-disease-associated manifestation, an overlap, or accompanying manifestations of an unrelated condition. Polyarticular and patterns of joint involvement have been described (Sandler et al., 2020). This study requires further in-depth research on the classification of joint patterns and the timing of onset.

There are certain limitations to our study. This research sample size is smaller, which recruited a limited number of patients with SSc., and still needs a multicenter, large sample, the long-term clinical observation confirmed that this conclusion. From a clinical point of view, different courses of disease, disease stages, and disease subsets need to be identified to facilitate personalized management approaches. The retrospective study design can also be considered a disadvantage, with treatment guiding

decisions rather than preventing physicians from standardizing the purpose of the study background. Therefore, high-quality, large-scale with longer follow-ups are needed to further compare safety and efficacy, and disease stages and other relevant cytokine assays may be increased. However, patient cases represent real-life scenarios, we exhibited abnormalities in T subsets and the production of their cytokines, as compared with those in HCs. These new insights into the pathogenesis of SSc may allow the development of novel therapeutic interventions targeting these cells and the cytokines they produce. Although there is no single direct correlation between cytokine and clinical parameters, they also contribute to the evaluation of SSc patients. These easily detected clinical indicators may be useful for the risk stratification of patients with SSc, therapeutic guidance, and monitoring of disease progression. Moreover, the imbalance or re-balance of T lymphocyte subsets and cytokines may be used as the parameters of diagnosis and therapeutic efficacy.

Data availability statement

The raw data supporting the conclusion of this article will be made available by the authors, without undue reservation.

Ethics statement

The studies involving human participants were reviewed and approved by the Ethics Committee of the Shanxi Medical University Second Affiliated Hospital. The patients/participants provided their written informed consent to participate in this study.

Author contributions

R-HG performed the data analyses and wrote the manuscript. HC, X-YZ, ZY, G-HW, S-YH and X-PG participated in the collection of samples and clinical data. HC participated in the study design and revising of the manuscript. H-YW provided intellectual input and supervision throughout the study and made a substantial contribution to manuscript drafting. All authors contributed to the article and approved the submitted version.

Funding

This study was supported by the Key Scientific Research Project of Medical Science of Shanxi Province (2021XM08), Basic Research Youth Project of Shanxi Province (202103021223442), and 2020 Shanxi Province Emerging Industry Leadership Project (2020-15).

Conflict of interest

The authors declare that the research was conducted in the absence of any commercial or financial relationships that could be construed as a potential conflict of interest.

Publisher's note

References

Abdel-Magied, R. A., Kamel, S. R., Said, A. F., Ali, H. M., Abdel Gawad, E. A., and Moussa, M. M. (2016). Serum interleukin-6 in systemic sclerosis and its correlation with disease parameters and cardiopulmonary involvement. *Sarcoidosis Vasc. Diffuse Lung Dis.* 33, 321–330.

Antiga, E., Quaglino, P., Bellandi, S., Volpi, W., Del Bianco, E., ComessAtti, A., et al. (2010). Regulatory T cells in the skin lesions and blood of patients with systemic sclerosis and morphoea. *Br. J. Dermatol.* 162, 1056–1063. doi:10.1111/j.1365-2133.2010.09633.x

Avouac, J., Walker, U. A., Hachulla, E., Riemekasten, G., Cuomo, G., Carreira, P. E., et al. (2016). Joint and tendon involvement predict disease progression in systemic sclerosis: A EUSTAR prospective study. *Ann. Rheum. Dis.* 75, 103–109. doi:10.1136/annrheumdis-2014-205295

Avouac, J., Walker, U., Tyndall, A., Kahan, A., Matucci-Cerinic, M., Allanore, Y., et al. (2010). Characteristics of joint involvement and relationships with systemic inflammation in systemic sclerosis: Results from the EULAR scleroderma trial and research group (EUSTAR) database. *J. Rheumatol.* 37, 1488–1501. doi:10.3899/jrheum.091165

Baraut, J., Farge, D., Jean-Louis, F., Kesmandt, H., Durant, C., VerrecchiaF., et al. (2012). Cytokines in systemic sclerosis. *Pathol. Biol.* 60, 127–139. doi:10.1016/j.patbio.2009.11.003

Baraut, J., Michel, L., Verrecchia, F., and Farge, D. (2010). Relationship between cytokine profiles and clinical outcomes in patients with systemic sclerosis. *Autoimmun. Rev.* 10, 65–73. doi:10.1016/j.autrev.2010.08.003

Boin, F., De Fanis, U., Bartlett, S. J., Wigley, F. M., Rosen, A., and Casolaro, V. (2008). T cell polarization identifies distinct clinical phenotypes in scleroderma lung disease. *Arthritis Rheum.* 58, 1165–1174. doi:10.1002/art.23406

Cutolo, M., Soldano, S., and Smith, V. (2019). Pathophysiology of systemic sclerosis: Current understanding and new insights. *Expert Rev. Clin. Immunol.* 15, 753–764. doi:10.1080/1744666x.2019.1614915

Distler, J. H., Jordan, S., Airo, P., Alegre-Sancho, J. J., Allanore, Y., Balbir Gurman, A., et al. (2011). Is there a role for TNFα antagonists in the treatment of SSc? EUSTAR expert consensus development using the delphi technique. *Clin. Exp. Rheumatol.* 29, S40–S45.

Fuschiotti, P. (2016). Current perspectives on the immunopathogenesis of systemic sclerosis. *Immunotargets Ther.* 5, 21–35. doi:10.2147/itt.S82037

Fuschiotti, P., Medsger, T. A., Jr., and Morel, P. A. (2009). Effector CD8+ T cells in systemic sclerosis patients produce abnormally high levels of interleukin-13 associated with increased skin fibrosis. *Arthritis Rheum.* 60, 1119–1128. doi:10.1002/art.24432

Georges, C., Chassany, O., Toledano, C., Mouthon, L., Tiev, K., Meyer, O., et al. (2006). Impact of pain in health related quality of life of patients with systemic sclerosis. *Rheumatol. Oxf.* 45, 1298–1302. doi:10.1093/rheumatology/kel189

Herrick, A. L., Pan, X., Peytrignet, S., Lunt, M., Hesselstrand, R., Mouthon, L., et al. (2017). Treatment outcome in early diffuse cutaneous systemic sclerosis: The European scleroderma observational study (ESOS). *Ann. Rheum. Dis.* 76, 1207–1218. doi:10.1136/annrheumdis-2016-210503

Hügle, T., O'Reilly, S., Simpson, R., Kraaij, M. D., Bigley, V., Collin, M., et al. (2013). Tumor necrosis factor-costimulated T lymphocytes from patients with systemic sclerosis trigger collagen production in fibroblasts. *Arthritis Rheum.* 65, 481–491. doi:10.1002/art.37738

Kang, S., Tanaka, T., Narazaki, M., and Kishimoto, T. (2019). Targeting interleukin-6 signaling in clinic. *Immunity* 50, 1007–1023. doi:10.1016/j.immuni.2019.03.026

Kataoka, H., Yasuda, S., Fukaya, S., Oku, K., Horita, T., Atsumi, T., et al. (2015). Decreased expression of Runx1 and lowered proportion of Foxp3$^+$ CD25$^+$ CD4$^+$ regulatory T cells in systemic sclerosis. *Mod. Rheumatol.* 25, 90–95. doi:10.3109/14397595.2014.899736

Lam, G. K., Hummers, L. K., Woods, A., and Wigley, F. M. (2007). Efficacy and safety of etanercept in the treatment of scleroderma-associated joint disease. *J. Rheumatol.* 34, 1636–1637.

Liu, M., Wu, W., Sun, X., Yang, J., Xu, J., Fu, W., et al. (2016). New insights into CD4(+) T cell abnormalities in systemic sclerosis. *Cytokine Growth Factor Rev.* 28, 31–36. doi:10.1016/j.cytogfr.2015.12.002

MacDonald, K. G., Dawson, N. A. J., Huang, Q., Dunne, J. V., Levings, M. K., and Broady, R. (2015). Regulatory T cells produce profibrotic cytokines in the skin of patients with systemic sclerosis. *J. Allergy Clin. Immunol.* 135, 946-.e9–955. doi:10.1016/j.jaci.2014.12.1932

O'Reilly, S., Hügle, T., and van Laar, J. M. (2012). T cells in systemic sclerosis: A reappraisal. *Rheumatol. Oxf.* 51, 1540–1549. doi:10.1093/rheumatology/kes090

Rodríguez-Reyna, T. S., Furuzawa-Carballeda, J., Cabiedes, J., Fajardo-Hermosillo, L. D., Martinez-Reyes, C., Diaz-Zamudio, M., et al. (2012). Th17 peripheral cells are increased in diffuse cutaneous systemic sclerosis compared with limited illness: A cross-sectional study. *Rheumatol. Int.* 32, 2653–2660. doi:10.1007/s00296-011-2056-y

Sakkas, L. I., Xu, B., Artlett, C. M., Lu, S., Jimenez, S. A., and Platsoucas, C. D. (2002). Oligoclonal T cell expansion in the skin of patients with systemic sclerosis. *J. Immunol.* 168, 3649–3659. doi:10.4049/jimmunol.168.7.3649

Sandler, R. D., Matucci-Cerinic, M., and Hughes, M. (2020). Musculoskeletal hand involvement in systemic sclerosis. *Semin. Arthritis Rheum.* 50, 329–334. doi:10.1016/j.semarthrit.2019.11.003

Sato, S., Hasegawa, M., and Takehara, K. (2001). Serum levels of interleukin-6 and interleukin-10 correlate with total skin thickness score in patients with systemic sclerosis. *J. Dermatol. Sci.* 27, 140–146. doi:10.1016/s0923-1811(01)00128-1

Saxena, A., Khosraviani, S., Noel, S., Mohan, D., Donner, T., and Hamad, A. R. A. (2015). Interleukin-10 paradox: A potent immunoregulatory cytokine that has been difficult to harness for immunotherapy. *Cytokine* 74, 27–34. doi:10.1016/j.cyto.2014.10.031

Slobodin, G., and Rimar, D. (2017). Regulatory T cells in systemic sclerosis: A comprehensive review. *Clin. Rev. Allergy Immunol.* 52, 194–201. doi:10.1007/s12016-016-8563-6

Stochmal, A., Czuwara, J., Trojanowska, M., and Rudnicka, L. (2020). Antinuclear antibodies in systemic sclerosis: An update. *Clin. Rev. Allergy Immunol.* 58, 40–51. doi:10.1007/s12016-018-8718-8

Tsou, P. S., Varga, J., and O'Reilly, S. (2021). Advances in epigenetics in systemic sclerosis: Molecular mechanisms and therapeutic potential. *Nat. Rev. Rheumatol.* 17, 596–607. doi:10.1038/s41584-021-00683-2

van den Hoogen, F., Khanna, D., Fransen, J., Johnson, S. R., Baron, M., Tyndall, A., et al. (2013). 2013 classification criteria for systemic sclerosis: An American college of rheumatology/European league against rheumatism collaborative initiative. *Ann. Rheum. Dis.* 72, 1747–1755. doi:10.1136/annrheumdis-2013-204424

Wang, Y. Y., Wang, Q., Sun, X. H., Liu, R. Z., Shu, Y., Kanekura, T., et al. (2014). DNA hypermethylation of the forkhead box protein 3 (FOXP3) promoter in CD4+ T cells of patients with systemic sclerosis. *Br. J. Dermatol.* 171, 39–47. doi:10.1111/bjd.12913

Wynn, T. A. (2004). Fibrotic disease and the T(H)1/T(H)2 paradigm. *Nat. Rev. Immunol.* 4, 583–594. doi:10.1038/nri1412

Yang, X., Yang, J., Xing, X., Wan, L., and Li, M. (2014). Increased frequency of Th17 cells in systemic sclerosis is related to disease activity and collagen overproduction. *Arthritis Res. Ther.* 16, R4. doi:10.1186/ar4430

Zhang, M., and Zhang, S. T. (2020). T cells in fibrosis and fibrotic diseases. *Front. Immunol.* 11, 1142. doi:10.3389/fimmu.2020.01142

Zhou, Y., Hou, W., Xu, K., Han, D., Jiang, C., Mou, K., et al. (2015). The elevated expression of Th17-related cytokines and receptors is associated with skin lesion severity in early systemic sclerosis. *Hum. Immunol.* 76, 22–29. doi:10.1016/j.humimm.2014.12.008

frontiers | Frontiers in Pharmacology

TYPE Original Research
PUBLISHED 22 November 2022
DOI 10.3389/fphar.2022.1033103

OPEN ACCESS

EDITED BY
Jian Gao,
Shanghai Children's Medical Center, China

REVIEWED BY
Shizhong Zheng,
Nanjing University of Chinese Medicine, China
Zhishen Xie,
Henan University of Chinese Medicine, China

*CORRESPONDENCE
Ping Liu,
liuliver@vip.sina.com
Jiamei Chen,
cjm0102@126.com

†These authors have contributed equally to this work and share first authorship

SPECIALTY SECTION
This article was submitted to Gastrointestinal and Hepatic Pharmacology, a section of the journal Frontiers in Pharmacology

RECEIVED 31 August 2022
ACCEPTED 09 November 2022
PUBLISHED 22 November 2022

CITATION
Hu Y, He X, Zhou X, Liang Y, Fu Y, Zhang L, Fang J, Liu W, Chen G, Mu Y, Zhang H, Cai H, Liu C, Liu P and Chen J (2022), Gypenosides ameliorate ductular reaction and liver fibrosis *via* inhibition of hedgehog signaling. *Front. Pharmacol.* 13:1033103. doi: 10.3389/fphar.2022.1033103

Gypenosides ameliorate ductular reaction and liver fibrosis *via* inhibition of hedgehog signaling

Yonghong Hu[1,2†], Xiaoli He[1,2†], Xiaoxi Zhou[1,2], Yue Liang[1,2], Yadong Fu[3], Linzhang Zhang[3], Jing Fang[1,2], Wei Liu[1,2], Gaofeng Chen[1,2], Yongping Mu[1,2], Hua Zhang[1,2], Hong Cai[4], Chenghai Liu[1,2], Ping Liu[1,2,3]* and Jiamei Chen[1,2]*

[1]Institute of Liver Diseases, Key Laboratory of Liver and Kidney Diseases (Ministry of Education), Shuguang Hospital Affiliated to Shanghai University of Traditional Chinese Medicine, Shanghai, China, [2]Shanghai Key Laboratory of Traditional Chinese Clinical Medicine, Shanghai, China, [3]Institute of Interdisciplinary Integrative Medicine Research, Shanghai University of Traditional Chinese Medicine, Shanghai, China, [4]Xiamen Hospital of Traditional Chinese Medicine, Xiamen, Fujian, China

Backgroud and aims: Ductular reaction (DR) is a common pathological change and thought to have a key role in the pathogenesis and progression of liver fibrosis. Our previous study reported Gypenosides (GPs) ameliorated liver fibrosis, however, the anti-fibrotic mechanisms of GPs are still unclear.

Methods: Liver fibrosis was induced in rats by carbon tetrachloride combining with 2-acerylaminofluorene (CCl_4/2-AAF), and Mdr2 knockout (*Mdr2*$^{-/-}$) mice to evaluate the anti-fibrotic role of GPs. *In vitro*, WB-F344 cells, a hepatic progenitor cells (HPCs) line, with or without Gli1 overexpressing lentiviral vectors, were induced by sodium butyrate (SB) to validate the mechanism of GPs and NPLC0393, the main ingredient of GPs.

Results: Both in CCl_4/2-AAF-treated rats and *Mdr2*$^{-/-}$ mice, GPs obviously reduced the deposition of collagen and hydroxyproline content, inhibited the activation of hepatic stellate cells and inflammatory cell infiltration. Notably, GPs reduced the expressions of Epcam, CK19, CK7, Dhh, Smo, Ptch2, Gli1 and Gli2. Furthermore, CK19$^+$ cells co-expressed Gli1, while the number of CK19$^+$/Gli1$^+$ cells was decreased by GPs. *In vitro*, GPs and NPLC0393 inhibited the differentiation of WB-F344 cells toward a biliary phenotype. Mechanistically, GPs and NPLC0393 protected against DR by inhibiting hedgehog signaling, which was supported by the results that DR, triggered directly by Gli1 overexpressing lentiviral vector was blocked by administration with GPs or NPLC0393.

Conclusion: GPs attenuated DR and liver fibrosis by inhibiting hedgehog signaling, which provided more evidences and a novel mechanism of anti-fibrotic effect of GPs.

KEYWORDS

gypenosides, liver fibrosis, ductular reaction, hedgehog signaling, NPLC0393

1 Introduction

Liver fibrosis, which is characterized by excessive deposition of extracellular matrix and the formation of fibrous scars (Parola and Pinzani, 2019), is a common pathological consequence of chronic liver injuries induced by various etiological factors, such as virus infection, alcoholism, chemical damage, and autoimmune disorders (Parola and Pinzani, 2019; Roehlen et al., 2020). If untreated, it ultimately leads to cirrhosis, end-stage liver diseases, and even hepatocellular carcinoma (HCC), becoming a major health challenge worldwide (Zhao et al., 2018; Asrani et al., 2019). Ductular reaction (DR) has been observed in acute and chronic liver injuries. It has been reported that in cholestatic liver injury, chronic viral hepatitis, and alcoholic hepatitis, ductular reactive cells extended into the hepatic parenchyma and played a key role in recruiting immune cells to create a proinflammatory and profibrogenic microenvironment, which correlated with the severity of fibrosis and short-term survival (Clouston et al., 2005; Zhao et al., 2018; Aguilar-Bravo et al., 2019). In our previous study, we demonstrated that abnormal proliferated cholangioctyes formed DR, exhibiting a profibrotic effect in rats with bile duct ligation (BDL), and the extent of DR was increased with the prolongation of molding time (Zhang et al., 2016). Although experimental data has proved that liver fibrosis, even early cirrhosis, is reversible through pharmacologic treatment or gene-editing technology. However, there are currently no effective FDA-approved drugs targeting liver fibrosis. Therefore, investigations searching for effective herbal medicines or bioactive compounds for anti-hepatic fibrosis have been a longstanding goal.

The Hedgehog (Hh) signaling is known to play a critical role in various acute and chronic liver diseases, including 70% partial hepatectomy (Ochoa et al., 2010), HBV/HCV infection (Pereira Tde et al., 2010), cholestatic liver injury (Gupta et al., 2020), alcoholic liver disease (Jung et al., 2008) and non-alcoholic fatty liver disease (Syn et al., 2012). Although temporary Hh signaling activation is required for efficient liver regeneration, dysregulated activation of Hh signaling in liver injuries encourages the development of the liver fibrosis and cirrhosis. As a result, inhibiting Hh signaling offers hope for the therapy of liver fibrosis.

Gypenosides (GPs) is one of the main pharmacologically active components extracted from *Gynostemma pentaphyllum* (Cui et al., 1999). GPs had effects on regulating lipid metabolism (Zhang et al., 2021), anti-inflammatory (Tu et al., 2021), anti-oxidative (Zhang et al., 2018), anti-cancer (Li et al., 2022), anti-diabetes (He et al., 2015), and hepatoprotection (Li et al., 2020). GPs have significant therapeutic effects on a variety of animal models of liver fibrosis. In addition, prior work has shown that the anti-fibrotic mechanisms of GPs were related to inhibiting the proliferation and activation of hepatic stellate cells (HSCs) (Chen et al., 2008), as well as reducing the damage caused by aldehydes and lipid peroxidation (Song et al., 2017). However, little work has been focused on the effect of GPs on DR.

In the present study, two rodent models of hepatic fibrosis induced by different pathogenic processes, including rats treated with carbon tetrachloride (CCl_4) combined with 2-acetylaminofluorene (2-AAF) and multidrug resistance gene 2 knockout (*Mdr2*$^{-/-}$) mice, and an *in vitro* model of differentiation of hepatic progenitor cells (HPCs) into cholangiocytes by sodium butyrate (SB) exposure, were used to elucidate the effect and mechanism of GPs on liver fibrosis. The findings demonstrated that GPs ameliorated DR and liver fibrosis by inhibiting hedgehog signaling.

2 Materials and methods

2.1 Animals

Female Fisher 344 rats, 6–8 weeks old, with 160–180 g, were purchased from Beijing Vital River Laboratory Animal Technology (Beijing, China). *Mdr2*$^{-/-}$ and wild-type (WT) mice were purchased from the Shanghai Research Center of Southern Model Organisms (Shanghai, China). All animals were housed at the Animal Experiment Center of Shanghai University of Traditional Chinese Medicine, with a 12-h light-dark cycle and free access to a chow diet and water. All animal experiments were approved by the Experimental Animal Ethics Committee of Shanghai University of Traditional Chinese Medicine (NO. PZSHUTCM190505002, and NO. PZSHUTCM200731007).

2.2 Drugs

CCl_4 (10006464) was purchased from Sinopharm Chemical Reagent Co. Ltd. (Shanghai, China). 2-AAF (53-96-3), GANT61 (G9048), and SB (B5887) were purchased from Sigma-Aldrich Co., Ltd. (America) GPs (180527) was purchased from Shanghai Winherb Medical Technology Co., Ltd. (Shanghai, China). NLPC0393 was gifted by Dr. Shanhua Fang from Shanghai Institute of Materia Medica, Chinese Academy of Sciences.

2.3 Liver fibrosis animal models and treatment with GPs

2.3.1 CCl_4 combined with 2-AAF -treated rats

All Fisher 344 rats were randomly divided into the CCl_4-injected group and the normal control group. The CCl_4-injected group was injected subcutaneously with 30% CCl_4 -olive oil solution at a dose of 2 ml/kg, body weight, twice a week for 6 weeks. At the beginning of the seventh week, all CCl_4-injected rats were randomly divided into three groups, including the CCl_4

combined with 2-AAF (10 mg/kg/d) -treated group (the CCl_4/2-AAF-treated group), the CCl_4/2-AAF plus GPs (100 mg/kg/d) -treated group (the GPs-treated group), and the CCl_4/2-AAF plus GANT61 (25 mg/kg/qod) -treated group (the GANT61-treated group). All drugs were administered orally according to different groups up to the end of the ninth week.

2.3.2 *Mdr2*$^{-/-}$ spontaneous primary sclerosing cholangitis model

A deficiency of canalicular phospholipid translocase in *Mdr2*$^{-/-}$ mice, resulted in lacking phospholipids in the bile further leading to the accumulation of toxic bile acids in hepatocytes and initiation of a profibrogenic ductular reaction, and spontaneously progressing to severe biliary fibrosis, resembling PSC (Popov et al., 2005). From the beginning of the eighth week after birth, *Mdr2*$^{-/-}$ mice were randomly divided into the *Mdr2*$^{-/-}$ model group and the GPs (200 mg/kg/d) -treated group. All mice were sacrificed at the end of the 11th week, liver tissues were collected for further experiments.

2.4 WB-F344 cells culture and treatment

WB-F344 cells, the HPC line, was purchased from Xiangf Bio (Shanghai, China), and cultured in high glucose DMEM supplemented with 10% fetal bovine serum, at 37°C humidified atmosphere with 5% CO_2. Cells were stimulated with 3.75 μM SB for 4 days to induce the differentiation into cholangiocytes, meanwhile treated for 4 days with or without GPs and NPLC0393 dissolved in DMSO with appropriate concentrations.

2.5 *Gli1* overexpressing lentivirus vectors

The *Gli1* gene overexpressing lentivirus vector and empty control lentivirus vector were prepared by Shanghai Genechem Co. Ltd. (Shanghai, China). The lentivirus vector carried a green fluorescent label (Vector name, GV367; element sequence, Ubi-MCS-SV40-EGFP-IRES-puromycin; control serial number, CON238). WB-F344 cells at the concentration of 1 × 10̇4 cell/mL were cultured in 12-well plates for 24 h and treated with lentivirus vector per well at a MOI = 50. After 12 h, the transfection medium was changed to the medium according to the experimental groups. Cells were collected for the subsequent examination after 72 h.

2.6 Histopathological and immunohistochemical analysis

Liver tissues were fixed in 10% neutral-buffered formalin solution for at least 48 h. Subsequently, liver tissues were paraffin-embedded and cut at a thickness of 4 μm for hematoxylin and eosin (H&E) and Sirius red (SR) staining according to the manufacturer's instructions.

Immunohistochemical staining was performed with the standard methods. Liver sections were firstly deparaffinized and washed, retrieved the antigens in citrate buffer, and inactivated the endogenous peroxidases with 3% hydrogen peroxide. Then blocked by 10% goat serum or 5% bovine serum, and incubated with primary antibodies at 4°C overnight. After three washes in PBST, sections were incubated with the corresponding secondary antibodies conjugated with HRP (GTVision III Immunohistochemical Detection Kit, HRP/DAB, anti-mouse/rabbit IgG, two-step, GK5005/5007, Gene Tech, Shanghai, China) for 30 min at 37°C in next day. Sections were then washed, colored with DAB, counterstained with hematoxylin, washed, dehydrated, and sealed. The staining images were acquired by a Leica SCN 400 slide scanner (Leica Microsystems Ltd., Mannheim, Germany) or bright-field microscopy (Olympus, Beijing, China). The detailed antibodies were provided in Supplementary Table S1.

2.7 Immunofluorescence analysis

Liver sections (8 μm) were fixed in pre-cooled (−20°C) acetone and cells were fixed in 4% paraformaldehyde for 10 min. After fixed, tissue sections and cells were treated with blocking solution (10% goat serum or 5% bovine serum in PBS) for 30–60 min at room temperature. Subsequently, primary antibodies were incubated at 4°C overnight. After three washes in PBST (5 min per wash), secondary antibodies were incubated at 37°C for 30 min in the next day. And 4′,6-diamidino-2 phenylindole (DAPI) was labeled the nuclear visualization. Fluorescent images were captured by a DP80 fluorescence inverted microscope (Olympus, Beijing, China) or a laser-scanning confocal microscope (Olympus, Beijing, China). The detailed antibodies were provided in Supplementary Table S2.

2.8 Western blot analysis

The liver tissues and cells were lysed by lysis buffer with protease and phosphatase inhibitors. After centrifugation (12000 rpm, 15 min) at 4°C, the supernatant was collected and the protein concentration was determined using the BCA assay. The samples were then mixed with 5× loading buffer and heated at 100°C for 8 min, fractionated by SDS-PAGE, and transferred to polyvinylidene fluoride (PVDF) membranes. The membranes were then incubated in blocking solution (5% bovine serum in PBS) for 60 min at RT, followed by overnight incubation at 4°C with the primary

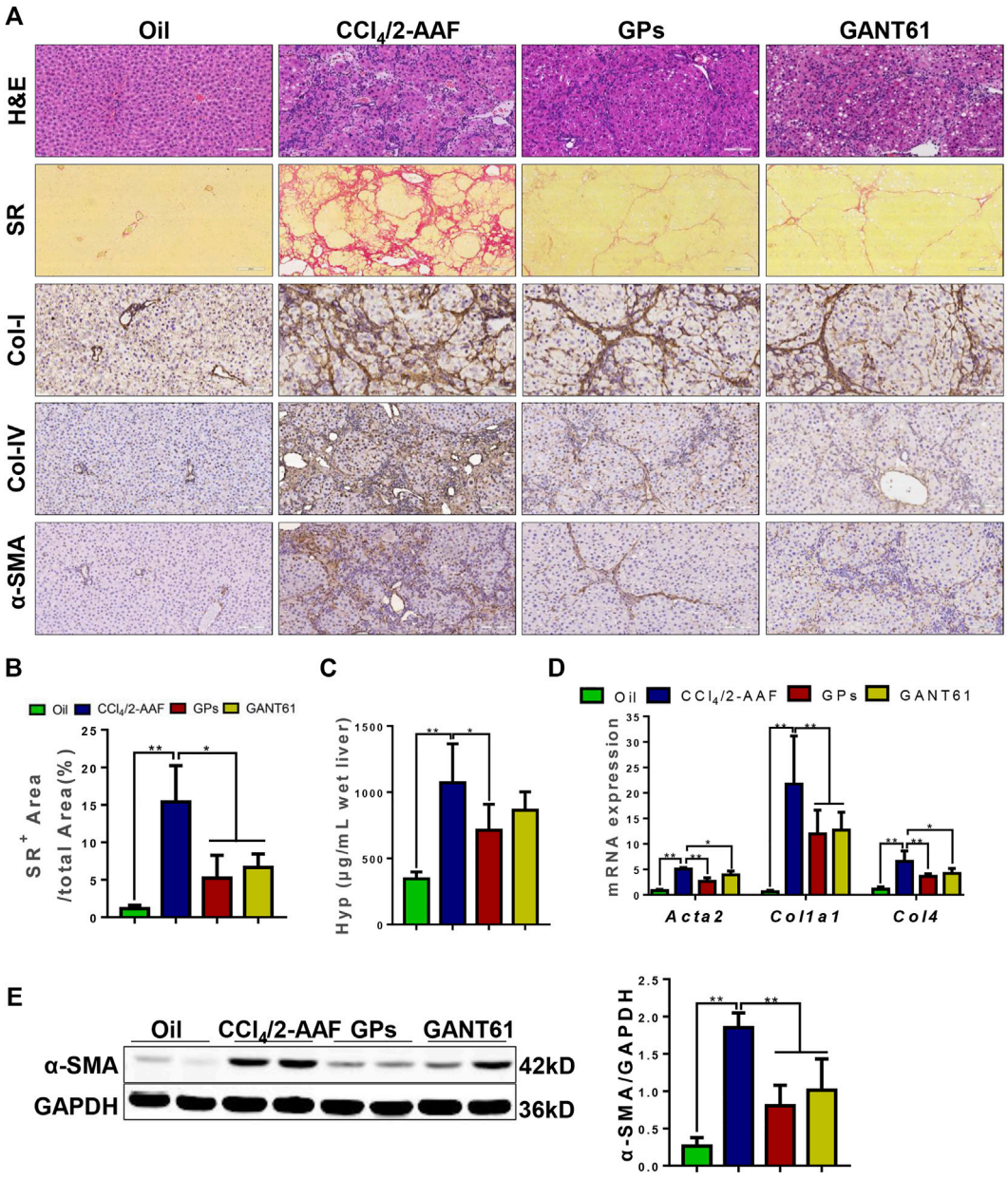

FIGURE 1
GPs alleviated CCl_4/2-AAF-induced liver fibrosis in rats. **(A)** Representative images of liver sections stained with H&E (200×), SR (100×), and immunohistochemical staining (200×). **(B)** Morphometric quantification of the SR-positive area (%). **(C)** The Hyp content. **(D)** The mRNA expressions of *Atca2*, *Col1a1,* and *Col4*. **(E)** Western blotting and the gray-level score for α-SMA. *, $p < 0.05$; **, $p < 0.01$. Oil: the control group; CCl_4/2-AAF: the CCl_4 combined with 2-AAF-treated group; GPs: the GPs-treated group; GANT61: the GANT61-treated group.

antibodies. After three washes in PBST (5 min each), the membrane was incubated with the appropriate secondary antibodies at RT for 1 h. After three more washes (5 min per wash) in PBST, the membranes were imaged by the Odyssey infrared imaging system (LiCor, America) or the ECL system (Tanon, Shanghai, China). The detailed antibodies were provided in Supplementary Table S3.

2.9 Quantitative real-time quantitative PCR

Quantitative real-time PCR was performed according to the manufacturer's instructions as follows. Total RNA was extracted from liver tissues and cells using the MagExtraction™ RNA kit (TOYOBO, NPK-201F). The total RNA was reverse transcribed

into cDNA by ReverTra Ace qPCR RT Master Mix with gDNA Remover (TOYOBO, FSQ-301). Real-time quantitative PCR was performed using the SYBR® Green Premix Pro Taq HS qPCR Kit (Accurate Biology, AG11701). The primer sequences used are listed in Supplementary Table S4 and Supplementary Table S5.

2.10 Statistical analysis

The data were subjected to statistical analysis including Student's t-test when appropriate or univariate analysis of variance (ANOVA) when more than two groups were compared, using the IBM SPSS 26.0 statistical package. p-value < 0.05 was considered significant.

3 Results

3.1 GPs ameliorated CCl_4/2-AAF-induced liver fibrosis in rats

To demonstrate whether GPs can improve liver fibrosis, a rat liver fibrosis model induced by CCl_4/2-AAF was first established. In this model, 2-AAF could inhibit hepatocyte proliferation, conversely promote the activation and proliferation of HPCs. H&E staining showed apparent damaged lobules, extensive inflammatory cell infiltration in the portal area, and fibrous septa were visible in the CCl_4/2-AAF-treated group. However, necroinflammatory hepatic lesions were markedly attenuated in the GPs or GANT61-treated group compared to the CCl_4/2-AAF-treated group (Figure 1A). SR staining revealed that a large amount of collagen fiber deposited and some extended into the liver parenchyma, which formed pseudo nodules in the CCl_4/2-AAF-treated group, in contrast, collagen deposition was significantly decreased after GPs or GANT61 treatment (Figure 1A). Consistently, the ratio of collagen-positive area and the hepatic Hyp content in the CCl_4/2-AAF-treated group were significantly increased ($p < 0.01$), which were remarkably decreased in the GPs or GANT61-treated group ($p < 0.05$) (Figures 1B,C). Immunostaining showed that in the CCl_4/2-AAF-treated group, collagen type I (Col-I), Col-IV, and alpha-smooth muscle actin (α-SMA) were mainly expressed in the fibrotic septa, and increased compared to the normal group, while GPs and GANT61 significantly reduced the expression of Col-I, Col-IV and α-SMA (Figure 1A). Moreover, *Col1a1*, *Col4,* and *Acta2* mRNA expressions were significantly increased in the CCl_4/2-AAF-treated group compared to the normal group ($p < 0.01$), whereas their expressions were decreased after administration with GPs or GANT61 ($p < 0.01$, $p < 0.05$) (Figure 1D). In addition, the α-SMA protein expression was significantly lower in the GPs-treated group and the GANT61-treated group than that in the CCl_4/2-AAF-treated group ($p < 0.01$) (Figure 1E). These results demonstrated that GPs and GANT61 significantly alleviated liver fibrosis induced by CCl_4/2-AAF in rats.

3.2 GPs ameliorated liver inflammation and collagen deposition in *Mdr2*$^{-/-}$ mice

The anti-fibrotic effect of GPs was continued to investigate in another hepatic fibrosis model, *Mdr2*$^{-/-}$ mice, which could spontaneously develop cholestatic liver injury and fibrosis. Similar to the results found in the CCl_4/2-AAF-treated rats, H&E staining also showed the hepatic lobule structure was disorganized and inflammatory cells infiltrated in *Mdr2*$^{-/-}$ mice, which were markedly improved after administration with GPs (Figure 2A). SR staining revealed that collagen deposition was increased, forming bridging fibrosis and complete pseudo nodule in *Mdr2*$^{-/-}$ mice, which was attenuated in GPs-treated group (Figure 2A). In addition, the Hyp content and SR-positive area were extensively reduced in GPs-treated group compared with the *Mdr2*$^{-/-}$ group ($p < 0.05$) (Figures 2B,C). Immunostaining showed that α-SMA expression in the liver was increased in *Mdr2*$^{-/-}$ mice, while significantly reduced after GPs administration ($p < 0.01$) (Figure 2E), which was consistent with mRNA expression of *Acta2* analyzed by qRT-PCR (Figure 2D). Besides that, GPs inhibited the mRNA expression of *Col1a1*, *Col3*, *Col4* and *Tgf-β1* ($p < 0.01$, $p < 0.05$) (Figure 2D). All these results proved that GPs alleviated liver fibrosis in *Mdr2*$^{-/-}$ mice.

3.3 GPs suppressed ductular reaction in fibrotic animals

DR is associated with liver fibrosis and the extent of DR parallels patient mortality (Sato et al., 2019). Immunostaining showed that OV6, an antigen-specific for rodent HPCs, was mainly expressed in the portal area in the normal group. In the CCl_4/2-AAF-treated rats, OV6 was widely found in the injured liver, which was lower in the GPs or GANT61-treated group. For analyzing the changes in DR, serial sections were stained with epithelial cell adhesion molecule (Epcam), keratin19 (CK19), and CK7 by immunohistochemistry, which were biomarkers of HPCs and cholangiocytes, respectively. In the CCl_4/2-AAF-treated group, Epcam was expressed in HPCs and reactive cholangiocytes located in the fibrous septa and occasionally in the scattered cells within hepatic lobules. CK19 and CK7 were expressed in pre-existing and reactive cholangiocytes. Further observation revealed that Epcam$^+$ cells also expressed CK19 and CK7. While the expression of Epcam, CK19, and CK7 were decreased in the GPs-treated

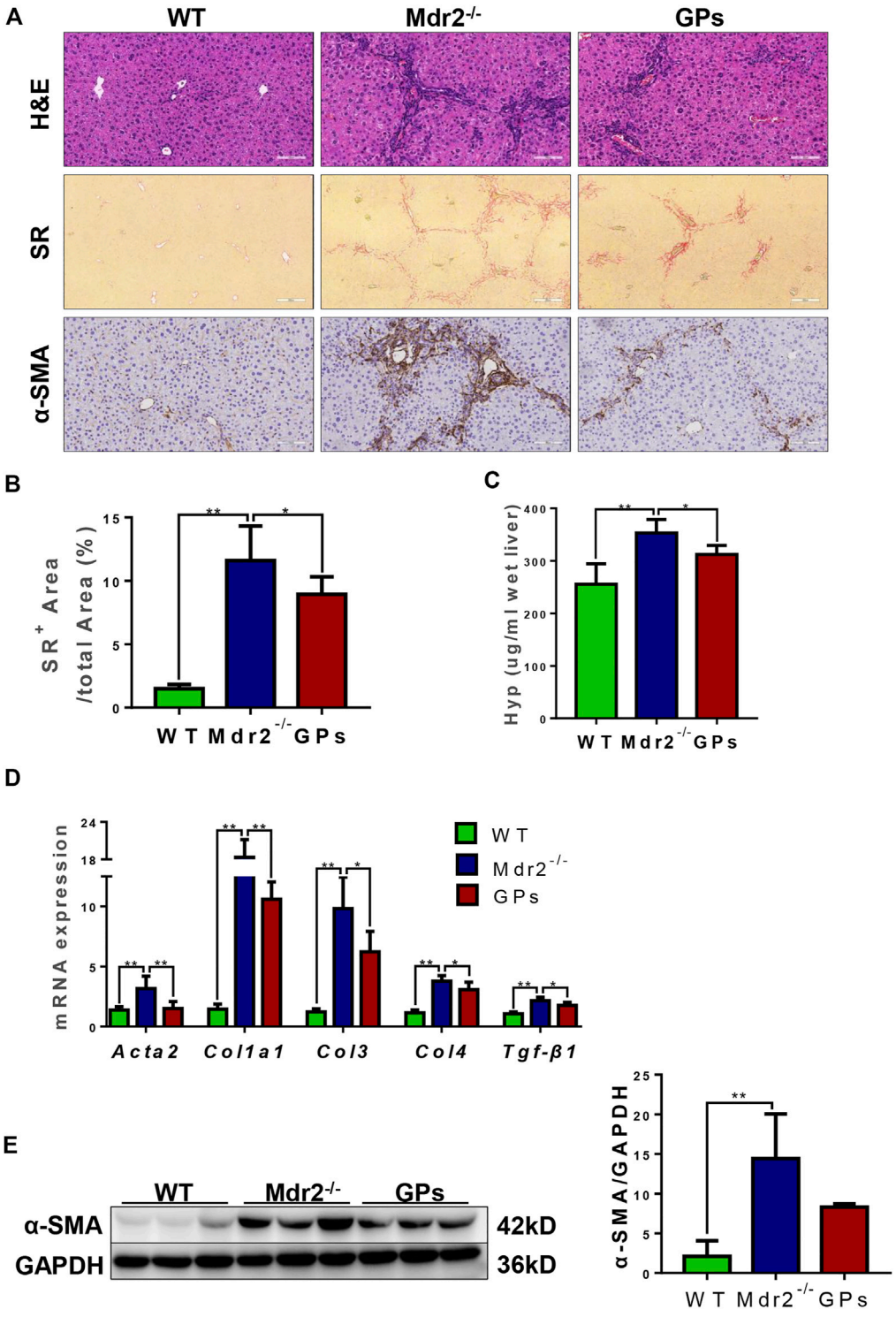

FIGURE 2
GPs ameliorated liver inflammation and collagen deposition in *Mdr2*$^{-/-}$ mice. **(A)** Representative images of liver sections stained with H&E (200×) and SR (100×), and immunohistochemical staining for α-SMA (200×). **(B)** Morphometric quantification of the SR-positive area (%). **(C)** The Hyp content. **(D)** The relative mRNA expressions of *Atca2*, *Col1a1*, *Col3*, *Col4*, and *Tgf-β1*. **(E)** Western blotting and the gray-level score for CK19. 0.05; **, $p < 0.01$. Mdr2$^{+/-}$: the WT control group; Mdr2$^{-/-}$: the Mdr2$^{-/-}$ mice group; GPs: the GPs-treated group.

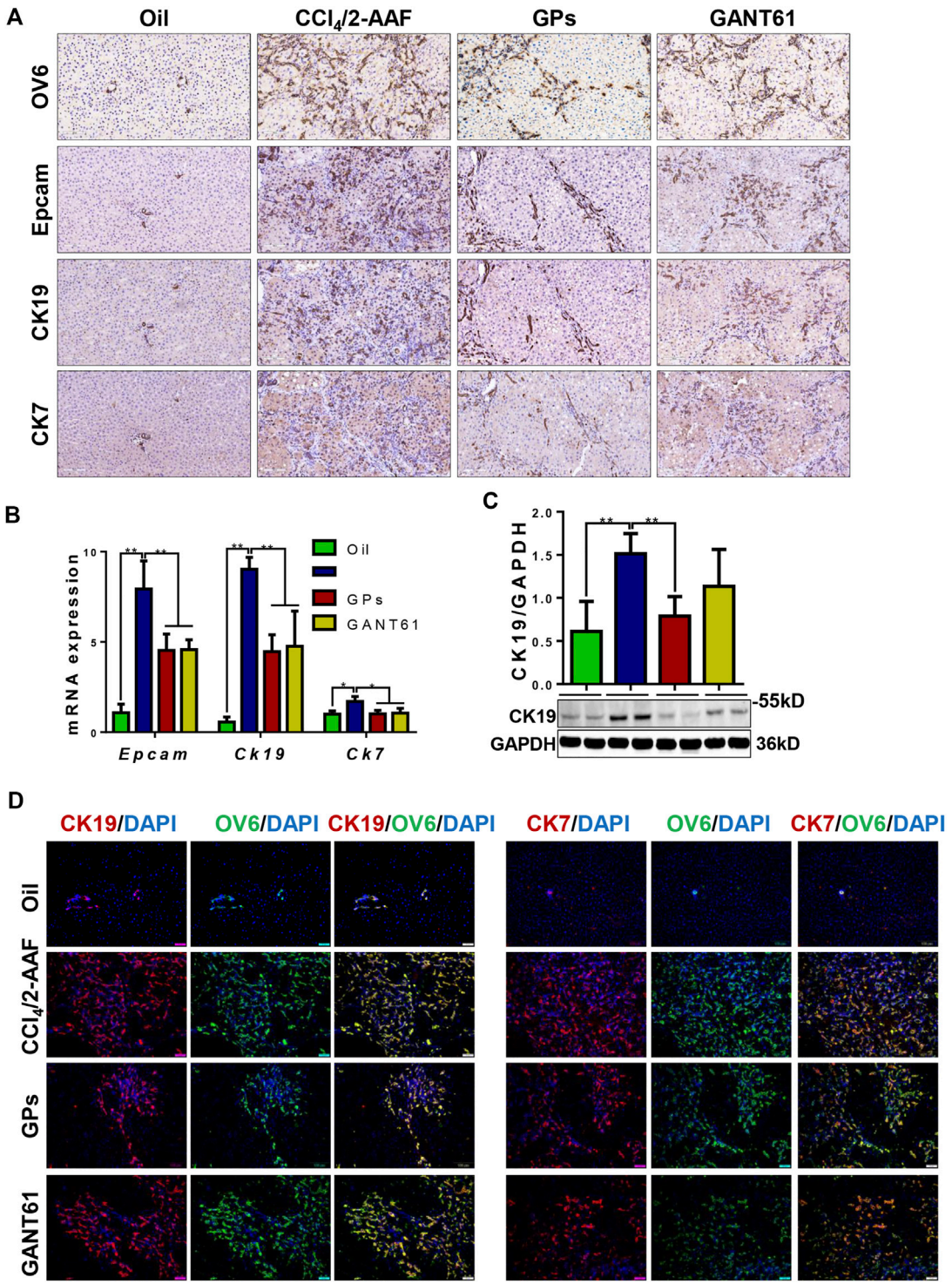

FIGURE 3
GPs suppressed DR in CCl_4/2-AAF-induced rats. **(A)** Representative immunohistochemical staining for OV6, Epcam, CK19, and CK7 (200×). **(B)** The mRNA expressions of *Epcam*, *Ck19*, and *Ck7*. **(C)** Western blotting and the gray-level score for CK19. **(D)** Confocal analysis of co-staining for CK19 (red) and OV6 (green), CK7 (red) and OV6 (green) (200×). *, $p < 0.05$; **, $p < 0.01$. Oil: the control group; CCl_4/2-AAF: the CCl_4 combined with 2-AAF-treated group; GPs: the GPs-treated group; GANT61: the GANT61-treated group.

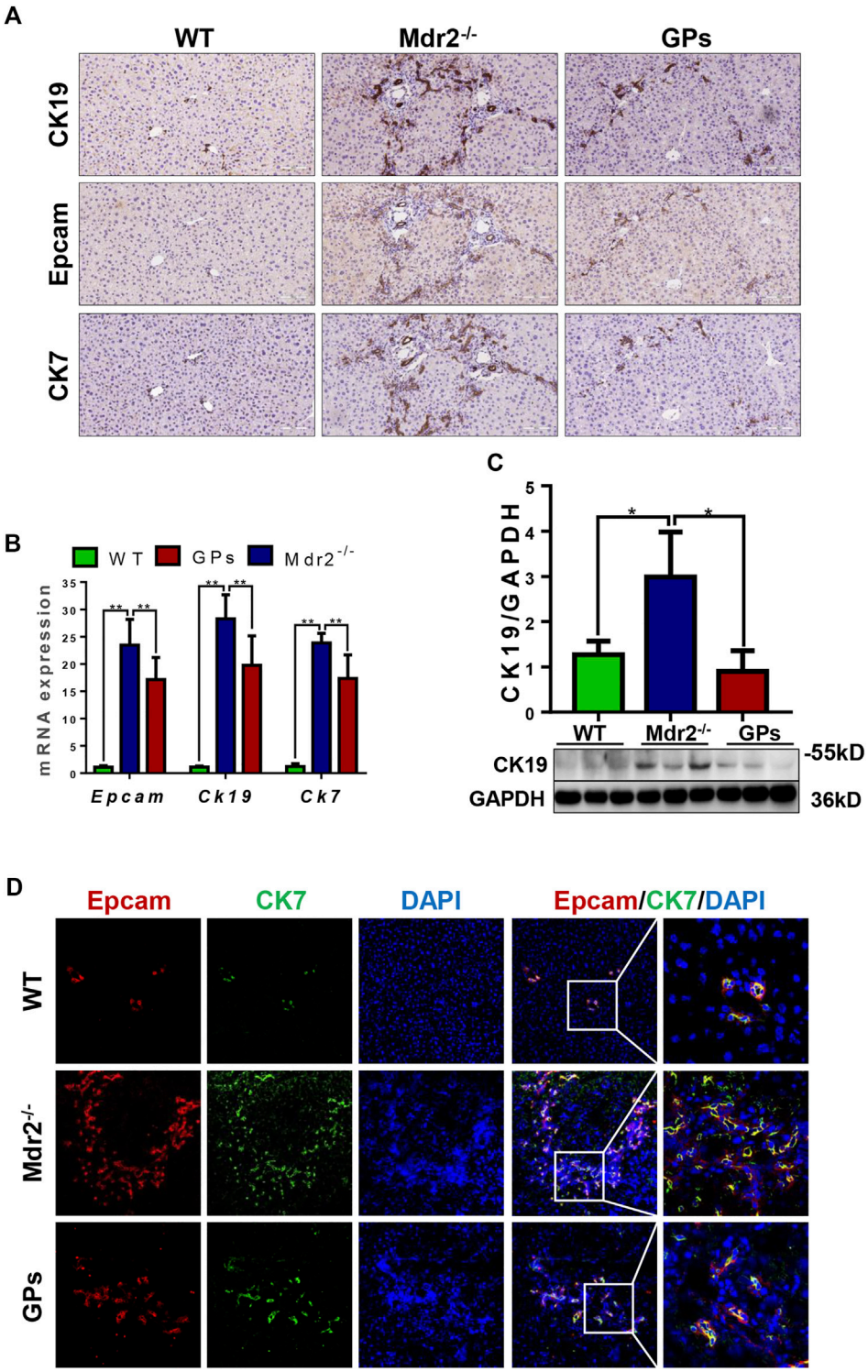

FIGURE 4
GPs inhibited DR in CCl_4/2-AAF-induced rats. **(A)** Representative immunohistochemical staining for CK19, Epcam, and CK7 (200×). **(B)** The mRNA expressions of *Epcam*, *Ck19*, and *Ck7*. **(C)** Western blotting and gray-level score of CK19. **(D)** Confocal analysis of co-staining for Epcam (red) and CK7 (green) (200×). *, $p < 0.05$; **, $p < 0.01$. $Mdr2^{+/-}$: the WT control group; $Mdr2^{-/-}$: the $Mdr2^{-/-}$ mice group; GPs: the GPs-treated group.

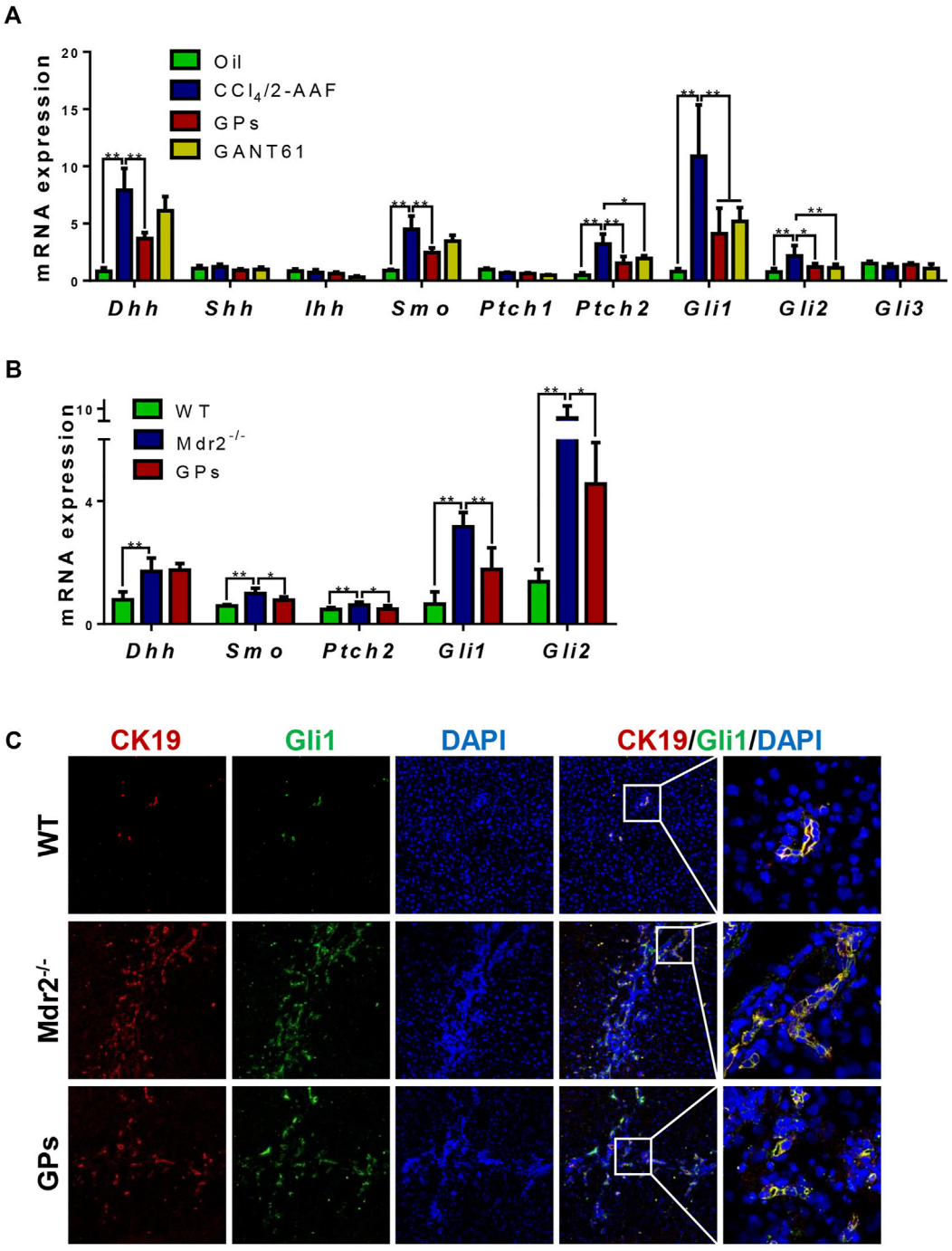

FIGURE 5
GPs attenuated DR via hedgehog pathway in fibrotic animals. **(A)** The mRNA expressions of *Dhh*, *Shh*, *Ihh*, *Smo*, *Ptch1*, *Ptch2*, *Gli1*, *Gli2*, and *Gli3* in CCl_4/2-AAF-induced rats. **(B)** The mRNA expressions of *Dhh*, *Smo*, *Ptch2*, *Gli1*, and *Gli2* in *Mdr2*$^{-/-}$ mice. **(C)** Confocal analysis of co-staining for CK19 (red) and Gli1 (green) (200×). *, $p < 0.05$; **, $p < 0.01$.

and GANT61-treated groups (Figure 3A). The mRNA expression of *Epcam*, *Ck19*, and *Ck7*, as well as the protein expression of CK19, were increased in the CCl_4/2-AAF-treated group, which were significantly reduced after administration of GPs or GANT61 ($p < 0.01$, $p < 0.05$) (Figures 3B,C). Moreover, double-immunofluorescence staining showed that CK19, CK7, and OV6 were co-localized in reactive cholangiocytes, while the numbers of

10.3389/fphar.2022.1033103

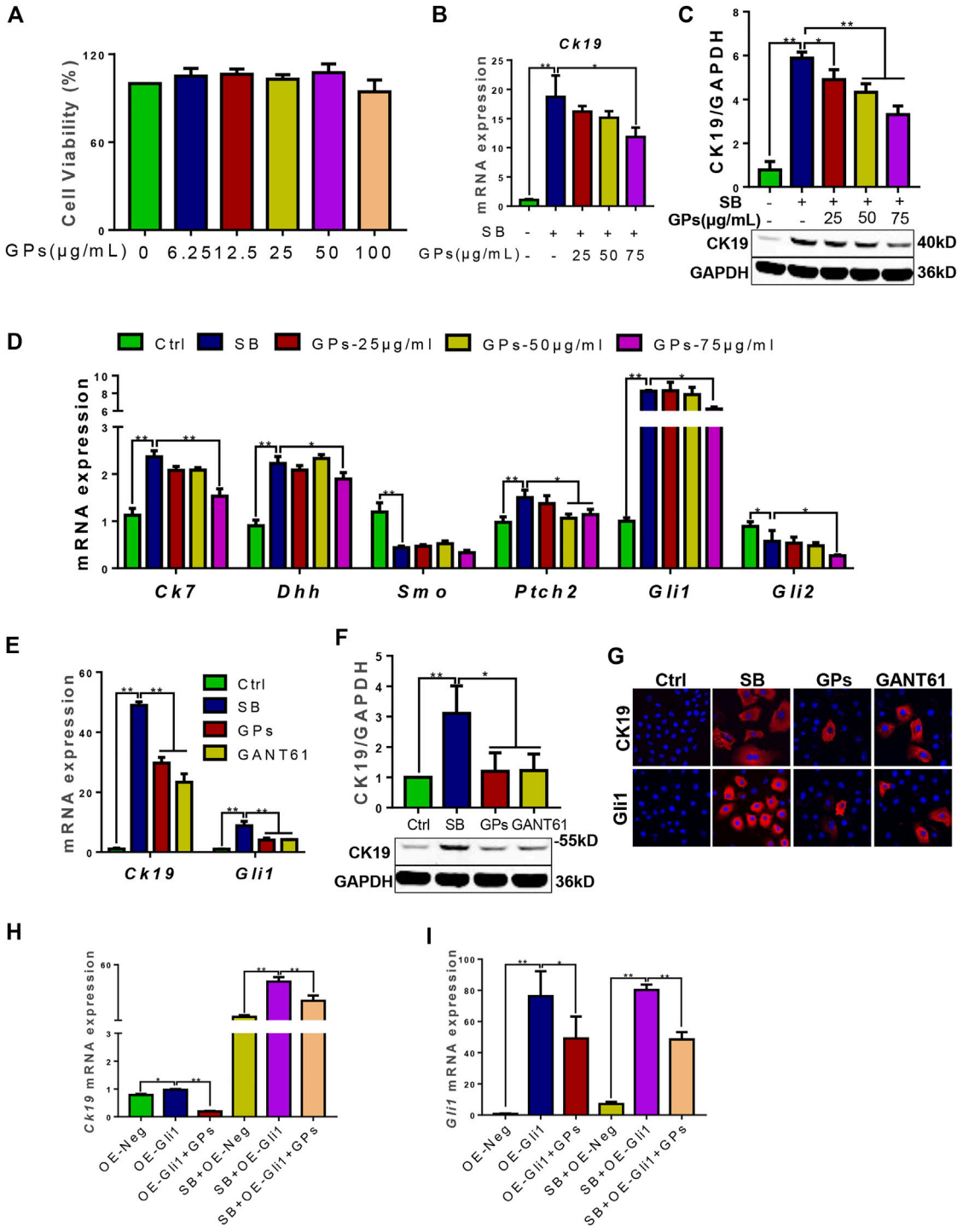

FIGURE 6
GPs inhibited the differentiation of WB-F344 cells into cholangiocytes via hedgehog signaling. **(A)** Cell viability of GPs on WB-F344 cells. **(B)** The mRNA expression of *Ck19*. **(C)** Western blotting and the gray-level score for CK19. **(D)** The mRNA expressions of *Ck7*, *Dhh*, *Smo*, *Ptch2*, *Gli1*, and *Gli2*. **(E)** The mRNA expressions of *Ck19* and *Gli1*. **(F)** Western blotting and the gray-level score for CK19. **(G)** Representative fluorescent cell images of WB-F344 cells stained with Gli1 and CK19 (600×). **(H)** The mRNA expression of *Ck19*. **(I)** The mRNA expression of *Gli1*. *, $p < 0.05$; **, $p < 0.01$.

$CK19^+/OV6^+$ and $CK7^+/OV6^+$ cells were reduced in the GPs-treated and GANT61-treated groups compared with the CCl_4/2-AAF-treated group (Figure 3D). Consistently with our finding in CCl_4/2-AAF-treated rats, GPs also reduced the expressions of CK19, Epcam, and CK7 in *Mdr2*$^{-/-}$ mice ($p < 0.01$, $p < 0.05$) (Figures 4A–C). And the number of $Epcam^+/CK7^+$ cells was obviously decreased after GPs treatment analyzed by double-immunofluorescence staining (Figure 4D). These results demonstrated that GPs inhibited DR in fibrotic models.

3.4 GPs suppressed the activation of hedgehog signaling *in vivo*

In CCl_4/2-AAF-treated rats, qRT-PCR showed that the mRNA expressions of *Dhh*, *Smo*, *Ptch2*, *Gli1,* and *Gli2*, the relative genes of hedgehog signaling, were upregulated in the CCl_4/2-AAF-treated rats ($p < 0.01$), which were downregulated in the GPs-treated group ($p < 0.01$, $p < 0.05$) (Figure 5A). GANT61, a direct small-molecule inhibitor of Gli1/Gli2, obviously reduced the mRNA expression of *Gli1, Gli2* and *Ptch2* ($p < 0.01$, $p < 0.05$) (Figure 5A). In addition, in *Mdr2*$^{-/-}$ mice, GPs decreased the expression of *Smo*, *Ptch2*, *Gli1* and *Gli2* ($p < 0.01$, $p < 0.05$) (Figure 5B). Importantly, double-immunofluorescence staining results showed Gli1 was expressed in the $CK19^+$ reactive cholangiocytes, and the number of $Gli1^+/CK19^+$ cells was significantly increased in *Mdr2*$^{-/-}$ mice, which was obviously reduced in the GPs-treated group (Figure 5C). These results indicated that GPs played an anti-fibrotic role by inhibiting hedgehog signaling.

3.5 GPs inhibited the differentiation of HPCs into cholangiocytes by inhibition of hedgehog signaling *in vitro*

To confirm whether GPs suppressed DR through hedgehog signaling, the *in vitro* model of differentiation of WB-F344 cells into cholangiocytes induced by SB was established. And the qRT-PCR result showed that the mRNA levels of *Dhh*, *Ptch2*, and *Gli1* were upregulated in the SB-treated group compared with the control group ($p < 0.01$) (Figure 6D), which suggested that Hh signaling plays an effect on the differentiation of WB-F344 cells into cholangiocytes. Based on the CCK8 assay showed that the different concentrations of GPs did not have a toxic effect on WB-F344 cells (Figure 6A). Then, GPs at the three concentrations (25, 50, 75 μg/ml) were selected to incubate WB-F344 cells for 4 days, and the results showed that GPs significantly decreased the expressions of CK19, CK7, Dhh, Ptch2 and Gli1 at 75 μg/ml compared with the SB-treated group ($p < 0.01$, $p < 0.05$) (Figures 6B–D), Further study found that the ability of GPs to inhibit CK19 and Gli1 expression was comparable to that of the Gli1 inhibitor, GANT61 (Figures 6E–G).

To further validate whether GPs inhibit the differentiation of WB-F344 cells into cholangiocytes in a Gli1-dependent manner, Gli1-overexpressing lentiviral vectors were transfected into WB-F344 cells. The results revealed that *Ck19* and *Gli1* expressions in the Gli1-overexpressing lentiviral vector-transfected group were upregulated compared with the empty vector-transfected group ($p < 0.05$, $p < 0.01$), which were remarkably downregulated after treatment with GPs ($p < 0.05$, $p < 0.01$) (Figures 6H,I). Even compared with the SB plus empty vector-transfected groups, the *Ck19* expression was notably increased in the SB plus Gli1-overexpressing lentiviral vector-transfected group ($p < 0.01$), which was also decreased after GPs treatment ($p < 0.01$) (Figure 6H). All these results demonstrated that Gli1 triggered and promoted the differentiation of WB-F344 cells into cholangiocytes, which could be inhibited by GPs.

3.6 NPLC0393, the natural compound of GPs, suppressed the differentiation of WB-F344 cells into cholangiocytes in a Gli1-dependent manner

NPLC0393 is a triterpene saponin constituent of GPs, which is isolated from the Chinese herb *Gynostemma pentaphyllum*. The total ion chromatograms (TIC) and extract ion chromatograms (EIC) of NLPC0393 in GPs and reference substances were shown in Figure 7A. The content of NPLC0393 in GPs was 2.6%. *In vitro* results showed that NPLC0393 at 20 μM reduced the expression of CK19 and Gli1 induced not only by SB stimulation but also by SB stimulation plus Gli1-overexpressing lentiviral vectors ($p < 0.05$, $p < 0.01$) (Figures 7B–H). In summary, NPLC0393, the compound of GPs also inhibited the differentiation of WB-F344 cells into cholangiocytes in a Gli1-dependent manner.

4 Discussion

Numerous candidates from Chinese herbs have been studied recently for treating liver fibrosis (Li, 2020). GPs are one of the triterpenoids mainly extracted from *Gynostemma pentaphyllum*. It has been reported that GPs had unambiguous hepatoprotective effects on liver injuries (Huang et al., 2019; Shen et al., 2020). Additionally, GPs significantly decreased the serum ALT and AST levels, ameliorated the histopathological changes in CCl_4 or DMN-induced liver fibrosis models (Feng et al., 2012; Chen et al., 2017). In this study, the obvious anti-fibrotic effect of GPs was also demonstrated by other two different rodent models, the CCl_4/2-AAF-induced hepatic fibrosis and *Mdr2*$^{-/-}$ mice. 2-AAF can block hepatocyte proliferation and induce the robust expansion of HPCs (Petersen et al., 1998). And the CCl_4/2-

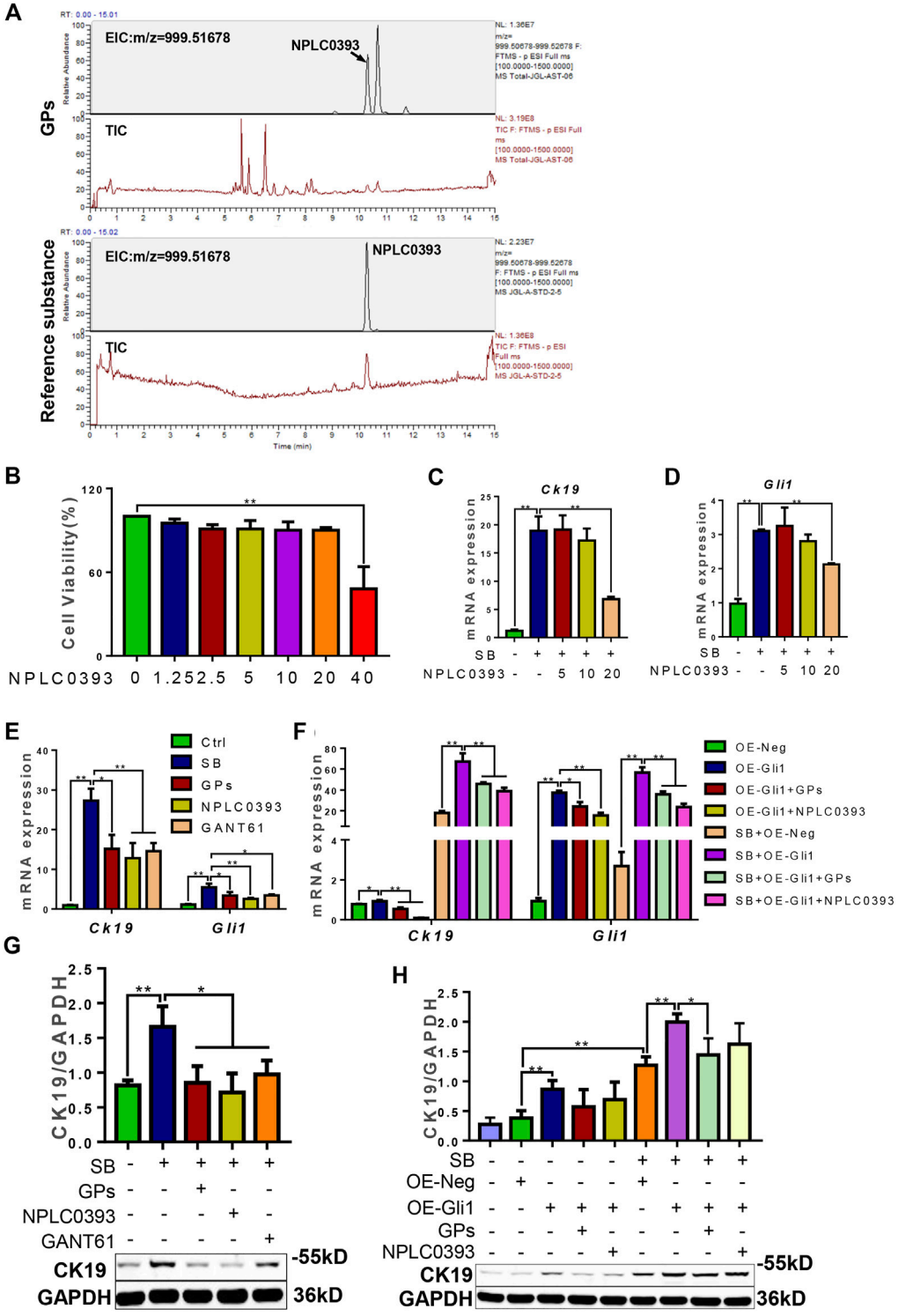

FIGURE 7
NPLC0393 suppressed the differentiation of WB-F344 cells toward a biliary phenotype in a Gli1-dependent manner. **(A)** The total ion chromatograms and extract ion chromatograms of NLPC0393 in GPs and reference substances (TIC and EIC). **(B)** Cell viability of NPLC0393 on WB-F344 cells. **(C)** The mRNA expressions of *Ck19*. **(D)** The mRNA expression of *Gli1*. **(E,F)** The mRNA expressions of *Ck19* and *Gli1*. **(G,H)** Western blotting and gray-level score of CK19. *, $p < 0.05$; **, $p < 0.01$.

AAF-induced DR-fibrosis model displays more severe fibrosis and even cirrhosis compared to the only CCl_4-induced fibrotic model, which recapitulated the events commonly observed in human fibrosis (Chobert et al., 2012). The ABCB4 gene was mutative in the *Mdr2*$^{-/-}$ mouse, which prevents the mice from secreting phospholipids into the bile. A histological look highly reminiscent of PSC patients results from the retained bile becoming corrosive and destroying cholangiocytes (Smit et al., 1993). The anti-fibrotic effect of GPs on these two models supplied more evidence that GPs ameliorated liver fibrosis induced by different pathogenic processes.

DR is a common typical response to injury in human liver diseases (Sato et al., 2019). Histologically, DR is described as the proliferation of ductular reactive cells, arising from the proliferation of pre-existing cholangiocytes, the differentiation of HPCs, or the biliary metaplasia of hepatocytes, which can exhibit a ductular phenotype and be identified of cholangiocyte markers, CK19 and CK7 (Sato et al., 2019). It is also described as a dynamic and complex process involving many other cells and reactions, such as inflammatory cells, extracellular matrix, and endothelial cells in the reactive lesions (Sato et al., 2019; Coll et al., 2022), which facilitates liver fibrosis and correlates with disease severity (Aguilar-Bravo et al., 2019). In contrast previous studies proposed that the anti-fibrotic effect of GPs may be related to altering glycolysis metabolism and protecting against the damage of aldehydes and lipid peroxidation (Song et al., 2017), and blocking the proliferation of HSCs (Chen et al., 2008), our study found that both in CCl_4/2-AAF-treated rats and *Mdr2*$^{-/-}$ mice, GPs down-regulated the Epcam, CK19 and CK7 expression, and decreased the number of CK19$^+$/OV6$^+$, Epcam$^+$/CK7$^+$ cells, which suggested that GPs suppressed DR. Further studies proved that GPs inhibited the differentiation of WB-F344 cells into a biliary phenotype inducing by SB *in vitro*. Both *in vivo* and *in vitro* results demonstrated that DR, the key pathological factor in liver fibrosis, could be obviously inhibited by GPs.

Hh signaling is vital for hepatic pathophysiology, which consists of four fundamental components: the ligand Hh (containing Shh, Dhh, and Ihh), the receptor Ptch, the signal transducer Smo, and the transcription factor Glis (including Gli1, Gli2, and Gli3). In normal adult livers, Hh signaling is quiescent. Once activated when the liver was injured, Hh signaling can regulate liver sinusoidal endothelial cells capillarization (Wu et al., 2021), stimulate the activation and proliferation of HSCs (Du et al., 2018), and promote biliary expansion (Jalan-Sakrikar et al., 2016), which leads to liver fibrosis (Chung et al., 2016). Thus, inhibiting Hh signaling will be an effective therapeutic target. It has been previously reported liver fibrosis was attenuated by Hh inhibitors, such as cyclopamine (Zhang et al., 2020), vismodegib (Pratap et al., 2012), and GANT61 (Jiayuan et al., 2020). The present study showed that GPs suppressed the activation of Hh signaling both in CCl_4/2-AAF-treated rats and *Mdr2*$^{-/-}$ mice. Of note, Gli1$^+$/CK19$^+$ cells were decreased after GPs treatment. Gli1 is one of the strongest downstream transcriptional activators of Hh signaling. Gli1$^+$ mesenchymal stem cell-like cells were proved to have a key ability to transition into myofibroblasts (Weiskirchen et al., 2019). Genetic ablation of Gli1$^+$ cells substantially improves injury-induced organ fibrosis, which provides a relevant therapeutic target in fibrotic diseases (Kramann et al., 2015). Based on our previous finding, Gli1-dependent Hh signaling triggered the differentiation of HPCs into cholangiocytes and promoted DR-induced fibrosis progression (Chen et al., 2020). The results *in vitro* showed that GPs suppressed the differentiation of WB-F344 cells into a biliary phenotype *via* inhibition of Hh signaling, which was further confirmed in cells transfected with over-expressing Gli1 lentiviral vectors. This is the first time to reveal that GPs alleviate DR and liver fibrosis *via* inhibition of Hh signaling.

NPLC0393 is a natural triterpene saponin constituent of the Chinese herb *Gynostemma pentaphyllum*. NPLC0393 accounts for 2.6% of GPs and is one of the main active ingredients. Previous studies demonstrated that NPLC0393, as a small molecular activator of PP2Cα, successfully ameliorated CCl_4- and BDL-induced fibrotic models (Wang et al., 2010). And it inhibited the activation of HSCs by regulating TGFβ1/NDRG2/MAPK signaling axis in CCl_4-induced liver fibrosis (Huang et al., 2020) Our study newly found that NLPC0393 inhibited the differentiation of WB-F344 cells into cholangiocytes in a Gli1-dependent manner. Additional *in vivo* experiments, of course, should be needed to verify the anti-fibrosis and anti-DR of NPLC0393. But the *in vitro* results of the previous study could provide stronger evidence for the important effects of GPs on ameliorating DR and liver fibrosis *via* inhibition of Hh signaling.

5 Conclusion

In summary, the present study provided more evidence supporting the therapeutic effect of GPs on liver fibrosis. And for the first time, we demonstrated that GPs alleviated DR and liver fibrosis *via* inhibition of hedgehog signaling. These results will provide new insights into the anti-fibrotic effects of GPs.

Data availability statement

The original contributions presented in the study are included in the article/Supplementary Material, further inquiries can be directed to the corresponding authors.

Ethics statement

The animal study was reviewed and approved by the Animal Experimentation of Shanghai University of Traditional Chinese Medicine.

Author contributions

PL and JC contributed to conception, YH, PL, and JC participated in research design. YH, XH, XZ, YL, YF, LZ, JF, WL, and HC conducted the experiments. WL, GC, YM, HZ, HC, and LC performed the statistical analysis. YH, XH, and JC edited and wrote the manuscript, designed and drew tables and figures. PL and JC revised the manuscript and were responsible for final approval. All authors read and approved the final manuscript.

Funding

This work was supported by the National Natural Science Foundation of China (81973613, 81603465) to JC, Shuguang Hospital affiliated to Shanghai University of Traditional Chinese Medicine (SGXZ-201908, SGKTLC-202013 to JC, SGKJ-202004 to YH), China Postdoctoral Science Foundation (2021M702218) to YH, Shanghai Post-doctoral Excellence Program (2020372) to YH, Fujian Provincial Department of Science and Technology (2021D006) to HC, and Xiamen Department of Science and Technology (3502Z20214ZD1150) to HC.

Acknowledgments

We thank Shanhua Fang from Shanghai Institute of Materia Medica, Chinese Academy of Sciences for providing NLPC0393.

Conflict of interest

The authors declare that the research was conducted in the absence of any commercial or financial relationships that could be construed as a potential conflict of interest.

Publisher's note

All claims expressed in this article are solely those of the authors and do not necessarily represent those of their affiliated organizations, or those of the publisher, the editors and the reviewers. Any product that may be evaluated in this article, or claim that may be made by its manufacturer, is not guaranteed or endorsed by the publisher.

Supplementary material

The Supplementary Material for this article can be found online at: https://www.frontiersin.org/articles/10.3389/fphar.2022.1033103/full#supplementary-material

References

Aguilar-Bravo, B., Rodrigo-Torres, D., Arino, S., Coll, M., Pose, E., Blaya, D., et al. (2019). Ductular reaction cells display an inflammatory profile and recruit neutrophils in alcoholic hepatitis. *Hepatology* 69 (5), 2180–2195. doi:10.1002/hep.30472

Asrani, S. K., Devarbhavi, H., Eaton, J., and Kamath, P. S. (2019). Burden of liver diseases in the world. *J. Hepatol.* 70 (1), 151–171. doi:10.1016/j.jhep.2018.09.014

Chen, J., Hu, Y., Fang, J., Chen, L., Mu, Y., Liu, W., et al. (2020). GLI1, but not smoothened-dependent, signaling in hepatic progenitor cells promotes a ductular reaction, which aggravates liver fibrosis. *J. Hepatology* 73, S511. doi:10.1016/s0168-8278(20)31497-5

Chen, J., Li, X., Hu, Y., Liu, W., Zhou, Q., Zhang, H., et al. (2017). Gypenosides ameliorate carbon tetrachloride-induced liver fibrosis by inhibiting the differentiation of hepatic progenitor cells into myofibroblasts. *Am. J. Chin. Med.* 45 (5), 1061–1074. doi:10.1142/S0192415X17500574

Chen, M. H., Chen, S. H., Wang, Q. F., Chen, J. C., Chang, D. C., Hsu, S. L., et al. (2008). The molecular mechanism of gypenosides-induced G1 growth arrest of rat hepatic stellate cells. *J. Ethnopharmacol.* 117 (2), 309–317. doi:10.1016/j.jep.2008.02.009

Chobert, M. N., Couchie, D., Fourcot, A., Zafrani, E. S., Laperche, Y., Mavier, P., et al. (2012). Liver precursor cells increase hepatic fibrosis induced by chronic carbon tetrachloride intoxication in rats. *Lab. Invest.* 92 (1), 135–150. doi:10.1038/labinvest.2011.143

Chung, S. I., Moon, H., Ju, H. L., Cho, K. J., Kim, D. Y., Han, K. H., et al. (2016). Hepatic expression of Sonic Hedgehog induces liver fibrosis and promotes hepatocarcinogenesis in a transgenic mouse model. *J. Hepatol.* 64 (3), 618–627. doi:10.1016/j.jhep.2015.10.007

Clouston, A. D., Powell, E. E., Walsh, M. J., Richardson, M. M., Demetris, A. J., and Jonsson, J. R. (2005). Fibrosis correlates with a ductular reaction in hepatitis C: roles of impaired replication, progenitor cells and steatosis. *Hepatology* 41 (4), 809–818. doi:10.1002/hep.20650

Coll, M., Arino, S., Martinez-Sanchez, C., Garcia-Pras, E., Gallego, J., Moles, A., et al. (2022). Ductular reaction promotes intrahepatic angiogenesis through Slit2-Roundabout 1 signaling. *Hepatology* 75 (2), 353–368. doi:10.1002/hep.32140

Cui, J., Eneroth, P., and Bruhn, J. G. (1999). Gynostemma pentaphyllum: identification of major sapogenins and differentiation from panax species. *Eur. J. Pharm. Sci.* 8 (3), 187–191. doi:10.1016/s0928-0987(99)00013-5

Du, K., Hyun, J., Premont, R. T., Choi, S. S., Michelotti, G. A., Swiderska-Syn, M., et al. (2018). Hedgehog-YAP signaling pathway regulates glutaminolysis to control activation of hepatic stellate cells. *Gastroenterology* 154 (5), 1465–1479. doi:10.1053/j.gastro.2017.12.022

Feng, Q., Li, X., Peng, J., Duan, X., Fu, Q., and Hu, Y. (2012). Effect of gypenosides on DMN-induced liver fibrosis in rats. *Zhongguo Zhong Yao Za Zhi* 37 (4), 505–508.

Gupta, V., Gupta, I., Park, J., Bram, Y., and Schwartz, R. E. (2020). Hedgehog signaling demarcates a niche of fibrogenic peribiliary mesenchymal cells. *Gastroenterology* 159 (2), 624–638. doi:10.1053/j.gastro.2020.03.075

He, Q., Li, J. K., Li, F., Li, R. G., Zhan, G. Q., Li, G., et al. (2015). Mechanism of action of gypenosides on type 2 diabetes and non-alcoholic fatty liver disease in rats. *World J. Gastroenterol.* 21 (7), 2058–2066. doi:10.3748/wjg.v21.i7.2058

Huang, H., Wang, K., Liu, Q., Ji, F., Zhou, H., Fang, S., et al. (2020). The active constituent from Gynostemma pentaphyllum prevents liver fibrosis through regulation of the TGF-β1/NDRG2/MAPK Axis. *Front. Genet.* 11, 594824. doi:10.3389/fgene.2020.594824

Huang, X., Chen, W., Yan, C., Yang, R., Chen, Q., Xu, H., et al. (2019). Gypenosides improve the intestinal microbiota of non-alcoholic fatty liver in mice and alleviate its progression. *Biomed. Pharmacother.* 118, 109258. doi:10.1016/j.biopha.2019.109258

Jalan-Sakrikar, N., De Assuncao, T. M., Lu, J., Almada, L. L., Lomberk, G., Fernandez-Zapico, M. E., et al. (2016). Hedgehog signaling overcomes an EZH2-dependent epigenetic barrier to promote cholangiocyte expansion. *PLoS One* 11 (12), e0168266. doi:10.1371/journal.pone.0168266

Jiayuan, S., Junyan, Y., Xiangzhen, W., Zuping, L., Jian, N., Baowei, H., et al. (2020). Gant61 ameliorates CCl4-induced liver fibrosis by inhibition of Hedgehog signaling activity. *Toxicol. Appl. Pharmacol.* 387, 114853. doi:10.1016/j.taap.2019.114853

Jung, Y., Brown, K. D., Witek, R. P., Omenetti, A., Yang, L., Vandongen, M., et al. (2008). Accumulation of hedgehog-responsive progenitors parallels alcoholic liver disease severity in mice and humans. *Gastroenterology* 134 (5), 1532–1543. doi:10.1053/j.gastro.2008.02.022

Kramann, R., Schneider, R. K., DiRocco, D. P., Machado, F., Fleig, S., Bondzie, P. A., et al. (2015). Perivascular Gli1+ progenitors are key contributors to injury-induced organ fibrosis. *Cell Stem Cell* 16 (1), 51–66. doi:10.1016/j.stem.2014.11.004

Li, H. (2020). Advances in anti hepatic fibrotic therapy with Traditional Chinese Medicine herbal formula. *J. Ethnopharmacol.* 251, 112442. doi:10.1016/j.jep.2019.112442

Li, H., Xi, Y., Xin, X., Tian, H., and Hu, Y. (2020). Gypenosides regulate farnesoid X receptor-mediated bile acid and lipid metabolism in a mouse model of non-alcoholic steatohepatitis. *Nutr. Metab.* 17, 34. doi:10.1186/s12986-020-00454-y

Li, X., Liu, H., Lv, C., Du, J., Lian, F., Zhang, S., et al. (2022). Gypenoside-induced apoptosis via the PI3K/AKT/mTOR signaling pathway in bladder cancer. *Biomed. Res. Int.* 2022, 9304552. doi:10.1155/2022/9304552

Ochoa, B., Syn, W. K., Delgado, I., Karaca, G. F., Jung, Y., Wang, J., et al. (2010). Hedgehog signaling is critical for normal liver regeneration after partial hepatectomy in mice. *Hepatology* 51 (5), 1712–1723. doi:10.1002/hep.23525

Parola, M., and Pinzani, M. (2019). Liver fibrosis: Pathophysiology, pathogenetic targets and clinical issues. *Mol. Asp. Med.* 65, 37–55. doi:10.1016/j.mam.2018.09.002

Pereira Tde, A., Witek, R. P., Syn, W. K., Choi, S. S., Bradrick, S., Karaca, G. F., et al. (2010). Viral factors induce Hedgehog pathway activation in humans with viral hepatitis, cirrhosis, and hepatocellular carcinoma. *Lab. Invest.* 90 (12), 1690–1703. doi:10.1038/labinvest.2010.147

Petersen, B. E., Zajac, V. F., and Michalopoulos, G. K. (1998). Hepatic oval cell activation in response to injury following chemically induced periportal or pericentral damage in rats. *Hepatology* 27 (4), 1030–1038. doi:10.1002/hep.510270419

Popov, Y., Patsenker, E., Fickert, P., Trauner, M., and Schuppan, D. (2005). Mdr2 (Abcb4)-/- mice spontaneously develop severe biliary fibrosis via massive dysregulation of pro- and antifibrogenic genes. *J. Hepatol.* 43 (6), 1045–1054. doi:10.1016/j.jhep.2005.06.025

Pratap, A., Singh, S., Mundra, V., Yang, N., Panakanti, R., Eason, J. D., et al. (2012). Attenuation of early liver fibrosis by pharmacological inhibition of smoothened receptor signaling. *J. Drug Target.* 20 (9), 770–782. doi:10.3109/1061186X.2012.719900

Roehlen, N., Crouchet, E., and Baumert, T. F. (2020). Liver fibrosis: Mechanistic concepts and therapeutic perspectives. *Cells* 9 (4), E875. doi:10.3390/cells9040875

Sato, K., Marzioni, M., Meng, F., Francis, H., Glaser, S., and Alpini, G. (2019). Ductular reaction in liver diseases: Pathological mechanisms and translational significances. *Hepatology* 69 (1), 420–430. doi:10.1002/hep.30150

Shen, S., Wang, K., Zhi, Y., Shen, W., and Huang, L. (2020). Gypenosides improves nonalcoholic fatty liver disease induced by high-fat diet induced through regulating LPS/TLR4 signaling pathway. *Cell Cycle* 19 (22), 3042–3053. doi:10.1080/15384101.2020.1829800

Smit, J. J., Schinkel, A. H., Oude Elferink, R. P., Groen, A. K., Wagenaar, E., van Deemter, L., et al. (1993). Homozygous disruption of the murine mdr2 P-glycoprotein gene leads to a complete absence of phospholipid from bile and to liver disease. *Cell* 75 (3), 451–462. doi:10.1016/0092-8674(93)90380-9

Song, Y. N., Dong, S., Wei, B., Liu, P., Zhang, Y. Y., and Su, S. B. (2017). Metabolomic mechanisms of gypenoside against liver fibrosis in rats: An integrative analysis of proteomics and metabolomics data. *PLoS One* 12 (3), e0173598. doi:10.1371/journal.pone.0173598

Syn, W. K., Agboola, K. M., Swiderska, M., Michelotti, G. A., Liaskou, E., Pang, H., et al. (2012). NKT-associated hedgehog and osteopontin drive fibrogenesis in non-alcoholic fatty liver disease. *Gut* 61 (9), 1323–1329. doi:10.1136/gutjnl-2011-301857

Tu, Q., Zhu, Y., Yuan, Y., Guo, L., Liu, L., Yao, L., et al. (2021). Gypenosides inhibit inflammatory response and apoptosis of endothelial and epithelial cells in LPS-induced ALI: A study based on bioinformatic analysis and *in vivo*/vitro experiments. *Drug Des. devel. Ther.* 15, 289–303. doi:10.2147/DDDT.S286297

Wang, L., Wang, X., Chen, J., Yang, Z., Yu, L., Hu, L., et al. (2010). Activation of protein serine/threonine phosphatase PP2Cα efficiently prevents liver fibrosis. *PLoS One* 5 (12), e14230. doi:10.1371/journal.pone.0014230

Weiskirchen, R., Weiskirchen, S., and Tacke, F. (2019). Organ and tissue fibrosis: Molecular signals, cellular mechanisms and translational implications. *Mol. Asp. Med.* 65, 2–15. doi:10.1016/j.mam.2018.06.003

Wu, X., Shu, L., Zhang, Z., Li, J., Zong, J., Cheong, L. Y., et al. (2021). Adipocyte fatty acid binding protein promotes the onset and progression of liver fibrosis via mediating the crosstalk between liver sinusoidal endothelial cells and hepatic stellate cells. *Adv. Sci.* 8 (11), e2003721. doi:10.1002/advs.202003721

Zhang, H., Chen, X., Zong, B., Yuan, H., Wang, Z., Wei, Y., et al. (2018). Gypenosides improve diabetic cardiomyopathy by inhibiting ROS-mediated NLRP3 inflammasome activation. *J. Cell. Mol. Med.* 22 (9), 4437–4448. doi:10.1111/jcmm.13743

Zhang, Q., Guo, X., Xie, C., Cao, Z., Wang, X., Liu, L., et al. (2021). Unraveling the metabolic pathway of choline-TMA-TMAO: Effects of gypenosides and implications for the therapy of TMAO related diseases. *Pharmacol. Res.* 173, 105884. doi:10.1016/j.phrs.2021.105884

Zhang, T., Li, Y., Song, Y., Chen, X., Li, J., Peng, Q., et al. (2020). Curcumin- and cyclopamine-loaded liposomes to enhance therapeutic efficacy against hepatic fibrosis. *Drug Des. devel. Ther.* 14, 5667–5678. doi:10.2147/DDDT.S287442

Zhang, X., Du, G., Xu, Y., Li, X., Fan, W., Chen, J., et al. (2016). Inhibition of notch signaling pathway prevents cholestatic liver fibrosis by decreasing the differentiation of hepatic progenitor cells into cholangiocytes. *Lab. Invest.* 96 (3), 350–360. doi:10.1038/labinvest.2015.149

Zhao, L., Westerhoff, M., Pai, R. K., Choi, W. T., Gao, Z. H., and Hart, J. (2018). Centrilobular ductular reaction correlates with fibrosis stage and fibrosis progression in non-alcoholic steatohepatitis. *Mod. Pathol.* 31 (1), 150–159. doi:10.1038/modpathol.2017.115

frontiers | Frontiers in Pharmacology

TYPE Review
PUBLISHED 23 November 2022
DOI 10.3389/fphar.2022.1033674

OPEN ACCESS

EDITED BY
Jian Gao,
Shanghai Children's Medical Center, China

REVIEWED BY
Han Cen,
Ningbo University, China
Tao Zhu,
Zhejiang University, China

*CORRESPONDENCE
Song Shao,
1255319122@qq.com

†These authors have contributed equally to this work

SPECIALTY SECTION
This article was submitted to Gastrointestinal and Hepatic Pharmacology, a section of the journal Frontiers in Pharmacology

RECEIVED 31 August 2022
ACCEPTED 02 November 2022
PUBLISHED 23 November 2022

CITATION
Wang X, Tang G, Liu Y, Zhang L, Chen B, Han Y, Fu Z, Wang L, Hu G, Ma Q, Sheng S, Wang J, Hu X and Shao S (2022), The role of IL-6 in coronavirus, especially in COVID-19.
Front. Pharmacol. 13:1033674.
doi: 10.3389/fphar.2022.1033674

The role of IL-6 in coronavirus, especially in COVID-19

Xinyi Wang[1†], Guozheng Tang[2†], Yuchen Liu[3†], Lizhi Zhang[4†], Bangjie Chen[5], Yanxun Han[3], Ziyue Fu[6], Liuning Wang[4], Guangzhi Hu[4], Qing Ma[4], Shuyan Sheng[4], Jianpeng Wang[4], Xinyang Hu[4] and Song Shao[2*]

[1]Department of Radiation Oncology, The First Affiliated Hospital of Anhui Medical University, Hefei, Anhui, China, [2]Department of Orthopaedics, Lu'an Hospital of Anhui Medical University, Lu'an, Anhui, China, [3]Department of Otolaryngology, Head and Neck Surgery, The First Affifiliated Hospital of Anhui Medical University, Hefei, Anhui, China, [4]First Clinical Medical College, Anhui Medical University, Hefei, Anhui, China, [5]Department of Oncology, The First Affiliated Hospital of Anhui Medical University, Hefei, Anhui, China, [6]Second Clinical Medical College, Anhui Medical University, Hefei, Anhui, China

Severe Acute Respiratory Syndrome Coronavirus 2 (SARS-CoV-2) infects both people and animals and may cause significant respiratory problems, including lung illness: Corona Virus Disease 2019 (COVID-19). Swabs taken from the throat and nose of people who have the illness or are suspected of having it have shown this pathogenic virus. When SARS-CoV-2 infects the upper and lower respiratory tracts, it may induce moderate to severe respiratory symptoms, as well as the release of pro-inflammatory cytokines including interleukin 6 (IL-6). COVID-19-induced reduction of IL-6 in an inflammatory state may have a hitherto undiscovered therapeutic impact. Many inflammatory disorders, including viral infections, has been found to be regulated by IL-6. In individuals with COVID-19, one of the primary inflammatory agents that causes inflammatory storm is IL-6. It promotes the inflammatory response of virus infection, including the virus infection caused by SARS-CoV-2, and provides a new diagnostic and therapeutic strategy. In this review article, we highlighted the functions of IL-6 in the coronavirus, especially in COVID-19, showing that IL-6 activation plays an important function in the progression of coronavirus and is a rational therapeutic goal for inflammation aimed at coronavirus.

KEYWORDS

IL-6, COVID-19, SARS, MERS, coronavirus

Introduction

Severe Acute Respiratory Syndrome Coronavirus 2 (SARS-CoV-2), a betacoronavirus closely related to Middle East Respiratory Syndrome Coronavirus (MERS-CoV) and Severe Acute Respiratory Syndrome Coronavirus (SARS-CoV), the organisms responsible for Middle East respiratory sickness (MERS) and severe acute respiratory syndrome (SARS), respectively (COVID-19). MERS-CoV and SARS-CoV cause high mortality, with the majority of cases resulting from an inflammatory viral pneumonia that progresses to acute respiratory distress syndrome 1 (ARDS1). ARDS2 was detected in 81 percent of fatal patients infected with COVID-19. In light of this, a recent letter published in The Lancet

recommends that all COVID-19 patients be examined for hyperinflammation to identify those who may benefit from immunosuppression or immunomodulation to prevent acute lung injury (ALI). The coronavirus family consists of four "established" human coronaviruses (HCOVs), two of which have been identified since the 1960s: HCOV-OC43 and HCOV-229E. These two viruses produce a milder respiratory illness and, after rhinoviruses, are the most frequent cause (10–30 percent) of the common cold (Hamre and Procknow, 1966; McIntosh et al., 1967; van der Hoek, 2007). Following increased coronavirus screening, two new HCoVs, HCoV-NL63 and HCoV-HKU1, were found lately (van der Hoek et al., 2004; Woo et al., 2005). Recent research suggests that HCoV-NL63, -229E, and -OC43 are also the result of zoonotic transmission from bats (de Wilde et al., 2018).

Considering the importance of interleukin 6 (IL-6) in airway disease, preliminary studies using humanized monoclonal antibodies against the IL-6 Receptor (Tocilizumab) to target this cytokine therapeutically in response to COVID-19 infection have shown promising results, but additional research is required. It has been shown that the antimalarial drug hydroxychloroquine (Plaquenil) inhibits the expression of toll-like receptors (TLRs) and the production of IL-6, and hence may have an anti-COVID-19 impact (Wang et al., 2020).

Overview of IL-6

IL-6 is a prototype cytokine with pleiotropic activity and functional redundancy that is necessary for host defense (Akira et al., 1993; Tanaka and Kishimoto, 2014; Tanaka et al., 2016a). Due to infection and tissue damage, IL-6 is produced rapidly by a variety of cells, including immune-mediated cells, mesenchymal cells, endothelial cells, fibroblasts and cancer cells, and even many other cells, which promotes host defense by stimulating acute phase reactions, hematopoiesis, and immune responses (Akira et al., 1993; Tanaka et al., 2014; Tanaka et al., 2016a). Because these processes are necessary for the elimination of pathogenic microorganisms and tissue healing, IL-6 is a crucial cytokine in host defense. Monocytes and macrophages produce IL-6 in response to infections or tissue injuries by stimulating pattern recognition receptors with pathogen-associated molecular patterns (PAMPs) or damage-associated molecular patterns (DAMPs) and serum IL-6 levels rise to several tens to hundreds of pg/ml, depending on the infection or injury, but in healthy condition, it is not higher than 4 pg/ml (Tanaka et al., 2012; Tanaka et al., 2014; Kang et al., 2015).

The role of IL-6 in inflammation

The purpose of acute inflammation is to transport white blood cells (neutrophils, lymphocytes, monocytes, etc.) and plasma proteins (complements, antibodies, etc.) to the inflammatory site to kill and remove inflammatory factors. In addition to these cells collected from local lesions, various cytokines, such as IL-6 and tumor necrosis factor-α (TNF-α), are also produced during inflammation (Kaur et al., 2020). In acute inflammation, IL-6 enters the liver through blood and induces a large number of acute phase proteins, such as C-reactive protein (CRP), serum amyloid A (SAA), etc. At the same time, the abnormal synthesis of IL-6 also plays a pathological role in chronic inflammation and autoimmunity. When the high concentration of SAA persists, it will promote the generation of chronic inflammatory disease complications and organ failure (Heinrich et al., 1990; Gillmore et al., 2001; Tanaka et al., 2014). Persistent acute inflammation will develop into chronic inflammation, which will eventually lead to tissue damage. IL-6 is an important regulator for the transformation of inflammation from the acute phase to the chronic phase.

The role of IL-6 in disease

IL-6 can mediate a variety of signaling pathways, regulate cell proliferation, differentiation, apoptosis, angiogenesis and metastasis, and play a role in a variety of diseases. In rheumatoid arthritis (RA), the expression of TLRs signaling pathway can be used as the activation pathway of IL-6. IL-6 plays a key role in osteoclast mediated bone resorption. In RA patients, the levels of IL-6 and IL-6R in serum and synovial fluid of affected joints are elevated (Pandolfi et al., 2020). STAT3 pathway is considered to be an important signal transducer downstream of gp130 signal. STAT3 itself is a carcinogenic gene and plays a key role in connecting inflammation and cancer. It can participate in tumor angiogenesis by up regulating the expression of matrix metalloproteinase-9 (MMP-9) (Kujawski et al., 2008; Yu et al., 2009; Kishimoto, 2010).

Signaling pathway of IL-6

IL-6 interacts with its specific receptor IL-6R, and its complex IL-6/IL-6R interacts with and activates gp130, which is a signal transducer shared by the IL-6 family of cytokines. The hexamer complex composed of IL-6/IL-6R/gp130 performs various physiological and biochemical functions of IL-6 by activating different signal pathways (including classic signaling and trans-signaling).

The combination of IL-6 and membrane-bound IL6R (mIL-6R) can mediate classic signaling, while the combination of IL-R and soluble IL-6R (sIL-6R) can mediate trans-signaling. The hexamer complex composed of IL-6/IL-6R/gp130 first activates Janus kinase (JAK) and starts the enzymatic reaction. Two common pathways include JAK/STAT pathway and SHP-2/

ERK pathway. Src homology phosphotyrosine phosphatase 2 (SHP-2) connects to mitogen-activated protein kinase (MAPK), phosphorylates growth factor receptor-bound protein 2 (GRB2) associated binding protein 1 (Gab1), and transfers it to the cell membrane to coordinate the ongoing activation of MAPK and phosphatidylinositol 3-kinase (PI3K). PI3K/Akt pathway contributes to the activation of nuclear factor kappa-B(NF-κB). (Heinrich et al., 2003; Mihara et al., 2012; Tanaka et al., 2014; Baran et al., 2018; Jiang et al., 2021).

When the level of IL-6 in serum is low, the classic signaling pathway plays a leading role, which can play an anti-inflammatory role; When the concentration of IL-6 increases, IL-6R starts trans-signaling transduction, and proinflammatory reaction occurs in a wider cell population (Lee et al., 2014).

Specificity of IL-6

IL-6 is an important member of the cytokine network, a central mediator of cytokine release syndrome (CRS) toxicity, and plays a central role in acute inflammatory response (Lee et al., 2014). IL-6 can induce the production of CRP and procalcitonin (PCT), which is directly related to inflammation and infection, facilitating the diagnosis of early inflammation and early warning of sepsis. Therefore, IL-6 can be used as a biomarker of disease severity and prognosis in CRS. A large number of clinical data show that CRS is related to the severity of COVID-19 and is the key cause of severe COVID-19 [26–28]. A variety of cytokines, including IL-6, are involved in severe COVID-19, and anti-inflammatory treatment is of great significance in the protection of severe patients. Therefore, the role of IL-6 in COVID-19 is irreplaceable by other cytokines.

The function of IL-6 in SARS-CoV and MERS-CoV

IL-6 in SARS-CoV

From 2002 to 2003, SARS-CoV, a new coronavirus, caused a severe respiratory epidemic worldwide (Yu et al., 2019). SARS is characterized by influenza-like symptoms, a high fever, myalgia, dyspnea, lymphopenia, and severe breathing problems caused by lung infiltrates (pneumonia) (De Clercq, 2006). The N proteins and RNA of SARS-CoV were found in lung, bronchial epithelial cells and macrophages, suggesting that these cells may be infected with SARS-CoV. Monoclonal antibodies against MCP-1 and TGF-1, as well as monoclonal antibodies against IL-6, substantially interacted with the angiotensin converting enzyme 2 (ACE2) and the S proteins of SARS-CoV produced by most cells (He et al., 2006). Sheng et al. (Sheng et al., 2005) collected information on SARS-associated coronavirus-infected hospitalized patients in Taiwan University Hospital, and determined a series of plasma inflammatory cytokines, including IL-1β, IL-6, IL-8 and TNF-α. The fast rise of the inflammatory cytokines IL-6, IL-8, and TNF-α was shown to be associated with the development of SARS-associated ARDS. The significance of IL-6 in the acute phase of SARS, however, remained unknown.

The IL-6 cytokine's mRNA expression was observed to be higher in SARS patients' peripheral blood mononuclear cell (PBMC) (Yu et al., 2005; Dosch et al., 2009). After sufficient immunosuppressive medication, the levels of IL-6 and TNF in the acute phase grew dramatically and recovered to normal, according to a study of SARS-CoV infected patients (Hsueh et al., 2004). Wang et al. (Bai et al., 2008) found that the S proteins of SARS-CoV was involved in the synthesis of pro-inflammatory cytokine during the virus-host cell contact stage. IL-6 is one of the primary cytokines released by activated macrophages in excess amounts. The level of IL-6 expression was found to be greater in SARS patients and was associated with the severity of their sickness (Liu et al., 2020a). Before and during the treatment of many early SARS patients, the amount of IL-6 and TNF-α induced by T cells or monocyte activators was higher than the normal value, and some people still increased after treatment. This indicated that SARS may cause long-term imbalance of cytokines. Future research should focus on improving antiviral therapy and trying to use relevant cytokine inhibitors to limit damage (Jones et al., 2004).

IL-6 in MERS-CoV

In 2012, MERS-CoV was discovered and causes a spectrum of severe respiratory disease known as MERS. There were 1,728 confirmed MERS infections in 27 countries as of 26 April 2016, with 624 deaths (Wise, 2012; Zaki et al., 2012; Hijawi et al., 2013; Korea Centers for Disease, 2015; de Wit et al., 2016) (http://www.who.int/csr/don/26-april-2016-mers-saudi-arabia/en/ (2016)).

MERS is most commonly referred to as lower respiratory tract (LRT) disease and involves cough, fever, dyspnea, and pneumonia. Between 20 and 40 percent of infected individuals may develop ARDS, multiple organ failure and death. MERS is another fatal zoonotic coronavirus illness, comparable to SARS; it causes respiratory failure and severe kidney damage (also has the effect on the growth of kidney cells under laboratory conditions). Patients with underlying diseases have been reported more frequently and more fatal. The majority of human MERS infections are linked to medical institution infection prevention and control (IPC) failures. According to reports, the detection rate of all viruses detected in health care workers (HCWs) is about 20%.

Rossigno et al. (Rossignol, 2016) reported that oral administration of 100 mg/kg nitazoxanide 2 h prior to a 1 ml intraperitoneal injection of 4 percent thioglycollate (TG)

decreased plasma IL-6 levels by 90 percent compared to vehicle-treated mice 6 h after TG administration. Although the clinical relevance of these results has not been determined, they suggest that nitazoxanide may improve the prognosis of MERS-CoV patients by reducing the overproduction of pro-inflammatory cytokines such as IL-6. According to recent research, the S protein of MERS-CoV does not increase the production of TNF or IL-6, but rather suppresses their generation by Lipopolysaccharide (LPS). This shows that the activation of these factors found in previous research was related to active viral replication, since macrophages were infected with an active virus at the time (Al-Qahtani et al., 2017). IL-6 expression was elevated in severe MERS-CoV infections compared to moderate ones (Liu et al., 2020a). Nitazoxanide is a broad-spectrum antiviral drug with *in vitro* activity against coronavirus, which can be used to treat viral respiratory infection and inhibit the production of IL-6 (Rossignol, 2016). A phase 2b/3 clinical trial by Haffizulla et al. (Haffizulla et al., 2014) showed that nitazoxanide 600 mg twice a day for five consecutive days was related to the shortening of the duration of symptoms in patients with acute non complex influenza. At present, nitazoxanide is a potential drug to treat MERS, so it is of great significance to evaluate its therapeutic effect when used alone or in combination with other candidate drugs such as oseltamivir (Rossignol et al., 2009).

IL-6 in COVID-19

In December 2019, COVID-19 first came into public view. Globally, as of 6: 49p.m. Central European summer Time (CEST), 26 August 2022, there have been 596, 873, 121 confirmed cases of COVID-19, including 6, 459,684 deaths, reported to World Health Organization (WHO). As of 23 August 2022, a total of 12, 449,443,718 vaccine doses have been administered (https://covid19.who.int/). The nucleic acid sequences of COVID-19 are coronavirus-specific, and they vary from the known human coronavirus specializations. These sequences are identical to those found in severe SARS or MERS coronavirus. The combination of the S protein and ACE2 in COVID-19 provides a severe public health danger to human transmission (Xu et al., 2020; Hu et al., 2021b).

Critical patients with COVID-19 had increased plasma levels of cytokines, similar to SARS, suggesting that an inflammatory storm is involved in illness development (Luo et al., 2020). Inflammatory cytokine (IL-6, IL-1, and IFN) blockade, stem cell therapy, immune cell reduction, transfusion of convalescent plasma, and artificial extracorporeal liver support are all potential therapies for COVID-19 (Al-Qahtani et al., 2017), and we believe that IL-6 blockade is a viable technique for COVID-induced CRS. CRS is a systemic inflammatory response defined by a rapid rise in a high number of pro-inflammatory cytokines (Teijaro, 2017; Norelli et al., 2018; Shimabukuro-Vornhagen et al., 2018), which may be induced by infection, certain medications and other situations. CRS is more frequent in immune-related conditions and treatments, such as chimeric antigen receptor-T (CAR-T) therapy, organ transplantation sepsis (Chousterman et al., 2017) and viral infections. We observed that elevated IL-6 levels were consistently reported in several COVID-19 studies (Huang et al., 2020; Lai et al., 2020; Xu et al., 2020; Hu et al., 2021b), suggesting that it might be used as a disease severity predictor (Luo et al., 2020). In patients with COVID-19, IL-6 levels were linked to death in a large retrospective cohort study (Tanaka et al., 2012). In the dendritic cell-T cell interaction, IL-6 is required for the production of T helper 17 (Th17) cells (Mackay and Arden, 2015). According to Xu et al. (McIntosh et al., 1967) elevated IL-6 might account for the highly active Th17 cells seen in COVID-19 patients. Animal investigations of SARS-CoV have shown that suppressing NF-κB, a critical transcription factor of IL-6, or infecting animals with SARS-CoV missing the coronavirus envelope (E) protein, a potent stimulant to NF-κB signaling, enhanced animal survival with lower IL-6 levels (Zhang et al., 2020). The E proteins of SARS-CoV-2 (Ref sequence QHD43418.1) and SARS-CoV (Ref sequence NP 828854.1) are 95 percent similar, as found. Given that the E protein is a virulence determinant and mediates the coronavirus immune response (Kai and Kai, 2020; Moore and June, 2020), it is reasonable to presume that both viruses provoke an identical immune response. Therefore, targeting IL-6 for COVID-induced CRS may be advantageous (Figure 1).

Patients with severe COVID-19 had a greater IL-6/IFN ratio than those with mild COVID-19, which might be due to a stronger cytokine storm promoting lung injury (Lagunas-Rangel and Chavez-Valencia, 2020). This raises the issue of whether IL-6 inhibition is exclusively helpful in individuals who have high IL-6 serum expression levels. If this is the case, IL-6 testing may become a necessary component of the rating system. Moreover, the expression level of IL-6 may not be sufficient to indicate its functional downstream effects. A test that distinguishes functional IL-6 from total IL-6 might be beneficial for directing treatment decisions. CRP, an acute-phase inflammatory protein generated by IL-6-dependent hepatic biosynthesis, is a reliable indicator of IL-6 bioactivity and is used to predict the severity of CRS and evaluate the success of IL-6 blocking in CAR-T cell-induced CRS patients (van der Hoek et al., 2004; de Wilde et al., 2018). Unknown is the CRP level in virus-induced CRS. With a few exceptions (Hu et al., 2021b), the majority of studies (Liu et al., 2020b; Luo et al., 2020; Smilowitz et al., 2021) found an association between elevated CRP levels and severe COVID-19. In the future, however, further biomarker research will be necessary for risk stratification and therapeutic effect monitoring. In the inflammatory network,

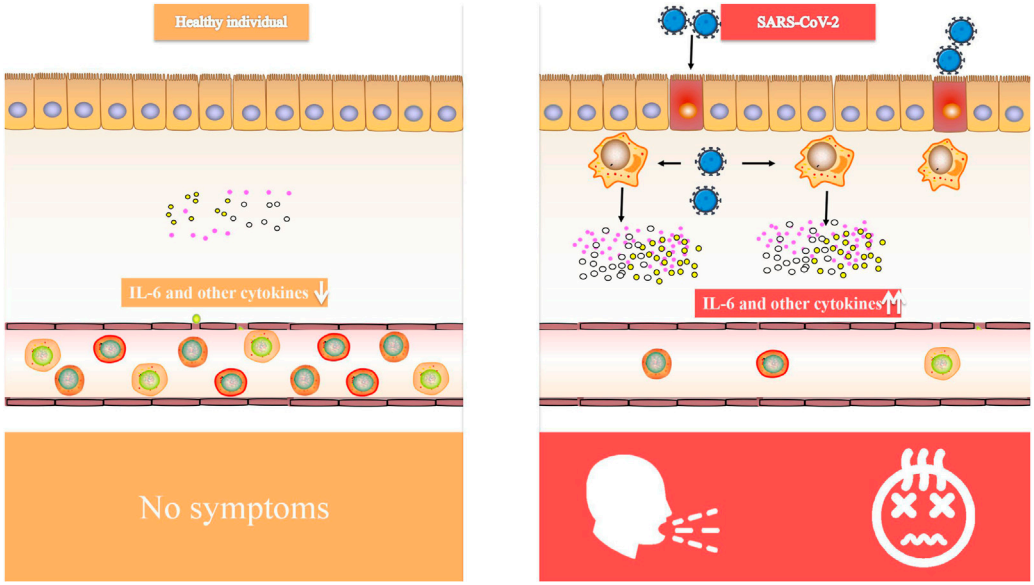

FIGURE 1
Comparison of IL-6 and other cytokines in healthy individual and SARS-CoV-2 infected people.

there are several pharmacological agents that target IL-1, IL-18, TNF, and IFN, as well as JAK/STAT signaling (Table 1). Regular testing for inflammatory cytokines should be performed if these medications are effective (Liu et al., 2020a). Relevant clinical trials showed that in the study on the treatment of COVID-19 inpatients with anti-IL-6 receptor antibody tocillizumab, there was no support for the conjecture that "the use of anti-IL-6 drug intervention can improve the symptoms of COVID-19, such as hypoxia and respiratory failure, and reduce the risk of death" (Stone et al., 2020; Declercq et al., 2021). However, tocillizumab may still be effective in severe patients, so further research should be conducted in the future (Soin et al., 2021).

Regulatory mechanisms of IL-6

The possible mechanism of CRS in severe COVID-19 patients is that SARS-CoV-2 infects with alveolar epithelial cells through ACE2 receptor. The loss of epithelial cells and increased cell permeability lead to the release of the virus. SARS-CoV-2 stimulates the innate immune system, leading macrophages and other innate immune cells, including IL-6, to generate a large number of cytokines and chemokines. Antigen-presenting cells may also initiate adaptive immunity (mainly dendritic cells). T cells and B cells are antiviral cells that indirectly or directly stimulate the generation of proinflammatory cytokines. In addition, when inflammatory chemicals stimulate the alveoli, a large amount of inflammatory exudate and erythrocytes enter the alveoli, resulting in dyspnea and respiratory arrest (Figure 2).

In an infected lesion, IL-6 generates warning signals in the whole body. Pathogen-recognition receptors (PRRs) on immune cells, including monocytes and macrophages, identify PAMPs in lesions (Kumar et al., 2011). Among the PRRs are TLRs, retinoic acid-inducible gene-1-like receptors, nucleotide-binding oligomerization domain-like receptors, and DNA receptors. They stimulate the synthesis of inflammatory cytokine mRNA such as IL-6, TNF and IL-1 by activating many signaling pathways, including NF-κB. Additionally, TNF and IL-1 activate transcription factors, leading to the generation of IL-6.

In the event of tissue damage, IL-6 also transmits a warning signal. DAMPs, which are produced by dead or damaged cells in noninfectious inflammations such as burns or trauma, either directly or indirectly exacerbate inflammation. During sterile surgical operations, an increase in serum IL-6 levels precedes an increase in body temperature and serum acute phase protein concentration (Nishimoto et al., 1989). DAMPs from damaged cells include, among others, mitochondrial DNA, high mobility group box 1 (HMGB1), and S100 proteins (Bianchi, 2007). HMGB1 binding to TLR2, TLR4, and the receptor for advanced glycation end products (RAGE) may trigger inflammation; nevertheless, blood mtDNA levels in trauma patients are hundreds of times higher than in controls, causing TLR9 stimulation and NF-κB activation (Zhang et al., 2010). The S100 family consists of more than 25 proteins, some of which interact with RAGE to generate sterile inflammation (Sims et al., 2010).

TABLE 1 Study on IL-6 in SARS-CoV-2, SARS-CoV and MERS-CoV.

Abbreviations	Terms
ACE2	angiotensin converting enzyme 2
ALI	acute lung injury
AP-1	activator protein 1
ARDS1	acute respiratory distress syndrome 1
CAR-T	chimeric antigen receptor-T
CEST	Central European summer Time
COVID-19	Corona Virus Disease 2019
CRP	C-reactive protein
CRS	cytokine release syndrome
DAMPs	Damage-associated molecular patterns
Gab1	GRB2 associated binding protein 1
GRB2	growth factor receptor-bound protein 2
GvHD	graft-versus-host disease
HCOVs	human coronaviruses
HCWs	health care workers
HMGB1	high mobility group box 1
IL	interleukin
IPC	infection prevention and control
IRF-1	interferon regulatory factor 1
JAK	Janus kinase
LPS	Lipopolysaccharide
LRT	lower respiratory tract
MAPK	mitogen-activated protein kinase
MAS	macrophage activation syndrome
MERS	Middle East respiratory sickness
MERS-CoV	Middle East Respiratory Syndrome Coronavirus
mIL-6R	membrane-bound IL6R
MMP-9	matrix metalloproteinase-9
NF-IL-6	nuclear factor IL-6
NF-κB	nuclear factor kappa-B
PAMPs	pathogen-associated molecular patterns
PBMC	peripheral blood mononuclear cell
PCT	procalcitonin
PI3K	phosphatidylinositol 3-kinase
PRRs	Pathogen-recognition receptors
RA	rheumatoid arthritis
RAGE	receptor for advanced glycation end products
SAA	serum amyloid A
SARS	severe acute respiratory syndrome
SARS-CoV	Severe Acute Respiratory Syndrome Coronavirus
SARS-CoV-2	Severe Acute Respiratory Syndrome Coronavirus 2
SHP-2	Src homology phosphotyrosine phosphatase 2
sIL-6R	soluble IL-6R
SP1	specificity protein 1
TG	thioglycollate
Th17	T helper 17
TLRs	toll-like receptors
TMPRSS2	transmembrane protease serine 2
TNF-α	tumor necrosis factor-α
WHO	World Health Organization

(Continued in next column)

In response to various stimuli, in addition to immune-mediated cells, IL-6 is generated by mesenchymal cells, endothelial cells, fibroblasts and a range of other cells (Akira et al., 1993). The stringent gene transcriptional and post-transcriptional regulation of IL-6 production is necessitated by the fact that IL-6 acts as a signal to alert the presence of an emergency. A multitude of transcription factors control the IL-6 gene's transcription (Figure 3). The 5′ flanking region of the human IL-6 gene has binding sites for NF-κB, specificity protein 1 (SP1), nuclear factor IL-6 (NF-IL-6), activator protein 1 (AP-1) and interferon regulatory factor 1 (IRF-1) (Libermann and Baltimore, 1990; Akira and Kishimoto, 1992; Matsusaka et al., 1993). The IL-6 promoter is active when cis-regulatory elements are stimulated by IL-1, TNF, TLR-mediated signal and forskolin (Tanaka et al., 2014).

The mechanism of COVID-19

ACE2 has been identified as the primary receptor for binding SARS-CoV S protein. Researchers have designed and discovered small molecule compounds and peptides that can bind to the SARS-CoV-specific receptor ACE2, preventing SARS-CoV S protein from binding to ACE2 and fusing with the host cell membrane to prevent viral infection (Zhang et al., 2020). This suggests that drugs targeting the virus-acting receptor can be designed. Xu et al. (Xu et al., 2020) confirmed ACE2 as the receptor of SARS-CoV-2 by studying the binding capacity of the structural model of SARS-CoV-2 S protein to human ACE2 receptor. SARS-transmembrane CoV's spike glycoprotein (S protein) binds to the cellular membrane ACE2; SARS-CoV then attaches to target cells, followed by SARS-CoV-S protein priming by cellular surface proteases such as transmembrane protease serine 2 (TMPRSS2), resulting in the fusion of viral and cellular membranes and SARS-CoV entry and replication in target cells. In addition, elimination of ACE2 reduces viral infection and replication considerably in mice infected with SARS-CoV. It is thus believed that the SARS-CoV S protein's binding to ACE2 is crucial for SARS-CoV infection (Kai and Kai, 2020). Alveolar epithelial cells bind to SARS-CoV-2. The virus then activates the innate and adaptive immune systems, resulting in a flood of cytokines, including IL-6, being produced (Figure 4).

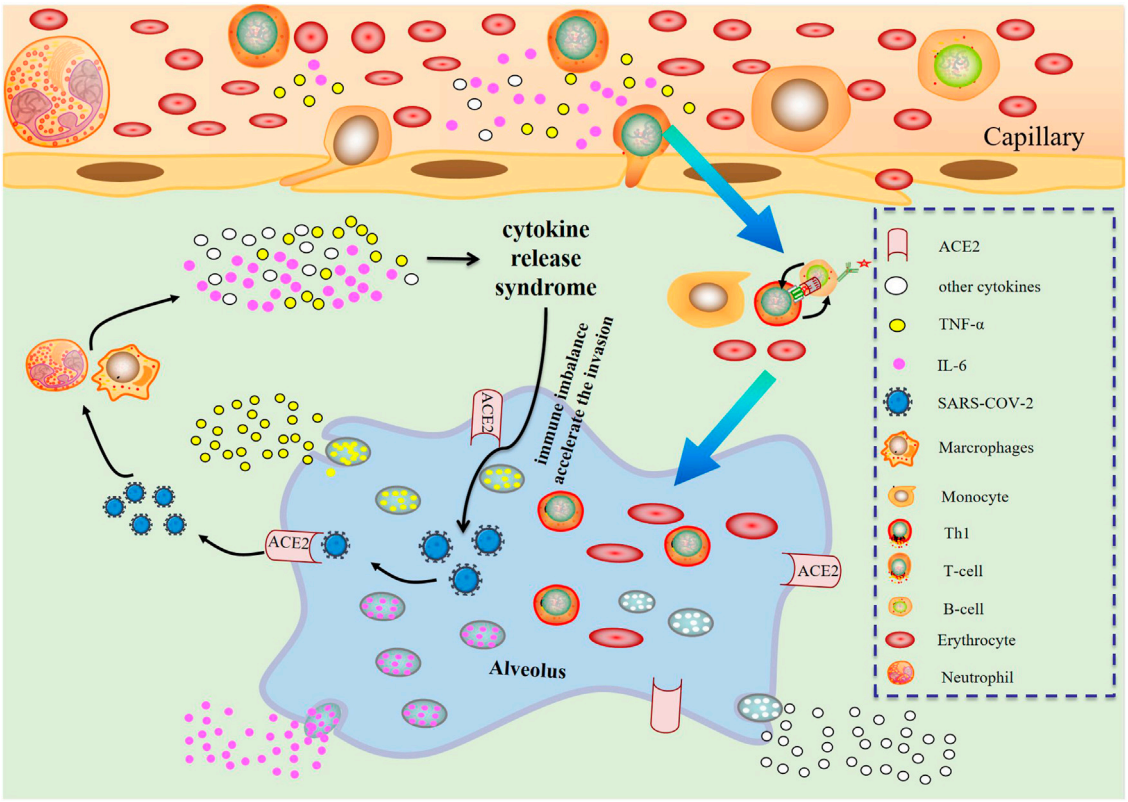

FIGURE 2
Changes of various immune cells and related substances in alveolus after SARS-CoV-2 invasion.

Future prospects

In controlled clinical trials throughout the world, IL-6 and IL-6R antagonists are being evaluated for the treatment of COVID-19 patients with severe respiratory difficulties. Unanswered is whether IL-6 antagonists and IL-6R antagonists will have varying degrees of effectiveness. Inhibitors of the IL-6R may disrupt both cis and trans signaling, as well as the recently identified trans presentation signaling. IL-6 binds to mIL-6R on immune cells, which then forms a complex with gp130 on Th17 cells, resulting in T cell signaling that may be involved in ARDS (Tanaka et al., 2016b; Heink et al., 2017; Kang et al., 2019). In contrast, IL-6 inhibitors can only suppress cis and trans signaling. The primary goal of IL-6 antagonistic therapy is to decrease the need for advanced treatment in individuals with severe COVID-19. The development of antivirals and immunizations that prevent or relieve illness should be a long-term goal.

Patients with severe COVID-19, similar to SARS and MERS patients, have been proposed to have a CRS defined by an elevation in IL-6, which indicates that it may aggravate lung damage, cause viral inflammatory response and death. A prior cohort analysis found that IL-6 expression was substantially higher in COVID-19 patients, but that it varied greatly across ICU and non-ICU patients (Liu et al., 2020a). Moreover, recent study has shown that the SARS-CoV S protein promotes an upregulation of IL-6 and TNF in murine macrophages, and IL-6 and IL-8 have been identified as significant SARS-CoV-induced epithelial cytokines (Yoshikawa et al., 2009). These data indicate that SARS-CoV-induced IL-6 and TNF play a role in the disease's pathogenesis, notably in terms of inflammation and high fever (Wang et al., 2014). Anti-IL6R antibody Tocilizumab is a humanized recombinant monoclonal antibody. Tocilizumab has shown potential for treating severe CRS. Sixty-nine percent of patients responded within 14 days after receiving one or two doses of tocilizumab, with fever and hypotension receding within hours and vasopressors being withdrawn within a few days (Kotch et al., 2019). Tocilizumab's effect has also been recorded in CRS linked with sepsis, graft-versus-host disease (GvHD) and macrophage activation syndrome (MAS), among others (Barut et al., 2017; Ibrahim et al., 2020; Melgarejo-Ortuno et al., 2021). However, there is not enough evidence to clearly show the clinical efficacy and safety of Tocilizumab for severe patients with COVID-19, and its clinical application and side effects need to be further explored (Cortegiani et al., 2021).

Given the worldwide urgency of containing the COVID-19 pandemic, there are a few cautions to consider. Corticosteroids are

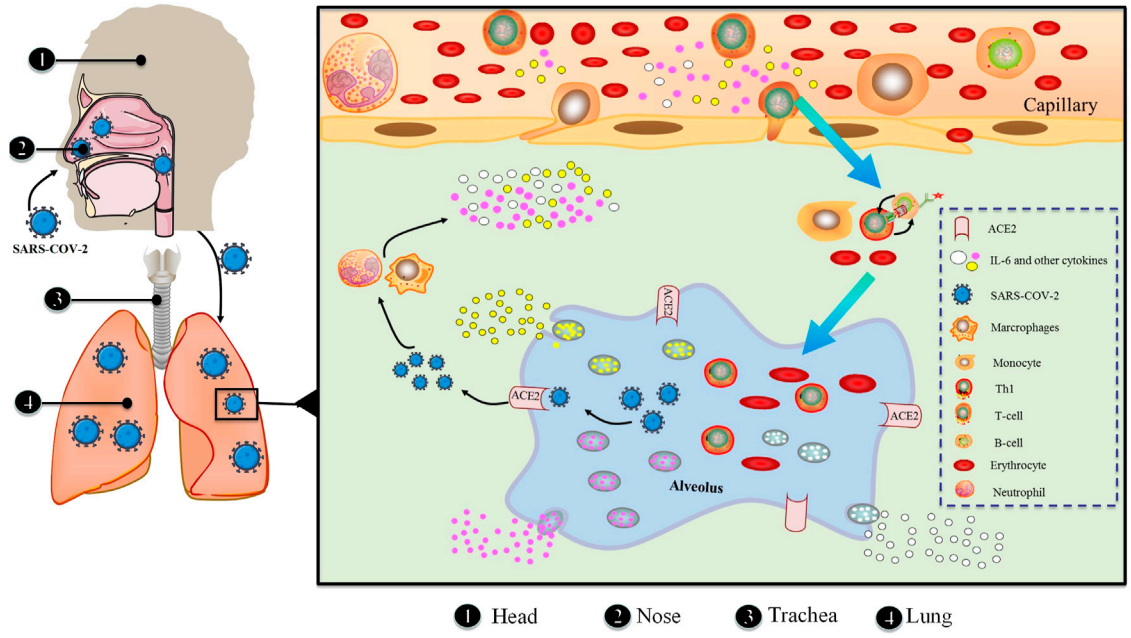

FIGURE 3
Macro and micro aspects of SARS-CoV-2 invading respiratory system.

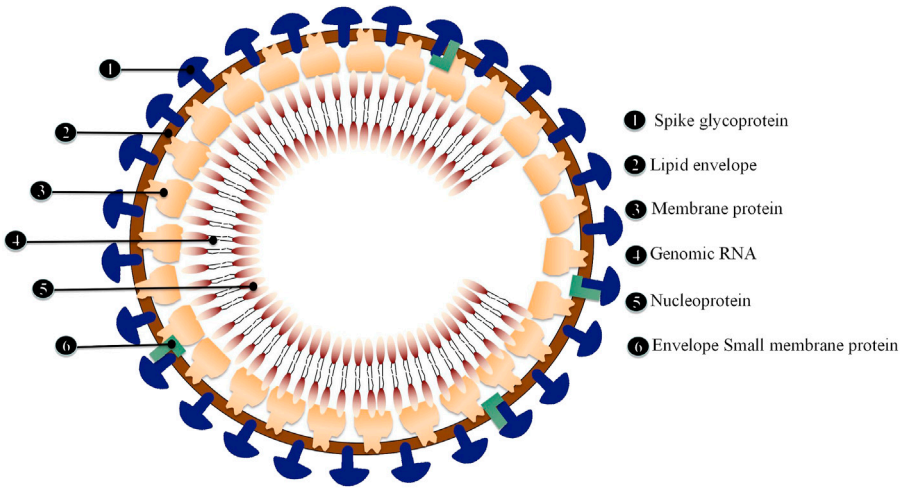

FIGURE 4
Schematic diagram of SARS-CoV-2 structure.

often used to treat ARDS caused by sepsis. However, in SARS and MERS patients, corticosteroids did not lower mortality and delayed viral clearance (Channappanavar and Perlman, 2017). Infectious disease authority and the WHO have thus decided that systemic corticosteroids should not be administered to COVID-19 patients at this time. The reduction in inflammation generated by IL-6 antagonism might, in theory, postpone viral clearance. Nevertheless, inhibiting IL-6 induces a rapid drop in serum IL-10, which may assuage concerns over the length of time required for viral clearance (Tanaka et al., 2016b). Furthermore, it is doubtful that one or two doses of an IL-6 antagonist would cause consequences like fungal infections or jaw osteonecrosis,

which are common in people using these medications on a monthly basis for chronic illnesses like RA. Tocilizumab was first approved for rheumatic illnesses, then for CRS in patients undergoing CAR-T cell treatment, and is now being repurposed for the COVID-19 pandemic. Diamanti et al. found that compared with HCWs, people using IL-6 inhibitors (such as RA patients) had significantly lower vaccine antibody titers, but almost all patients had antibody specific reactions induced in their bodies. In the investigated RA patients, BNT162b2 vaccine showed good safety (Picchianti-Diamanti et al., 2021).

Conclusion

As the pandemic grows, experts throughout the globe are working to better understand the virus's pathophysiology and identify new targets and promising medications that may be used to fight SARS-CoV-2. There are no confirmed antiviral medicines with particular action against SARS-CoV-2, despite some insights about viral pathophysiology and prospective targets. Future pandemics involving more viruses, may use IL-6-targeted treatments Chen et al., 2010, Hu et al., 2021a, Kim et al., 2021, Li et al., 2016, Soy et al., 2020.

Author contributions

SOS and XW designed the idea, XW, GT, and YL wrote the manuscript, LZ, BC, YH, and ZF drew the figures and chart, LW, GH, QM, SHS, JW, and XH revised the manuscript.

Funding

This project was supported by the Innovative Training Program for College Students in Anhui Province (AHMU20220018, chaired by XW).

Conflict of interest

The authors declare that the research was conducted in the absence of any commercial or financial relationships that could be construed as a potential conflict of interest.

Publisher's note

All claims expressed in this article are solely those of the authors and do not necessarily represent those of their affiliated organizations, or those of the publisher, the editors and the reviewers. Any product that may be evaluated in this article, or claim that may be made by its manufacturer, is not guaranteed or endorsed by the publisher.

Supplementary material

The Supplementary Material for this article can be found online at: https://www.frontiersin.org/articles/10.3389/fphar.2022.1033674/full#supplementary-material

References

Akira, S., and Kishimoto, T. (1992). IL-6 and NF-IL6 in acute-phase response and viral infection. *Immunol. Rev.* 127, 25–50. doi:10.1111/j.1600-065x.1992.tb01407.x

Akira, S., Taga, T., and Kishimoto, T. (1993). Interleukin-6 in biology and medicine. *Adv. Immunol.* 54, 1–78. doi:10.1016/s0065-2776(08)60532-5

Al-Qahtani, A. A., Lyroni, K., Aznaourova, M., Tseliou, M., Al-Anazi, M. R., Al-Ahdal, M. N., et al. (2017). Middle East respiratory syndrome corona virus spike glycoprotein suppresses macrophage responses via DPP4-mediated induction of IRAK-M and PPARγ. *Oncotarget* 8 (6), 9053–9066. doi:10.18632/oncotarget.14754

Bai, B., Hu, Q., Hu, H., Zhou, P., Shi, Z., Meng, J., et al. (2008). Virus-like particles of SARS-like coronavirus formed by membrane proteins from different origins demonstrate stimulating activity in human dendritic cells. *PLoS One* 3 (7), e2685. doi:10.1371/journal.pone.0002685

Baran, P., Hansen, S., Waetzig, G. H., Akbarzadeh, M., Lamertz, L., Huber, H. J., et al. (2018). The balance of interleukin (IL)-6, IL-6.soluble IL-6 receptor (sIL-6R), and IL-6.sIL-6R.sgp130 complexes allows simultaneous classic and trans-signaling. *J. Biol. Chem.* 293 (18), 6762–6775. doi:10.1074/jbc.RA117.001163

Barut, K., Adrovic, A., Sahin, S., and Kasapcopur, O. (2017). Juvenile idiopathic arthritis. *Balk. Med. J.* 34 (2), 90–101. doi:10.4274/balkanmedj.2017.0111

Bianchi, M. E. (2007). DAMPs, PAMPs and alarmins: All we need to know about danger. *J. Leukoc. Biol.* 81 (1), 1–5. doi:10.1189/jlb.0306164

Channappanavar, R., and Perlman, S. (2017). Pathogenic human coronavirus infections: Causes and consequences of cytokine storm and immunopathology. *Semin. Immunopathol.* 39 (5), 529–539. doi:10.1007/s00281-017-0629-x

Chen, J., Lau, Y. F., Lamirande, E. W., Paddock, C. D., Bartlett, J. H., Zaki, S. R., et al. (2010). Cellular immune responses to severe acute respiratory syndrome coronavirus (SARS-CoV) infection in senescent BALB/c mice: CD4+ T cells are important in control of SARS-CoV infection. *J. Virol.* 84 (3), 1289–1301. doi:10.1128/JVI.01281-09

Chousterman, B. G., Swirski, F. K., and Weber, G. F. (2017). Cytokine storm and sepsis disease pathogenesis. *Semin. Immunopathol.* 39 (5), 517–528. doi:10.1007/s00281-017-0639-8

Cortegiani, A., Ippolito, M., Greco, M., Granone, V., Protti, A., Gregoretti, C., et al. (2021). Rationale and evidence on the use of tocilizumab in COVID-19: A systematic review. *Pulmonology* 27 (1), 52–66. doi:10.1016/j.pulmoe.2020.07.003

De Clercq, E. (2006). Potential antivirals and antiviral strategies against SARS coronavirus infections. *Expert Rev. anti. Infect. Ther.* 4 (2), 291–302. doi:10.1586/14787210.4.2.291

de Wilde, A. H., Snijder, E. J., Kikkert, M., and van Hemert, M. J. (2018). Host factors in coronavirus replication. *Curr. Top. Microbiol. Immunol.* 419, 1–42. doi:10.1007/82_2017_25

de Wit, E., van Doremalen, N., Falzarano, D., and Munster, V. J. (2016). SARS and MERS: Recent insights into emerging coronaviruses. *Nat. Rev. Microbiol.* 14 (8), 523–534. doi:10.1038/nrmicro.2016.81

Declercq, J., Van Damme, K. F. A., De Leeuw, E., Maes, B., Bosteels, C., Tavernier, S. J., et al. (2021). Effect of anti-interleukin drugs in patients with COVID-19 and signs of cytokine release syndrome (COV-aid): A factorial, randomised, controlled trial. *Lancet. Respir. Med.* 9 (12), 1427–1438. doi:10.1016/S2213-2600(21)00377-5

Dosch, S. F., Mahajan, S. D., and Collins, A. R. (2009). SARS coronavirus spike protein-induced innate immune response occurs via activation of the NF-kappaB

pathway in human monocyte macrophages *in vitro*. *Virus Res.* 142 (1-2), 19–27. doi:10.1016/j.virusres.2009.01.005

Gillmore, J. D., Lovat, L. B., Persey, M. R., Pepys, M. B., and Hawkins, P. N. (2001). Amyloid load and clinical outcome in AA amyloidosis in relation to circulating concentration of serum amyloid A protein. *Lancet* 358 (9275), 24–29. doi:10.1016/S0140-6736(00)05252-1

Haffizulla, J., Hartman, A., Hoppers, M., Resnick, H., Samudrala, S., Ginocchio, C., et al. (2014). Effect of nitazoxanide in adults and adolescents with acute uncomplicated influenza: A double-blind, randomised, placebo-controlled, phase 2b/3 trial. *Lancet. Infect. Dis.* 14 (7), 609–618. doi:10.1016/S1473-3099(14)70717-0

Hamre, D., and Procknow, J. J. (1966). A new virus isolated from the human respiratory tract. *Proc. Soc. Exp. Biol. Med.* 121 (1), 190–193. doi:10.3181/00379727-121-30734

He, L., Ding, Y., Zhang, Q., Che, X., He, Y., Shen, H., et al. (2006). Expression of elevated levels of pro-inflammatory cytokines in SARS-CoV-infected ACE2+ cells in SARS patients: Relation to the acute lung injury and pathogenesis of SARS. *J. Pathol.* 210 (3), 288–297. doi:10.1002/path.2067

Heink, S., Yogev, N., Garbers, C., Herwerth, M., Aly, L., Gasperi, C., et al. (2017). Corrigendum: Trans-presentation of IL-6 by dendritic cells is required for the priming of pathogenic TH17 cells. *Nat. Immunol.* 18 (1), 474–485. doi:10.1038/ni0417-474b

Heinrich, P. C., Behrmann, I., Haan, S., Hermanns, H. M., Muller-Newen, G., and Schaper, F. (2003). Principles of interleukin (IL)-6-type cytokine signalling and its regulation. *Biochem. J.* 374 (1), 1–20. doi:10.1042/BJ20030407

Heinrich, P. C., Castell, J. V., and Andus, T. (1990). Interleukin-6 and the acute phase response. *Biochem. J.* 265 (3), 621–636. doi:10.1042/bj2650621

Hijawi, B., Abdallat, M., Sayaydeh, A., Alqasrawi, S., HaddAdin, A., JaarourN., et al. (2013). Novel coronavirus infections in Jordan, April 2012: Epidemiological findings from a retrospective investigation. *East. Mediterr. Health J.* 19 (1), S12–S18. doi:10.26719/2013.19.supp1.s12

Hsueh, P. R., Chen, P. J., Hsiao, C. H., Yeh, S. H., Cheng, W. C., Wang, J. L., et al. (2004). Patient data, early SARS epidemic, Taiwan. *Emerg. Infect. Dis.* 10 (3), 489–493. doi:10.3201/eid1003.030571

Hu, B., Huang, S., and Yin, L. (2021). The cytokine storm and COVID-19. *J. Med. Virol.* 93 (1), 250–256. doi:10.1002/jmv.26232

Hu, S., Li, Z., Chen, X., and Liang, C. H. (2021). Computed tomography manifestations in super early stage 2019 novel coronavirus pneumonia. *Acta Radiol.* 62 (3), 360–367. doi:10.1177/0284185120924806

Huang, C., Wang, Y., Li, X., Ren, L., Zhao, J., Hu, Y., et al. (2020). Clinical features of patients infected with 2019 novel coronavirus in Wuhan, China. *Lancet* 395 (10223), 497–506. doi:10.1016/S0140-6736(20)30183-5

Ibrahim, Y. F., Moussa, R. A., Bayoumi, A. M. A., and Ahmed, A. F. (2020). Tocilizumab attenuates acute lung and kidney injuries and improves survival in a rat model of sepsis via down-regulation of NF-κB/JNK: A possible role of P-glycoprotein. *Inflammopharmacology* 28 (1), 215–230. doi:10.1007/s10787-019-00628-y

Jiang, Z., Liao, R., Lv, J., Li, S., Zheng, D., Qin, L., et al. (2021). IL-6 trans-signaling promotes the expansion and anti-tumor activity of CAR T cells. *Leukemia* 35 (5), 1380–1391. doi:10.1038/s41375-020-01085-1

Jones, B. M., Ma, E. S., Peiris, J. S., Wong, P. C., Ho, J. C. M., Lam, B., et al. (2004). Prolonged disturbances of *in vitro* cytokine production in patients with severe acute respiratory syndrome (SARS) treated with ribavirin and steroids. *Clin. Exp. Immunol.* 135 (3), 467–473. doi:10.1111/j.1365-2249.2003.02391.x

Kai, H., and Kai, M. (2020). Interactions of coronaviruses with ACE2, angiotensin II, and RAS inhibitors-lessons from available evidence and insights into COVID-19. *Hypertens. Res.* 43 (7), 648–654. doi:10.1038/s41440-020-0455-8

Kang, S., Tanaka, T., and Kishimoto, T. (2015). Therapeutic uses of anti-interleukin-6 receptor antibody. *Int. Immunol.* 27 (1), 21–29. doi:10.1093/intimm/dxu081

Kang, S., Tanaka, T., Narazaki, M., and Kishimoto, T. (2019). Targeting interleukin-6 signaling in clinic. *Immunity* 50 (4), 1007–1023. doi:10.1016/j.immuni.2019.03.026

Kaur, S., Bansal, Y., Kumar, R., and Bansal, G. (2020). A panoramic review of IL-6: Structure, pathophysiological roles and inhibitors. *Bioorg. Med. Chem.* 28 (5), 115327. doi:10.1016/j.bmc.2020.115327

Kim, J. S., Lee, J. Y., Yang, J. W., Lee, K. H., Effenberger, M., Szpirt, W., et al. (2021). Immunopathogenesis and treatment of cytokine storm in COVID-19. *Theranostics* 11 (1), 316–329. doi:10.7150/thno.49713

Kishimoto, T. (2010). IL-6: From its discovery to clinical applications. *Int. Immunol.* 22 (5), 347–352. doi:10.1093/intimm/dxq030

Korea Centers for Disease, C. (2015). Prevention Middle East respiratory syndrome coronavirus outbreak in the republic of Korea, 2015. *Osong Public Health Res. Perspect.* 6 (4), 269–278.

Kotch, C., Barrett, D., and Teachey, D. T. (2019). Tocilizumab for the treatment of chimeric antigen receptor T cell-induced cytokine release syndrome. *Expert Rev. Clin. Immunol.* 15 (8), 813–822. doi:10.1080/1744666X.2019.1629904

Kujawski, M., Kortylewski, M., Lee, H., Herrmann, A., Kay, H., and Yu, H. (2008). Stat3 mediates myeloid cell-dependent tumor angiogenesis in mice. *J. Clin. Investig.* 118 (10), 3367–3377. doi:10.1172/JCI35213

Kumar, H., Kawai, T., and Akira, S. (2011). Pathogen recognition by the innate immune system. *Int. Rev. Immunol.* 30 (1), 16–34. doi:10.3109/08830185.2010.529976

Lagunas-Rangel, F. A., and Chavez-Valencia, V. (2020). High IL-6/IFN-gamma ratio could be associated with severe disease in COVID-19 patients. *J. Med. Virol.* 92 (10), 1789–1790. doi:10.1002/jmv.25900

Lai, X., Wang, M., Qin, C., Tan, L., Ran, L., Chen, D., et al. (2020). Coronavirus disease 2019 (COVID-2019) infection among health care workers and implications for prevention measures in a tertiary hospital in wuhan, China. *JAMA Netw. Open* 3 (5), e209666. doi:10.1001/jamanetworkopen.2020.9666

Lee, D. W., Gardner, R., Porter, D. L., Louis, C. U., Ahmed, N., Jensen, M., et al. (2014). Current concepts in the diagnosis and management of cytokine release syndrome. *Blood* 124 (2), 188–195. doi:10.1182/blood-2014-05-552729

Li, S. W., Wang, C. Y., Jou, Y. J., Huang, S. H., Hsiao, L. H., Wan, L., et al. (2016). SARS coronavirus papain-like protease inhibits the TLR7 signaling pathway through removing lys63-linked polyubiquitination of TRAF3 and TRAF6. *Int. J. Mol. Sci.* 17 (5), E678. doi:10.3390/ijms17050678

Libermann, T. A., and Baltimore, D. (1990). Activation of interleukin-6 gene expression through the NF-kappa B transcription factor. *Mol. Cell. Biol.* 10 (5), 2327–2334. doi:10.1128/mcb.10.5.2327

Liu, B., Li, M., Zhou, Z., Guan, X., and Xiang, Y. (2020). Can we use interleukin-6 (IL-6) blockade for coronavirus disease 2019 (COVID-19)-induced cytokine release syndrome (CRS)? *J. Autoimmun.* 111, 102452. doi:10.1016/j.jaut.2020.102452

Liu, F., Li, L., Xu, M., Wu, J., Luo, D., Zhu, Y., et al. (2020). Prognostic value of interleukin-6, C-reactive protein, and procalcitonin in patients with COVID-19. *J. Clin. Virol.* 127, 104370. doi:10.1016/j.jcv.2020.104370

Luo, X., Zhou, W., Yan, X., Guo, T., Wang, B., Xia, H., et al. (2020). Prognostic value of C-reactive protein in patients with coronavirus 2019. *Clin. Infect. Dis.* 71 (16), 2174–2179. doi:10.1093/cid/ciaa641

Mackay, I. M., and Arden, K. E. (2015). MERS coronavirus: Diagnostics, epidemiology and transmission. *Virol. J.* 12, 222. doi:10.1186/s12985-015-0439-5

Matsusaka, T., Fujikawa, K., Nishio, Y., MukaidaN.Matsushima, K., KishimoTo, T., et al. (1993). Transcription factors NF-IL6 and NF-kappa B synergistically activate transcription of the inflammatory cytokines, interleukin 6 and interleukin 8. *Proc. Natl. Acad. Sci. U. S. A.* 90 (21), 10193–10197. doi:10.1073/pnas.90.21.10193

McIntosh, K., Dees, J. H., Becker, W. B., Kapikian, A. Z., and Chanock, R. M. (1967). Recovery in tracheal organ cultures of novel viruses from patients with respiratory disease. *Proc. Natl. Acad. Sci. U. S. A.* 57 (4), 933–940. doi:10.1073/pnas.57.4.933

Melgarejo-Ortuno, A., Escudero-Vilaplana, V., Revuelta-Herrero, J. L., Bailen, R., Collado-Borrell, R., Gomez-Centurion, I., et al. (2021). Tocilizumab as salvage treatment of refractory pulmonary acute graft-versus-host disease. *J. Oncol. Pharm. Pract.* 27 (3), 751–755. doi:10.1177/1078155220948934

Mihara, M., Hashizume, M., Yoshida, H., Suzuki, M., and Shiina, M. (2012). IL-6/IL-6 receptor system and its role in physiological and pathological conditions. *Clin. Sci.* 122 (4), 143–159. doi:10.1042/CS20110340

Moore, J. B., and June, C. H. (2020). Cytokine release syndrome in severe COVID-19. *Science* 368 (6490), 473–474. doi:10.1126/science.abb8925

Nishimoto, N., Yoshizaki, K., Tagoh, H., MondenM.KiShimoto, S., Hirano, T., et al. (1989). Elevation of serum interleukin 6 prior to acute phase proteins on the inflammation by surgical operation. *Clin. Immunol. Immunopathol.* 50 (3), 399–401. doi:10.1016/0090-1229(89)90147-5

Norelli, M., Camisa, B., Barbiera, G., Falcone, L., Purevdorj, A., Genua, M., et al. (2018). Monocyte-derived IL-1 and IL-6 are differentially required for cytokine-release syndrome and neurotoxicity due to CAR T cells. *Nat. Med.* 24 (6), 739–748. doi:10.1038/s41591-018-0036-4

Pandolfi, F., Franza, L., Carusi, V., Altamura, S., Andriollo, G., and Nucera, E. (2020). Interleukin-6 in rheumatoid arthritis. *Int. J. Mol. Sci.* 21 (15), E5238. doi:10.3390/ijms21155238

Picchianti-Diamanti, A., Aiello, A., Lagana, B., Agrati, C., Castilletti, C., Meschi, S., et al. (2021). ImmunosuppressiveTherapies differently modulate humoral- and T-cell-specific responses to COVID-19 mRNA vaccine in rheumatoid arthritis

patients. *Front. Immunol.* 12, 740249. Supplementary Materials. doi:10.3389/fimmu.2021.740249

Rossignol, J. F., La Frazia, S., Chiappa, L., Ciucci, A., and Santoro, M. G. (2009). Thiazolides, a new class of anti-influenza molecules targeting viral hemagglutinin at the post-translational level. *J. Biol. Chem.* 284 (43), 29798–29808. doi:10.1074/jbc.M109.029470

Rossignol, J. F. (2016). Nitazoxanide, a new drug candidate for the treatment of Middle East respiratory syndrome coronavirus. *J. Infect. Public Health* 9 (3), 227–230. doi:10.1016/j.jiph.2016.04.001

Sheng, W. H., Chiang, B. L., Chang, S. C., Ho, H. N., Wang, J. T., Chen, Y. C., et al. (2005). Clinical manifestations and inflammatory cytokine responses in patients with severe acute respiratory syndrome. *J. Formos. Med. Assoc.* 104 (10), 715–723.

Shimabukuro-Vornhagen, A., Godel, P., Subklewe, M., Stemmler, H. J., SchloBer, H. A., Schlaak, M., et al. (2018). Cytokine release syndrome. *J. Immunother. Cancer* 6 (1), 56. doi:10.1186/s40425-018-0343-9

Sims, G. P., Rowe, D. C., Rietdijk, S. T., Herbst, R., and Coyle, A. J. (2010). HMGB1 and RAGE in inflammation and cancer. *Annu. Rev. Immunol.* 28, 367–388. doi:10.1146/annurev.immunol.021908.132603

Smilowitz, N. R., Kunichoff, D., Garshick, M., Shah, B., Pillinger, M., Hochman, J. S., et al. (2021). C-reactive protein and clinical outcomes in patients with COVID-19. *Eur. Heart J.* 42 (23), 2270–2279. doi:10.1093/eurheartj/ehaa1103

Soin, A. S., Kumar, K., Choudhary, N. S., Sharma, P., Mehta, Y., Kataria, S., et al. (2021). Tocilizumab plus standard care versus standard care in patients in India with moderate to severe COVID-19-associated cytokine release syndrome (COVINTOC): An open-label, multicentre, randomised, controlled, phase 3 trial. *Lancet. Respir. Med.* 9 (5), 511–521. doi:10.1016/S2213-2600(21)00081-3

Soy, M., Keser, G., Atagunduz, P., Tabak, F., Atagunduz, I., and Kayhan, S. (2020). Cytokine storm in COVID-19: Pathogenesis and overview of anti-inflammatory agents used in treatment. *Clin. Rheumatol.* 39 (7), 2085–2094. doi:10.1007/s10067-020-05190-5

Stone, J. H., Frigault, M. J., Serling-Boyd, N. J., Fernandes, A. D., Harvey, L., Foulkes, A. S., et al. (2020). Efficacy of tocilizumab in patients hospitalized with covid-19. *N. Engl. J. Med.* 383 (24), 2333–2344. doi:10.1056/NEJMoa2028836

Tanaka, T., and Kishimoto, T. (2014). The biology and medical implications of interleukin-6. *Cancer Immunol. Res.* 2 (4), 288–294. doi:10.1158/2326-6066.CIR-14-0022

Tanaka, T., Narazaki, M., and Kishimoto, T. (2014). IL-6 in inflammation, immunity, and disease. *Cold Spring Harb. Perspect. Biol.* 6 (10), a016295. doi:10.1101/cshperspect.a016295

Tanaka, T., Narazaki, M., and Kishimoto, T. (2016). Immunotherapeutic implications of IL-6 blockade for cytokine storm. *Immunotherapy* 8 (8), 959–970. doi:10.2217/imt-2016-0020

Tanaka, T., Narazaki, M., and Kishimoto, T. (2012). Therapeutic targeting of the interleukin-6 receptor. *Annu. Rev. Pharmacol. Toxicol.* 52, 199–219. doi:10.1146/annurev-pharmtox-010611-134715

Tanaka, T., Narazaki, M., Masuda, K., and Kishimoto, T. (2016). Regulation of IL-6 in immunity and diseases. *Adv. Exp. Med. Biol.* 941, 79–88. doi:10.1007/978-94-024-0921-5_4

Teijaro, J. R. (2017). Cytokine storms in infectious diseases. *Semin. Immunopathol.* 39 (5), 501–503. doi:10.1007/s00281-017-0640-2

van der Hoek, L. (2007). Human coronaviruses: What do they cause? *Antivir. Ther.* 12 (4), 651–658. doi:10.1177/135965350701200s01.1

van der Hoek, L., Pyrc, K., Jebbink, M. F., Vermeulen-Oost, W., Berkhout, R. J. M., Wolthers, K. C., et al. (2004). Identification of a new human coronavirus. *Nat. Med.* 10 (4), 368–373. doi:10.1038/nm1024

Wang, C., Fei, D., Li, X., Zhao, M., and Yu, K. (2020). IL-6 may be a good biomarker for earlier detection of COVID-19 progression. *Intensive Care Med.* 46 (7), 1475–1476. doi:10.1007/s00134-020-06065-8

Wang, S. F., Tseng, S. P., Yen, C. H., Yang, J. Y., Tsao, C. H., Shen, C. W., et al. (2014). Antibody-dependent SARS coronavirus infection is mediated by antibodies against spike proteins. *Biochem. Biophys. Res. Commun.* 451 (2), 208–214. doi:10.1016/j.bbrc.2014.07.090

Wise, J. (2012). Patient with new strain of coronavirus is treated in intensive care at London hospital. *BMJ* 345, e6455. doi:10.1136/bmj.e6455

Woo, P. C., Lau, S. K., Chu, C. M., Chan, K. h., Tsoi, H. w., Huang, Y., et al. (2005). Characterization and complete genome sequence of a novel coronavirus, coronavirus HKU1, from patients with pneumonia. *J. Virol.* 79 (2), 884–895. doi:10.1128/JVI.79.2.884-895.2005

Xu, X., Chen, P., Wang, J., Feng, J., Zhou, H., Li, X., et al. (2020). Evolution of the novel coronavirus from the ongoing Wuhan outbreak and modeling of its spike protein for risk of human transmission. *Sci. China. Life Sci.* 63 (3), 457–460. doi:10.1007/s11427-020-1637-5

Yoshikawa, T., Hill, T., Li, K., Peters, C. J., and Tseng, C. T. (2009). Severe acute respiratory syndrome (SARS) coronavirus-induced lung epithelial cytokines exacerbate SARS pathogenesis by modulating intrinsic functions of monocyte-derived macrophages and dendritic cells. *J. Virol.* 83 (7), 3039–3048. doi:10.1128/JVI.01792-08

Yu, H., Pardoll, D., and Jove, R. (2009). STATs in cancer inflammation and immunity: A leading role for STAT3. *Nat. Rev. Cancer* 9 (11), 798–809. doi:10.1038/nrc2734

Yu, P., Hu, B., Shi, Z. L., and Cui, J. (2019). Geographical structure of bat SARS-related coronaviruses. *Infect. Genet. Evol.* 69, 224–229. doi:10.1016/j.meegid.2019.02.001

Yu, S. Y., Hu, Y. W., Liu, X. Y., Xiong, W., Zhou, Z. T., and Yuan, Z. H. (2005). Gene expression profiles in peripheral blood mononuclear cells of SARS patients. *World J. Gastroenterol.* 11 (32), 5037–5043. doi:10.3748/wjg.v11.i32.5037

Zaki, A. M., van Boheemen, S., Bestebroer, T. M., Osterhaus, A. D., and Fouchier, R. A. (2012). Isolation of a novel coronavirus from a man with pneumonia in Saudi Arabia. *N. Engl. J. Med.* 367 (19), 1814–1820. doi:10.1056/NEJMoa1211721

Zhang, X., Li, S., and Niu, S. (2020). ACE2 and COVID-19 and the resulting ARDS. *Postgrad. Med. J.* 96 (1137), 403–407. doi:10.1136/postgradmedj-2020-137935

Zhang, Z. W., Zhang, Q. Y., Zhou, M. T., Liu, N. X., Chen, T. K., Zhu, Y. F., et al. (2010). Antioxidant inhibits HMGB1 expression and reduces pancreas injury in rats with severe acute pancreatitis. *Dig. Dis. Sci.* 55 (9), 2529–2536. doi:10.1007/s10620-009-1073-0

Glossary

ACE2 angiotensin converting enzyme 2
ALI acute lung injury
AP-1 activator protein 1
ARDS1 acute respiratory distress syndrome 1
CAR-T chimeric antigen receptor-T
CEST central european summer time
COVID-19 corona virus disease 2019
CRP C-reactive protein
CRS cytokine release syndrome
DAMPs damage-associated molecular patterns
Gab1 GRB2 associated binding protein 1
GRB2 growth factor receptor-bound protein 2
GvHD graft-versus-host disease
HCOVs human coronaviruses
HCWs health care workers
HMGB1 high mobility group box 1
IL interleukin
IPC infection prevention and control
IRF-1 interferon regulatory factor 1
JAK janus kinase
LPS lipopolysaccharide
LRT lower respiratory tract
MAPK mitogen-activated protein kinase
MAS macrophage activation syndrome
MERS middle east respiratory sickness
MERS-CoV middle east respiratory syndrome coronavirus
mIL-6R membrane-bound IL6R
MMP-9 matrix metalloproteinase-9
NF-IL-6 nuclear factor IL-6
NF-κB nuclear factor kappa-B
PAMPs pathogen-associated molecular patterns
PBMC peripheral blood mononuclear cell
PCT procalcitonin
PI3K phosphatidylinositol 3-kinase
PRRs pathogen-recognition receptors
RA rheumatoid arthritis
RAGE receptor for advanced glycation end products
SAA serum amyloid A
SARS severe acute respiratory syndrome
SARS-CoV severe acute respiratory syndrome coronavirus
SARS-CoV-2 severe acute respiratory syndrome coronavirus 2
SHP-2 Src homology phosphotyrosine phosphatase 2
sIL-6R soluble IL-6R
SP1 specificity protein 1
TG thioglycollate
Th17 T helper 17
TLRs toll-like receptors
TMPRSS2 transmembrane protease serine 2
TNF-α tumor necrosis factor-α
WHO World Health Organization

frontiers | Frontiers in Pharmacology

TYPE Original Research
PUBLISHED 08 December 2022
DOI 10.3389/fphar.2022.1056865

OPEN ACCESS

EDITED BY
Jian Gao,
Shanghai Children's Medical Center, China

REVIEWED BY
Ming Hong,
Zhongshan People's Hospital (ZSPH), China
Yi Lu,
Fudan University, China

*CORRESPONDENCE
Chenghai Liu,
chenghailiu@hotmail.com
Yanyan Tao,
taoyanyan1023@126.com

†These authors have contributed equally to this work and share first authorship

SPECIALTY SECTION
This article was submitted to Gastrointestinal and Hepatic Pharmacology, a section of the journal Frontiers in Pharmacology

RECEIVED 29 September 2022
ACCEPTED 07 November 2022
PUBLISHED 08 December 2022

CITATION
Wang F, Wang S, Wang J, Huang K, Chen G, Peng Y, Liu C and Tao Y (2022), Pharmacological mechanisms of Fuzheng Huayu formula for Aristolochic acid I–induced kidney fibrosis through network pharmacology. *Front. Pharmacol.* 13:1056865. doi: 10.3389/fphar.2022.1056865

Pharmacological mechanisms of Fuzheng Huayu formula for Aristolochic acid I–induced kidney fibrosis through network pharmacology

Fan Wang[1†], Siyuan Wang[1†], Jing Wang[1†], Kai Huang[2], Gaofeng Chen[1], Yuan Peng[1], Chenghai Liu[1,2,3*] and Yanyan Tao[1,2,3*]

[1]Institute of Liver Diseases, Shuguang Hospital affiliated to Shanghai University of Traditional Chinese Medicine, Shanghai, China, [2]Shanghai Key Laboratory of Traditional Chinese Clinical Medicine, Shanghai, China, [3]Key Laboratory of Liver and Kidney Diseases, Ministry of Education, Shanghai University of Traditional Chinese Medicine, Shanghai, China

Renal fibrosis, characterized by the destruction of renal tubules and interstitial capillaries and the accumulation of extracellular matrix proteins, is a common outcome of chronic renal diseases and has a wide spectrum of etiologies. Fibrosis can affect any organ and has similar pathological mechanisms. Fuzheng Huayu formula (FZHY), as the approved anti-liver fibrosis medicine in China, also can inhibit the kidney fibrosis induced by $HgCl_2$ or unilateral ureteral obstruction. However, little is known about the mechanisms underlying the beneficial effects of FZHY on renal fibrosis. This study aimed to identify the mechanisms of FZHY acts on renal fibrosis through network pharmacological analysis and *in vivo* experiments. Data from online databases were mined and screened to predict the target related genes of FZHY acts on renal fibrosis. The STRING and Cytoscape were used to construct the protein-protein interaction (PPI) networks for FZHY and CKD target proteins. Mouse models with CKD induced by Aristolochic Acid I (AAI) were used to validate the effects of FZHY on renal fibrosis and their underlying mechanisms by detecting kidney function, renal fibrosis, and related intersection genes. A total of 129 FZHY–CKD crossover proteins were filtered and constructed into a protein–protein interaction network complex and designated as the potential targets of FZHY. One of the highest-scoring genes, *FOS*, and its related signaling pathways were more activated in CKD. The results demonstrated that FZHY can exert an anti-renal fibrosis effect by improving the levels of serum creatinine and blood urea nitrogen and alleviating excessive collagen deposition in kidney tissue, FZHY also could reduce the levels of *TNF-α*, *IL-1β*, and *IL-6* and inhibit the expression of *MAPK*/*FOS* signal molecules. Our study findings provide insights into predicting the effects of FZHY on CKD through network pharmacology. FZHY can protect the kidney from inflammatory injury caused by AAI and can antagonize inflammatory factor-stimulated *MAPK*/*FOS* activation in fibrotic kidneys. These effects constitute the mechanisms of FZHY for renal fibrosis.

KEYWORDS

renal fibrosis, Aristolochic acid I, Fuzheng Huayu formula, network pharmacology, mechanisms

1 Introduction

Chronic kidney disease (CKD) is defined as the kidney dysfunction and abnormality. Renal fibrosis is the primary pathological process of CKD and has an overall prevalence of 10.8% in China; however, treatment options are limited (Zhang et al., 2012). Current treatments to reverse the progression of many CKDs are neither effective nor safe enough for clinical application (Klinkhammer et al., 2017). Although angiotensin receptor blockers and angiotensin converting enzyme inhibitors are commonly used together to treat CKD, their effect is unsatisfactory (Qin et al., 2020). One meta-analysis revealed that N-acetylcysteine (NAC) can improve renal function in patients with CKD, and the most frequent side effects are nausea and vomiting (Ye et al., 2021). In a previous study, 11% of stage 3 CKD cases progress into end-stage renal disease (i.e., kidney failure). The only therapeutic regimen for renal disease is dialysis or transplantation (Collins et al., 2015). CKD has also become an urgent public health problem in China. In 2015, 1.06 million patients with incident dialysis were admitted at a cost of 106 billion Chinese Renminbi (Yang et al., 2020).

Traditional Chinese Medicine (TCM) is one therapeutic option for CKD. Several studies have documented that TCM can delay CKD progress and improve patient survival and quality of life (Xi et al., 2020; Xia et al., 2020). The Fuzheng Huayu formula (FZHY) is a well-studied empirical prescription that consists of six Chinese medicinal herbs: *Radix Salvia Miltiorrhizae, Cordyceps, Semen Persicae, Gynostemma Pentaphyllammak, Pollen Pini,* and *Fructus Schisandrae Chinensis*. FZHY was approved by the Chinese State Food and Drug Administration (SFDA) as a drug (No. Z20050547), and it is widely used to treat hepatic fibrosis in China. Additionally, our previous studies have suggested that FZHY significantly decreases kidney collagen deposition and attenuates renal interstitial fibrosis (Wang et al., 2010; Wang et al., 2020). Fibrosis is characterized by dysfunction of capillary networks and the accumulation of fibrillary collagens, which activates myofibroblasts and inflammatory cells (Kang et al., 2015). Similarly, liver fibrosis and kidney fibrosis exhibit common pathological changes. FZHY, an anti-liver fibrotic TCM, also has an anti-renal fibrotic effect. However, the potential therapeutic effect of FZHY on CKD and the pharmacological mechanisms of FZHY require further research.

Network pharmacology can be used to create a complex interactive network based on target molecules, biological functions, and biologically active compounds, which addresses the natural feature of Chinese medicine recipes and systematically reflects the intervention mechanisms of TCM (Luo et al., 2020). In the present study, network pharmacology was used to further elucidate potential target genes and signaling pathways of FZHY for renal fibrosis. Furthermore, the molecular mechanisms underlying the effects of FZHY on renal fibrosis were examined using *in vivo* experiments.

2 Materials and methods

2.1 Prediction of chronic kidney disease-Related genes from Gene Expression Omnibus profiles

The raw data of renal biopsy from 53 patients with CKD were obtained from the Gene Expression Omnibus under GEO Series (GSE) (accession number: GSE66494) (Nakagaw et al., 2015). The eight normal human adult genome, retrieved from GPL6480, were used as the control.

By incorporating the Affy and Limma software packages in the R language (Ritchie et al., 2015), differentially expressed genes (DEGs) of patients with and without CKD were analyzed. The Affy package removes systematic errors in the original data to obtain standardized gene expression data, and the Limma package is used for the differential expression analysis of normal tissue and kidney injury tissue data after normalization. An adjusted p-value of <0.05 and a $\log_2|\text{fold change (FC)}| \geq 1.2$ were selected as the cutoff criteria. Finally, the upregulated and downregulated differential genes were identified. Finally, the Pheatmap package was used to draw heat maps and volcano maps.

2.2 Identification of associated molecular targets of Fuzheng Huayu

The potential molecular targets of FZHY were predicted using the Traditional Chinese Medicine Systems Pharmacology (TCMSP) (Ru et al., 2014), BATMAN (Liu et al., 2016), and Drug Bank (Wishart et al., 2018) databases. The target information of each ingredient was retrieved from TCMSP and Drug Bank to construct the potential target group of the active ingredients of FZHY. The meridian information of each medicinal component in the prescription was obtained from the 2015 edition of the *Chinese Pharmacopoeia*. Candidate components were screened and selected based on the following two parameters to evaluate the levels of oral absorption, usability, and biological activity: 1) oral

bioavailability of ≥30% and 2) druglikeness of ≥0.18 (Xu et al., 2020).

2.3 Screening of targets associated with chronic kidney disease

Information on the various genes associated with CKD was obtained from the GeneCards database (Stelzer et al., 2016) and the Online Mendelian Inheritance in Man (OMIM) database (Amberger & Hamosh, 2017), which are databases for human genes and genetic disorders. The keywords searched in the three databases were "Renal interstitial fibrosis," "Glomerulosclerosis" and "renal failure" and the results were exported online.

2.4 Fuzheng Huayu component-chronic kidney disease target protein–protein interaction network construction

To clarify the interaction between FZHY-related targets and CKD targets, FZHY multicomponent target genes and CKD target genes were genetically deduplicated. The R language was used to program the intersection of the two targets and create the Venn diagram. The intersection targets were submitted to the STRING11.0 database (Szklarczy et al., 2017), where the parameter related to the organism was set to "*Homo sapiens*," other basic settings were set to default values, and the isolated proteins were hidden. The data were analyzed and exported to the protein–protein interaction (PPI) network diagram. The PPI analysis model was limited to "multiple proteins," the species was set as "*Homo sapiens*," and the minimum required interaction score was set to 0.4 with a confidence of ≥0.7 to hide isolated proteins.

2.5 Gene ontology functional enrichment analysis and Kyoto Encyclopedia of Genes and Genomes pathway enrichment analysis

To determine the target genes associated with functional annotations and pathway enrichment, gene ontology (GO) annotation and Kyoto Encyclopedia of Genes and Genomes (KEGG) analysis were used. The GO annotation shows the molecular function (MF), biological process (BP), and cellular components (CC) of target genes. Additionally, the pathway enrichment analysis was conducted using the clusterprofiler package (Zhou et al., 2019), and the results were visualized using the enrichplot and DOSE Bioconductor packages (Yu et al., 2015). Enrichment with a p-value of <0.05 was considered statistically significant, and the adjusted p-value of <0.05 was set as the threshold.

3 Reagents and materials

3.1 Reagents

Serum creatinine (Scr, Cat. No. 20150526), blood urea nitrogen (BUN, Cat. No. 20150511), and hematoxylin-eosin stain (Cat. No. D006-1-1) were obtained from the Nanjing Jiancheng Institute of Biotechnology (Nanjing, China). Trizol reagent (Cat. No. F919KB3054) and a total RNA Isolation Kit (Cat. No. B511321) were purchased from Sangon Biotech (Shanghai, China). TB Green Premix Ex Taq (Cat. No. RR420A) and PrimeScript RT Reagent Kit with gDNA Eraser (Cat. No. RR047A) were purchased from Takara Biotechnology (Beijing, China). An Immunohistochemical Staining Kit (Lot No.16E06K04C1627) was purchased from Boster Biological Technology (Wuhan, China). Anti-c-Fos antibody (No. ab222699) and anti-JNK1 antibody (No. ab199380) were purchased from Abcam (Cambridge, United Kingdom). The primary antibodies against a-SMA (No. 19245), p-c-Fos (No. 5348), p-SAPK/JNK (Thr183/Tyr185) (No. 4668), p44/42 MAPK (Erk1/2) (No. 4695), p-p44/42 MAPK (Erk1/2) (No. 4370), and GAPDH (No. 5174) were produced by Cell Signaling Technology (Danvers, MA, United States). Enzyme-linked immunosorbent assay (ELISA) kits of IL-6 (Cat. No. 88-7064-88), TNF alpha (Cat. No. 88-7324-88), and IL-1β (Cat. No. 88-7013-88) were purchased from Thermo-Fisher Scientific (MA, United States).

3.2 Animals

3.2.1 Dynamic experiment

Fifty male C57BL/6 mice (8 weeks old, 25 ± 2 g) were purchased from Beijing Vital River Laboratory Animal [License No. SCXK (Jing) 2014-0001] and housed in the Shanghai Model Organisms Center [License No. SYXK (Shanghai) 2017-0012]. The environment was free of specific pathogens, and the average relative humidity and temperature were 55%–60% and 25 ± 1°C, respectively. A 12-h light–dark cycle was used. All experiments were approved by the Institutional Laboratory Animal Care and Use Committee (IACUC) of the Shanghai Model Organisms Center (Approval No. IACUC 2018-0026).

3.2.2 Pharmacodynamic experiment

Fifty C57BL/6 mice (8 weeks old, half male and half female, 25 ± 2 g) were purchased from Beijing Vital River Laboratory Animal [License No. SCXK (Jing) 2014-0001] and housed in the Laboratory Animal Center at the Shanghai University of Traditional Chinese Medicine [No. SYXK (Shanghai) 2020-

0009]. All experiments were in accordance with the requirements of the Animal Ethics Committee of the Shanghai University of Traditional Chinese Medicine. The ethics committee registration number was PZSHUTCM200821017.

3.3 Chemicals and drugs

Aristolochic acid I (AAI) with the molecular formula of $C_{17}H_{11}NO_7$ was purchased from Shanghai Standard Technology. The purity of AAI was 98.5% (Batch No. 3503). Sodium carboxymethyl cellulose (Batch No. F20051103) was obtained from Sinopharm Chemical Reagent Shanghai. FZHY extract powder was provided from Sundise Medicine Technology (SFDA approval No. Z20050546; Batch No. 20190608, the extract yield was 14.28% from Fuzheng Huayu formula). NAC (tradename: Flumucil) was obtained from Hainan Zambon Pharmaceutical (Cat. No. 1001542).

3.4 Animal groups and experimental design

3.4.1 Dynamic experiment

Mice were randomly divided into a normal group (n = 12), 4-week model group (n = 12), 8-week model group (n = 12), and 12-week model group (n = 14). To prepare the AAI-induced renal fibrosis model, mice in model groups were intraperitoneally injected with 4 mg/kg AAI dissolved in 0.5% sodium carboxymethyl cellulose at a concentration of 1 mg/ml twice weekly for 12 weeks. Normal mice received 0.5% sodium carboxymethyl cellulose only. Mice were euthanized at 4 weeks, 8 weeks, and 12 weeks after AAI administration, respectively. The renal tissue and blood samples were collected. The blood was centrifuged at 3,000 rpm for 15 min to obtain the serum, and the kidneys were harvested and stored at −80°C or fixed in 4% paraformaldehyde solution.

3.4.2 Pharmacodynamic experiment

Mice were randomly divided into a normal group (n = 10), model group (n = 10), FZHY low-dose (FL) group (n = 10), FZHY high-dose (FH) group (n = 10), and NAC group (n = 10). Preparation for the renal fibrosis model was the same as that for the dynamic experiment. Beginning from the fourth week of AAI injection, mice in the FL and FH groups were intragastrically administered FZHY at doses of 1.44 and 2.88 g/kg per day for 8 weeks, respectively. Mice in the NAC group was administered NAC at a dose of 3.0 g/kg per day for 8 weeks. Mice in the normal and AAI model groups were treated with an equal amount of vehicle. Mice were euthanized 12 weeks after AAI administration for renal tissue and blood sampling. Blood and kidney tissue sample processing was consistent with that described in the dynamic experiment section.

3.5 Biochemical assays in serum

Serum levels of Scr and BUN in mice were measured using the BIO-TEK multifunctional microplate reader (Molecular Devices, Sunnyvale, CA, United States) in accordance with the manufacturer's instructions.

3.6 Hematoxylin-eosin and Sirius Red staining

Kidney tissue was cut along the horizontal plane. Half of the tissue was fixed with 4% formaldehyde for 48 h, dehydrated using an automated dehydrator, and embedded in paraffin. The tissue was then cut into 4-μm paraffin sections for hematoxylin-eosin staining to assess renal injury and for Sirius Red staining to assess collagen deposition.

3.7 Quantitative reverse transcription-polymerase chain reaction

Based on the results of the network pharmacology, the top 10 potential hub genes were selected for quantitative reverse transcription-polymerase chain reaction (qRT-PCR) verification and screening. The National Center for Biotechnology Information online primer design software Primer-Blast was used to design primers (*INS2*, *IL-6*, *VEGFA*, *CASP3*, *MAPK8*, *MYC*, *ESR1*, *FOS*, *CCND1*, and *β-actin*), which were synthesized by Shanghai Sangon Biotech. *EGFR* primer sequences were provided by BIOTNT (see Table 1 for gene names and primer sequences). Total RNA was extracted from mice renal tissue by using Trizol reagent. Reverse transcription was performed using a reverse transcription kit, and cDNA amplification was performed using an SYBR Premix Ex Taq II fluorescent quantitative kit. Each sample was tested three times. The $2^{-\triangle\triangle CT}$ method was used for analysis and quantification, and *β-actin* was the internal reference.

3.8 Immunohistochemistry staining

The tissue sections were dewaxed and hydrated in graded ethanol and microwaved in sodium citrate buffer to repair antigens. Endogenous peroxidase activity was reduced using 3% H_2O_2 for 10 min. Each sample was blocked with 5% bovine serum albumin for 20–30 min and then incubated with the primary antibody against a-SMA (1:400), Fos (1:2000) at 4°C overnight. On the next day, the sections were incubated with a biotin-labeled goat antirabbit secondary antibody for 1 h and then stained with 3,3-diaminobenzidine and counterstained with hematoxylin. After dehydration and drying, the sections were mounted with neutral gum and observed under a microscope.

Aperio Image Scope software was used to perform image analysis.

3.9 Western blot analysis

Kidney tissues were homogenized in RIPA lysis buffer [50 mM Tris-HCl (pH 7.4), 150 mM NaCl, 0.1% sodium dodecyl sulfate (SDS), 1% Nonidet P-40, 1 mM EDTA, 1 mM PMSF, and 1 × Roche Complete Mini protease inhibitor cocktail]. The supernatants were collected after centrifugation at 10,000 × *g* at 4°C for 15 min. The protein concentration was determined using a bicinchonic acid protein assay kit. An equal amount of protein was separated through 10% SDS gel electrophoresis under denaturing conditions and was then transferred to the nitrocellulose membrane. The membrane was blocked with 5% nonfat milk in TBST at room temperature for 1 h and incubated with a primary antibody [a-SMA, 1:1000; c-Fos, 1:1000; JNK1, 1:1000; p-c-Fos, 1:1000; p-JNK, 1:1000; p44/42 MAPK (Erk1/2), 1:1000; p-p44/42 MAPK (p-Erk1/2), 1:2000] or GAPDH (1:2000) at 4°C overnight. After being washed in TBST, the blots were incubated with a horseradish-conjugated secondary antibody (No.8884). The signals were visualized using the Odyssey infrared laser imaging system by obtaining with photographs of bands, and ImageJ software was used to analyze the grey value.

3.10 Enzyme-linked immunosorbent assay

The concentrations of *IL-1*β, *IL-6*, and *TNF*-α in kidney tissues were determined using an enzyme-linked immunosorbent assay (ELISA) kit. Kidney homogenates were obtained after homogenizing in 50 mM PBS buffer (pH 7.4) in an ice water bath and centrifuging at 10,000 × *g* for 15 min at 4°C. For each assay, 100 μl of kidney homogenates from all mice were serially diluted to ensure that values obtained were within the linear range of the standards provided with each kit. The manufacturer's instructions (Thermo-Fisher Scientific) were strictly followed during the ELISA experiments.

3.11 Statistical analysis

The experimental data were statistically analyzed using SPSS 26.0 and were represented as the mean ± standard deviation (SD). One-way analysis of variance was used to compare groups, and $p < 0.05$ indicated a statistically significant difference. GraphPad Prism eight software was used for mapping.

4 Results

4.1 Prediction of chronic kidney disease-Related genes from Gene Expression Omnibus profiles

To further illustrate the pathological mechanisms of CKD in humans, DEGs between healthy donors and patients with CKD were screened (Figure 1). In total, 815 genes in the kidney biopsy samples were expressed among patients with CKD and not among those without CKD. Of the 815 genes, 129 genes were upregulated, and 686 genes were downregulated. The heatmap (Figure 1A) shows the top 40 DEGs in the two groups. Patients with CKD expressed the following genes which different from the individuals without CKD: *RPS4Y1*, *RPS4Y2*, *HBA1*, *HBD*, *HBA2*, *ITLN1*, *ACTG2*, *OR5L2*, *C5orf58*, and *IL4I1*. The volcano plot (Figure 1B) was applied to demonstrate the distribution of gene expression differences; the horizontal axis is the logarithm of the fold differences, and the vertical axis is the negative logarithm of the *p*-value for multiple significant differences. Red dots represent significantly upregulated genes, and green dots represent significantly downregulated genes ($p < 0.05$ and log |FC| ≥1.2).

4.2 Potential hub genes through which Fuzheng Huayu acts on chronic kidney disease

A Venn diagram (Figure 2A) was drawn to illustrate the common genes between FZHY and CKD. In total, 129 genes were potential hub genes responsible for the effects of FZHY on CKD. To further illustrate the relationship between FZHY and CKD target proteins, PPI network (Figure 2B) was constructed using the Search Tool for the Retrieval of Interacting Genes/Proteins public database. The bar plot (Figure 2C) was used to display the top 30 potential hub genes through which FZHY acts on CKD, such as *INS*, *IL-6*, *VEGFA*, *EGFR*, *CASP3*, *MAPK8*, and *MYC*.

4.3 Gene ontology and Kyoto Encyclopedia of Genes and Genomes pathway analysis

GO annotations of the 129 potential therapeutic target genes were performed to identify the biological activity of FZHY against renal fibrosis. The top 20 significantly enriched terms in the categories of BP, CC, and MF are shown in Figure 3. The BP (Figure 3A) was mainly related to the cellular response to

chemical stress, response to steroid hormone production, response to ketone, and response to oxidative stress. The CC (Figure 3B) was related to the membrane raft, membrane microdomain, membrane region, vesicle lumen, and secretory granule lumen. The MF (Figure 3C) was related to DNA-binding transcription factor binding, nuclear receptor activity, ligand-activated transcription factor activity, and steroid binding. Furthermore, the KEGG pathway analysis (Figure 3D) indicated that the lipid and atherosclerosis pathways, prostate cancer pathway, apoptosis pathway, fluid shear stress and atherosclerosis pathways, and TNF signaling pathway may be correlated with the therapeutic effects of FZHY on renal fibrosis.

4.4 Effect of Fuzheng Huayu on renal function and fibrosis caused by Aristolochic acid I

The dynamic and pharmacodynamic AAI mice models were used to verify the network pharmacology results. The hematoxylin-eosin staining results (Figure 4A) revealed that the renal tissue structure of the normal group was intact, and no obvious abnormality nor inflammatory cell infiltration was presented in the renal interstitium. However, renal tissue structure destruction was evident in the model group. Tubular dilatation and edema indicated clear interstitial inflammatory cell infiltration. The basement membrane of the renal tubules was incomplete, and the epithelial cells of the proximal convoluted tubule were sloughed off when the tubulointerstitium widened. Compared with the model group, the FZHY group exhibited reduced inflammatory cell infiltration, along with the alleviation of the damage to renal tubules. As shown in Figure 4B, after AAI injection, the Scr and BUN levels increased gradually over time and were significantly higher at 8 weeks and 12 weeks, respectively ($p < 0.01$), compared with the normal group (Figure 4B). After the use of FZHY, the Scr and BUN levels significantly decreased compared with the 12 weeks model group ($p < 0.01$). Sirius Red staining (Figure 4C) demonstrated the collagen deposition. As the result, after AAI administration, significant renal collagen deposition was observed in mice, which was reduced by using FZHY or NAC (Figure 4E). IHC (Figure 4D) and WB (Figure 4G) analysis of a-SMA were used to demonstrate the degree of renal fibrosis in mice. Compared with the normal group, the degree of renal fibrosis was increased after AAI injection, and alleviated by FZHY(Figures 4F,H).

Based on the results of the network pharmacology, the top 10 genes were selected to verify their reliability through qRT-PCR. Analysis of the renal tissues of the AAI dynamic mice model revealed that among the top 10 potential hub genes, the expression of *INS*, *EGFR*, *IL-6*, *CASP3*, *MAPK8*, *FOS*, *MYC*, *CCND*, and *VEGFA* was higher than that in the normal group. Of these, the differential expression was most pronounced with the *FOS* gene. Especially, the amount of mouse *FOS* gene expression in the 12w model group was about 10 times of that in the normal group ($p < 0.01$). (Figure 5A).

According to the literature, *FOS* is a downstream transcription factor, which can form AP-1 with *JUN*. We selected the *FOS* gene for subsequent studies as it plays the crucial role in regulating cell proliferation and death (Shaulian & Karin, 2002). In the mouse pharmacodynamic model of AAI, *FOS* gene expression decreased in the FZHY group and the positive drug NAC group compared with the 12-week model group ($p < 0.01$) (Figure 5A). Consistent with the qRT-PCR results, the Western blot analysis results demonstrated that *FOS* may be the target gene for the FZHY decoction against renal fibrosis (Figures 5B,C). According to the immunohistochemistry results, *FOS* protein mainly located in the renal tubular epithelial cells, most of which are present in the cytoplasm and only a few are located in the nucleus (Figures 5D,E). These results revealed that *FOS* is mainly expressed in tubular epithelial cells and serves as a potential target gene against CKD.

4.5 Role of mitogen-activated protein kinase family/FOS signaling pathways in Fuzheng Huayu against renal fibrosis

As one of the immediate early response genes, *FOS* expression is regulated by several extracellular signaling molecules, including those involved in the MAPK signaling pathways (mainly JNK and ERK signaling pathways) (Dalhäusser et al., 2022). Based on the GO annotation and KEGG analysis data, we selected p-c-FOS, JNK, p-JNK, ERK, and p-ERK for further validation.

As shown in Figures 6A,B, p-c-FOS, p-JNK, ERK, and p-ERK expression significantly increased at both 8 weeks and 12 weeks after AAI administration. After FZHY gavage, the expression levels of JNK and ERK proteins did not significantly change, and the expression levels of p-c-FOS p-JNK, and p-ERK significantly decreased compared with those in the model group ($p < 0.01$). The results suggest that the protective effect of FZHY on renal fibrosis may be related to the inhibition of the stimulation of the MAPK signaling pathways.

Because the activation of the MAPK signaling pathways was correlated with inflammatory factors, ELISA was conducted (Figures 7A,B). The levels of *IL-6*, *IL-1β*, and *TNF-α* significantly increased after AAI administration, and the levels of *IL-6*, *IL-1β*, and *TNF-α* decreased after FZHY administration, suggesting that FZHY alleviates the inflammatory response induced by AAI.

Generally, after the stimulation of MAPKs by inflammatory factors, the phosphorylated JNK, ERK

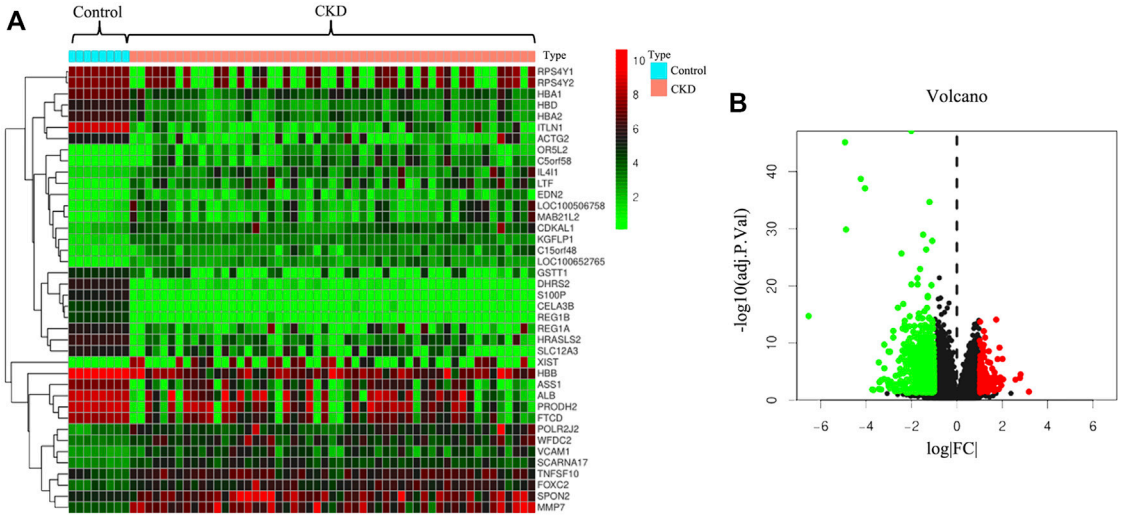

FIGURE 1
Prediction of differentially expressed genes between patients with chronic kidney disease (CKD) and healthy donors. **(A)** Heatmap of differentially expressed genes in human kidney tissues with or without CKD. **(B)** Volcano plot of distribution of differentially expressed genes.

TABLE 1 qRT-PCR primer sequences of each gene.

Gene	Forward Primer(5′-3′)	Reverse Primer(5′-3′)
INS	CCATCAGCAAGCAGGAAGGTA	GGCTGGGTTGAGGATAGCAAA
IL6	TAGTCCTTCCTACCCCAATTTCC	TTGGTCCTTAGCCACTCCTTC
VEGFA	GGCTGCTGTAACGATGAA	CTGCTGTGCTGTAGGAAG
EGFR	AACAGGCTTTTTGCTGATTCA	TGACCATGTTGCTTTGTTCTG
CASP3	AGGCAAACACTGAAGGCAGA	TAGCCAGGTTTAGGGACACC
MAPK8	GAGGAACGAACTAAGAATGGA	ATTGACAGACGGCGAAGA
MYC	TGTAGTAATTCCAGCGAGAG	CAGATTGTAAGTTCCAGTGAG
ESR1	TGCTCCTAACTTGCTCCT	GATGTGGTCCTTCTCTTCC
FOS	TGAAGACCGTGTCAGGAG	CGCTTGGAGTGTATCTGTC
CCND1	CAGAAGTGCGAAGAGGAG	GGATAGAGTTGTCAGTGTAGA
β-actin	TGACGAGGCCCAGAGCAAGA	ATGGGCACAGTGTGGGTGAC

proteins enter the nucleus and promote the transcription of the *c-fos* gene, which in turn can further promote fibrosis. Our research shows that FZHY could alleviate AAI-induced renal injuries and inflammatory responses through the MAPK/FOS signaling pathways (Figure 8).

5 Discussion

CKD has the characteristics of high incidence, high prevalence, and complex mechanisms. End-stage kidney disease caused by CKD affects countless people worldwide. According to statistics, approximately 10% of adults were affected by CKD (GBD Chronic Kidney Disease Collaboration., 2020). Concomitant with high prevalence, CKD also has a high mortality rate. According to statistical studies, the number of deaths due to CKD is expected to reach 2.2 to 4 million by 2040 (Foreman et al., 2018). As the hallmark of progressive CKD, renal fibrosis is mainly characterized by glomerulosclerosis, tubular atrophy, and renal interstitial fibrosis (Yan et al., 2021). Renal fibrosis is the final pathway in virtually all chronic progressive kidney diseases, regardless of initial etiology (Humphreys., 2018). Renal fibrosis has a complex pathogenesis involving multiple signaling pathways, such as the TGF-β, angiotensin II, and Wnt signaling pathways (Yuan et al., 2022). Although drugs targeting the inflammatory factors associated with signaling pathways have been approved for

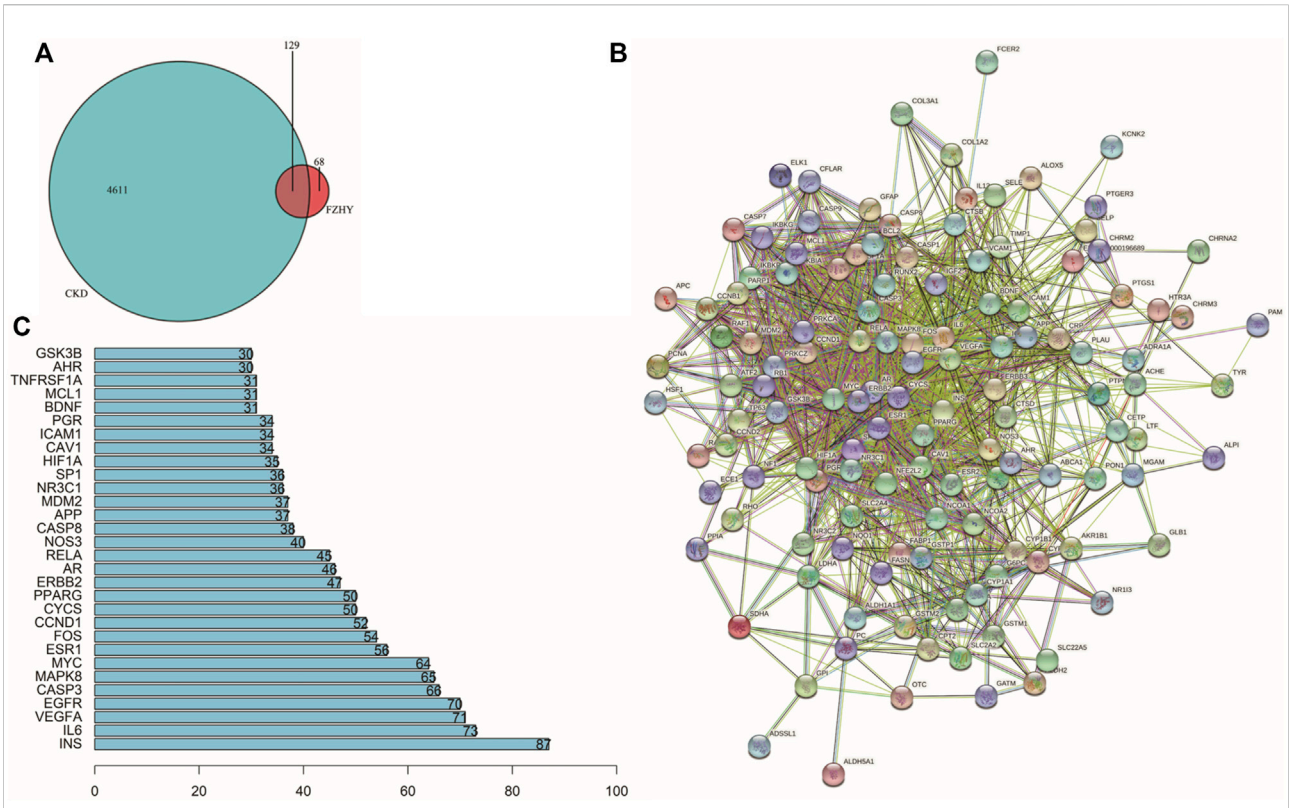

FIGURE 2
Construction of PPI network. **(A)** Venn diagram of 129 target genes of Fuzheng Huayu (FZHY) and chronic kidney disease (CKD). Overlaps are considered potential target genes of FZHY acting on CKD. **(B)** Protein–protein interaction network constructed using STRING. **(C)** Bar plot of potential hub proteins. *Y*-axis represents name of the protein. *X*-axis represents number of adjacent proteins. Height denotes the number of protein connections.

testing in clinical trials, no major advances have been made specifically in treatment strategies for renal fibrosis (Prakoura et al., 2019).

In the last decades, TCM has attracted worldwide attention for its curative effects, relatively low toxicity, and low cost (Luo et al., 2020). As a clinical prescription, FZHY has been shown to improve liver function, reduce Child Pugh scores, and alleviate symptoms in clinical studies (Chen et al., 2019). Multicenter phase II clinical trials in the United States have revealed that FZHY has a positive effect on hepatitis C liver fibrosis (Hassanein et al., 2022). Our previous studies have indicated that FZHY can effectively treat $HgCl_2$-induced renal interstitial fibrosis associated with *TGF-β1*-induced epithelial-to-mesenchymal transition (Wang et al., 2010) and peroxidation (Yuan et al., 2017). A randomized, double-blind, multicenter clinical trial was conducted to evaluate the efficacy of FZHY for CKD (2019ZX09201001-001-006). TCM has multitarget characteristics. Therefore, exploring the mechanisms of FZHY against renal fibrosis is essential to understand how to best use FZHY.

In this study, we identified 815 genes that were differentially expressed in patients with CKD compared with normal individuals in their kidney tissues, of which 129 genes were upregulated and 686 genes were downregulated (Figure 1). Then, after searching the public database, the target network of FZHY against CKD was constructed and analyzed. The Venn diagram indicated 129 potential genes. The PPI network of FZHY–CKD was used to explore the interaction between the formula and disease. GO annotations and the KEGG pathway were used for the functional analysis of related target genes. We identified 1753 GO terms that were significantly associated with FZHY treatment (Figure 3). Several terms were also associated with biological processes relevant to renal diseases, including the response to chemical stress (Kitamura., 2008), response to oxidative stress (Aranda-Rivera et al., 2021), response to drugs (Cybulsky., 2017), and epithelial cell proliferation (Bonventre., 2014). These terms may be associated with the ability of FZHY to inhibit renal fibrosis.

Our KEGG pathway analyses also revealed 128 pathways that were differentially regulated in response to FZHY treatment (Figure 3), including the PI3K–Akt signaling pathway, MAPK signaling pathways (Yuan et al., 2022), and TNF signaling pathway (Al-Lamki & Mayadas., 2015),

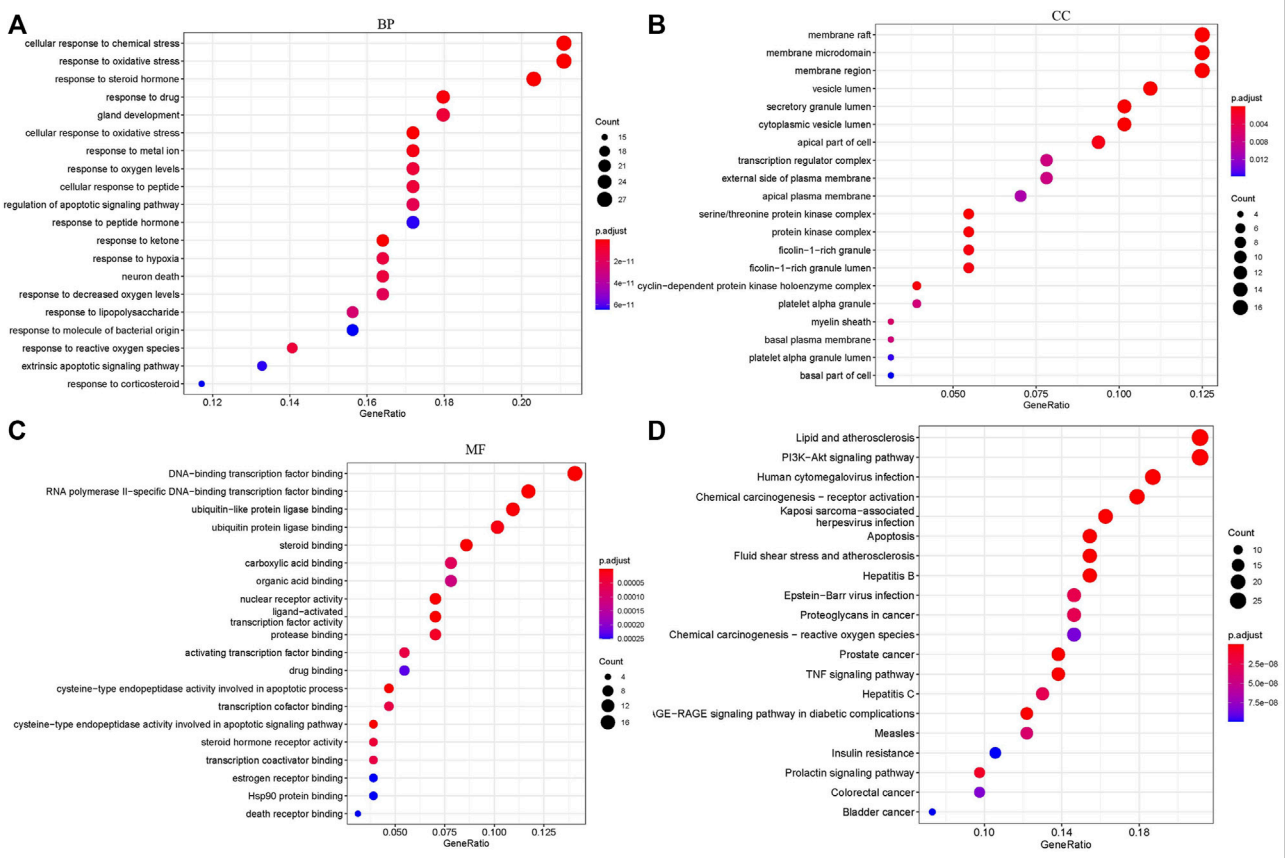

FIGURE 3
Target biological function analysis: GO and KEGG analysis. **(A)** BP analysis of 129 FZHY–CKD target genes. **(B)** CC analysis of 129 FZHY–CKD target genes. **(C)** MF analysis of 129 FZHY–CKD target genes. **(D)** KEGG pathway enrichment analysis of 129 FZHY–CKD target genes. KEGG, Kyoto Encyclopedia of Genes and Genomes; BP, biological process; MF, molecular function; CC, cellular component.

all of which are related to the development of renal fibrosis. These results jointly indicate that FZHY can reverse renal fibrosis by regulating the aforementioned signaling pathways, although additional research is required to validate these findings. The bar plot presents the top 30 potential hub genes through which FZHY acts on CKD, such as *IL-6* (Feigerlová & Battaglia-Hsu., 2017), *EGFR* (Rayego-Mateos et al., 2018), *MAPK8*, and *FOS* (Grynberg et al., 2017). These proteins are also associated with the development of renal disease.

CKD can be caused by various factors, including the inappropriate use of drugs (Romagnani et al., 2017) and prolonged exposure to a toxicant–contaminated environment (i.e., Balkan endemic nephropathy due to AAI) (Lukinich-Gruia et al., 2022). Aristolochic acids (AAs), which are produced by *Aristolochia* and *Asarum*, have been widely used as herbal TCMs (Anger et al., 2020). AAI and AAII are active components in AAs (Jadot et al., 2017). AA nephropathy (AAN) is clinically characterized by rapidly progressive interstitial fibrosis, including impaired proximal tubular function (Luciano & Perazella, 2015). The mechanisms of AAI-induced kidney disease include oxidative stress, apoptosis, and an inflammatory response (Anger et al., 2020). Studies have demonstrated that AAs can cause transitional cell carcinoma of the renal pelvis, ureter, and bladder epithelium by binding to cellular DNA and forming AA–DNA adducts (Stiborová et al., 2017).

Currently, many Chinese herbal medicines containing AAI have been banned, but Aristolochiaceae plants are still applied in clinical treatment due to their relatively low AAI content. Based on the pathological characteristics and pathogenic mechanisms of AAN, AAI was used to establish the CKD mice model in this study.

The dynamic model of AAI at 12 weeks in mice and the pharmacodynamic model of AAI plus FZHY were used for network pharmacological validation. After AAI administration, the Scr and BUN levels of the model group

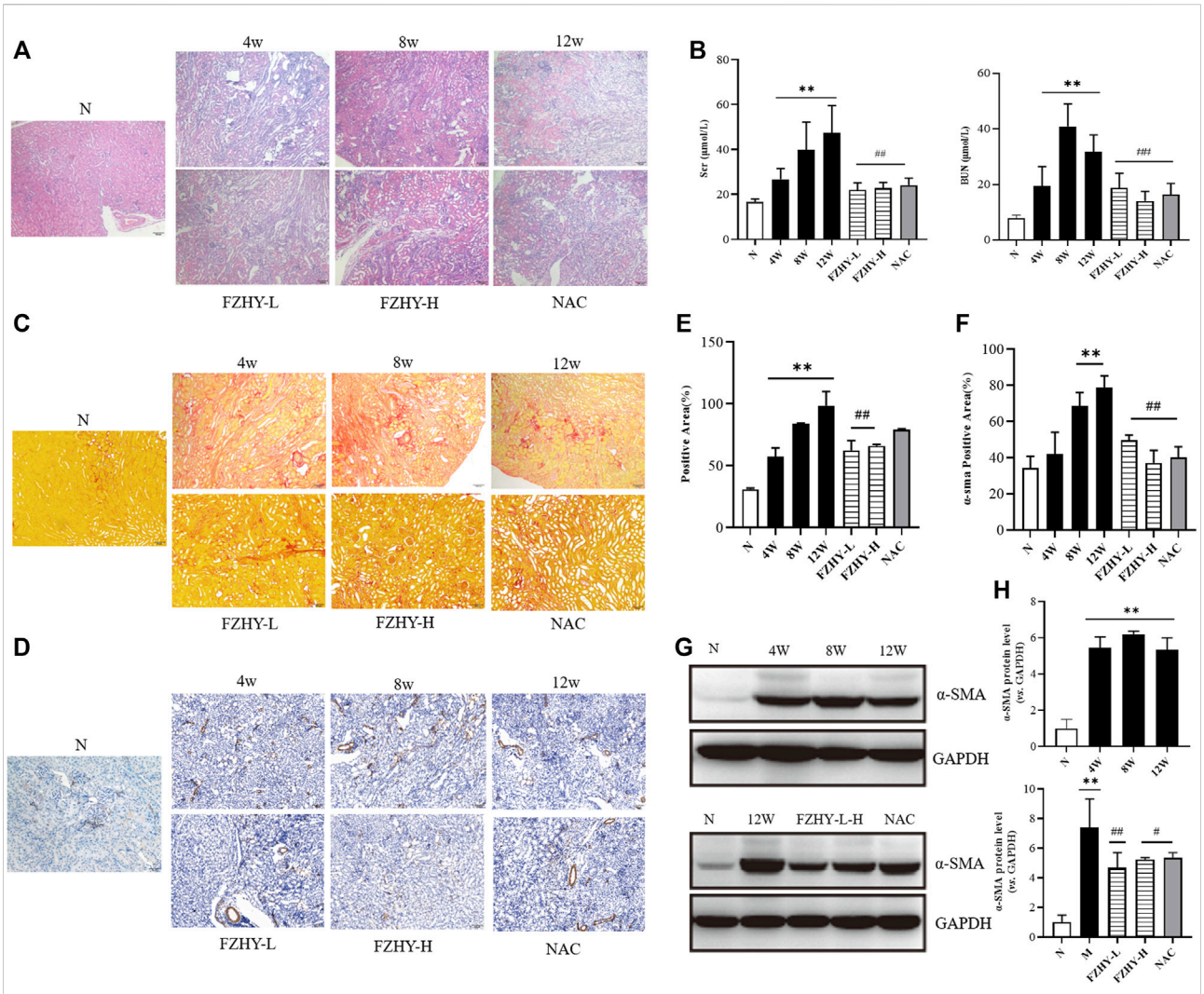

FIGURE 4
Fuzheng Huayu (FZHY) alleviates renal fibrosis induced by Aristolochic Acid I (AAI) *in vivo*. Dynamic experimental model mice were intraperitoneal injected with AAI (4 mg/kg body weight) twice a week and sacrificed at 4 weeks, 8 weeks, and 12 weeks. Pharmacodynamic experimental model mice were intraperitoneal injected with AAI (4 mg/kg body weight) twice a week for 12 weeks. From fourth week of AAI injection, mice were intragastrically administered FZHY (1.44 g/kg, 2.88 g/kg body weight) or NAC (3.0 g/kg body weight) daily for 8 weeks. All mice were sacrificed. Hematoxylin-eosin **(A)** staining of mouse renal tissue sections demonstrated degree of renal injury. Levels of serum creatinine and blood urea nitrogen **(B)** were used to detect renal function. The collagen deposition was shown by using Sirius Red staining **(C)**. Significant renal collagen deposition was observed in mice after AAI administration, which was then reduced by using FZHY or NAC **(E)**. IHC **(D,F)** and WB **(G,H)** analysis of a-SMA showed the degree of renal fibrosis, which increased after AAI injection and alleviated by FZHY (Figures 4F,H). FL, Fuzheng Huayu low-dose; FH, Fuzheng Huayu high-dose. Bar = 100 μm; $^{*}p < 0.05$, compared with normal group; $^{**}p < 0.01$, compared with normal group; $^{\#}p < 0.05$, compared with model group; $^{\#\#}p < 0.01$, compared with model group.

were higher than those of the normal group, and the BUN level significantly decreased after using FZHY (Figure 4B). Hematoxylin-eosin staining revealed that in the AAI model, the renal tissue structure was significantly disrupted, with obvious tubular dilatation, interstitial inflammatory cell infiltration, epithelial cell sloughing, and atrophy in the proximal convoluted tubules. Compared with the model group, the FZHY group exhibited slightly reduced infiltration of inflammatory cells, and renal tubular damage was alleviated (Figure 4A). Moreover, the collagen deposition and the degree of fibrosis in the FZHY and NAC groups decreased compared with that in the model group (Figures 4C,D). Therefore, the results suggest that FZHY can improve, to some degree, renal interstitial fibrosis induced by AAI.

Based on the network pharmacological results, we selected the top 10 genes to perform the qRT-PCR and verify their reliability. Among the top 10 genes, the expression of *EGFR*, *INS*, *IL-6*, *CASP3*, *MAPK8*, *FOS*, *MYC*, *CCND*, and *VEGFA*

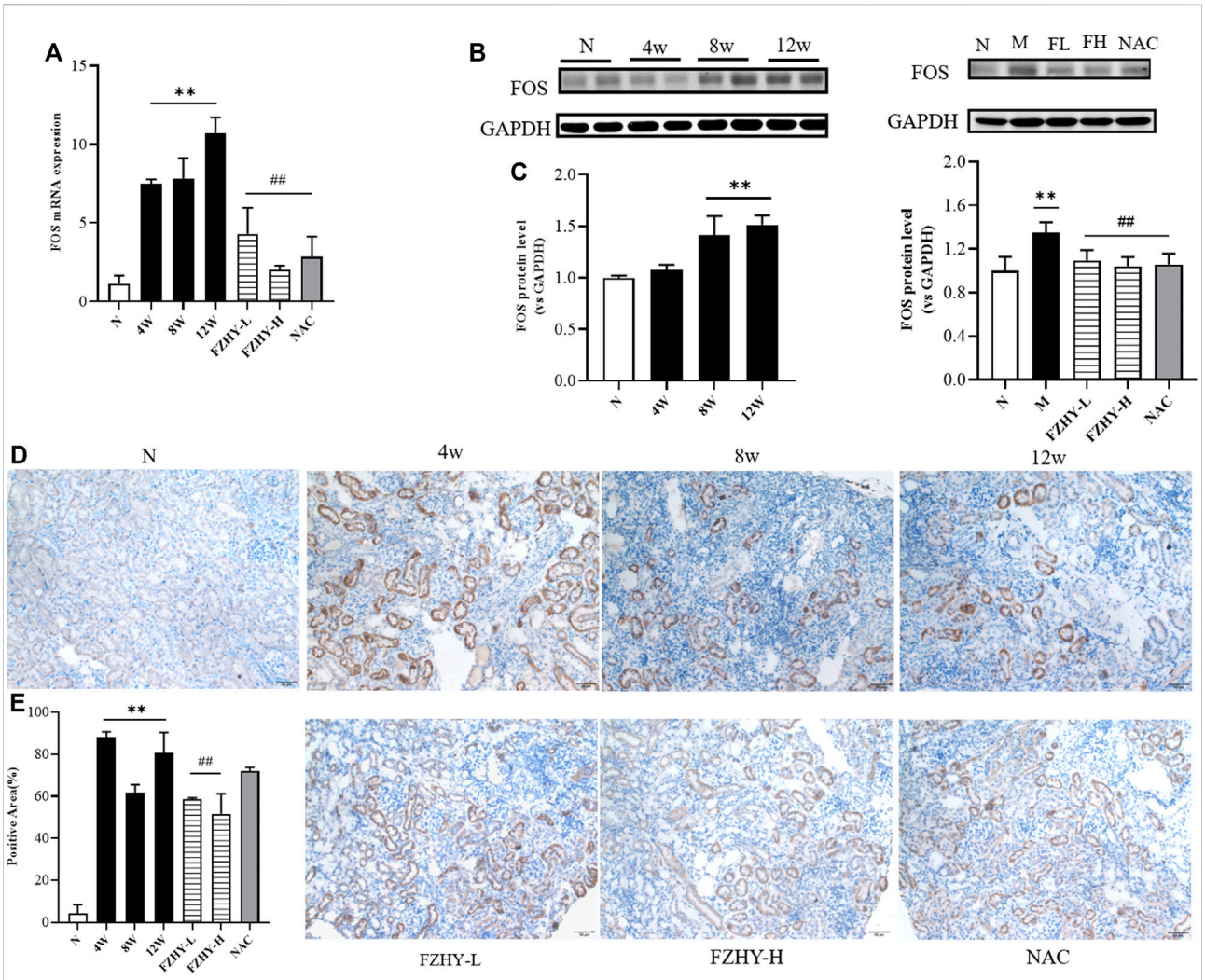

FIGURE 5
FOS may serve as key gene for FZHY to act on chronic kidney disease. Dynamic experimental model mice were intraperitoneal injected with Aristolochic Acid I (AAI) (4 mg/kg body weight) twice a week and sacrificed at 4 weeks, 8 weeks, and 12 weeks, respectively. Pharmacodynamic experimental model mice were intraperitoneal injected with AAI (4 mg/kg body weight) twice a week for 12 weeks. From fourth week of AAI injection, mice were intragastrically administered FZHY (1.44 g/kg, 2.88 g/kg body weight) or NAC (3.0 g/kg body weight) per day for 8 weeks. All mice were sacrificed. Quantitative real-time polymerase chain reaction analysis of mice renal tissues **(A)** shows that *FOS* gene expression significantly increased at 4 weeks, 8 weeks, and 12 weeks compared with normal group and decreased after use of FZHY. Western blot exhibited **(B)** *FOS* protein expression in mice renal tissue. *FOS* protein significantly increased at 8 weeks and 12 weeks compared with normal group and decreased after a high dose of FZHY or NAC **(C)**. Immunohistochemistry was used for locating *FOS* protein **(D)** and quantifying **(E)** in paraffin sections of mice renal tissue. *FOS* protein is mainly expressed in tubular epithelial cells, mostly in cytoplasm, and some are expressed in nucleus. Bar = 50 μm; $^{*}p < 0.05$, compared with normal group; $^{**}p < 0.01$, compared with normal group; $^{\#}p < 0.05$, compared with model group; $^{\#\#}p < 0.01$, compared with model group.

increased compared with that in the normal group. *FOS* elevation was the most prominent and remained high at 12 weeks (Figure 5A). Immunohistochemistry indicated that *FOS* is mainly localized in tubular epithelial cells and expressed in the cytoplasm, with some located in the nucleus (Figure 5D). Similarly, the results of the Western blot analysis demonstrated that *FOS* may serve as a target gene through which FZHY exerts its effects against renal fibrosis (Figures 5B,C).

The proto-oncogene c-Fos is a gene coding for the 62-kDa protein comprising 380 amino acids (Alfonso-Gonzalez & Riesgo-Escovar, 2018). The c-Fos protein is a regulator of cell functions, such as differentiation, proliferation, and transformation (Tsiambas et al., 2020). Based on the characteristics of the *FOS* gene and the role of the MAPK signaling pathways in inflammation and injury (Bhosale et al., 2022), we performed a WB analysis of p-c-Fos, JNK, p-JNK,

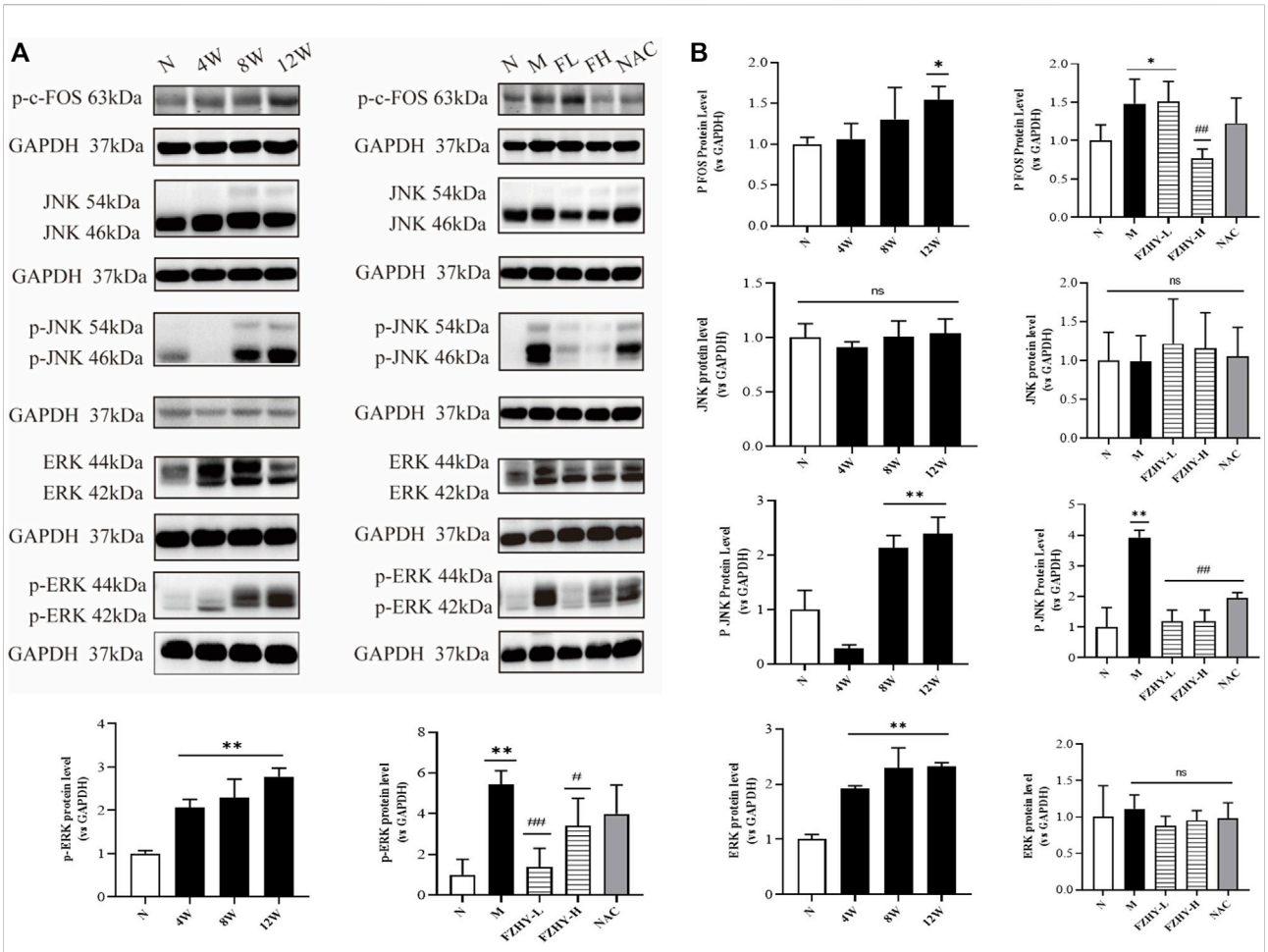

FIGURE 6
Western blot analyses further illustrate the mechanisms of FZHY against renal fibrosis. Dynamic experimental model mice were intraperitoneal injected with Aristolochic Acid I (AAI) (4 mg/kg body weight) twice a week and sacrificed at 4 weeks, 8 weeks, and 12 weeks. Pharmacodynamic experimental model mice were intraperitoneal injected with AAI (4 mg/kg body weight) twice a week for 12 weeks. From the fourth week of AAI injection, mice were intragastrically administered FZHY (1.44 g/kg, 2.88 g/kg body weight) or NAC (3.0 g/kg body weight) per day for 8 weeks. All mice were sacrificed. p-c-fos, JNK, p-JNK, ERK, and p-ERK expression in mice renal tissues were analyzed using Western blot analysis **(A)**. p-JNK, ERK, and p-ERK significantly increased at both 8 weeks and 12 weeks after AAI administration **(B)**. After the FZHY gavage, protein expression levels of JNK and ERK did not change significantly, but expression levels of p-JNK and p-ERK significantly decreased compared with model group **(B)**. $^{*}p < 0.05$, compared with normal group; $^{**}p < 0.01$, compared with normal group; $^{\#}p < 0.05$, compared with model group; $^{\#\#}p < 0.01$, compared with model group; ns, no significance, compared with model group.

ERK, and p-ERK expression. p-JNK, ERK, and p-ERK expression significantly increased in the AAI model at 8 and 12 weeks (Figures 6A,B). However, the protein expression levels of JNK and ERK did not change significantly, and the expression levels of p-JNK and p-ERK significantly decreased compared with those in the model group ($p < 0.01$), suggesting that the protective effect of FZHY on the kidney may be related to the inhibition of the MAPK signaling pathways. Studies have shown that AAI can lead to renal inflammatory responses (Anger et al., 2020), such as the expression of the proinflammatory factors IL6, TNF-α (Li et al., 2021), IL-1β. These factors, in turn, can activate the MAPK signaling pathway (Gaestel et al., 2009; Garbers et al., 2018). ELISA results showed that FZHY could inhibit the inflammatory response caused by AAI (Figures 7A,B).

Collectively, FZHY could alleviate AAI-induced renal injuries and inflammatory responses by inhibiting the MAPK/FOS signaling pathways (Figure 8). Our study identified that *FOS* may play a vital role in how the FZHY formula acts on CKD, and the *MAPK* signaling pathway may serve as the key point. However, further research is necessary both *in vivo* and *in vitro*.

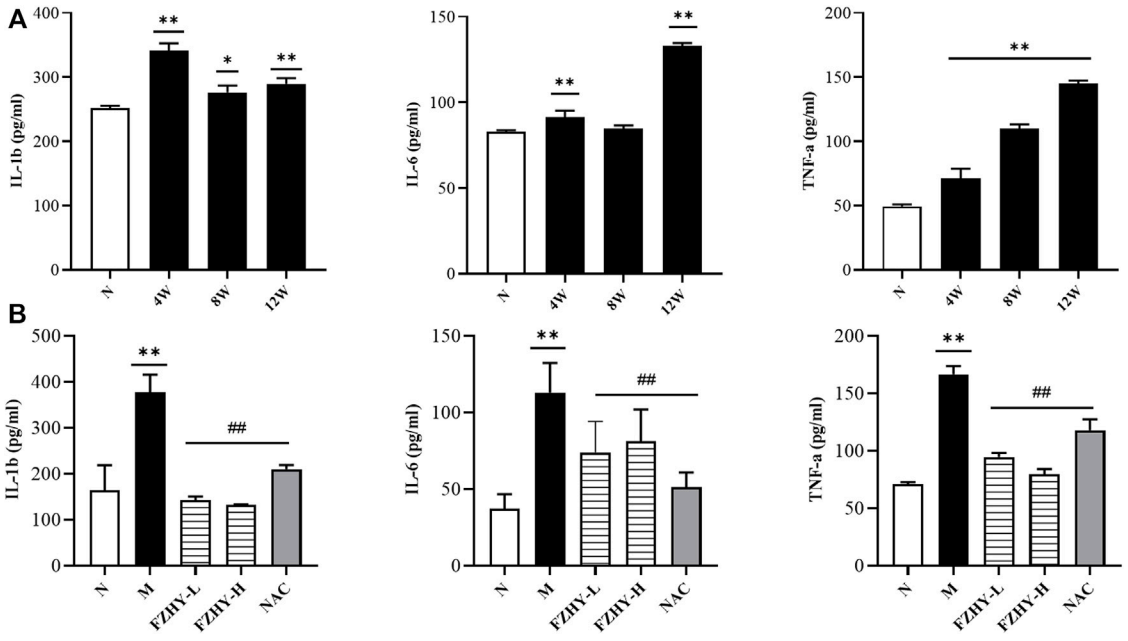

FIGURE 7
Enzyme-linked immunosorbent assay (ELISA) analyses demonstrate the changes of inflammatory response during FZHY against renal fibrosis. Dynamic experimental model mice were intraperitoneal injected with Aristolochic Acid I (AAI) (4 mg/kg body weight) twice a week and sacrificed at 4 weeks, 8 weeks, and 12 weeks. Pharmacodynamic experimental model mice were intraperitoneal injected with AAI (4 mg/kg body weight) twice a week for 12 weeks. From the fourth week of AAI injection, mice were intragastrically administered FZHY (1.44 g/kg, 2.88 g/kg body weight) or NAC (3.0 g/kg body weight) per day for 8 weeks. All mice were sacrificed. ELISA analysis was employed to detect inflammatory factors. Levels of *IL-6*, *IL-1β*, and *TNF-α* significantly increased after AAI administration **(A)**, and levels of *IL-6*, *IL-1β*, and *TNF-α* decreased after FZHY **(B)**.

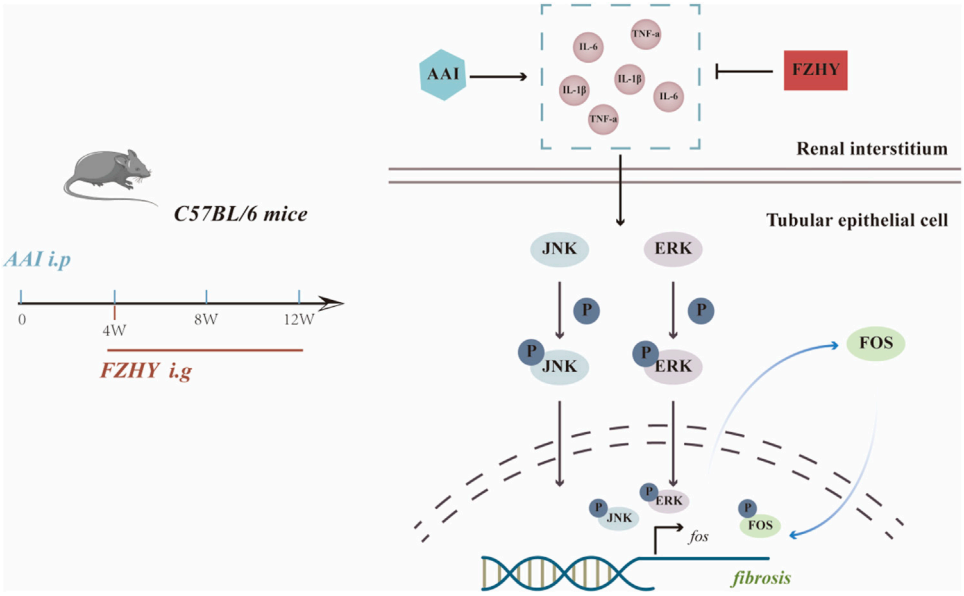

FIGURE 8
Diagram depicting the potential mechanism of FZHY against the renal fibrosis induced by AAI.

6 Conclusion

The mechanisms of the FZHY formula that alleviate renal fibrosis in CKD have been preliminarily explored using network pharmacological predictions and *in vivo* validation. Functional enrichment analyses demonstrated that FZHY may achieve therapeutic efficacy by modulating MAPK and PI3K-AKT signaling and reactive oxygen species. However, further research is necessary to validate the role of FZHY in functional contexts. Our work also revealed that FZHY can protect the kidney from inflammatory injuries caused by AAI and antagonize inflammatory factor-stimulated MAPK/FOS activation.

Data availability statement

The datasets presented in this study can be found in online repositories. The names of the repository/repositories and accession number(s) can be found in the article/Supplementary Material.

Ethics statement

The animal study was reviewed and approved by Experimental Animal Ethics Committee of Shanghai University of Traditional Chinese Medicine.

Author contributions

YT and CL conceived and designed the project; FW, SW, JW, GC, and KH conducted the experiments; FW and YT analyzed the data and wrote the manuscript; CL revised the manuscript; YT made the final critical revision to the manuscript.

Funding

This work was supported by the Science and Technology Innovation Action Plan of the Shanghai Municipal Science and Technology Commission (No. 19401901500), the National Science and Technology Major Project "Key New Drug Creation and Manufacturing Program" (No. 2 019ZX09201001) and the Three-Year Action Plan of for the Development of TCM in Shanghai [No. ZY-(2018-2020)-CCCX-5001].

Conflict of interest

The authors declare that the research was conducted in the absence of any commercial or financial relationships that could be construed as a potential conflict of interest.

Publisher's note

All claims expressed in this article are solely those of the authors and do not necessarily represent those of their affiliated organizations, or those of the publisher, the editors and the reviewers. Any product that may be evaluated in this article, or claim that may be made by its manufacturer, is not guaranteed or endorsed by the publisher.

Supplementary material

The Supplementary Material for this article can be found online at: https://www.frontiersin.org/articles/10.3389/fphar.2022.1056865/full#supplementary-material

References

Al-Lamki, R. S., and Mayadas, T. N. (2015). TNF receptors: Signaling pathways and contribution to renal dysfunction. *Kidney Int.* 87 (2), 281–296. doi:10.1038/ki.2014.285

Alfonso-Gonzalez, C., and Riesgo-Escovar, J. R. (2018). Fos metamorphoses: Lessons from mutants in model organisms. *Mech. Dev.* 154, 73–81. doi:10.1016/j.mod.2018.05.006

Amberger, J. S., and Hamosh, A. (2017). Searching online mendelian inheritance in man (OMIM): A knowledgebase of human genes and genetic phenotypes. *Curr. Protoc. Bioinforma.* 58, 1–7. doi:10.1002/cpbi.24.2.1–1.2.12

Anger, E. E., Yu, F., and Li, J. (2020). Aristolochic acid-induced nephrotoxicity: Molecular mechanisms and potential protective approaches. *Int. J. Mol. Sci.* 21 (3), 1157. doi:10.3390/ijms21031157

Aranda-Rivera, A. K., Cruz-Gregorio, A., Aparicio-Trejo, O. E., and Pedraza-Chaverri, J. (2021). Mitochondrial redox signaling and oxidative stress in kidney diseases. *Biomolecules* 11 (8), 1144. doi:10.3390/biom11081144

Bhosale, P. B., Kim, H. H., Abusaliya, A., Vetrivel, P., Ha, S. E., Park, M. Y., et al. (2022). Structural and functional properties of activator protein-1 in cancer and inflammation. *Evid. Based. Complement. Altern. Med.* 2022, 9797929. doi:10.1155/2022/9797929

Bonventre, J. V. (2014). Primary proximal tubule injury leads to epithelial cell cycle arrest, fibrosis, vascular rarefaction, and glomerulosclerosis. *Kidney Int. Suppl.* 4 (1), 39–44. doi:10.1038/kisup.2014.8

Chen, J., Hu, Y., Chen, L., Liu, W., Mu, Y., and Liu, P. (2019). The effect and mechanisms of Fuzheng Huayu formula against chronic liver diseases. *Biomed. Pharmacother.* 114, 108846. doi:10.1016/j.biopha.2019.108846

Collins, A. J., Foley, R. N., Gilbertson, D. T., and Chen, S. C. (2015). United States Renal Data System public health surveillance of chronic kidney disease and end-stage renal disease. *Kidney Int. Suppl.* 5 (1), 2–7. doi:10.1038/kisup.2015.2

Cybulsky, A. V. (2017). Endoplasmic reticulum stress, the unfolded protein response and autophagy in kidney diseases. *Nat. Rev. Nephrol.* 13 (11), 681–696. doi:10.1038/nrneph.2017.129

Dalhäusser, A. K., Rössler, O. G., and Thiel, G. (2022). Resveratrol stimulates c-Fos gene transcription via activation of ERK1/2 involving multiple genetic elements. *Gene* 821, 70–75. doi:10.1016/j.gene.2018.03.008

Feigerlová, E., and Battaglia-Hsu, S. F. (2017). IL-6 signaling in diabetic nephropathy: From pathophysiology to therapeutic perspectives. *Cytokine Growth Factor Rev.* 37, 57–65. doi:10.1016/j.cytogfr.2017.03.003

Foreman, K. J., Marquez, N., Dolgert, A., Fukutaki, K., Fullman, N., McGaughey, M., et al. (2018). Forecasting life expectancy, years of life lost, and all-cause and cause-specific mortality for 250 causes of death: Reference and alternative scenarios for 2016-40 for 195 countries and territories. *Lancet* 392 (10159), 2052–2090. doi:10.1016/S0140-6736(18)31694-5

Gaestel, M., Kotlyarov, A., and Kracht, M. (2009). Targeting innate immunity protein kinase signalling in inflammation. *Nat. Rev. Drug Discov.* 8 (6), 480–499. doi:10.1038/nrd2829

Garbers, C., Heink, S., Korn, T., and Rose-John, S. (2018). Interleukin-6: Designing specific therapeutics for a complex cytokine. *Nat. Rev. Drug Discov.* 17 (6), 395–412. doi:10.1038/nrd.2018.45

Gbd Chronic Kidney Disease Collaboration (2020). Global, regional, and national burden of chronic kidney disease, 1990-2017: A systematic analysis for the global burden of disease study 2017. *Lancet* 395 (10225), 709–733. doi:10.1016/S0140-6736(20)30045-3

Grynberg, K., Ma, F. Y., and Nikolic-Paterson, D. J. (2017). The JNK signaling pathway in renal fibrosis. *Front. Physiol.* 8, 829. doi:10.3389/fphys.2017.00829

Hassanein, T., Tai, D., Liu, C., Box, T. D., Tong, M. J., Rossaro, L., et al. (2022). Efficacy and safety of a botanical formula Fuzheng Huayu for hepatic fibrosis in patients with CHC: Results of a phase 2 clinical trial. *Evid. Based. Complement. Altern. Med.* 2022, 4494099. doi:10.1155/2022/4494099

Humphreys, B. D. (2018). Mechanisms of renal fibrosis. *Annu. Rev. Physiol.* 80, 309–326. DOI: doi:10.1146/annurev-physiol-022516-034227

Jadot, I., Declèves, A. E., Nortier, J., and Caron, N. (2017). An integrated view of aristolochic acid nephropathy: Update of the literature. *Int. J. Mol. Sci.* 18 (2), 297. doi:10.3390/ijms18020297

Kang, H. M., Ahn, S. H., Choi, P., Ko, Y. A., Han, S. H., Chinga, F., et al. (2015). Defective fatty acid oxidation in renal tubular epithelial cells has a key role in kidney fibrosis development. *Nat. Med.* 21 (1), 37–46. doi:10.1038/nm.3762

Kitamura, M. (2008). Endoplasmic reticulum stress in the kidney. *Clin. Exp. Nephrol.* 12 (5), 317–325. doi:10.1007/s10157-008-0060-7

Klinkhammer, B. M., Goldschmeding, R., Floege, J., and Boor, P. (2017). Treatment of renal fibrosis-turning challenges into opportunities. *Adv. Chronic Kidney Dis.* 24 (2), 117–129. doi:10.1053/j.ackd.2016.11.002

Li, L., Tao, S., Guo, F., Liu, J., Huang, R., Tan, Z., et al. (2021). Genetic and pharmacological inhibition of fatty acid-binding protein 4 alleviated inflammation and early fibrosis after toxin induced kidney injury. *Int. Immunopharmacol.* 96, 107760. doi:10.1016/j.intimp.2021.107760

Liu, Z., Guo, F., Wang, Y., Li, C., Zhang, X., Li, H., et al. (2016). BATMAN-TCM: A Bioinformatics analysis Tool for molecular mechANism of traditional Chinese medicine. *Sci. Rep.* 6, 21146. doi:10.1038/srep21146

Luciano, R. L., and Perazella, M. A. (2015). Aristolochic acid nephropathy: Epidemiology, clinical presentation, and treatment. *Drug Saf.* 38 (1), 55–64. doi:10.1007/s40264-014-0244-xAristolochic acid nephropathy

Lukinich-Gruia, A. T., Nortier, J., Pavlović, N. M., Milovanović, D., Popović, M., Drăghia, L. P., et al. (2022). Aristolochic acid I as an emerging biogenic contaminant involved in chronic kidney diseases: A comprehensive review on exposure pathways, environmental health issues and future challenges. *Chemosphere* 297, 134111. doi:10.1016/j.chemosphere.2022.134111

Luo, T. T., Lu, Y., Yan, S. K., Xiao, X., Rong, X. L., and Guo, J. (2020). Network pharmacology in research of Chinese medicine formula: Methodology, application and prospective. *Chin. J. Integr. Med.* 26 (1), 72–80. doi:10.1007/s11655-019-3064-0

Nakagawa, S., Nishihara, K., Miyata, H., Shinke, H., Tomita, E., Kajiwara, M., et al. (2015). Molecular markers of tubulointerstitial fibrosis and tubular cell damage in patients with chronic kidney disease,. *PloS one* 10 ((8)), e0136994. DOI: doi:10.1371/journal.pone.0136994

Prakoura, N., Hadchouel, J., and Chatziantoniou, C. (2019). Novel targets for therapy of renal fibrosis. *J. Histochem. Cytochem.* 67 (9), 701–715. doi:10.1369/0022155419849386

Qin, T., Wu, L., Hua, Q., Song, Z., Pan, Y., and Liu, T. (2020). Prediction of the mechanisms of action of shenkang in chronic kidney disease: A network pharmacology study and experimental validation. *J. Ethnopharmacol.* 246, 112128. doi:10.1016/j.jep.2019.112128

Rayego-Mateos, S., Rodrigues-Diez, R., Morgado-Pascual, J. L., Valentijn, F., Valdivielso, J. M., Goldschmeding, R., et al. (2018). Role of epidermal Growth factor receptor (EGFR) and its ligands in kidney inflammation and damage. *Mediat. Inflamm.* 2018, 8739473. doi:10.1155/2018/8739473

Ritchie, M. E., Phipson, B., Wu, D., Hu, Y., Law, C. W., Shi, W., et al. (2015). Limma powers differential expression analyses for RNA-sequencing and microarray studies. *Nucleic Acids Res.* 43 (7), e47. doi:10.1093/nar/gkv007

Romagnani, P., Remuzzi, G., Glassock, R., Levin, A., Jager, K. J., Tonelli, M., et al. (2017). Chronic kidney disease. *Nat. Rev. Dis. Prim.* 3, 17088. doi:10.1038/nrdp.2017.88

Ru, J., Li, P., Wang, J., Zhou, W., Li, B., Huang, C., et al. (2014). Tcmsp: A database of systems pharmacology for drug discovery from herbal medicines. *J. Cheminform.* 6, 13. doi:10.1186/1758-2946-6-13

Shaulian, E., and Karin, M. (2002). AP-1 as a regulator of cell life and death. *Nat. Cell Biol.* 4 (5), E131–E136. doi:10.1038/ncb0502-e131

Stelzer, G., Rosen, N., Plaschkes, I., Zimmerman, S., Twik, M., Fishilevich, S., et al. (2016). The GeneCards suite: From gene data mining to disease genome sequence analyses. *Curr. Protoc. Bioinforma.* 54, 1. doi:10.1002/cpbi.5.30.1–1.30.33

Stiborová, M., Arlt, V. M., and Schmeiser, H. H. (2017). DNA adducts formed by aristolochic acid are unique biomarkers of exposure and explain the initiation phase of upper urothelial cancer. *Int. J. Mol. Sci.* 18 (10), 2144. doi:10.3390/ijms18102144

Szklarczyk, D., Morris, J. H., Cook, H., Kuhn, M., Wyder, S., Simonovic, M., et al. (2017). The STRING database in 2017: Quality-controlled protein-protein association networks, made broadly accessible. *Nucleic Acids Res.* 45 (D1), D362-D368–D368. doi:10.1093/nar/gkw937

Tsiambas, E., Mastronikolis, N., Fotiades, P. P., Kyrodimos, E., Chrysovergis, A., Papanikolaou, V., et al. (2020). c-Jun/c-Fos complex in laryngeal squamous cell carcinoma. *J. BUON* 25 (2), 618–620.PMID: 32521843

Wang, Q. L., Tao, Y. Y., Xie, H. D., Liu, C. H., and Liu, P. (2020). Fuzheng Huayu recipe, a traditional Chinese compound herbal medicine, attenuates renal interstitial fibrosis via targeting the miR-21/PTEN/AKT axis. *J. Integr. Med.* 18 (6), 505–513. doi:10.1016/j.joim.2020.08.006

Wang, Q. L., Yuan, J. L., Tao, Y. Y., Zhang, Y., Liu, P., and Liu, C. H. (2010). Fuzheng Huayu recipe and vitamin E reverse renal interstitial fibrosis through counteracting TGF-beta1-induced epithelial-to-mesenchymal transition. *J. Ethnopharmacol.* 127 (3), 631–640. doi:10.1016/j.jep.2009.12.011

Wishart, D. S., Feunang, Y. D., Guo, A. C., Lo, E. J., Marcu, A., Grant, J. R., et al. (2018). DrugBank 5.0: A major update to the DrugBank database for 2018. *Nucleic Acids Res.* 46 (D1), D1074-D1082–D1082. doi:10.1093/nar/gkx1037

Xi, Y., Lu, X., Zhu, L., Sun, X., Jiang, Y., He, W., et al. (2020). Clinical trial for conventional medicine integrated with traditional Chinese medicine (TCM) in the treatment of patients with chronic kidney disease. *Medicine* 99 (21), e20234. doi:10.1097/MD.0000000000020234

Xia, P., Gao, K., Xie, J., Sun, W., Shi, M., Li, W., et al. (2020). Data mining-based analysis of Chinese medicinal herb formulae in chronic kidney disease treatment. *Evid. Based. Complement. Altern. Med.* 2020, 9719872. doi:10.1155/2020/9719872

Xu, T., Wang, Q., and Liu, M. (2020). A network pharmacology approach to explore the potential mechanisms of huangqin-baishao herb pair in treatment of cancer. *Med. Sci. Monit.* 26, e923199. doi:10.12659/MSM.923199

Yan, H., Xu, J., Xu, Z., Yang, B., Luo, P., and He, Q. (2021). Defining therapeutic targets for renal fibrosis: Exploiting the biology of pathogenesis. *Biomed. Pharmacothe* 143, 112115. doi:10.1016/j.biopha.2021.112115

Yang, C., Wang, H., Zhao, X., Matsushita, K., Coresh, J., Zhang, L., et al. (2020). CKD in China: Evolving spectrum and public health implications. *Am. J. Kidney Dis.* 76 (2), 258–264. doi:10.1053/j.ajkd.2019.05.032

Ye, M., Lin, W., Zheng, J., and Lin, S. (2021). N-Acetylcysteine for chronic kidney disease: A systematic review and meta-analysis. *Am. J. Transl. Res.* 13 (4), 2472–2485.PMCID: PMC8129408

Yu, G., Wang, L. G., Yan, G. R., and He, Q. Y. (2015). Dose: An R/bioconductor package for disease ontology semantic and enrichment analysis. *Bioinformatics* 31 (4), 608–609. doi:10.1093/bioinformatics/btu684

Yuan, J. L., Tao, Y. Y., Wang, Q. L., Shen, L., and Liu, C. H. (2017). Fuzheng Huayu Formula prevents rat renal interstitial fibrosis induced by HgCl2 via antioxidative stress and down-regulation of nuclear factor-kappa B activity. *Chin. J. Integr. Med.* 23 (8), 598–604. doi:10.1007/s11655-016-2540-z

Yuan, Q., Tang, B., and Zhang, C. (2022). Signaling pathways of chronic kidney diseases, implications for therapeutics. *Signal Transduct. Target. Ther.* 7 (1), 182. doi:10.1038/s41392-022-01036-5

Yuan, Q., Tang, B., and Zhang, C. (2022). Signaling pathways of chronic kidney diseases, implications for therapeutics. *Signal Transduct. Target. Ther.* 7 (1), 182. doi:10.1038/s41392-022-01036-5

Zhang, L., Wang, F., Wang, L., Wang, W., Liu, B., Liu, J., et al. (2012). Prevalence of chronic kidney disease in China: A cross-sectional survey. *Lancet (London, Engl.* 379 (9818), 815–822. doi:10.1016/S0140-6736(12)60033-6

Zhou, R. S., Zhang, E. X., Sun, Q. F., Ye, Z. J., Liu, J. W., Zhou, D. H., et al. (2019). Integrated analysis of lncRNA-miRNA-mRNA ceRNA network in squamous cell carcinoma of tongue. *BMC cancer* 19 (1), 779. doi:10.1186/s12885-019-5983-8

Glossary

AAI Aristolochic acid I

ACEIs Angiotensin converting enzyme inhibitors

ACTG2 Actin gamma 2

ANOVA One-way analysis of variance

ARBs Angiotensin receptor blockers

a-SMA Alpha-smooth muscle actin

BATMAN a Bioinformatics Analysis Tool for Molecular mechANism of Traditional Chinese Medicine

BCA Bicinchoninic acid assay

BP Biological process

BSA Bovine serum albumin

BUN Blood urea nitrogen

C5orf58 Chromosome 5 open reading frame 58

CC Cellular component

CCND1 Cyclin D1

CKD Chronic kidney disease

DAB Diaminobenzidine

DEGs Differentially expressed genes

DL DrugLikeness

EDTA Ethylene diamine tetraacetic acid

EGFR Epidermal growth factor receptor

ELISA Enzyme-linked immunosorbent assay

EMT Epithelial-to-mesenchymal transition

ERK Extracellular regulated protein kinases

ESR1 Estrogen receptor 1

ESRD End-stage renal disease

FH FZHY high-dose

FL FZHY low-dose

FOS FBJ murine osteosarcoma viral oncogene homolog/Fos proto-oncogene

FZHY Fuzheng Huayu formula/decoction/recipe

GAPDH Glyceraldehyde-3-phosphate dehydrogenase

GEO Gene expression omnibus

GO Gene ontology

HBA1 Hemoglobin subunit alpha 1

HBA2 Hemoglobin subunit alpha 2

HBD Hemoglobin subunit delta

H-E Hematoxylin-eosin

IACUC Institutional laboratory animal care and use committee

IHC Immunohistochemistry

IL-1β Interleukin-1 beta

IL4I1 Interleukin 4 induced 1

IL-6 Interleukin-6

INS Insulin

ITLN1 Intelectin 1

JNK/MAPK8 Mitogen-activated protein kinase 8

KDIGO Kidney disease improving global outcomes

KEGG Kyoto encyclopedia of genes and genomes

MAPKs Mitogen-activated protein kinase family

MF Molecular function

MYC MYC proto-oncogene

NAC N-acetylcysteine

NCBI National center for biotechnology information

OB Oral bioavailability

OMIM Online mendelian inheritance in man

OR5L2 Olfactory receptor family 5 subfamily L member 2

PBS Phosphate buffer saline

PBST Phosphate buffer saline with Tween® 20

P-ERK Phospho-extracellular regulated protein kinases

P-JNK Phospho-mitogen-activated protein kinase 8

PMSF Phenylmethylsulfonyl fluoride

PPI Protein-protein interaction

qRT-PCR Quantitative real-time PCR

RIPA Radio immunoprecipitation assay

RPS4Y1 Ribosomal protein S4 Y-linked 1

RPS4Y2 Ribosomal protein S4 Y-linked 2

Scr Serum creatinine

SD Standard deviation

SDS Sodium dodecyl sulfate

SDS-PAGE Sodium dodecyl sulfate polyacrylamide gel electrophoresis

SFDA State food and drug administration

SPF Specific pathogen Free

SPSS Statistical product service solutions

STRING Search tool for the retrieval of interaction gene/proteins

TBS Tris buffered saline

TBST Tris buffered saline with Tween® 20

TCM Traditional Chinese Medicine

TCMSP Traditional Chinese Medicine systems pharmacology database and analysis platform

TMB 3, 3′,5 ,5′-Tetramethylbenzidine

TNF-α Tumor necrosis factor-alpha

UUO Unilateral ureteral obstruction

VEGFA Vascular endothelial growth factor A

WB Western blot

frontiers | Frontiers in Pharmacology

TYPE Original Research
PUBLISHED 09 January 2023
DOI 10.3389/fphar.2022.1086206

OPEN ACCESS

EDITED BY
Xiaoxi Lv,
Institute of Materia Medica, Chinese Academy of Medical Sciences and Peking Union Medical College, China

REVIEWED BY
Xiao-Wei Zhang,
Institute of Materia Medica, Chinese Academy of Medical Sciences and Peking Union Medical College, China
Shanshan Liu,
Second Xiangya Hospital, Central South University, China

*CORRESPONDENCE
Hongliang Dong,
hldongscmc@163.com
Jian Gao,
gaojianayfy@163.com

SPECIALTY SECTION
This article was submitted to Respiratory Pharmacology, a section of the journal Frontiers in Pharmacology

RECEIVED 01 November 2022
ACCEPTED 22 December 2022
PUBLISHED 09 January 2023

CITATION
Huang Y, Cheng M, Wang X, Dong H and Gao J (2023), Dang Gui Bu Xue Tang, a conventional Chinese herb decoction, ameliorates radiation-induced heart disease *via* Nrf2/HMGB1 pathway. *Front. Pharmacol.* 13:1086206. doi: 10.3389/fphar.2022.1086206

Dang Gui Bu Xue Tang, a conventional Chinese herb decoction, ameliorates radiation-induced heart disease *via* Nrf2/HMGB1 pathway

Yifan Huang[1,2], Minghan Cheng[1], Xiaoye Wang[1,3], Hongliang Dong[1]* and Jian Gao[1]*

[1]Pediatric Translational Medicine Institute, Shanghai Children's Medical Center, School of Medicine, Shanghai Jiao Tong University, Shanghai, China, [2]School of Public Health, Suzhou Medical College of Soochow University, Suzhou, China, [3]School of Pharmacy, Anhui University of Chinese Medicine, Hefei, China

Introduction: Radiation-induced heart disease (RIHD), characterized by cardiac dysfunction and myocardial fibrosis, is one of the most common complications after cardiothoracic radiotherapy. Dang Gui Bu Xue Tang (DBT) is a conventional Chinese herb decoction composed of Radix Astragali membranaceus (RAM) and Radix Angelicae sinensis (RAS) at a ratio of 5:1, famous for its "blood-nourishing" effect. In this study, we aimed to investigate the cardioprotective effect of DBT on RIHD.

Methods: C57BL mice at 8 weeks of age were divided into five groups, namely Control, Radiation, RDBT51 (Radiation with DBT, RAM:RAS = 5:1), RDBT11 (Radiation with DBT, RAM:RAS = 1:1), and RDBT15 (Radiation with DBT, RAM:RAS = 1:5).

Results: We mainly found that radiation in the cardiothoracic region led to significant left ventricular systolic dysfunction, myocardial fibrotic lesions and cardiac injury accompanied by abnormally increased myocardial HMGB1 protein levels. Administration of conventional DBT significantly ameliorated left ventricular systolic dysfunction, alleviated myocardial fibrosis, and counteracted cardiac injury, all of which supported the protective effect of DBT on RIHD, involving upregulation of myocardial Nrf2 protein levels and downregulation of HMGB1 protein levels as underlying mechanisms.

Conclusions: DBT exerts a significant protective effect on RIHD, and the Nrf2/HMGB1 pathway probably plays an important role in this protective effect.

KEYWORDS

myocardial fibrosis (MF), radix angelicae sinensis (RAS), radix astragali membranaceus (RAM), galectin-3 (Gal-3), systolic dysfunction, cardiac injury

1 Introduction

Despite being widely used in cancer patients and improving survival rates for many cancers, radiation therapy involves some inevitable complications (Wang et al., 2019; Quintero-Martinez et al., 2021). Radiation-induced myocardial fibrosis, characterized by decreased ventricular elasticity and distensibility, is a potentially lethal clinical complication of chest radiotherapy and a final stage of radiation-induced heart disease (RIHD) (Wang et al., 2020). The development of radiation-induced myocardial fibrosis is a slow but constantly progressive process, with clinical symptoms occurring several years after irradiation. However, the exact underlying mechanism involving radiation-

induced myocardial fibrosis is still not completely clarified (Sarkozy et al., 2021), and accurately diagnosing and identifying patients who may progress to radiation-induced myocardial fibrosis has been challenging (Wang et al., 2020).

High mobility group box 1 (HMGB1), a highly conservative nucleoprotein, was a multifunctional protein involved in the regulation of inflammation, cancer and fibrosis progression (Wang and Zhang, 2020). As an important late inflammatory cytokine, the role of HMGB1 in fibrotic diseases has become one of the hot issues during the past years. The expression of HMGB1 is up-regulated in pulmonary fibrosis and participates in the occurrence and development of pulmonary fibrosis. Many studies have shown that inhibiting the production of HMGB1 can effectively reduce the inflammatory reaction-related damage in the body. Our previous studies demonstrated that Nrf2 attenuated the epithelial mesenchymal transition process in pulmonary fibrosis through inhibition of HMGB1 pathway (Zhang et al., 2018; Qu et al., 2019).

The role of HMGB1 in cardiovascular disease and cardiac fibrosis has been increasingly concerned in recent years, and a series of progress has also been made. Many studies have shown that HMGB1 acts on the RAGE receptor on the surface of cardiac fibroblasts, making it form heterodimer with some TLRs (such as TLR2/4/9) or β - integrin Mac-1, and stimulate cardiac fibroblasts to obtain the characteristics of proliferation, migration and fibrosis promotion through NF-κB, MAPKs and JAK/STAT (Turner, 2016). In the cardiac fibrosis model induced by diabetes, silencing HMGB1 can inhibit cardiac fibrosis and improve cardiac function through MAPK pathway (Wang et al., 2014). All these data showed that HMGB1 is a very promising target for cardiac fibrosis treatment, but whether the therapeutic strategy targeting HMGB1 plays a protective role in patients still needs more evidence. In RIHD, whether HMGB1 is involved in the process of myocardial injury and cardiac fibrosis is still unknown.

Dang Gui Bu Xue Tang (DBT), a combination of *Radix Astragali membranaceus* (RAM) and *Radix Angelicae sinensis* (RAS) at a conventional ratio of 5:1, is a widely used herbal decoction in traditional Chinese medicine promote or invigorate the "blood". DBT has been proved to mediate potent cardioprotective and anti-cardiac fibrosis effects (Mak et al., 2006), while the underlying mechanisms remain to be elaborated. In the present study, we developed *in vivo* and *in vitro* models of RIHD. Through these models, we revealed that DBT-mediated Nrf2 activation could downregulate radiation-induced increase in cardiac HMGB1, improve abnormal weight loss, and reduce cardiac fibrosis. These findings uncovered a Nrf2-HMGB1 axis mediating the protective effect of DBT on cardiac fibrosis, providing a useful clue for a clinical strategy against the disease.

2 Materials and methods

2.1 Animal and cell preparation

The animal study was reviewed and approved by the Animal Ethics Committee of Soochow University. A total of 45 male C57BL mice at 7 weeks of age were purchased from the Beijing Vital River Laboratory (Beijing Vital River Laboratory Animal Technology Co., Ltd., China). All mice were housed in a temperature- and humidity-controlled facility without specific pathogen at 12-h light and dark cycles, with water and food *ad libitum*.

Neonatal mice (born within 48 h, Beijing Vital River Laboratory Animal Technology Co., Ltd., China) were euthanized by decapitation and then the neonatal mouse myocardial fibroblasts were isolated and cultured according to the methods we described previously (Zhang et al., 2022). Briefly, mouse ventricular myocardial tissues were minced and rinsed in D-Hanks balanced salt solution, and subsequently digested in D-Hanks solution containing 10 μg/ml Liberase TH (Roche, 5,401,151,001), incubated at 37°C for 30 min. High glucose Dulbecco's Modified Eagle's Medium (DMEM) (HyClone, United States of America) supplemented with 10% foetal bovine serum (FBS) (Gibco, United States of America) was added to the digested supernatant to terminate the digestion, followed by centrifugation at 100 *g* for 10 min to collect suspended cells. All isolated cells were pre-plated in a humidified incubator at 37°C with 5%CO_2 for 1 hour, after which the unattached cells were discarded and the attached cells were myocardial fibroblasts. Isolated myocardial fibroblasts were cultured in high glucose DMEM with 10% FBS for further *in vitro* experiments.

2.2 DBT preparation

The preparation of DBT was based on previous studies (Chunhua et al., 2017; Zhou et al., 2018). In short, a total weight of 600 g RAM and RAS at ratios of 5:1 (DBT51), 1:1 (DBT11), and 1:5 (DBT15) were immersed respectively for 1 hour with 8 times the volume of distilled water (4.8 L). The medicinal materials were decocted twice at 100°C for 1 hour, and subsequently the decocted liquids were collected and merged together. After filtration, the decocted liquid was concentrated to 500 ml by water bath, resulting in a final DBT concentration of 1.2 g/ml. For cell experiments, some DBT was diluted to a final concentration of 1 mg/ml by using DMEM with 2% FBS and sterilized by filtration (Zhou et al., 2018).

2.3 RIHD model and DBT treatment

2.3.1 In vivo study

After 1 week adaptation period, all mice were randomly divided into five groups: Control (n = 5); Radiation (n = 10); RDBT51 (Radiation with DBT, RAM:RAS = 5:1, n =10); RDBT11 (Radiation with DBT, RAM:RAS = 1:1, n = 10); RDBT15 (Radiation with DBT, RAM:RAS = 1:5, n = 10). The precordial area of each mouse in radiation groups was exposed to X-ray irradiation individually to establish a murine RIHD model. After all mice had been anesthetized with isoflurane anaesthesia (2%) using a mask, the hair on the chest was removed, and irradiation was applied with a 6 MV X-ray beam energy at a single dose of 20 Gy using an X-RAD 320ix Irradiator (Precision X-Ray Inc., United States). For 8 consecutive weeks starting from the day of radiation, distilled water or diverse DBT (10 μl/g body weight, equivalent to 12 g/kg body weight) were administered to mice once daily *via* oral gavage. This DBT dose of 12 g/kg was designed based on the previous study (Chunhua et al., 2017; Liu et al., 2018) and our preliminary experiments. All mice were sacrificed at the end of the 8 weeks after irradiation. Mouse serum was obtained by centrifugation of blood at 1000× g for 10 min at 4°C, and cardiac tissue was isolated and stored for the following experiments.

2.3.2 In vitro study

Primary neonatal mouse myocardial fibroblasts cultured in high glucose DMEM with 10% FBS were seeded in 6-well plate

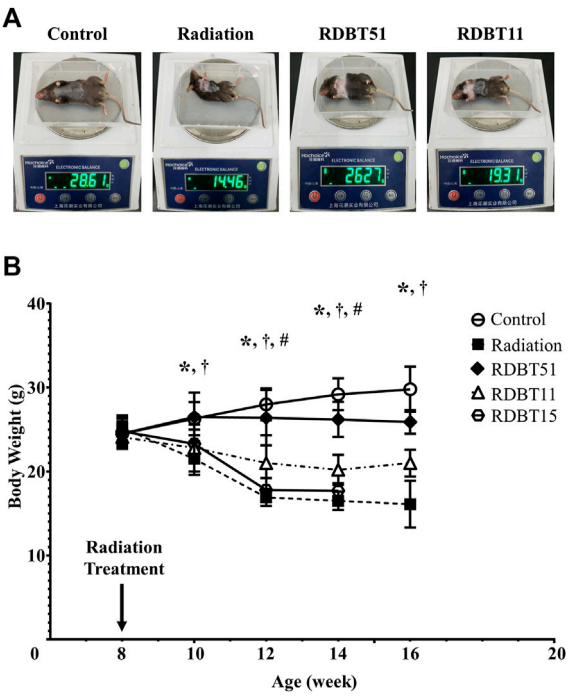

FIGURE 1
The protective effect of DBT on the radiation-induced abnormal weight loss. **(A)** The representative images of body weighing at 8 weeks after radiation; **(B)** Trends in body weight change. *$p < 0.05$ of Radiation versus Control; †$p < 0.05$ of RDBT51 versus Radiation; #$p < 0.05$ of RDBT11 versus Radiation. DBT, Dang Gui Bu Xue Tang; RAM, *Radix Astragali membranaceus*; RAS, *Radix Angelicae sinensis*; RDBT51, Radiation with DBT (RAM: RAS = 5:1); RDBT11, Radiation with DBT (RAM: RAS = 1:1); RDBT15, Radiation with DBT (RAM: RAS = 1:5); The "R" in the "RDBT" stands for Radiation, while the two digits following RDBT represent the ratio between RAM and RAS, the same below.

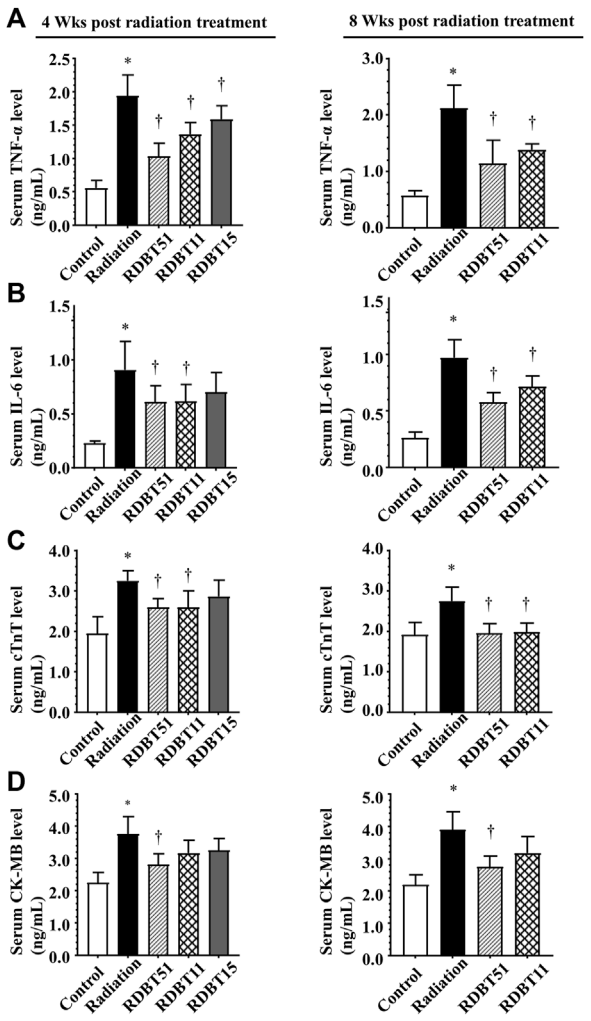

FIGURE 2
The DBT ameliorates the inflammation- and myocardial injury-related biomarkers in the serum of mice at 4 and 8 weeks after radiation. **(A)** TNF-α; **(B)** IL-6; **(C)** cTnT; **(D)** CK-MB. *$p < 0.05$ versus Control; †$p < 0.05$ versus Radiation. DBT, Dang Gui Bu Xue Tang; RAM, *Radix Astragali membranaceus*; RAS, *Radix Angelicae sinensis*; RDBT51, Radiation with DBT (RAM: RAS = 5:1); RDBT11, Radiation with DBT (RAM: RAS = 1:1); RDBT15, Radiation with DBT (RAM: RAS = 1:5).

and randomly divided into five groups: Control; Radiation; RDBT51 (Radiation with DBT, RAM:RAS = 5:1); RDBT11 (Radiation with DBT, RAM:RAS = 1:1); RDBT15 (Radiation with DBT, RAM:RAS = 1:5). At 70%–80% confluency, myocardial fibroblasts in radiation groups were irradiated with a single dose of 4 Gy at a dose rate of 2 Gy/min using an X-RAD 320ix Irradiator (Precision X-Ray Inc., United States). After administration, myocardial fibroblasts immediately received fresh control culture medium or concerning DBT medium (1 mg/ml) with 2%FBS. The specific inhibitor ML385 (1 μM, MCE, United States of America) was used to inhibit Nrf2 in fibroblasts. After 24 or 48 h, culture medium was collected and centrifuged at 10,000 g for 5 min, and then the supernatant was kept for further ELISA assay.

2.4 Echocardiography

At 4 and 8 weeks after irradiation, the mice were anesthetized with inhaled isoflurane (1%) and imaged using a 40 MHz linear array transducer attached to a preclinical ultrasound system (Vevo 2100, Fujifilm VisualSonics, Toronto, ON, Canada) with nominal in-plane spatial resolution of 40 μm (axial) × 80 μm (lateral). M-mode and 2-D parasternal short-axis scans (133 frames/second) at the level of the papillary muscles were employed to assess the changes in left ventricular (LV) end-systolic inner diameter, LV end-diastolic inner diameter, LV posterior wall thickness in end-diastole and end-systole, fractional shortening (FS), and ejection fraction (EF).

2.5 Histological analysis

Cardiac tissues were routinely collected, fixed, processed and sectioned into 5 μm slices. The cardiac collagen deposition was determined by Sirius red (Shanghai Yuanye Biotechnology, Shanghai, China) staining as previously described (Zhang et al., 2022).

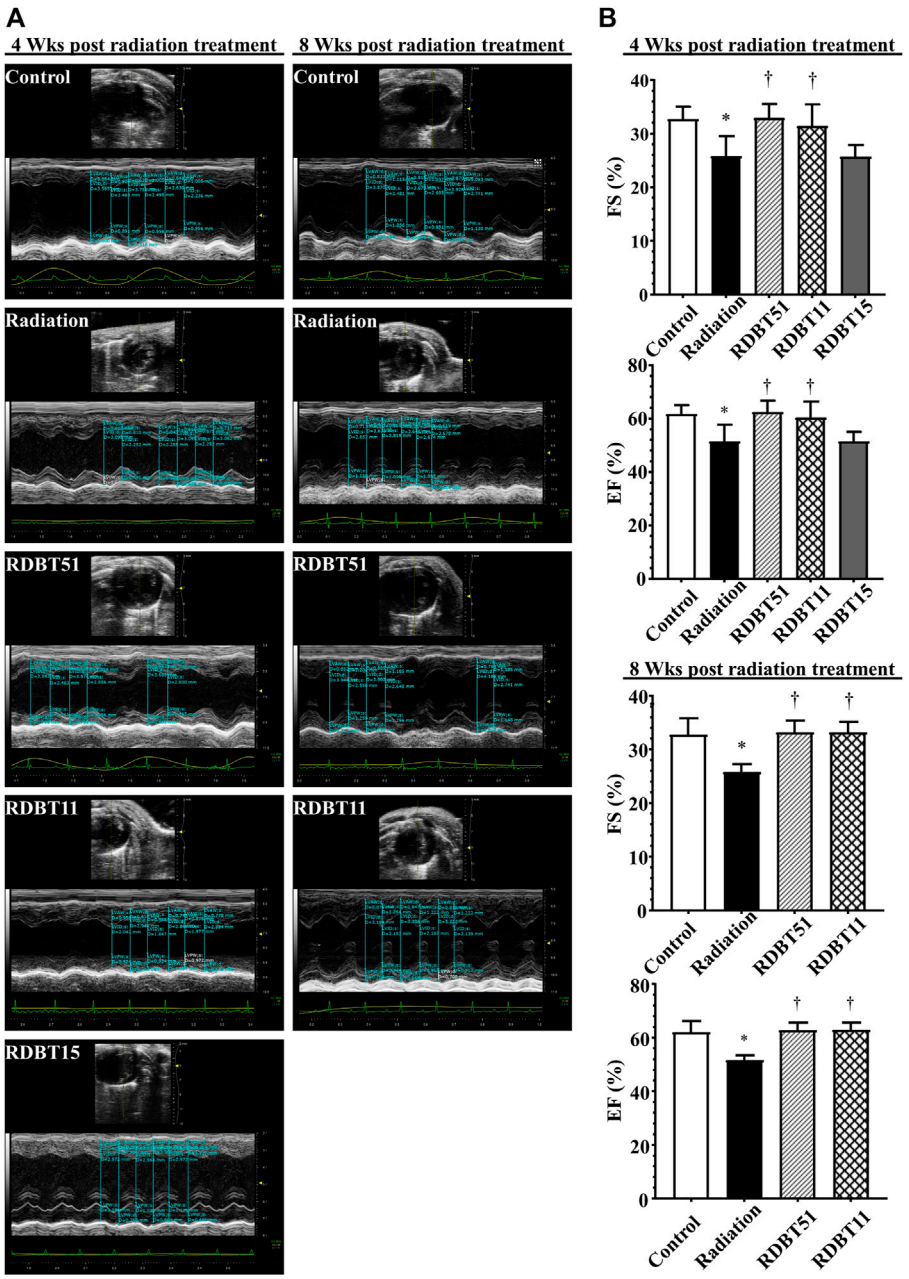

FIGURE 3
The DBT improves radiation-induced left ventricular systolic dysfunction. **(A)** Representative echocardiograms obtained at 4 and 8 weeks after radiation treatment; **(B)** Quantitative statistical analyses of FS and EF. The other concerning quantitative statistical analyses of cardiac function related parameters are summarized in Table 1. DBT, Dang Gui Bu Xue Tang; EF, ejection fraction; FS, fractional shortening; RAM, *Radix Astragali membranaceus*; RAS, *Radix Angelicae sinensis*; RDBT51, Radiation with DBT (RAM: RAS = 5:1); RDBT11, Radiation with DBT (RAM: RAS = 1:1); RDBT15, Radiation with DBT (RAM: RAS = 1:5).

2.6 Western blot and real-time qPCR analysis

Cardiac tissues or myocardial fibroblasts were harvested in RIPA Digest Buffer. The supernatant was collected, and protein concentration was measured using the BCA Protein Assay Reagent Kit. Equal amounts of protein were electrophoretically separated in SDS-polyacrylamide gels and then transferred onto polyvinylidene difluoride membranes (PVDF, IPVH00010, Millipore, United States). The blot was blocked with 5% skim milk for 1 h at room temperature and probed overnight at 4°C by incubation with the primary antibodies, including anti-Nrf2 (ab31163, Abcam, Cambridge, United Kingdom), anti-HMGB1 (3935, CST, Boston, United States of America) and anti-GAPDH (2118, CST, Boston, United States of America) antibodies. After being washed with Tris Buffered Saline with Tween (TBST), the membranes were subsequently incubated with secondary horseradish peroxidase conjugated anti-rabbit antibodies at 25°C for 2 h. Finally, membranes were analysed. Total RNA was extracted using the TRIzol reagent (Takara, Tokyo, Japan) according to the manufacturer's instructions, and then was analysed *via* the real-time qPCR as described before (Zhang et al., 2022). The sequences of primers are as follows: *Collagen-I,*

TABLE 1 Left ventricular systolic function and morphologic data obtained from echocardiographic measurement.

	4 weeks					8 weeks			
	Control	Radiation	RDBT51	RDBT11	RDBT15	Control	Radiation	RDBT51	RDBT11
LVAWd (mm)	0.68 ± 0.08	0.73 ± 0.09	0.74 ± 0.17	0.69 ± 0.07	0.58 ± 0.27	0.81 ± 0.06	0.63 ± 0.12	0.66 ± 0.15	0.72 ± 0.17
LVAWs (mm)	1.02 ± 0.12	0.95 ± 0.15	1.04 ± 0.20	0.94 ± 0.05	0.90 ± 0.26	1.08 ± 0.10	0.87 ± 0.21	0.93 ± 0.23	1.01 ± 0.21
LVIDd (mm)	3.82 ± 0.26	3.66 ± 0.46	3.35 ± 0.48	3.32 ± 0.38	3.55 ± 0.46	3.79 ± 0.18	3.63 ± 0.52	3.67 ± 0.32	3.47 ± 0.25
LVIDs (mm)	2.57 ± 0.16	2.72 ± 0.40	2.26 ± 0.39	2.28 ± 0.29	2.64 ± 0.36	2.55 ± 0.14	2.69 ± 0.33	2.45 ± 0.17	2.31 ± 0.14
LVPWd (mm)	0.66 ± 0.08	0.67 ± 0.05	0.65 ± 0.15	0.64 ± 0.07	0.68 ± 0.09	0.72 ± 0.14	0.66 ± 0.10	0.68 ± 0.19	0.67 ± 0.12
LVPWs (mm)	1.04 ± 0.14	0.94 ± 0.15	0.94 ± 0.12	0.92 ± 0.08	1.01 ± 0.08	1.07 ± 0.11	0.92 ± 0.15	1.10 ± 0.33	0.97 ± 0.04
IVSd (mm)	0.69 ± 0.08	0.74 ± 0.09	0.74 ± 0.17	0.70 ± 0.07	0.58 ± 0.27	0.81 ± 0.06	0.63 ± 0.12	0.67 ± 0.15	0.73 ± 0.17
IVSs (mm)	1.02 ± 0.09	1.00 ± 0.09	1.11 ± 0.21	1.03 ± 0.06	0.73 ± 0.38	1.20 ± 0.15	0.88 ± 0.23	0.96 ± 0.29	1.11 ± 0.29

Data are presented as mean ± standard deviation, N = 5–7/group. Abbreviations: DBT, Dang Gui Bu Xue Tang; RAM, *Radix Astragali membranaceus*; RAS, *Radix Angelicae sinensis*; RDBT51, Radiation with DBT (RAM: RAS, 5:1); RDBT11, Radiation with DBT (RAM: RAS, 1:1); RDBT15, Radiation with DBT (RAM: RAS, 1:5); LVAW, left ventricular anterior wall; LVID, left ventricular internal diameter; LVPW, left ventricular posterior wall; IVS, interventricular septum; -d, in diastole; -s, in systole.

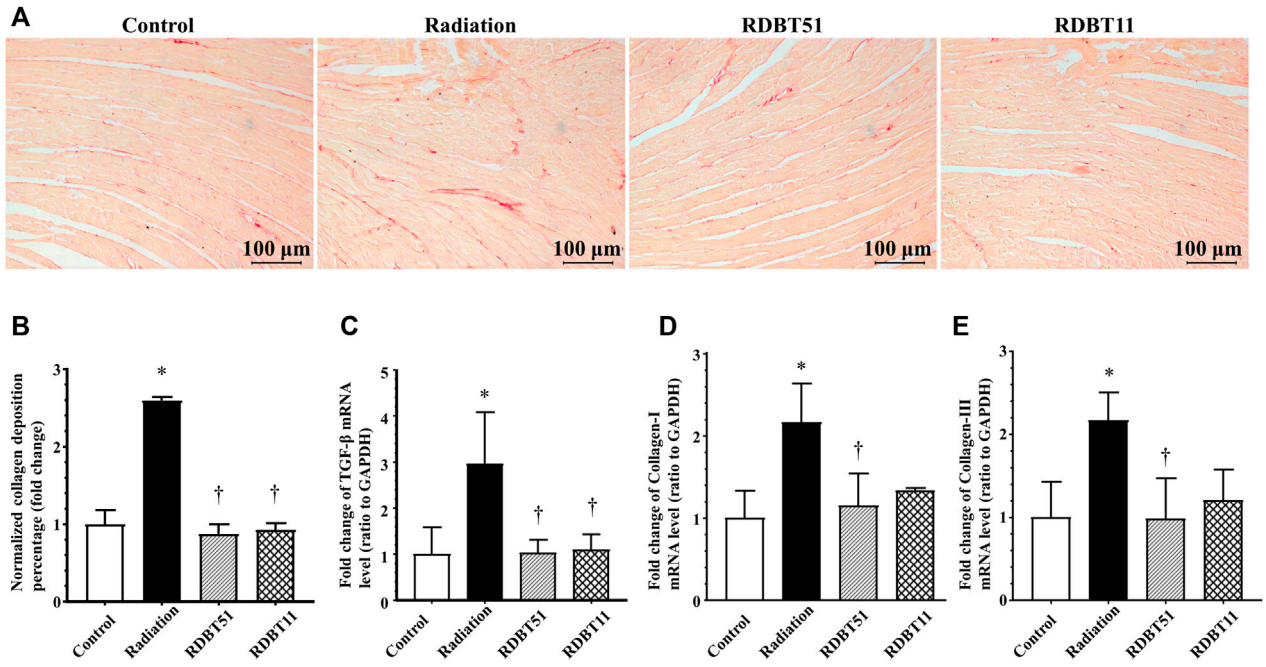

FIGURE 4
The DBT alleviates radiation-induced cardiac fibrosis. **(A)** Representative microphotographs of Sirius red staining obtained at 8 weeks after radiation; **(B)** Quantitative results of collagen deposition percentage; **(C)**, **(D)**, and **(E)** The myocardial mRNA levels of TGF-β, Collagen-I and Collagen-III relative to GAPDH were analysed by real-time qPCR. *$p < 0.05$ versus Control; †$p < 0.05$ versus Radiation. DBT, Dang Gui Bu Xue Tang; RAM, *Radix Astragali membranaceus*; RAS, *Radix Angelicae sinensis*; RDBT51, Radiation with DBT (RAM: RAS = 5:1); RDBT11, Radiation with DBT (RAM: RAS = 1:1).

Forward-GCAAGAGGCGAGAGAGGTTT and Reverse-TGCACCACC AACTGCTTAGC; *Collagen-III*, Forward-ACGTAGATGAATTGGGAT GCAG and Reverse-GGGTTGGGGCAGTCTAG; *TGF-β*, Forward-TGGGCACCATCCATGACAT and Reverse-TCTTCTCTGTGGAGCT GAAGCA; *GAPDH*, Forward-GGATGCAGGGATGATGTTCT and Reverse-TGCACCACCAACTGCTTAGC.

2.7 ELISA

The serum levels of HMGB1 and Galectin-3 were assayed by using ELISA kits (eBioscience, United States) according to the manufacturer's instructions. Standard curves were established using mouse recombinant cytokines provided in the kits.

2.8 Statistical analysis

Data are presented as mean ± standard deviation. The analysis of variance followed by the Bonferroni test was adopted for multiple comparisons among groups.

3 Results

3.1 The DBT protected mice against radiation-induced weight loss

The radiation treatment led to an obvious body weight loss in mice, as shown in Figure 1. The body weight of mice in the radiation group started to be significantly lower than that in the control group from 2 weeks after radiation and continued through 8 weeks (all $p < 0.05$). The body weight of mice in the RDBT51 group was consistently significantly higher than that of mice in the radiation group (all $p < 0.05$). Similarly, the mice in the RDBT11 group inclined to have higher body weights than those in the radiation group, but only at 4 and 6 weeks after radiation there were significant differences in body weight between the radiation and RDBT11 group.

3.2 The DBT reduced radiation-induced elevation of serum inflammatory and myocardial injury biomarkers

As shown in Figure 2, the radiation treatment led to a significant elevation of serum inflammatory biomarkers, *i.e.,* TNF-α and IL-6, as well as myocardial injury biomarkers such as cTnT and creatine kinase - MB (CK-MB), at 4 and 8 weeks after radiation (all $p < 0.05$). Notably, the serum levels of TNF-α, IL-6, cTnT, and CK-MB were consistently lower in the RDBT51 group than in the radiation group (all $p < 0.05$). Except for CK-MB, the above biomarkers were also lower in the RDBT11 group than in the radiation group, while there was no significant difference in the serum IL-6, cTnT, and CK-MB levels between the mice in the radiation and RDBT15 group.

3.3 The DBT improved radiation-induced myocardial systolic dysfunction

The improvement effect of DBT on radiation-induced left ventricular systolic dysfunction was summarized in Figure 3 and Table 1. The mice in the radiation group had lower EF and FS compared with the mice in the control group, accordingly, the EF and FS of mice in both RDBT51 and RDBT11 groups were significantly higher than those in the radiation group (all $p < 0.05$). Nevertheless, significant differences were found neither in EF nor in FS between the radiation and RDBT15 group.

3.4 The DBT alleviated radiation-induced myocardial fibrosis

The beneficial effect of DBT on radiation-induced myocardial fibrosis were summarized in Figure 4, which were comparable to the results concerning myocardial systolic function. The mice in the radiation group had a significantly higher degree of myocardial fibrosis compared with the mice in the control group, based on the myocardial collagen deposition and the mRNA levels of TGF-β, Collagen-I, and Collagen-III across groups (all $p < 0.05$). On this basis, the degree of myocardial fibrosis was lower in the RDBT51 group than in the radiation group. Meanwhile, the mice in the RDBT11 group also had a lower degree of myocardial fibrosis compared with the mice in the control group, despite the fact that there was no significant difference between groups in the mRNA level of myocardial Collagen-I and Collagen-III.

The results derived from assessment of myocardial fibroblasts supernatant and serum Galectin-3 levels, the indicator of fibrosis, were consistent with the differences in myocardial fibrosis among groups described above (Figure 5 and Figure 6). At 24 and 48 h after radiation treatment, the levels of Galectin-3 were significantly higher in the fibroblast culture medium of the radiation group than that in the fibroblast culture medium of the control, RDBT51, and RDBT11 groups (Figure 5, all $p < 0.05$). In parallel, at 4 weeks and 8 weeks after radiation treatment, the mouse serum levels of Galectin-3 were also significantly higher than those in the control and RDBT51 groups (Figure 6, all $p < 0.05$). The above differences were neither observed between the radiation and RDBT11 group, nor between the radiation and RDBT15 group, except for the serum Galectin-3 level between the radiation and the RDBT11 group at the time point of 4 weeks post-radiation.

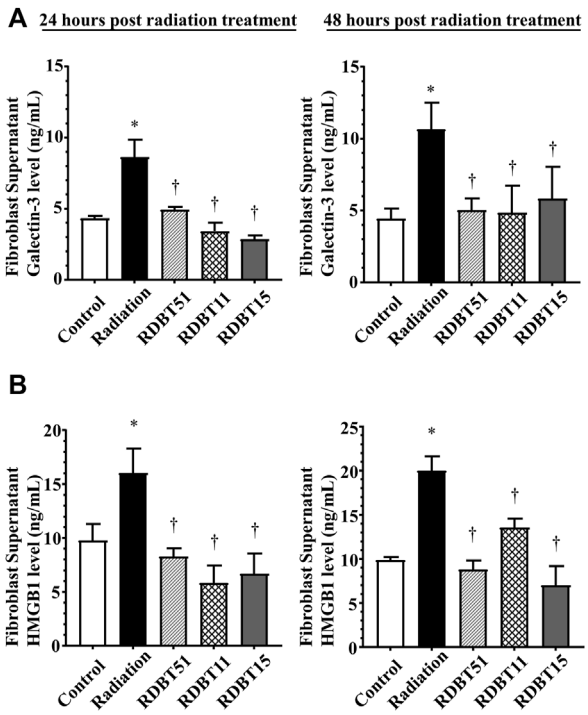

FIGURE 5
The DBT reduces the fibrosis-related biomarkers in the neonatal mouse myocardial fibroblast culture supernatant at 24 and 48 h after radiation. **(A)** Galectin-3; **(B)** HMGB1. *$p < 0.05$ versus Control; †$p < 0.05$ versus Radiation. DBT, Dang Gui Bu Xue Tang; HMGB1, high mobility group box 1; RAM, *Radix Astragali membranaceus*; RAS, *Radix Angelicae sinensis*; RDBT51, Radiation with DBT (RAM: RAS = 5:1); RDBT11, Radiation with DBT (RAM: RAS = 1:1); RDBT15, Radiation with DBT (RAM: RAS = 1:5).

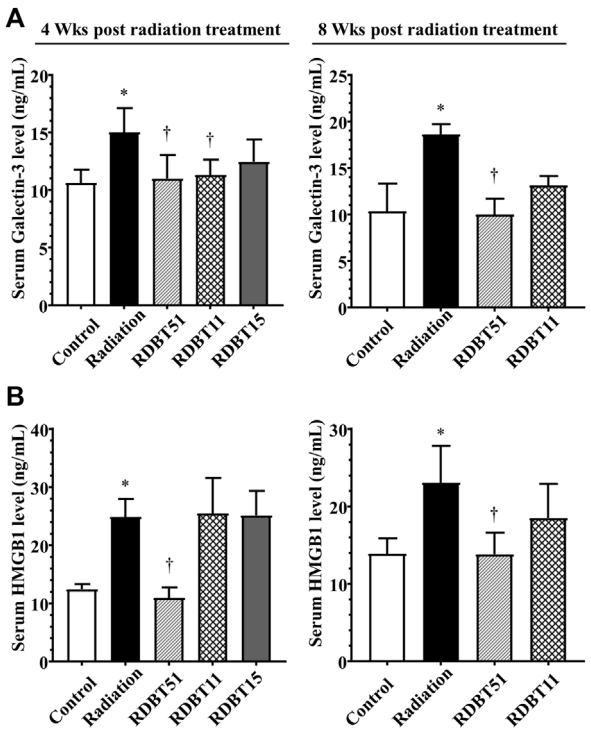

FIGURE 6
The DBT reduces the fibrosis-related biomarkers in the serum of mice at 4 and 8 weeks after radiation. **(A)** Galectin-3; **(B)** HMGB1. *p < 0.05 versus Control; †p < 0.05 versus Radiation. DBT, Dang Gui Bu Xue Tang; HMGB1, high mobility group box 1; RAM, *Radix Astragali membranaceus*; RAS, *Radix Angelicae sinensis*; RDBT51, Radiation with DBT (RAM: RAS = 5:1); RDBT11, Radiation with DBT (RAM: RAS = 1:1); RDBT15, Radiation with DBT (RAM: RAS = 1:5).

3.5 The DBT increased myocardial Nrf2 expression and decreased the radiation-induced elevated expression of myocardial HMGB1

As shown in Figure 5 and Figure 6, the levels of HMGB1 in fibroblast culture supernatant or mouse serum of the radiation group were highest among fibroblast culture groups or mouse groups at the corresponding time points. Correspondingly, at the end of 8 weeks after radiation treatment, the myocardial HMGB1 protein level in the radiation group, as well as the myocardial Nrf2 protein level in the RDBT51 group, was highest among all mouse groups. Although the myocardial HMGB1 protein level in the RDBT11 group tended to be lower than that in the radiation group, the difference was not significant (Figure 7).

By inhibiting Nrf2 *via* ML385 in fibroblasts in the RDBT group, we furthermore validated the mediating role of Nrf2/HMGB1 in the protective effect of DBT. As shown in Figure 8, in line with the results from the *in vivo* study, the level of Nrf2 was higher in the RDBT51 group than in the radiation and RDBT51 + ML385 groups, whereas the expression levels of HMGB1, TGF-β, Collagen-I and Collagen-III were higher in the RDBT51 + ML385 group than in the RDBT group (all $p < 0.05$).

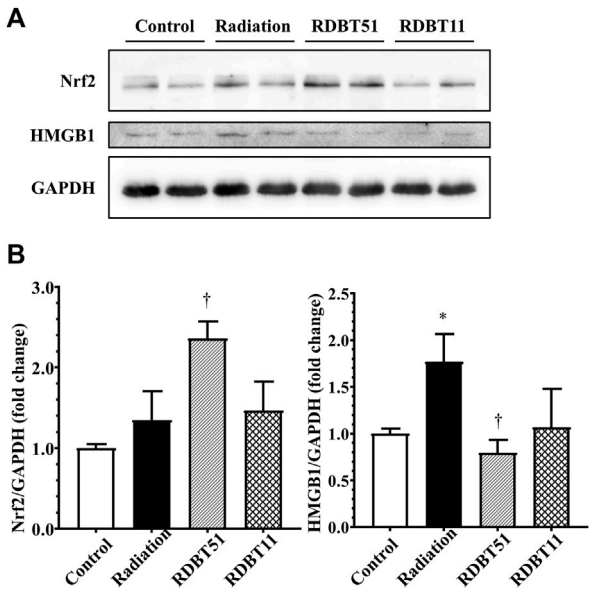

FIGURE 7
The regulatory effect of radiation and DBT on mouse myocardial Nrf2 and HMGB1 protein levels. **(A)** Representative western blot bands; **(B)** Quantitative results of Western blot. *p < 0.05 versus Control; †p < 0.05 versus Radiation. DBT, Dang Gui Bu Xue Tang; HMGB1, high mobility group box 1; RAM, *Radix Astragali membranaceus*; RAS, *Radix Angelicae sinensis*; RDBT51, Radiation with DBT (RAM: RAS = 5:1); RDBT11, Radiation with DBT (RAM: RAS = 1:1).

4 Discussion

In this study, we mainly found the significant deleterious side effect of radiation treatment in cardiothoracic region, which is characterized by body weight loss, cardiac systolic dysfunction and myocardial fibrosis, can be effectively ameliorated by the supplementation of DBT. In addition, the implicated abnormal expression of Nrf2, HMGB1 and Galectin-3 may play important roles during the whole disease development.

4.1 Exploration of the rationality of RAM to RAS ratio

Previous studies have demonstrated that the application of RAM and RAS individually, or in combination, may exert potential cardioprotective effect through anti-inflammatory and anti-oxidative mechanisms. In this study, we designated three herb weight-to-weight ratios, namely RAM and RAS in the ratios of 5:1 (conventional formulation of DBT), 1:1 and 1:5, in order to investigate whether RAM and RAS protect against RIHD, furthermore, to compare the efficacy differences across ratios. The results revealed that the DBT with a ratio of RAM to RAS at 5:1 most effectively ameliorated the abnormal weight loss, myocardial injury and fibrosis caused by radiation treatment among three ratio groups, supporting the rationality of the conventional formulation.

Numerous previous studies also demonstrated the rationality of maintaining the RAM to RAS ratio at 5:1. Dong *et al.* found that the contents of main active components such as astragaloside IV, calycosin, formononetin and ferulic acid were highest when the extraction ratio of RAM to RAS was 5:1, and the DBT extracted in

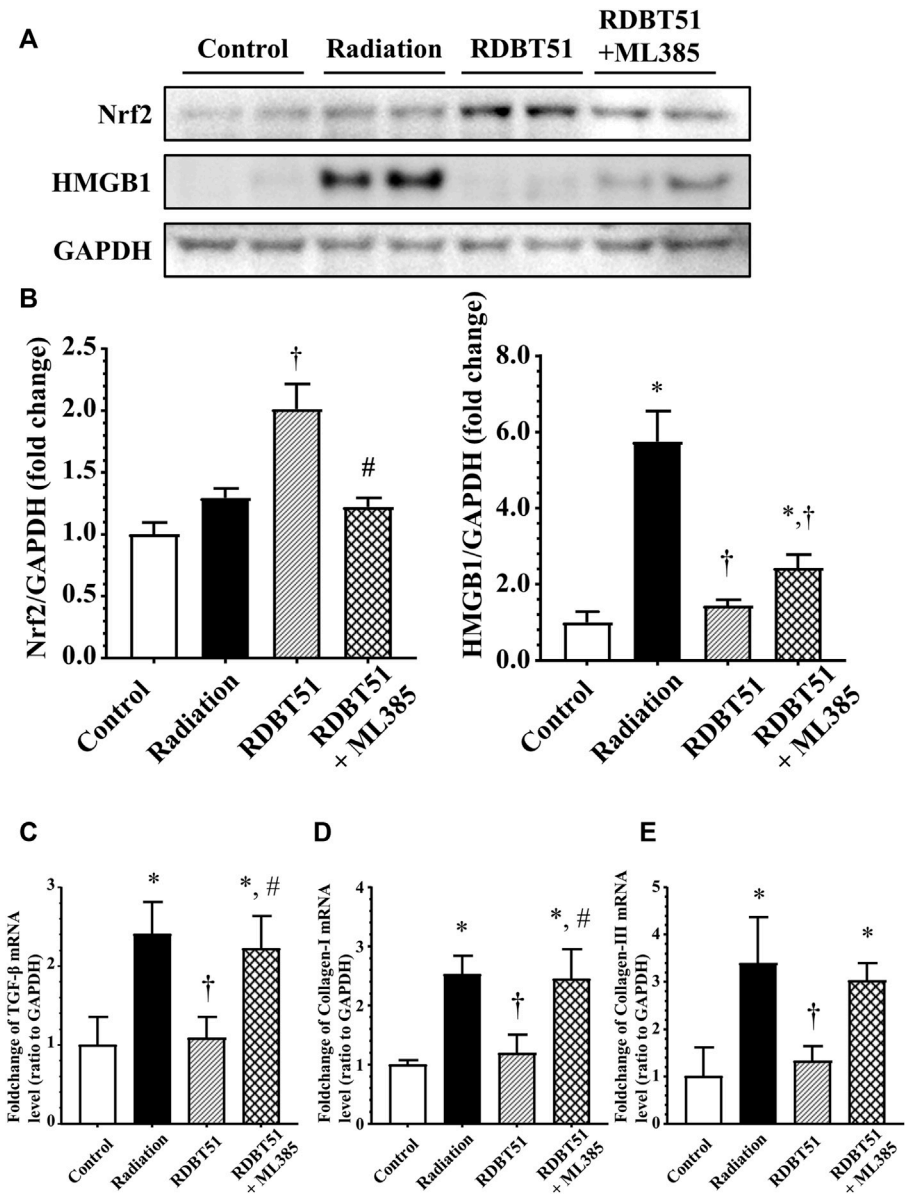

FIGURE 8
Inhibition of Nrf2 compromises the protective effect of DBT on radiation-induced deleterious changes in myocardial fibroblasts. After administration of radiation, myocardial fibroblasts were immediately changed to fresh normal medium, DBT51 medium (1 mg/ml), or DBT51 medium with 1 μM ML385 (specific inhibitor of Nrf2) for 48 h and then collected for analyses. **(A)** Representative western blot bands; **(B)** Quantitative results of Western blot; **(C)**, **(D)**, and **(E)** Quantitative results of real-time qPCR for TGF-β, Collagen-I and Collagen-III. *$p < 0.05$ versus Control; †$p < 0.05$ versus Radiation; #$p < 0.05$ versus DBT51. DBT, Dang Gui Bu Xue Tang; HMGB1, high mobility group box 1; RAM, *Radix Astragali membranaceus*; RAS, *Radix Angelicae sinensis*; RDBT51, Radiation with DBT (RAM: RAS = 5:1).

this ratio achieved the best chemical composition and biological effect (Dong et al., 2006). In parallel, Mak *et al.* found that the RAM extracts seemed to play more important roles than RAS extracts in DBT, since RAM extracts contained more bioactive components than RAS extract (Mak et al., 2006). Thus, it is understandable that Liu *et al.* found that the DBT based on this ratio exerted a significant ameliorative effect on heart injury, including inhibition of the NF-κB pathway as probable mechanisms (Liu et al., 2018). To a certain degree, the above studies also provide the probable reasons why conventional DBT (RAM: RAS = 5:1) has the most significant beneficial effect among groups.

4.2 The Nrf2/HMGB1 pathway in the development of RIHD

During the past years, emerging evidence indicates that increased HMGB1 is closely associated with fibrotic disease models, and moreover, targeted inhibition of HMGB1-related pathways significantly resists fibrosis. For instance, Wu *et al.* found that inhibition of HMGB1 significantly counteracted the isoproterenol-induced cardiac fibrosis by recovering TLR2-mediated autophagy suppression (Wu et al., 2018). Likewise, we demonstrated in the rat model of pulmonary fibrosis, the increased expression of HMGB1 was

closely associated with the generation of extracellular matrix components, accompanied by increased expression of TGF-β (Li et al., 2015). Nrf2 has been considered to be a robust therapeutic target for cardiovascular diseases because of its ability to regulate the expression of numerous antioxidants. It is noteworthy that our previous results suggested the regulatory role of Nrf2 for HMGB1. Based on Nrf2 knockout mice, we verified that Nrf2 activation remarkably downregulated the expression of HMGB1, inhibited the TGF-β-induced epithelial-mesenchymal transition and reactive oxygen species generation, subsequently ameliorated the development of pulmonary fibrosis (Qu et al., 2019). Considering that in the present study, myocardial Nrf2 levels were lower, while HMGB1 and TGF-β levels were higher in the radiation group than that in the control group, it is reasonable to infer the Nrf2/HMGB1 pathway at least partially contributes to the radiation-induced myocardial pathological changes.

4.3 The underlying mechanism of DBT resistance to RIHD

According to previous relevant studies, DBT contains sorts of biological active ingredients including astragaloside IV, calycosin, formononetin, ferulic acid, total flavonoids, total saponins, and total polysaccharides (Dong et al., 2006). Astragaloside IV has been demonstrated to attenuate the inflammatory reaction *via* inhibition of HMGB1 (Huang et al., 2012; Li et al., 2016). Decreased HMGB1 level was observed in livers from mice fed with calycosin enhanced diet (Cheng et al., 2020), while in a previous *in vitro* study, administration of formononetin also led to downregulation of HMGB1 (Wang et al., 2018). When it comes to total flavonoids, Shen *et al.* have investigated the interaction between quercetin, isoquercitrin, rutin and HMGB1 through a comprehensive spectral and *in silico* analysis, and eventually they concluded that all the above three flavonoids could directly interact with HMGB1, caused conformational changes and then reduced pro-inflammatory activity of HMGB1.

Couples of studies also have investigated the effect of DBT, or some of its main active ingredients, on Nrf2. Results from Li *et al.* showed that RAM-derived astragaloside IV activated Nrf2 signaling pathway and attenuated inflammatory response (Li H et al., 2018). Li *et al.* described that calycosin and ferulic acid probably contribute to the protective of Yiqi Huoxue Decoction on ischemia/hypoxia-induced oxidative stress injury in H9c2 cardiomyocytes, involving increased Nrf2 expression as underlying mechanisms (Li F et al., 2018). Additionally, flavonoids were reported to be capable of activating Nrf2 pathway in many disease models (Suraweera et al., 2020). In terms of polysaccharides, results of several studies similarly suggested the regulatory function of astragalus polysaccharides on Nrf2 (Farag et al., 2019; Zhang et al., 2021).

However, it is important to note that, to date, few studies have directly investigated the cardioprotective effect of DBT under the radiation condition. Furthermore, many data on the regulatory role of DBT in Nrf2/HMGB1 pathway have come from other organs, with very limited data from the heart. Our results suggested that DBT may be a promising clinical treatment for RIHD, but more population studies, especially well-designed randomized double-blind controlled trials, are needed to verify it in future.

In conclusion, radiation treatment significantly leads to weight loss, cardiac dysfunction and myocardial fibrosis, which can be ameliorated by consumption of DBT, involving regulation of Nrf2/HMGB1 pathway as probable underlying mechanisms.

Data availability statement

The original contributions presented in the study are included in the article/supplementary material, further inquiries can be directed to the corresponding authors.

Ethics statement

The animal study was reviewed and approved by Ethical Committee of Soochow University.

Author contributions

YH, HD, and JG contributed to conception and design of the study. YH, MC, and XW performed the study and organized the database. YH and MC performed the statistical analysis. YH and HD wrote sections of the manuscript. All authors contributed to manuscript revision, read, and approved the submitted version.

Funding

This research was supported by the National Natural Science Foundation of China. (No. 81274172, 81473267 and 81973637); The National Traditional Chinese Medicine Inheritance and Innovation "Hundreds and Thousands" Talent Project: Young Qihuang Scholar Support Project of the State Administration of Traditional Chinese Medicine in 2020.

Acknowledgments

The authors would like to express their gratitude to the Animal Centre of Soochow University and Lulu Zhang for providing suggestion.

Conflict of interest

The authors declare that the research was conducted in the absence of any commercial or financial relationships that could be construed as a potential conflict of interest.

Publisher's note

References

Cheng, X., Liu, N., Liu, H., Huang, N., Sun, X., and Zhang, G. (2020). Bioinformatic and biochemical findings disclosed anti-hepatic steatosis mechanism of calycosin. *Bioorg. Chem.* 100, 103914. doi:10.1016/j.bioorg.2020.103914

Chunhua, M., Hongyan, L., Weina, Z., Xiaoli, H., Yajie, Z., and Jie, R. (2017). Dang Gui Bu Xue Tang ameliorates coronary artery ligation-induced myocardial ischemia in rats. *Biomed. Pharmacother.* 88, 617–624. doi:10.1016/j.biopha.2017.01.079

Dong, T. T., Zhao, K. J., Gao, Q. T., Ji, Z. N., Zhu, T. T., Li, J., et al. (2006). Chemical and biological assessment of a Chinese herbal decoction containing Radix Astragali and Radix Angelicae sinensis: Determination of drug ratio in having optimized properties. *J. Agric. Food Chem.* 54 (7), 2767–2774. doi:10.1021/jf053163l

Farag, M. R., Elhady, W. M., Ahmed, S. Y., Taha, H. S., and Alagawany, M. (2019). Astragalus polysaccharides alleviate tilmicosin-induced toxicity in rats by inhibiting oxidative damage and modulating the expressions of HSP70, NF-kB and Nrf2/HO-1 pathway. *Res. veterinary Sci.* 124, 137–148. doi:10.1016/j.rvsc.2019.03.010

Huang, L., Yao, Y., Li, J., Zhang, S., Li, W., Dong, N., et al. (2012). The effect of Astragaloside IV on immune function of regulatory T cell mediated by high mobility group box 1 protein *in vitro*. *Fitoterapia* 83 (8), 1514–1522. doi:10.1016/j.fitote.2012.08.019

Li, F., Guo, S., Wang, H., Huang, X., Tan, X., Cai, Q., et al. (2018). Yiqi Huoxue decoction attenuates ischemia/hypoxia-induced oxidative stress injury in H9c2 cardiomyocytes. *J. Traditional Chin. Med. Sci.* 5 (3), 271–282. doi:10.1016/j.jtcms.2018.07.002

Li, H., Wang, P., Huang, F., Jin, J., Wu, H., Zhang, B., et al. (2018). Astragaloside IV protects blood-brain barrier integrity from LPS-induced disruption via activating Nrf2 antioxidant signaling pathway in mice. *Toxicol. Appl. Pharmacol.* 340, 58–66. doi:10.1016/j.taap.2017.12.019

Li, J., Huang, L., Wang, S., Yao, Y., and Zhang, Z. (2016). Astragaloside IV attenuates inflammatory reaction via activating immune function of regulatory T-cells inhibited by HMGB1 in mice. *Pharm. Biol.* 54 (12), 3217–3225. doi:10.1080/13880209.2016.1216133

Li, L-C., Li, D-L., Xu, L., Mo, X-T., Cui, W-H., Zhao, P., et al. (2015). High-mobility group box 1 mediates epithelial-to-mesenchymal transition in pulmonary fibrosis involving transforming growth factor-β1/Smad2/3 signaling. *J. Pharmacol. Exp. Ther.* 354 (3), 302–309. doi:10.1124/jpet.114.222372

Liu, K., Ren, X. M., You, Q. S., Gu, M. M., Wang, F., Wang, S., et al. (2018). Ameliorative effect of dangguibuxue decoction against cyclophosphamide-induced heart injury in mice. *Biomed. Res. Int.* 2018, 8503109. doi:10.1155/2018/8503109

Mak, D. H., Chiu, P. Y., Dong, T. T., Tsim, K. W., and Ko, K. M. (2006). Dang-Gui Buxue Tang produces a more potent cardioprotective effect than its component herb extracts and enhances glutathione status in rat heart mitochondria and erythrocytes. *Phytother. Res.* 20 (7), 561–567. doi:10.1002/ptr.1904

Qu, J., Zhang, Z., Zhang, P., Zheng, C., Zhou, W., Cui, W., et al. (2019). Downregulation of HMGB1 is required for the protective role of Nrf2 in EMT-mediated PF. *J. Cell. Physiology* 234 (6), 8862–8872. doi:10.1002/jcp.27548

Quintero-Martinez, J. A., Cordova-Madera, S. N., and Villarraga, H. R. (2021). Radiation-induced heart disease. *J. Clin. Med.* 11 (1), 146. doi:10.3390/jcm11010146

Sarkozy, M., Varga, Z., Gaspar, R., Szucs, G., Kovacs, M. G., Kovacs, Z. Z. A., et al. (2021). Pathomechanisms and therapeutic opportunities in radiation-induced heart disease: From bench to bedside. *Clin. Res. Cardiol.* 110 (4), 507–531. doi:10.1007/s00392-021-01809-y

Suraweera, T. L. S., Rupasinghe, H. P. V., Dellaire, G., and Xu, Z. (2020). Regulation of nrf2/ARE pathway by dietary flavonoids: A friend or foe for cancer management? *Antioxidants (Basel)* 9 (10), 973. doi:10.3390/antiox9100973

Turner, N. A. (2016). Inflammatory and fibrotic responses of cardiac fibroblasts to myocardial damage associated molecular patterns (DAMPs). *J. Mol. Cell. Cardiol.* 94, 189–200. doi:10.1016/j.yjmcc.2015.11.002

Wang, B., Wang, H., Zhang, M., Ji, R., Wei, J., Xin, Y., et al. (2020). Radiation-induced myocardial fibrosis: Mechanisms underlying its pathogenesis and therapeutic strategies. *J. Cell. Mol. Med.* 24 (14), 7717–7729. doi:10.1111/jcmm.15479

Wang, H., Wei, J., Zheng, Q., Meng, L., Xin, Y., Yin, X., et al. (2019). Radiation-induced heart disease: A review of classification, mechanism and prevention. *Int. J. Biol. Sci.* 15 (10), 2128–2138. doi:10.7150/ijbs.35460

Wang, J., Wang, L., Zhou, J., Qin, A., and Chen, Z. (2018). The protective effect of formononetin on cognitive impairment in streptozotocin (STZ)-induced diabetic mice. *Biomed. Pharmacother.* 106, 1250–1257. doi:10.1016/j.biopha.2018.07.063

Wang, S., and Zhang, Y. (2020). HMGB1 in inflammation and cancer. *J. Hematol. Oncol.* 13 (1), 116. doi:10.1186/s13045-020-00950-x

Wang, W., Wang, B., Lu, Q., Zhang, W., Qin, W., Liu, X., et al. (2014). Inhibition of high-mobility group box 1 improves myocardial fibrosis and dysfunction in diabetic cardiomyopathy. *Int. J. Cardiol.* 172 (1), 202–212. doi:10.1016/j.ijcard.2014.01.011

Wu, R-N., Yu, T-Y., Zhou, J-C., Li, M., Gao, H-K., Zhao, C., et al. (2018). Targeting HMGB1 ameliorates cardiac fibrosis through restoring TLR2-mediated autophagy suppression in myocardial fibroblasts. *Int. J. Cardiol.* 267, 156–162. doi:10.1016/j.ijcard.2018.04.103

Zhang, M., Zhong, H., Cao, T., Huang, Y., Ji, X., Fan, G. C., et al. (2022). Gamma-aminobutyrate transaminase protects against lipid overload-triggered cardiac injury in mice. *Int. J. Mol. Sci.* 23 (4), 2182. doi:10.3390/ijms23042182

Zhang, Q., Liu, J., Duan, H., Li, R., Peng, W., and Wu, C. (2021). Activation of Nrf2/HO-1 signaling: An important molecular mechanism of herbal medicine in the treatment of atherosclerosis via the protection of vascular endothelial cells from oxidative stress. *J. Adv. Res.* 34, 43–63. doi:10.1016/j.jare.2021.06.023

Zhang, Z., Qu, J., Zheng, C., Zhang, P., Zhou, W., Cui, W., et al. (2018). Nrf2 antioxidant pathway suppresses Numb-mediated epithelial-mesenchymal transition during pulmonary fibrosis. *Cell Death Dis.* 9 (2), 83. doi:10.1038/s41419-017-0198-x

Zhou, L-P., Wong, K-Y., Yeung, H-T., Dong, X-L., Xiao, H-H., Gong, A. G-W., et al. (2018). Bone protective effects of danggui buxue tang alone and in combination with tamoxifen or raloxifene *in vivo* and *in vitro*. *Front. Pharmacol.* 9, 779. doi:10.3389/fphar.2018.00779

frontiers | Frontiers in Pharmacology

TYPE Original Research
PUBLISHED 30 January 2023
DOI 10.3389/fphar.2023.1064307

OPEN ACCESS

EDITED BY
Yang Zhou,
Brown University, United States

REVIEWED BY
Davide Piloni,
San Matteo Hospital Foundation (IRCCS), Italy
Koike Haruki,
Nagoya University, Japan

*CORRESPONDENCE
Jin Woo Song,
jwsongasan@gmail.com

†These authors have contributed equally to this work and share first authorship

SPECIALTY SECTION
This article was submitted to Respiratory Pharmacology, a section of the journal Frontiers in Pharmacology

RECEIVED 08 October 2022
ACCEPTED 18 January 2023
PUBLISHED 30 January 2023

CITATION
Kim MJ, Lee D, Choe J and Song JW (2023), Long-term clinical course and outcomes of patients with microscopic polyangiitis-associated interstitial lung disease.
Front. Pharmacol. 14:1064307.
doi: 10.3389/fphar.2023.1064307

Long-term clinical course and outcomes of patients with microscopic polyangiitis-associated interstitial lung disease

Min Jee Kim[1†], Donghee Lee[2†], Jooae Choe[3] and Jin Woo Song[4*]

[1]Department of Internal Medicine, Asan Medical Center, University of Ulsan College of Medicine, Seoul, South Korea, [2]University of Ulsan College of Medicine, Seoul, South Korea, [3]Department of Radiology, Asan Medical Center, University of Ulsan College of Medicine, Seoul, South Korea, [4]Department of Pulmonary and Critical Care Medicine, Asan Medical Center, University of Ulsan College of Medicine, Seoul, South Korea

Background: Interstitial lung disease (ILD) is a significant complication associated with microscopic polyangiitis (MPA) that has a poor prognosis. However, the long-term clinical course, outcomes, and prognostic factors of MPA-ILD are not well defined. Hence, this study aimed to investigate the long-term clinical course, outcomes, and prognostic factors in patients with MPA-ILD.

Methods: Clinical data of 39 patients with MPA-ILD (biopsy proven cases, n = 6) were retrospectively analyzed. High resolution computed tomography (HRCT) patterns were assessed based on the 2018 idiopathic pulmonary fibrosis diagnostic criteria. Acute exacerbation (AE) was defined as the worsening of dyspnea within 30 days, with new bilateral lung infiltration that is not fully explained by heart failure or fluid overload and that does not have identified extra-parenchymal causes (pneumothorax, pleural effusion, or pulmonary embolism).

Results: The median follow-up period was 72.0 months (interquartile range: 44–117 months). The mean age of the patients was 62.7 years and 59.0% were male. Usual interstitial pneumonia (UIP) and probable usual interstitial pneumonia patterns on high resolution computed tomography were identified in 61.5 and 17.9% of the patients, respectively. During the follow-up, 51.3% of patients died, and the 5- and 10-year overall survival rates were 73.5% and 42.0%, respectively. Acute exacerbation occurred in 17.9% of the patients. The non-survivors had higher neutrophil counts in bronchoalveolar lavage (BAL) fluid and more frequent acute exacerbation than the survivors. In the multivariable Cox analysis, older age (hazard ratio [HR], 1.07; 95% confidence interval [CI], 1.01–1.14; p = 0.028) and higher BAL counts (HR, 1.09; 95% CI, 1.01–1.17; p = 0.015) were found to be the independent prognostic factors associated with mortality in patients with MPA-ILD.

Conclusion: During the 6 years-follow-up, about half of patients with MPA-ILD died and approximately one-fifth experienced acute exacerbation. Our results suggest that older age and higher BAL neutrophil counts mean poor prognosis in patients with MPA-ILD.

Abbreviations: AE, Acute exacerbation; ANCA, Antineutrophil cytoplasmic antibodies; ATS, American Thoracic Society; BAL, Bronchoalveolar lavage; DAH, Diffuse alveolar hemorrhage; ERS, European Respiratory Society; HR, Hazard ratio; HRCT, High resolution computed tomography; ILD, Interstitial lung disease; IPF, Idiopathic pulmonary fibrosis; PF, Pulmonary fibrosis; SD, Standard deviation; TLC, Total lung capacity; UIP, Usual interstitial pneumonia.

KEYWORDS
interstitial lung disease, microscopic polyangiitis, survival, prognosis, risk factor

1 Introduction

Microscopic polyangiitis (MPA) is a non-granulomatous necrotizing vasculitis involving small vessels and a type of antineutrophil cytoplasmic antibody-associated vasculitis (AAV) (Chung and Seo, 2010). Lung and renal involvement are the most common complications in patients with MPA and have a significant impact on survival (Corral-Gudino et al., 2011). While the kidney is the most commonly affected organ, lung involvement can be observed in 25%–55% of patients with MPA (Chung and Seo, 2010). Although interstitial lung disease (ILD) is a rare manifestation in patients with MPA, it is associated with poor survival (Fernandez Casares et al., 2015).

In previous studies, the long-term survival of patients with MPA-ILD was reported to range from 50% to 60% at 5 years; additionally, the main cause of death was worsening of pulmonary fibrosis (PF), which accounts for 40%–60% of cases (Homma et al., 2004; Hervier et al., 2009; Comarmond et al., 2014; Fernandez Casares et al., 2015). The presence of myeloperoxidase (MPO) specific antineutrophil cytoplasmic antibodies (ANCA), a usual interstitial pneumonia (UIP) pattern on high resolution computed tomography (HRCT), and induction therapy with glucocorticoids have been identified as unfavorable prognostic factors in patients with MPA-ILD (Homma et al., 2013; Comarmond et al., 2014; Fernandez Casares et al., 2015; Watanabe et al., 2019). However, the long-term clinical course and the prognostic factors of MPA-ILD are still not well defined. Therefore, this study aimed to investigate the clinical course, outcomes, and prognostic factors in patients with MPA-ILD.

2 Materials and methods

2.1 Study population

Between January 2000 and December 2019, 65 patients with MPA were diagnosed at Asan Medical Center, Seoul, South Korea. ILD was confirmed on HRCT images in 39 patients (biopsy proven cases, $n = 6$) and they were included in this study. All patients were diagnosed with MPA based on the European Medicines Agency algorithm and Chapel Hill Consensus Conference criteria (Watts et al., 2007; Jennette et al., 2013). The study was approved by the Institutional Review Board of Asan Medical Center (2019-0861), and the requirement for informed consent was waived due to the retrospective nature of this study.

2.2 Clinical data

The clinical and survival data were retrospectively collected from medical records and/or the records of the National Health Insurance of Korea. The spirometric parameters, total lung capacity (TLC) by plethysmography, and diffusing capacity of the lung for carbon monoxide (DL_{CO}) were measured according to the American Thoracic Society (ATS)/European Respiratory Society (ERS) recommendations (Macintyre et al., 2005; Miller et al., 2005; Wanger et al., 2005). The results were expressed as percentages of normal predicted values. A 6-min walk test (6MWT) was performed according to the ERS/ATS recommendations (Holland et al., 2014). Bronchoalveolar lavage (BAL) was performed according to the ATS guidelines (Meyer et al., 2012).

The data from follow-up visits at 3–6-month intervals or from hospitalization were reviewed to determine the development of complications, such as acute exacerbation (AE), pneumonia, diffuse alveolar hemorrhage (DAH), or malignant tumors. AE was defined based on the criteria proposed by Collard et al. (2016), as a worsening of dyspnea within 30 days, with new bilateral lung infiltration that is not fully explained by heart failure or fluid overload and that does not have any identified extra-parenchymal causes (pneumothorax, pleural effusion, or pulmonary embolism). Pneumonia was defined as focal or unilateral lung infiltration with identified causative organism; however, when a causative pathogen was not identified and infection was strongly suspected clinically (symptoms such as purulent sputum, rapid and significant response to antibiotic treatment alone), it was also diagnosed as pneumonia (Kwon et al., 2022). DAH was defined according to the following criteria: 1) diffuse ground-glass opacity and/or consolidation on HRCT without alternative cause 2) hemoptysis, bronchoscopic evidence of hemorrhage, or bloody BAL fluid (Hozumi et al., 2021). Disease progression or improvement was defined as a relative decline or increase of at least 10% of the forced vital capacity (FVC) predicted value (% predicted) (Richeldi et al., 2012). The changes in lung function that did not meet these criteria were classified as stabilization. The relative FVC changes were calculated as follows: (FVC % predicted at follow-up − FVC % predicted at baseline)/FVC % predicted at baseline × 100 (%).

2.3 HRCT image evaluation

HRCT scans were performed in accordance with standard protocols at full inspiration without contrast enhancement. The HRCT scanned images were reviewed by a radiologist (J.C.) without the clinical and pathologic information provided. Overall, HRCT patterns were categorized as UIP, probable UIP, indeterminate UIP, or alternative diagnosis, based on the idiopathic pulmonary fibrosis (IPF) diagnostic criteria (Raghu et al., 2018). Based on the HRCT findings, the patients were also classified based on whether they had a UIP-like pattern or not. A UIP-like pattern was diagnosed when HRCT findings were consistent with a UIP or probable UIP pattern (Jacob et al., 2019). A UIP-like pattern was defined as a reticular pattern with traction bronchiectasis or bronchiolectasis with or without honeycombing and the absence of findings compatible with a UIP pattern, such as extensive ground-glass opacities, micro-nodules, discrete cysts, or segmental/lobar consolidations.

2.4 Statistical analysis

All data are expressed as mean ± standard deviation (SD) or median [interquartile range (IQR)] for continuous variables and as percentages for categorical variables. The continuous variables were compared using the Student's t-test or Mann-Whitney *U* test, and categorical variables were compared using Pearson's chi-squared or

TABLE 1 Comparison of baseline characteristics between the non-survivors and survivors among patients with MPA-ILD.

	Total	Non-survivors	Survivors	*p*-value
Number of patients	39	20	19	
Age at ILD diagnosis	62.7 ± 9.8	66.0 ± 7.9	59.3 ± 10.6	0.031
Male sex	23 (59.0)	14 (70.0)	9 (47.4)	0.151
Ever-smokers	21 (53.8)	12 (60.0)	9 (47.4)	0.429
Sequence of diagnosis				
ILD first	26 (66.7)	15 (75.0)	11 (57.9)	0.257
MPA first	1 (2.6)	1 (5.0)	0	>0.999
Concurrence	12 (30.8)	4 (20.0)	8 (42.1)	0.135
Extra-pulmonary involvement				
Kidney	30 (76.9)	15 (75.0)	15 (78.9)	>0.999
Peripheral nervous system	13 (33.3)	8 (40.0)	5 (26.3)	0.365
Autoantibody				
MPO-ANCA titer, IU/mL	116.0 (38.0–134.0)	121.0 (64.0–154.0)	116.0 (32.0–134.0)	0.221
MPO-ANCA positivity	36 (92.3)	18 (90.0)	18 (94.7)	>0.999
ANA positivity	5 (12.8)	2 (10.5)	3 (16.7)	0.660
CRP, mg/dL	6.9 ± 6.7	7.8 ± 6.9	5.9 ± 6.6	0.386
Pulmonary function test				
FVC, % predicted	77.0 ± 15.3	75.8 ± 15	78.3 ± 16	0.625
DLco, % predicted	59.8 ± 14.8	60.6 ± 17.4	58.9 ± 11.9	0.733
TLC, % predicted	78.4 ± 13.1	78.7 ± 14.6	78.1 ± 11.6	0.887
6-min walk test				
Distance, meter	392.8 ± 143.8	360.3 ± 154.0	427.0 ± 127.6	0.162
The lowest SpO_2, %	93.0 ± 4.9	92.2 ± 5.8	93.8 ± 3.7	0.331
Bronchoalveolar lavage				
WBC/mm^3	317.9 ± 300.9	295.1 ± 254	345.6 ± 358.0	0.650
Neutrophil, %	10.9 ± 8.7	13.1 ± 9.8	7.6 ± 6.0	0.110
Lymphocyte, %	15.0 ± 9.0	15.7 ± 10.7	14.2 ± 6.7	0.639

The data are presented as mean ± standard deviation, median (interquartile range), or number (%).
MPA, microscopic polyangiitis; ILD, interstitial lung disease; MPO-ANCA, myeloperoxidase-antineutrophil cytoplasmic antibodies; ANA, antinuclear antibody; CRP, C-reactive protein; FVC, forced vital capacity; DLco, diffusing capacity of the lung for carbon monoxide; TLC, total lung capacity; WBC, white blood cell; SpO_2, oxygen saturation measured by pulse oximetry.

Fisher's exact test. A Kaplan-Meier survival analysis and the log-rank test were performed to analyze the survival rate. The survival time was calculated as the number of months from the date of ILD diagnosis until death or the end of the follow-up period. The patients were censored if they were alive on 21 July 2022. The Cox analysis was performed to identify the prognostic factors for mortality in patients with MPA-ILD. In the multivariable Cox analysis, baseline variables with p-value < 0.1 in the unadjusted analysis were included in the multivariable models. All p-values were two-tailed, with the statistical significance set at a p-value < 0.05. All statistical analyses were performed using IBM SPSS Statistics for Windows, Version 26.0 (IBM Corp., Armonk, NY, United States).

3 Results

3.1 Baseline characteristics

The baseline characteristics of the study population are shown in Table 1. The mean age was 62.7 years, and 59.0% of patients were male. The median follow-up period was 72.0 months (IQR: 44.0–117.0 months), and 20 patients (51.3%) died. The 1-, 5-, and 10-year cumulative survival rates of patients were 89.7, 73.5, and 42.0%, respectively (Figure 1). Overall, ILD was the initial

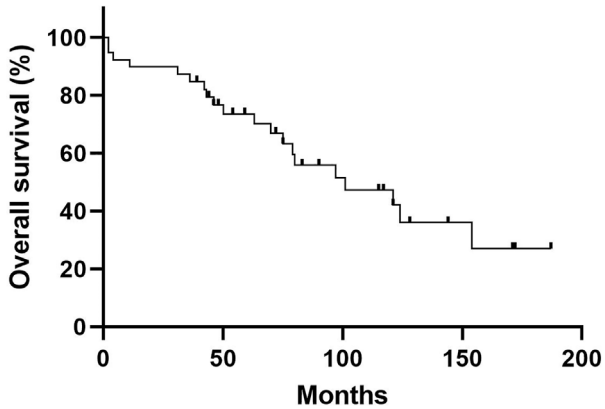

FIGURE 1
Overall Kaplan—Meier survival curve of patients with MPA-ILD. The 5-year and 10-year overall survival rates of patients with MPA-ILD were 73.5% and 42.0%, respectively. MPA, microscopic polyangiitis; ILD, interstitial lung disease.

TABLE 2 Comparison of the clinical course between the non-survivors and survivors among patients with MPA-ILD.

	Total	Non-survivors	Survivors	*p*-value
Number of patients	39	20	19	
Complications				
Pneumonia	9 (23.1)	6 (30.0)	3 (15.8)	0.501
Diffuse alveolar hemorrhage	7 (17.9)	3 (15.0)	4 (21.1)	0.695
Acute exacerbation	7 (17.9)	7 (35.0)	0	0.015
Lung cancer	3 (7.7)	3 (15.0)	0	0.231
FVC changes (6 months), % predicted	2.9 ± 13.7	1.4 ± 14.1	4.4 ± 13.6	0.541
FVC changes (12 months), % predicted	2.7 ± 13.2	−0.9 ± 13.5	6.4 ± 12.1	0.117
Pulmonary function change				
Improved	7 (21.2)	4 (23.5)	3 (18.8)	>0.999
Stabilization	20 (60.6)	8 (47.1)	12 (75.0)	0.101
Progression	6 (18.2)	5 (29.4)	1 (6.3)	0.175

The data are presented as mean ± standard deviation or number (%).
MPA, microscopic polyangiitis; ILD, interstitial lung disease; FVC, forced vital capacity.

manifestation of MPA in 66.7% of patients, and extra-pulmonary organ involvement was found in 92.3% of patients, of which renal involvement was the most common, accounting for 83% of extra-pulmonary organ involvement, followed by peripheral nerve involvement (36%). The non-survivors showed older age and higher BAL neutrophil counts than the survivors (Table 1); however, other variables, including lung function and exercise capacity, did not vary between the two groups.

3.2 Clinical course

Table 2 presents the clinical course of patients with MPA-ILD. Pneumonia was the most frequent pulmonary complication (23.1%), followed by AE, DAH, and lung cancer. AE occurred in 7 (17.9%) patients during the follow-up, and all of them died. During the follow-up, the non-survivors developed AE more frequently than the survivors (Table 2). However, there was no difference in the development of pneumonia, DAH, and lung cancer between the two groups.

Overall, pulmonary function was stabilized in 60.6% of patients, improved in 21.2% of patients, and progressed in 18.2% of patients (Table 2). The changes in lung function did not vary between the non-survivors and survivors; however, the non-survivors showed numerically lower improvement in FVC during the 6- or 12-month follow-up periods than the survivors without statistical significance.

In terms of treatment, 38 (97.4%) patients received steroid alone (n = 12) or with cyclophosphamide (n = 26) as an induction therapy. Maintenance therapy included steroid only (n = 8) or immunosuppressant (n = 30; azathioprine = 22, mycophenolate mofetil = 5, methotrexate = 2, cyclosporine = 1) with or without steroid.

3.3 Clinical course according to the HRCT patterns

Of all patients, 24 (61.5%) were classified as having a UIP pattern on HRCT, 7 (17.9%) as having probable UIP, 5 (12.8%) as having indeterminate UIP, and 3 (7.7%) as having an alternative diagnosis. A UIP-like pattern on HRCT was identified in 31 (79.5%) patients. The baseline characteristics of patients according to the HRCT patterns are summarized in Table 3. Patients with a UIP-like pattern showed a tendency for higher BAL neutrophil counts than those without; however, there was no difference in the frequency of complications between the two groups except a tendency for a higher prevalence of lung cancer in patients with a non-UIP-like pattern (Table 4). There was no significant difference in the baseline lung function between the two groups; however, patients with a UIP-like pattern showed numerically lower improvement in FVC over a 6- or 12-month follow-up period without statistical significance (Tables 3, 4).

The Kaplan—Meier survival curve of patients with MPA-ILD according to the HRCT patterns is shown in Figure 2. There was no statistical difference in overall survival according to the HRCT patterns in patients with MPA-ILD (Figure 2A); the median survival period was 97.0 months for a UIP pattern, 124.0 months for probable UIP, 101.0 months for indeterminate UIP, and 154.0 months for alternative diagnosis (p = 0.985). There was also no difference in the overall survival between patients with UIP-like and non-UIP-like patterns on HRCT (median survival period, 97.0 vs. 101.0 months, p = 0.969) (Figure 2B).

3.4 Risk factors for mortality

In the unadjusted Cox analysis, older age, male sex, higher BAL neutrophil counts, AE, and greater changes in the FVC (12 months) were significant prognostic factors for mortality in patients with MPA-ILD (Table 5). In the multivariable Cox analysis, older age (hazard ratio [HR], 1.072; 95% confidence interval [CI], 1.008–1.141; p = 0.028) and higher BAL neutrophil counts (HR, 1.091; 95% CI, 1.017–1.170; p = 0.015) were independent prognostic factors in patients with MPA-ILD.

4 Discussion

In this study, during a follow-up of 6 years, about half of patients with MPA-ILD died and approximately one-fifth of patients experienced AE. Our results suggest that older age and higher BAL neutrophil counts were independent prognostic

TABLE 3 Comparison of the baseline characteristics according to the HRCT patterns in patients with MPA-ILD.

	Total	UIP-like	Non-UIP-like	*p*-value
Number of patients	39	31	8	
Age at ILD diagnosis	62.7 ± 9.8	63.6 ± 9.2	59.4 ± 11.8	0.281
Male sex	23 (59.0)	19 (61.3)	4 (50.0)	0.694
Ever-smokers	21 (53.8)	18 (58.1)	3 (37.5)	0.432
Sequence of diagnosis				
ILD first	26 (66.7)	20 (64.5)	6 (75.0)	0.694
MPA first	1 (2.6)	1 (3.2)	0	>0.999
Concurrence	12 (30.8)	10 (32.3)	2 (25.0)	>0.999
Extra-pulmonary involvement				
Kidney	30 (76.9)	23 (74.2)	7 (87.5)	0.653
Peripheral nervous system	13 (33.3)	10 (32.3)	3 (37.5)	>0.999
Autoantibody				
MPO-ANCA titer, IU/mL	116.0 (38.0–134.0)	108.0 (35.0–134.0)	134.0 (87.5–165.0)	0.094
MPO-ANCA positivity	36 (92.3)	29 (93.5)	7 (87.5)	>0.999
ANA positivity	5 (12.8)	3 (10.3)	2 (25.0)	0.564
CRP, mg/dL	6.9 ± 6.7	7.4 ± 7.1	4.8 ± 4.6	0.358
Pulmonary function test				
FVC, % predicted	77.0 ± 15.3	79.0 ± 14.7	69.4 ± 16.1	0.116
DLco, % predicted	59.8 ± 14.8	58.6 ± 14.3	69.4 ± 17.0	0.317
TLC, % predicted	78.4 ± 13.1	80.1 ± 13.1	71.3 ± 11.3	0.110
6-min walk test				
Distance, meter	392.8 ± 143.8	382.0 ± 153.6	439.0 ± 83.5	0.352
The lowest SpO_2, %	93.0 ± 4.9	93.1 ± 4.8	92.6 ± 5.4	0.813
Bronchoalveolar lavage				
WBC/mm^3	317.9 ± 300.9	348.0 ± 326.9	189.0 ± 78.0	0.249
Neutrophil, %	10.9 ± 8.7	11.9 ± 8.7	7.5 ± 8.8	0.290
Lymphocyte, %	15.0 ± 9.0	13.5 ± 7.2 1	21.3 ± 13.3	0.216

Data are presented as mean ± standard deviation, median (interquartile range) or number (%).
MPA, microscopic polyangiitis; ILD, interstitial lung disease; MPO-ANCA, myeloperoxidase-antineutrophil cytoplasmic antibodies; ANA, antinuclear antibody; CRP, C-reactive protein; FVC, forced vital capacity; TLC, total lung capacity; DLco, diffusing capacity of the lung for carbon monoxide; WBC, white blood cell; SpO_2, oxygen saturation measured by pulse oximetry.

TABLE 4 Comparison of the clinical course according to the HRCT patterns in patients with MPA-ILD.

	Total	UIP-like	Non-UIP-like	*p*-value
Number of patients	39	31	8	
Complications				
Pneumonia	9 (23.1)	6 (19.4)	3 (37.5)	0.538
Diffuse alveolar hemorrhage	7 (17.9)	6 (19.4)	1 (12.5)	>0.999
Acute exacerbation	7 (17.9)	6 (19.4)	1 (12.5)	>0.999
Lung cancer	3 (7.7)	1 (3.2)	2 (25.0)	0.101
FVC changes (6 months), % predicted	2.9 ± 13.7	1.1 ± 10.6	11.1 ± 22.8	0.338
FVC changes (12 months), % predicted	2.7 ± 13.2	2.2 ± 12.3	4.9 ± 17.8	0.662
Pulmonary function change				
Improvement	7 (17.9)	5 (18.5)	2 (33.3)	0.584
Stabilization	20 (51.3)	17 (63.0)	3 (50.0)	0.659
Progression	6 (15.4)	5 (18.5)	1 (16.7)	>0.999

Data are presented as mean ± standard deviation or number (%).
MPA, microscopic polyangiitis; ILD, interstitial lung disease; FVC, forced vital capacity.

factors for mortality in patients with MPA-ILD. However, HRCT patterns were not associated with prognosis in patients with MPA-ILD.

In our study, the clinical characteristics of patients with MPA-ILD were similar to those in previous reports (Tzelepis et al., 2010; Huang et al., 2014; Fernandez Casares et al., 2015). In a previous study

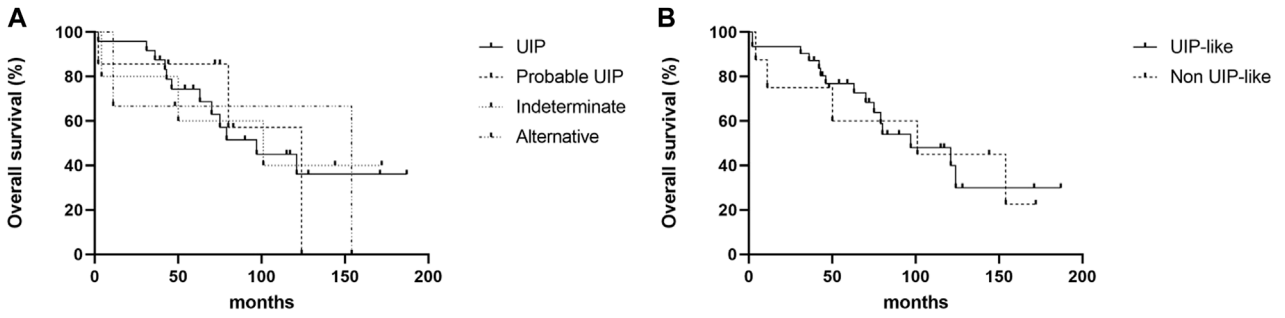

FIGURE 2
Kaplan—Meier survival curve of patients with MPA-ILD according to HRCT patterns. **(A)** Comparison of overall survival according to the HRCT patterns, **(B)** Comparison of overall survival between patients with UIP-like pattern and non-UIP-like pattern. **(A)** There were no differences in overall survival rates according to the HRCT patterns; the median survival period was 97.0 months for a UIP pattern, 124.0 months for probable UIP, 101.0 months for indeterminate UIP, and 154.0 months for alternative diagnosis (log-rank test, p = 0.985). **(B)** There was no difference in the overall survival between patients with UIP-like and non-UIP-like pattern on HRCT; the median survival period was 97.0 months for UIP-like pattern, and 101.0 months for non-UIP-like pattern (log-rank test, p = 0.969). MPA, microscopic polyangiitis; ILD, interstitial lung disease; HRCT, high resolution computed tomography; UIP, usual interstitial pneumonia.

TABLE 5 Prognostic factors for mortality in patients with MPA-ILD assessed by Cox regression analysis.

	Unadjusted analysis		
Variables	HR	95% CI	*p*-value
Age at ILD diagnosis	1.081	1.018–1.148	0.011
Male sex	2.294	0.871–6.039	0.093
MPA first	3.072	0.392–24.075	0.285
Ever smoker	1.767	0.714–4.374	0.218
CRP mg/dL	1.030	0.969–1.095	0.342
FVC, % predicted	0.993	0.968–1.018	0.575
DLco, % predicted	1.009	0.979–1.040	0.561
TLC, % predicted	1.001	0.967–1.036	0.950
6MWT, lowest SpO_2, %	0.936	0.860–1.018	0.121
6MWT, distance (meter)	0.999	0.996–1.003	0.743
BAL, Neutrophil, %	1.075	1.006–1.149	0.034
BAL, Lymphocyte, %	0.993	0.940–1.049	0.795
UIP-like pattern	0.980	0.349–2.755	0.969
FVC changes (6 months), % predicted	0.977	0.939–1.016	0.243
FVC changes (12 months), % predicted	0.952	0.907–0.999	0.045
Acute exacerbation	4.203	1.616–10.933	0.003
Multivariate analysis[a]			
Variables	HR	95% CI	*p*-value
Age at ILD diagnosis	1.072	1.008–1.141	0.028
Male sex	2.190	0.699–6.866	0.179
BAL, Neutrophil, %	1.091	1.017–1.170	0.015

ILD: interstitial lung disease, MPA: microscopic polyangiitis, CRP: C-reactive protein, FVC: forced vital capacity, DLco: diffusing capacity of the lung for carbon monoxide, TLC: total lung capacity, 6MWT: 6-min walk test, SpO_2: oxygen saturation measured by pulse oximetry, BAL: bronchoalveolar lavage, UIP: usual interstitial pneumonia.
[a]Only baseline variables with p-value < 0.1 in the unadjusted analysis were entered into the multivariable models.

including nine patients with MPA and PF (MPA-PF) (Fernandez Casares et al., 2015), there was a slight predominance of males (55.6%), and our study also revealed a male predominance of 59.0%. In our study, 92.3% of patients presented MPO-ANCA positivity, and the development of ILD preceded that of vasculitis in 66.7% of patients. These features corresponded with those reported in the study by Fernandez Casares et al. (2015); they showed that 32.1% of 28 patients with MPA had ILD, and ILD was the initial manifestation in 55.5% of those with ILD. Likewise, ILD preceded extra-pulmonary manifestations in other studies (Tzelepis et al., 2010; Huang et al., 2014). Tzelepis et al. (2010) compared the clinical characteristics and outcomes of patients with MPA with and without ILD, and revealed that ILD preceded extra-pulmonary manifestations in 53.8% of patients with MPA-ILD (n = 13). Additionally, Huang et al. (2014) reported that ILD was observed to precede the diagnosis of MPA in 68.4% of 19 patients with MPA-ILD.

In our study, higher BAL neutrophil counts were associated with poor prognosis in patients with MPA-ILD. The significant difference in neutrophil count between the non-survivors and the survivors might be explained by the correlation of increase in BAL neutrophils with disease severity and prognosis of IPF (Meyer et al., 2012). A previous study by Foucher et al. (1999) also suggested that the MPO antibody-related autoimmune response contributes to lung injury after the local release of products of activated neutrophils, which supports a pathogenic role of MPO antibody in pulmonary lesions. Moreover, a study by Birnbaum et al. (2007) involving patients with MPA-PF, showed that vasculitis with neutrophilic degranulation may have triggered fibroblastic foci and the development of ILD. Consistently, a recent study by Koike et al. (2022) comparing sural nerve biopsy specimens between patients with MPA and those with non-systemic vasculitic neuropathy (NSVN) demonstrated that neutrophils adhere to vascular endothelial cells, migrate to the extravascular spaces, and release neutrophil components in the extracellular spaces in patients with MPA; however, these findings were not observed in those with NSVN.

Pulmonary complications, including DAH, chronic respiratory failure, and AE, are significant causes of death and are associated with a high mortality rate in patients with MPA-ILD (Hozumi et al., 2021). PF with respiratory failure contributes to 40%–100% of deaths in patients with MPA-ILD (Tzelepis et al., 2010; Comarmond et al., 2014; Huang et al., 2014; Fernandez Casares et al., 2015), suggesting that survival is more closely associated with PF than with vasculitis itself. In our study, AE occurred in approximately 20% of patients during follow-up, and all the patients died. The exact incidence of AE in patients with MPA-ILD is not known; however, a previous study, involving 80 patients with MPA-ILD, suggested that the 1-year cumulative incidence of AE was 7.2%, similar to that of IPF (8.5% of 1-year incidence) (Kim et al., 2006; Hozumi et al., 2021). In the unadjusted Cox regression analyses of our study, AE was a significant risk factor for mortality, which was in line with the results of previous studies demonstrating that AE accounts for up to 20%–60% of the causes of death in patients with AAV-ILD (Hosoda et al., 2016; Watanabe et al., 2019).

In our study, a UIP pattern on HRCT was the dominant HRCT pattern, consistent with previous studies (Arulkumaran et al., 2011; Fernandez Casares et al., 2015). The most common fibrosis pattern on HRCT in patients with MPA-ILD was a UIP pattern, accounting for 77.7% and 57.1% of patients with MPA-ILD in previous studies by Arulkumaran et al. (2011) and Fernandez Casares et al. (2015), respectively. However, unlike other connective tissue disease-associated ILDs (Koo et al., 2019), whether HRCT patterns affect the survival of patients with MPA-ILD has not been clarified. Comarmond et al. (2014) reported that the UIP pattern and atypical UIP or NSIP patterns on HRCT were not associated with an increased risk of mortality in 49 patients with PF associated with AAV (HR, 5.01; 95% CI, 0.63–39.92; p = 0.13 and HR, 3.54; 95% CI, 0.21–58.61; p = 0.38). Furthermore, in our study, there was no significant difference in the overall survival according to the HRCT patterns in patients with MPA-ILD. Moreover, Hozumi et al. (2021) showed that there was no difference in the overall survival between the UIP group and the non-UIP group in 84 patients with MPA-ILD (5-year cumulative survival rate, 35.8% vs. 54.2%, p = 0.18).

Our study has some limitations. First, it was a retrospective observational study performed at a single center, and this may limit the generalizability of our results. However, the baseline characteristics of the subjects were similar to those reported in other studies (Homma et al., 2004; Foulon et al., 2008; Comarmond et al., 2014; Fernandez Casares et al., 2015). Second, the number of patients was small, and this would have limited the ability to produce statistically significant results. The subjects in our study also received various treatments, which may lead to the different patients outcome. However, even considering a small number of patients, our results identify prognostic factors for survival in patients with MPA-ILD. The results of our study need to be confirmed in other studies with larger cohorts. Finally, the definition of a UIP-like pattern used in this study was modified from the HRCT classification of IPF diagnostic guidelines. In the absence of a consensus on the definition of the UIP-like pattern in fibrosing ILDs other than IPF, the modification may be inevitable in some subtypes of ILDs. Despite these limitations, the inclusion of patients with MPA-ILD—rather than just those with ANCA positivity and the assessment of their long-term clinical outcomes are the strengths of this study.

In conclusion, during a follow-up of 6 years, it was observed that about 50% and 20% of patients with MPA-ILD experienced death and AE, respectively. Our results suggest that older age and higher BAL neutrophil counts signify poor prognosis in patients with MPA-ILD.

Data availability statement

The original contributions presented in the study are included in the article/supplementary material, further inquiries can be directed to the corresponding author.

Ethics statement

The studies involving human participants were reviewed and approved by Institutional Review Board of the Asan Medical Center. Written informed consent for participation was not required for this study in accordance with the national legislation and the institutional requirements.

Author contributions

JWS: Conceptualization; Data curation; Funding acquisition; Methodology; Project administration; Resources; Supervision; Validation; Writing-review and Editing. MJK: Formal analysis; Investigation; Methodology; Visualization; Writing-original draft. DL: Formal analysis; Investigation; Methodology; Visualization; Writing-original draft. JC: Formal analysis; Validation; Writing-review and Editing; Resources.

Funding

This study was supported by grants from the Basic Science Research Program (NRF-2022R1A2B5B02001602) and the Bio and Medical Technology Development Program (NRF-2022M3A9E4082647) of the National Research Foundation of Korea (NRF) funded by the Ministry of Science and ICT, South Korea, and also supported by the National Institute of Health research project (2021ER120701) and by Korea Environment Industry and Technology Institute through Core Technology Development Project for Environmental Diseases Prevention and Management Program funded by Korea Ministry of Environment (ARQ202201450001), South Korea.

Acknowledgments

The authors thank Seokchan Hong for his help with confirming the diagnosis of patients with microscopic polyangiitis (Department of Rheumatology, Asan Medical Center, University of Ulsan College of Medicine) and Na Young Kim for her statistical consultation (Department of Clinical Epidemiology and Biostatistics, Asan Medical Center).

Conflict of interest

The authors declare that the research was conducted in the absence of any commercial or financial relationships that could be construed as a potential conflict of interest.

Publisher's note

All claims expressed in this article are solely those of the authors and do not necessarily represent those of their affiliated organizations, or those of the publisher, the editors and the reviewers. Any product that may be evaluated in this article, or claim that may be made by its manufacturer, is not guaranteed or endorsed by the publisher.

References

Arulkumaran, N., Periselneris, N., Gaskin, G., Strickland, N., Ind, P. W., Pusey, C. D., et al. (2011). Interstitial lung disease and ANCA-associated vasculitis: A retrospective observational cohort study. *Rheumatol. Oxf.* 50, 2035–2043. doi:10.1093/rheumatology/ker236

Birnbaum, J., Danoff, S., Askin, F. B., and Stone, J. H. (2007). Microscopic polyangiitis presenting as a "pulmonary-muscle" syndrome: Is subclinical alveolar hemorrhage the mechanism of pulmonary fibrosis? *Arthritis Rheum.* 56, 2065–2071. doi:10.1002/art.22633

Chung, S. A., and Seo, P. (2010). Microscopic polyangiitis. *Rheum. Dis. Clin. North Am.* 36, 545–558. doi:10.1016/j.rdc.2010.04.003

Collard, H. R., Ryerson, C. J., Corte, T. J., Jenkins, G., Kondoh, Y., Lederer, D. J., et al. (2016). Acute exacerbation of idiopathic pulmonary fibrosis. An international working group report. *Am. J. Respir. Crit. Care Med.* 194, 265–275. doi:10.1164/rccm.201604-0801CI

Comarmond, C., Crestani, B., Tazi, A., Hervier, B., Adam-Marchand, S., Nunes, H., et al. (2014). Pulmonary fibrosis in antineutrophil cytoplasmic antibodies (ANCA)-associated vasculitis: A series of 49 patients and review of the literature. *Med. Baltim.* 93, 340–349. doi:10.1097/MD.0000000000000217

Corral-Gudino, L., Borao-Cengotita-Bengoa, M., Del Pino-Montes, J., and Lerma-MāRQUEZ, J. L. (2011). Overall survival, renal survival and relapse in patients with microscopic polyangiitis: A systematic review of current evidence. *Rheumatol. Oxf.* 50, 1414–1423. doi:10.1093/rheumatology/ker112

Fernandez Casares, M., Gonzalez, A., Fielli, M., Caputo, F., Bottinelli, Y., and Zamboni, M. (2015). Microscopic polyangiitis associated with pulmonary fibrosis. *Clin. Rheumatol.* 34, 1273–1277. doi:10.1007/s10067-014-2676-1

Foucher, P., Heeringa, P., Petersen, A. H., Huitema, M. G., Brouwer, E., Tervaert, J. W., et al. (1999). Antimyeloperoxidase-associated lung disease. An experimental model. *Am. J. Respir. Crit. Care Med.* 160, 987–994. doi:10.1164/ajrccm.160.3.9807139

Foulon, G., Delaval, P., Valeyre, D., Wallaert, B., Debray, M. P., Brauner, M., et al. (2008). ANCA-Associated lung fibrosis: Analysis of 17 patients. *Respir. Med.* 102, 1392–1398. doi:10.1016/j.rmed.2008.04.023

Hervier, B., Pagnoux, C., Agard, C., Haroche, J., Amoura, Z., Guillevin, L., et al. (2009). Pulmonary fibrosis associated with ANCA-positive vasculitides. Retrospective study of 12 cases and review of the literature. *Ann. Rheum. Dis.* 68, 404–407. doi:10.1136/ard.2008.096131

Holland, A. E., Spruit, M. A., Troosters, T., Puhan, M. A., Pepin, V., Saey, D., et al. (2014). An official European respiratory society/American thoracic society technical standard: Field walking tests in chronic respiratory disease. *Eur. Respir. J.* 44, 1428–1446. doi:10.1183/09031936.00150314

Homma, S., Matsushita, H., and Nakata, K. (2004). Pulmonary fibrosis in myeloperoxidase antineutrophil cytoplasmic antibody-associated vasculitides. *Respirology* 9, 190–196. doi:10.1111/j.1440-1843.2004.00581.x

Homma, S., Suzuki, A., and Sato, K. (2013). Pulmonary involvement in ANCA-associated vasculitis from the view of the pulmonologist. *Clin. Exp. Nephrol.* 17, 667–671. doi:10.1007/s10157-012-0710-7

Hosoda, C., Baba, T., Hagiwara, E., Ito, H., Matsuo, N., Kitamura, H., et al. (2016). Clinical features of usual interstitial pneumonia with anti-neutrophil cytoplasmic antibody in comparison with idiopathic pulmonary fibrosis. *Respirology* 21, 920–926. doi:10.1111/resp.12763

Hozumi, H., Kono, M., Hasegawa, H., Yasui, H., Suzuki, Y., Karayama, M., et al. (2021). Clinical significance of interstitial lung disease and its acute exacerbation in microscopic polyangiitis. *Chest* 159, 2334–2345. doi:10.1016/j.chest.2021.01.083

Huang, H., Wang, Y. X., Jiang, C. G., Liu, J., Li, J., Xu, K., et al. (2014). A retrospective study of microscopic polyangiitis patients presenting with pulmonary fibrosis in China. *BMC Pulm. Med.* 14, 8. doi:10.1186/1471-2466-14-8

Jacob, J., Hirani, N., Van Moorsel, C. H. M., Rajagopalan, S., Murchison, J. T., Van Es, H. W., et al. (2019). Predicting outcomes in rheumatoid arthritis related interstitial lung disease. *Eur. Respir. J.* 53, 1800869. doi:10.1183/13993003.00869-2018

Jennette, J. C., Falk, R. J., Bacon, P. A., Basu, N., Cid, M. C., Ferrario, F., et al. (2013). 2012 revised international Chapel Hill consensus conference nomenclature of vasculitides. *Arthritis Rheum.* 65, 1–11. doi:10.1002/art.37715

Kim, D. S., Park, J. H., Park, B. K., Lee, J. S., Nicholson, A. G., and Colby, T. (2006). Acute exacerbation of idiopathic pulmonary fibrosis: Frequency and clinical features. *Eur. Respir. J.* 27, 143–150. doi:10.1183/09031936.06.00114004

Koike, H., Furukawa, S., Mouri, N., Fukami, Y., Iijima, M., and Katsuno, M. (2022). Early ultrastructural lesions of anti-neutrophil cytoplasmic antibody-versus complement-associated vasculitis. *Neuropathology* 42, 420–429. doi:10.1111/neup.12821

Koo, S. M., Kim, S. Y., Choi, S. M., and Lee, H. K.Korean Interstitial Lung Diseases Study Group (2019). Korean guidelines for diagnosis and management of interstitial lung diseases: Part 5. Connective tissue disease associated interstitial lung disease. *Tuberc. Respir. Dis. Seoul.* 82, 285–297. doi:10.4046/trd.2019.0009

Kwon, B. S., Lee, H. Y., Choe, J., Chae, E. J., Hong, S., and Song, J. W. (2022). Acute respiratory deterioration in rheumatoid arthritis-associated interstitial lung disease: A single-center study. *Chest* 162, 136–144. doi:10.1016/j.chest.2022.01.007

Macintyre, N., Crapo, R. O., Viegi, G., Johnson, D. C., Van, D. G. C. P., Brusasco, V., et al. (2005). Standardisation of the single-breath determination of carbon monoxide uptake in the lung. *Eur. Respir. J.* 26, 720–735. doi:10.1183/09031936.05.00034905

Meyer, K. C., Raghu, G., Baughman, R. P., Brown, K. K., Costabel, U., Du Bois, R. M., et al. (2012). An official American thoracic society clinical practice guideline: The clinical utility of bronchoalveolar lavage cellular analysis in interstitial lung disease. *Am. J. Respir. Crit. Care Med.* 185, 1004–1014. doi:10.1164/rccm.201202-0320ST

Miller, M. R., Hankinson, J., Brusasco, V., Burgos, F., Casaburi, R., Coates, A., et al. (2005). Standardisation of spirometry. *Eur. Respir. J.* 26, 319–338. doi:10.1183/09031936.05.00034805

Raghu, G., Remy-Jardin, M., Myers, J. L., Richeldi, L., Ryerson, C. J., Lederer, D. J., et al. (2018). Diagnosis of idiopathic pulmonary fibrosis. An official ATS/ERS/JRS/ALAT clinical practice guideline. *Am. J. Respir. Crit. Care Med.* 198, e44–e68. doi:10.1164/rccm.201807-1255ST

Richeldi, L., Ryerson, C. J., Lee, J. S., Wolters, P. J., Koth, L. L., Ley, B., et al. (2012). Relative versus absolute change in forced vital capacity in idiopathic pulmonary fibrosis. *Thorax* 67, 407–411. doi:10.1136/thoraxjnl-2011-201184

Tzelepis, G. E., Kokosi, M., Tzioufas, A., Toya, S. P., Boki, K. A., Zormpala, A., et al. (2010). Prevalence and outcome of pulmonary fibrosis in microscopic polyangiitis. *Eur. Respir. J.* 36, 116–121. doi:10.1183/09031936.00110109

Wanger, J., Clausen, J. L., Coates, A., Pedersen, O. F., Brusasco, V., Burgos, F., et al. (2005). Standardisation of the measurement of lung volumes. *Eur. Respir. J.* 26, 511–522. doi:10.1183/09031936.05.00035005

Watanabe, T., Minezawa, T., Hasegawa, M., Goto, Y., Okamura, T., Sakakibara, Y., et al. (2019). Prognosis of pulmonary fibrosis presenting with a usual interstitial pneumonia pattern on computed tomography in patients with myeloperoxidase anti-neutrophil cytoplasmic antibody-related nephritis: A retrospective single-center study. *BMC Pulm. Med.* 19, 194. doi:10.1186/s12890-019-0969-5

Watts, R., Lane, S., Hanslik, T., Hauser, T., Hellmich, B., Koldingsnes, W., et al. (2007). Development and validation of a consensus methodology for the classification of the ANCA-associated vasculitides and polyarteritis nodosa for epidemiological studies. *Ann. Rheum. Dis.* 66, 222–227. doi:10.1136/ard.2006.054593

frontiers | Frontiers in Pharmacology

TYPE Original Research
PUBLISHED 03 February 2023
DOI 10.3389/fphar.2023.1089812

OPEN ACCESS

EDITED BY
Carol Artlett,
College of Medicine, Drexel University, United States

REVIEWED BY
Bi-Sen Ding,
Sichuan University, China
Yanqiu Liu,
Shandong University of Traditional Chinese Medicine, China

*CORRESPONDENCE
Jian Gao,
gaojianayfy@163.com
Minghan Cheng,
305017097@qq.com

†These authors have contributed equally to this work

SPECIALTY SECTION
This article was submitted to Respiratory Pharmacology, a section of the journal Frontiers in Pharmacology

RECEIVED 04 November 2022
ACCEPTED 25 January 2023
PUBLISHED 03 February 2023

CITATION
Ji H, Dong H, Lan Y, Bi Y, Gu X, Han Y, Yang C, Cheng M and Gao J (2023), Metformin attenuates fibroblast activation during pulmonary fibrosis by targeting S100A4 *via* AMPK-STAT3 axis . *Front. Pharmacol.* 14:1089812. doi: 10.3389/fphar.2023.1089812

Metformin attenuates fibroblast activation during pulmonary fibrosis by targeting S100A4 *via* AMPK-STAT3 axis

Huimin Ji[1,2†], Hongliang Dong[1†], Yuejiao Lan[1,3], Yuqian Bi[1], Xuan Gu[1,4], Yongyue Han[1], Chongyang Yang[1], Minghan Cheng[1*] and Jian Gao[1*]

[1]Pediatric Translational Medicine Institute, Shanghai Children's Medical Center, School of Medicine, Shanghai Jiao Tong University, Shanghai, China, [2]The Second Affiliated Hospital, Dalian Medical University, Dalian, Liaoning, China, [3]Jilin Province People's Hospital, Changchun, Jilin, China, [4]3201 Hospital, Hanzhong, Shaanxi, China

Fibroblasts activation is a crucial process for development of fibrosis during idiopathic pulmonary fibrosis pathogenesis, and transforming growth factor (TGF)-β1 plays a key regulatory role in fibroblast activation. It has been reported that metformin (MET) alleviated bleomycin (BLM)-induced pulmonary fibrosis (PF) by regulating TGF-β1-induced fibroblasts activation, but the underlying mechanisms still deserve further investigations. In this study, MET blocked α-smooth muscle actin (α-SMA) accumulation *in vivo* accompanied with S100A4 expression and STAT3 phosphorylation inhibition, resulting in attenuating the progression of lung fibrosis after BLM administration. We determined that S100A4 plays critical roles in fibroblasts activation *in vitro*, evidenced by siRNA knockdown of S100A4 expression downregulated TGF-β1 induced α-SMA production in Human fetal lung fibroblast (HFL1) cells. Importantly, we found for the first time that the expression of S100A4 in fibroblasts was regulated by STAT3. Stattic, an effective small molecule inhibitor of STAT3 phosphorylation, reduced S100A4 level in TGF-β1- treated HFL1 cells accompanied with less α-SMA production. We further found that MET, which inhibits STAT3 phosphorylation by AMPK activation, also inhibits fibroblasts activation by targeting S100A4 *in vitro*. Together all these results, we conclude that S100A4 contributes to TGF-β1- induced pro-fibrogenic function in fibroblasts activation, and MET was able to protect against TGF-β1-induced fibroblasts activation and BLM-induced PF by down-regulating S100A4 expression through AMPK-STAT3 axis. These results provide a useful clue for a clinical strategy to prevent PF.

KEYWORDS

pulmonary fibrosis, metformin, fibroblast activation, S100A4, STAT3

1 Introduction

Pulmonary Fibrosis (PF) is a chronic progressive lung interstitial disease, characterized by distorted alveolar structure, excessive proliferation of lung mesenchymal cells and abnormal deposition of extracellular matrix (ECM), which results in reduced lung compliance, gas exchange impairment, and irreversible decline in pulmonary function (Yang et al., 2019; Kasam et al., 2020). PF with unknown etiology is termed idiopathic pulmonary fibrosis (IPF). The incidence of idiopathic pulmonary fibrosis (IPF) is related to gender (male: female ratio, 7:3)

and age (Raghu et al., 2018; Wijsenbeek and Cottin, 2020). Nearly half of IPF patients die from respiratory failure on average within 2–4 years after diagnosis (Richeldi et al., 2017). The COVID-19 pandemic rapidly spreads around the world, and it ranges in severity from asymptomatic through to severe acute respiratory distress, which can lead to respiratory failure and death. It has rapidly become evident that COVID-19 patients infected with SARS-CoV-2 virus can develop features of interstitial pulmonary fibrosis (John, Joseph, Jenkins and Tatler, 2021). In recent years, pirfenidone and nintedanib, two drugs approved from Food and Drug Administration (FDA), are available for treating IPF (Somogyi, Chaudhuri, Torrisi, Kahn, Muller and Kreuter, 2019). However, neither of them provides a cure, and both of them are associated with several serious drug-related side effects, including gastrointestinal events, rash and photosensitivity (Richeldi et al., 2014; Cottin and Maher, 2015; Zhang et al., 2019). Therefore, it is an urgent need to elucidate the molecular mechanism and key targets of PF for developing effective therapeutic drugs. A large number of studies support the view that fibroblasts activation plays a crucial role in the progression of PF. During fibroblasts activation, lung-resident fibroblasts proliferate and differentiate into contractile mesenchymal cells, named myofibroblasts, which secret α-smooth muscle actin (α-SMA), and participate in excessive deposition of ECM and distortion of alveolar architecture (Kuhn and McDonald, 1991; Sontake et al., 2017; Wijsenbeek and Cottin, 2020).

S100A4, a calcium-binding protein, also termed fibroblast-specific protein-1(FSP-1), was previously considered as a marker of fibroblasts, regulating cellular biological functions, such as cell mobility, proliferation, or metastasis (Bresnick et al., 2015). In addition, S100A4 is involved in the pathogenesis of inflammation, autoimmune diseases and fibrosis (Fei, Qu, Li, Wang, Li and Zhang, 2017; Austermann et al., 2018). Increased expression levels of S100A4 have been reported in the lungs of IPF patients, including in mesenchymal progenitor cells, suggesting the involvement of S100A4 in IPF pathogenesis through modulating mesenchymal progenitor cell fibrogenicity (Xia et al., 2017; Lee et al., 2020). Like other members of the S100 family, S100A4 has intracellular as well as extracellular functions. Extracellular S100A4 produced and released by macrophages has been proved to be a key driver of lung fibroblast activation (Li et al., 2018; Zhang et al., 2018; Li et al., 2020), but the roles of intracellular S100A4 produced within fibroblasts in the process of fibroblast activation are still unclear.

Signal transducer and activator of transcription 3 (STAT3), a member of STATs family, is activated by multiple cytokines, including interleukin-6 and transforming growth factor (TGF)-β1 (Chakraborty et al., 2017). Upon binding of these ligands to their receptors, STAT3 is activated by phosphorylation at Tyr-705 in the STAT3 transactivation domain, and translocates to the nucleus, modulating the transcription of target genes (Bharadwaj, Kasembeli, Robinson and Tweardy, 2020). Activated STAT3 is elevated in the fibrotic lungs of patients with IPF and the Bleomycin (BLM) -induced mice PF model. On the other hand, STAT3 contributes to activating fibroblasts to transform into myofibroblasts, finally leading to abnormal accumulation of ECM (Pedroza et al., 2016). Therefore, STAT3 may be a potential therapeutic target in PF.

Many studies have reported the therapeutic effects of MET in PF. It has been suggested that intraperitoneal administration of MET attenuates BLM-induced lung fibrosis in mice *via* NADPH oxidase 4 (NOX4) suppression (Sato et al., 2016). MET reversed established lung fibrosis in both BLM- or silica-induced PF model, suggesting activation of AMP-activated protein kinase (AMPK) as key underlying signaling event, leading to downregulation of α-SMA and collagen (Rangarajan et al., 2018; Cheng et al., 2021). MET alters the fate of myofibroblasts and accelerates fibrosis resolution by inducing myofibroblast-to-lipofibroblast transdifferentiation (Kheirollahi et al., 2019). Our previous research showed that MET suppressed the proliferation of fibroblasts in PF by AMPK (Gu et al., 2021). Given that proliferation is a process of fibroblast activation, it is worth to further explore the effects of MET on fibroblasts activation in PF and its underlying molecular mechanisms. In this study, we established the BLM-induced PF model *in vivo* and TGF-β1-induced fibroblasts activation model *in vitro,* and found that MET was able to alleviate TGF-β1-induced fibroblasts activation and BLM-induced mice PF by down-regulating S100A4 expression through AMPK-STAT3 axis.

2 Materials and methods

2.1 Chemicals and materials

Bleomycin (Cat. No. 20026111) was purchased from Hanhui Pharmaceuticals Co., Ltd. Metformin (Cat. No. D150959) was purchased from Sigma-Aldrich. Stattic (Cat. No. HY-13818) was obtained from MedChemExpress, and Recombinant Human TGF-β1 (Cat. No. 100-21) was purchased from PeproTech.

2.2 BLM-induced PF model

This study performed on the mice conforms to the Guidelines from the National Institutes of Health and was approved by the Research Ethics Committee of Dalian medical University (animal ethics approval No. AEE19013). Male C57BL/6J mice (8–10 weeks of age, SPF grade) were purchased from Institute of Genome Engineered Animal Models for Human disease of Dalian Medical University. Mice were randomly divided into Saline groups, BLM groups, BLM + MET groups, and MET groups (n = 20 per group). Intratracheal instillation of BLM with 4.5 mg/kg (Gu et al., 2021) was performed to induce PF model in mice of BLM groups, and the mice of Saline groups received an equal volume of normal saline. Day 7 after administration of BLM or saline, mice in BLM + MET groups and MET groups were intraperitoneal injected with MET (65 mg/kg, Sigma, D150959) (Rangarajan et al., 2018) for every other day. At 21 days of BLM insult, mice lungs were collected for further assay.

2.3 Histology and immunohistochemistry

In brief, mice lungs were fixed in 4% paraformaldehyde and embedded in paraffin. Sequentially, lung was were sliced into 5 μm slices, then, lung slices were stain with Hematoxylin and Eosin (H&E) and Masson's trichrome for observing the lung structure and collagen deposition. Lung slices were subjected to immunohistochemical (IHC) staining according to standard procedures. Briefly, lung slices were incubated with a primary antibody specific for S100A4 (Abcam, ab27957, 1:200) and p-STAT3 (Tyr705) antibody (Abcam, ab76315, 1:100) at 4°C overnight. Second day, lung slices were incubated with

10.3389/fphar.2023.1089812

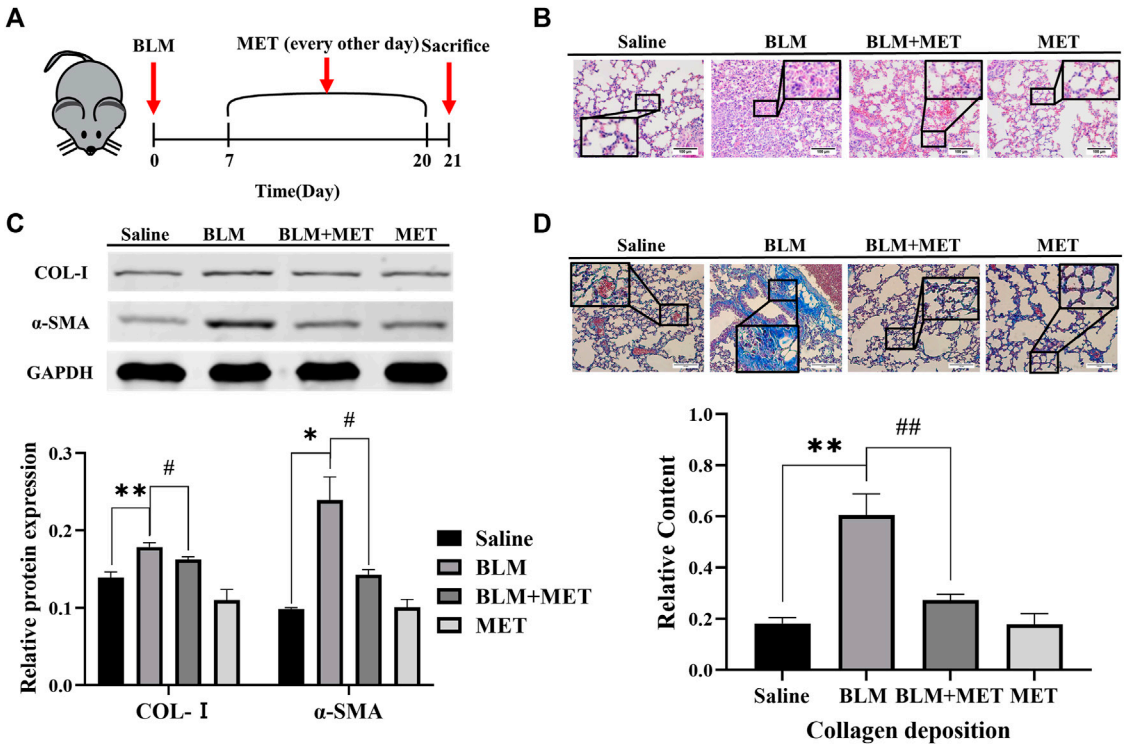

FIGURE 1
MET protected against Pulmonary fibrosis induced by BLM in C57BL/6J mice. **(A)** C57BL/6J mice were intraperitoneally given either MET (65 mg/kg) or normal saline every other day after administrated saline or BLM (4.5 mg/kg, n = 3). **(B)** Lung tissues of mice were collected after 21 days of intratracheal instillation of BLM or normal saline. Lung histology was observed through H&E staining. Scale bars represent 100 μm. **(C)** The expression level of Col-I and α-SMA from mice lung was measured by Western Blot analysis. **(D)** Masson's trichrome staining was for observing collagen deposition. Scale bars represent 100 μm. Data are shown as the mean ± SD (n = 3, per group). $^{*}p < 0.05$, $^{**}p < 0.01$, compared with the saline group. $^{\#}p < 0.05$, $^{\#\#}p < 0.01$ compared with the BLM group.

secondary antibodies and DAB solution. The Histology and protein level of lung slices were viewed under the microscope (Leica, DM 2000). The staining intensity was quantified using ImageJ software V.1.4.3.67.

2.4 Cell culture

Human fetal lung fibroblast (HFL1, Cat. No. SCSP5049) was purchased from the Chinese Academy of Sciences Cell Bank (Shanghai, China) and cultured in Ham's F-12K (Procell, PM150910) medium supplemented with 10% fetal bovine serum (FBS) (Gibco, 10099141C) and 1% penicillin-streptomycin Solution (Hyclone, SV30010) in an incubator at 37°C with 5% CO_2 atmosphere.

2.5 Transfection with small interfering RNA

When confluence of fibroblasts reached 60%–70% in the 6-well plates, S100A4 siRNA or scramble siRNA (negative control siRNA) mixed with Lipofectamine 2000 (Invitrogen, 11668-027) according to the manufacturer's instructions. HFL1 cells were transfected with S100A4 siRNA or Scrambled siRNA separately before TGF-β1 stimulation. S100A4 siRNA and scramble siRNA were synthesized by GenePharma. The sequences of S100A4 siRNA were shown as follows: the forward primer was 5′-GCAUCGCCAUGAUGUGUAATT-3′, and the reverse primer was 5′-UUACAGAUCAUGGCGAUGCTT-3'.

2.6 Western blot analysis

Lung tissues or fibroblasts were lysed with RIPA lysis buffer (Beyotime, P0013B) containing Phenylmethanesulfonyl fluoride (PMSF) (Beyotime, ST506) and phosphatase inhibitor (Beyotime, P1081), then protein concentrations were measured using BCA protein assay kit (Beyotime, P0010S). Protein extracts mixed with loading buffer were separated by sulfate-polyacrylamide gel electrophoresis (SDS-PAGE, 10%–15%) and then were transferred to polyvinylidene difluoride (PVDF, 0.22 μm and 0.45 μm) membranes (Millipore). After being blocked with 5% skim milk, the membranes were incubated overnight at 4°C with primary antibodies, including anti-p-STAT3 (Abcam, ab27957, 1:1,000), anti-p-STAT3 (Tyr705) (Abcam, ab76315, 1:1,000), anti-STAT3 (Cell signaling technology, 30835S, 1:1,000), anti-AMPK (Cell signaling technology, 2,532, 1:1,000), anti-p-AMPK (Cell signaling technology, 2,535, 1:500), anti-SMA (Abcam, 5,694, 1:1,000), anti-Col-I (Bioss, bs-10423R, 1:1,000) and anti-GAPGH (Cell signaling technology, 2,118, 1:1,500). On the second day, after being incubated with anti-rabbit IgG (H + L) (Invitrogen, 35568), the protein bands on the membranes were detected by the Oddessy Clx. GAPDH was used for normalizing the expressed level of relative protein.

10.3389/fphar.2023.1089812

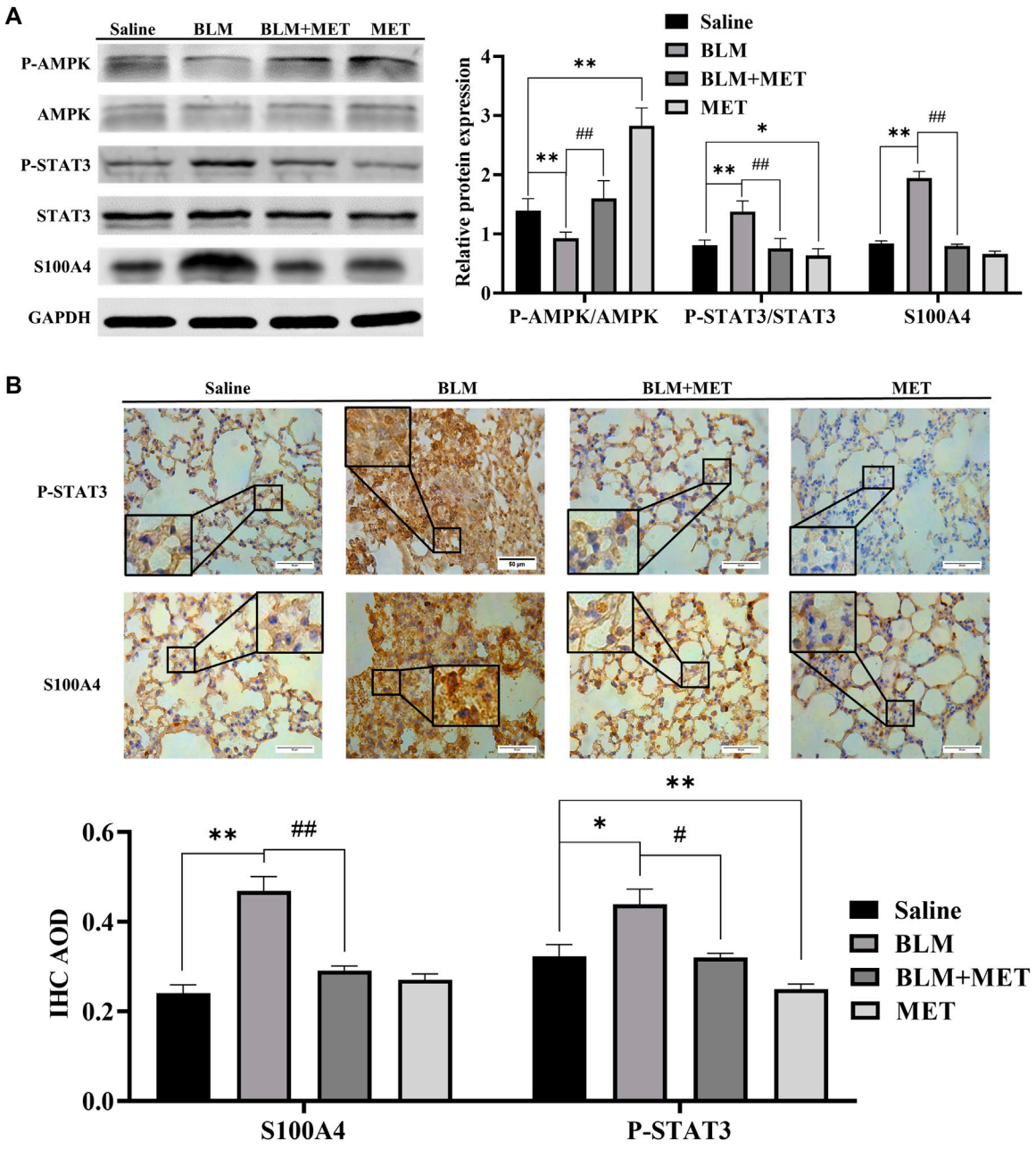

FIGURE 2
MET downregulated the expression of S100A4 and STAT3 Activation in BLM-induced PF mice. **(A)** Western blot analysis in lung using AMPK, p-AMPK, STAT3, p-STAT3 and S100A4 antibodies. **(B)** Representative images of IHC-stained lung section from mice using S100A4 and p-STAT3 antibodies, respectively. Scale bars represent 50 μm. Data were shown as mean ± SD (n = 3 per group). *$p < 0.05$, **$p < 0.01$, compared with the Saline group; $^{\#\#}p < 0.01$, compared with the BLM group.

2.7 Scratch wound healing assay

The cells were seeded in 6-well plates and grown to confluence. A linear wound was performed to each confluent monolayer using a pipette tip and washed 3 times with PBS. Thereafter, the cells were cultured with serum free medium (Gibco, 31985-070), and the images of scratches were captured at 0 h and 24 h. The area of the cell gap was determined by the ImageJ software V.1.4.3.67. The following equation was used to evaluate the migrated area (%): [(cell gap area at 0 h − cell gap area at 24 h)/cell gap at 0 h] × 100%.

2.8 Immunofluorescence analysis

Cells were fixed in 4% paraformaldehyde, then permeabilized with 0.3% Triton X-100 (Byotime, ST795), and blocked with goat serum (Dalian Meilunbio, MB4508). Thereafter, cells were incubated with primary antibodies for S100A4 (1:200), p-STAT3 (Tyr705, 1:500) or α- SMA (Santa Cruz, sc-53142, 1:50) respectively, overnight at 4°C and then combined with TRITC- conjugated goat anti-mouse IgG (ZSGB-BIO, ZF-0313, 1:100) or FITC-conjugated goat anti-rabbit IgG (ZSGB-BIO, ZF-0311; 1:100). Cell nuclei were stained with DAPI (Byotime, C1005, 1:100)

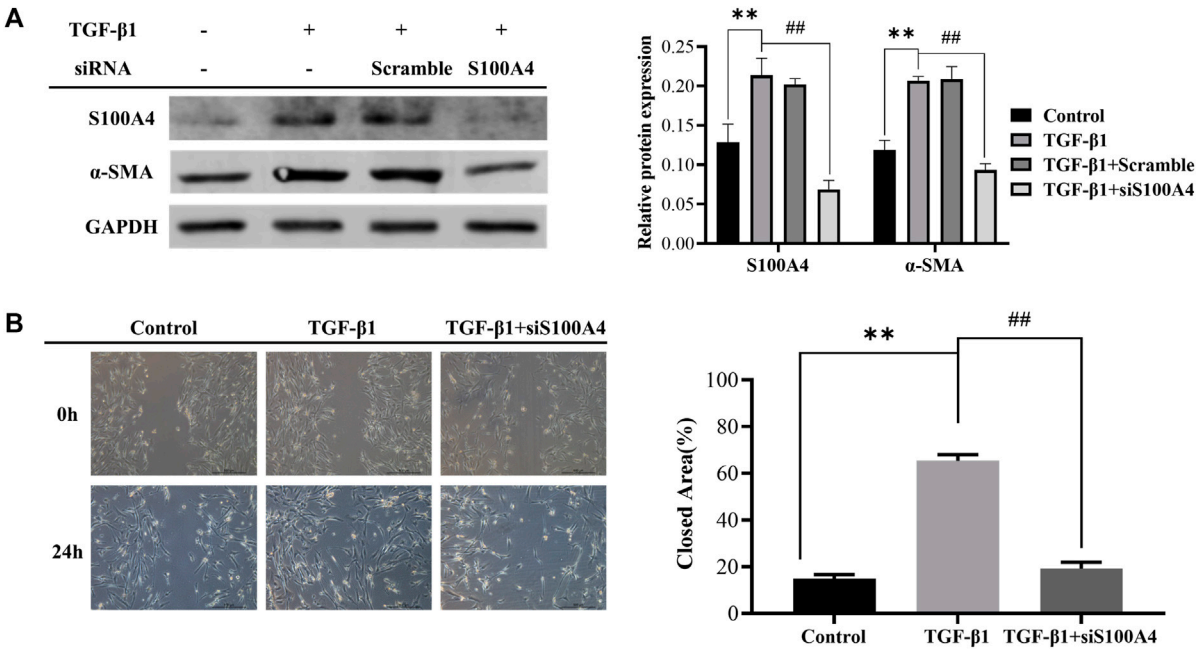

FIGURE 3
Knockdown of S100A4 attenuated TGF-β1-induced fibroblasts activation. HFL1s were transfected by S100A4 siRNA or Scrambled siRNA, and then stimulated with TGF-β1 (10 ng/mL) for 24 h. **(A)** The protein expression levels of α-SMA and S100A4 were measured by western blot in fibroblasts. **(B)** The migration abilities of fibroblasts were detected by scratch assay at 0 h and 24 h after treatment with TGF-β1, respectively. The closed area (%) of the scratch was calculated by equation: [(cell gap area at 0 h - cell gap area after 24 h)/cell gap area at 0 h] ×100%. Scale bars represent 500 μm. Data were shown as mean ± SD (n = 3), $^{**}p < 0.01$ compared with Control group; $^{\#\#}p < 0.01$ compared with TGF-β1 group.

for 5 min at room temperature. The fluorescence images were captured by Inverted fluorescence Microscope (Leica, DMI3000B).

2.9 Statistical analysis

Data are present as mean ± standard deviation (SD) for three independent experiments. Data of two groups are analyzed using Student test (t-test), and data of multiple groups are analyzed by one-way analysis of variance (ANOVA). All statistical analysis is performed by SPSS software and column graphs are using GraphPad prism 8.3. In all cases, $p < 0.05$ was considered statistically significant.

3 Results

3.1 MET mediated anti-fibrosis effects in BLM-induced PF model accompanied with downregulation of S100A4 and phosphorylation of STAT3 expression

MET has been known to mediate anti-fibrosis effects in PF, but its underlying mechanisms deserves further investigation (Sato et al., 2016; Rangarajan et al., 2018; Cheng et al., 2021). In this study, we first confirmed MET-mediated anti-fibrosis effects *in vivo* by employing BLM-induced PF model (Figure 1A). HE staining results showed that MET significantly ameliorated BLM induced severe disruption of alveolar structure, thicker alveolar septa, infiltration of inflammatory cells (Figure 1B). The expression of collagen I (Col-I) and α-SMA in lung tissues, which were hallmarks of the degree of PF, were inhibited by MET treatment (Figure 1C). Masson staining results showed that MET treatment rescued BLM-induced collapse of alveolar spaces and pulmonary interstitial collagen deposition (Figure 1D). Together these data indicated that MET alleviated BLM-induced PF in C57BL/6J mice, which is consistent with previous findings (Sato et al., 2016; Rangarajan et al., 2018).

Based upon the key roles of S100A4 in PF process (Xia et al., 2017; Lee et al., 2020), we further investigated the regulatory effects of MET on the expression of S100A4 in lung tissues of BLM-induced PF mice. Both the WB (Figure 2A) and IHC (Figure 2B) data showed that the protein level of S100A4 was significantly increased after BLM treatment, but MET administration reversed this change, indicating that MET mediated anti-fibrosis in PF by targeting S100A4. Notably, in lung tissues of BLM-induced PF model, BLM treatment induced STAT3 phosphorylation level upregulation and AMPK signaling inhibition also reversed by MET administration (Figures 2A, B). It is reasonable to speculate AMPK pathway, and STAT3 phosphorylation contributes to MET-mediated anti-fibrosis effects, but whether MET downregulated the expression of S100A4 *via* activating AMPK pathway and STAT3 phosphorylation needs further investigations.

3.2 Knockdown of S100A4 attenuated TGF-β1-induced fibroblasts activation

Differentiation of fibroblasts and production of collagen caused by TGF-β1 contribute to the pathogenesis of PF (Wynn and Ramalingam, 2012). In this work, we treated lung fetal fibroblasts (HFL1) with TGF-β1 (10 ng/mL) for 24 h to induce fibroblast activation

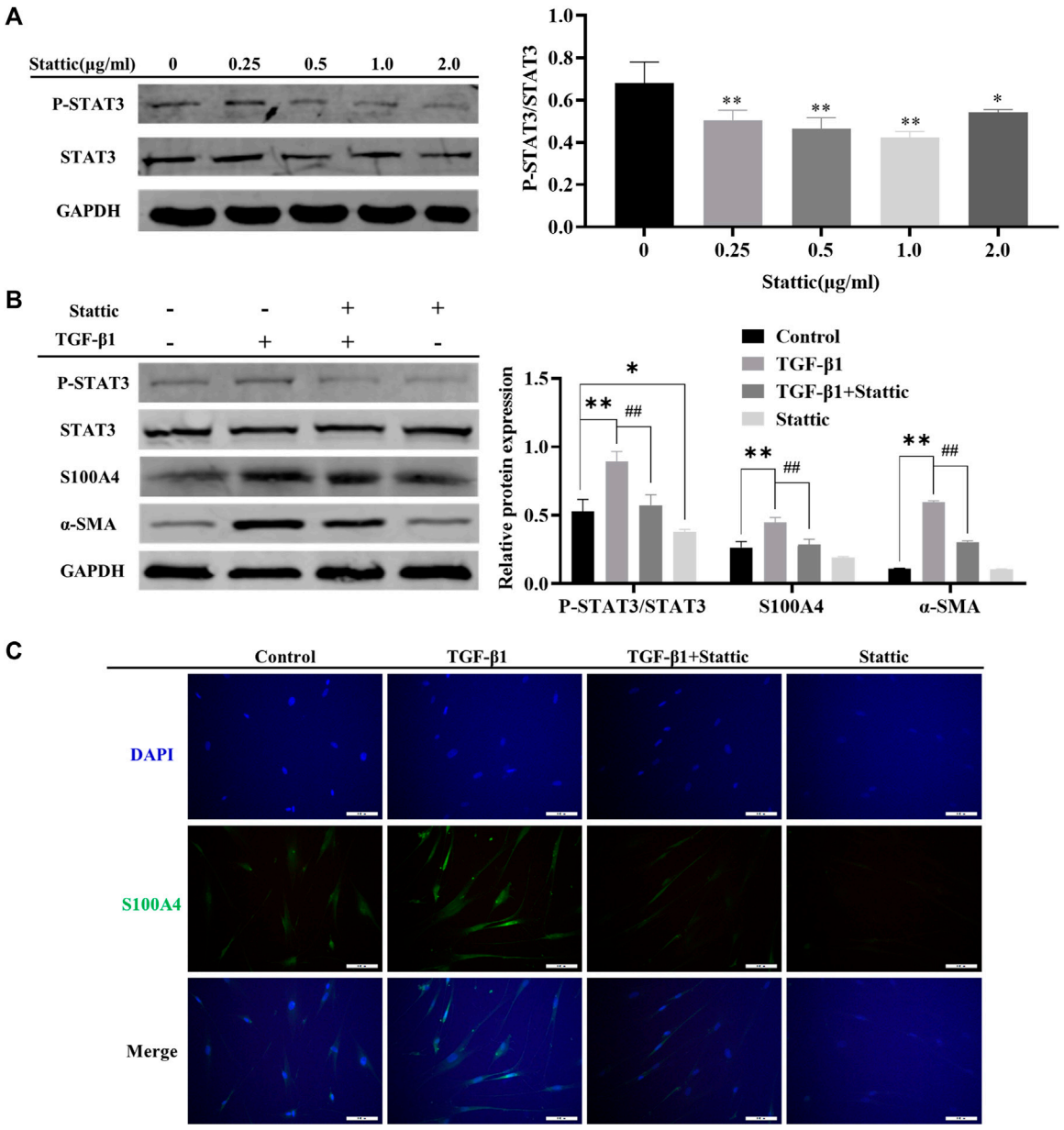

FIGURE 4
Inhibition of STAT3 activation alleviated TGF-β1 mediated S100A4 expression and fibroblast activation. **(A)** HFL1 cells were treated with different concentrations of Stattic (0 μg/mL–2.0 μg/mL) for 48 h. The phosphorylation level of STAT3 was measured by Western Blot. **(B, C)** Stattic treatment was started 24 h before TGF-β1 stimulation and the expression of protein were measured by western blot and immunofluorescence after 24 h treatment with TGF-β1. Scale bars represent 100 μm. Data were shown as mean ± SD ($n = 3$), $*p < 0.05$, $**p < 0.01$, compared with Control group; $\#\#p < 0.01$, compared with TGF-β1 group.

in vitro. We found that TGF-β1 increased the expression of S100A4 (Figure 3A), which is consistent with the changes of α-SMA expression, a hallmark of differentiation of fibroblasts into myofibroblasts. These data indicated that S100A4 expression is positively related to fibroblasts activation and actively involved in PF. In order to further confirm the roles of intracellular S100A4 in fibroblasts activation, we knockdown S100A4 expression in TGF-β1 treated HFL1 cells using small interfering RNA, and the results showed that knockdown the expression of S100A4 reduced TGF-β1 induced α-SMA upregulation (Figure 3A) and inhibited migration abilities of fibroblasts induced by TGF-β1 (Figure 3B). Collectively, these results indicated that S100A4 contributes to TGF-β1 induced α-SMA accumulation in fibroblasts activation, which plays critical roles in PF pathology. Targeting S100A4 might provide us a potential therapeutic strategy for PF.

3.3 Inhibition of STAT3 activation alleviated TGF-β1 mediated S100A4 expression and fibroblast activation

As shown in Figures 2A, B, MET downregulated the expression of S100A4 accompanied with AMPK pathway activation and

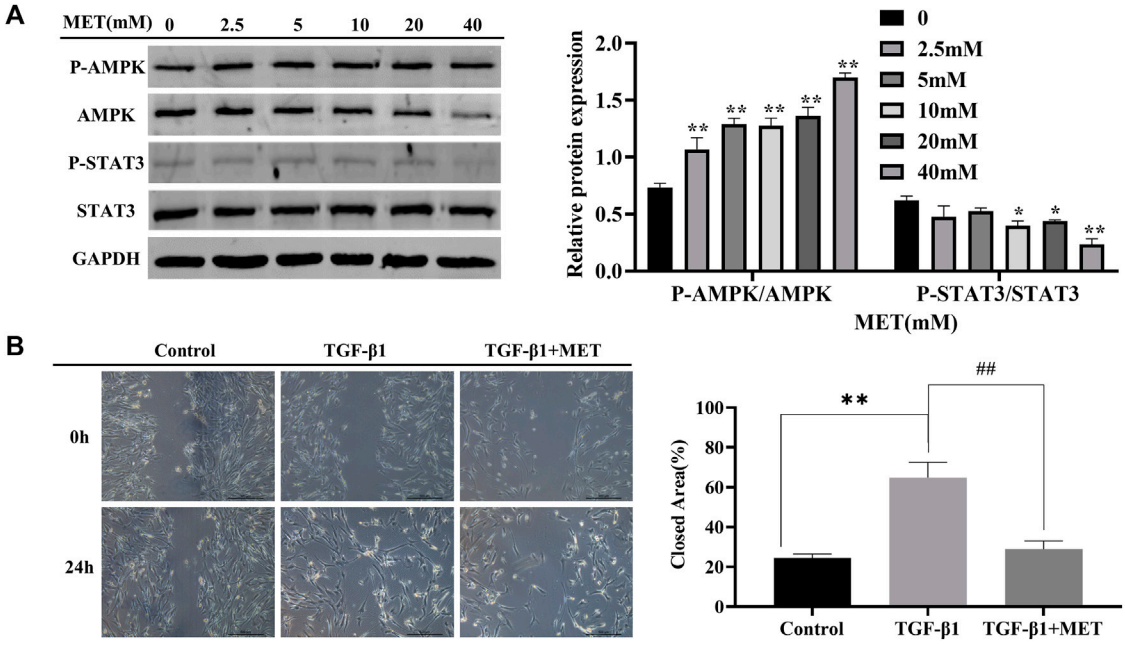

FIGURE 5
MET suppressed TGF-β1-induced fibroblasts activation. **(A)** HFL1 cells were treated with MET (0 mM–40 mM) for 24 h. Western blot was performed to measure the expression level of p-AMPK, AMPK, STAT3 and p-STAT3. **(B)** HFL1 cells were pretreated with MET (10 mM) for 24 h and then incubated with TGF-β1 (10 ng/mL) for 24 h. The migration abilities of fibroblasts were detected by scratch assay at 0 h and 24 h after treatment with TGF-β1, respectively. Scale bars represent 500 μm. The closed area (%) of the scratch was calculated by equation: [(cell gap area at 0 h - cell gap after 24 h)/cell gap area at 0 h] ×100%. **(C)** The expression of p-STAT3 and α-SMA were measured by immunofluorescence after 24 h treatment with TGF-β1. Scale bars represent 100 μm. Data were shown as mean ± SD (n = 3), *p < 0.05, **p < 0.01, compared with Control group; ##p < 0.01, compared with TGF-β1 group.

STAT3 phosphorylation (Figures 2A, B). It has been reported that MET inhibits phosphorylation of STAT3 by activating AMPK(Lee et al., 2017; Ge, Wang, Miao and Yan, 2018; Bharadwaj, Kasembeli, Robinson and Tweardy, 2020). However, whether S100A4 expression in fibroblasts is regulated by phosphorylation of STAT3 is still unknown. As shown in Figure 4A, static inhibited STAT3 phosphorylation effectively and downregulated TGF-β1 induced the expression of S100A4 and fibroblasts activation (using α-SMA as a hallmark) in HFL1 cells (Figures 4B, C). All of these results indicated that inhibition of STAT3 activation alleviates fibroblast activation by regulating S100A4.

3.4 MET suppressed fibroblasts activation by targeting S100A4 *via* AMPK-STAT3 axis

Next, we wonder if MET-mediated downregulation of S100A4 expression is dependent on AMPK-STAT3 pathway. Firstly, AMPK activation and significant decrease of phosphorylated STAT3 in a dose dependent manner were observed after MET administration in HFL1 cells (Figure 5A). Furthermore, we found that increased migration abilities of fibroblasts induced by TGF-β1 stimulation were reversed by MET pretreatment (Figure 5B). Immunofluorescence data also further confirmed that MET pretreatment down-regulated α-SMA and STAT3 phosphorylation induced by TGF-β1 (Supplementary Figure S1). These data implied that MET exerts obvious inhibitory effects on fibroblasts activation by possibly regulating STAT3 phosphorylation.

In TGF-β1-induced fibroblasts activation system *in vitro*, the expression level of α-SMA, phosphorylated STAT3 and S100A4 in HFL1 cells increased. However, pretreatment with MET upregulated the protein level of activated AMPK, but significantly downregulated α-SMA, phosphorylated STAT3 and S100A4 (Figure 6A). Meanwhile, pretreatment of MET weakened the immunofluorescence activity of S100A4 induced by TGF-β1 (Figure 6B). Together all these data, we conclude that MET exerts inhibitory effect on fibroblast activation by targeting S100A4 *via* AMPK-STAT3 axis.

4 Discussion

IPF is a progressive interstitial lung disease characterized by fibroblasts activation and excessive ECM deposition. At present, only Nintedanib and Pirfenidone have been approved for treating IPF in Europe and the United States. However, serious adverse drug reaction limits their clinical applications (Richeldi et al., 2014; Cottin and Maher, 2015). It is necessary to explore the pathogenesis of IPF and develop novel therapeutic strategies. An important finding of this study is that fibroblasts activation can be inhibited by targeting S100A4 through downregulating STAT3 phosphorylation (Figures 4B, C), providing us a novel potential therapeutic strategies of IPF.

S100A4 was first known as specific marker of fibroblasts, and a great deal of evidence emphasizes the role of S100A4 in tissue fibrosis (Schneider et al., 2008; Louka and Ramzy, 2016; Qian

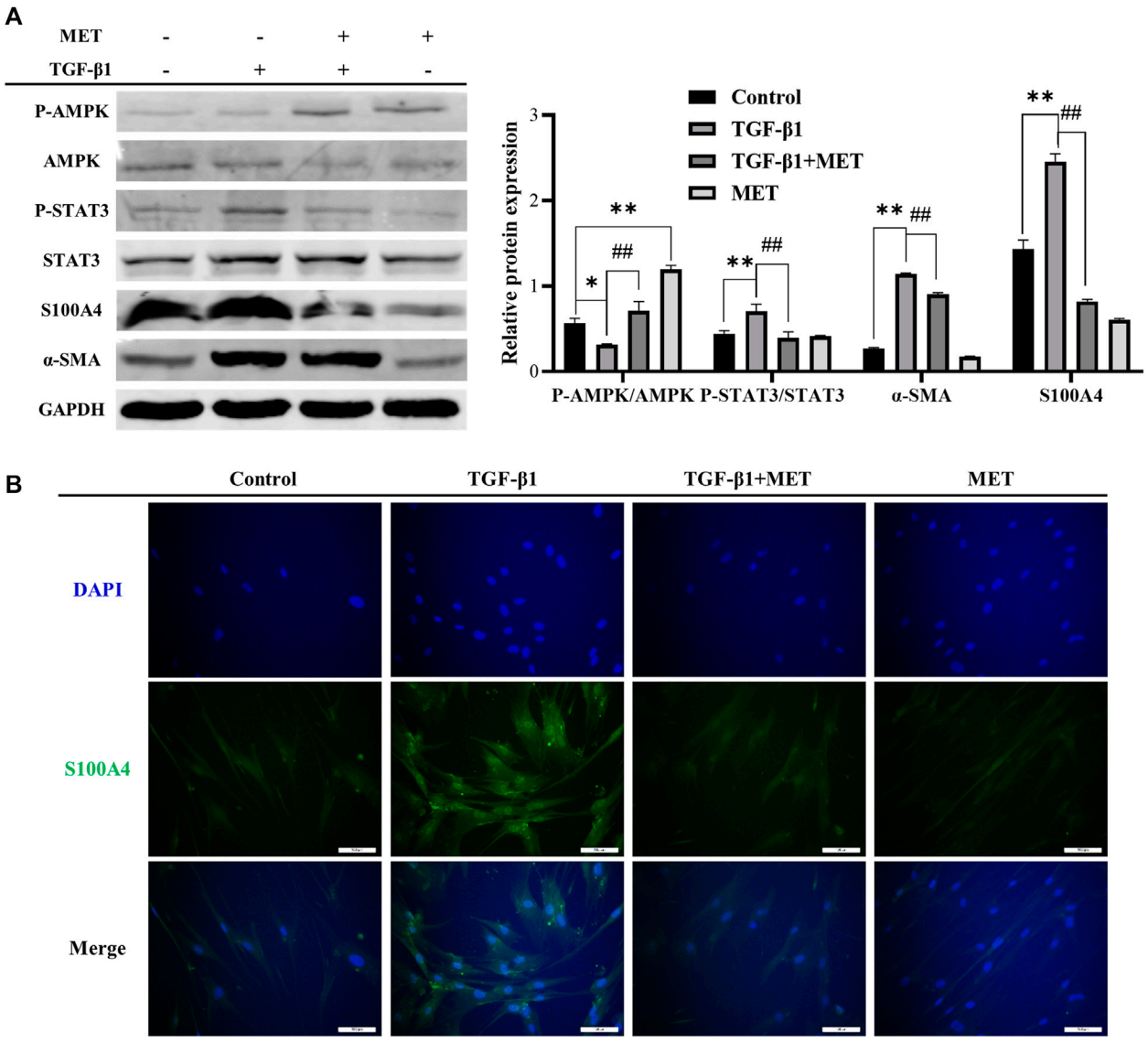

FIGURE 6
MET inhibited S100A4 *via* AMPK-STAT3 axis during fibroblasts activation *in vitro*. MET treatment was started 24 h before TGF-β1 stimulation. The expressions of protein were measured by western blot **(A)** and Immunofluorescence analysis **(B)**. Scale bars represent 100 μm. Data were shown as mean ± SD (n = 3), $^{*}p < 0.05$, $^{**}p < 0.01$, compared with Control group; $^{\#\#}$<0.01, compared with TGF-β1 group.

et al., 2018). In fibrotic cardiac tissue, S100A4 is mainly expressed by hematopoietic cells and endothelial cells (Kong, Christia, Saxena, Su and Frangogiannis, 2013), while S100A4 secreted by subpopulation of macrophage activates hepatic stellate cells during liver fibrosis (Osterreicher et al., 2011; Chen et al., 2015). In PF, subpopulations of macrophages and fibroblasts are the major sources of S100A4 (Lawson et al., 2005; Li et al., 2018). Endonuclear S100A4 confers mesenchymal progenitor cell fibrogenicity through promoting p53 degradation in the progression of IPF (Xia et al., 2017). Previous studies mainly focus on extracellular S100A4 derived from macrophage promotes fibroblasts activation during PF (Li et al., 2018; Zhang et al., 2018; Li et al., 2020), while the regulatory effect of intracellular S100A4 on fibroblasts activation is still unclear. In the present study, we found S100A4 increased in lung tissues of BLM-induced PF mice and TGF-β1-treated HEF1 cells (Figures 2A, B), blocking S100A4 expression by siRNA exhibited anti-fibrosis effects (Figures 3A, B) or inhibiting STAT3 phosphorylation with a small molecule inhibitor static (Figures 4B, C), as well as MET (Figures 5, 6).

Therapeutic strategies by targeting S100A4 go beyond the field of lung fibrosis. Like in PF, S100A4, as a downstream mediator of the stimulatory effects of TGF-β1, amplifies TGF-β1-induced fibroblasts activation in systemic sclerosis (Tomcik et al., 2015). Silencing S100A4 with siRNA or blocking S100A4 with niclosamide inhibited fibroblasts activation in amyotrophic lateral sclerosis (Milani et al., 2021). S100A4 released from highly bone-metastatic breast cancer cells plays a critical role in osteolysis (Kim et al., 2019). Targeting S100A4 by employing chemotherapeutic drugs such as MET, antibodies, or small-molecule inhibitors might provide a new potential therapy for systemic sclerosi, amyotrophic lateral sclerosis and cancers.

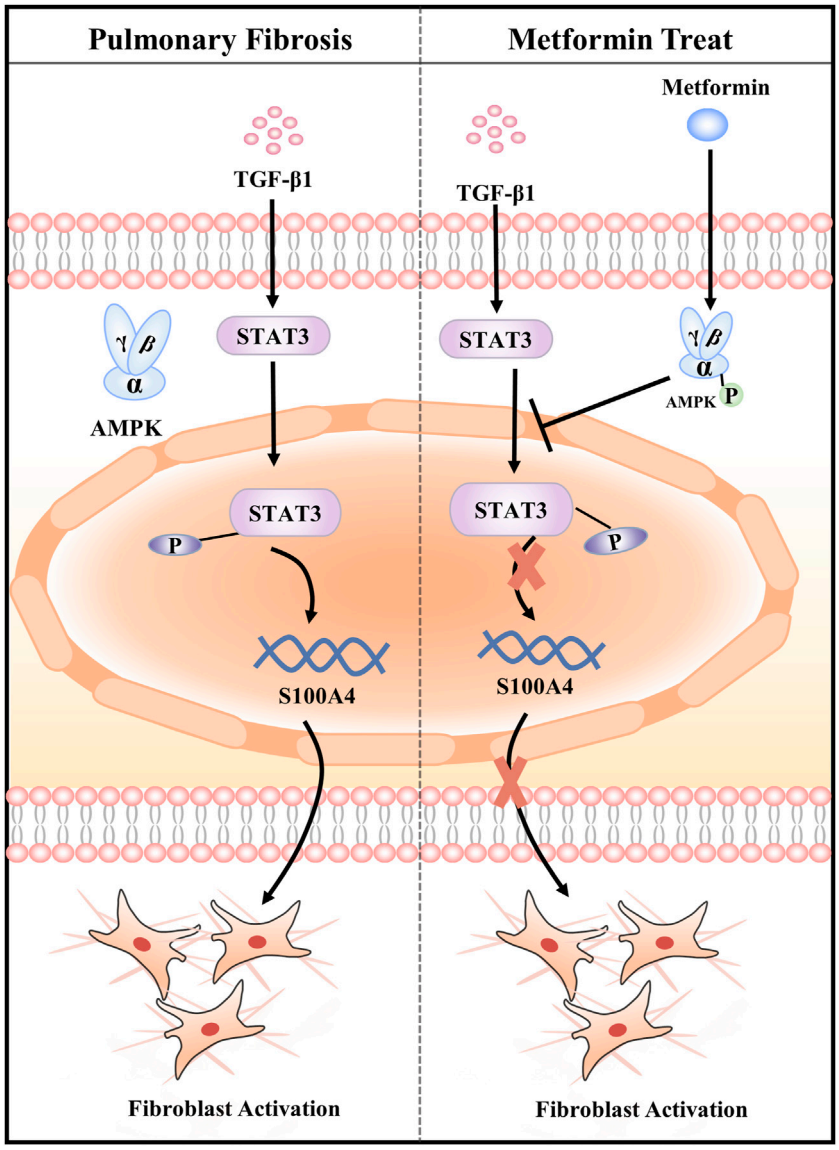

FIGURE 7
Graphical abstract of the mechanisms. Metformin attenuates Fibroblast Activation during Pulmonary Fibrosis by Targeting S100A4 *via* AMPK-STAT3 axis.

As a member of STATs family, STAT3 is activated by multiple cytokines including interleukin-6 and TGF-β1 (Chakraborty et al., 2017). The level of STAT3 phosphorylation is elevated in the fibrotic lungs of patients with IPF and BLM-induced PF mice. On the other hand, STAT3 contributes to activating fibroblasts to transform into myofibroblasts, finally leading to abnormal accumulation of ECM (Pedroza et al., 2016). Previous studies show the role of STAT3 in tissue fibrosis, which activation of STAT3 contributes to PF and TGF-β1-induced fibroblast activation (Knight et al., 2011; Zehender et al., 2018). Stattic is a small non-peptide molecule that selectively targets the function of the tyrosinylation site (Tyr705) and the SH2 domain of STAT3, thereby inhibiting STAT3 phosphorylation and dimerization of activated STAT3 and nuclear transport (Schust, Sperl, Hollis, Mayer and Berg, 2006). Here, we reported that Stattic inhibited STAT3 activation and attenuated the fibroblasts activation by inhibiting S100A4 expression. Interestingly, macrophage-derived S100A4 activates STAT3 in hepatocytes followed by the upregulation of inflammatory factor gene expression, leading to inflammation, but suppresses lipid accumulation during chronic ethanol-induced fatty liver (Yuan et al., 2019). In PF, further study deserves to be carried out for investigating whether extracellular S100A4 activates STAT3 in fibroblasts, leading to fibroblasts activation.

Although many studies showed that the first-line antidiabetic drug, MET, is a potential therapeutic drug for PF (Rangarajan et al., 2018; Kheirollahi et al., 2019; Cheng et al., 2021), the underlying mechanisms needs to be further clarified. In this manuscript, we demonstrate that MET alleviated deposition of collagen, distorted alveolar structure in BLM-induced mice PF *in vivo*, and inhibited lung fibroblasts activation *in vitro* by targeting S100A4 *via* AMPK-ATAT3 axis. In addition, there were no abnormal

findings in the vital signs and physical examination of the mice, suggesting to some extent that MET did not cause obvious adverse drug reaction in this study. Our findings provide novel important explanation for MET mediated a variety of favorable biological and therapeutic activities such as anti-fibrosis, anti-tumor, and anti-inflammation.

5 Conclusion

In summary, our data demonstrates that MET protects against BLM-induced PF of mice *in vivo* and attenuates TGF-β1-induced fibroblasts activation *in vitro* by targeting S100A4 *via* AMPK-STAT3 axis (Figure 7). Our study might provide a new potential therapy for S100A4-involved diseases including PF.

Data availability statement

The original contributions presented in the study are included in the article/Supplementary Material, further inquiries can be directed to the corresponding authors.

Ethics statement

The animal study was reviewed and approved by Research Ethics Committee of Dalian medical University.

Author contributions

HJ, HD, and JG conceived and designed the study. HJ performed the experiments, analyzed data, and wrote the manuscript. YL, YB, YH, XG, and CY friendly helped the animal experiment. MC and JG modified the manuscript.

Funding

This study was supported by the National Natural Science Foundation of China (No. 81274172, 81473267, and 81973637) and the National Traditional Chinese Medicine Inheritance and Innovation "Hundreds and Thousands" Talent Project: Young Qihuang Scholar Support Project of the State Administration of Traditional Chinese Medicine in 2020.

Conflict of interest

The authors declare that the research was conducted in the absence of any commercial or financial relationships that could be construed as a potential conflict of interest.

Publisher's note

All claims expressed in this article are solely those of the authors and do not necessarily represent those of their affiliated organizations, or those of the publisher, the editors and the reviewers. Any product that may be evaluated in this article, or claim that may be made by its manufacturer, is not guaranteed or endorsed by the publisher.

Supplementary material

The Supplementary Material for this article can be found online at: https://www.frontiersin.org/articles/10.3389/fphar.2023.1089812/full#supplementary-material

SUPPLEMENTARY FIGURE 1
HFL1 cells were pretreated with MET (10 mM) for 24 h and then incubated with TGF-β1 (10 ng/ml) for 24 h. The expression of P-STAT3 and α-SMA were measured by immunofluorescence after 24 h treatment with TGF-β1. Scale bars represent 100 μm.

References

Austermann, J., Spiekermann, C., and Roth, J. (2018). S100 proteins in rheumatic diseases. *Nat. Rev. Rheumatol.* 14, 528–541. doi:10.1038/s41584-018-0058-9

Bharadwaj, U., Kasembeli, M. M., Robinson, P., and Tweardy, D. J. (2020). Targeting janus kinases and signal transducer and activator of transcription 3 to treat inflammation, fibrosis, and cancer: Rationale, progress, and caution. *Pharmacol. Rev.* 72, 486–526. doi:10.1124/pr.119.018440

Bresnick, A. R., Weber, D. J., and Zimmer, D. B. (2015). S100 proteins in cancer. *Nat. Rev. Cancer* 15, 96–109. doi:10.1038/nrc3893

Chakraborty, D., Sumova, B., Mallano, T., Chen, C. W., Distler, A., Bergmann, C., et al. (2017). Activation of STAT3 integrates common profibrotic pathways to promote fibroblast activation and tissue fibrosis. *Nat. Commun.* 8, 1130. doi:10.1038/s41467-017-01236-6

Chen, L., Li, J., Zhang, J., Dai, C., Liu, X., Wang, J., et al. (2015). S100A4 promotes liver fibrosis via activation of hepatic stellate cells. *J. Hepatol.* 62, 156–164. doi:10.1016/j.jhep.2014.07.035

Cheng, D., Xu, Q., Wang, Y., Li, G., Sun, W., Ma, D., et al. (2021). Metformin attenuates silica-induced pulmonary fibrosis via AMPK signaling. *J. Transl. Med.* 19, 349. doi:10.1186/s12967-021-03036-5

Cottin, V., and Maher, T. (2015). Long-term clinical and real-world experience with pirfenidone in the treatment of idiopathic pulmonary fibrosis. *Eur. Respir. Rev.* 24, 58–64. doi:10.1183/09059180.00011514

Fei, F., Qu, J., Li, C., Wang, X., Li, Y., and Zhang, S. (2017). Role of metastasis-induced protein S100A4 in human non-tumor pathophysiologies. *Cell Biosci.* 7, 64. doi:10.1186/s13578-017-0191-1

Ge, A., Wang, S., Miao, B., and Yan, M. (2018). Effects of metformin on the expression of AMPK and STAT3 in the spinal dorsal horn of rats with neuropathic pain. *Mol. Med. Rep.* 17, 5229–5237. doi:10.3892/mmr.2018.8541

Gu, X., Han, Y. Y., Yang, C. Y., Ji, H. M., Lan, Y. J., Bi, Y. Q., et al. (2021). Activated AMPK by metformin protects against fibroblast proliferation during pulmonary fibrosis by suppressing FOXM1. *Pharmacol. Res.* 173, 105844. doi:10.1016/j.phrs.2021.105844

John, A. E., Joseph, C., Jenkins, G., and Tatler, A. L. (2021). COVID-19 and pulmonary fibrosis: A potential role for lung epithelial cells and fibroblasts. *Immunol. Rev.* 302, 228–240. doi:10.1111/imr.12977

Kasam, R. K., Ghandikota, S., Soundararajan, D., Reddy, G. B., Huang, S. K., Jegga, A. G., et al. (2020). Inhibition of Aurora Kinase B attenuates fibroblast activation and pulmonary fibrosis. *EMBO Mol. Med.* 12, e12131. doi:10.15252/emmm.202012131

Kheirollahi, V., Wasnick, R. M., Biasin, V., Vazquez-Armendariz, A. I., Chu, X., Moiseenko, A., et al. (2019). Metformin induces lipogenic differentiation in myofibroblasts to reverse lung fibrosis. *Nat. Commun.* 10, 2987. doi:10.1038/s41467-019-10839-0

Kim, H., Kim, B., Il Kim, S., Kim, H. J., Ryu, B. Y., Chung, J., et al. (2019). S100A4 released from highly bone-metastatic breast cancer cells plays a critical role in osteolysis. *Bone Res.* 7, 30. doi:10.1038/s41413-019-0068-5

Knight, D., Mutsaers, S. E., and Prele, C. M. (2011). STAT3 in tissue fibrosis: Is there a role in the lung? *Pulm. Pharmacol. Ther.* 24, 193–198. doi:10.1016/j.pupt.2010.10.005

Kong, P., Christia, P., Saxena, A., Su, Y., and Frangogiannis, N. G. (2013). Lack of specificity of fibroblast-specific protein 1 in cardiac remodeling and fibrosis. *Am. J. Physiol. Heart Circ. Physiol.* 305, H1363–H1372. doi:10.1152/ajpheart.00395.2013

Kuhn, C., and McDonald, J. A. (1991). The roles of the myofibroblast in idiopathic pulmonary fibrosis. Ultrastructural and immunohistochemical features of sites of active extracellular matrix synthesis. *Am. J. Pathol.* 138, 1257–1265.

Lawson, W. E., Polosukhin, V. V., Zoia, O., Stathopoulos, G. T., Han, W., Plieth, D., et al. (2005). Characterization of fibroblast-specific protein 1 in pulmonary fibrosis. *Am. J. Respir. Crit. Care Med.* 171, 899–907. doi:10.1164/rccm.200311-1535OC

Lee, J. U., Chang, H. S., Shim, E. Y., Park, J. S., Koh, E. S., Shin, H. K., et al. (2020). The S100 calcium-binding protein A4 level is elevated in the lungs of patients with idiopathic pulmonary fibrosis. *Respir. Med.* 171, 105945. doi:10.1016/j.rmed.2020.105945

Lee, S. Y., Moon, S. J., Kim, E. K., Seo, H. B., Yang, E. J., Son, H. J., et al. (2017). Metformin suppresses systemic autoimmunity in roquin(san/san) mice through inhibiting B cell differentiation into plasma cells via regulation of AMPK/mTOR/STAT3. *J. Immunol.* 198, 2661–2670. doi:10.4049/jimmunol.1403088

Li, Y., Bao, J., Bian, Y., Erben, U., Wang, P., Song, K., et al. (2018). S100A4(+) macrophages are necessary for pulmonary fibrosis by activating lung fibroblasts. *Front. Immunol.* 9, 1776. doi:10.3389/fimmu.2018.01776

Li, Z., Li, Y., Liu, S., and Qin, Z. (2020). Extracellular S100A4 as a key player in fibrotic diseases. *J. Cell Mol. Med.* 24, 5973–5983. doi:10.1111/jcmm.15259

Louka, M. L., and Ramzy, M. M. (2016). Involvement of fibroblast-specific protein 1 (S100A4) and matrix metalloproteinase-13 (MMP-13) in CCl4-induced reversible liver fibrosis. *Gene* 579, 29–33. doi:10.1016/j.gene.2015.12.042

Milani, M., Mammarella, E., Rossi, S., Miele, C., Lattante, S., Sabatelli, M., et al. (2021). Targeting S100A4 with niclosamide attenuates inflammatory and profibrotic pathways in models of amyotrophic lateral sclerosis. *J. Neuroinflammation* 18, 132. doi:10.1186/s12974-021-02184-1

Osterreicher, C. H., Penz-Osterreicher, M., Grivennikov, S. I., Guma, M., Koltsova, E. K., Datz, C., et al. (2011). Fibroblast-specific protein 1 identifies an inflammatory subpopulation of macrophages in the liver. *Proc. Natl. Acad. Sci. U. S. A.* 108, 308–313. doi:10.1073/pnas.1017547108

Pedroza, M., Le, T. T., Lewis, K., Karmouty-Quintana, H., To, S., George, A. T., et al. (2016). STAT-3 contributes to pulmonary fibrosis through epithelial injury and fibroblast-myofibroblast differentiation. *FASEB J.* 30, 129–140. doi:10.1096/fj.15-273953

Qian, L., Hong, J., Zhang, Y., Zhu, M., Wang, X., Zhang, Y., et al. (2018). Downregulation of S100A4 alleviates cardiac fibrosis via wnt/β -catenin pathway in mice. *Cell Physiol. Biochem.* 46, 2551–2560. doi:10.1159/000489683

Raghu, G., Remy-Jardin, M., Myers, J. L., Richeldi, L., Ryerson, C. J., Lederer, D. J., et al. (2018). Diagnosis of idiopathic pulmonary fibrosis. An official ATS/ERS/JRS/ALAT clinical practice guideline. *Am. J. Respir. Crit. Care Med.* 198, e44–e68. doi:10.1164/rccm.201807-1255ST

Rangarajan, S., Bone, N. B., Zmijewska, A. A., Jiang, S., Park, D. W., Bernard, K., et al. (2018). Metformin reverses established lung fibrosis in a bleomycin model. *Nat. Med.* 24, 1121–1127. doi:10.1038/s41591-018-0087-6

Richeldi, L., Collard, H. R., and Jones, M. G. (2017). Idiopathic pulmonary fibrosis. *Lancet* 389, 1941–1952. doi:10.1016/S0140-6736(17)30866-8

Richeldi, L., du Bois, R. M., Raghu, G., Azuma, A., Brown, K. K., Costabel, U., et al. (2014). Efficacy and safety of nintedanib in idiopathic pulmonary fibrosis. *N. Engl. J. Med.* 370, 2071–2082. doi:10.1056/NEJMoa1402584

Sato, N., Takasaka, N., Yoshida, M., Tsubouchi, K., Minagawa, S., Araya, J., et al. (2016). Metformin attenuates lung fibrosis development via NOX4 suppression. *Respir. Res.* 17, 107. doi:10.1186/s12931-016-0420-x

Schneider, M., Hansen, J. L., and Sheikh, S. P. (2008). S100A4: A common mediator of epithelial-mesenchymal transition, fibrosis and regeneration in diseases? *J. Mol. Med. Berl.* 86, 507–522. doi:10.1007/s00109-007-0301-3

Schust, J., Sperl, B., Hollis, A., Mayer, T. U., and Berg, T. (2006). Stattic: A small-molecule inhibitor of STAT3 activation and dimerization. *Chem. Biol.* 13, 1235–1242. doi:10.1016/j.chembiol.2006.09.018

Somogyi, V., Chaudhuri, N., Torrisi, S. E., Kahn, N., Muller, V., and Kreuter, M. (2019). The therapy of idiopathic pulmonary fibrosis: What is next? *Eur. Respir. Rev.* 28, 190021. doi:10.1183/16000617.0021-2019

Sontake, V., Wang, Y., Kasam, R. K., Sinner, D., Reddy, G. B., Naren, A. P., et al. (2017). Hsp90 regulation of fibroblast activation in pulmonary fibrosis. *JCI Insight* 2, e91454. doi:10.1172/jci.insight.91454

Tomcik, M., Palumbo-Zerr, K., Zerr, P., Avouac, J., Dees, C., Sumova, B., et al. (2015). S100A4 amplifies TGF-beta-induced fibroblast activation in systemic sclerosis. *Ann. Rheum. Dis.* 74, 1748–1755. doi:10.1136/annrheumdis-2013-204516

Wijsenbeek, M., and Cottin, V. (2020). Spectrum of fibrotic lung diseases. *N. Engl. J. Med.* 383, 958–968. doi:10.1056/NEJMra2005230

Wynn, T. A., and Ramalingam, T. R. (2012). Mechanisms of fibrosis: Therapeutic translation for fibrotic disease. *Nat. Med.* 18, 1028–1040. doi:10.1038/nm.2807

Xia, H., Gilbertsen, A., Herrera, J., Racila, E., Smith, K., Peterson, M., et al. (2017). Calcium-binding protein S100A4 confers mesenchymal progenitor cell fibrogenicity in idiopathic pulmonary fibrosis. *J. Clin. Invest.* 127, 2586–2597. doi:10.1172/JCI90832

Yang, D. C., Li, J. M., Xu, J., Oldham, J., Phan, S. H., Last, J. A., et al. (2019). Tackling MARCKS-PIP3 circuit attenuates fibroblast activation and fibrosis progression. *FASEB J.* 33, 14354–14369. doi:10.1096/fj.201901705R

Yuan, Q., Hou, S., Zhai, J., Tian, T., Wu, Y., Wu, Z., et al. (2019). S100A4 promotes inflammation but suppresses lipid accumulation via the STAT3 pathway in chronic ethanol-induced fatty liver. *J. Mol. Med. Berl.* 97, 1399–1412. doi:10.1007/s00109-019-01808-7

Zehender, A., Huang, J., Gyorfi, A. H., Matei, A. E., Trinh-Minh, T., Xu, X., et al. (2018). The tyrosine phosphatase SHP2 controls TGFβ-induced STAT3 signaling to regulate fibroblast activation and fibrosis. *Nat. Commun.* 9, 3259. doi:10.1038/s41467-018-05768-3

Zhang, W., Ohno, S., Steer, B., Klee, S., Staab-Weijnitz, C. A., Wagner, D., et al. (2018). S100a4 is secreted by alternatively activated alveolar macrophages and promotes activation of lung fibroblasts in pulmonary fibrosis. *Front. Immunol.* 9, 1216. doi:10.3389/fimmu.2018.01216

Zhang, Y., Lu, W., Zhang, X., Lu, J., Xu, S., Chen, S., et al. (2019). Cryptotanshinone protects against pulmonary fibrosis through inhibiting Smad and STAT3 signaling pathways. *Pharmacol. Res.* 147, 104307. doi:10.1016/j.phrs.2019.104307

Frontiers in Pharmacology

Explores the interactions between chemicals and living beings

The most cited journal in its field, which advances access to pharmacological discoveries to prevent and treat human disease.

Discover the latest Research Topics

See more →

Frontiers

Avenue du Tribunal-Fédéral 34
1005 Lausanne, Switzerland
frontiersin.org

Contact us

+41 (0)21 510 17 00
frontiersin.org/about/contact